GEOLOGY, GEOCHRONOLOGY AND ALTERATION OF THE LORRAINE ALKALIC PORPHYRY CU-AU DEPOSIT, BRITISH COLUMBIA, CANADA

by

Adam Brian Bath

B.Sc Hons (University of Tasmania)

Submitted in fulfilment of the requirements for the degree of Doctor of Philosophy

University of Tasmania

Australia

November, 2010

Declaration of Originality

This thesis contains no material which has been accepted for the award of any other degree or diploma by the University or any other institution, except by way of background information and duly acknowledged in the thesis, and to the best of my knowledge and belief no material previously published or written by another person except where due acknowledgement is made in the text of the thesis, nor does the thesis contain any material that infringes copyright.

Date: 01/ 11 /2010

Signature: 

Authority of Access

This thesis is not to be made available for loan or copy for twelve months following the date this statement was signed. Following that time, the thesis may be made available for loan and limited copying in accordance with the Copyright Act 1968.

01/11/2010

Statement of Ethical Conduct

The research associated with this thesis abides by the international and Australian codes on human and animal experimentation, the guidelines by the Australian Government' Office of the Gene Technology Regulator and the rulings of the Safety, Ethics and Institutional Biosafety Committees of the University.

Abstract

The present study assesses ore-forming processes and the timing of mineralisation in the Lower Main Zone of the Lorraine porphyry Cu deposit, north-central British Columbia. The deposit is hosted in an intrusion complex that comprises pre-mineral and post-mineral shoshonitic ultrabasic to syenite rock types. New U-Pb zircon ages of pre- and post-mineralisation dykes constrain the timing of mineralisation between 178.8 and 178.4 Ma. Intrusions in the Lower Main Zone have undergone several stages of alteration, which include early-, transitional- and late-stage assemblages. Early stage alteration includes; (1) pervasive biotite and K-feldspar alteration of wall rocks; (2) veins and patches of magnetite-diopside ± albite and (3) early coarse-grained K-feldspar-biotite veins that are locally associated with bornite and chalcopyrite. Transitional-stage mineralisation has produced distinctive sulphide zonation patterns consisting of a bornite-chalcocite core grading outwards to domains of bornite-chalcopyrite, chalcopyrite, chalcopyrite>pyrite, and a peripheral domain of pyrite with minor chalcopyrite. The sulphide zonation pattern is tilted and has overprinted numerous rock-types and the early-formed alteration assemblages. Syenite in the inner bornite-chalcopyrite zone typically contains abundant turbid K-feldspar (i.e. >70 %), whereas syenite marginal to the bornite-chalcopyrite core contains 50-70 % K-feldspar, indicating an increase in K-metasomatism of syenites towards the core of the deposit.

Transitional-stage mineralisation at Lorraine predominantly occurs as fine-grained disseminated sulphides in syenite, biotite pyroxenite and fine-grained K-feldspar biotite rock. Rare net-textured chalcopyrite and bornite mineralisation has also been identified in some biotite pyroxenites. Earlier workers speculated that biotite pyroxenites with net-textured sulphides at Lorraine may represent a 'deep' magmatic component of the porphyry system. However textural analysis of mineralised biotite pyroxenite appears to be at odds with this concept. In particular the current study has shown that: (1) primary diopside, which form contacts with sulphides, have corroded and actinolite-altered margins, suggesting alteration of primary minerals; (2) primary diopside and biotite do not contain primary sulphide in-

clusions and therefore there appears to be no evidence of a primary magmatic sulphide melt; (3) irregular-shaped relicts of biotite and diopside occur in sulphides, suggesting sulphides have replaced primary minerals and (4) deposit-scale sulphide zonation patterns overprints numerous lithology types, including biotite pyroxenites with net-textured sulphides. These findings support the author's contention that primary magmatic biotite and diopside were replaced or partially replaced by sulphide minerals, and are consistent with an influx of Cu and S during transitional-stage alteration and subsequent replacement of primary magmatic minerals (e.g., biotite) as opposed to the precipitation of primary magmatic sulphides from a Cu-rich ultrabasic magma source.

Analysis of oxygen and hydrogen isotopes from F-rich biotite in early altered fine-grained K-feldspar biotite rock and fine-grained biotite in altered syenite has revealed the composition of fluids in equilibrium with early alteration assemblages. Fluid compositions define a range between +6.1 ‰ and +7.6 ‰ for $\delta^{18}O$, and -53 ‰ and -47 ‰ for δD. These values are consistent with the range for magmatic-derived aqueous fluids or metamorphic fluids. A magmatic fluid source is consistent with the close timing of alteration and mineralisation and the emplacement of syenite intrusions, and biotite geothermometry indicates that early alteration occurred at approximately 550 °C.

The current study also investigated the chemical composition of unaltered shoshonitic rocks from Lorraine. The study concluded that biotite pyroxenite and syenite from Lorraine have major and trace element compositions that plot along a single trend, which is similar to fractionation trends for arc-related Fijian shoshonite lavas or shoshonitic glasses from the Nicola Group lavas (British Columbia). It is inferred that geochemical trends for Lorraine rocks reflect fractionation trends, and it is also inferred that syenite dykes were sourced from magma chambers at depth, or from fractionating melt in mature crystal mush columns. Ultrabasic rocks at Lorraine (i.e. biotite pyroxenite; ~42 to 48 wt. % SiO_2) include: (1) depletion in high field strength elements in comparison with rare earth elements; (2) enrichment in large ion lithophile elements and P in comparison with rare earth elements; (3) $^{87}Sr/^{86}Sr$ (avg. = 0.7036), εNd (avg. = + 4.7) and stable isotope $\delta^{18}O$ (diopside

= 5.89) compositions that are similar to post-collisional shoshonites from the Mariana arc and Fiji and (4) an abundance of P (avg. ~0.87 wt. % P_2O_5) and Sr (avg. ~1200 ppm), which is higher or similar in abundance to Fijian shoshonites respectively. Some workers have related the high P and Sr in western Pacific shoshonites to the melting of slab-derived carbonate- and phosphorous-rich sediments in the mantle, which could also explain the enrichment of these elements in Lorraine shoshonites.

Acknowledgements

First and foremost, I would like to thank my wife Ena, for her endless and unconditional support and encouragement over the years. You have made our home a wonderful place to live and work, and for that I am very grateful. Doumo arigatou gozaimasu!!

This study has benefited from collaboration with organisations outside of the University of Tasmania. An enormous thanks goes out to the major sponsors of the alkalic project including Amarc Resources Ltd., Anglogold-Ashanti, Barrick Gold Corp., Imperial Metals Corp., Lysander Minerals Corp., Newcrest Mining Corp., Teck Ltd., Nova Gold Resources Inc., NSERC Collaborative Research and Development program and Geoscience BC for financial and logistical support throughout the duration of this project. Financial and logistical support was also provided by the British Columbia Ministry for Energy, Mines and Petroleum Resources for which I am very grateful. Generous scholarships were also provided by CODES, Geoscience BC and the Society of Economic Geologists, and I would like to thank them all for their support. I would like to send a sincere thanks to Teck Ltd. for providing me with accommodation, transportation and an endless amount of logistical support throughout my time in the field at Lorraine and in Vancouver. Teck Ltd. were an outstanding company to be involved with and a wonderful group of people to work with. This thesis simply would not exist without the support shown by them.

A special thanks goes to the people on-site at Lorraine (support crews and geologist alike) who made living in camp for several months an absolute pleasure. The exploration team of Paul Baxter, Fionnula Devine, Andrew Davies, Claire Chamberlain, Paul Jago and Amber Henry all provided stimulating and insightful discussions during my time in the field, and this project has benefitted enormously from all their input. Exceptional work on the district-scale geology by the above geologist has provided me with a foundation to work from. Without this foundation it would have been impossible to fully appreciate the geology of the Lower Main Zone and Lorraine area. Visits to Lorraine by Mitch Mihalynuk (British Columbia Geological Survey), Glenn Garratt (Eastfield Resources Ltd.), David Cooke and Dick Sillitoe also provided invaluable insights into the geology and alteration history at Lorraine.

I owe many thanks to my team of supervisors. In particular, I owe special thanks to Prof. David Cooke for his unrelenting support (both in and out of the field), encouragement and detailed reviews. Dave has provided stimulating and insightful discussions on the geology at Lorraine. Dave has also been a wealth of information on alkalic porphyries, and I have learnt a great deal from him over the past 4 years. Without Dave's involvement in this project, my life would have been far more difficult. I would also like to thank Prof. Dima Kamenetsky and Prof. Tony Crawford for providing support and encouragement throughout this project. Dima offered sound advice with petrography and geochemical studies,

and has offered constructive criticism throughout the course of this study. Since I first came to CODES, Dima has encouraged me to think more critically about scientific problems, and has taught me some of the finer points of analytical techniques. I thank Tony for sharing some of his extensive knowledge in petrology. Tony has freely shared some of his data, offered constructive criticism and reviewed a number of chapters in this thesis. Since I first arrived at CODES, Tony has provided me with unwavering support and sound scientific advice, for which I am very grateful.

Jim Logan, Mitch Mihalynuk, Ray Lett and Graham Nixon of the British Columbia Ministry for Energy, Mines and Petroleum Resources are all thanked for providing support at various stages during this project. It was Mitch and Jim who first encouraged me to come to Canada and work on the alkalic rocks in British Columbia. Jim got me involved in a mapping project in the summer of 2005, and it was during this period that I decided that I wanted to do a PhD on alkalic porphyries. Jim was a wonderful bloke to work with, and I've learnt a great deal from him over the years. I certainly have some great memories of our time together in the field! Mitch was the first person to introduce me to professional field mapping in British Columbia, and I certainly consider myself very lucky to have had the opportunity to work under Mitch. The few people that do get the opportunity to work with Mitch quickly realise that he is an amazing role model, and a person that truly leads by example. I would like to thank Graham for providing important samples, data and insights into the rocks at Lorraine. Graham's work on Lorraine in 2003, was a platform from which I could work from. I was particularly amazed at the quality and quantity of data that Graham has provided, based on only two weeks in the field! Graham was also a really great person to have a beer with and discuss ideas.

Ron Berry, Andrew McNeill, Paul Davidson, Mawson Croaker, Rod Maier, Heidi Pass, Mitch Mihalynuk and Jim Logan all reviewed chapters in this thesis, and during the course of this project they have all provided stimulating and insightful discussions, which have improved the content of this thesis. I am grateful to CODES and the School of Earth Sciences (staff and student alike), who have provided an environment that promotes the collaboration of ideas and learning. Enormous thanks goes to the support staff at CODES for expert advice in sample preparation, lapidary and geochemical analyses. A special thanks also goes to staff and students at Mineral Deposit Research Unit of the University of British Columbia, for the collaboration of data and ideas, and expert advice on geochronology. I also thank Roland Maas of Melbourne University and Kevin Faure from GNS for providing sound advice and high quality data for the isotope study.

Last but certainly not least, I would like to thank my wonderful parents, Brian and Heather. They have shown unwavering support throughout my life, and they have shown my sister and I that love is the cord that connects parent and child.

Table of Contents

List of Figures

List of Tables

List of Appendices

Appendices are provided electronically on accompanying CD.

List of Abbreviations

ab	albite
act	actinolite
A-F	alkali feldspar
ah	anhydrite
AK	Alaska
alu	alunite
amu	atomic mass unit
An	anorthite
ANA	ancestral North America
anh	anhedral
ank	ankerite
ap	apatite
apfu	atoms per formula unit
avg.	average
AZ	Arizona
BC	British Columbia
BCR-2	Basaltic glass standard
bio	biotite, phlogopite
BL	blueschist
bn	bornite
BS	bulk sediment
BSE	back-scatter electron
bx	breccia
C	centigrade
CA	California
ca.	circa
cal	calcite
car	carbonate
CaTs	tschermakitic component
CC	Cache Creek Terrane
cc	chalcocite
ce	celsian
cha	chalocedony
chl	chlorite
CIPW	Cross, Iddings, Pirsson and Washington normative calculation
Ck.	Creek
CL	cathodoluminescence
clz	clinozoisite
cm	centimetres
CO	Colorado
CODES	Centre of Excellence in Ore Deposits
conf.	confidence
cps	counts per second
cpx	clinopyroxene
cpy	chalcopyrite
CSL	Central Science Laboratory

D	deuterium
DB.1	Phase 1 Duckling Creek polymictic K-feldspar-magnetite-diopside-sulphide rock
DCz.2	Phase 2 Duckling Creek K-feldspar-phyric syenite with mafic groundmass
DE.?	Duckling Creek plagioclase porphyry monzonite (Phase unknown)
DF.0	Duckling Creek fine-grained K-feldspar biotite rock
di	diopside
dic	dickite
dist.	district
DK.3	Phase 3 Duckling Creek coarse-grained K-feldspar syenite
DL.3	Phase 3 Duckling Creek leucosyenite
DM.2	Phase 2 Duckling Creek monzonite
dol	dolomite
DP.1	Phase 1 Duckling Creek biotite pyroxenite
DP.2	Phase 2 Duckling Creek biotite pyroxenite and feldspathic pyroxenite
DPk.2	Phase 2 Duckling Creek K-feldspar phyric pyroxenite
DPp.2	Phase 2 Duckling Creek pseudoleucite feldspathic pyroxenite
DS.1	Phase 1 Duckling Creek syenite
DS.2	Phase 2 Duckling Creek syenite
DSk.2	Phase 2 Duckling Creek flow-foliated K-feldspar-phyric syenite
DSr.1	Phase 1 Duckling Creek rhythmically layered syenite
E	east
EC	eclogite
EDS	energy dispersive spectrometers
el	electrum
EMII	ocean island basalt mantle source
E-MORB	enriched mid ocean ridge basalt
en	enargite/ tennantite
ENE	east-northeast
ep	epidote
EPMA	electron probe microanalyser
euh	euhedral
fd	feldspar
Fig.	figure
fl	fluorite
flinc	fluid inclusion(s)
Fo	forsterite
g	grams
g/cm^3	grams per cubic centimetre
g/t	grams per metric ton
gn	garnet, grandite
hal	halite
hb	hornblende
HFSE	high field strength element(s)
hm	hematite
HREE	heavy rare earth element(s)
Hz	hertz
ICP-MS	inductively-coupled plasma mass spectrometer (or spectrometry)
ID	Idaho

ID-TIMS	isotope dilution ionisation mass spectrometer (or spectrometry)
il	ilmenite
ill	illite
IMA	Internation Mineral Association
Indo.	Indonesia
IP	induced polarisation
IUGS	International Union of Geological Sciences
Kazakh.	Kazakhstan
kbar	kilobar
keV	kilo electron volt
Kfd	K-feldspar, orthoclase
kg	kilogram
Km	kilometre(s)
KO	Kootnay terrane
L	litre
LA-ICP-MS	laser ablation inductively-coupled plasma mass spectrometer (or spectrometry)
LILE	large ion lithophile element(s)
LREE	light rare earth element(s)
Ltd.	Limited
lTr	Late Triassic
m	metre
µl	micro litre
µm	micrometre
M	molar
m.y.	million years
Ma	mega annum (millions of years before present)
mal	malachite
MDRU	Mineral Deposit Research Unit
mE	eastings
mg	magnesium
mg	milligram
ml	millilitre
MLA	mineral liberation analysis (software package)
mm	millimetre
mN	northings
mnt	montmorillonite
MORB	mid ocean ridge basalt
MREE	medium rare earth element(s)
MSWD	mean squared weighted deviations
mt	magnetite
MT	Montana
Mt.	Mount
mTr	Middle Triassic
mus	muscovite
N	north
nA	nano-ampere
NAD83	North American Datum 1983
NB	New Brunswick

ne	nepheline
NE	northeast
NIST612	International standard glass
nm	nanometre
NM	New Mexico
N-MORB	normal mid ocean ridge basalt
NS	Nisling terrane
NSW	New South Wales
NV	Nevada
OIB	ocean island basalt
ON	Ontario
opq	opaque
Or	orthoclase
P	Permian
PFA	perfluoroalkoxy
pg	pictogram
PGE	platinum group elements
Phil.	Philippines
pi	pitch-limonite
pl	plagioclase
plag	plagioclase
PNG	Papua New Guinea
ppb	parts per billion
pph	pyrophanite
ppi	pyrophyllite
ppm	parts per million
PTFE	polytetrafluoroethylene
py	pyrite
QN	Quesnel terrane
qz	quartz
REE	rare earth element(s)
rh	rhodochrosite
rt	rutile
S	south
SE	southeast
sec	seconds
SEM	scanning electron microscope
ser	sericite
SHRIMP-RG	sensitive high resolution ion microprobe – reverse geometry
SM	Slide Mountain
sph	sphalerite
srb	celestine
ST	Stikine terrane
stdev.	standard deviation
sub	subhedral
SUMAC	Stanford University and United States Geological Survey Microanlytical Centre
SW	southwest
ten	tennantite

ti	titanite, sphene
Tr	Triassic
tre	tremolite
TX	Texas
U.S.	United States
UBC	University of British Columbia
ur	uralite
UT	Utah
Utas	University of Tasmania
UTM	universal transverse Mercator
UV	ultraviolet
Uzbek	Uzbekistan
VS	volcaniclastic sediment
vs.	versus
VSMOW	Vienna standard mean ocean water
W	west
WA	Washington
Wo	wollastonite
WSW	west-southwest
wt	weight
wt. %	weight percent
X	mole fraction
XRF	x-ray fluorescence
YTT	Yukon Tanana terrane
ze	zeolite
zr	zircon

CHAPTER 1
INTRODUCTION

1.1. Introduction

Over the past four decades, an intensive and sustained research effort has constrained many of the characteristics of porphyry Cu systems globally. Over that period researchers have arrived at a range of viewpoints on ore-forming processes, magma sources, timing of mineralisation and sources of metals (e.g., Lowell and Guilbert, 1970; Beane, 1982; Titley, 1982; Seedorff, 1988; Cline and Bodnar, 1991; Vila and Sillitoe, 1991; Anthony and Titley, 1994; Cline and Bodnar, 1994; Lowenstern, 1994; Baker et al., 1997; Keith et al., 1997; Heinrich et al., 1999; Ulrich, 1999; Dilles et al., 2000; Sillitoe, 2000; Audetat et al., 2002; Landtwing et al., 2002; Arif and Baker, 2004; Redmond et al., 2004; Rusk et al., 2004; Candela and Piccoli, 2005; Cannell et al., 2005; Cooke et al., 2005; Heinrich, 2005; Seedorff et al., 2005; Holliday and Cooke, 2007; Rusk et al., 2008). In British Columbia, investigations of the Late Triassic to Early Jurassic alkalic porphyry Cu-Au deposits of the Quesnel and Stikine terranes have focused on the timing of mineralisation, intrusion paragenesis, brecciation events, and alteration and/or isotopic zonation patterns (e.g., Sutherland Brown and Cathro, 1976; Fraser, 1994; Lang et al., 1994; Schroeter, 1995; Lang et al., 1995a; Logan and Mihalynuk, 2005a, b; Logan, 2005; Micko, 2007; Byrne et al., 2008; Jackson et al., 2008; Jackson, 2008; Jago, 2008; Jago and Tosdal, 2008; Micko et al., 2008; Pass et al., 2008; Jago and Tosdal, in prep.; Micko et al., in prep.; Pass et al., in prep.). However, details of ore-forming processes, magma sources and the source(s) of ore-forming metals in these systems remain poorly understood.

The present study investigates the Lower Main Zone of the Lorraine porphyry Cu-Au deposit, which is hosted in the Quesnel terrane, north-central British Columbia. The Lorraine deposit has been classified as a silica-undersaturated alkalic porphyry Cu-Au deposit (e.g., Lang et al., 1995b), but has textural features unusual for porphyry deposits. In particular mineralisation is hosted by massive to foliated fine-grained K-feldspar-biotite-rich rocks, and by biotite pyroxenite and syenite. Copper-gold mineralisation predominantly occurs as fine-grained disseminations, and locally as Cu-bearing net-textured sulphides hosted in biotite pyroxenites rather than fracture or vein fillings more typical to porphyry deposits. Net-textured sulphides are typical of magmatic sulphide deposits, and this has led some workers (e.g., Bishop et al., 1995) to interpret them as evidence for Lorraine being a 'deep' crustal root zone of a porphyry deposit. Other workers have doubted this hypothesis based on their recognition of metasomatic alteration of the mineralised zones (e.g., Nixon and Peatfield, 2003).

More recently, Sillitoe (2007) demonstrated the presence of tilted porphyry-style sulphide zonation patterns at Lorraine. The sulphide mineralisation overprints numerous rock types, including biotite pyroxenite, with local net-textured sulphides and these rocks have been intruded by younger biotite pyroxenite and syenite dykes (Sillitoe, 2007). Hence, the Lorraine deposit has alteration and sulphide zonation patterns that formed in an active magmatic complex, consistent with modern concepts of porphyry formation. One of the aims of this study is to investigate the enigmatic relationships between disseminated epigenetic sulphides and their host rocks, which are atypical of most fracture/vein-hosted porphyry systems (e.g., Titley and Beane, 1981; Seedorff et al., 2005). In particular, the sulphides in biotite pyroxenite, syenite and fine-grained K-feldspar biotite rocks are investigated in order to constrain the relative timing of mineralisation and processes of disseminated ore deposition in the Lower Main Zone.

The occurrence of multiple, pre- and post-mineralisation biotite pyroxenites at Lorraine provide an opportunity to study ultrabasic rocks associated with porphyry-style mineralisation. Keith et al. (1998) noted that wet, oxidised mafic alkaline magmas generated in the mantle may be capable of transferring high concentrations of S, H_2O, Cl, and chalcophile metals to the base of an ore-related magma chamber if they rise rapidly through the crust, without stagnating and fractionating sulphide or sulphate minerals. Halter et al. (2005) suggested that the introduction of a wet (6 wt. % H_2O), Cu-rich (~200 ppm) mafic source into a rhyodacitic magma chamber was important for generating ore fluids at the Bajo de la Alumbrera porphyry deposit, Argentina. The occurrence of co-magmatic biotite pyroxenite at Lorraine provides an opportunity to investigate the role of alkaline ultrabasic magmas with respect to porphyry mineralisation. To test this, detailed petrographic studies are conducted here to determine if there is any evidence of magmatic sulphide globules in Lorraine rocks, which may have formed as a result of primary magmatic sulphide saturation in melts.

The petrological characteristics of the alkaline ultrabasic rocks at Lorraine have also been investigated in detail as part of this study. The major element, trace element and Sr, Nd, Pb, O and H isotopic composition of least altered biotite pyroxenites, syenites and monzonites from Lorraine were determined and are compared to assess their petrogenetic relationships. In addition, the geochemistry of biotite pyroxenites is compared with OIB, N-MORB and arc shoshonites from the western Pacific, Nicola Group shoshonites from the Quesnel terrane, and with diopside-hosted melt inclusions from the Nicola Group shoshonites. Through these comparisons, an attempt is made to constrain the possible source(s) of parental melts for ultrabasic rocks at Lorraine.

1.2. What is a porphyry deposit?

According to Seedorff et al. (2005), porphyry deposits are magmatic-hydrothermal deposits in which oxide and sulphide minerals are precipitated from aqueous solutions at elevated temperatures. Porphyry deposits are thought to form by orthomagmatic-hydrothermal processes related to the emplacement of intermediate to felsic intrusives (Candela and Piccoli, 2005), and the term 'porphyry' relates to the porphyritic texture of dyke and plug-like intrusions that are spatially associated and genetically related to ore deposition (e.g., Seedorff et al., 2005). In the case of Lorraine, porphyritic rocks are uncommon in mineralised zones, and Sillitoe (2007) has inferred that the causative intrusive body is most likely concealed at depth.

A key feature of porphyry deposits is the alteration of wall rocks by hydrothermal fluids which exsolved from intermediate to felsic magmas. Hydrothermal alteration is interpreted to have occurred at temperatures both above and below the magmatic solidus (e.g., ~200 to 750 °C; Hemley and Jones, 1964; Wilson et al., 1980; Titley and Beane, 1981; Ulrich et al., 2001; Seedorff et al., 2005), and the style of alteration is dictated by magmatic fluid composition, wall-rock composition and fluid-to-rock ratio (Seedorff et al., 2005). Porphyry deposits are typically laterally (and vertically) zoned on a scale of hundreds to thousands of metres, and commonly exhibit a crudely concentric pattern of alteration types (Lowell and Guilbert, 1970; Rose, 1970); from a central potassic zone grading out to propylitic alteration zones (Lowell and Guilbert, 1970; Rose, 1970; Rose and Burt, 1979). Potassic alteration zones result from interactions between magmatic fluids and wall rocks and are spatially associated with hypogene ore, typically as stockwork veins, hydrothermal breccia and/or as disseminated sulphides in wall rocks. Propylitic zones tend to form in the outer zones of porphyry systems where more reduced external fluids mix and are heated by magmatic fluids or thermal gradients (Seedorff et al., 2005). Deeper formation waters may be heated by thermal diffusion from magma chambers resulting in deep sodic-calcic alteration zones in some porphyries (e.g., Dilles et al., 2000; Seedorff et al., 2005). Potassic and propylitic assemblages can be overprinted by late stage hydrolytic assemblages (Gustafson and Hunt, 1975). As magmatic fluids cool, HCl tends to dissociate, and thus lowers the pH of hydrothermal fluids (Montoya and Hemley, 1975), which promotes sericite alteration of earlier potassic zones as the system wanes (Rose and Burt, 1979).

According to Seedorff et al. (2005), porphyry deposits can be divided into five classes based on their principal economic metals (Table 1-1). The main classes, in terms of economics are; porphyry Au (e.g., Lobo, Chile; Sillitoe, 2000), porphyry Cu (e.g., Yerrington dist., Nevada; Dilles et al., 2000), porphyry Mo (e.g., Henderson, Colorado; Seedorff, 1988), porphyry W (e.g., Mount Pleasant, New Brunswick; Kooiman et al., 1986) and porphyry Sn (e.g., Cerro Rico, Bolivia; Sillitoe et al., 1975). These classes can be subdi-

vided based on the composition of causative intrusives (Table 1-1). Porphyry Au deposits are typically associated with dioritic rocks, whereas porphyry Mo and porphyry Cu deposits can be associated with a range of intrusive rocks. In particular porphyry Cu deposits are associated with tonalitic-granodioritic rocks (e.g., Batu Hijau, Indonesia; Garwin, 2000), mostly dioritic rocks (e.g., Philippines; Sillitoe and Gappe, 1984), monzonitic rocks (e.g., Mt. Milligan, British Columbia; Barrie, 1993; Bingham Canyon, Utah; Waite et al., 1997) and syenitic rocks (e.g., Galore Creek, British Columbia; Enns et al., 1995; Logan, 2005). According to Seedorff et al. (2005), Lorraine and Mt. Polley are examples of syenite porphyry Cu-(Au) deposits (Table 1-1).

1.3. Alkalic porphyry-Cu Au deposits

Alkalic porphyry Cu-Au deposits have been identified in a limited number of arc-related provinces worldwide, where they are associated with silica-saturated to silica-undersaturated 'shoshonitic' series monzonites or syenites. In addition to their association with shoshonitic magmatism, alkalic porphyry Cu-Au deposits can also be distinguished from calc-alkalic deposits based on metal association, ore-related alteration, peripheral alteration and quartz veining (e.g., Schroeter, 1995; Wilson, 2003; Seedorff et al., 2005; Table 1-2). Well known examples occur in the Mesozoic arcs of British Columbia (Schroeter, 1995; Logan and Mihalynuk, 2005a,b; Logan, 2005; Tosdal et al., 2008), and the Late Ordovician Lachlan Fold Belt of New South Wales (Wilson, 2003), and isolated examples have been identified in the Philippines (Dinkidi; Wolfe, 2001) and Greece (Skouries; Kroll et al., 2002). The alkalic porphyry Cu-Au deposits are considered to be small compared to their calc-alkalic equivalents, but can be comparatively higher grade and in some cases well endowed with Au (e.g., Ridgeway NSW, Australia; Wilson et al., 2003). Some alkalic porphyry deposits are also associated with small volume pipe-like intrusives and intensely developed hydrothermal alteration zones that are restricted to within a few hundred meters of the intrusive complex (Cooke et al., 2007).

Detailed studies indicate that alkalic porphyry deposits in New South Wales, Philippines (Dinkidi) and British Coumbia are zoned (*see* below; Heithersay and Walshe, 1995; Lang et al., 1995a; Jensen and Barton, 2000; Wolfe, 2001; Wilson et al., 2003; Wilson et al., 2007; Byrne et al., 2008; Jackson et al., 2008; Jago and Tosdal, 2008; Micko et al., 2008; Pass et al., 2008). Recent studies of alteration assemblages associated with Late Triassic to Early Middle Jurassic porphyry Cu-Au deposits of British Columbia have indicated that the silica-undersaturated Galore Creek and Mt. Polley and silica-saturated Mount Milligan alkalic porphyry deposits are characterised by sulphide zonation patterns which grade from bornite-chalcopyrite cores outwards chalcopyrite>pyrite and outer zones of pyrite ± minor chalcopyrite. These are consistent with zonation patterns in other porphyry systems

Table 1-1. Classification scheme for the porphyry deposit types (after Seedorff et al., 2005).

Classes	Porphyry gold		Porphyry copper					Porphyry molybdenum				Porphyry tungsten	Porphyry tin
Sub-classes	Dioritic porphyry Au	Tonalitic-granodioritic porphyry Cu-(Au-Mo)	Quartz monzodioritic-grantitic porphyry Cu-(Mo)	Monzonitic porphyry Cu-(Au-Mo)	Syenitic porphyry Cu-(Au)	Monzonitic porphyry Cu-(Au)	Syenitic porphyry Mo	Quartz monzonitic-grantitic porphyry Mo-Cu	Grantitic porphyry Mo	Trond-hjemitic porphyry Mo	Rhyolitic porphyry Mo	Rhyolitic porphyry W-Mo	Rhyodacitic porphyry Sn
Example	Cerro Casale, Aldebarán dist., Chile; Lobo, Chile; Marte, Chile; Palmetto, NV; Pancho, Refugio dist., Chile; Verde, Refugio dist., Chile; Zule, CA	Batu Hijau, Indo.; Dizon, Phil.; Dos Pobres, Safford dist., AZ; Far Southeast, Phil., Island Copper, BC; Kal'makyr, Almalyk dist., Uzbek.; Oyu Tolgoi, Mon golia; Panguna, PNG; Qonyrat, Kazakh.; Sar Cheshmeh, Iran; Tanamá, Puerto Rico	Ann-Mason, Yerington dist., NV; Cananea, Sonora; Chuquicamata, Chile: El Salvador, Chile; Highland Valley, BC; La Es con-dida, Chile; Morenci, AZ; Re solu-tion, Supe-rior dist, AZ; San Manuel-Kalamazoo, AZ; Santa Rita , NM; Sierrita-Esperanza, AZ	Bingham, UT; Bisbee, AZ; Dinkidi, Phil.; Goonumbla, NSW; Kharmagtai, Mongolia; Mouywa , Myanmar: Mount Milligan, BC; Ok Tedi, PNG; Peschanka, Russia; Rialto, NM; Russia; Robinson, NV; Skouries, Greece; Yulong, China	Galore Creek, BC; Lorraine, BC; Mount Polley (Cari-boo-Bell), BC; Rayfield River, BC	Central City, CO; Golden Sunlight, MT; Jamestown, CO; Three Rivers, NM	Big Ben, MT; Bord-vika-Vragla, Norway; Cave Peak, TX; Malmb-jerg, Werner Bjerge, Greenland; Marinkas Kwela, Namibia; Nordli, Norway	Buckinulram, NV; Can-nivan Gulch, MT; Cumobabi, Sonora; East Qonyrat, Kazakh., Hall(Nevada Moly), NV; Kadzaran , Armenia ; Montezuma, CO; Mount Tolman , WA; New Boston-Blue Ribbon, NV; Opodepe (El Crestón) , Sonora	Adanac (Ruby Creek), BC; Burroughs Bay, AK; Endako, BC; Kitsault, Alice Arm dist., BC; Quartz Hill, AK; Roundy Creek, BC; Thompson Creek, ID	Bald H ll, New Ze aland; Kirki , Greece; Mink Lake, ON; Trout Lake, BC; Setting Net Lake , ON	Bear Mountain, AK; Climax, CO; Henderson, CO; Mount Hope, NV; Mount Em-mons, CO; Pine Grove, UT; Questa, NM; Redwell Basin, CO; Silver Creek (Rico), CO; Urad, CO	Mount Pleasant, NB; True Hill, NB	Cerro Rico (Potosí), Bolivia; Chorolque, Bolivia; Llallagua, Bolivia; Majuba Hill, NV; Oruro, Bolvia

Abbreviations: AK = Alaska; AZ = Arizona; BC = British Columbia, dist. = dist rict ; CA = California; CO = Colorado; JD = Idaho; Indo. = Indonesia; Kazakh. = Kazakhstan ; MT = Montana; NB = New Brunswick; NM = New Mexico; NSW = New South Wales; NV = Nevada ; ON = Ontario; Phil. = Philippines; PNG = Papua New Guinea; TX = Texas; UT = Utah; Uzbek. = Uzbekistan; WA : Washington

(e.g., Cadia, NSW; Wilson et al., 2003; El Teniente, Chile; Cannell et al., 2005). Alteration zonation patterns of British Columbia alkalic porphyries are reported as (1) inner, intensely developed potassic alteration assemblages of K-feldspar, biotite, magnetite and/or hematite dusting, (2) inner to peripheral zones of diopside, actinolite, albite and/or garnet and (3) outer zones of chlorite, epidote, hematite, albite, calcite and/or sericite (Byrne et al., 2008; Jackson et al., 2008; Jago and Tosdal, 2008; Micko et al., 2008; Pass et al., 2008; Jago and Tosdal, in prep.; Micko et al., in prep.; Pass et al., in prep.).

The Late Ordovician alkalic porphyry Au-Cu deposits in New South Wales show alteration zonation patterns and sulphide zonation patterns similar to the alkalic porphyry deposits of BC. The NSW alkalic porphyry deposits are characterised by (1) early albite, biotite, magnetite and orthoclase, (2) transitional-stage assemblages of quartz, biotite, orthoclase with (3) peripheral garnet, epidote, calcite, albite, illite, muscovite and/or calcite and (4) distal magnetite and hematite (Wilson, 2003). One notable difference between the NSW and BC alkalic porphyries is the absence of quartz veining accompanying mineralisation in the BC deposits, with the exception of Red Chris and Mt. Milligan (e.g., Baker et al., 1997; Jago, 2008; Jago and Tosdal, in prep.).

Table 1-2. Summary of characteristics of alkalic versus calc-alkalic porphyry deposits, from Wilson (2003).

Feature	Alkalic	Calc-alkalic
Metal association	Au-Cu; Cu-Au	Cu-Au-Mo (high-K)
	rare Mo	Cu-Mo(-Au), Cu-Au-Mo (med-K)
Ore-related alteration	*Potassic*: bio-Kfd-mt-ab-chl±ah	*Potassic*: bio-Kfd-ab ± mt ± ah
	Calc-potassic: act-bio-mt-ep; gn-Kfd-bi ± ap ± ah	*Phyllic*: qz-mus-py
Peripheral alteration	*Sodic-calcic*: ab-di-ep-chl-cal	*Argillic*: mnt-ill-py
	Sodic: ab-chl-py	*Propylitic*: chl-ep-cal ± act
	Propylitic: chl-ab-ep-cal	*Advanced argillic*: qz-alu-dic-ppl
Quartz veining	Rare in BC deposits; abundant in other regions	Ubiquitous
Type examples	Galore Creek, Copper Mountain, Mount Polley, British Columbia; Skouries, Greece; Dinkidi, Philippines	Escondida, Chuquicamata, El Salvador, Spence, Chile; Bingham Canyon, Utah; Bajo del Alumbrera, Argentina

Abbreviations: ab = albite, act = actinolite, alu = alunite, ah = anhydrite, ap = apatite, bio = biotite, cal = calcite, chl = chlorite, di = diopside, dic = dickite, ep = epidote, gn = garnet, ill = illite, Kfd =K-feldspar, orthoclase, mt = magnetite, mnt = montmorillonite, mus = muscovite, py = pyrite, ppl = pyrophyllite, qz = quartz.

1.4. Objectives of this dissertation

The current study presents results of detailed geological mapping and core logging of the Lower Main Zone, coupled with new U-Pb geochronology data, detailed petrographical observations and geochemical data. The principal aims of the study have been to:

- Describe the geology of the Lower Main Zone, including:
  - Characteristies the intrusives and their relationship to mineralisation.
  - Determine absolute and relative ages of the intrusive phases.
  - Delineate alteration and mineralisation patterns.
- Characterise the geochemistry of intrusive rocks of the Lower Main Zone.
- Use the major element, trace element and isotopic compositions of Lorraine rocks to constrain the parental magma source of ultrabasic rocks at Lorraine.
- Generate a genetic model for Cu-Au mineralisation at Lorraine.

1.5. Location and Access

The Lorraine porphyry Cu-Au deposit is situated about 280 kilometres northwest of Prince George and 55 kilometers west-northwest of Germansen Landing (55°55.6'N, 125°26.5'W; MINFILE 093N/014). The terrain ranges in elevation from 1050 to 2000m above mean sea level (Fig. 1-1a-d). The deposit is situated near the headwaters of Duckling Creek in the Omineca Mountains of north-central British Columbia. They are accessible via four wheel drive roads from either Fort St. James and Germansen Landing off the Omineca Mining Road, or via the Kemess Access Corridor from Mackenzie to adjoining logging roads that follow the Osilinka River and Haha Creek to north-west of the Lorraine-Jajay property. The property is also access by helicopter (approximately 1 hour from Smithers or 1.3 hours from Fort St James).

1.6. Exploration history of the Lorraine area

This brief summary of exploration milestones for the Lorraine prospect has been synthesised from a recent report by Garratt and Lindinger (2008). For a comprehensive history of exploration in the Lorraine area, the reader is referred to the above report. Exploration milestones are:

- Early 1900s prospectors noted malachite-stained bluffs on Lorraine Mountain, and the property was first staked in 1931.

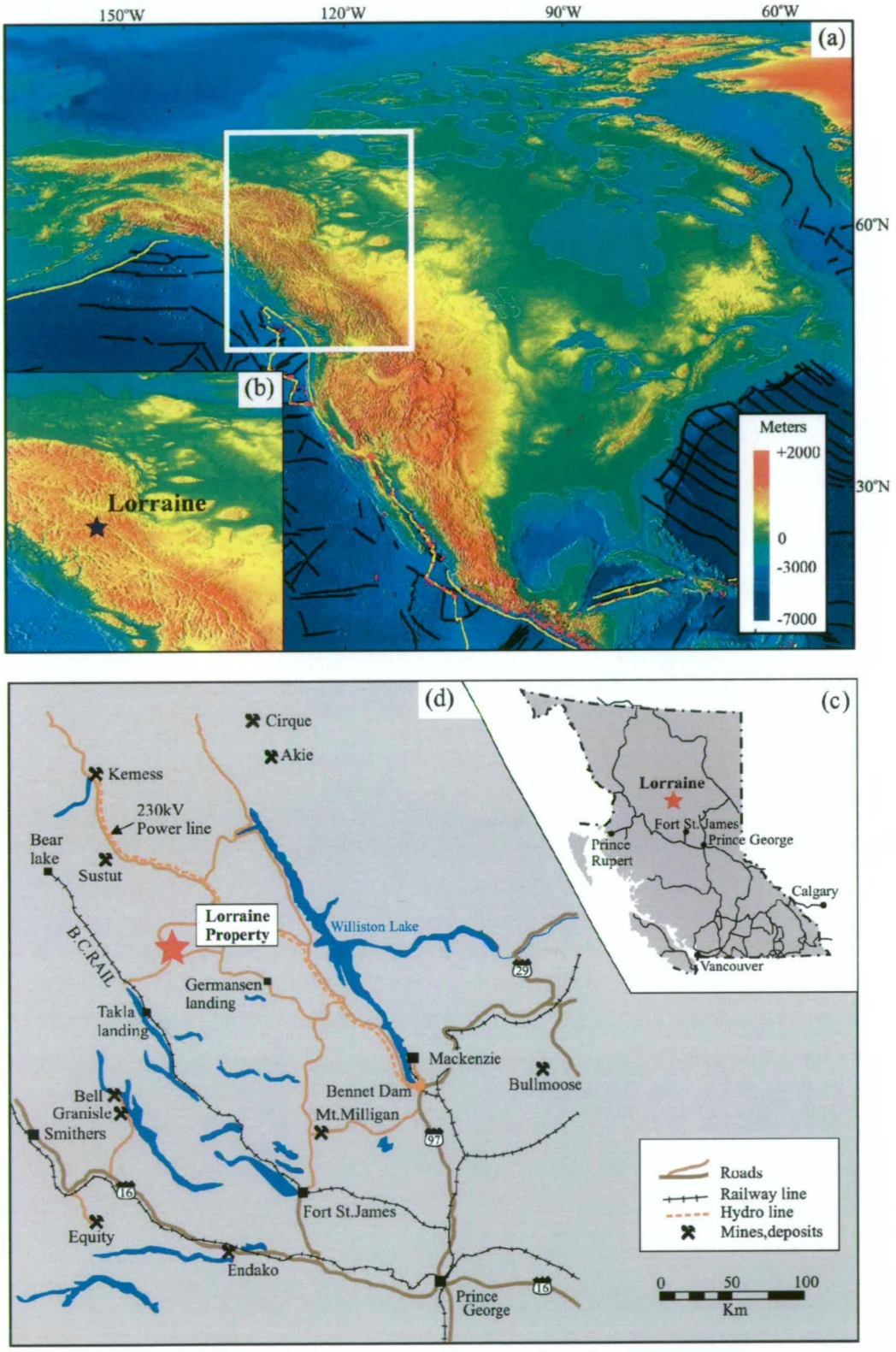

Figure 1-1. **(a)** Digital land surface and sea floor elevation map of North America with major modern-day faults (black and yellow lines). The white rectangle denotes the area of British Columbia shown in "b". Modified from National Geophysical Data Center (2009). **(b)** Digital land surface and sea floor elevation maps of British Columbia, and the location of the Lorraine porphyry Cu-Au deposit. Modified from National Geophysical Data Center (2009). **(c-d)** Location map of the Lorraine porphyry Cu-Au deposit of British Columbia, Canada, relative to major infrastructure. Modified from Garratt and Lindinger (2008).

• Drilling of the Main Zone by Northwestern Exploraion Limited was first conducted in 1949 with five widely spaced diamond drill holes. Drilling results were mixed.'

• Between 1970 and 1973 Granby Mining Company Ltd carried out a total of 3,992 metres of diamond drilling and 2470 metres of percussion drilling on the Main Zone and Lower Main Zone. An estimate of 5.5 Mt (inferred) grading 0.6 % Cu and 0.1 g/t Au for the Lower Main Zone and 4.5 Mt at 0.75 % Cu and 0.34 g/t Au for the Main Zone was made based on the new drilling results.

• In 1991 Kennecott completed twelve diamond drill holes (totalling 2392 metres) in the Lorraine area and delineated mineralisation in the Bishop Zone.

• Between 1994 and 1997 Lysander Gold Corporation optioned the property from Kennecott, drilled over 40 diamond drill holes in the Lorraine area, and intersected 64 metres of 0.58 % Cu and 0.24 g/t Au in the Bishop Zone (drill hole 1997-47).

• In 2000 Eastfield Resources optioned the Lorraine-Jajay property from Lysander Minerals Corporation and between 2000 and 2004 conducted further diamond drilling in the Lorraine area that expanded the area of known mineralisation to the south and west.

• An exploration program, funded by Teck Ltd was conducted between 2005 and 2008, including extensive induced polarisation (IP) and magnetic geophysical surveys, detailed geological mapping of the Lorraine district and diamond drilling. New mineralised zones were identified to the south of the Lorraine deposit in the Duckling Creek Syenite Complex (e.g., Slide area).

1.7. Structure of this thesis

In addition to this introductory chapter, this thesis has been divided into the following chapters:

• *Chapter 2* discusses the geology of the Canadian Cordillera and interpretated tectonic setting. The chapter also introduces the regional- and district-scale geology of the Lorraine district.

• *Chapter 3* describes the geology of the Lower Main Zone, and presents an interpretation map and cross-sections of the Lower Main Zone. The chapter also presents six new U-Pb zircon ages for intrusives of the Lower Main Zone.

• *Chapter 4* presents the early, transitional and late-stage alteration assemblages of the Lower Main Zone. The chapter also presents alteration maps and cross-

sections of the Lower Main Zone.

• *Chapter 5* describes in detail transitional stage alteration and mineralisation of the Lower Main Zone. Detailed petrographic descriptions are provided and relationships between sulphides and host rocks are discussed.

• *Chapter 6* compares the major and trace element chemistry of mineral phases in altered and unaltered rocks. The comparison demostrates geochemical differences between magmatic phases and phases formed as a result of alteration. The chapter also compares the mineral chemistry of unaltered shoshonites with other arc-related shoshonites.

• *Chapter 7* presents major and trace element whole rock geochemistry of the Lorraine deposit, and compares the composition of unaltered shoshonites from Lorraine with global arc-related shoshonites. The comparison demonstrates notable similarities between Lorraine shoshonites and Fijian shoshonites.

• *Chapter 8* presents new radiogenic Sr, Nd and Pb data for Lorraine and new O and D stable isotope results. The isotope composition of mineral phases in altered rocks are compared with unaltered rocks. In addition the isotopic composition of Lorraine rocks are compared with other arc-related shoshonites.

• *Chapter 9* concludes the thesis by presenting a tectonic model to explain the emplacement of shoshonitic intrusions at Lorraine in light of the new isotopic and whole rock geochemistry. The chapter discusses reactions and conditions during the deposition of sulphides at Lorraine.

CHAPTER 2
REGIONAL AND DISTRICT SCALE GEOLOGY

2.1. Introduction

The aim of this chapter is to review the tectonic environment in which the Lorraine porphyry Cu-Au deposit formed, and to describe the district scale geology of the area. Lorraine is located in the Canadian Cordillera, an orogenic collage that includes rocks with island arc affinities, oceanic plateaus, accretionary complexes, active and passive continental margins and cratons consisting of rocks which range in age from Palaeoproterozoic to Holocene (Parfenov et al., 1999; Monger and Price, 2000; Johnston and Borel, 2007). Much of the Canadian Cordillera was formed outboard of the craton and accreted during major orogenic events during the Middle Jurassic to Early Tertiary (Monger and Price, 2000). Alkalic porphyry Cu-Au mineralisation occurred before and closely following accretion of the Quesnel and Stikine island arc terranes, and was associated with the emplacement of silica-saturated to -undersaturated alkalic intrusives in the Late Triassic and Early Middle Jurassic (McMillan et al., 1995; Lang et al., 1995b).

2.2. Terranes of the Canadian Cordillera

The Canadian Cordillera can be divided into six main belts (Fig. 2-1), which includes from east to west: (1) the passive margin sequences of the Cordillera Foreland, (2) the pericratonic belt, (3) the Cache Creek terrane, (4) the accreted Stikine and Quesnel arc terranes, (5) Coastal Mountain Plutonic belt and (6) the Insular belt (Johnston and Borel, 2007).

2.2.1. Foreland passive margin

Rocks of the Cordillera Foreland extend from the Canadian-American (Washington to Montana) border in the south to the Yukon-Alaskan border in the north, and consist of Palaeozoic to Middle Jurassic shallow water carbonates and deeper water argillaceous sediments and Paleoproterozoic to Neoproterozoic clastic and carbonate sequences (Monger and Price, 2000; Johnston and Borel, 2007). These shallow and deeper water sediments were deposited along the western margin of ancestral North America (or Laurentia), and can be divided into a landward carbonate belt (the Rocky Mountain or Mackenzie platform), a medial shale basin (Selwyn Basin/Kechika Trough), and an outer or oceanward carbonate belt (e.g., Cassiar platform), from east to west respectively (Fig. 2-1; Johnston and Borel, 2007; Nelson and Colpron, 2007). During the accretion of island arc (Quesnellia and Stikinia) and oceanic (Cache Creek and Slide Mountain) terranes in the Middle Jurassic, rocks of the foreland were deformed into an extensive fold and thrust belt (Monger and Price, 2000).

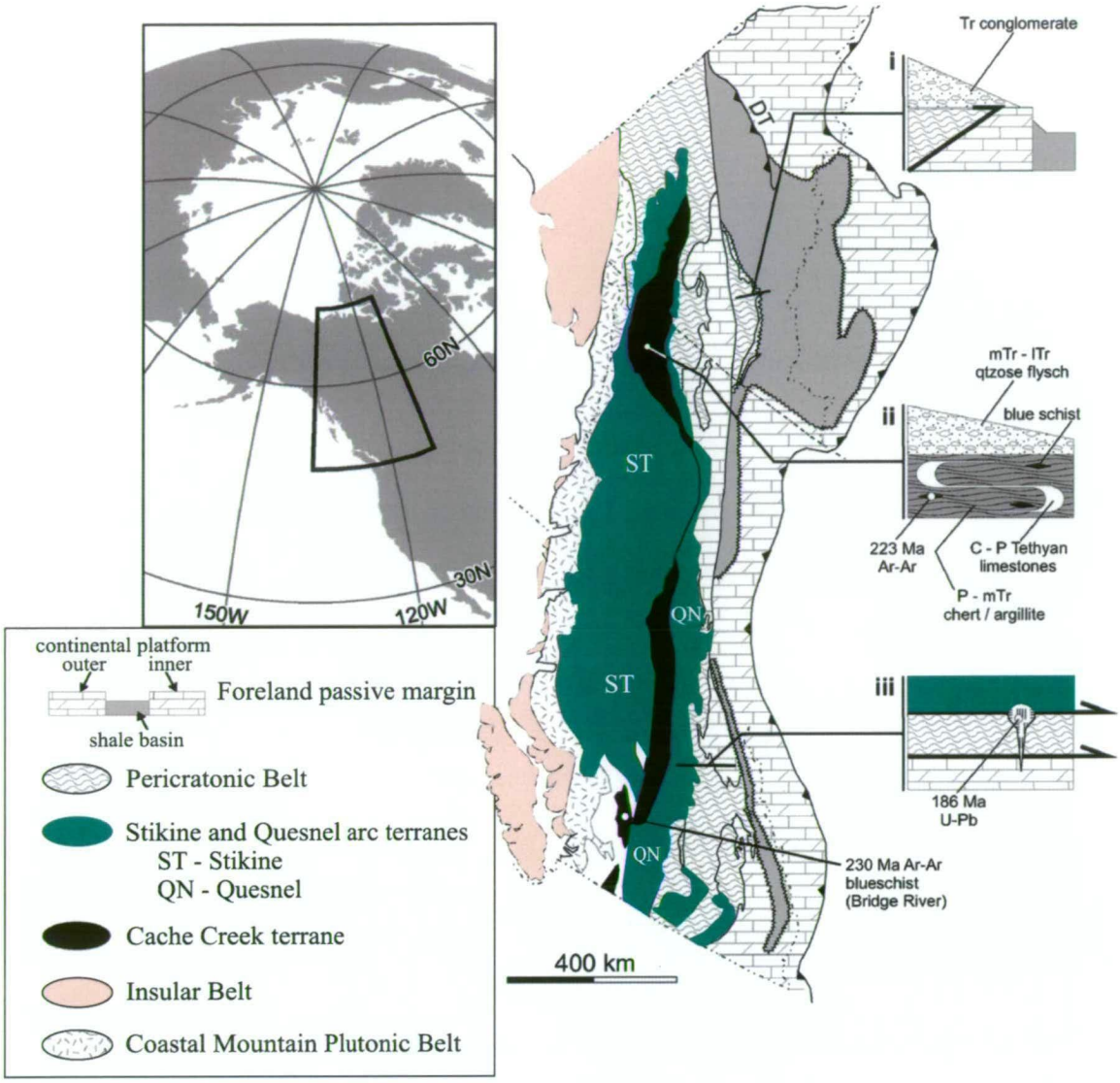

Figure 2-1. Tectonic map of the Canadian Cordillera illustrating the arrangement of terranes. Cross-sections (i, ii and iii) indicate relative and absolute timing constraints. Insert shows location of the main map of northwestern North America. Timing constraints are **(i)** Triassic conglomerate unconformably overlying a thrust that places crystalline rocks of the pericratonic belt over outboard continental platform (Johnston and Borel, 2007); **(ii)** Middle Triassic and younger flysch, interpreted to be derived from Stikinia, unconformably overlying folded and metamorphosed (blueschist facies) Cache Creek strata (Monger, 1975; Mihalynuk et al. 1993); **(iii)** 186 million year pluton intruding and stitching together previously imbricated strata of the Quesnel arc terrane, the pericratonic belt and the outboard continental platform (Nixon et al. 1993; Johnston and Erdmer, 1995). Modified from Johnston and Borel (2007).

2.2.2. Pericratonic belt

The pericratonic belt occurs to the west of the foreland passive margin and east of the accreted rocks of Quesnel and Cache Creek terranes in British Columbia and in south-central Yukon. The pericratonic belt also extends around the western side of the Stikine arc terrane in north-western British Columbia and south-western Yukon Territory (Fig. 2-1).

The pericratonic belt consists of the Nisling, Yukon-Tanana and Kootenay terranes (Johnston and Borel, 2007), which are variably metamorphosed quartzose rocks that formed along a continental margin (Patchett and Gehrels, 1998; Johnston and Borel, 2007). The three terranes contain voluminous Late Devonian, Carboniferous, and Permian arc-related volcanic and plutonic suites (Mortensen, 1992). Dismembered Upper Devonian to Permian ophiolite rocks, referred to as the Slide Mountain terrane, define the eastern margin of the pericratonic belt, and are interpreted as remnants of a marginal basin that developed landward of the arc (Johnston and Borel, 2007). Erdmer et al. (1998) reported blueschist and eclogite facies rocks with cooling ages ranging from Carboniferous to the Triassic in the Slide Mountain and Yukon-Tanana terranes and suggested that they represent a record of middle Paleozoic, late Paleozoic, and early Mesozoic subduction.

The pericratonic belt was overthrust by late Triassic to Early Jurassic arc rocks of the Stikine-Quesnel accreted arc terranes. The pericratonic belt and Stikine-Quesnel terranes are stitched by ca. 186 Ma cross-cutting intrusive rocks, indicating that accretion occurred no later than the Middle Jurassic in the northern area of the Canadian Cordillera (Nixon et al., 1993; Johnston and Erdmer, 1995).

2.2.3. Cache Creek terrane

The Cache Creek terrane is an accretionary complex comprising mafic-ultramafic volcanic-plutonic complexes and extensive shallow water reefal carbonates with distinctive Upper Carboniferous to Triassic Tethyan fauna that are exotic with respect to other terranes of the Cordillera and to autochthonous North America strata (e.g., the Permian Verbeekinid fusilinids; Monger and Ross, 1971; Johnston and Borel, 2007). Exotic fossil-bearing carbonates stratigraphically overlie basalts with geochemical compositions consistent with origins as ocean island basalts or within-plate tholeiites (English et al., 2002; English et al., 2010), and it is inferred that seamounts and oceanic plateau with carbonate reefs were scraped off the down-going slab along the forearc region of the Stikine and Quesnel arcs during subduction (Monger, 1977; Gabrielse, 1991; Mihalynuk et al., 1994a).

Permian to Early Jurassic palinspastic reconstructions, geochemical affinities and the presence of far travelled 'exotic' fossils of Tethyan fauna, suggests that Cache Creek seamounts were conveyed by an east-dipping slab subducting beneath Stikine and Quesnel arc terranes (Fig. 2-2; Mihalynuk et al., 1994a; Monger and Price, 2000; English et al., 2002; Mihalynuk et al., 2004). The accretion of seamounts is recorded by pre-Late Triassic isoclinal folding of the Cache Creek strata and blueschist facies metamorphism (Gabrielse, 1991; Johnston and Borel, 2007). Blueschist cooling ages of 230 Ma to 220 Ma are con-

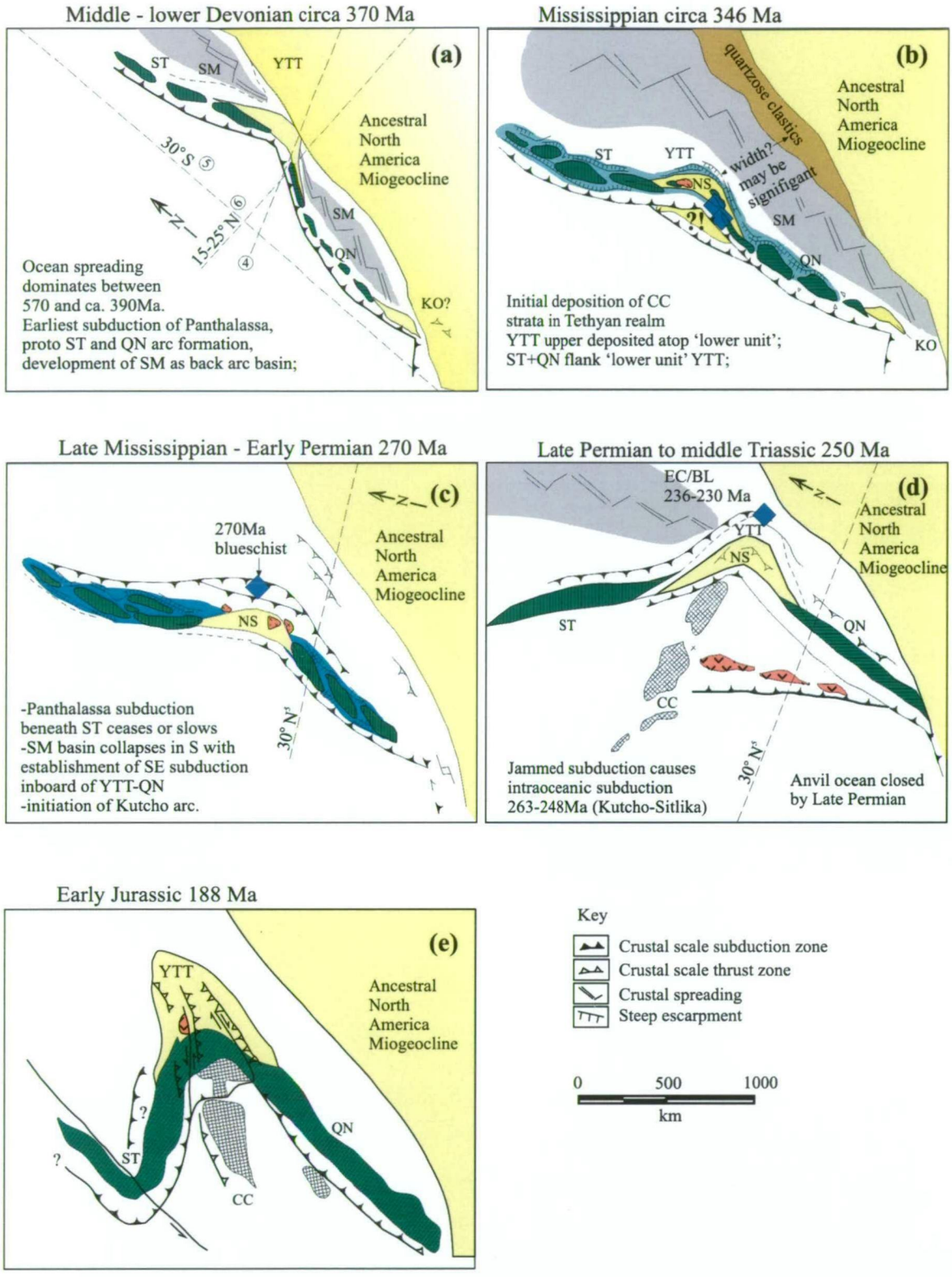

Figure 2-2. Scaled palinspatic maps of the west coast of ancestral North America at **(a)** ~370 Ma, **(b)** ~346 Ma, **(c)** ~270 Ma, **(d)** ~250 Ma and **(e)** 188 Ma as proposed by Mihalynuk et al. (1994a). The palinspatic maps show the location of the Quesnel (QN) and Stikine (ST) arc terranes relative to the pericratonic Yukon-Tanana (YTT) Nisling (NS) and Kootenay (KO), and the Slide Mountain (SM) terrane assemblages, which are inferred to have formed as a rifted marginal basin that developed landward of the Quesnel and Stikinia arc. The palinspatic maps also depict the translation and collision of the Cache Creek terrane (CC) from the Late Permian to the Early Jurassic which is thought to have led to oroclinal folding of the QN-ST arc. Additional acronyms include eclogite (EC) and blueschist (BS; modified from M.G. Mihalynuk, written commun., 2008).

sistent with exhumation following Early Triassic entry into a subduction zone of the Cache Creek seamounts (Ghent et al., 1996). Johnston and Borel (2007) linked the Late Permian to Early Triassic period of arc quiescence to seamount and plateau accretion in the forearc. Continued subduction beneath the arc is evident from Late Triassic to late Early Jurassic arc magmatism and Early Jurassic blueschist metamorphism within the Cache Creek accretionary complex (Mihalynuk et al., 1994a).

2.2.4. Stikine and Quesnel arc terranes

The Quesnel terrane forms a ribbon (<100 km wide) of arc-derived rocks that trend northwest through the central region of British Columbia (Fig. 2-1). It extends from south of the American-Canada border to north of the British Columbia-Yukon border. To the east, the Quesnel terrane is bounded by pericratonic and foreland rocks, and to the west the Quesnel terrane is faulted against the Cache Creek and Stikine terranes.

The Stikine terrane forms a belt of rocks up to 250 km wide that extends from southern British Columbia as far north as south-central Yukon. Stikinia is separated from the Coastal Belt to the west by a series of faults (Gabrielse et al., 1991) and is structurally juxtaposed against rocks of the Cache Creek and Quesnel terranes to the east. Although presently exposed on opposite sides of the Cache Creek complex, the Stikine and Quesnel terranes are believed to have formed a single, continuous magmatic arc that lay east of the Cache Creek accretionary complex in the Paleozoic and early Mesozoic (Wernicke and Klepacki, 1988; Mihalynuk et al., 1994a; Johnston and Borel, 2007). The medial position of the Cache Creek accretionary complex between Stikine and Quesnel terranes is inferred to have resulted from either strike-slip displacement (Wernicke and Klepacki, 1988) or oroclinal bending of the arc (Mihalynuk et al., 1994a; Fig. 2-2).

The accretion of the Cache Creek seamounts to Stikine and Quesnel terranes occurred in the Middle to Upper Triassic (Mihalynuk et al., 1994a), and the collision of Stikine and Quesnel terranes with the pericratonic belt-Cassiar platform occurred between 190 and 180 Ma (Johnston and Borel, 2007). Two schools of thought exist over the location of the pericratonic belt-Cassiar platform relative to ancestral North America during its collision with the amalgamated Stikine, Quesnel and Cache Creek terranes. Either the pericratonic belt and Cassiar platform collided with Cache Creek, Stikine and Quesnel terranes at a distance of >4000 km west of ancestral North American (between 190 and 180 Ma) and were later accreted to ancestral North America at about 150 Ma (Johnston and Borel, 2007), or the pericratonic belt and Cassiar platform formed outboard of ancestral North America and was thrust onto it during the accretion of Stikine, Quesnel and Cache Creek terranes in the late Early Jurassic (Monger and Irving, 1980; Wernicke and Klepacki, 1988; Mihalynuk et al., 1994a; Monger and Price, 2000; Mihalynuk et al., 2004). For more de-

tailed insights into the models for the accretion of Cache Creek to Stikine and Quesnel terranes the reader is referred to Wernicke and Klepacki (1988), Mihalynuk et al. (1994a), Mihalynuk et al. (2004) and Johnston and Borel (2007).

2.2.4.1. Geology of the Stikine and Quesnel terranes

The Stikine terrane comprises arc rocks of the Lower to lower Middle Jurassic Hazelton Group and Upper Triassic Stuhini and Lewis River groups. These packages overlie Paleozoic arc and sedimentary successions collectively known as the Stikine assemblage (Monger, 1977; Logan and Koyanagi, 1994; Mihalynuk et al., 1994b; Evenchick et al., 2004). The Stikine assemblage is characterised by a basal Devonian quartzose turbidite (Mihalynuk et al., 1994b), Devonian to Permian carbonate, calc-alkaline arc volcanic and volcaniclastic rocks (Monger, 1977), Upper Permian to Middle Triassic argillite, chert and conglomerate (Brown et al., 1991; Logan and Koyanagi, 1994), and Upper Triassic sequences characterised by alkalic (shoshonitic) arc volcanic and intrusive rocks as well as coral reefs (Brown et al., 1991; Johnston and Borel, 2007).

The geology of the Quesnel terrane is similar to that of Stikinia comprising Upper Triassic and Lower Jurassic calc-alkalic to alkalic (shoshonitic) volcanics and associated sedimentary rocks (i.e. Takla, Slocan, Rossland and Nicola Groups). The Quesnel terrane also includes Triassic to early Jurassic calc-alkaline to alkalic intrusives (e.g., Hogem Batholith). Quesnel rocks overlie or have intruded Paleozoic rocks of the Harper Ranch Group and Lay Range assemblage in central-northern British Columbia (Ferri, 1997; Monger and Price, 2000). These Paleozoic sequences comprise latest Devonian chert-pebble conglomerate, sandstone, shale and Middle to Late Carboniferous, and Early to Middle Permian limestone, volcaniclastic, graded siliceous argillite and siltstone (Ferri et al., 1993; Ferri, 1997; Monger and Price, 2000). Rocks of the Quesnel and Stikine terranes are predominantly metamorphosed to grades of prehnite-pumpellyite or zeolite facies assemblages (Monger and Price, 2000), although greenschist facies metamorphism is recognised locally (Gabrielse et al., 1991).

2.3. Mineral deposits of the Stikine and Quesnel arc terranes

The oldest known ore deposits in the Stikine terrane are Devonian-Carboniferous VMS deposits such as Tulsequah Chief and Foremore, which occur in the north-western part of the terrane (Logan, 2004; Nelson and Colpron, 2007). To the author's knowledge there are no significant Devonian-Carboniferous VMS mineral occurrences in the Quesnel terrane.

The Quesnel and Stikine arc terranes host Late Triassic to Middle Jurassic Cu-Au and Cu-Mo porphyry deposits (Fig. 2-3). The Highland Valley, Gibraltar, Copper Mountain, Brenda, Afton, Mt. Polley and Kemess deposits have been mined or are being mined (Bysouth et al., 1995; Casselman et al., 1995; Fraser et al., 1995; Rebagliati et al., 1995; Stanley et al., 1995; Weeks et al., 1995; Logan and Mihalynuk, 2005). There are plans for future mines at Galore Creek and Mt. Milligan (Enns et al., 1995; Sketchley et al., 1995); and unexploited resources occur at Lorraine, Red Chris and Schaft Creek (Bishop et al., 1995; Newell and Peatfield, 1995; Spilsbury, 1995; Nelson and Colpron, 2007). The porphyry-related intrusives range from ca. 210 Ma (Galore Creek and Highland Valley) to ca. 180 Ma (Lorraine and Mount Milligan respectively). The most common ages of magmatism are ca. 205 to 202 Ma (e.g., Mount Polley, Afton; Mortensen, 1995; Logan et al., 2007; Fig. 2-3). Intrusives associated with porphyry-style mineralisation range from calc-alkalic (e.g., Highland Valley, Brenda, Gibraltar, Kemess and Schaft Creek) to shoshonitic/alkalic affinities (e.g., Lorraine, Copper Mountain, Mt. Polley, Red Chris and Galore Creek; McMillan et al., 1995; Fig. 2-3), and are thought to have been emplaced when the Stikine and Quesnel terranes were in a state of compression or sinistral trans-

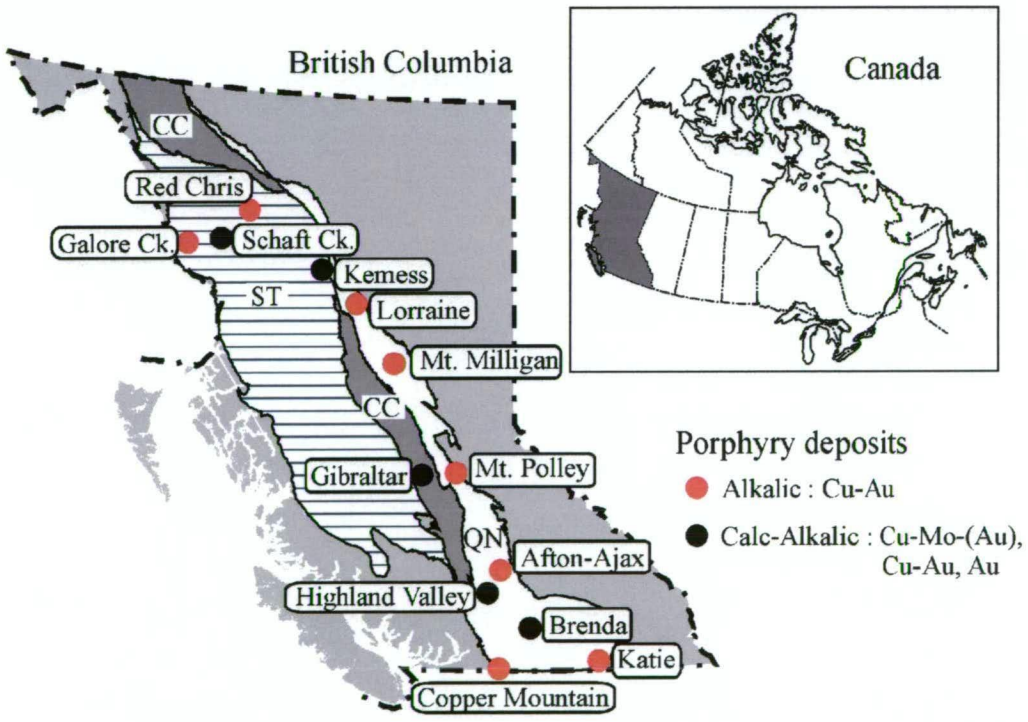

Figure 2-3. Tectono-stratigraphic setting and location of the Lorraine deposit along with other Late Triassic to Early Middle Jurassic Cu-Au porphyry deposits in British Columbia. Terranes; Stikine (ST); Cache Creek (CC); Quesnel (QN; modified from Nixon and Peatfield, 2003). Labels show the location of Late Triassic to Early Jurassic calc-alkalic and alkalic porphyry deposits in the Quesnel and Stikine terranes (McMillan et al., 1995). Inserted is a map of Canada with provincial and territorial boarders. Grey filled area represents the province of British Columbia.

pression (Nelson and Colpron, 2007). A compressional and sinistral transpresssional tectonic setting has been inferred by the occurrence of constrained Triassic-Jurassic folded rocks and reverse faults, unconformities, and a transition from predominantly marine conditions in the Triassic to widespread subaerial and shallow submarine volcanism in the Jurassic (Nelson and Colpron, 2007).

In addition to porphyry deposits, other epigenetic deposit types of similar age occur within the Stikine and Quesnel terranes, including gold skarns (e.g., Hedley and Quesnel River). The Quesnel terrane also contains Triassic to late Early Jurassic Alaskan-type intrusive complexes with chromite and platinum group element (PGE) mineralisation (e.g., Nixon et al., 1993; Nixon et al., 1997).

2.4. District-scale geology of the Lorraine Deposit

The Quesnel terrane, in the vicinity of the Lorraine Cu-Au deposit, is composed of Takla Group volcanic and sedimentary rocks intruded by Late Triassic to mid-Cretaceous plutons of the Hogem Batholith. The Quesnel terrane is bounded by the Findlay-Ingenika-Pinchi fault system to the west (Fig. 2-4; Garnett, 1978; Schiarizza and Tan, 2005), and to the east by the Manson fault zone (Garnett, 1978; Nixon and Peatfield, 2003; Schiarizza and Tan, 2005).

2.4.1. Takla Group

The Takla Group crops out to the east of Lorraine in the Germansen Landing area (Fig. 2-4), where it was mapped by Ferri et al. (1992; 1993) and Ferri and Melville (1994). The area around Johansen Lake was mapped by Schiarizza and Tan (2005), and to the east and south within the Mount Milligan and Discovery Creek areas by Nelson and Bellefontaine (1996; Fig. 2-4). The Takla Group to the east of the Hogem Batholith has been subdivided into two main successions; (1) a lower primarily sedimentary unit, the Slate Creek succession is characterised by phyllite, argillite, limestone and lesser tuffs, mafic volcanics and coarse epiclastic rocks (Ferri and Melville, 1994) and (2) an upper, arc-proximal volcanic succession, the Plughat Mountain succession, which is characterised by thick sequences of augite-bearing, mafic and intermediate (?) calc-alkaline to alkaline pyroclastic rocks, feldspar-pyroxene-phyric pillow basalt, volcanic sandstone, breccia and local discontinuous units of siltstone and limestone (Ferri and Melville, 1994). The oldest rocks of the Takla Group near Lorraine belong to the Slate Creek succession, and include limestone with Middle to Late Triassic conodonts (Ferri and Melville, 1994; Nelson and Bellefontaine, 1996). Monger (1977) described Late Triassic microfossils from various localities within the siltstone-limestone and sandstone-carbonate subunits of the Plughat

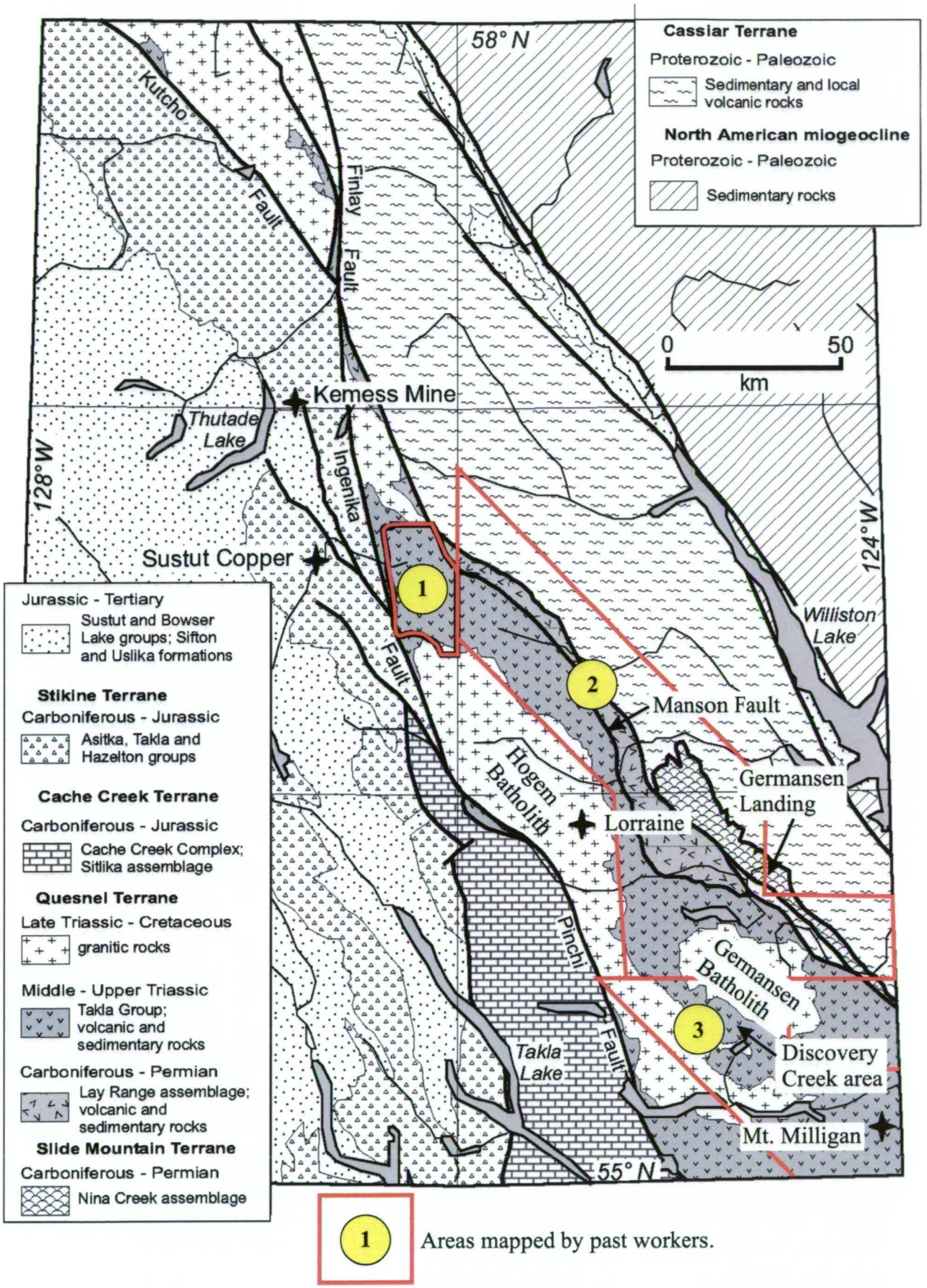

Figure 2-4. Geological setting of the Lorraine and Hogem Batholith area, showing the location of major mineral deposits and lithologies. Areas mapped by previous authors include: (1) Schiarizza and Tan (2005); (2) Ferri et al. (1992; 1993) and Ferri and Melville (1994); (3) Nelson and Bellefontaine (1996). Modified from Schiarizza and Tan (2005).

Mountain succession. Schiarizza and Tan (2005) also reported Late Triassic age conodonts from the lower units of the Plughat Mountain succession.

2.4.2. Hogem Batholith

The Hogem Batholith in the Lorraine area can be divided into five distinct complexes (Fig. 2-5; Nixon and Peatfield, 2003), which in chronological order includes; (1) the Late Triassic (?) to Early Jurassic Hogem granodiorite comprising the central area, (2) a peripheral zone of Late Triassic (?) to Early Jurassic diorite, monzodiorite and quartz monzodiorite of the Thane and Detni plutons, (3) inner subordinate zone of the latest Early Jurassic Duckling Creek Syenite Complex, composed of leucosyenite, syenite, biotite pyroxenite, monzonite and K-feldspar pegmatitic rocks, (4) the localised Early to mid-Cretaceous Osilinka granodiorite and granite and (5) the early to mid-Cretaceous Mesilinka Plutons in the northern area of the Hogem Batholith, which consist of quartz diorite, monzodiorite and granodiorite (Fig. 2-5; Eadie, 1976; Woodsworth, 1976; Garnett, 1978; Woodsworth et al., 1991; Mortensen, 1995; Nixon and Peatfield, 2003). Lorraine is hosted in the Duckling Creek Syenite Complex. Minor alteration and veining also occurs in the older Hogem granodiorite and monzonite (Garratt and Lindinger, 2008).

2.4.2.1. Duckling Creek Syenite Complex

The geology of the Duckling Creek Syenite Complex has been described in a number of reports, maps and publications (e.g., Garnett, 1974; Wilkinson et al., 1976; Garnett, 1978; Bishop et al., 1995; Nixon, 2003; Nixon and Peatfield, 2003; Baxter and Devine, 2007;

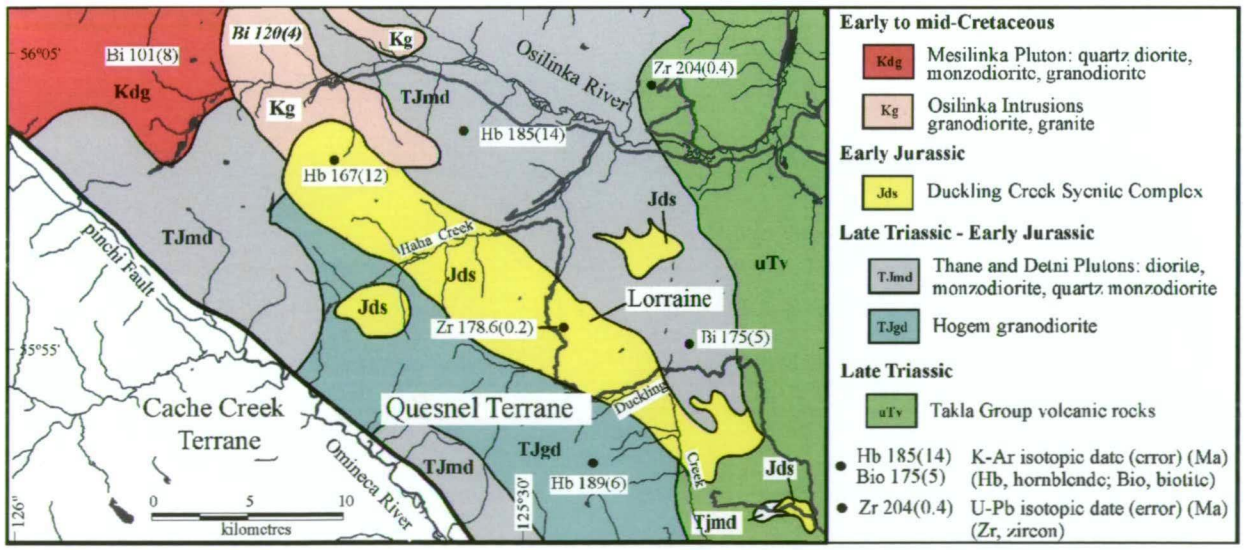

Figure 2-5. Regional geology around the Lorraine deposit, showing the location of published historical K-Ar and U-Pb isotopic ages for the Hogem Batholith. Isotopic data from Eadie (1976), Woodsworth (1976), Garnett (1978), Woodsworth et al. (1991), Mortensen (1995) and *this* study. Modified from Nixon and Peatfield (2003).

Garratt and Lindinger, 2008). Recent detailed mapping on the Lorraine-Jajay and Jan-Tam-Misty properties by Baxter and Devine (2007) and Devine et al. (2007) has significantly revised the geology for the Duckling Creek Syenite Complex in the southern to central area of the complex; however, the content of this map has not been made available to the general public. To the author's knowledge the northern area of the Duckling Creek Syenite Complex has not been mapped in detail; however, earlier work by Garnett (1978) indicates the northern area is dominated by syenite, diorite and other granitic units.

The southern to central area of the Duckling Creek Syenite Complex is composed of seven main lithological units; (1) biotite pyroxenite, (2) syenite, (3) strongly altered rocks of uncertain affinities, (4) mafic megacrystic syenite, (5) leucocratic megacrystic syenite, (6) monzonite and (7) diorite (Fig. 2-6; Devine et al., 2007). These have been grouped into three phases (Devine et al., 2007), based on their relative timing of emplacement with respect to mineralisation and tilting at Lorraine. Phase 1 rocks are the host to main-stage

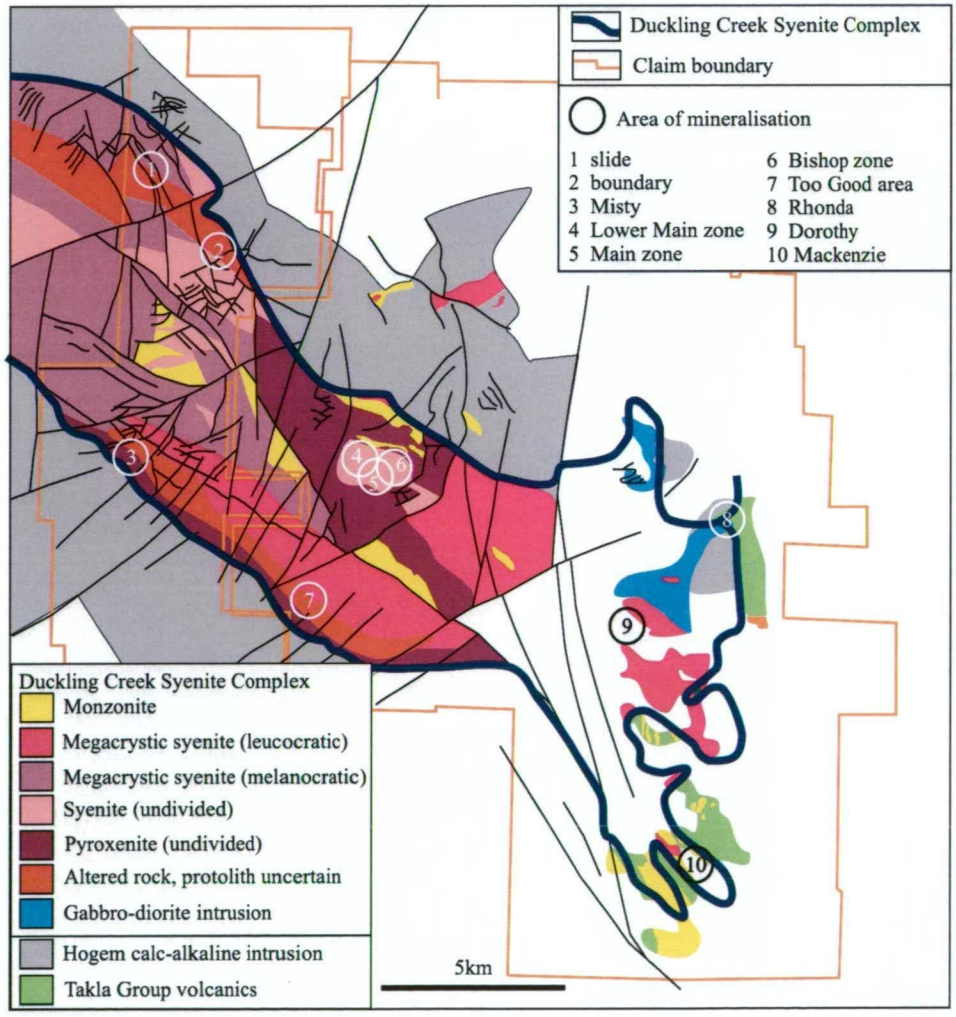

Figure 2-6. Geology of the Duckling Creek Syenite Complex within the Jan-Tam-Misty and Lorraine-Jajay properties. Modified after Garratt and Lindinger (2008).

Table 2-1. Petrographic characteristics of intrusive phases of the Duckling Creek Syenite Complex within the Lorraine area. Intrusives are listed from oldest (bottom) to youngest (top), based on cross-cutting relationships. "Field term" refers to the name assigned to the rock unit based on macroscopic examination of hand specimen and historical names. Following petrographic examination, rocks were classified by modal mineral abundance using the QAP diagram of the IUGS (Le Maitre, 1989).

Map code	Field term	IUGS classification	Texture	Average grain size	Assemblage
DE.?	Plagioclase porphyry monzonite	Plagioclase porphyry monzonite	Porphyritic	Groundmass <0.5 mm, phenocryst 4-6 mm	Euh pl, fine-grained groundmass, anh qz (local)
DL.3	Leucosyenite	Syenite	Equigranular	2-3 mm	Sub Kfd, sub qz, sub pl
DK.3	Kfd-phyric syenite dyke	Kfd megacrysts-biotite syenite	Pegmatitic	1-8 cm	Euh Kfd, booklets of bio
DM.2	Monzonite	Monzonite	Equigranular	2-4 mm	Euh to sub di, interlocking sub Kfd + pl
DCz.2	Kfd megacrystic syenite (leucocratic)	Kfd megacrystic syenite with leucocratic groundmass	Porphyritic	1-3 mm, Kfd phenocrysts 1-7 cm	Euh Kfd / groundmass alkali feldspar
DCm.2	Kfd megacrystic syenite (Melanocratic)	Kfd megacrystic syenite with melanocratic groundmass	Porphyritic	1-3 mm, Kfd phenocrysts 1-7 cm	Euh Kfd, euh di, sub to anh feldspar
DS.2	Syenite	Syenite	Equigranular to porphyritic	1-3 mm (phenocrysts up to 3 cm)	Euh to sub Kfd with anh ab + bio + ap
DP.2	Biotite pyroxenite to feldspathic pyroxenite	Biotite pyroxenite + biotite-diopside syenite	Equigranular to porphyritic	2-3 mm (phenocrysts up to 3 cm)	Euh to sub di, anh bio, euh to sub ap + mt, local euh Kfd phenocrysts, anh pl
DSr.1	Rhythmically layered syenite	Diopside syenite	Layered	<1-2 mm	Sub di, anh Kfd, anh pl, anh bio, sub mt
DS.1	Syenite	Syenite	Equigranular to porphyritic	1-3 mm (phenocrysts up to 3 cm)	Euh to sub Kfd, anh ab + bio, euh to sub ap
DP.1	Biotite pyroxenite to feldspathic pyroxenite	Biotite pyroxenite + diopside-biotite syenite	Equigranular to porphyritic	2-3 mm (phenocrysts up to 3 cm)	Euh to sub di, anh bio, euh to anh mt + ap, anh alkali feldspar + pl (up to 40 %)
DF.1	Fine grained K-feldspar biotite rock	Not primary igneous	Equigranular sugary textured	0.5-1 mm	Sub grey Kfd with anh bio

Abbreviation : ab = albite, act = actinolite, anh= anhedral, ap = apatite, bio = biotite, phlogopite, bn = bornite, chl = chlorite, clz = clinozoisite, cpy = chalcopyrite, di = diopside, ep = epidote, euh = euhedral, fl = fluorite, gn = garnet, grandite, hm = hematite, Kfd = K-feldspar, orthoclase, mal = malachite, mt = magnetite, mus = muscovite, pl = plagioclase, pph = pyrophanite, py = pyrite, qz = quartz, sub = subhedral.

mineralisation and dip moderately towards the southwest. Phase 2 intrusives cross-cut mineralised rocks and have sub-vertical dips. Phase 3 rocks are a minor component of the Duckling Creek Syenite Complex. They have cross-cut Phase 1 and 2 rocks and are inferred to be late relative to main-stage mineralisation (Table 2-1).

2.4.2.2. Mineral deposits of the Duckling Creek Syenite Complex

Ten main mineralised zones have been identified (e.g., Baxter and Devine, 2007; Garratt and Lindinger, 2008) within the southern and central areas of the Duckling Creek Syenite Complex on the Lorraine-Jajay-Jan-Tam-Misty property (e.g., Baxter and Devine, 2007; Garratt and Lindinger, 2008; Fig 2-7). The mineralised zones are spatially associated with areas of strong to intense K-feldspar alteration that predominantly occurs along the margins of the syenite complex (Baxter and Devine, 2007; Garratt and Lindinger, 2008; Fig. 2-7). A number of the mineralised zones within the margins of the Duckling Creek Syenite Complex coincide with areas of strong ductile deformation (e.g., Misty and Boundary

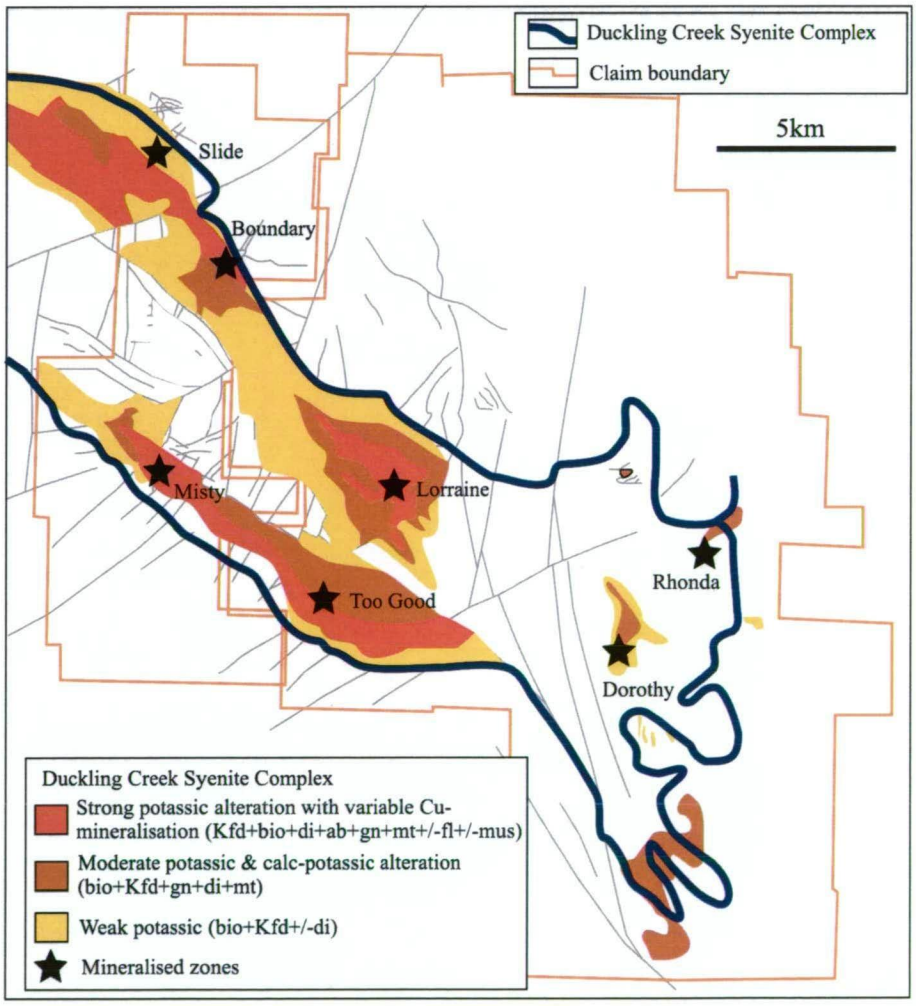

Figure 2-7. General alteration map of the Duckling Creek Syenite Complex in the Jan-Tam-Misty and Lorraine-Jajay areas after Garratt and Lindinger (2008). Abbreviations: ab = albite, bio = biotite, di = diopside, fl = fluorite, gn = garnet, Kfd = K-feldspar, mt = magnetite, mus = muscovite.

areas; Garratt and Lindinger, 2008). In the Misty area, alteration and mineralisation are focused along a ductile deformation zone, where weak to strongly foliated grey K-feldspar ± biotite contains patches of disseminated chalcopyrite and bornite mineralisation (Baxter and Devine, 2007; Garratt and Lindinger, 2008). In other areas, mineralisation occurs in rocks that are not reported to be deformed (e.g., Bishop Zone; Sillitoe, 2007; Garratt and Lindinger, 2008).

2.4.3. Lorraine deposit

The Lorraine deposit is divided into three zones the Bishop, Lower Main and Main zones (Fig. 2-8). They occur along strike over a distance of approximately 1.5 kilometres, contain a measured and inferred resource of ca. 32 million tonnes grading 0.66 wt. % copper and 0.26 g/t gold at a cut-off grade of 0.4 wt. % copper (Table 2-2; based on a resource estimate in 1996 by Lysander Gold Corporation; Nixon and Peatfield, 2003; Garratt and Lindinger, 2008). The Lower Main Zone occurs furthest to the northwest, the Bishop Zone furthest to the southeast and the Main Zone 500 m southeast of the Lower Main Zone (Fig. 2-8). Northeast-trending faults with unknown displacement separate the Bishop Zone from the Main Zone and the Main Zone from the Lower Main Zone (Wilkinson et al., 1976; Bishop et al., 1995).

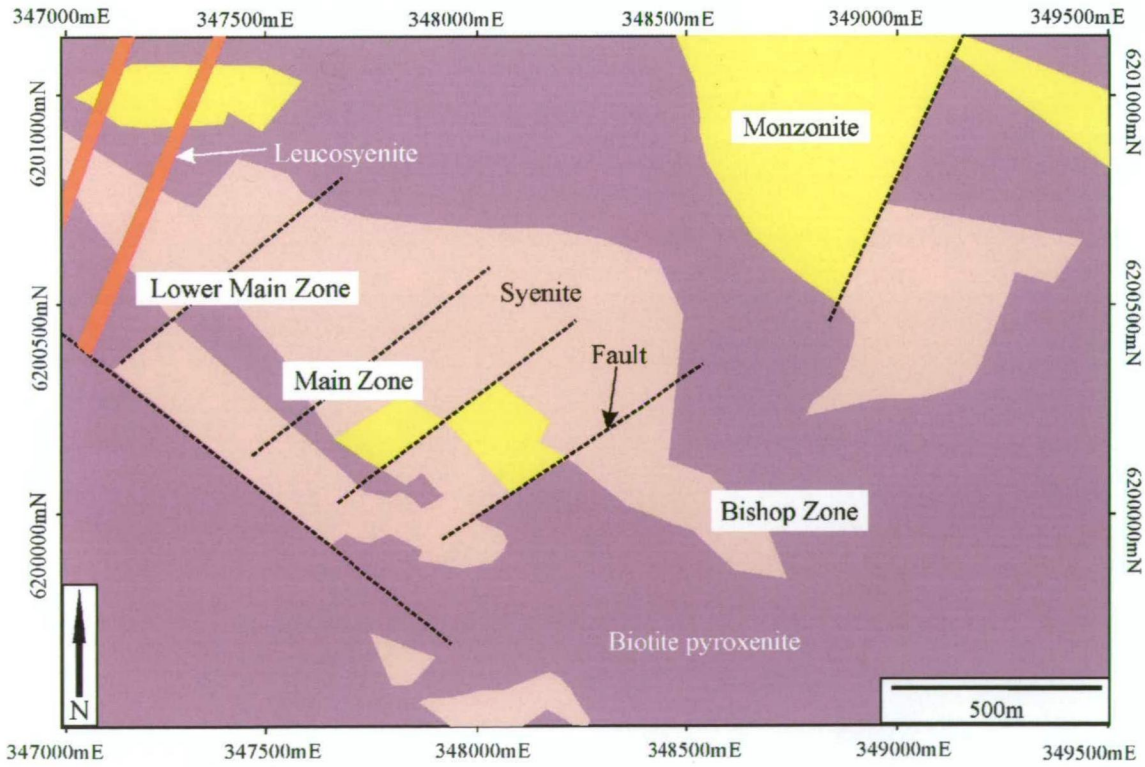

Figure 2-8. Simplified geological map of the Duckling Creek Syenite Complex in the Lorraine area showing the Lower Main Zone, Main Zone and the Bishop Zone (modified from Devine et al., 2007).

Table 2-2. Lorraine resource summary (modified after Garratt and Lindinger, 2008).

Zone	Tonnes (million)	Cu (wt. %)	Au (g/t)
Upper Main (measured and indicated)	11.89	0.71	0.26[a]
Upper Main (inferred)	3.96	0.70	0.25[a]
Bishop (measured and indicated)	7.72	0.64	0.07[a]
Bishop (inferred)	2.87	0.62	0.05[a]
Lower Main (inferred)	5.50	0.60	0.10[a]
Total measured and indicated	19.61	0.68	0.19[a]
Total inferred	12.33	0.63	0.14[a]

[a]gold analyses incomplete

Calculation predates national policy 43-10 implementation and is therefore a "historical estimate". Calculation made by Dr G.R.Peatfield (Garratt and Lindinger, 2008).

The Lower Main, Bishop and Main zones all occupy a northwest-trending corridor dominated by syenite, and are surrounded by biotite pyroxenite (Fig. 2-8). The Early (Phase 1) biotite pyroxenite and syenite have north-westerly trending contacts parallel to the regional trend of the Duckling Creek Complex and Hogem Batholith (Garnett, 1978; Nixon and Peatfield, 2003). Recent work by Teck Ltd. (e.g., Devine et al., 2007) and Sillitoe (2007) suggested that mineralised intrusives are components of a dyke-swarm complex that was tilted following main-stage mineralisation (Fig. 2-9). Phase 1 units at Lorraine are cross-cut by unmineralised sub-vertically dipping Phase 2 biotite pyroxenites, K-feldspar megacrystic syenite, syenite and monzonite dykes, and Phase 3 leucosyenites and K-feldspar pegmatite dykes.

2.5. Summary

The Canadian Cordillera is composed of a collage of accreted terranes; including island arcs, ocean seamounts and accretionary complexes. Most authors agree that by ca. 186 Ma the Quesnel arc terrane had been accreted to the western margin of ancestral North America. Also at this time, ongoing calc-alkaline to alkaline arc-related magmatism is recorded in the Lorraine district of the Quesnel terrane, with emplacement of calc-alkaline to high-K intrusives of the Hogem Batholith, which included;

- Late Triassic? to Early Jurassic Hogem granodiorite: calc-alkaline granodiorite (189 ± 6 Ma; hornblende K-Ar cooling age).
- Late Triassic? to Early Jurassic Thane and Detni Plutons: calc-alkaline to high-K diorite and monzodiorite (185 ± 14 Ma hornblende K-Ar cooling age).

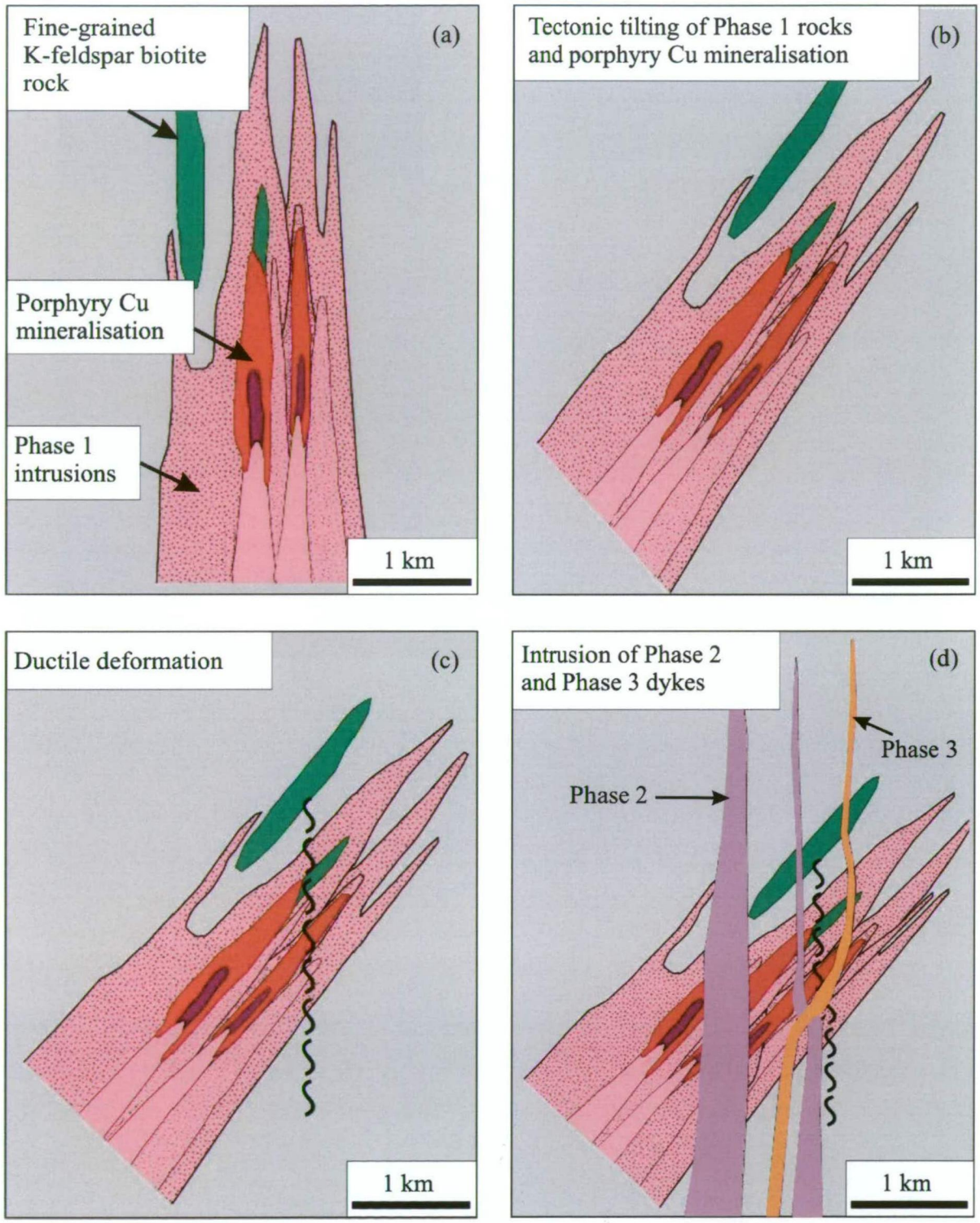

Figure 2-9. An interpretation of geological events at Lorraine as suggested by Sillitoe (2007) and Garratt and Lindinger (2008). **(a)** Emplacement of porphyry Cu-Au mineralisation in a dyke swarm complex of pyroxenite through to syenite, followed by **(b)** tilting of porphyry mineralisation and early Phase 1 dykes. **(c)** Localised ductile shearing, and **(d)** intrusion of late Phase 2 and 3 alkaline pyroxenite to leucosyenite dykes. Grey area represents older wall rocks (undivided) of the Hogem Batholith. Modified from Garratt and Lindinger (2008).

Following accretion of the Quesnel terrane to ancestral North America, and early calc-alkaline magmatism there was a pulse of 'shoshonitic' arc-related magmatism at Lorraine, which resulted in the formation of;

- latest Early Jurassic Duckling Creek Syenite Complex: shoshonitic biotite pyroxenite, monzonite and syenite (ca. 179 Ma; zircon U-Pb).

Accompanying this pulse of shoshonitic magmatism was the formation of the Lorraine porphyry Cu-Au deposit within the Duckling Creek Syenite Complex. Following deposition, but prior to cessation of shoshonitic magmatism, the Lorraine porphyry Cu-Au deposit (i.e. Lower Main, Main and Bishop zones) was tilted, locally deformed (Main and Lower Main zones only) and intruded by post main-stage dykes (Sillitoe, 2007; Garratt and Lindinger, 2008).

CHAPTER 3
GEOLOGY AND GEOCHRONOLOGY OF THE LOWER MAIN ZONE

3.1 Introduction

In this chapter the geology of the Lower Main Zone is described with the aims of documenting the geological environment in which the ore body formed. Much of the interpretation of the geological framework reported in this chapter was influenced by the work of Teck Ltd geologists on the property-scale features on the Lorraine-Jajay-Jan-Tam-Misty area (Devine et al., 2007; Chapter 2).

To establish the timing of mineralisation and intrusive events in the Lower Main Zone, the current study determined the absolute crystallisation dates of rocks by conventional Isotope Dilution Thermal Ionisation Mass Spectrometer (ID-TIMS) and Sensitive High Resolution Ion Micro Probe – Reverse Geometry (SHRIMP-RG) analyses. These new dates constrain the absolute timing of various magmatic pulses, mineralisation, tilting and deformation in the Lower Main Zone.

3.1.1. Methods: mapping, core logging and presentation of data

Bedrock mapping of the Lower Main Zone was carried out at 1:1000 scale and in more detailed (1:500 scale) in complex areas. Maps were constructed using the "Anaconda" method with five layers of transparent mylar over an 8.5" x 11" black and white orthophoto base. The mylar overlays were used to record lithology, structure, alteration, mineralisation and veining.

Detailed graphic core logging was carried out at the 1:250 scale and includes columns showing grain size, graphic illustrations of lithology and structures, abundance of various mineral types, mineralisation and written descriptions (Appendix I). Individual core logs were compiled onto 1:1000 scale interpretative cross-sections. For the purpose of this compilation, maps and cross-sections were reduced to approximately 1:3000 and 1:3500 scales to fit on A3 and A4 pages respectively. Co-ordinates provided in the current study are North American Datum 1983 (NAD 83), Universal Transverse Mercator Zone 10, and altitudes are in metres above mean sea level.

3.1.2. Nomenclature

The Lorraine deposit is hosted by a number of different rock types, most of which have been interpreted as intrusives, with the exception of fine-grained K-feldspar biotite rocks

which are thought to be metasomatised felsic wall rocks. Intrusive rocks at Lorraine are referred to as pyroxenite, syenite and monzonite (e.g., Bishop et al., 1995; Nixon and Peatfield, 2003). According to the IUGS classification system, a pyroxenite is a plutonic rock with M (primary: micas, amphiboles, pyroxenes, olivines, opaque minerals, epidote, garnet and carbonates) equal or greater than 90 and ol/(ol+opx+cpx) less than 40 (Neuendorf et al., 2005). At Lorraine rocks referred to as biotite pyroxenite commonly include 40-60 % diopside and 35-45 % biotite, but contain no olivine. However, individual outcrops of biotite pyroxenite can show lateral variations in modal abundance of alkali feldspar, and as noted by Nixon and Peatfield (2003) "*difficulties arise in the rigorous application of this nomenclature to pyroxenite.*" In this study the author uses the term feldspathic pyroxenite for pyroxenites which have variations in alkali feldspar abundance from greater than 10 % and locally up to 40%.

Monzonite and syenite at Lorraine have mineral compositions which can be classified using the IUGS system; although in some cases, rocks that have been inferred to be syenite have undergone pervasive K-feldspar alteration, which makes determination of the igneous protolith ambiguous. CIPW normative compositions (wt. %) were calculated using the IGPET 2005 software program (assuming a $Fe^{3+}/(Fe^{3+}+ Fe^{2+})$ ratio of 0.15). Normative calculations indicate that most felsic intrusive rocks of the Lower Main Zone are nepheline normative, and hence syenites plot in the foid-bearing syenite to foid-bearing monzonite fields, whereas monzonite plots in the foid-bearing monzonite to foid-bearing monzodiorite fields (Fig. 3-1a-b).

According to Streckeisen (1976), plutonic rocks should be formally classified based on actual mineral estimates. Detailed work using the scanning electron microscope (SEM) failed to identify nepheline or other feldspathoidal phases in monzonite or syenite, and point counting using the energy dispersive spectrometers (EDS)-SEM showed that actual alkali feldspar to plagioclase ratios were higher than the calculated CIPW normative compositions have predicted. The high CIPW nepheline normative composition of Lorraine rocks likely reflects the fact that normative calculations will underestimate biotite, which has low SiO_2 compared to pyroxene and K-feldspar. Thus unaltered intrusive rocks from Lorraine have been classified using field and EDS-SEM determined mineral modal estimates as opposed to the CIPW method.

3.2. Geology of the Lorraine Deposit

The Lower Main, Bishop and Main zones all occur in a northwest-trending corridor dominated by syenite. The mineralised corridor is surrounded by biotite pyroxenite (Fig. 2-8). Pre-mineralisation biotite pyroxenite and syenite dykes have north-westerly trending contacts parallel to the regional trend of the Duckling Creek Complex and Hogem

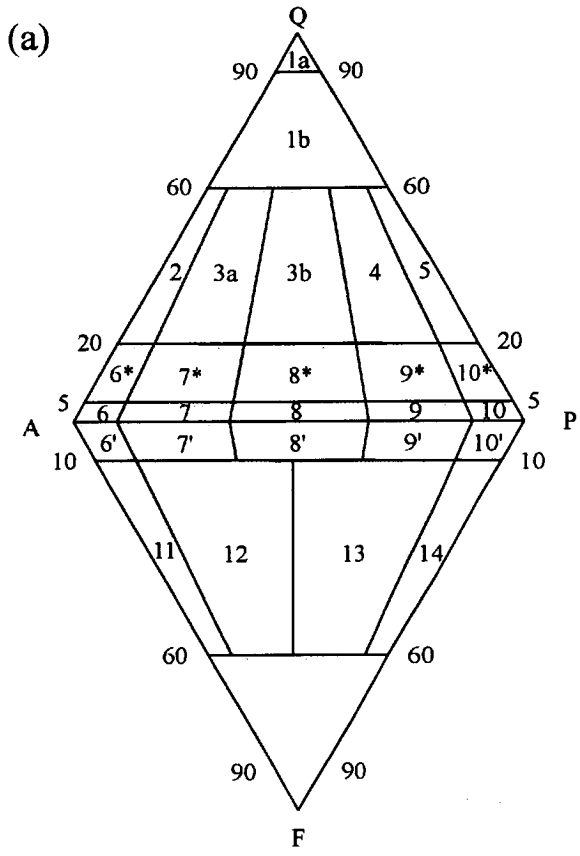

1a quartzolite
1b quartzrich granitoids
2 alkali feldspar granite
3a syenogranite
3b monzogranite
4 granodiorite
5 tonalite
6* quartz alkali feldspar syenite
7* quartz syenite
8* quartz monzonite
9* quartz monzodiorite
10* quartz diorite
6 alkali feldspar syenite
7 syenite
8 monzonite
9 monzodionite
10 diorite
6' foid-bearing alkali feldspar syenite
7' foid-bearing syenite
8' foid-bearing monzonite
9' foid-bearing monzodiorite
10' foid-bearing diorite
11 foid syenite
12 foid monzosyenite
13 foid monzodiorite
14 foid diorite

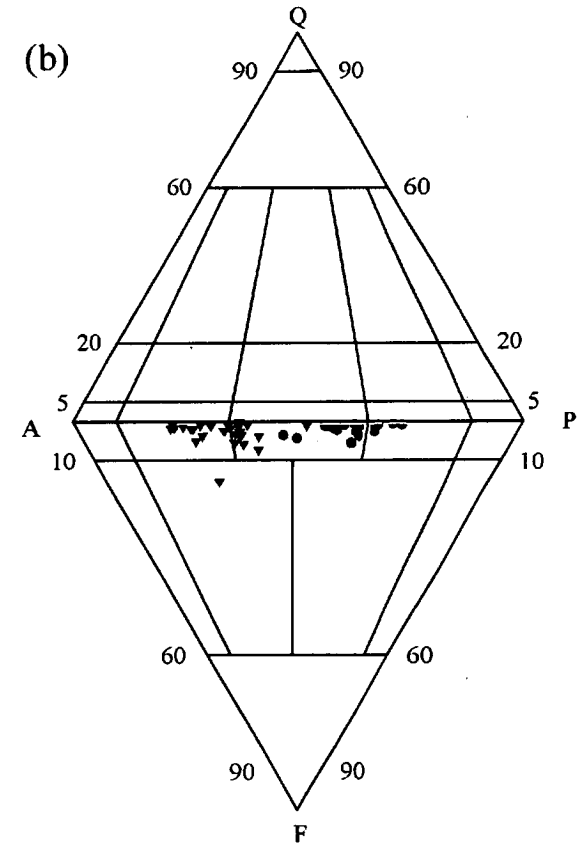

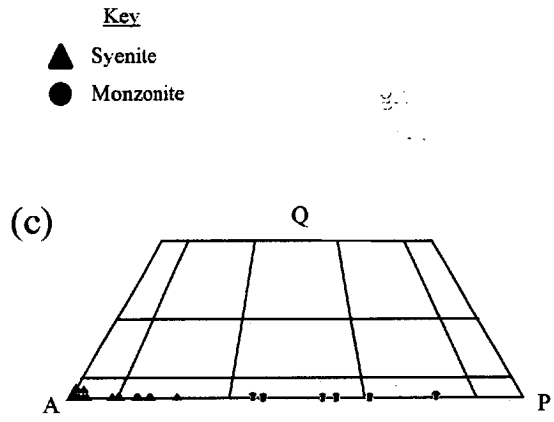

Figure 3-1. **(a)** IUGS classification of plutonic rocks of Le Maitre (1989). **(b)** Classification of syenites and monzonites from the Lorraine deposit based on CIPW normative compositions (includes whole rock data from this study and Nixon and Peatfield 2003). **(c)** Classification of syenite and monzonite from the Lorraine deposit based on EDS-SEM point counting method (*see* text).

Batholith (Garnett, 1978; Nixon and Peatfield, 2003). Recent work by Teck Ltd and Sillitoe (2007) proposes that mineralised intrusives are components of a dyke-swarm complex, which was tilted some time after main-stage mineralisation. Devine et al. (2007) referred to the tilted intrusives as Phase 1, which includes biotite pyroxenite, feldspathic pyroxenite and syenites in the Lorraine area. The tilted and mineralised (in parts of the Lower Main Zone) Phase 1 dykes are cross-cut by unmineralised sub-vertical Phase 2 biotite pyroxenite, feldspathic pyroxenite, syenite, monzonite and Phase 3 leucosyenite and coarse-grained K-feldspar dykes (Devine et al., 2007). Hence Phase 1 dykes are pre-mineralisation, whereas Phase 2 and 3 intrusives are post-mineralisation. The classification system devised by Devine et al. (2007) is adopted in the current study. In addition, the current study describes rhythmic layered diopside syenite dykes of the Lower Main Zone and the fine-grained biotite K-feldspar rocks, which are inferred to represent altered wall rocks that pre-date Phase 1 dykes.

3.3. Geology of the Lower Main Zone

The Lower Main Zone crops out on the western side of Lorraine peak over an area of approximately 500 m x 500 m (Figs. 3-2 and 3-3). Basement rocks predominantly crop out along narrow tracks and escarpments in the northern part of the Lower Main Zone. Syenite and fine-grained K-feldspar biotite rock are predominant in the southern and central areas, and pyroxenite and monzonite are abundant in the north and north-central areas.

Figure 3-2. Photo of the southern slope of the Lower Main Zone taken from Ekland Ridge (looking northwards). Dotted white line is an approximate outline of the mapped area of the Lower Main Zone (Fig. 3-3), and white dashed lines highlights the late north-northeast trending faults that cut the Main Zone.

→

Figure 3-3. Interpretive geological map of the Lower Main Zone based on 1:1000 scale mapping conducted during the current study.

Combined outcrop and interpretation geological map of the Lower Main Zone

Mapping by Adam B. Bath

0 50 100
metres

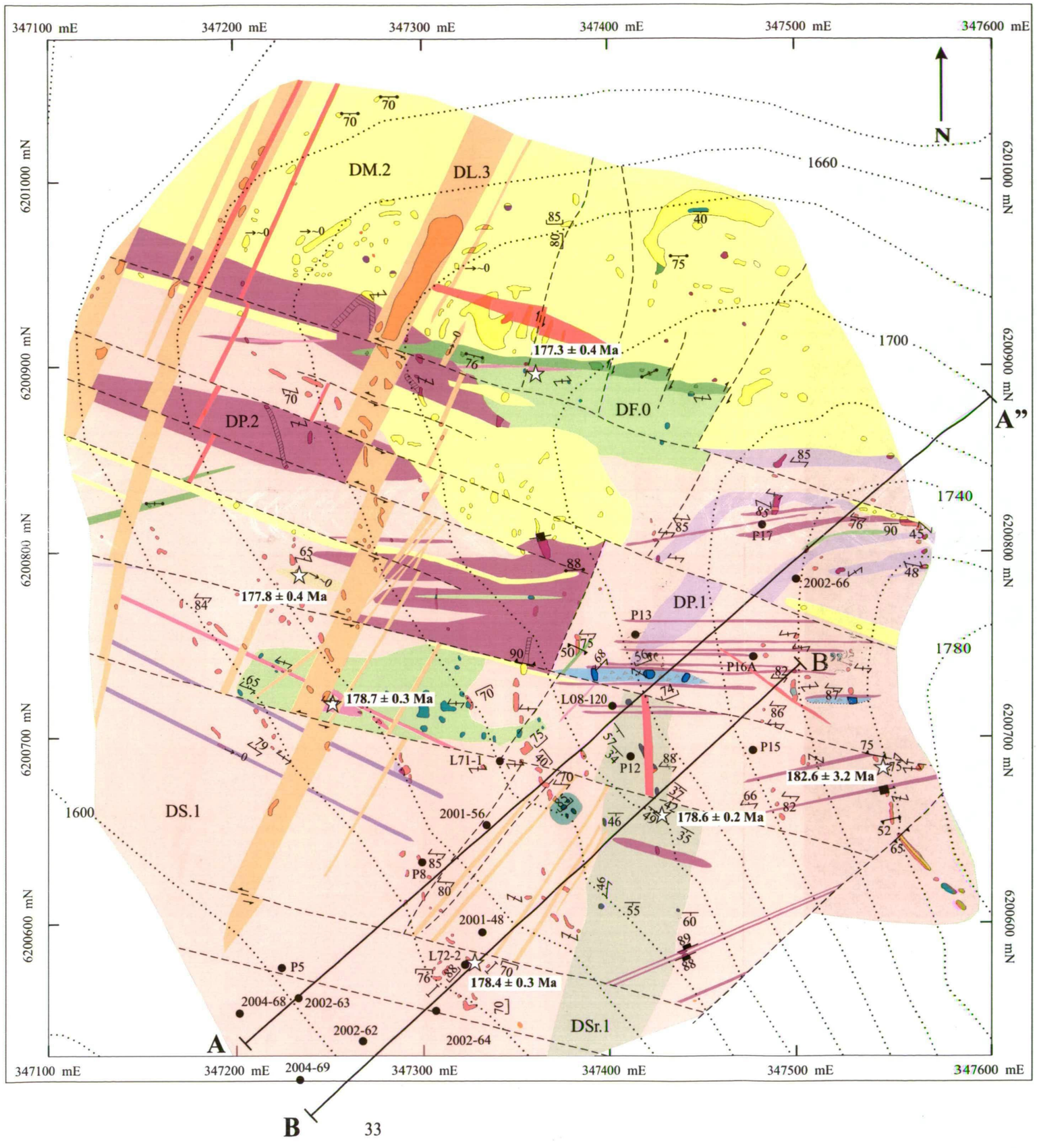

Legend

Outcrop / interpretation

DE.2 Plagioclase porphyry monzonite with aphanitic to fine-grained groundmass. Plagioclase phenocrysts 1 to 4 mm in size

Phase 3 (Late relative to main-stage mineralisation : latest Early Jurassic)

DL.3 Leucosyenite dyke. Ranges from quartz phyric with fine-grained sugary K-feldspar groundmass to fine grained sugary texture

DK.3 Coarse-grained K-feldspar syenite dykes. K-feldspar typically 1 to 5 cm in size

Phase 2 (Post main-stage mineralisation : latest Early Jurassic)

DM.2 Monzonite with medium grained equal granular plagioclase and K-feldspar. Mafics dominated by diopside with subordinate hornblende and biotite

DS.2 K-feldspar phyric syenite dyke, K-feldspar <2cm and K-feldspar is commonly aligned parallel to dyke margins

DCz.2 K-feldspar-phyric syenite. Phenocrysts up to 6 cm long, euhedral and zoned. Groundmass comprises medium grained euhedral medium grained clinopyroxene. Flow foliated

DSk.2 K-feldspar phyric flow foliated syenite porphyry with medium-grained diopside + feldspar groundmass

DPk.2 K-feldspar phyric feldspathic pyroxenite. K-feldspar phenocrysts range from 1cm to 3cm and are aligned sub-parallel to dyke margins. Flow foliated

DPp.2 Pseudoleucite feldspathic pyroxenite. Euhedral to subhedral pseudoleucite (up to 3cm). Euhedral to subhedral diopside with biotite, feldspar, apatite and magnetite

DP.2 Biotite pyroxenite to feldspathic pyroxenite. Euhedral to subhedral diopside (1-8mm) with biotite, feldspar, apatite and magnetite

Phase 1 (Host rocks to mineralisation : latest Early Jurassic)

DB.1 Polymictic K-feldspar-magnetite-diopside-Cu-Fe sulphide cement breccia and K-feldspar-magnetite-diopside-Cu-Fe sulphide rock

DSr.1 Fine- to medium-grained rhythmically layered syenite. Layering ranges from 1mm to 3cm and is inferred to be primary igneous layering

DS.1 Syenite (undivided) fine to medium grained K-feldspar with variable amounts of anhedral biotite and subhedral diopside

DP.1 Biotite pyroxenite and feldspathic pyroxenite. Euhedral to subhedral diopside (1-8mm) with biotite, feldspar, apatite and magnetite

Altered wall rocks inferred to pre-date Phase 1 intrusives

DF.0 Fine-grained K-feldspar biotite rock. Local textural variations range from layered to massive

Structural symbols

- Lithological contact, measured
- Subvertical lithological contact, measured
- Subvertical lithological contact inferred
- Primary igneous layering
- Tabular mineral trend
- Primary igneous foliation (alignment of di or Kfd)
- Solid-state deformation fabric (alignment of bio)
- Joint
- Fault movement
- Fault observed

Line and symbol types

- Fault, inferred
- Contour
- Drill hole location

Lithology symbols

- Outcrop
- Subcrop

Geochronology

☆ Locations for zircon U-Pb geochronology carried out in this study using ID-TIMS or SHRIMP-RG (*see* text)

Figure 3-3

One of the difficulties with mapping and core logging in the Lower Main Zone is that Phase 1 biotite pyroxeite, feldspathic pyroxenite and syenite are not always distinguishable from their Phase 2 equivalent. This is a problem in areas where contacts and cross-cutting relationships cannot be established, and in areas where rocks are not mineralised. In a number of cases interpretations on the distribution of Phase 1 and 2 rocks has been made based on extrapolation between well constrained areas into areas where rocks are poorly constrained. Due to the similarities between Phase 1 biotite pyroxenite, feldspathic pyroxenite and syenite and their Phase 2 equivalent, the author has decided to describe the main characteristics of these rocks together in this chapter. This is to avoid redundancy. The reader is referred to Chapters 4 and 5 for detailed descriptions of alteration and mineralisation of Phase 1 rocks.

3.3.1. Fine-grained K-feldspar biotite rocks (pre-mineralisation)

Fine-grained K-feldspar biotite rocks crop out in the central and northern areas of the Lower Main Zone (Fig. 3-3). They also occur as relic (?) lensoidal to irregular-shaped bodies that are cross-cut by Phase 1 biotite pyroxenite and syenite, and by Phase 2 and 3 rocks (Figs. 3-3 and 3-4a, b). Fine-grained K-feldspar biotite rocks are mineralised and have a strong sub-vertically dipping east-trending foliation defined by the alignment of biotite in the central area of the Lower Main Zone (Figs. 3-5a-d). In this area, they have been intruded by medium grained mineralised syenite dyklets which appear to have exploited the pre-existing deformation fabric (*see* below; Figs. 3-5a). However in some areas K-feldspar veins (or neosomes?) are folded (Fig. 3-5c), and it is inferred that early veins and/or neosomes pre-date or are synchronous with the foliation.

3.3.1.1. Petrographic description of fine-grained K-feldspar biotite rocks

Fine-grained K-feldspar biotite rocks are characterised by subhedral to anhedral alkali feldspar with anhedral biotite, magnetite and clinopyroxene (Fig. 3-5d-g). K-feldspar is the dominant alkali feldspar (35 to 75 %) and is fine-grained (0.5-1 mm), light translucent grey to pink coloured and contains inclusions of biotite and clinopyroxene (<50 μm in size). Strained K-feldspar crystals show strong to moderate undulatory extinction (Fig. 3-5g), others had tartan twinning and are microcline. Simple twining in K-feldspar was also observed in some samples, indicating the presence of orthoclase. Plagioclase (1 to 20 %) is fine-grained (<0.8 mm) and translucent light grey to white, whereas biotite (10 to 35 %), is fine-grained (0.3-1 mm), subhedral, dark brown, bladed, shows undulatory extinction (Fig. 3-5g), and is fluorine-rich (up to 3.2 wt. % F, Chapter 6). Some biotites

Figure 3-4. **(a)** Geological cross-section A-A' of the Lower Main Zone. **(b)** Geological cross-section B-B' of the Lower Main Zone. See Figure 3-3 for legend and location of cross-sections.

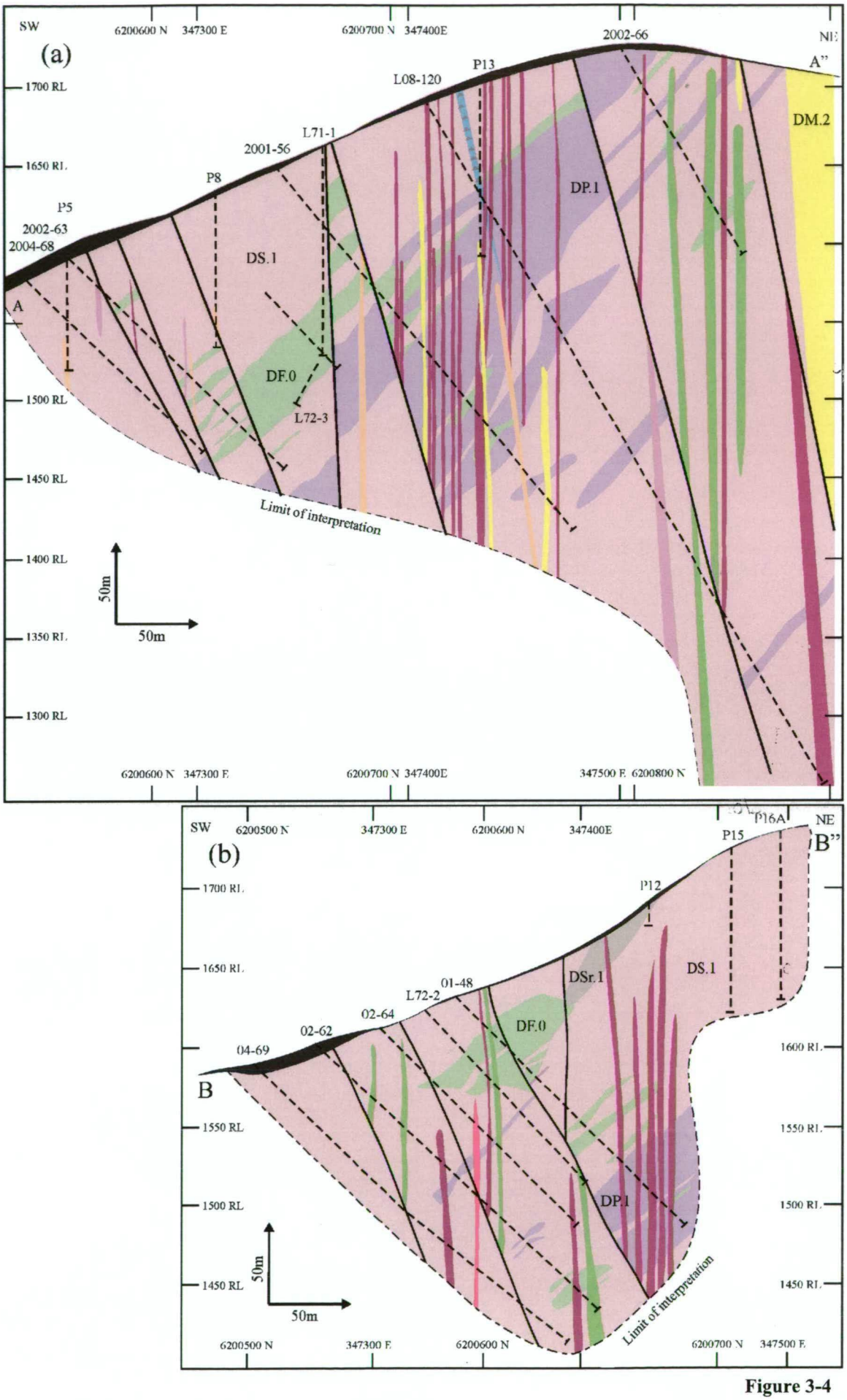
SW
(a)
6200600 N 347300 E
6200700 N 347400E
2002-66
NE
A"
P13
L08-120
L71-1
2001-56
P8
P5
2002-63
2004-68
A
DS.1
DF.0
L72-3
DP.1
DM.2
1700 RL
1650 RL
1500 RL
1450 RL
1400 RL
1350 RL
1300 RL
Limit of interpretation
50m
50m
6200600 N 347300 E
6200700 N 347400E
347500 E 6200800 N
SW
(b)
6200500 N
347300 E
6200600 N
347400E
P16A
NE
B"
P15
P12
1700 RL
1650 RL
1550 RL
1500 RL
1450 RL
1600 RL
01-48
L72-2
02-64
02-62
04-69
B
DSr.1
DS.1
DF.0
DP.1
50m
50m
Limit of interpretation
6200500 N
347300 E
6200600 N
6200700 N
347500 E

Figure 3-4

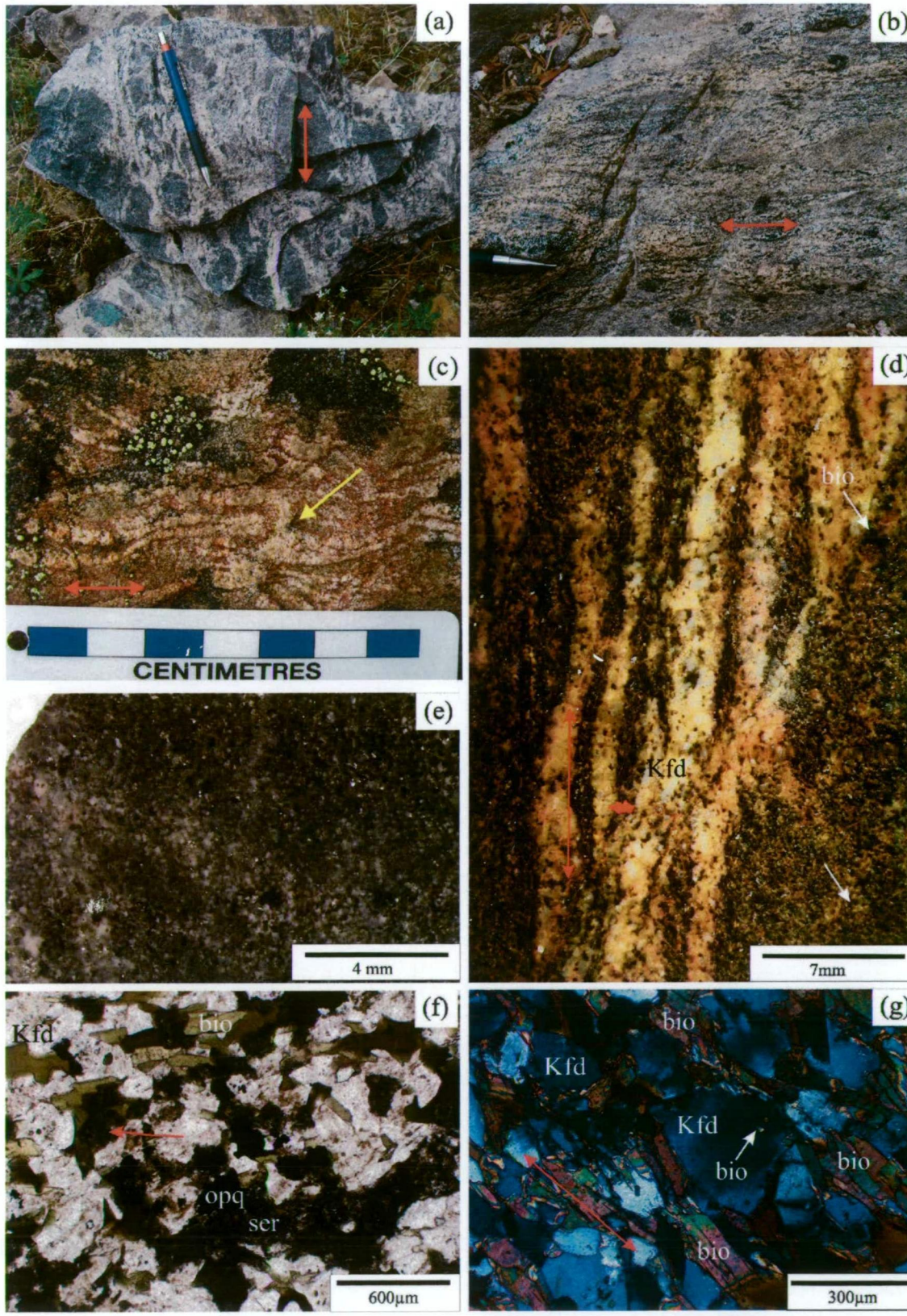

Figure 3-5. Examples of fine-grained K-feldspar biotite rocks from the Lower Main Zone. **(a)** Syenite that has intruded foliated fine-grained K-feldspar biotite rock. Malachite staining (bottom left of photo) is related to abundant disseminated bornite and chalcopyrite in biotite-rich wall rocks (07AB14-2; 347325mE, 6200720mN). **(b)** Strongly banded fine-grained K-feldspar biotite rock with aligned sub-parallel neosomes (?) oriented 080/75S in the central area of the Lower Main Zone (347360mE, 6200693mN). **(c)** Folded K-feldspars veins (or neosomes?) in foliated fine-grained K-feldspar biotite rocks in the central area of the

Figure 3-5. ***continued***
Lower Main Zone (07AB-40; 347295mE, 6200720mN). **(d)** Sample from the central area of the Lower Main Zone. The rock has a strong E-striking sub-vertical foliation defined by the alignment of biotite and K-feldspar bands (parallel to red arrow; sample 07AB-40; 347295mE, 6200720mN). **(e)** Sample from the northern area of the Lower Main Zone with fine-grained disseminated sulphides (drill hole 2002-66_30.4m). **(f)** Photomicrograph (in plane-polarised light), of fine-grained K-feldspar biotite rock showing anhedral K-feldspar, anhedral biotite and opaques. The rock also contains sericite-altered biotite and clinopyroxene. The red arrow indicates a pseudomorph of clinopyroxene. Sericite patches occur with opaque phases magnetite and chalcopyrite (drill hole 2001-56_88.8m). **(g)** Foliated fine-grained K-feldspar biotite rock from the central area of the Lower Main Zone (cross-polarised light). Photomicrograph shows unaltered K-feldspar with biotite inclusions, and larger aligned biotite crystals. Biotite and K-feldspar both show undulatory extinction consistent with deformation (sample 07AB-40; 347295mE, 6200720mN; also see Fig. 3-6a). Mineral abbreviations: bio = biotite, di = diopside, Kfd = K-feldspar, mt = magnetite and opq = opaque.

are unaltered; others are pervasively replaced by sericite, muscovite, chlorite, titanite, Cu-Fe sulphides, quartz and/or pyrite (Chapters 4 and 5). Fine-grained K-feldspar biotite rocks include accessory apatite (<0.1-1 %), titanite (<0.1-1 %) zircon (trace), and opaque phases (<0.1-3 %). Opaque phases include fine-grained magnetite (0-0.2 %), pyrite (0-2.5 %), chalcopyrite (0-1.5 %) and bornite (0-0.1 %).

3.3.2. Biotite pyroxenite and feldspathic pyroxenite (pre-mineralisation phase 1 and post-mineralisation phase 2)

Biotite pyroxenite and feldspathic pyroxenites are abundant in the Lower Main Zone, occurring as <1 to ~10 m thick bodies which strike east to southeast (Figs. 3-3 and 3-4a, b). Lensoidal bodies and dykes of biotite pyroxenite and feldspathic pyroxenite are sub-vertical (Phase 2; Fig. 3-6) or dip moderately towards the south-southwest (Phase 1; Fig. 3-7a, b). Phase 1 biotite pyroxenites pre-date mineralisation and have been intruded by, and have irregular southward-dipping contacts with, Phase 1 syenite. Phase 1 biotite pyroxenite also occurs as xenoliths in mineralized and barren Phase 1 syenite (Fig. 3-7c, d).

Phase 2 biotite pyroxenites post-date mineralisation, crop out primarily in the north-central and north-western areas of the Lower Main Zone and have sub-vertical east-trending contacts with Phase 1 rocks. In at least one location in the western part of the Lower Main Zone an east-trending sub-vertical dipping Phase 2 K-feldspar-phyric feldspathic pyroxenite cross-cuts Phase 1 foliated syenite (Fig. 3-6). At this location the Phase 2 pyroxenite dyke is sub-parallel to the prominent sub vertical E-trending foliation in the Phase 1 syenite (Fig. 3-6).

3.3.2.1. Petrographic descriptions of biotite pyroxenites

Biotite pyroxenites (phases 1 and 2) are characterised by euhedral to subhedral green diopside (40-60%) with anhedral biotite (35-45 %), anhedral K-feldspar (1-5 %), anhedral pla-

Figure 3-6. Biotite-banded foliated syenite intruded by undeformed feldspathic pyroxenite (locally K-feldspar phyric) in the east-central area of the Lower Main Zone (347508mE, 6200733mN). Note that blue eraser pen is used as scale and is approximately 13cm long.

gioclase (albite to andesine, 1-5 %), accessory apatite (1-3 %) and magnetite (1-3 %; Figs. 3-8a, b and 3-9a-d). Diopside is unaltered, weakly pleochroic, shows exsolution lamellae, has sharp extinction angles and has spherical or euhedral inclusions of magnetite and apatite (Fig. 3-9a-d). In some samples diopside crystals are aligned (red arrow, Fig. 3-8a), which is inferred to represent a primary igneous flow foliation as opposed to solid-state deformation (*see* below). Anhedral biotite grains are unaltered and have straight or undulatory extinction. They are intergrown with magnetite and have small (50-100 μm) inclusions of apatite and magnetite (Fig. 3-9a, c). Anhedral feldspar has simple twinning in places, and comprises both albite and K-feldspar. Based on petrographic observations, the crystallisation sequence of biotite pyroxenite is (from oldest to youngest); (1) euhedral to subhedral diopside with magnetite and apatite and (2) anhedral biotite with feldspar, apatite and magnetite.

3.3.2.2. Petrographic description of feldspathic pyroxenite

Feldspathic pyroxenite can be divided into four types based on textures and mineralogy. These are: (1) biotite-phyric feldspathic pyroxenite (phase 1 and 2; Fig. 3-8c, d), (2) eqigranular feldspathic pyroxenite (phase 1 and 2), (3) pseudoleucite-bearing feldspathic pyroxenite (Phase 2?; Fig. 3-10a) and (4) K-feldspar-phyric feldspathic pyroxenite (Phase 2; Fig. 3-10b). Pseudoleucite-bearing feldspathic pyroxenites crop out in only one part of the Lower Main Zone (Fig. 3-3). Phase 2 K-feldspar-phyric feldspathic pyroxenites were

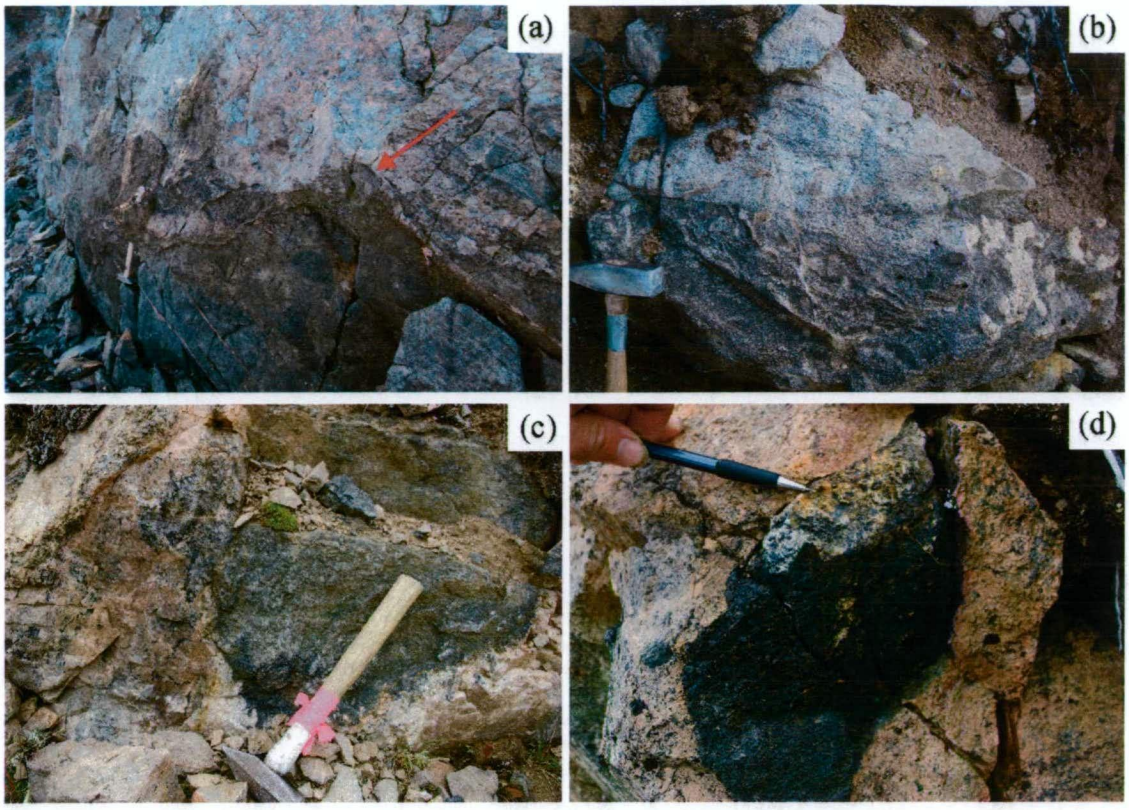

Figure 3-7. Cross-cutting relationships between Phase 1 biotite pyroxenite and Phase 1 syenite in the Lower Main Zone. **(a)** Contact between Phase 1 biotite pyroxenite and Phase 1 syenite along the northern slope of the Lorraine peak. The contact between the two units (red arrow) is irregular and dips moderately towards the south (347568mE, 6200794mN). **(b)** Contact between Phase 1 feldspathic pyroxenite and Phase 1 syenite, with anatomising dyklets of syenite that have intruded the biotite pyroxenite (347355mE, 6200711mN). **(c-d)** Xenoliths of Phase 1 biotite pyroxenite in a foliated (defined by biotite-bands) Phase 1 syenite. Foliation is locally overprinted by strong salmon pink fabric destructive K-feldspar alteration (347528mE, 6200735mN).

mostly observed in the northern area of the Lower Main Zone (Fig. 3-3). Hence, pseudoleucite-bearing and K-feldspar-phyric pyroxenites are only minor components of the Lower Main Zone. They are not host rocks to mineralisation, and for these reasons they are not described in detail in the current study. However, K-feldspar-phyric feldspathic pyroxenite commonly contain aligned K-feldspar phenocrysts (Fig. 3-10b), which are parallel to intrusive contacts. These aligned phenocrysts are inferred to be a primary igneous flow foliation (*see* below).

Biotite-phyric feldspathic pyroxenite comprise fine- to medium-grained euhedral diopside (40-60 %), coarse-grained anhedral biotite (up to 4mm), fine- to medium-grained anhedral K-feldspar and coarse-grained oikocrysts of K-feldspar (10-30 %), fine-grained anhedral plagioclase (1-8 %, albite to andesine) and fine-grained accessory magnetite and apatite (Fig. 3-11a-d). Phase 1 biotite-phyric feldspathic pyroxenites also contain Cu-Fe sulphides (*see* Chapter 5). Diopside is subhedral to euhedral and pleochroic, which varies from green to bluish-green, and likely reflects Fe-rich diopside compositions (e.g., Deer et al.,

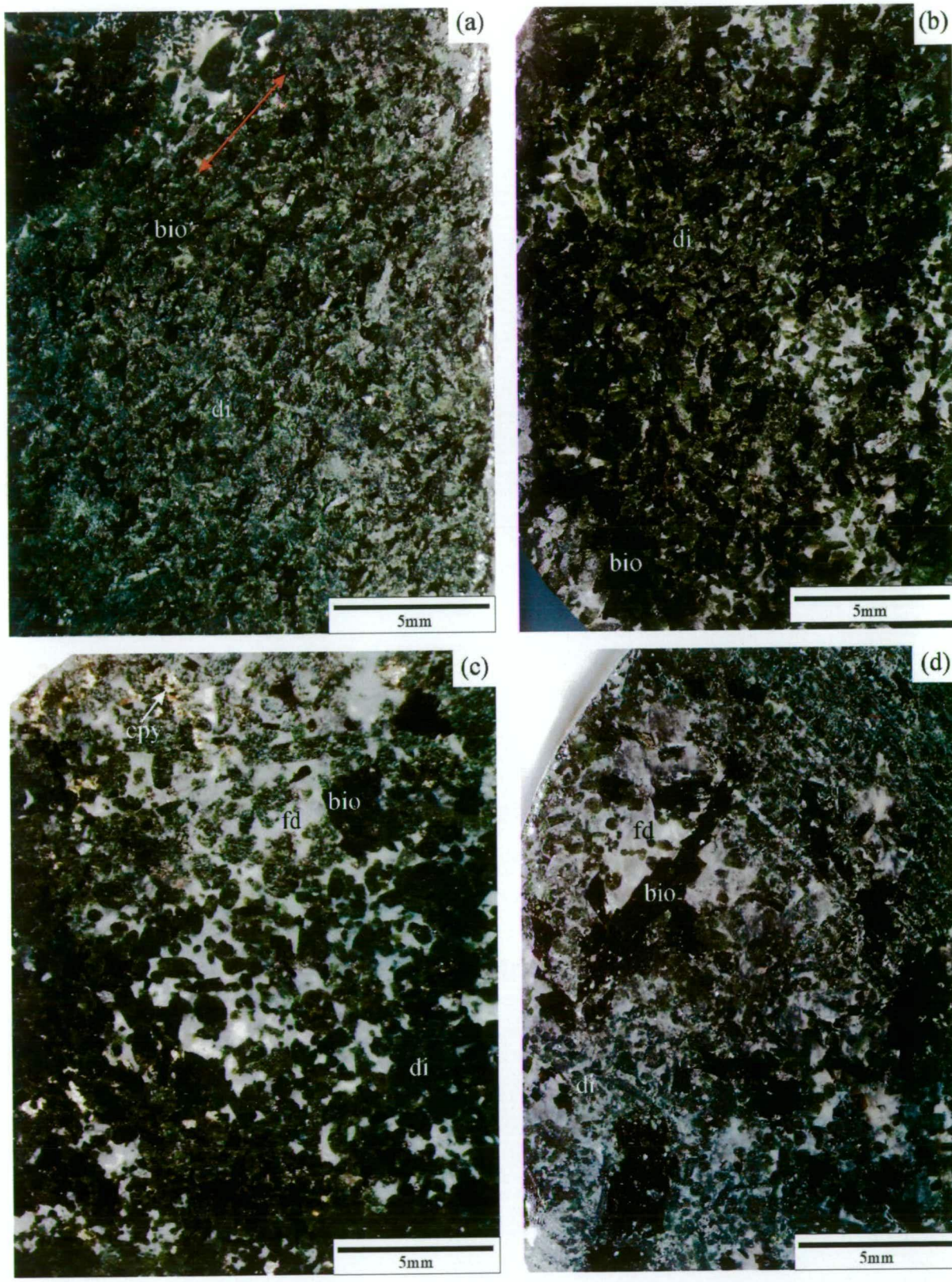

Figure 3-8. Samples of biotite pyroxenite and feldspathic pyroxenite from the Lower Main Zone. **(a)** Phase 2 biotite pyroxenite with aligned (red arrows) diopside crystals (drill hole 2001-48_195m). **(b)** Phase 2 biotite pyroxenite with local patches of anhedral feldspar (drill hole 2001-56_283m). **(c)** Biotite-phyric feldspathic pyroxenite from the Lower Main Zone (chalcopyrite mineralised; drill hole 2001-56_157 m). **(d)** Phase 2 biotite-phyric feldspathic pyroxenite from the Lower Main Zone (drill hole 2001-56_184m). Mineral abbreviations: bio = biotite, cpy = chalcopyrite, di = diopside, fd = feldspar, Kfd = K-feldspar and mt = magnetite.

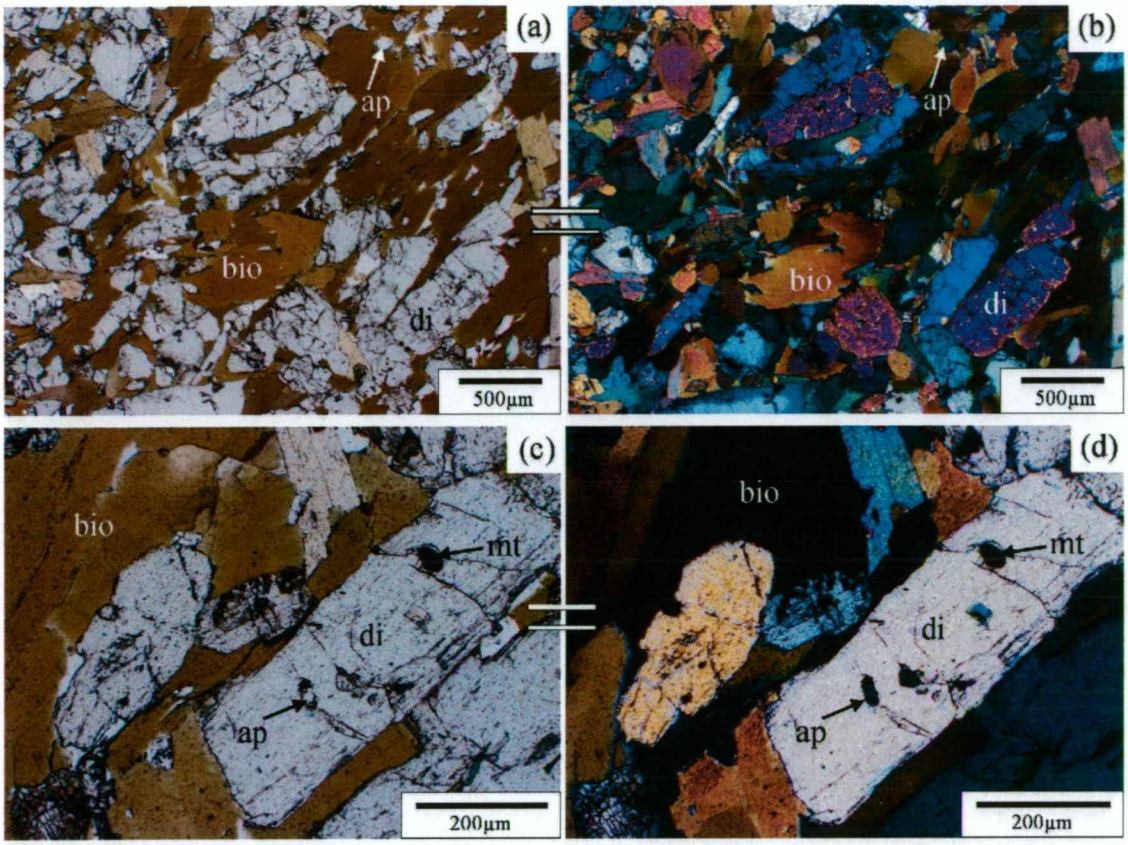

Figure 3-9. Photomicrographs of a Phase 2 biotite pyroxenite dyke from the Lower Main Zone. **(a)** Biotite pyroxenite in plane-polarised light, showing the alignment of subhedral diopside, and anhedral biotite with apatite. **(b)** Same as "a" except in cross-polarised light. **(c)** Subhedral diopside with inclusions of apatite and magnetite. **(d)** Same as "c" except in cross-polarised light. All photomicrographs are from drill hole 2001-56_283m (also see Fig. 3-10b). Mineral abbreviations: ap = apatite, bio = biotite, di = diopside and mt = magnetite.

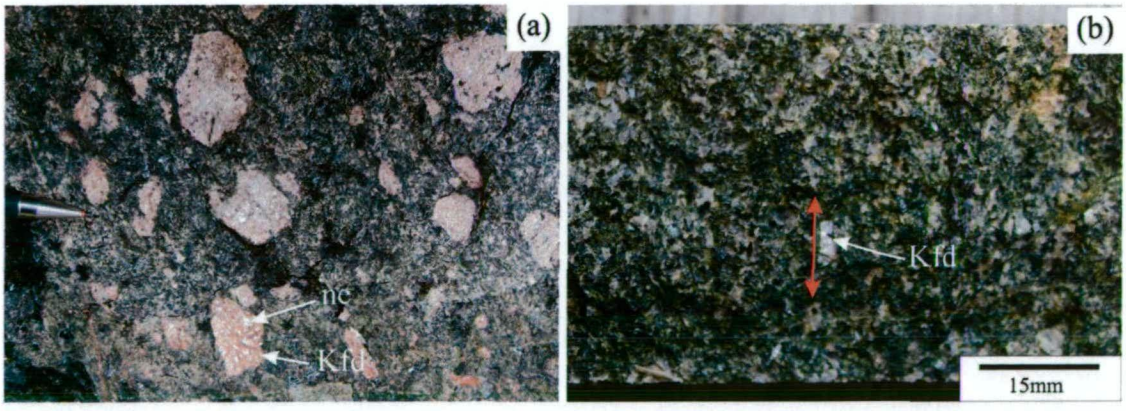

Figure 3-10. **(a)** Phase 2 pseudoleucite-bearing feldspathic pyroxenite from the central area of the Lower Main Zone. Pseudoleucite comprises pink to grey K-feldspar (Kfd) with white nepheline? (ne). The pen is approximately 1 cm in diameter (07AB-G1; 347232mE, 6200795mN). **(b)** Phase 2 K-feldspar-phyric pyroxenite from the Lower Main Zone. The rock consists of aligned euhedral K-feldspar (Kfd) laths (red arrow), which defined a primary igneous flow foliation (red arrow; drill hole 2002-63_33.2m). Mineral abbreviations: Kfd = K-feldspar and ne = nepheline(?).

1992). Diopside also includes small globular-shaped inclusions of magnetite and apatite. Phenocrysts of biotite are unaltered and pleochroic, ranging from medium to dark brown, which most likely reflects a high Fe content (e.g., Deer et al., 1992). In addition, biotite contains inclusions of diopside, plagioclase (albite to andesine; Chapter 6) and magnetite.

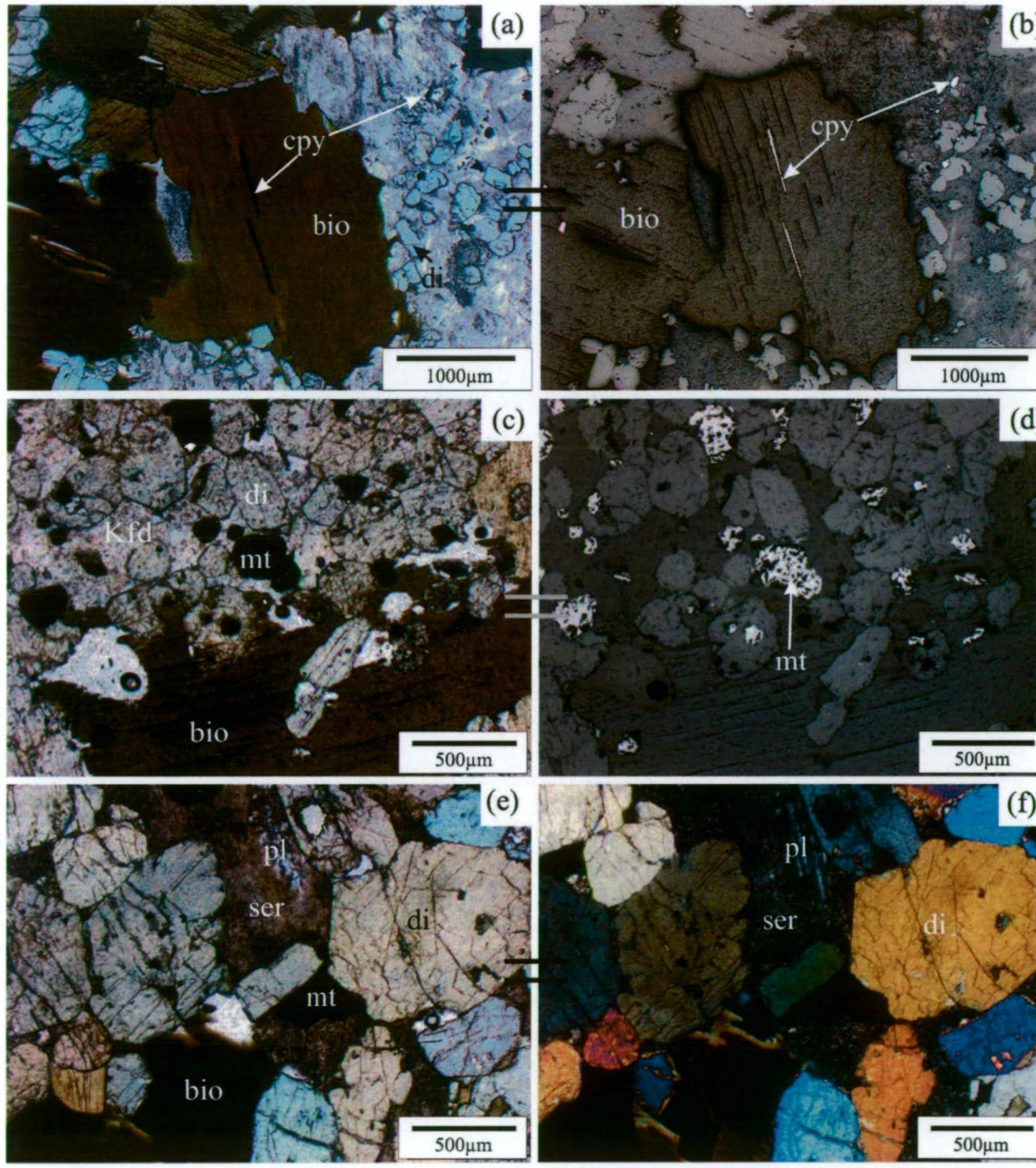

Figure 3-11. Thin section photomicrographs of feldspathic pyroxenite. **(a)** Phase 1 biotite-phyric feldspathic pyroxenite with chalcopyrite from the Lower Main Zone viewed in plane polarised light (drill hole 2001-56_157m, also *see* Fig. 3-8c). **(b)** Same as "a" except in reflected light. **(c)** Phase 2 unaltered biotite-phyric feldspathic pyroxenite from the Lower Main Zone consisting of diopside and coarse biotite phenocrysts. The rock includes large (up to 3 mm) K-feldspar oikocrysts that show simple twinning (not shown; viewed in plane polarised light; drill hole 2001-56_184m; also see 3-10d). **(d)** Same as "c" except in reflected light. **(e)** Phase 2 feldspathic biotite pyroxenite from the Bishop Zone in plane-polarised light, and showing diopside with green-blue pleochroism (drill hole 1996-43_116m). **(f)** Same as "e" except in cross-polarised light and showing relicts of plagioclase, which has been altered to sericite. Mineral abbreviations: bio = biotite, cpy = chalcopyrite, di = diopside, Kfd = K-feldspar, mt = magnetite, pl = plagioclase and ser = sericite.

Oikocrysts of K-feldspar are up to several millimetres in sizes and show simple twinning (i.e. consistent with orthoclase). Plagioclase is anhedral, shows multiple twinning in places, and in some samples is altered to sericite (Fig. 3-11e, f). The sequence of crystallisation for biotite-phyric feldspathic pyroxenite, from oldest to youngest, is; (1) euhedral to subhedral diopside, plagioclase, apatite and magnetite, (2) phenocrysts of biotite, magnetite, apatite and (3) anhedral plagioclase and orthoclase.

Equigranular feldspathic pyroxenites are very similar to biotite-phyric feldspathic pyroxenite, biotite phenocrysts. In contrast biotite is medium grained and anhedral. Diopsides in some equigranular feldspathic pyroxenites are aligned, which is inferred to represent a primary igneous flow foliation (*see* below).

3.3.3. Syenite (premineralisation phase 1 and post-mineralisation phase 2)

Phase 1 syenites are the dominant rock type of the Lower Main Zone. They range from fine- to medium-grained, equigranular to rarely porphyritic and massive to foliated (Figs. 3-12a-c and 3-13a, b). Syenites are mostly salmon pink in the central and southern areas

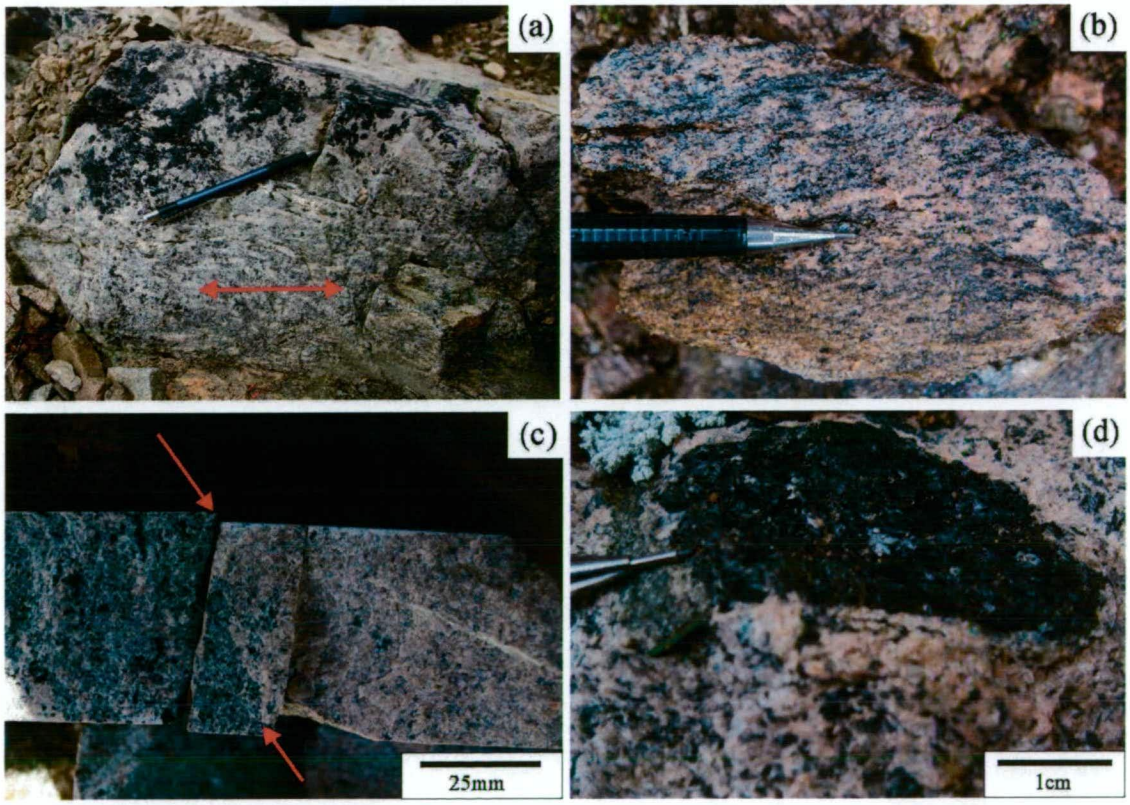

Figure 3-12. **(a)** K-feldspar flow foliated porphyry syenite (347569mE, 6200631mN), **(b)** mineralised Phase 1 syenite from the Lower Main Zone with biotite-rich banding (347354mE, 6200708mN), **(c)** Contact between Phase 1 altered syenite and Phase 1 altered biotite-diopside syenite (drill hole 2001-56_85m). **(d)** A xenolith of altered biotite pyroxenite in unaltered Phase 2 syenite (07AB-G2; 347273mE, 6200709mN).

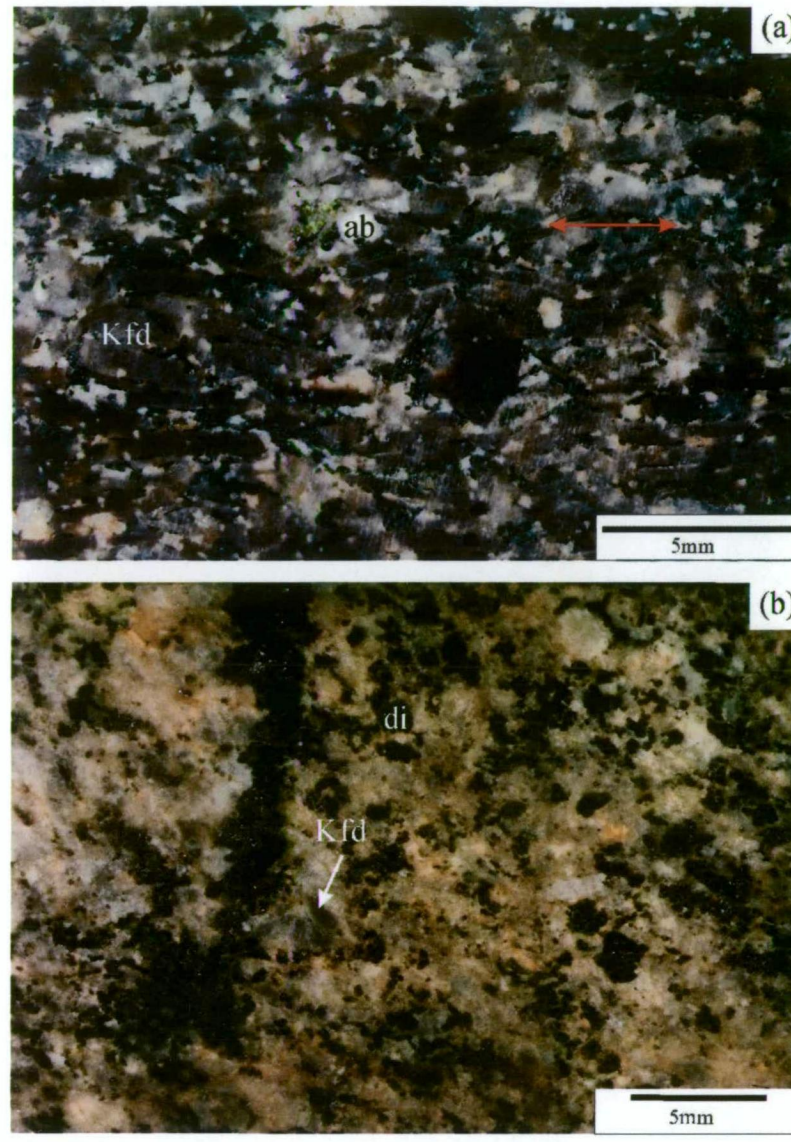

Figure 3-13. Syenite from the Lower Main Zone. **(a)** Phase 2 diopside-biotite syenite from the central area of the Lower Main Zone with aligned K-feldspar and diopside crystals defining a primary igneous flow foliation (sample 07AB-G2; 347255mE, 6200715mN). **(b)** Phase 1 diopside-biotite syenite from the Lower Main Zone (drill hole 2001-56_292.9m).

of the Lower Main Zone, and the pink colour is inferred to result from hematite alteration. In the northern area of the Lower Main Zone, syenite ranges from light grey to salmon pink. Syenites have a foliation defined by either the alignment of K-feldspar laths, which is inferred to be a primary igneous foliation (Fig. 3-12a), or aligned biotite-rich bands, which are inferred to be solid-state deformation fabrics (Fig. 3-12b; also *see* below). Phase 1 syenites range from diopside- and biotite-rich (i.e. >15 %) to mafic-poor and with contacts between individual units that vary from sharp to diffuse (Figs. 3-12c).

Phase 2 syenite dykes are commonly <4m wide and have cross-cut deformed and mineralised Phase 1 rocks in the central area of the Lower Main Zone, and include xenoliths of mineralised Phase 1 biotite pyroxenite (Fig. 3-12d). Phase 2 syenites contain euhedral to subhedral grey K-feldspar laths, diopside, biotite and accessory apatite and magnetite. K-feldspar and diopside in some Phase 2 syenites are aligned parallel to intrusive contacts, and define primary igneous flow foliations.

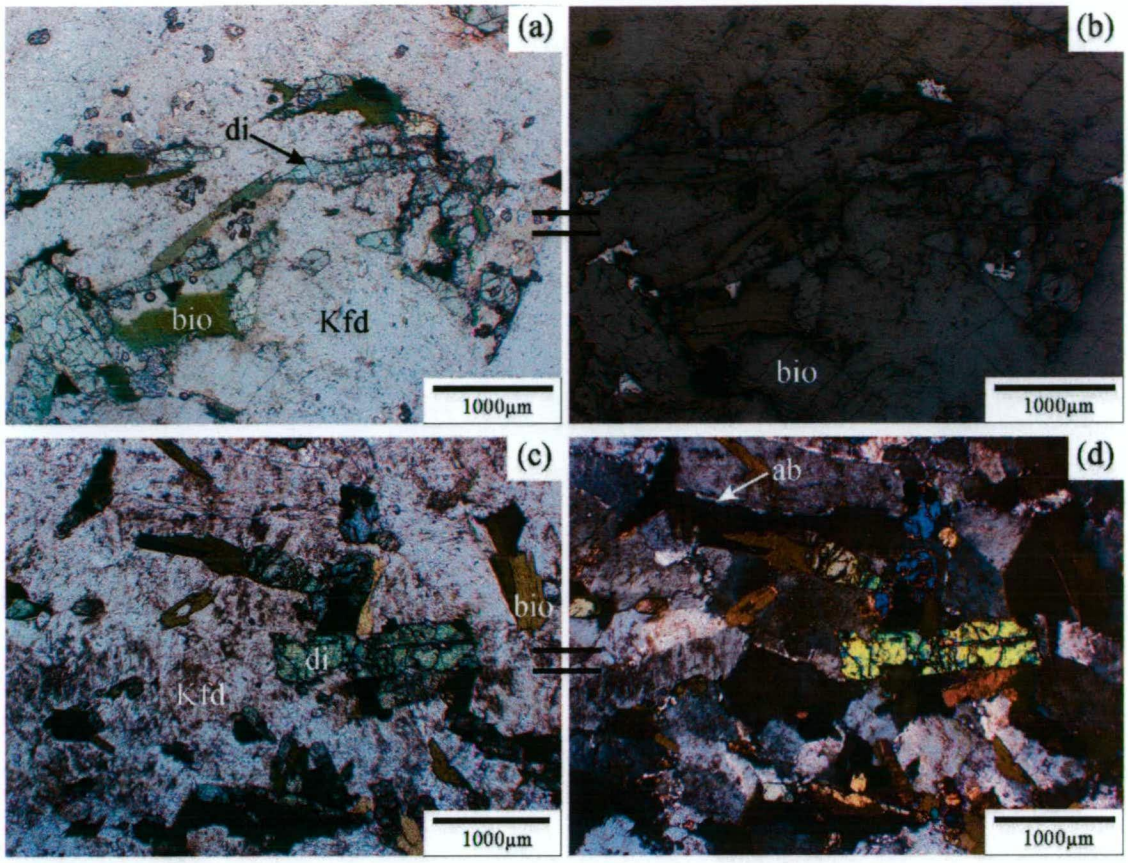

Figure 3-14. Photomicrographs of Phase 2 syenite from the Lower Main Zone. **(a)** Syenite with coarse-grained euhedral K-feldspar, fine to medium grained biotite and diopside and fine-grained magnetite viewed in plane polarised light. Magnetite is spatially associated with mafic minerals (07AB-G2; 347255mE 6200715mN). **(b)** Same as "a" except in reflected light. **(c)** Syenite with medium-grained turbid K-feldspar and fine to medium grained subhedral diopside and subhedral biotite viewed in plane polarised light (07AB-G5, 347365mE, 6200895mN). **(d)** Same as "c" except in cross-polarised light. Mineral abbreviations: ab = albite, bio = biotite, di = diopside, Kfd = K-feldspar and mt = magnetite.

3.3.3.1. Petrographic description of syenites

Phase 1 and 2 syenites are dominated by fresh to turbid euhedral to subhedral K-feldspar (50 to 70 %), which is medium- to coarse-grained and dominantly shows simple twinning (Fig. 3-14a-d). Plagioclase (5 to 15 %) is fine- to medium-grained, subhedral to anhedral, and ranges in composition from albite to oligoclase in composition (Chapter 6). Fine-grained albite occurs along K-feldspar grain boundaries (Fig. 3-14d). Mafic phases are dominated by fine- to medium-grained euhedral to subhedral diopside (1 to 20 %) and fine- to medium-grained anhedral biotite (5 to 20%; Fig. 3-14a-d); both minerals are strongly pleochroic, which reflects a high Fe-content. The syenites contain fine-grained anhedral to subhedral magnetite inferred to be of primary origin (<1%, Fig. 3-14b). Other accessory phases include trace apatite and titanite.

3.3.4. Rhythmic layered diopside syenite (pre-mineralisation Phase 1)

Rhythmic layered diopside syenite crops out in the south-eastern area of the Lower Main Zone. This dark to medium grey-green, fine- to medium-grained rock shows millimetre- to centimetre-scale compositional layering defined by variations in the abundance of diopside and biotite, and in the grain size of diopside, biotite and feldspar (Fig. 3-15a). The layering dips shallowly to moderately southwards (Fig. 3-3), and the rock has been cut by K-feldspar veins that are orientated both parallel and discordant to layering.

3.3.4.1. Petrographic description of rhythmic layered diopside syenite (Phase 1)

The rhythmic layered diopside syenite consists of subhedral to anhedral fine- to medium-grained pleochroic green to bluish-green diopside associated with variable amounts of fine-grained biotite and anhedral medium grained light grey feldspar (Fig. 3-15b-d). Stain-

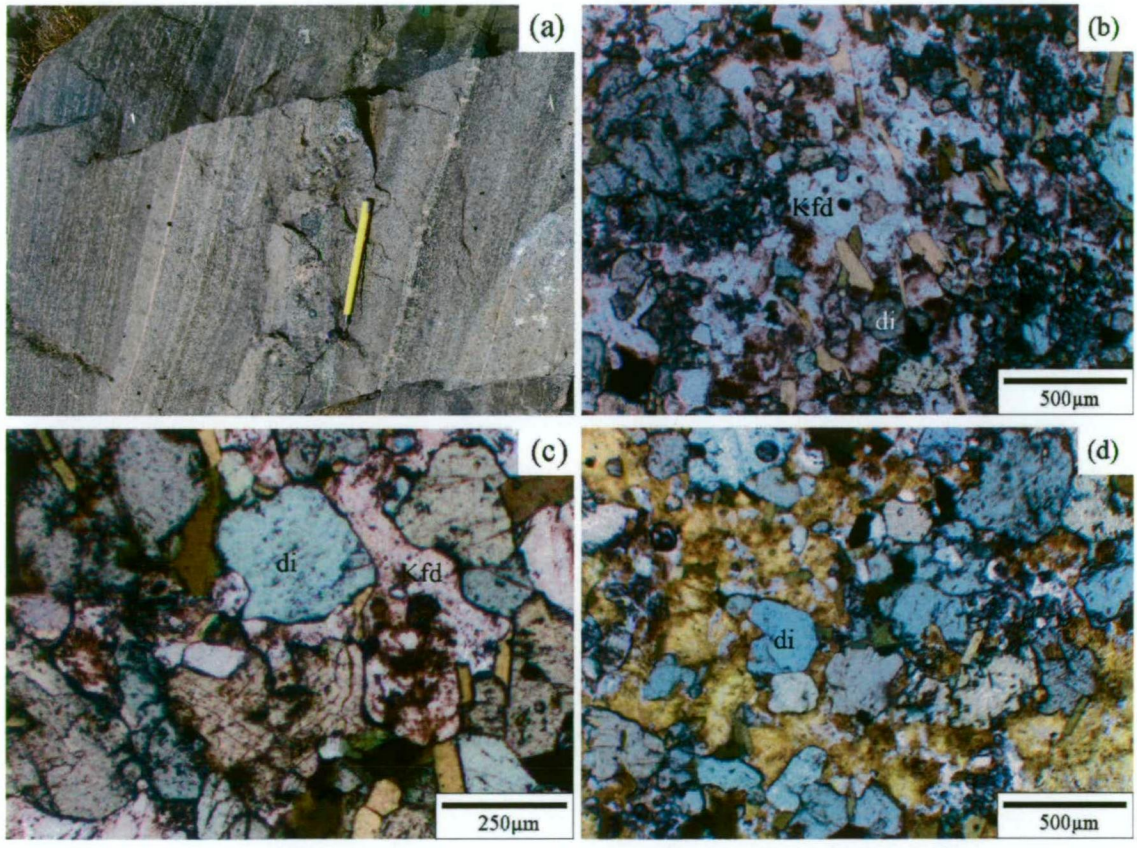

Figure 3-15. **(a)** Fine to medium grained rhythmic layered syenite from the south-central area of the Lower Main Zone. Pen magnet is for scale, and is approximately 12cm long. **(b-c)** Photomicrograph of the above rock in plane-polarised light showing unaltered subhedral diopside, which shows green to bluish green pleochroism, and anhedral K-feldspar and biotite. **(d)** Staining of feldspar demonstrates that K-feldspar is the dominant feldspar in this sample. Also note that the right side of "b" shows finer grained areas of the rock in thin section (R-side of yellow dashed line), and it is difficult to recognise clear boundaries between coarser grained layers and finer grained layers in thin section (347430mE, 6200660mN).

ing has revealed that K-feldspar is dominant with < 5% anhedral plagioclase (Fig. 3-15d). K-feldspar shows simple twinning in thin section suggesting that orthoclase is the dominant K-feldspar polymorph. Feldspars, biotite and diopside have weak undulatory extinctions. The foliation is visible in outcrop, but is not obvious in thin section.

3.3.5. K-feldspar-magnetite-albite-diopside-chalcopyrite-bornite rock (pre-mineralisation Phase 1)

K-feldspar-magnetite-albite-diopside-chalcopyrite-bornite rock crops out in the east-central and eastern area of the Lower Main Zone, and was also intercepted at ~65 m depth in drill hole L08-140 (Fig. 3-4a). The mineralised magnetite-K-feldspar-albite-diopside rock is up to 5m wide and appears to extend up slope for at least 50m on an easterly trend, where it is locally brecciated. Based on the distribution of this rock in outcrop and drill core, the individual zones are inferred to be steeply dipping (Fig. 3-4a).

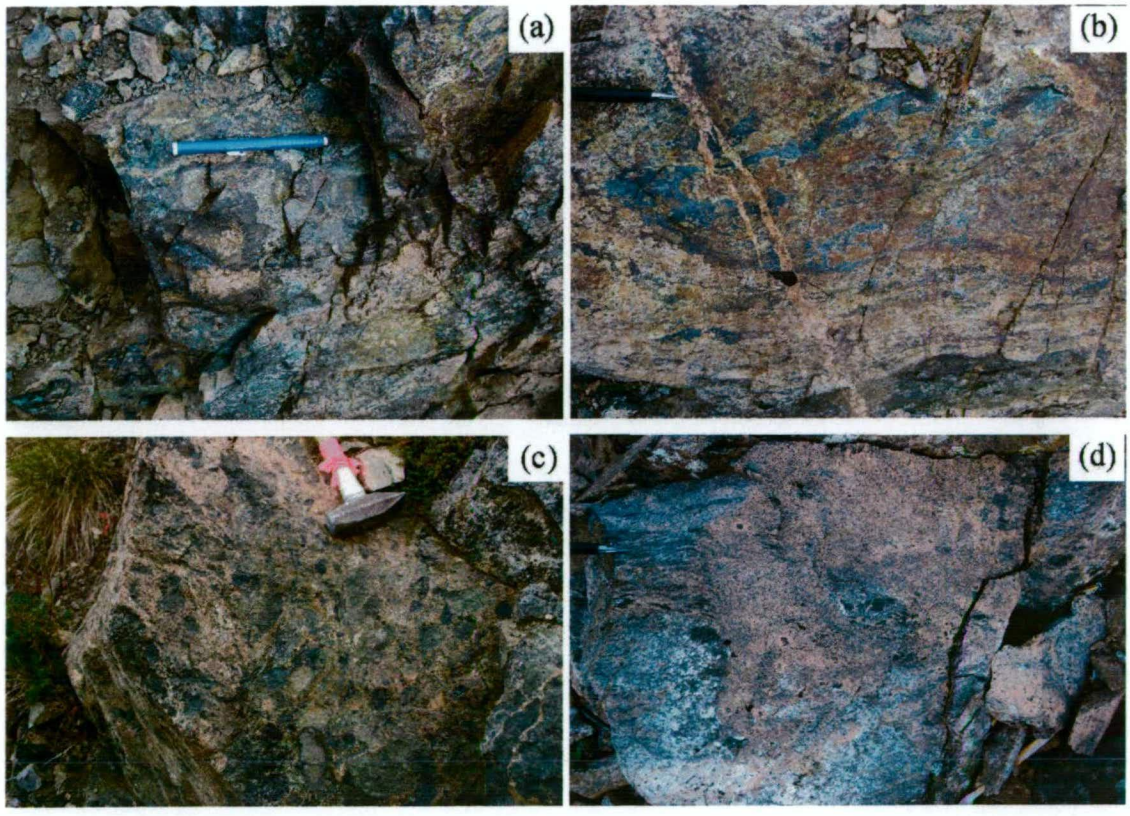

Figure 3-16. (a-b) K-feldspar-magnetite-albite-diopside altered rock in the central area of the Lower Main Zone (347423mE, 6200734mN). **(b)** In places K-feldspar-magnetite-albite-diopside altered rock is strongly foliated and appears to include folded magnetite veins that are cross-cut by late leucosyenite veins or dyklets (347423mE, 6200734mN). **(c)** In the eastern area of the Lower Main Zone the K-feldspar-magnetite-albite-diopside altered rock is locally brecciated (347530mE, 6200720mN), and **(d)** includes halo of salmon pink K-feldspar alteration that has overprinted biotite-banded Phase 1 syenites adjacent to the breccia.

The K-feldspar-magnetite-albite-diopside-chalcopyrite-bornite rock occurs in an area where the east-trending sub-vertical foliation is most strongly developed in the Lower Main Zone (Fig. 3-16a, b), and some areas include magnetite veins that appear to have been folded (?) (Fig. 3-16b). It is inferred that magnetite, albite, diopside and Cu-Fe sulphides predate solid-state deformation. In contrast, in the easternmost area of the Lower Main Zone, the K-feldspar-magnetite-albite-diopside-chalcopyrite-bornite rock is brecciated and includes a halo of K-feldspar alteration that overprints the dominant east-trending fabric in the adjacent syenite wall rocks. It is inferred that brecciation and associated K-feldspar alteration post-dated solid-state deformation (Fig. 3-16c, d).

3.3.6. Monzonite (post-mineralisation Phase 2)

Phase 2 monzonite is the dominant rock type in the northern part of the Lower Main Zone (Fig. 3-3). Small monzonite stocks and dykes have intruded unmineralised Phase 2(?) bi-

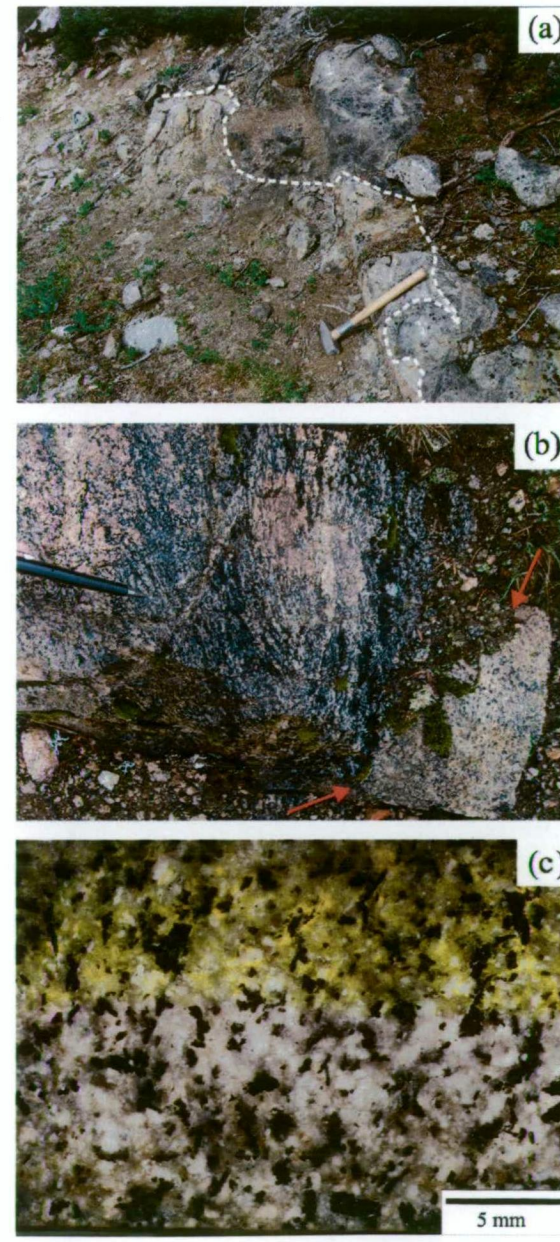

Figure 3-17. **(a)** Sub-vertical northeast trending contact between Phase 2 monzonite (left side of white dashed line) and Phase 2(?) biotite pyroxenite (right side of white dashed line) in the north-central area of the Lower Main Zone (347363mE, 6200808mN). **(b)** Phase 1 syenite with biotite-rich bands (to the left of red arrows) intruded by undeformed Phase 2 monzonite (right of red arrows) in the northern area of the Lower Main Zone. Red arrows indicate the sharp contact between monzonite and Phase 1 syenite. Foliation is sub-vertical and strikes 090 (347543mE 6200941mN). **(c)** K-feldspar stained (top third) polished rock slab of monzonite from the Lower Main Zone, which contains light grey K-feldspar and white plagioclase (347272mE, 6200828mN).

otite pyroxenite (Fig. 3-17a). Monzonites have steep sub-vertical contacts with biotite pyroxenite in the north-western area of the Lower Main Zone, and cross-cuts strongly foliated syenite in the northern area of the Lower Main Zone. It is inferred that monzonites were emplaced after solid-state deformation in the Lower Main Zone (Fig. 3-17b). Texturally, monzonites are generally massive (Fig. 3-17c), although some outcrops show a weak east-trending alignment of feldspar laths that are sub-parallel to the dyke or stock contacts along the southern margin. The alignment of feldspar laths appears to be consistent with a magmatic flow-foliation (*see* below).

3.3.6.1. Petrographic description of monzonite

Monzonite comprises medium grained euhedral to subhedral tabular plagioclase and anhedral to subhedral K-feldspar (Fig. 3-18a, b). Plagioclase shows multiple twinning in cross-polarised light and ranges from albite to labradorite in composition (Fig. 3-18b; Chapter 6). K-feldspar commonly shows simple twinning (Fig. 3-18a, b). The most abundant ferromagnesian minerals are fine to medium grained biotite and euhedral diopside. Accessory phases include euhedral amber coloured titanite, and fine-grained magnetite.

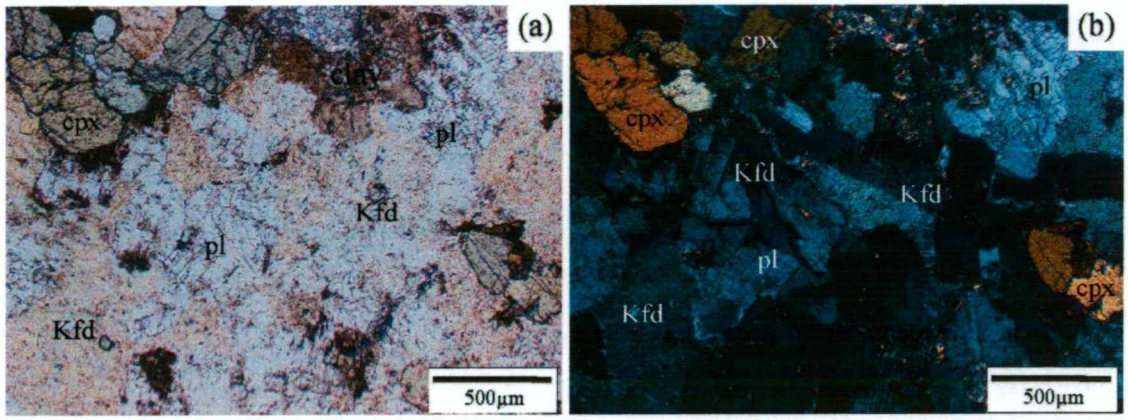

Figure 3-18. **(a)** Photomicrograph of stained thin section of monzonite showing abundant K-feldspar and plagioclase viewed under plane polarised light. **(b)** Same as "a" except in cross-polarised light, showing K-feldspar with Carlsbad twinning (i.e. orthoclase; 347272mE, 6200828mN).

3.3.7. Leucosyenite and coarse-grained K-feldspar syenite dykes (post-mineralisation Phase 3)

Late northeast-trending, steeply dipping massive equigranular leucosyenite (Phase 3) and flow-foliated coarse-grained K-feldspar-phyric syenite (Phase 3) dykes have cross-cut all of the previously described rock types in the Lower Main Zone (Figs. 3-3 and 3-19a, b). These dykes represent the last major magmatic event in the area. Leucosyenite dykes range in thickness up to 25 m in width and have been off-set, up to 20 m by northwest-trending faults. In the northern area of the Lower Main Zone, coarse-grained K-feldspar syenite dykes are cross-cut by steeply dipping northeast-trending faults.

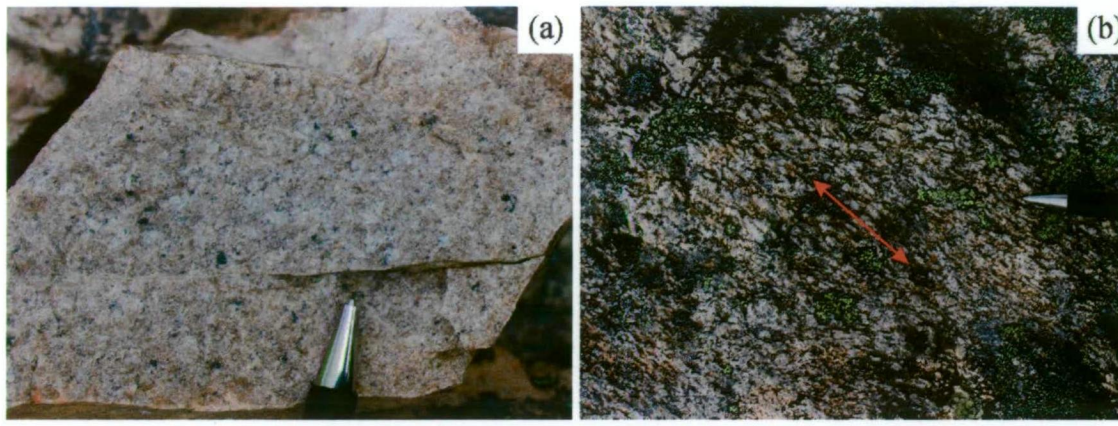

Figure 3-19. **(a)** A representative example of a late Phase 3 quartz-bearing leucosyenite. **(b)** A phase 3 coarse-grained K-feldspar syenite from the Lorraine district.

3.4. Foliation

This section discusses the types of foliation observed in the Lower Main Zone, and constrains the origins of the various foliations. Foliation in intrusive rocks can be magmatic or solid-state in origin (e.g., Vernon, 1983; Urai et al., 1986; Vernon et al., 1988; Paterson et al., 1989). The alignment of igneous minerals or the alignment of elongated enclaves parallel to the intrusive contact in the absence of plastic deformation or recrystallisation is a useful criteria for identifying magmatic foliations (e.g., Reesor, 1958; Johnson and Pollard, 1973a, 1973b; Bateman et al., 1983; Shelley, 1985; Vernon et al., 1988; Paterson et al., 1989). In contrast, solid-state deformation may be evident in minerals that show evidence of plastic deformation (e.g., undulatory extinction, kinking in feldspar and mica), or recrystallisation of minerals to fine-grained aggregates or folia, such as lenticular aggregates of muscovite, biotite, and sphene (e.g., Vernon, 1983; Urai et al., 1986; Paterson et al., 1989). Other features such as folded aplite veins that have a foliation parallel to the axial planes of the folds may also be used to identify solid-state deformation (e.g., Hobbs, 1966; Paterson et al., 1989). Solid-state deformation can be tectonic in origin or be related to deformation of the wall rocks during the emplacement of intrusions (Vernon and Johnson, 2004).

At least three types of foliation have been identified in the Lower Main Zone, which includes (1) the alignment of K-feldspar and diopside phenocrysts parallel to intrusive contacts (Figs. 3-12a and 3-9a), (2) rhythmic layering in diopside syenite (Fig. 3-15a) and (3) the alignment of biotite bands and cleavage(s) in fine-grained K-feldspar biotite rocks and syenites (Fig. 3-5b).

Table 3-1. A summary of the various rock types within the Lower Main Zone that exhibit primary igneous layering, magmatic flow foliation (defined by the alignment of phenocrysts) or a solid-state deformation foliation.

	Rock type	Primary igneous foliation	Orientation	Solid-state deformation fabric	Orientation
Phase 1	**Fine grained K-feldspar biotite rock**	-	-	Strong to weak, defined by the alignment of biotite	Strikes 090-110, Dips 65N-90
	Biotite pyroxenite/feldspathic pyroxenite	Defined by the alignment of diopside + K-feldspar laths	Trends 090	Localised alignment of biotite	Observed in drill core only. Orientation unknown
	Syenite	Defined by the alignment of feldspar laths + diopside	Trends 090	Defined by the alignment of biotite bands	Strikes 090-110, Dips 60N-45S
	Rhythmically layered diopside syenite	Defined by compositional layers with variable feldspar + ferromagnesian minerals and grainsize	Strikes 090-160, Dips 34-60 S/SW	Local weak alignment of biotite bands	090/88N
	K-feldspar-albite-magnetite-clinopyroxene-chalcopyrite-bornite rock (locally brecciated)	-	-	Defined by the alignment of folded (?) magnetite veins	Strikes 080-110, Dips 68N-90
Phase 2	**Biotite pyroxenite to feldspathic biotite pyroxenite**	Alignment of K-feldspar phenocrysts	Trend 90	-	-
	Syenite	Localised alignment of feldspar laths parallel to contact	Variable but dominantly 090	-	-
	Flow foliated K-feldspar megacrystic syenite	Defined by the alignment of K-feldspar megacrysts subparallel to contact	Trend 110	-	-
	Monzonite	Moderate to weak alignment of feldspar laths	Trend 090-110	-	-
Phase 3	**Leucosyenite dyke**	-	-	-	-
	K-feldspar pegmatitic dyke	Defined by the alignment of K-feldspar laths	0-020	-	-

3.4.1. Alignment of K-feldspar and diopside phenocrysts

The alignment of K-feldspar and diopside phenocrysts parallel to intrusive contacts in biotite pyroxenite, feldspathic pyroxenite, syenite, monzonite and coarse-grained K-feldspar syenite dykes appears to be consistent with a magmatic foliation (e.g., Figs. 3-9a, 3-10b, 3-12a, 3-13a and 3-19b). The crystals show no evidence of plastic deformation or recrystallisation. As outlined by Vernon (1968, 1976, 1986) and Paterson et al. (1989), euhedral feldspar phenocrysts generally do not grow in unmelted metamorphic rocks.

3.4.2. Rhythmic layering in diopside syenite

Layering in rhythmic layered diopside syenite is millimetre- to centimetre-scale, and minerals in rhythmic layered diopside syenite appear unstrained. K-feldspar shows simple twinning (i.e. orthoclase). According to Eggleston and Buseck (1980) solid-state deformation typically inverts orthoclase to microcline, and therefore it is inferred that orthoclase in rhythmic layered syenites is most likely igneous in origin. The layering in the diopside syenite does not appear to be cumulate layering; it is defined by variations in grain size. Nixon and Peatfield (2003) described the body as a multi-phase dyke with millimetre to centimetre-scale compositional layering defined by the modal abundance of feldspar and ferromagnesian minerals and localised, internal, finer-grained "chill" zones. The layering appears similar to the finely laminated igneous layering in the Balut Dyke from the Dinkidi alkalic porphyry Cu-Au deposit (Philippines), which is also composed of millimetre- to centimetre-scale alternating layers dominated by diopside-apatite-magnetite and perthite (Wolfe, 2001). Wolfe (2001) noted that layering in the Balut Dyke is vertical and parallel to the contact with wall rocks. Only relatively small outcrops of the rhythmic layered diopside syenite are exposed in the Lower Main Zone, and it was not possible to determine the relationship between layering and contacts. It was also not possible to determine if layering is symmetrical across the intrusive body. However layering is sub-parallel to contacts of Phase 1 biotite pyroxenite and syenite dykes, and it is inferred that the layering in rhythmic layered syenite is likely parallel to a contact. It is also inferred here that layering has been tilted along with other Phase 1 intrusives; although the emplacement of layering at an inclined angle cannot be ruled out based on the available data.

3.4.3. Biotite-rich bands in syenite and fine-grained K-feldspar biotite rock

Based on property-scale mapping by Teck Ltd (e.g., Devine et al., 2007), the biotite-rich banding appears to be mainly restricted to Phase 1 rocks of the Lower Main and Main zones; although a ductile foliation has also been identified at Misty and Slide Mountain (Baxter and Devine, 2007; Garratt and Lindinger, 2008). The intensity of the foliation ranges from weak to intense across the Lower Main Zone, and is strongest in a 50 to 100m

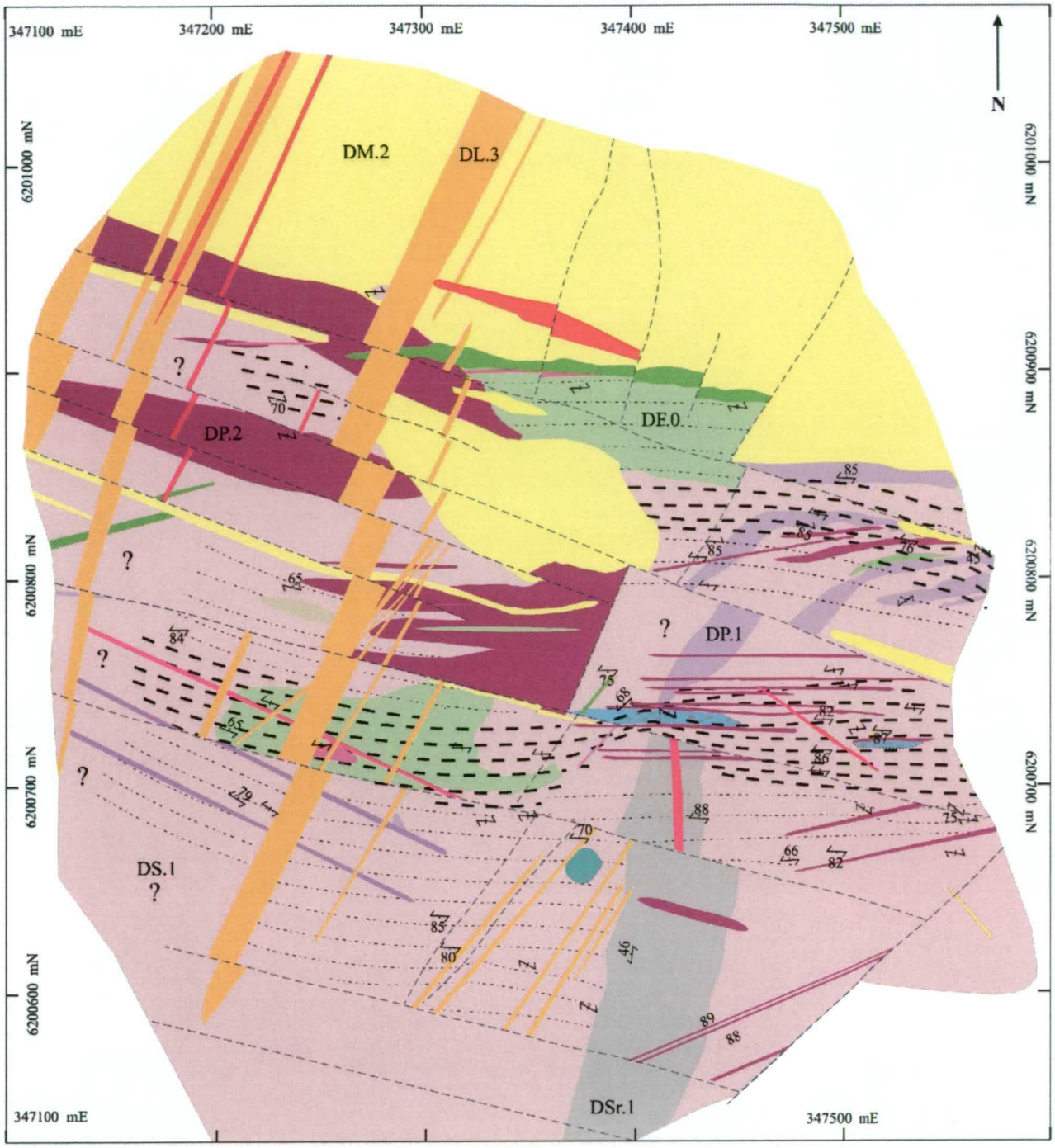

Figure 3-20. Interpreted geological map of the Lower Main Zone showing the distribution and intensity of the ductile fabric across the Lower Main Zone. Question marks (?) highlight areas where outcrops are sparse and the distribution of the fabric is poorly constrained. *See* Figure 3-3 for detailed legend.

wide band that runs eastward across the central area of the Lower Main Zone and into the Main Zone (Fig. 3-20). The foliation has an average orientation of 279/89N (Fig. 3-21).

The foliation is defined by the alignment of biotite-rich bands in syenite and fine-grained

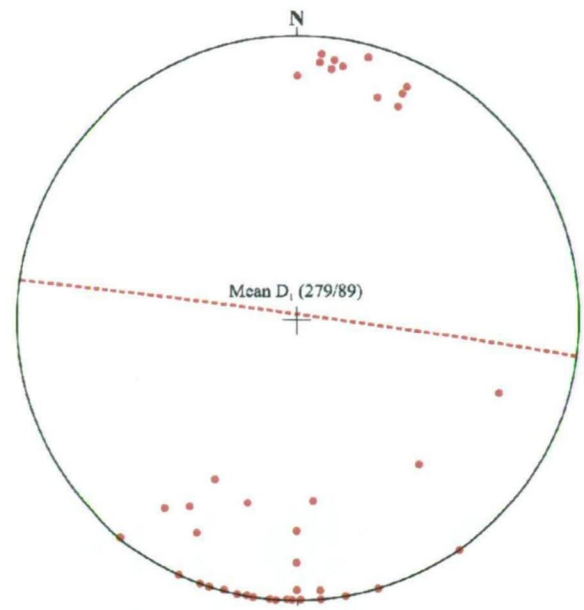

Figure 3-21. Stereonet projection of poles to cleavage for the dominant steeply dipping east-trending foliation defined by biotite-rich banding across the Lower Main Zone. Projections and mean cleavage orientation were plotted and calculated respectively using GEOrient 9.2 (Holcombe, 2006).

K-feldspar biotite rock (Figs. 3-5a-c, 3-12b, 3-17b and 3-23a). Fine-grained K-feldspar biotite rocks are thought to represent metasomatised wall rocks, and therefore the alignment of biotite in these rocks probably represents a solid-state foliation. Kinked biotite and folded K-feldspar veins (Fig. 3-5c) with undulatory extinction (Fig. 3-5g) in fine-grained K-feldspar biotite rock, and Phase 1 syenite, appears consistent with solid-state deformation. The solid-state deformation fabric could be related to a tectonic event or related to deformation during the emplacement of dykes (*see* discussion).

3.5. Late brittle north-northeast-and northwest-trending fault sets

North-northeast and west-northwest trending brittle fault sets were identified in outcrop along the upper easternmost road (Fig. 3-3), and also in drill core as clay-rich fault gouge commonly associated with calcite and/or chalcedony veins in adjacent wall rocks. In the northern and eastern areas of the Lower Main Zone, faults were inferred in areas where Phase 3 leucosyenite dykes and coarse-grained K-feldspar syenite dykes appear to have been offset. In the northern area of the Lower Main Zone, small creeks that have incised the slope towards the north have cut monzonite and coarse-grained K-feldspar syenite dykes, these are inferred to be eroding along N-trending faults. In one particular location a sub-vertical K-feldspar pegmatitic body appears to have been dextrally offset on either side of a north-trending creek and hence a relative dextral movement is inferred (Fig. 3-3). In contrast, north-northeast trending sub-vertical Phase 3 leucosyenite dykes display sinistral off-set along west-northwest trending faults. The relative timing between the two above fault sets is unclear, because no outcrops contained fault intersections. The last

kinematic displacement along these faults post-dates the last known intrusive event in the Lower Main Zone.

Brittle fault sets were reported in the Johanson Lake area, to the north of the Hogem Batholith, by Schiariazza and Tan (2005) and Zhang and Hynes (1994). Schiariazza and Tan (2005) reported dextral and sinistral displacement along northwest to north-trending faults and predominant sinistral displacements along northeast-trending faults, with the latter thought to be faults related to the Finlay-Ingenika Fault Zone (Zhang and Hynes, 1992, 1994). In the Lower Main Zone, northeast to north-trending faults have a dextral sense of displacement, and northwest to west-trending faults also show sinistral sense displacement. Thus the late brittle fault sets in the Lower Main Zone show displacements that could potentially be related to the dextral movement along major fault zones including the Manson Fault Zone to the east and Pinchi-Finlay-Ingenika Fault Zone to the west (Fig. 3-22). Dextral movement is thought to have occurred along the Manson Fault Zone and Pinchi- Finlay-Ingenika Fault Zone between the Late Cretaceous to Early Tertiary (Ferri and Melville, 1994; Zhang and Hynes, 1994), and the late faults in the Lower Main Zone may be related to deformation of similar ages.

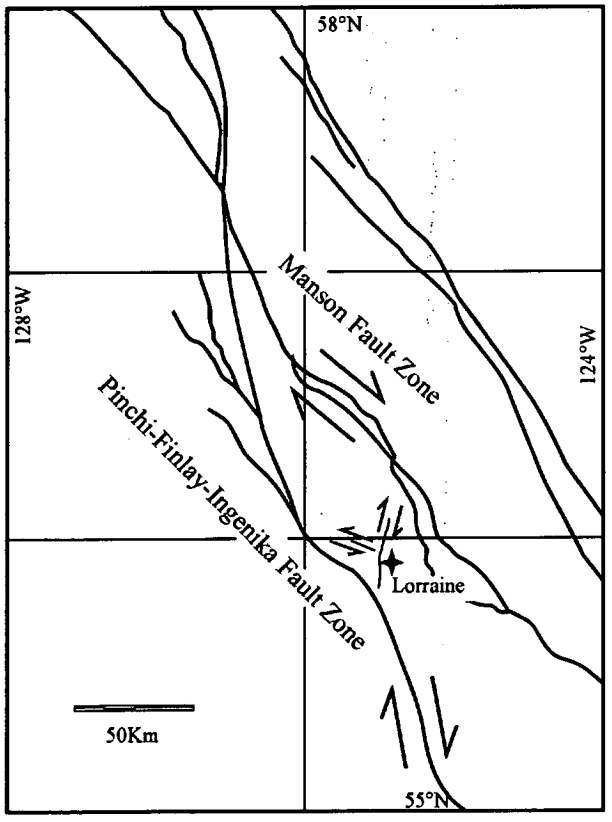

Figure 3-22. Regional-scale map of the Lorraine area showing the location and orientation of the Manson and Pinchi-Finlay-Ingenika Fault Zones, which formed as a result of dextral displacement in the Late Cretaceous to Tertiary. The map also shows the location of Lorraine, and the orientations and senses of movement of along the late north-northeast and northwest brittle fault sets in the Lower Main Zone (grey lines). The orientation of the faults and the sense of movement along faults appear consistent with conjugate faults related to the major dextral fault zones in the region, suggesting that the late faults may have formed during the Late Cretaceous to Tertiary (modified after Schiarizza and Tan, 2005).

3.6. Geochronology of igneous rocks

Zircon fractions from five igneous rock samples of the Lower Main Zone were dated using the conventional Isotope Dilution Thermal Ionization Mass Spectrometer (ID-TIMS) method at the Pacific Centre for Isotopic and Geochemical Research in the Department of Earth and Ocean Sciences, University of British Columbia. Also fifteen zircon grains from a syenite with biotite-rich bands from the Lower Main Zone were dated using SHRIMP-RG at the joint Stanford University and U.S. Geological Survey Microanalytical Centre (SUMAC) in California. Geochronology was carried out with the aim of; (1) estimating the crystallisation age of Phase 1 and Phase 2 rocks, (2) constraining the timing of mineralisation in the Lower Main Zone and (3) constraining the timing of solid-state deformation that developed biotite banding and tilting of the Lower Main Zone.

3.6.1. Methods

3.6.1.1. Sampling and zircon separation

Rock fragments from individual outcrops were liberated using a 5 kg sledgehammer, and pebble to cobble size fragments free of veins were collected into 20 L pails. Approximately 20 to 30 kg of each sample was submitted to the Pacific Centre for Isotopic and Geochemical Research in the Department of Earth and Ocean Sciences, University of British Columbia for zircon separation. All zircon was separated from samples using conventional crushing, grinding, and Wilfley table techniques, followed by final concentration using heavy liquid and magnetic separations. Mineral fractions for analysis were selected on the basis of grain quality, size, magnetic susceptibility and morphology.

3.6.1.2. Analytical techniques and data interpretation for SHRIMP-RG U-Pb dating

Cathodoluminescence (CL) imaging of zircon grains (Fig. 3-24a-d) and SHRIMP-RG analyses were carried out by Dr Richard M. Tosdal (MDRU, University of British Columbia) at the joint Stanford University and U.S. Geological Survey Microanalytical Centre (SUMAC). Zircon separates were mounted in epoxy, polished to expose zircon cores and carbon coated before being observed in CL using the JEOL JSM 5600 scanning electron microscope (SEM). The CL images were further enhanced for contrast and detail using Adobe Photoshop™. The epoxy mount was gold-coated and placed in the sample chamber of the SHRIMP-RG.

Prior to analysis, an 8 nA $^{16}O_2$-primary ion beam was rastered across grains for two minutes to remove the gold coating and surface contamination. Positive secondary ions were then

collected by excavating an approximately 1 μm deep flat-floored, rounded to elliptical pit (~20–30 μm diameter). For each analysis, six scans of peaks at $^{90}Zr_2{}^{16}O$, ^{204}Pb, ^{206}Pb, ^{207}Pb, ^{238}U, $^{232}Th^{16}O$ were collected. Beam tuning was done using the $^{238}U^{16}O$ peak, with maximum count times for ^{206}Pb and ^{207}Pb of 20 seconds. Uranium concentrations were obtained by comparison with zircon standard CZ3 (550 ppm). Common Pb correction is based on average crust model of Stacey and Kramer (1975), and data reduction was undertaken using SQUID 1.02 (Ludwig, 2001).

3.6.1.3. Analytical techniques and data interpretation for ID-TIMS U-Pb dating

ID-TIMS analysis was carried out by Dr Rich Friedman (MDRU, University of British Columbia). Geochemical separation and mass spectrometry on zircon were carried out at the Pacific Centre for Isotopic and Geochemical Research in the Department of Earth and Ocean Sciences, University of British Columbia. All zircon was air abraded prior to dissolution to minimise the effects of post-crystallisation Pb-loss, using the technique of Krogh (1982). Single zircon grains were dissolved in sub-boiled 48% HF and 14 M HNO_3 (ratio of ~10:1, respectively) in the presence of a mixed $^{233\text{-}235}U$-^{205}Pb tracer. Zircons were then placed in 300 μL PTFE or PFA microcapsules contained in high pressure vessels (Parr™ acid digestion vessels with 125 mL PTFE liners) for 40 hours at 240 °C. Sample solutions were then dried to salts at ~130 °C. Zircon residues were redissolved in ~100 μL of ultra clean 6.2 M HCl for 12 hours at 210 °C in high pressure vessels. These solutions were transferred to 7 mL PFA beakers, dried to a small droplet after addition of 2 μL of 0.5 M H_3PO_4. Samples were then loaded on single, degassed zone-refined Re filaments in 5 μL of a silica gel phosphoric acid emitter (Gerstenberger and Haase, 1997). Isotopic ratios were measured using a modified single collector VG-54R thermal ionisation mass spectrometer equipped with an analogue Daly photomultiplier. Measurements were done in peak-switching mode on the Daly detector. Analytical blanks during the course of this study were 0.2 pg for U and 1-2 pg for Pb. Uranium fractionation was determined directly on individual runs using the $^{233\text{-}235}U$ tracer, and Pb isotopic ratios were corrected for fractionation of 0.23 %/amu, based on replicate analyses of the NBS-982 Pb standard and the values recommended by Thirlwall (2000). Reported precisions for Pb/U and Pb/Pb dates were determined by numerically propagating all analytical uncertainties through the age calculation using the technique of Roddick et al. (1987). Standard concordia diagrams were constructed and regression intercepts, concordia ages and weighted means calculated with Isoplot 3.00 (Ludwig, 2003).

3.6.2. Results

A total of six samples were selected for zircon U-Pb dating. Results from the analysis are summarised in Tables 3-2 and 3-3, and in Figures 3-25 and 3-28. Uranium-Pb age data

for zircons from the Lower Main Zone samples collectively exhibit limited dispersion, with the entire dataset on concordia between ca. 174 and 179 Ma. Considered individually, the samples also display minor dispersion, with younger grains likely recording minor Pb-loss and no strong evidence for the presence of older inherited cores or high concentrations of Zr from whole rock geochemistry (i.e. 70 to 50 ppm); although the pseudoleucite-bearing pyroxenite does have anomalous Zr (i.e. ~100 ppm), and therefore assimilation of zircon in this sample cannot be ruled out. Given the minor Pb-loss that is interpreted to have affected some grains, age interpretations have been based on the oldest $^{238}U/^{206}Pb$ results for each of the respective rocks.

3.6.2.1. Syenite (Phase 1) sample 07AB-G4

A mineralised syenite with a strong sub-vertical east-west shear foliation fabric (Phase 1) was collected from the Lower Main Zone to determine the crystallisation age of syenites, to place a maximum age constraint on the timing of main-stage mineralisation and ductile deformation (Figs. 3-23a, b). Zircon grains were observed under CL, and cores and rims of zircon were analysed using SHRIMP-RG (Figs. 3-24a-d). Catholuminecence showed that zircon grains are characterised by complex zonations; however ages determined from isotopic data indicate that cores are not markedly older than rims, suggesting no evidence for inherited cores. Some zones in zircon have significantly lower than average $^{206}Pb/^{238}U$ ratios which may be attributed to loss of radiogenic Pb. The age estimated based on the weighted averages of all of the data is 182.6 ± 3.2 Ma (2σ; Fig. 3-25a, b). The weighted average has a calculated MSWD of 23, which indicates scatter beyond that of analytical precision (i.e. MSWD >2). Thus the age is considered to be only a crude estimation of the crystallisation age of the Phase 1 syenite.

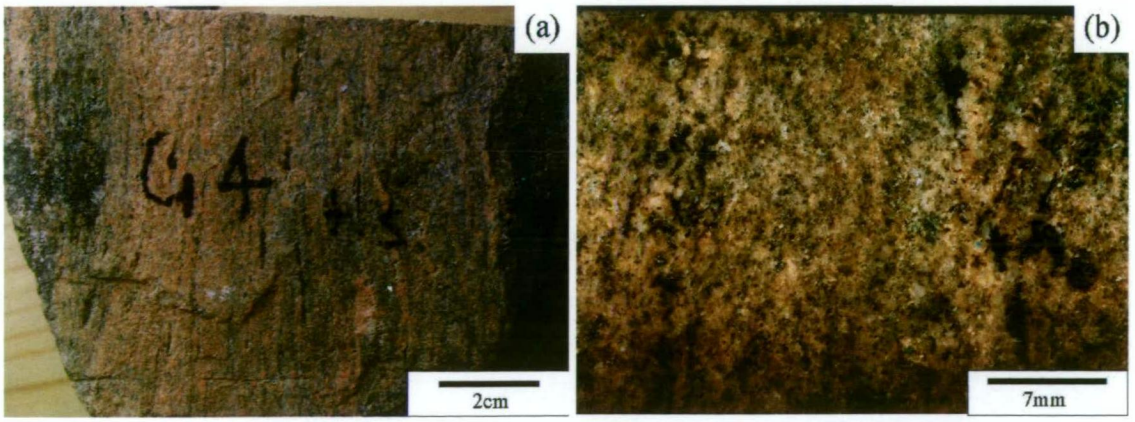

Figure 3-23. (a-b) Altered Phase 1 syenite with biotite-rich banding. This rock was collected from the eastern area of the Lower Main Zone for zircon U-Pb SHRIMP-RG dating (Sample 07AB-G4, 347550mE, 6200680mN).

Table 3-2. SHRIMP-RG U-Pb zircon analytical data for foliated Phase 1 syenite from the Lower Main Zone (sample 07AB-G4).

Grain[1]	U (ppm)	Th (ppm)	$^{232}Th/^{238}U$	$^{204}Pb/^{206}Pb$	^{206}Pb[2] (%)	Isotopic ratios ±1σ,%[3] $^{206}Pb/^{238}U$	$^{207}Pb/^{235}U$	$^{207}Pb/^{206}Pb$	corr. coef.	%[4] discordant	Apparent ages ±1σ,Ma[5] $^{206}Pb/^{238}U$
1C	413	217	0.54	0.000115	<0.01	.0275 ± 0.7	0.18 ± 3.3	.0479 ± 3.2	.211	-46	175.0 ± 1.2
2C	231	123	0.55	0.000106	0.53	.0287 ± 0.9	0.21 ± 4.0	.0524 ± 3.9	.230	65	182.7 ± 1.6
3C	172	115	0.69	0.000267	0.03	.0276 ± 1.1	0.17 ± 7.3	.0459 ± 7.2	.153	-105	175.5 ± 1.9
4C	300	111	0.38	0.000084	0.38	.0288 ± 0.9	0.20 ± 3.5	.0515 ± 3.3	.267	44	183.2 ± 1.7
5R	767	514	0.69	0.000048	0.06	.0274 ± 0.5	0.19 ± 2.3	.0494 ± 2.2	.230	-5	174.0 ± 0.9
6C	248	119	0.50	0.000180	0.21	.0284 ± 0.9	0.19 ± 4.6	.0487 ± 4.5	.197	-26	180.3 ± 1.6
7C	792	935	1.22	0.000000	0.15	.0287 ± 0.5	0.20 ± 1.9	.0509 ± 1.8	.258	30	182.2 ± 0.9
8R	1113	802	0.74	0.000000	0.09	.0288 ± 0.4	0.20 ± 1.5	.0505 ± 1.5	.261	18	182.9 ± 0.7
9C	333	140	0.43	0.000078	0.04	.0290 ± 0.9	0.20 ± 3.4	.0490 ± 3.3	.264	-20	184.5 ± 1.6
10C	273	153	0.58	0.000000	0.27	.0278 ± 0.8	0.20 ± 3.2	.0518 ± 3.1	.261	56	176.6 ± 1.5
11C	138	57	0.43	0.000185	0.07	.0288 ± 1.2	0.19 ± 6.0	.0476 ± 5.9	.195	-57	182.9 ± 2.1
12R	245	78	0.33	0.000000	0.01	.0292 ± 0.9	0.20 ± 3.4	.0498 ± 3.3	.260	1	185.6 ± 1.6
13R	776	466	0.62	0.000031	0.16	.0299 ± 0.5	0.21 ± 1.9	.0507 ± 1.9	.246	20	190.0 ± 0.9
14R	721	527	0.75	0.000000	<0.01	.0300 ± 0.5	0.20 ± 1.9	.0493 ± 1.9	.256	-14	190.8 ± 0.9
15C	61	21	0.36	0.000000	0.14	.0291 ± 1.8	0.20 ± 6.8	.0509 ± 6.6	.258	28	185.1 ± 3.2

Uncertainties given at the 1σ level.

[1]Grain number and spot location on rim (R) and core (C). Also *see* Fig. 3-22.

[2]Percentage of ^{206}Pb that is common.

[3]Isotopic ratios corrected for common ^{204}Pb

[4]% discordance to origin.

[5]Age calculations are based on U decay constants of Jaffey et. al. (1971).

Initial common Pb compositions based on Stacey and Kramers (1975) model Pb.

Table 3-3. ID-TIMS U-Pb zircon analytical data for Phase 1 and 2 rocks of the Lower Main Zone.

Grain[1]	Wt[2] (μg)	U[3] (ppm)	Pb*[4] (ppm)	$^{206}Pb/^{204}Pb$[5]	Pb*/Pbc[6]	Pb[7] (pg)	Th/U[8]	Isotopic ratios ±1σ,%[9] $^{206}Pb/^{238}U$	$^{207}Pb/^{235}U$	$^{207}Pb/^{206}Pb$	corr. coef.	% discordant[10]	Apparent ages ±2σ,Ma[11] $^{206}Pb/^{238}U$	$^{207}Pb/^{235}U$	$^{207}Pb/^{206}Pb$
07ABG7															
A	6.0	367.7	11.5	3845	68.9	1.0	0.750	0.02812 ± 0.18	0.1925 ± 0.23	0.04965 ± 0.16	0.722	-0.1	178.8 ± 0.7	178.8 ± 0.8	178.6 ± 7.4/7.4
B	5.3	419.5	12.9	3515	63.9	1.1	0.790	0.02753 ± 0.12	0.1879 ± 0.38	0.04951 ± 0.34	0.446	-1.7	175.0 ± 0.4	174.8 ± 1.2	172.1 ± 15.7/15.9
C	6.2	287.7	9.5	2308	43.4	1.4	1.010	0.02805 ± 0.11	0.1928 ± 0.31	0.04987 ± 0.29	0.402	5.6	178.3 ± 0.4	179.0 ± 1.0	188.7 ± 13.3/13.4
D	3.7	445.0	13.5	1772	30.9	1.6	0.706	0.02764 ± 0.15	0.1885 ± 0.39	0.04946 ± 0.36	0.421	-3.5	175.7 ± 0.5	175.3 ± 1.3	169.8 ± 16.6/16.7
E	3.8	554.8	16.9	3222	57.5	1.1	0.733	0.02763 ± 0.36	0.1884 ± 0.54	0.04946 ± 0.38	0.716	-3.5	175.7 ± 1.3	175.3 ± 1.8	169.9 ± 17.6/17.8
07ABG3															
A	10.9	914.8	26.5	1600	26.5	10.9	0.522	0.02772 ± 0.08	0.1901 ± 0.27	0.04974 ± 0.23	0.571	3.6	176.3 ± 0.3	176.7 ± 0.9	182.8 ± 10.6/10.6
B	5.0	1033.4	29.8	674	10.8	13.6	0.445	0.02809 ± 0.09	0.1924 ± 0.32	0.04967 ± 0.28	0.619	0.7	178.6 ± 0.3	178.7 ± 1.1	179.8 ± 12.8/12.9
C	5.1	750.8	22.0	432	6.9	15.9	0.516	0.02805 ± 0.14	0.1918 ± 0.56	0.04959 ± 0.50	0.530	-1.6	178.3 ± 0.5	178.2 ± 1.8	175.7 ± 22.9/23.3
D	4.6	434.4	13.8	267	4.5	13.9	0.824	0.02812 ± 0.16	0.1929 ± 0.69	0.04975 ± 0.61	0.605	2.6	178.8 ± 0.6	179.1 ± 2.3	183.5 ± 28.2/28.7
E	2.8	1266.2	39.1	512	8.7	12.5	0.709	0.02812 ± 0.14	0.1923 ± 0.41	0.04958 ± 0.34	0.645	-1.9	178.8 ± 0.5	178.6 ± 1.3	175.4 ± 15.6/15.8
07ABG2															
B	3.3	1086.9	40.6	6960	148.3	0.9	1.540	0.02816 ± 0.27	0.1933 ± 0.34	0.04978 ± 0.18	0.840	3.1	179.0 ± 1.0	179.4 ± 1.1	184.8 ± 8.6/8.6
C	6.9	658.2	22.4	5471	109.4	1.4	1.173	0.02772 ± 0.08	0.1898 ± 0.16	0.04966 ± 0.12	0.636	1.7	176.3 ± 0.3	176.5 ± 0.5	179.3 ± 5.8/5.8
D	3.4	1061.7	37.4	7435	149.8	0.9	1.271	0.02809 ± 0.11	0.1928 ± 0.16	0.04976 ± 0.10	0.780	2.9	178.6 ± 0.4	179.0 ± 0.5	183.9 ± 4.8/4.8
E	3.9	358.6	12.3	2511	48.8	1.0	1.144	0.02811 ± 0.12	0.1923 ± 0.21	0.04962 ± 0.15	0.685	-1.0	178.7 ± 0.4	178.6 ± 0.7	177.0 ± 7/7.1
07ABG5															
B	3.7	166.6	4.7	1798	28.9	0.6	0.359	0.02790 ± 0.12	0.1902 ± 0.32	0.04946 ± 0.29	0.421	-4.7	177.4 ± 0.4	176.8 ± 1.0	169.5 ± 13.5/13.6
C	3.5	396.7	12.5	2276	41.4	1.1	0.821	0.02787 ± 0.20	0.1909 ± 0.37	0.04967 ± 0.31	0.541	1.4	177.2 ± 0.7	177.4 ± 1.2	179.8 ± 14.6/14.7
D	3.7	267.4	7.9	1924	32.8	0.9	0.591	0.02776 ± 0.20	0.1903 ± 0.34	0.04974 ± 0.30	0.477	3.5	176.5 ± 0.7	176.9 ± 1.1	182.8 ± 14.1/14.2
E	2.0	418.1	12.0	1609	26.5	0.9	0.476	0.02777 ± 0.18	0.1901 ± 0.40	0.04964 ± 0.35	0.488	0.9	176.6 ± 0.6	176.7 ± 1.3	178.1 ± 16.1/16.2
07ABG1															
A	3.7	693.8	23.2	4814	91.6	0.9	1.057	0.02796 ± 0.11	0.1910 ± 0.20	0.04956 ± 0.15	0.677	-2.0	177.8 ± 0.4	177.5 ± 0.7	174.2 ± 6.9/7
C	2.4	365.8	11.5	1922	34.6	0.8	0.819	0.02780 ± 0.45	0.1902 ± 0.49	0.04963 ± 0.19	0.924	0.6	176.8 ± 1.6	176.8 ± 1.6	177.7 ± 8.6/8.7
D	1.2	584.0	18.4	1041	18.6	1.2	0.795	0.02807 ± 0.09	0.1921 ± 0.36	0.04964 ± 0.32	0.470	-0.3	178.4 ± 0.3	178.4 ± 1.2	177.9 ± 15/15.1

[1]A, B, zircon grain identifier; all are air-abraded single grains.

[2]Grain mass determined on Sartorious SE2 ultra-microbalance to ± 0.1 microgram.

[3]U concentration corrected for spike, blank 0.2 pg ± 50% at 2 sigma, and mass fractionation, which is directly determined with ^{233}U-^{235}U double spike.

[4]Radiogenic Pb; corrected for spike, fractionation, blank and initial common Pb. Mass fractionation correction of 0.23% /amu ± 40% (2 sigma) is based on analysis of NBS-982 Pb reference material throughout course of study. Blank Pb of 0.5-1.5 pg and 5.0 pg 07ABG3 ± 40% for all (2 sigma) with composition of $^{206}Pb/^{204}Pb = 18.50 \pm 2\%$; $^{207}Pb/^{204}Pb = 15.50 \pm 2\%$; $^{208}Pb/^{204}Pb = 36.40 \pm 2\%$, all at 2 sigma. Initial common Pb compositions based on Stacey and Kramers (1975) model Pb at 179 Ma.

[5]Measured ratio corrected for spike and fractionation.

[6]Ratio of radiogenic to common Pb.

[7]Total weight of common Pb calculated assuming blank isotopic composition.

[8]Model Th/U ratio calculated from radiogenic $^{208}Pb/^{206}Pb$ ratio and $^{207}Pb/^{206}Pb$ age.

[9]Corrected for spike, fractionation, blank and initial common Pb.

[10]% discordance to origin.

[11]Age calculations are based on U decay constants of Jaffey et. al. (1971)

Table 3-4. Interpreted U-Pb ages for rocks from the Lower Main Zone of the Lorraine deposit.

Rock type	Sample no.	Area	Intrusive phase	Easting	Northing	Mineral for dating	Age (Ma) 2σ	Comments
SHRIMP-RG								
Biotite-banded syenite	07AB G4	Lower Main Zone	Phase 1	347550	6200680	zircon	182.6 ±3.2	All data, mean ^{207}Pb corrected ^{206}Pb/^{238}U (95% conf.)
ID-TIMS								
Rhythmically layered K-feldspar-diopside rock	07AB G3	Lower Main Zone	Phase 1	347430	6200665	zircon	178.6 ±0.2	Based on 4 point weighted average of ^{206}Pb/^{238}U dates
Syenite	07AB G7	Lower Main Zone	Phase 1	347330	6200580	zircon	178.4 ±0.3	Based on 2 point weighted average of ^{206}Pb/^{238}U dates; minimum age
Diopside-biotite syenite	07AB G2	Lower Main Zone	Phase 2	347255	6200715	zircon	178.7 ±0.3	Based on 3 point weighted average of ^{206}Pb/^{238}U dates
Pseudoleucite-bearing pyroxenite	07AB G1	Lower Main Zone	Phase 2	347225	6200775	zircon	178.4 ±0.4	Based on oldest grain; minimum age
Syenite	07AB G5	Lower Main Zone	Phase 2	347365	6200895	zircon	177.3 ±0.4	Based on 2 point weighted average of ^{206}Pb/^{238}U dates; minimum age

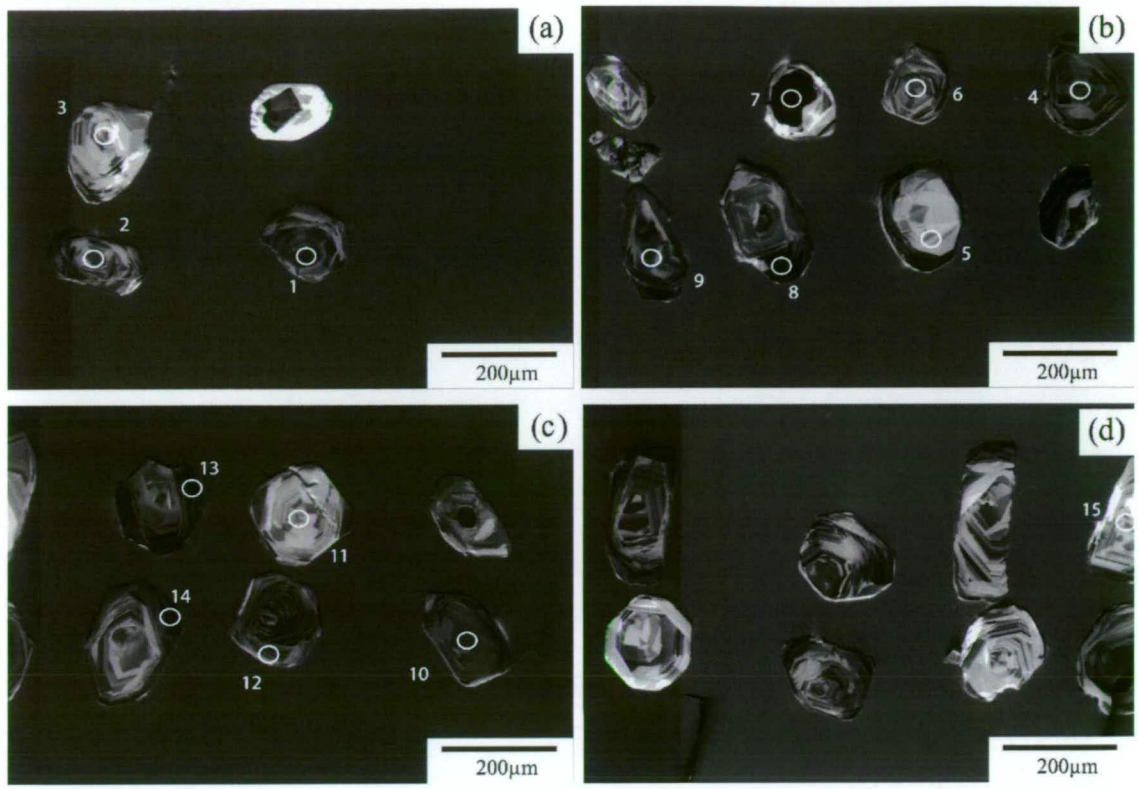

Figure 3-24. (a-d) Images of growth zones of zircon grains and spot location (white circles) in CL. Zircon grains were used for isotopic analysis using the SHRIMP-RG method (sample 07AB-G4, 347550mE, 6200680mN).

3.6.2.2. Syenite (Phase 1) sample 07AB-G7

A chalcopyrite mineralised syenite from the southern area of the Lower Main Zone was collected to determine the crystallisation age and to place a maximum age constraint on the timing of main-stage mineralisation (Fig. 3-27c, d). The syenite is non-foliated, and crops out to the south of mineralised syenite that has a shallow to moderately steep dipping, west northwest-trending foliation. An age of 178.4 ± 0.3 Ma was calculated based on 2 point weighted average $^{206}Pb/^{238}U$ (Fig. 3-27c, d; Table 3-2; MSWD = 1.5). Three of the five fractions were discarded based the inference of Pb-loss, and hence the above age is considered as a minimum age estimate for the crystallisation age of the syenite.

3.6.2.3. Rhythmic layered diopside syenite (Phase 1) sample 07AB-G3

A sample of rhythmic layered diopside syenite, from the south-central area of the Lower Main Zone was collected to determine its crystallisation age and to place a maximum age constraint on the timing of tilting of the Lower Main Zone (Fig. 3-15a-d). The diopside syenite in most parts does not show evidence in thin section of a shear foliation; although two outcrops showed minor evidence of a ductile deformation fabric. In the central area of the Lower Main Zone the rhythmic layered diopside syenite has very weak chalcopyrite and pyrite mineralisation and is therefore thought to pre-date or be synchronous with main-stage mineralisation. An age estimate of 178.6 ± 0.2 Ma was calculated based on a 4 point

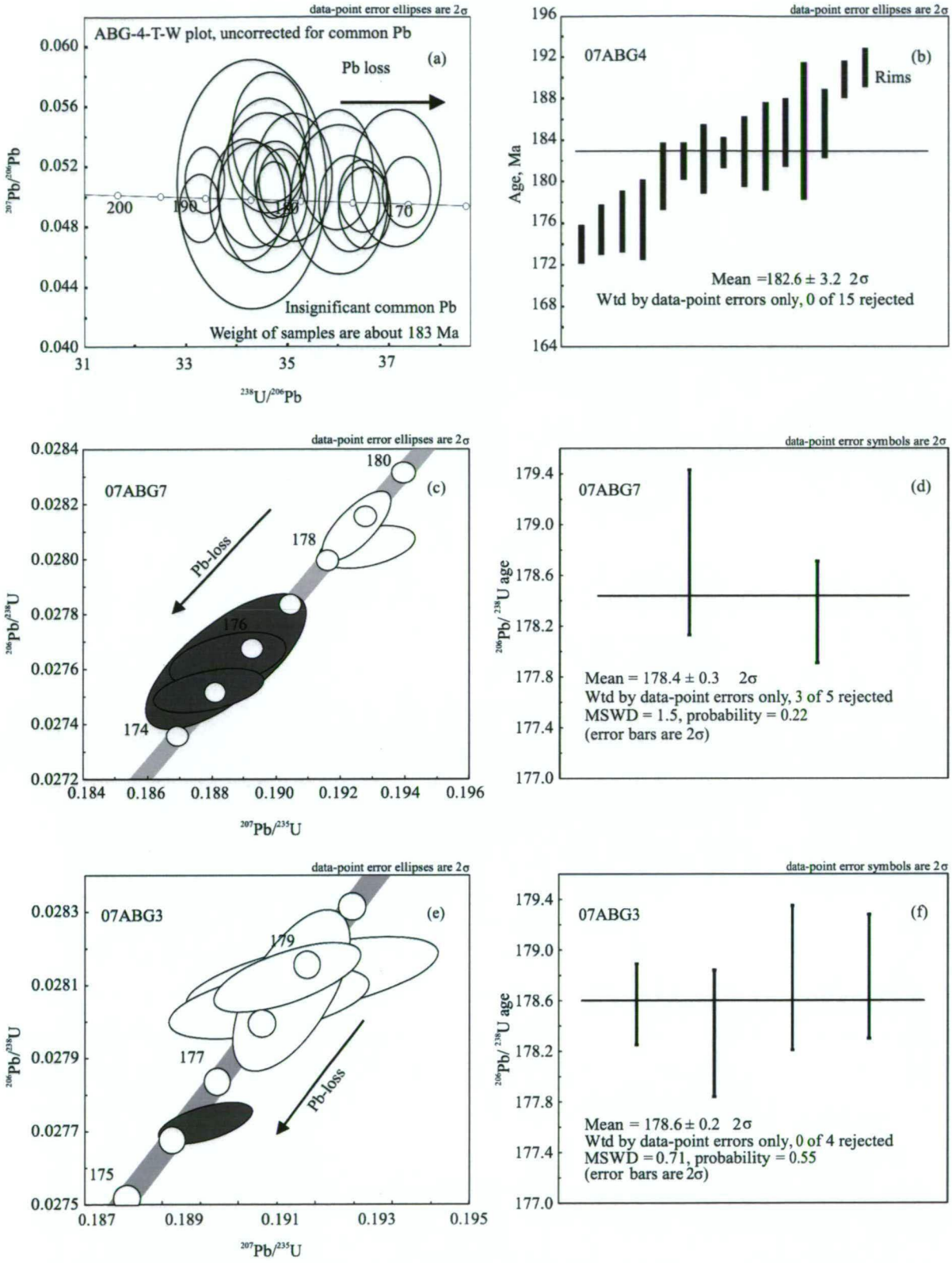

Figure 3-25. Conventional U-Pb concordia plots and weighted mean ^{204}Pb corrected $^{206}Pb/^{238}U$ plots with uncertainty bars used to interpret the ages of dated rocks from the Lower Main Zone, Lorraine. **(a-b)** SHRIMP-RG data from Phase 1 syenite 07AB-G4, **(c-d)** ID-TIMS data from Phase 1 altered syenite (sample 07AB-G7). **(e-f)** ID-TIMS data from Phase 1 rhythmic layered syenite (sample 07AB-G3).

Figure 3-26. Altered Phase 1 syenite from the Lower Main Zone with patches of early coarse diopside and magnetite alteration. Zircons from this sample dated by conventional ID-TIMS (see Chapter 4, sample 07AB-G7, 347330mE, 6200580mN).

weighted average of $^{206}Pb/^{238}U$. The youngest zircon fraction was rejected on the interpretation of Pb-loss. The multiple overlapping concordant results shown here provides a robust age interpretation (Fig. 3-25e, f; Table 3-2; MSWD = 0.71). This crystallisation age places a maximum age constraint on the timing of ductile deformation, tilting and mineralisation within the Lower Main Zone.

3.6.2.4. Diopside-biotite syenite (Phase 2) sample 07AB-G2

Phase 2 syenite from the central area of the Lower Main Zone cross-cuts mineralised biotite pyroxenite and strongly foliated mineralised fine-grained K-feldspar biotite rock, and was dated to place a minimum age constraint on the timing of mineralisation and the east-trending biotite-rich solid-state deformation fabric (Fig. 3-27a, b). The Phase 2 syenite has been cross-cut by a Phase 3 leucosyenite dyke which places a maximum age constraint on the leucosyenite dykes (Fig. 3-27a). The phase 2 syenite was analysed using ID-TIMS, and an age of 178.7 ± 0.3 Ma was calculated based on 3 point weighted average of $^{206}Pb/^{238}U$. One of the four zircon fractions was rejected for the weighted age based on the assumption of radiogenic Pb-loss (Fig. 3-28a-b; Table 3-2; MSWD = 0.36).

3.6.2.5. Diopside-biotite syenite (Phase 2) sample 07AB-G5

A barren Phase 2 syenite from the northern area of the Lower Main Zone has cross-cut the foliated fine-grained K-feldspar biotite rock with a sub-vertical contact. This Phase 2 syenite was dated to place minimum age constraints on the sub-vertical east-trending foliation and Phase 1 fine-grained K-feldspar biotite rocks in the northern area of the Lower

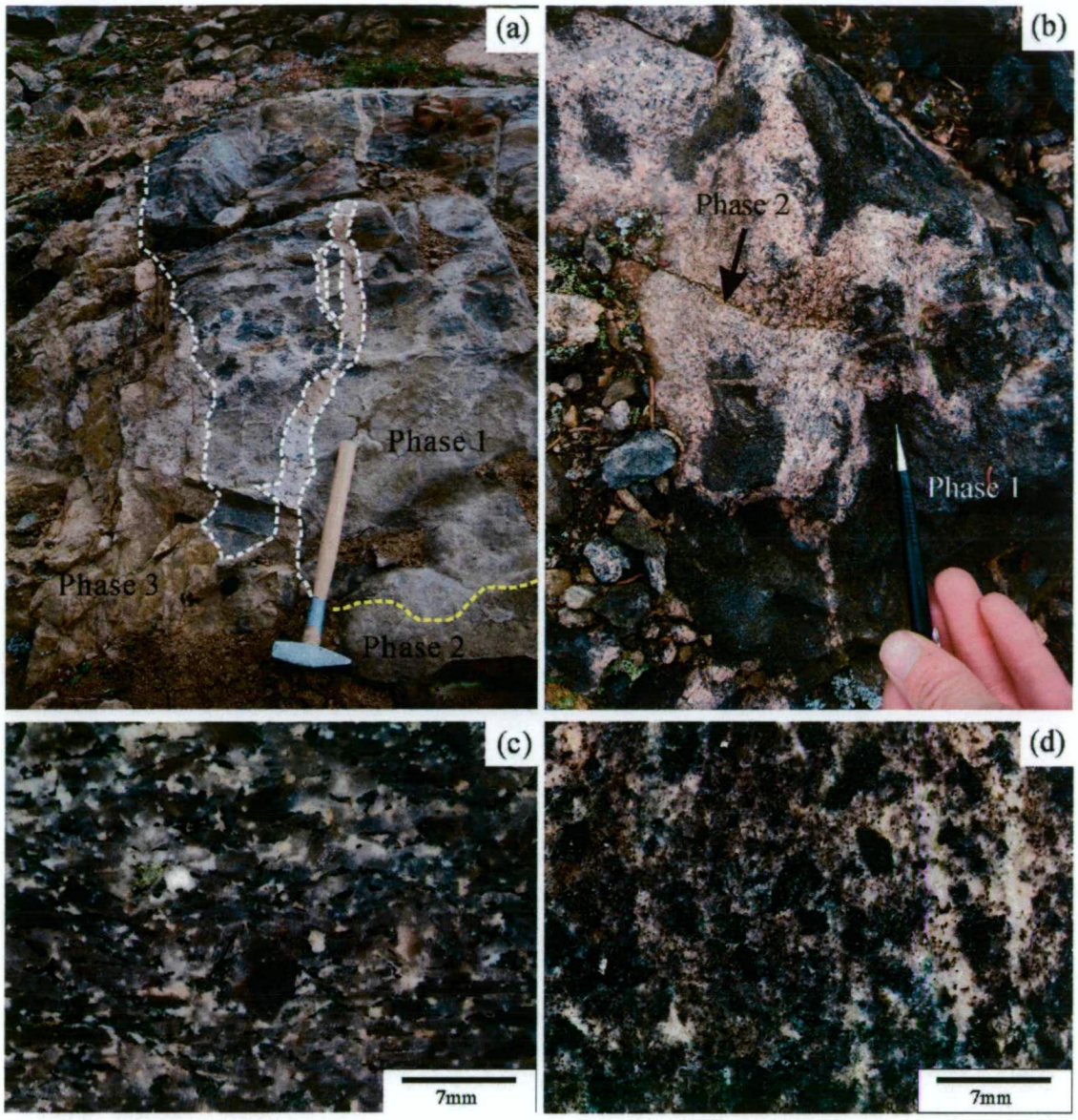

Figure 3-27. **(a)** Outcrop in the Lower Main Zone consisting of strongly foliated altered fine-grained K-feldspar biotite rock that is cross-cut by unaltered Phase 2 syenite (07AB-G2) and Phase 3 leucosyenite (347249mE, 6200715mN). **(b)** Phase 2 syenite (07AB-G2) from a dyke in the Lower Main Zone that has cross-cut altered and mineralised biotite pyroxenite (347273mE, 6200709mN, NAD83). **(c)** Phase 2 syenite (07AB-G2, 347249mE, 6200715mN). **(d)** Phase 2 biotite altered diopside syenite from a steeply dipping body in the northern area of the Lower Main Zone; this rock has cross-cut unaltered fine-grained K-feldspar rock (*see* Fig. 3-5b). The diopside syenite was dated using the ID-TIMS method (07AB-G5, 347365mE, 6200895mN).

Main Zone (Fig. 3-27d). An age of 177.3 ± 0.4 Ma was calculated based on a 2 point weighted average of $^{206}Pb/^{238}U$ (Fig. 3-28c-d; Table 3-2; MSWD = 0.16). Two zircon fractions were omitted from the weighted age calculation because they showed signs of radiogenic Pb-loss. The above age estimation is considered here to be a minimum crystallisation age.

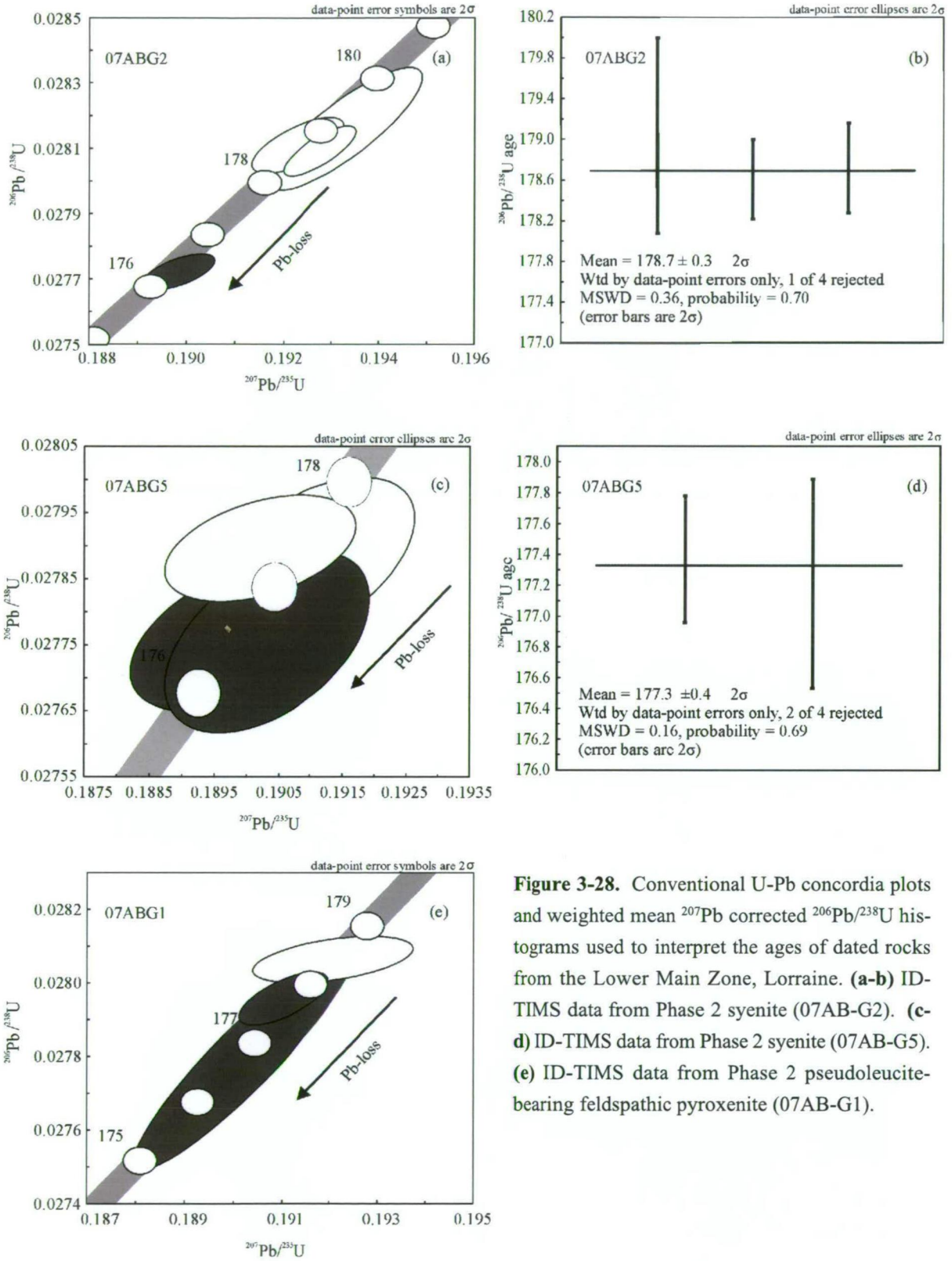

Figure 3-28. Conventional U-Pb concordia plots and weighted mean ^{207}Pb corrected $^{206}Pb/^{238}U$ histograms used to interpret the ages of dated rocks from the Lower Main Zone, Lorraine. **(a-b)** ID-TIMS data from Phase 2 syenite (07AB-G2). **(c-d)** ID-TIMS data from Phase 2 syenite (07AB-G5). **(e)** ID-TIMS data from Phase 2 pseudoleucite-bearing feldspathic pyroxenite (07AB-G1).

3.6.2.6. Pseudoleucite-bearing feldspathic pyroxenite (Phase 2) sample 07AB-G1

Pseudoleucite-bearing feldspathic pyroxenite with a medium-grained biotite and diopside groundmass was analysed to determine the age of late mafic magmatism in the Lower Main Zone (Fig. 3-10a). The pseudoleucite-bearing feldspathic pyroxenite occurs as a sub-vertical east-trending body that cuts weakly mineralised syenite. The oldest grain has undergone the least and possibly negligible Pb-loss, and therefore best represents the age of the sample. An age interpretation of 178.4 ± 0.3 Ma is considered here to represent the minimum crystallisation age for the Phase 2 pseudoleucite-bearing feldspathic pyroxenite (Fig. 3-28e). However this age assumes that this rock has not assimilated zircon from wall rocks, which cannot be ruled out based on a relatively high concentration of Zr in this sample (i.e. ~100 ppm).

3.7. Discussion and Conclusions

3.7.1. Constraints on the timing of geological events in the Lower Main Zone

Phase 1 rhythmic layered diopside syenite is inferred to dip moderately to shallowly towards the south, is in part weakly mineralised, and is thought to have been emplaced sub-vertically prior to tilting and likely during the waning stages of main-stage mineralisation. Zircons from Phase 1 rhythmic layered diopside syenite yielded a crystallisation age of 178.6 ± 0.2 Ma that places a maximum age constraint on the timing of tilting of the Lower Main Zone at 178.8 Ma. A minimum age constraint on the timing of tilting is constrained by the minimum age of Phase 2 syenite which dip sub-vertically and cross-cut mineralised Phase 1 rocks. Phase 2 syenite from the central area cross-cut mineralised fine-grained K-feldspar biotite rock, and places a lower age constraint on the timing of tilting and mineralisation at 178.4 Ma. Thus from the data set, tilting and mineralisation of the Lower Main Zone is estimated to have occurred between 178.8 and 178.4 Ma (Fig. 3-29).

Tilted and in part weakly mineralised rhythmic layered diopside syenite rocks in the central area of the Lower Main Zone show a weak E-W sub-vertical ductile fabric at one outcrop, but in all other areas appear unstrained. Hence the maximum age of rhythmic layered diopside syenite places a maximum age constraint on the timing of (at least minor) ductile deformation at 178.8 Ma. In contrast unstrained Phase 2 syenite cross-cuts strongly deformed rocks in the central area of the Lower Main Zone and place a minimum age constraint on the timing of ductile deformation at 178.4 Ma. Thus the timing of ductile deformation of the Lower Main Zone is also estimated to have occurred between 178.8 Ma and 178.4 Ma (Fig. 3-29).

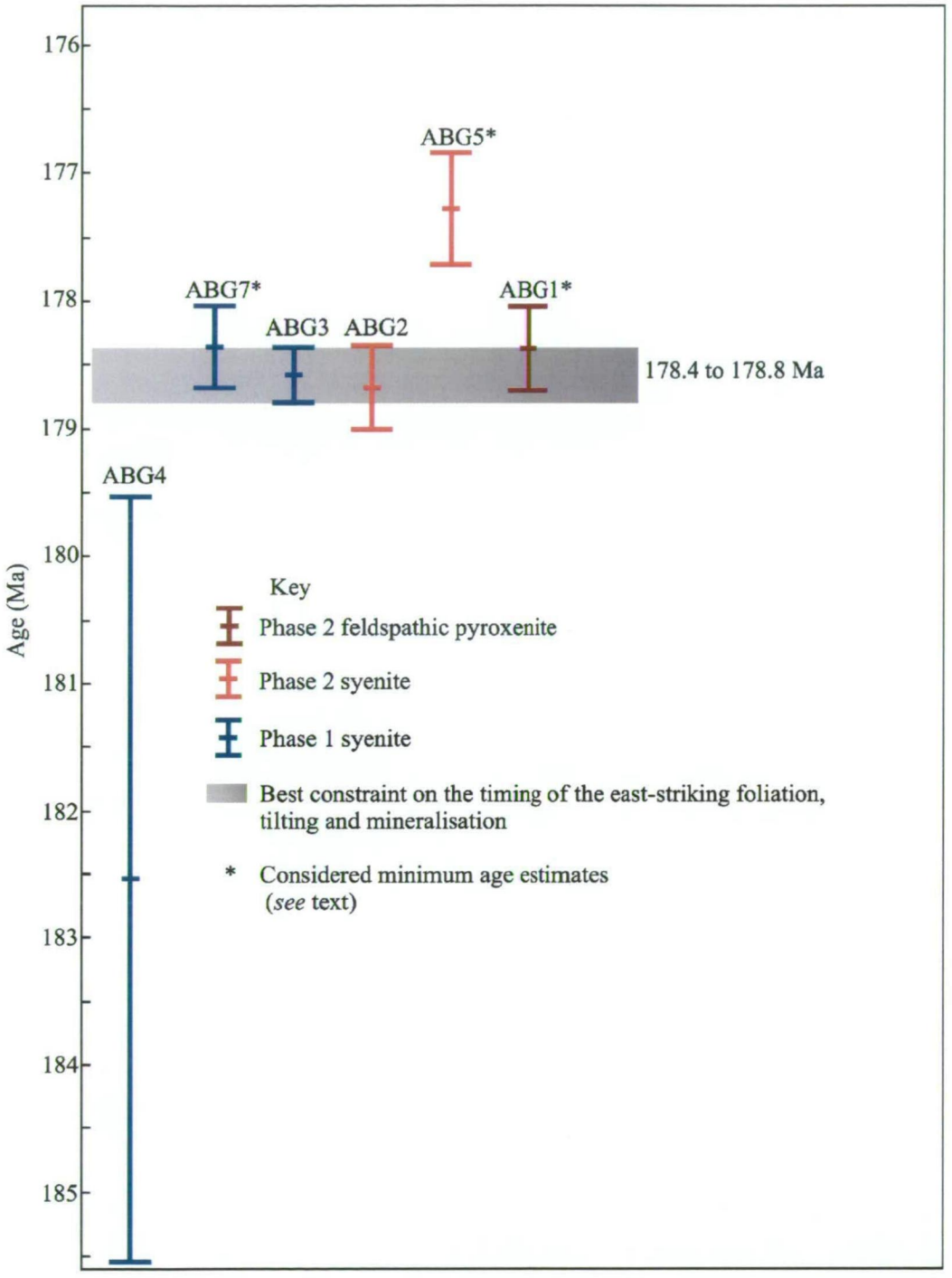

Figure 3-29. Compilation of zircon ages obtain from Phase 1 and Phase 2 rocks from the Lower Main Zone. Isotopic analysis of zircon was carried out using the SHRIMP-RG and ID-TIMS methods. Based on data collected during this study it appears that the timing of mineralisation tilting and ductile deformation is constrained between 178.8 and 178.4 Ma (*see* text for details).

The final main magmatic events involve the intrusion of leucosyenite and coarse-grained K-feldspar syenite dykes at ca. 177 Ma. These dykes have been cross-cut by brittle steeply dipping NNE-trending faults which have no minimum age constraint; although regional mapping to the north of the Hogem Batholith showed that late brittle faults with similar orientations are related to Late Cretaceous to Early Tertiary deformation events (Zhang and Hynes, 1992, 1994; Schiarizza and Tan, 2005).

3.7.2. Solid-state deformation

The strong dominantly east-trending sub-vertical ductile deformation fabric in the Lower Main Zone is constrained to the latest Early Jurassic based on the U-Pb zircon ages and cross-cutting relationships. Based on property-scale mapping by Teck Ltd, the solid-state deformation fabric appears to be a feature mainly restricted to Phase 1 rocks of the Lower Main Zone and parts of the Main Zone; although localised ductile shear zones have also been identified in other parts of the Duckling Creek Syenite Complex (i.e. Misty and Slide Mountain areas; Baxter and Devine, 2007). Significant variations in the intensity of the ductile fabric across the Lower Main Zone, and the noted absence of the fabric in Phase 1 rocks outside of the Lower Main and Main zones support the notion that the ductile fabric formed in localised shear zones (Sillitoe, 2007; Garratt and Lindinger, 2008). Cross-cutting relationships combined with absolute ages suggest that ductile deformation occurred during a time of active magmatism, and hence the Lower Main Zone was likely anomalously hot and therefore rheologically weak compared with adjacent wall rocks. In particular, as noted by Fournier (1999) the brittle-plastic transition commonly occurs at about 370 ° to 400 °C within presently active continental hydrothermal systems, as water allows plastic behaviour to occur at lower temperatures (e.g., Carter and Tsenn, 1986). Alternatively, high temperature deformation may have also occurred around the margin of dykes, due to stretching and ductile deformation of adjacent wall rocks (e.g., Vernon and Johnson, 2004).

3.7.3. Geological model for the genesis of the Lower Main Zone

The model shown in Figure 3-30 is largely based on concepts by Sillitoe (2007), Teck Ltd and Garratt and Lindinger (2008) for the Lorraine deposit. Modifications to the model include the development of an early pervasive fine-grained fluorine-rich biotite and K-feldspar alteration event, an early pre-mineral and pre-tilting ductile fabric and rotation of mineralised roof rocks along possible faults above a magma chamber.

- Stage 1 includes pervasive early alteration of a felsic wall rock with Fe-K- and F-rich fluid followed by the emplacement of Phase 1 biotite pyroxenite and syenite

intrusives (Fig. 3-30a).

• Stage 2 includes a pre-main stage mineralisation ductile deformation fabric that is in turn overprinted by K-feldspar alteration and main-stage mineralisation (Fig. 3-30b).

• Stage 3 includes rotation and tilting of the Lower Main Zone, along with ductile deformation. Following deformation Phase 2 and Phase 3 intrusives were emplaced (Fig. 3-30c). Late brittle faults (not shown in Fig. 3-30) cut all ductile features and Phase 3 intrusives.

3.7.3.1. Concluding remarks

The model indicates that an early pre-mineral deformation event occurred, and this was followed by mineralisation. Tilting and a deformation event post-dates mineralisation. The former is concluded based on the fact that the sulphide zonation pattern in the Lower Main Zone is tilted. Hence it is unlikely that all these events occurred simultaneously. Some events may overlap, such as the emplacement of dykes, and heating of the wall rocks. These hot rocks would have been rheologically weak compared with adjacent wall rocks, and thus prone to deformation. It is also possible that emplacement of the dykes themselves, in some cases invoked solid-state deformation in the adjacent wall rocks. In most cases, however it did not appear to be obvious that solid state deformation intensified around the margin of individual dykes.

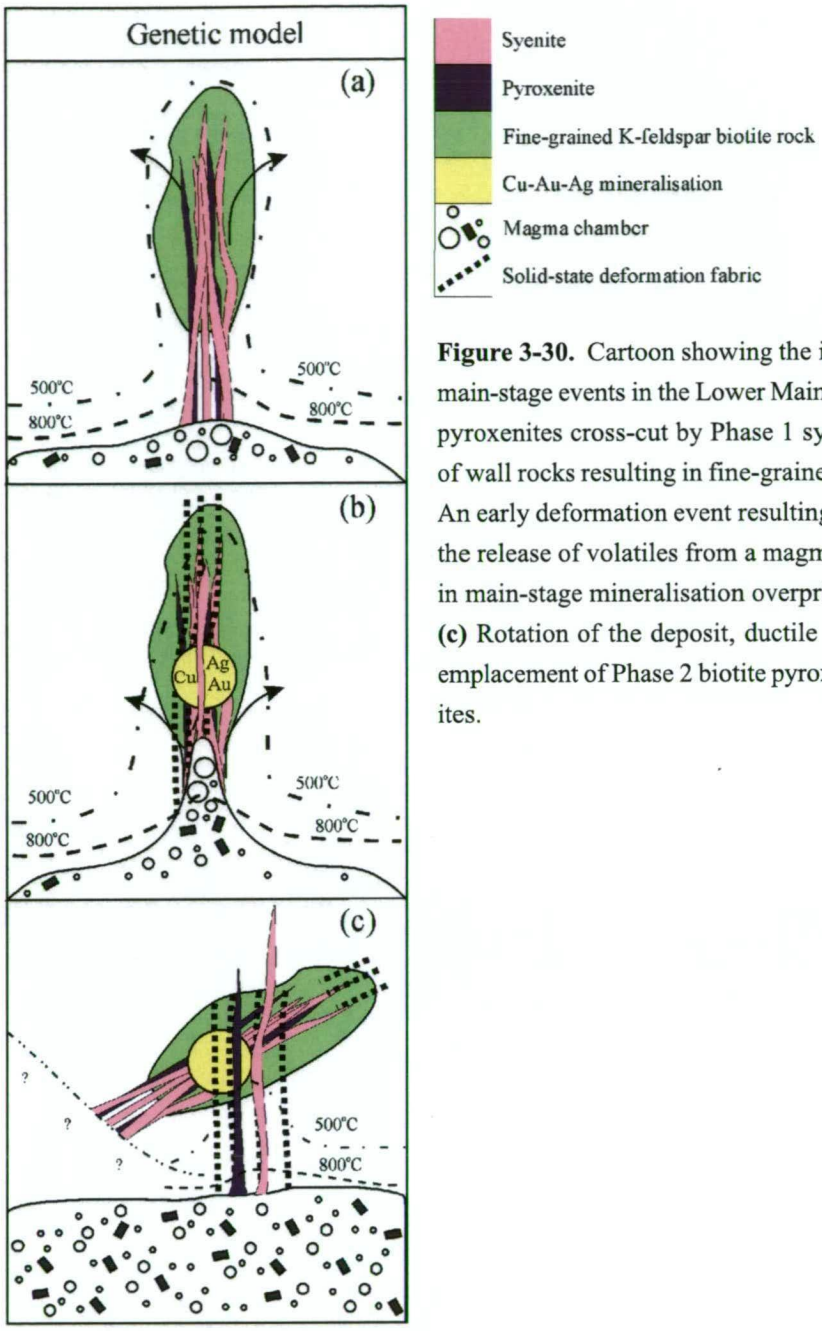

Figure 3-30. Cartoon showing the interpreted early, syn and post main-stage events in the Lower Main Zone. **(a)** The Phase 1 biotite pyroxenites cross-cut by Phase 1 syenites and the metasomatism of wall rocks resulting in fine-grained K-feldspar biotite rock. **(b)** An early deformation event resulting in ductile fabric followed by the release of volatiles from a magma chamber at depth, resulting in main-stage mineralisation overprinting the early ductile fabric. **(c)** Rotation of the deposit, ductile deformation followed by the emplacement of Phase 2 biotite pyroxenite and Phase 2 and 3 syenites.

CHAPTER 4
OVERVIEW OF ALTERATION AND MINERALISATION IN THE LOWER MAIN ZONE

4.1. Introduction

Porphyry-style ore deposits are commonly zoned, and an understanding of their alteration zonation patterns and temporal relationships can aid in the reconstruction of their original geometries (e.g. Lowell and Guilbert, 1970; Titley, 1982). As outlined in Chapter 1, alkalic Cu-Au porphyry deposits are considered to be small compared to their calc-alkalic equivalents (e.g., Cooke et al., 2007; Tosdal et al., 2008), but can occur as higher grade ore bodies, and in some cases are significantly enriched in Au (e.g., Ridgeway NSW, Australia; Wilson et al., 2003). They are also known to be associated with small volume pipe-like intrusives and intensely developed hydrothermal alteration zones that are restricted to within a few hundred meters of the intrusive complex (Cooke et al., 2007). Hence a detailed understanding of spatial alteration patterns and paragenetic relationships are important for understanding their architecture and genesis.

4.1.1. Terminology

The terms for alteration used in this study are based on definitions by Titley (1982); with the additional term "patches", which has been added to characterise highly irregular zones partially or totally infilled with secondary minerals (Table 4-1).

Table 4-1. Terminology for alteration and mineralisation used in the current study, modified from Titley (1982).

Term	Definition
Pervasive alteration	Alteration in which original rock textures and mineralogy have been completely changed
Selective-pervasive alteration	Alteration in which select mineral(s) of the original rock have been altered. This type of alteration is not texturally destructive
Patches	Highly irregular isolated zones partially or totally infilled with secondary minerals. Typically <30cm in size
Vein-veinlet	Fractures with planar to irregular margins that have been partially or totally infilled with secondary minerals. Vein = >5mm wide, veinlet = 5mm wide
Stringer	A series of veinlets occurring in a discontinuous subparallel pattern in wall rock
Alteration envelope	Pervasive or selective-pervasive alteration of wallrock adjacent to patches, veins or veinlets

4.2. Alteration and mineralisation at Lorraine

4.2.1. Previous work

A number of previous studies have described alteration and mineralisation of the Lorraine deposit (e.g., Koo, 1968; Wilkinson et al., 1976; Bishop et al., 1995; Nixon and Peatfield, 2003; Baxter and Devine, 2007; Sillitoe, 2007). Findings of previous work on alteration at Lorraine include;

- Koo (1968) suggested that the Lorraine property consists of syenite or fenite formed by the metasomatism of the fractured Hogem diorite. Metasomatic fluids were believed to have been derived from a hypothetical alkalic magma source that existed beneath the diorite body. Koo (1968) suggested seven successive stages of alteration within the Main Zone, which included; (1) biotite, (2) albite, (3) orthoclase, (4) quartz, (5) sericite, (6) chlorite and (7) epidote.

- Wilkinson et al. (1976) noted that the Lower Main and Main zones are characterised by high biotite and chlorite content, K-feldspar replacement, pervasive sericitisation and the presence of accessory epidote and magnetite with mineralisation. Wilkinson et al. (1976) also noted sulphide zonation in the Lower Main Zone as erratically distributed individual lenses with cores of *bornite with minor chalcopyrite* grading outwards to *chalcopyrite with minor bornite* and outer rims of *chalcopyrite with minor pyrite*.

- Bishop et al. (1995) reported three major alteration assemblages within the Bishop Zone, which included; (1) early potassium metasomatism resulting in secondary biotite, (2) main-stage K-feldspar alteration; and (3) late-stage, weak sericitisation and propylitisation (chlorite-epidote-carbonate). Bishop et al. (1995) also hypothesised that net-textured Cu-Fe sulphides in pyroxenites at Lorraine may be related to a possible magmatic sulphide component in a 'deep' crustal root zone of the deposit (*see* Chapter 5).

- Nixon and Peatfield (2003) described potassic alteration in the Main and Lower Main zone as pale to salmon pink, massive to locally foliated, with mineralised rocks characterised by pervasive flooding of potassium feldspar. Nixon and Peat-

field (2003) also noted irregular dark brown-grey zones of fine-grained biotite-magnetite ± potassium feldspar ± sulphide which are superimposed on K-feldspar alteration, and in turn are crosscut by stringers of potassium feldspar, and subsequently by epidote, chlorite, carbonate, sericite and clay alteration.

• More recently, Baxter and Devine (2007) and Sillitoe (2007) documented early-stage, main-stage and late-stage alteration assemblages within the Bishop, Main and Lower Main zones. Early alteration consists of magnetite-diopside ± apatite ± biotite locally associated with irregular hydrothermal breccia bodies. Main-stage sulphide mineralisation was reported to occur with local pervasive K-feldspar alteration of syenite and biotite alteration of mafic minerals. Late-stage alteration consisted of an earlier assemblage of epidote and hematite, and pale-green to white muscovite and fine-grained calcite alteration of coarse-grained syenite. Sillitoe (2007) also reported unambiguous well developed sulphide zoning in the Bishop zone, with a bornite and chalcocite core that grades outwards

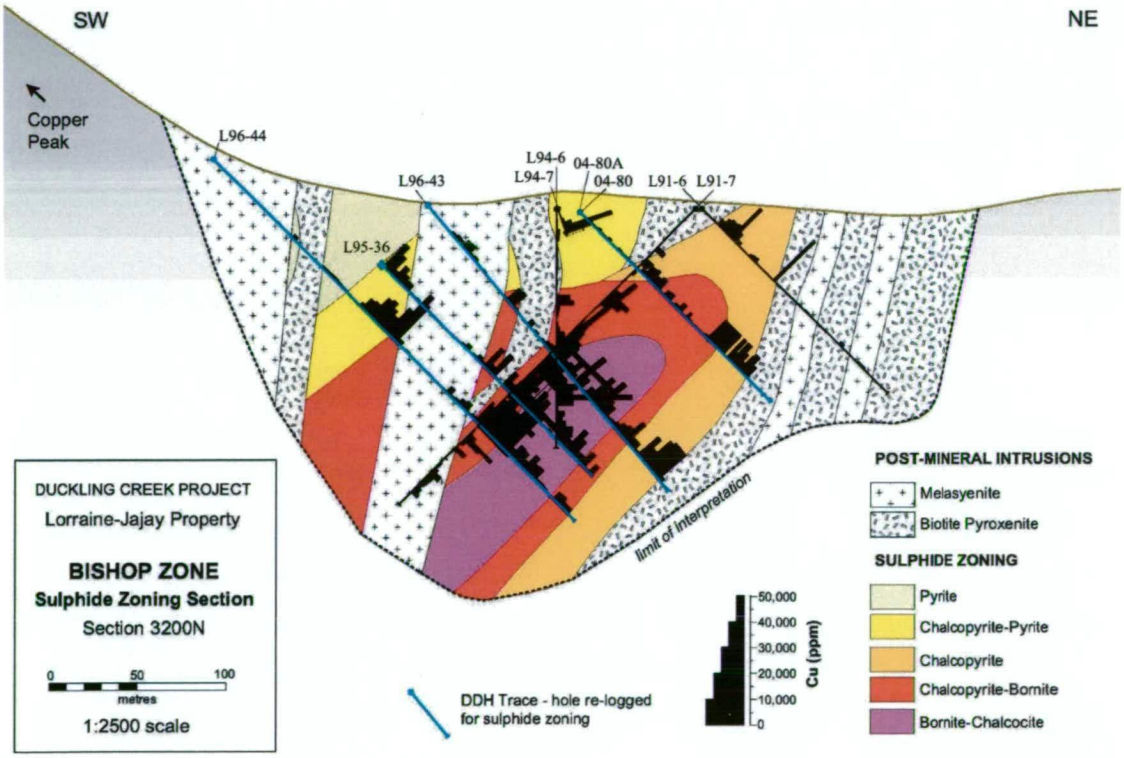

Figure 4-1. Interpreted cross-section of sulphide zonation within the Bishop Zone (section 3200N) at Lorraine. The cross-section also shows that mineralised rocks are cross-cut by post-mineralisation syenites and biotite pyroxenites (after Sillitoe, 2007).

through chalcopyrite-bornite and chalcopyrite-pyrite zones to a pyrite-only halo. Mineralisation forms a body that dips 40° south- to southwest (Fig. 4-1), sub-parallel to a regional primary magmatic flow fabric defined by the alignment of phenocrysts (Devine et al., 2007). Sulphide zonation was also recognised in the Main Zone with a similar pattern to the Bishop Zone; however the core zone is represented by chalcopyrite and bornite rather than bornite-chalcocite and the outer pyritic zone in the hanging wall is interpreted to have been eroded (Sillitoe, 2007).

4.3. The Lower Main Zone ore body

The boundary of the Lower Main Zone ore body is defined by contours of 0.2 wt. % Cu, 50 ppb Au and 1 ppm Ag. The orebody dips moderately to shallowly towards the south-southwest, varies in thickness from <50 m to 200 m and has been traced southwards down dip for at least 300 m (Figs. 4-2a-c and 4-3a-c). In places the ore contours are irregular, which is partly related to the intrusion of post-main stage dykes that have caused local dilution.

The contour patterns for Cu, Au and Ag show that areas of abundant Cu correlate with Au- and Ag-rich zones (Figs. 4-2a and 4-3a). Scatter plots of Cu versus Au and Ag show positive correlations (Fig. 4-4a, b), and there is no obvious difference in Cu:Au or Cu:Ag ratios between the various host rocks, suggesting that the host rock composition (biotite pyroxenite, fine-grained biotite K-feldspar rock or syenite), did not cause detectable fractionation between Cu, Au and Ag. Electrum inclusions have been identified in bornite from the Bishop Zone (e.g., Fig 4-5a, b), and the presence of electrum inclusions in Cu-Fe sulphides may also explain the positive correlations of Cu with Ag and Au in the Lower Main Zone.

Palladium, which was analysed in three drill holes (i.e. 2001-56, 2001-48 and 2002-62), is on average enriched in mineralised biotite pyroxenite (i.e. Pd up to ~40 ppb) compared to syenite and fine-grained K-feldspar biotite rocks (i.e. Pd <20 ppb; Figs. 4-4d and 4-6). The drill log of hole 2001-56 in Figure 4-6 shows lithology, sulphide mineralogy, Pd and Cu abundance, and shows that Pd is most enriched in Phase 1 biotite pyroxenite from bornite-chalcocite and chalcopyrite-pyrite zones. Mineralised syenite in the top 90 m of drill hole 2001-56 is notably poor in Pd, compared with barren Phase 2 biotite pyroxenite and pyrite ± chalcopyrite mineralised syenite in the lowest 65 m of the drill hole. At Lorraine merenskyite ($PdTe_2$) and melonite (Ni, Pd, Pt)Te_2 (Pt <15 ppb in Lower Main Zone) occur as inclusions in bornite, chalcocite and albite (Nixon et al., 2004). Nixon et al. (2004) also demonstrated that at Lorraine the bornite lattice does not contain PGE.

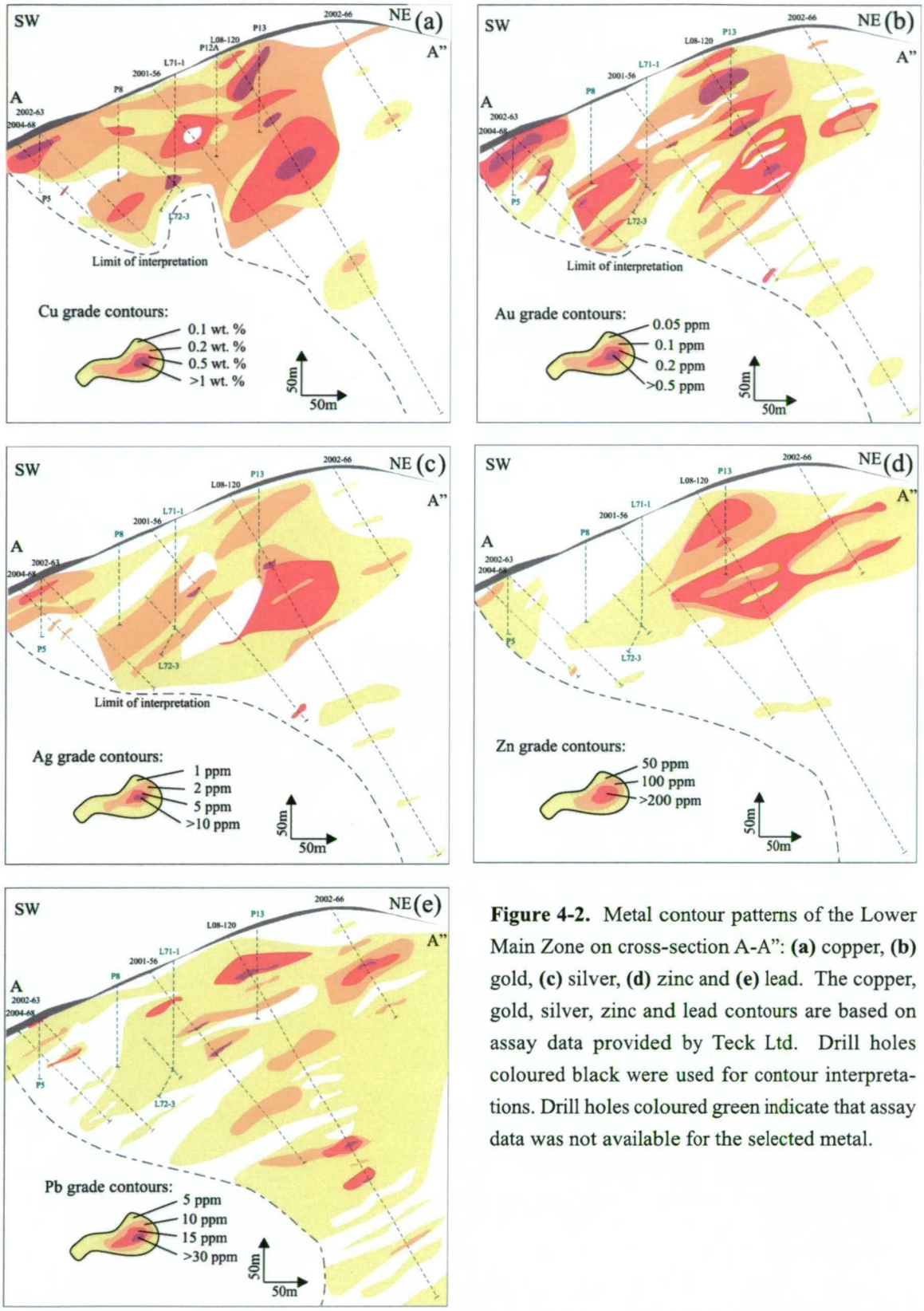

Figure 4-2. Metal contour patterns of the Lower Main Zone on cross-section A-A": **(a)** copper, **(b)** gold, **(c)** silver, **(d)** zinc and **(e)** lead. The copper, gold, silver, zinc and lead contours are based on assay data provided by Teck Ltd. Drill holes coloured black were used for contour interpretations. Drill holes coloured green indicate that assay data was not available for the selected metal.

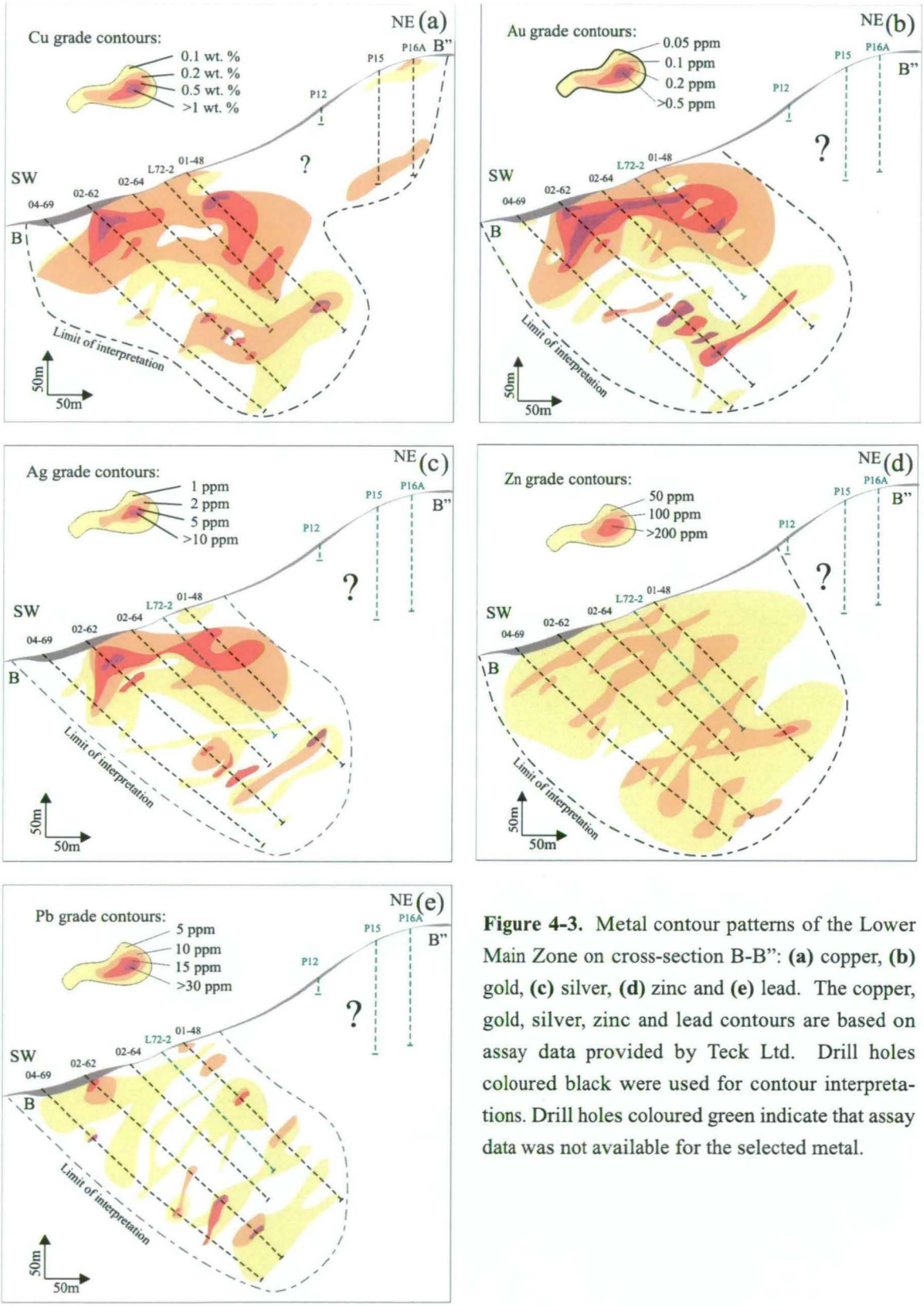

Figure 4-3. Metal contour patterns of the Lower Main Zone on cross-section B-B": **(a)** copper, **(b)** gold, **(c)** silver, **(d)** zinc and **(e)** lead. The copper, gold, silver, zinc and lead contours are based on assay data provided by Teck Ltd. Drill holes coloured black were used for contour interpretations. Drill holes coloured green indicate that assay data was not available for the selected metal.

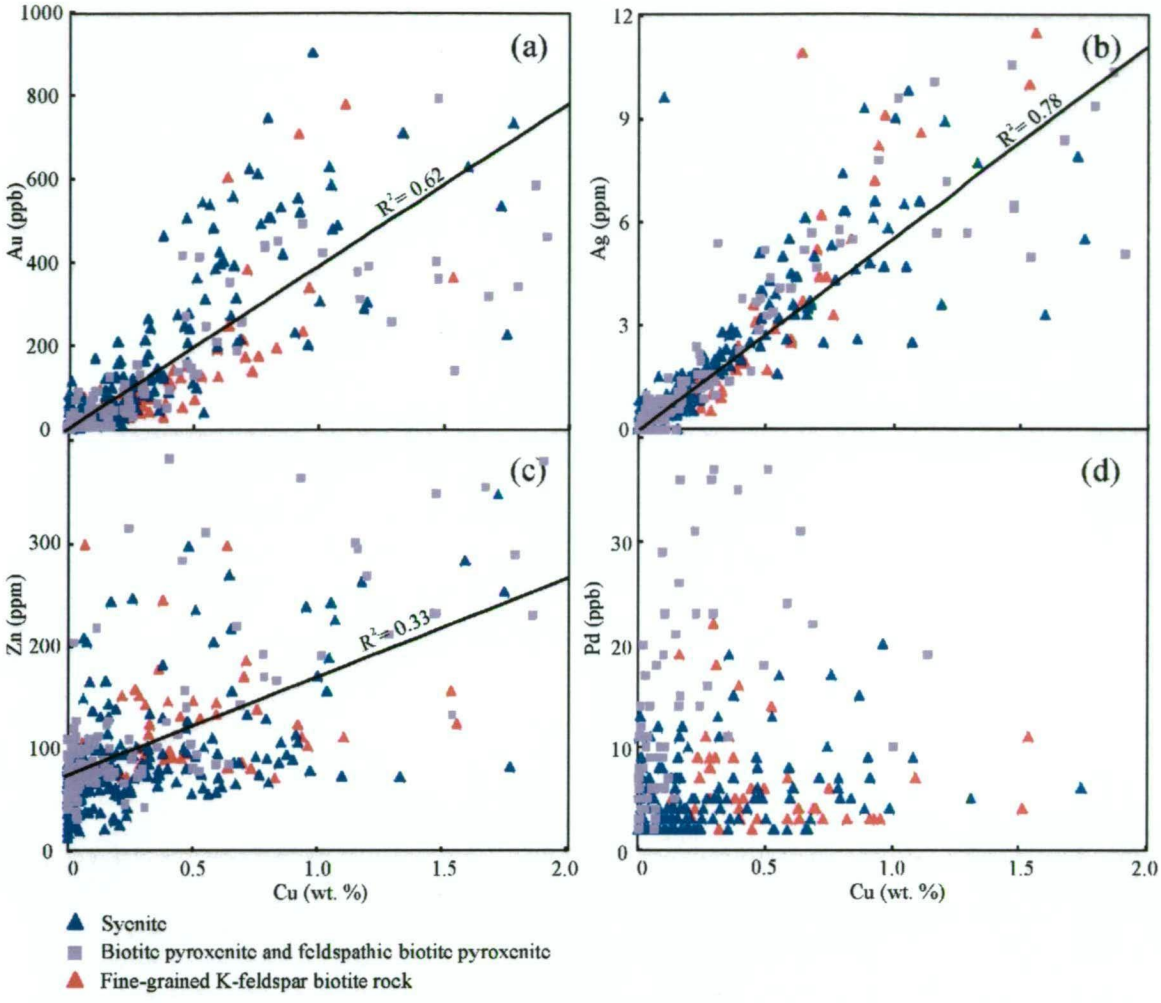

Figure 4-4. Scatter plots of assay data. **(a)** Gold versus copper, **(b)** silver versus copper, **(c)** zinc versus copper and **(d)** palladium versus copper for assay data from drill holes 2002-63, 2001-56, L08-120 and 2002-66. Drill holes are from cross-section A-A" of the Lower Main Zone. Assay data was provided by Teck Ltd.

The zinc content of bornite-chalcopyrite mineralised rocks is higher in the north-eastern area of the Lower Main Zone than in the southern area of the Lower Main Zone (i.e. up to 450 ppm; Fig. 4-2d). The association of elevated Zn with Cu, Au and Ag in mineralised rocks suggests that minor Zn was also deposited during main-stage mineralisation (most likely as sphalerite (?), Chapter 5; Figs. 4-2d and 4-3d). The relative increase of Zn in mineralised rocks in the north-eastern area of the Lower Main Zone compared to the southern area may be evidence of minor host rock control on Zn-deposition. Lead in contrast has no obvious zonation pattern and is variability enriched in the Lower Main Zone (i.e. up to 65 ppm; Figs. 4-2e and 4-3e).

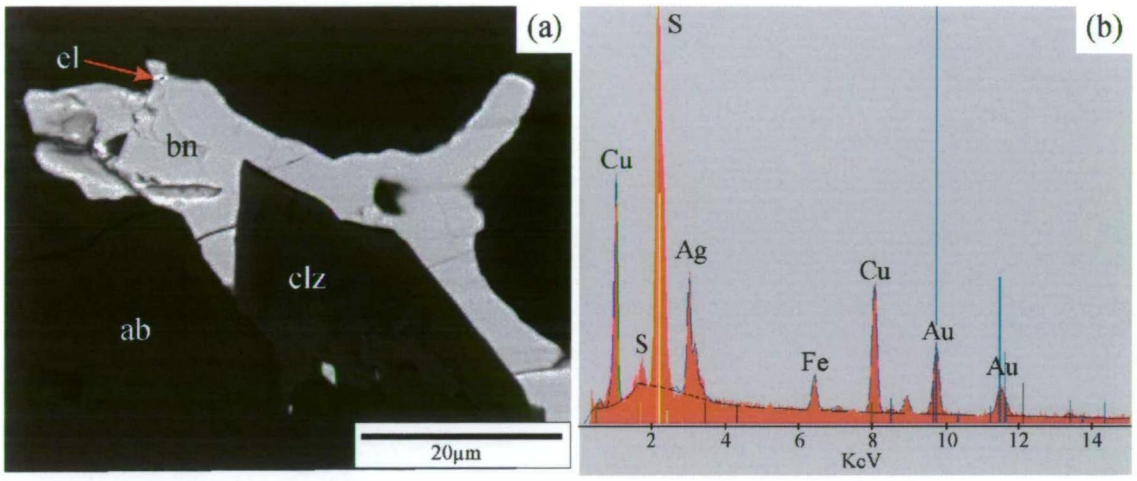

Figure 4-5. **(a)** Back-scatter electron image of bornite mineralisation in syenite. Note that bornite includes a small inclusion of electrum (?). **(b)** Energy dispersive spectrum (EDS) of the electrum (?) inclusion (Au and Ag) in bornite (Cu, Fe and S) as shown in "a". Syenite from the Bishop Zone (drill hole 1996-43_167m). Mineral abbreviations ab = albite, bn = bornite, clz = clinozoisite and el = electrum.

4.3.1. Abundance of copper in host rocks

Bar graphs showing the abundance of copper are compared to assess the variation in copper between different rock types (Figs. 4-7 and 4-8). The comparison between Cu-grades and lithology demonstrates that the abundance of copper changes sharply between different host-rock types. In particular contacts between fine-grained K-feldspar biotite rock and syenite show sharp changes in the abundance of copper (Figs. 4-7), with syenite in some areas showing significantly lower grades than adjacent fine-grained K-feldspar biotite rocks. Biotite pyroxenite show sharp spikes in copper abundance in drill holes 2001-56 and 2001-48 (Fig. 4-7). Sharp decreases in the abundance of copper occur where Phase 1 mineralised biotite pyroxenites have been cross-cut by dykes of barren Phase 2 biotite pyroxenite, monzonite or Phase 2 syenite; however sharp decreases in copper also occur where Phase 1 mineralised biotite pyroxenites have been cross-cut by weakly mineralised Phase 1 syenite.

Figure 4-6. Simplified geology, sulphide mineralogy, and copper- and palladium-grades of drill hole 2001-56 from cross-section A-A" of the Lower Main Zone. Assay data provided by Teck Ltd.

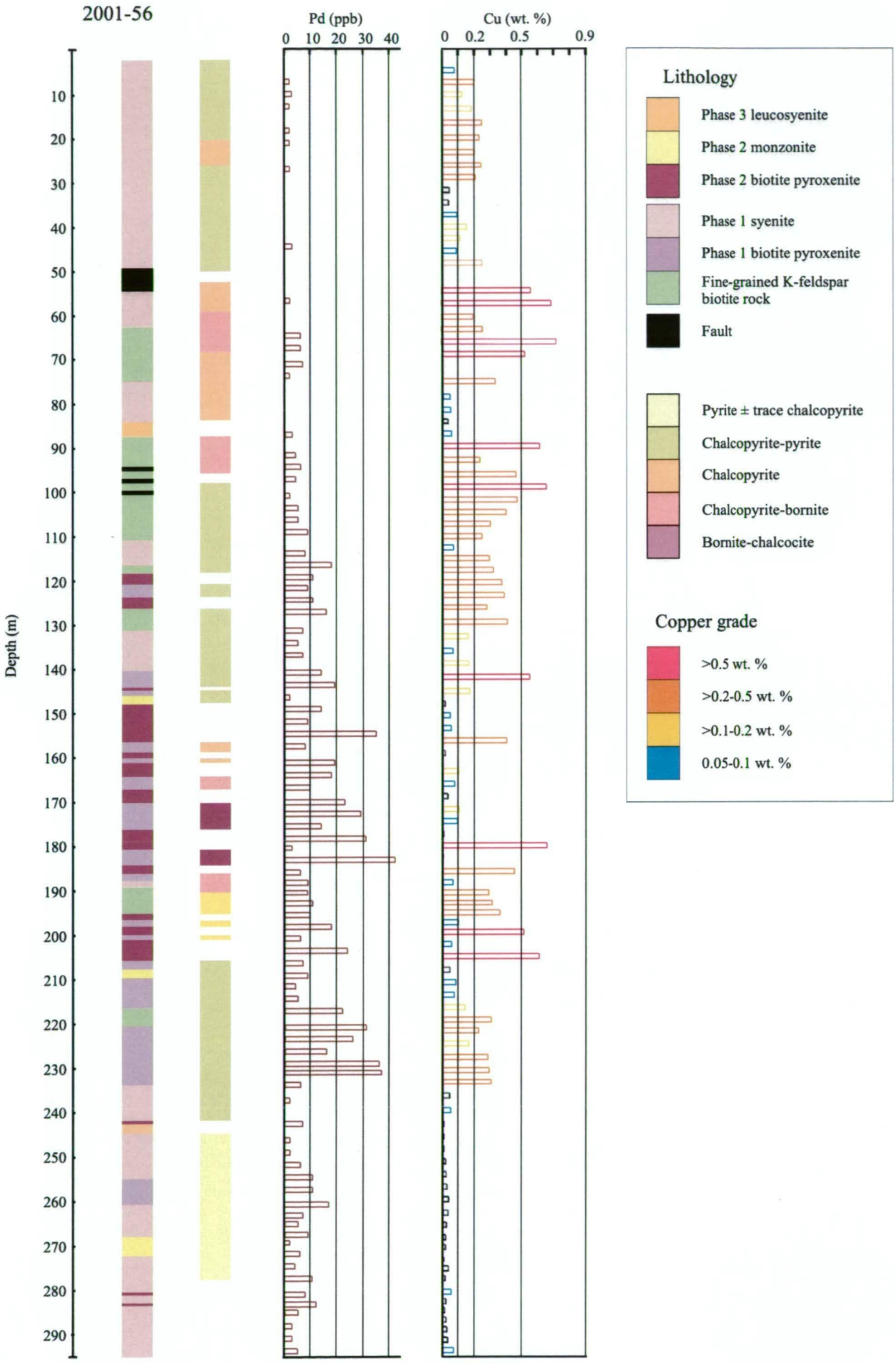
2001-56
Pd (ppb)
0 10 20 30 40
Cu (wt. %)
0 0.2 0.5 0.9
Depth (m)
10 20 30 40 50 60 70 80 90 100 110 120 130 140 150 160 170 180 190 200 210 220 230 240 250 260 270 280 290
Lithology
Phase 3 leucosyenite
Phase 2 monzonite
Phase 2 biotite pyroxenite
Phase 1 syenite
Phase 1 biotite pyroxenite
Fine-grained K-feldspar biotite rock
Fault
Pyrite ± trace chalcopyrite
Chalcopyrite-pyrite
Chalcopyrite
Chalcopyrite-bornite
Bornite-chalcocite
Copper grade
>0.5 wt. %
>0.2-0.5 wt. %
>0.1-0.2 wt. %
0.05-0.1 wt. %

4.4. Alteration and mineralisation in the Lower Main Zone

Hypogene alteration and mineralisation assemblages are well exposed in the central part of the Lower Main Zone, and include; (1) early metasomatised wall rocks that consist of fine-grained anhedral fluorine-rich biotite and grey K-feldspar, (2) veins and patches of magnetite-diopside ± albite, (3) local coarse-grained K-feldspar-biotite veins and patches that are locally associated with bornite and chalcopyrite, and (4) main-stage mineralisation defined by sulphide zonation patterns that consist of a bornite-chalcocite core (observed in one area of the Lower Main Zone) grading outwards to bornite-chalcopyrite, chalcopyrite, chalcopyrite>pyrite and pyrite with minor chalcopyrite domains. Syenite in the inner bornite-chalcopyrite zone typically contains abundant hematite-stained K-feldspar (i.e. >70 wt. %), whereas syenite peripheral to the bornite-chalcopyrite core contains 50-70% K-feldspar (*see* section 4.4.). Biotite pyroxenite from the inner bornite-chalcopyrite zone is characterised by patches of coarse biotite, which have been overprinted by magnetite and Cu-Fe sulphides with localised patches of coarse-grained apatite. Adjacent to the potassic alteration zone is a peripheral zone characterised by patchy alteration assemblages of pyrite, chlorite, albite, sericite and/or epidote (Table 4-2; Fig. 4-9).

Post main-stage alteration events include (1) albite and diopside patches and veins (2) weak to moderate selective pervasive alteration of plagioclase and diopside with epidote ± pyrite and hematite, (3) coarse-grained K-feldspar ± biotite veins, (4) late sparse quartz ± pyrite-chalcopyrite vein-veinlets spatially associated with late Phase 3 leucosyenite, (5) pervasive calcite-sericite alteration of wall rocks adjacent to late faults and (6) rare blue tremolite veinlets (Table 4-2; Fig. 4-9).

Figure 4-7. Simplified geology of selected drill holes from cross-section A-A" of the Lower Main Zone, showing copper grades. Note that copper grades in some areas change abruptly across different lithological boundaries. Abrupt changes in copper grades may indicate weakly mineralised Phase 1 syenites were emplaced late during the waning stages of main-stage mineralisation or may indicate weakly mineralised Phase 2 syenite. Arrows along drill hole 2001-56 signify intervals of Phase 1 syenite with significantly lower Cu-grades relative to adjacent wall rocks. Assay data provided by Teck Ltd.

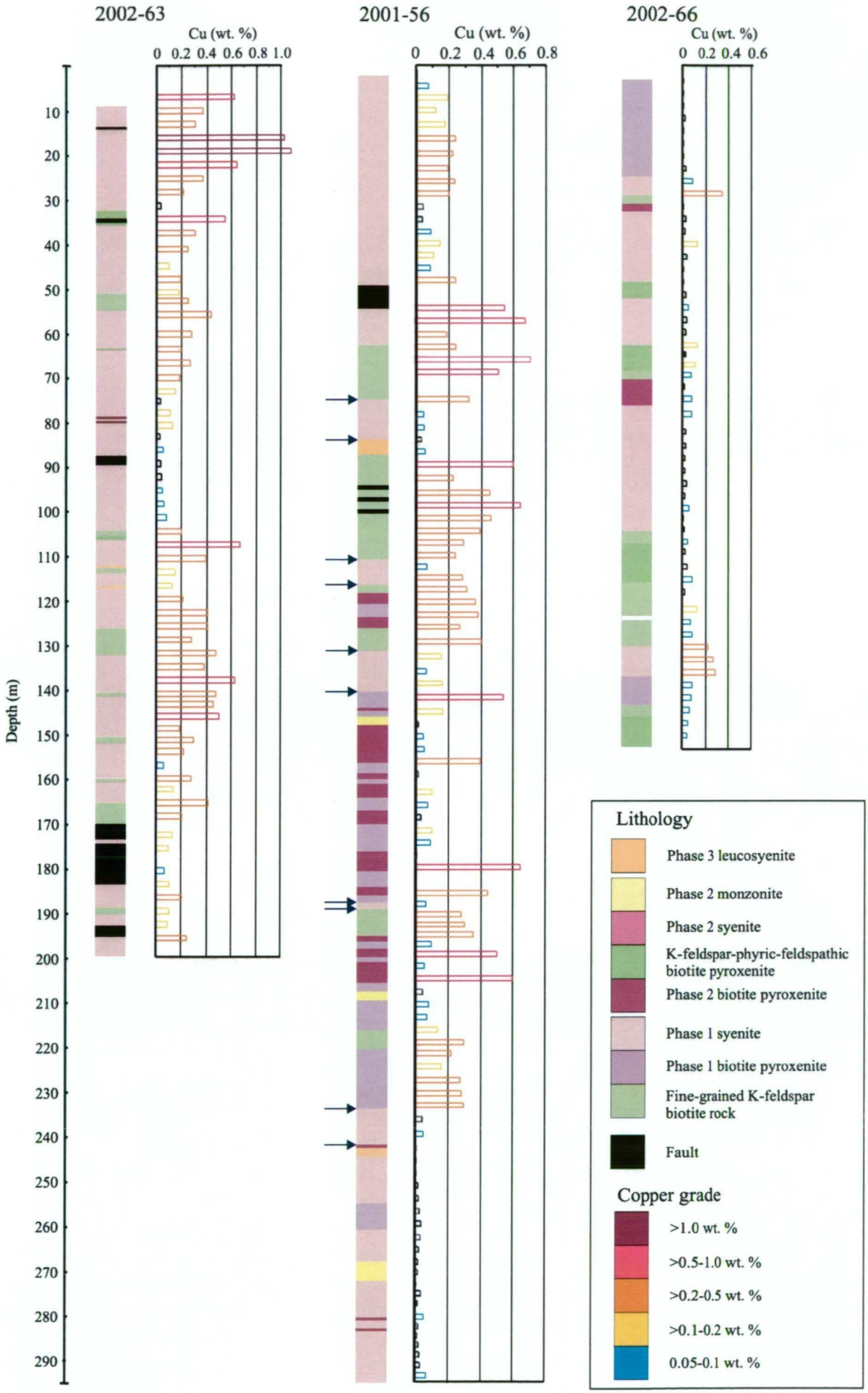
2002-63
Cu (wt. %)
0 0.2 0.4 0.6 0.8 1.0
2001-56
Cu (wt. %)
0 0.2 0.4 0.6 0.8
2002-66
Cu (wt. %)
0 0.2 0.4 0.6
Depth (m)
10 20 30 40 50 60 70 80 90 100 110 120 130 140 150 160 170 180 190 200 210 220 230 240 250 260 270 280 290
Lithology
Phase 3 leucosyenite
Phase 2 monzonite
Phase 2 syenite
K-feldspar-phyric-feldspathic biotite pyroxenite
Phase 2 biotite pyroxenite
Phase 1 syenite
Phase 1 biotite pyroxenite
Fine-grained K-feldspar biotite rock
Fault
Copper grade
>1.0 wt. %
>0.5-1.0 wt. %
>0.2-0.5 wt. %
>0.1-0.2 wt. %
0.05-0.1 wt. %

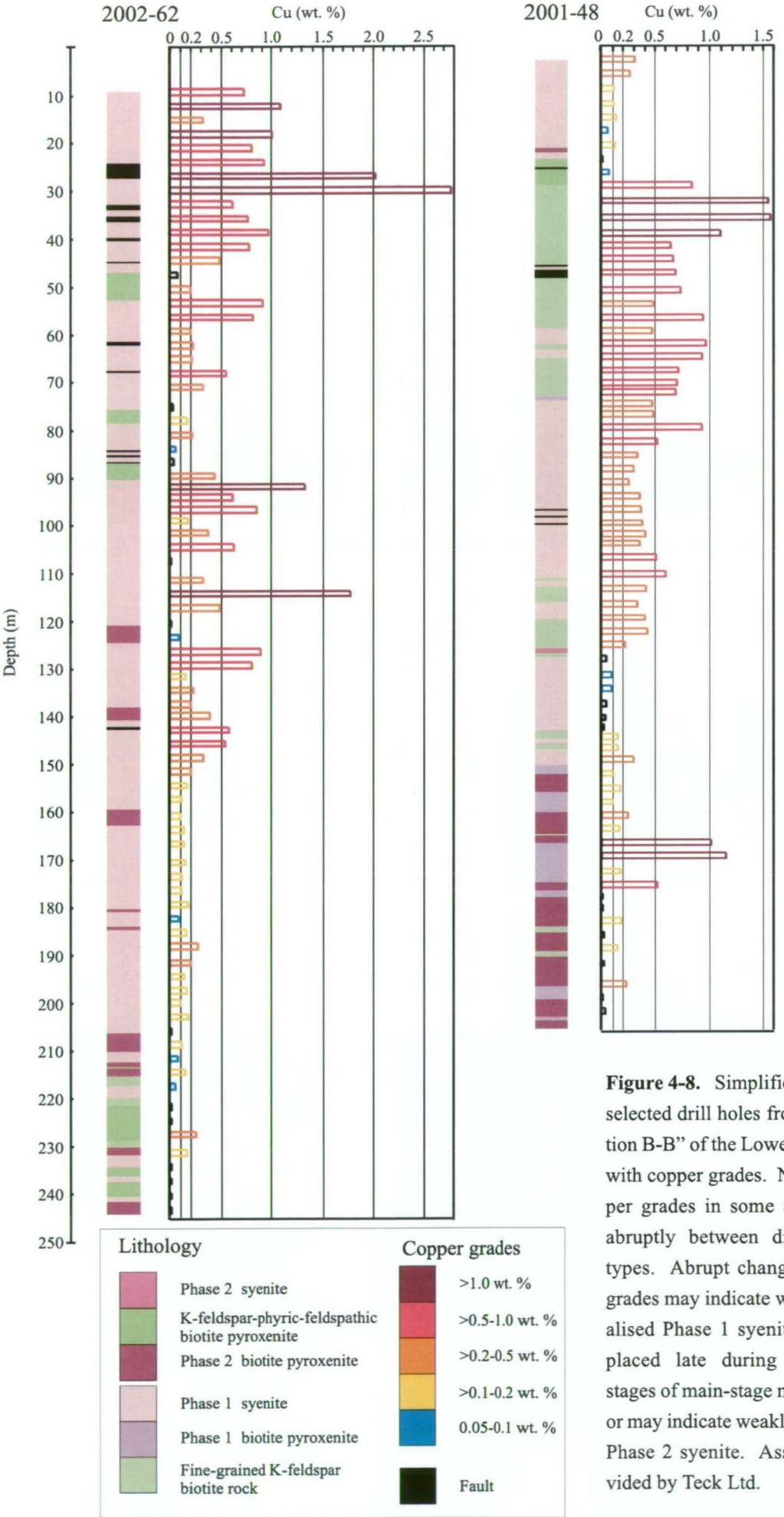

Figure 4-8. Simplified geology of selected drill holes from cross-section B-B" of the Lower Main Zone, with copper grades. Note that copper grades in some areas change abruptly between different rock types. Abrupt changes in copper grades may indicate weakly mineralised Phase 1 syenites were emplaced late during the waning stages of main-stage mineralisation or may indicate weakly mineralised Phase 2 syenite. Assay data provided by Teck Ltd.

Table 4-2. Alteration assemblages and their spatial and temporal relationships in the Lower Main Zone.

Alteration assemblage[1]	Major Minerals	Minor Minerals	Alteration intensity and style[2]	Spatial and temporal associations
Early stage alteration				
Potassic	Bio, Kfd		Strong to moderate pervasive alteration of a felsic-protolith wall rock to form fine grained K-feldspar biotite rock	Alteration is inferred to have affected older(?) wall rocks only. Relicts of fine grained K-feldspar biotite rock occur throughout the Lower Main Zone, and are intruded by Phase 1 biotite pyroxenite and syenite
Calcic / calcic-sodic	Di, mt	Ab, kfd, bio, bn, cpy, ap, ti	Veins and patches composed of coarse grained magnetite with rims of green diopside. Some patches are also associated with coarse grained K-feldspar, biotite and Cu-Fe sulphides	Alteration has affected all Phase 1 rocks. Patches are in localised in the southern area of the Lower Main Zone. Folded veins also occur in strongly foliated rocks in the eastern area of the Lower Main Zone
Potassic	Kfd, bio	Bn, cpy, ap	Veins with irregular margins that are composed of coarse grained euhedral K-feldspar and biotite books. Veins include interstitial apatite and in some cases Cu-Fe sulphides	Veins have cross-cut all phase 1 rock types. Veins dominantly occur in Phase 1 syenite in the southern area of the Lower Main Zone
Transitional stage alteration				
Inner Zone : felsic rocks				
Potassic	Kfd	Ab, clz, ti, cpy, bn, mt, fl, qz, gn, act	Strong to moderate pervasive locally texturally destructive K-feldspar alteration of syenite and fine grained K-feldspar biotite rock. Altered rocks include interstitial albite, clinozoisite, bornite and chalcopyrite. Selective-pervasive replacement of primary and secondary biotite and diopside by Cu-Fe sulphides	Alteration has affected fine grained K-feldspar biotite rock and Phase 1 syenite. Strongest pervasive texturally destructive alteration occurs in bornite-chalcopyrite mineralised rocks in the southern area of the Lower Main Zone
Inner Zone : biotite pyroxenite				
		Ap, cpy, bn, ti, mt, pph, ab act	Strong to moderate selective-pervasive replacement of biotite by Cu-Fe sulphide, magnetite and titanite. Weak selective-pervasive replacement of diopside by Cu-Fe sulphide + actinolite	Alteration has affected Phase 1 biotite pyroxenite
Sodic-calcic	Ab	Py, cpy, ser,chl, mus, ti, ep, clz, hm	Moderate to weak selective-pervasive replacement of plagioclase with milky white albite, clinozoisite, pyrite and muscovite. Diopside show weak selective-pervasive chlorite and epidote alteration, and biotite show weak to strong selective-pervasive chlorite, titanite and pyrite	Alteration has affected Phase 1 rocks. Strongest albite selective-pervasive alteration occurs in Phase 1 syenites beneath the Lower Main Zone are body in the northeastern area
Late stage alteration				
Sodic-calcic	Ab, di	Mt	Localised vein-veinlets and patches. Veins have planar to irregular margins	Vein-veinlets and patches overprint Phase 1 rocks and Phase 2 biotite pyroxenite. Alteration has cross-cut mineralised rocks and locally diluted ore grades
Calcic	Ep	Py	Weak to locally strong selective-pervasive replacement of plagioclase and diopside by epidote±pyrite	Affects Phase 1 and Phase 2 rocks. Is most prevalent in monzonite and biotite pyroxenite, which contain Ca-rich plagiocase and/or abundant mafics
Potassic	Kfd, bio		Planar vein-veinlets composed of coarse K-feldspar with minor biotite	Vein-veinlets have cross-cut Phase 1 and Phase 2 rocks. Vein sets are common thoughout the Lower Main Zone and predominantly strike east to northeast and dip sub vertically
Silicate	Qz	Py, cpy, mal, mus	Planar to irregular colourless to while quartz vein-veinlets. Some veins include alteration envelopes of selective-pervasive replacement of biotite with muscovite strong hematite dusting of feldspar	Vein-veinlets commonly occur adjacent to Phase 3 leucosyenite dykes and are inferred to be genetically linked
Phyllic	Mus	Py	Selective-pervasive replacement of biotite by muscovite and pyrite. Feldspar show strong hematite dusting	Alteration is restricted to Phase 3 coarse K-feldspar dykes.

[1] Alteration assemblages are listed in chronological order from oldest (top) to youngest (bottom)

[2] Definition of alteration terms by Titley (1982 ; *see* Table 4-1)

Abbreviation : ab = albite, act = actinolite, ap = apatite, bio = biotite, phlogopite, bn = bornite, chl = chlorite, clz = clinozoisite, cpy = chalcopyrite, di = dioside, ep = epidote, fl = fluorite, gn = garnet, hm = hematite, Kfd = K-feldspar, orthoclase, mal = malachite, mt = magnetite, mus = muscovite, pph = pyrophanite, py = pyrite, qz = quartz, ser = sericite, ti = titanite (sphene)

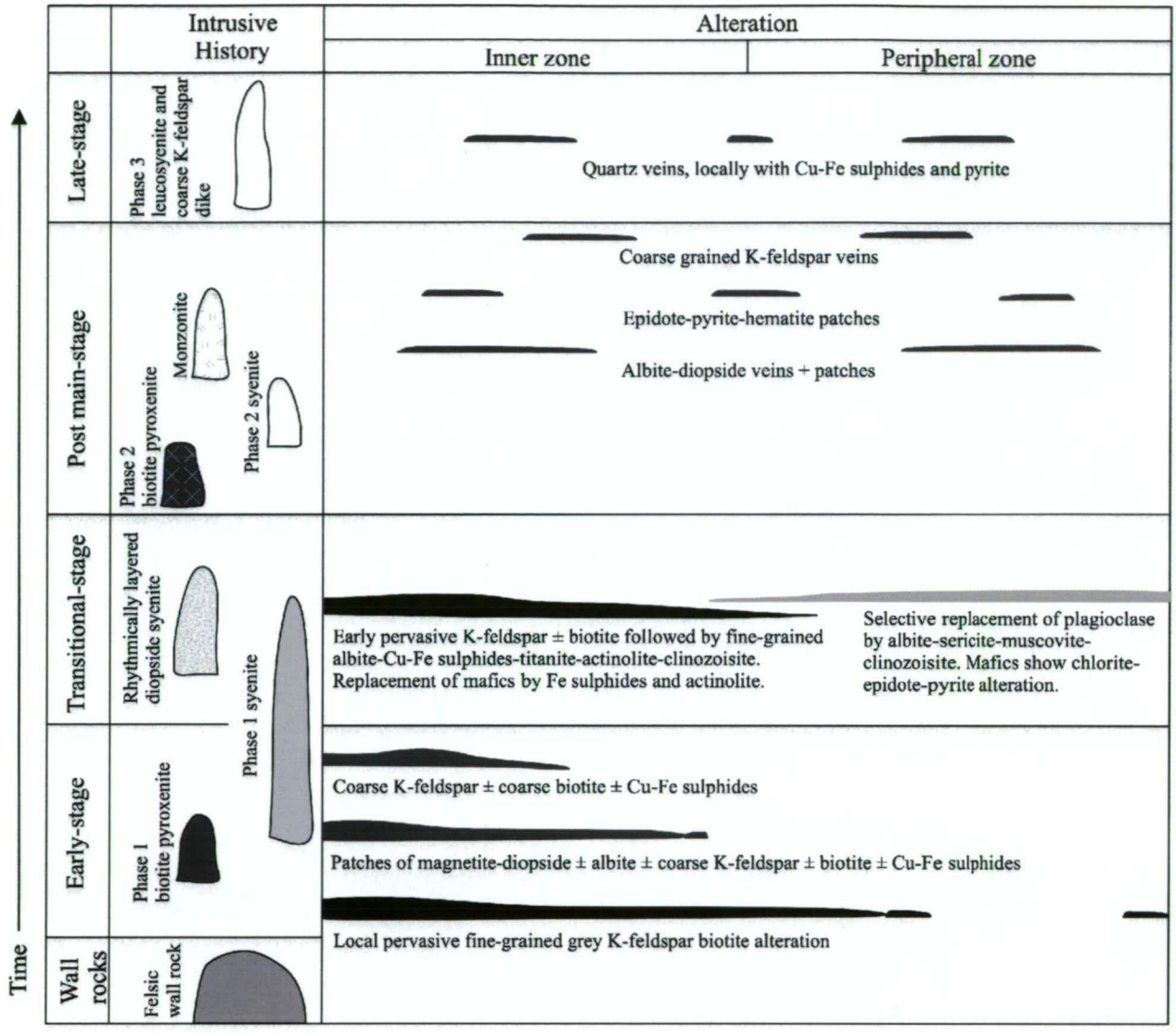

Figure 4-9. Schematic space-time diagram of intrusive history and alteration genesis of the Lower Main Zone. Pervasive alteration is shown as black, local veining or patchy alteration is shown as medium grey and selective replacement alteration is shown in light grey.

4.4.1. Early-stage

4.4.1.1. Pervasive biotite-K-feldspar alteration

Evidence for early-stage, strongly developed, pervasive K-feldspar-biotite metasomatism is recognised in relict bodies or xenoliths of fine-grained K-feldspar biotite rocks (Fig. 4-10a). Moderate K-feldspar biotite alteration is also evident in some syenite within the Lower Main Zone (Fig. 4-10b). The fine-grained biotite-K-feldspar altered rocks (Fig. 4-10c, d) are cross-cut by local magnetite-diopside veins, and light salmon pink K-feldspar-biotite veins (Fig. 4-10d), which in turn are overprinted by main-stage mineralisation with anhedral biotite replaced by Cu-Fe sulphides.

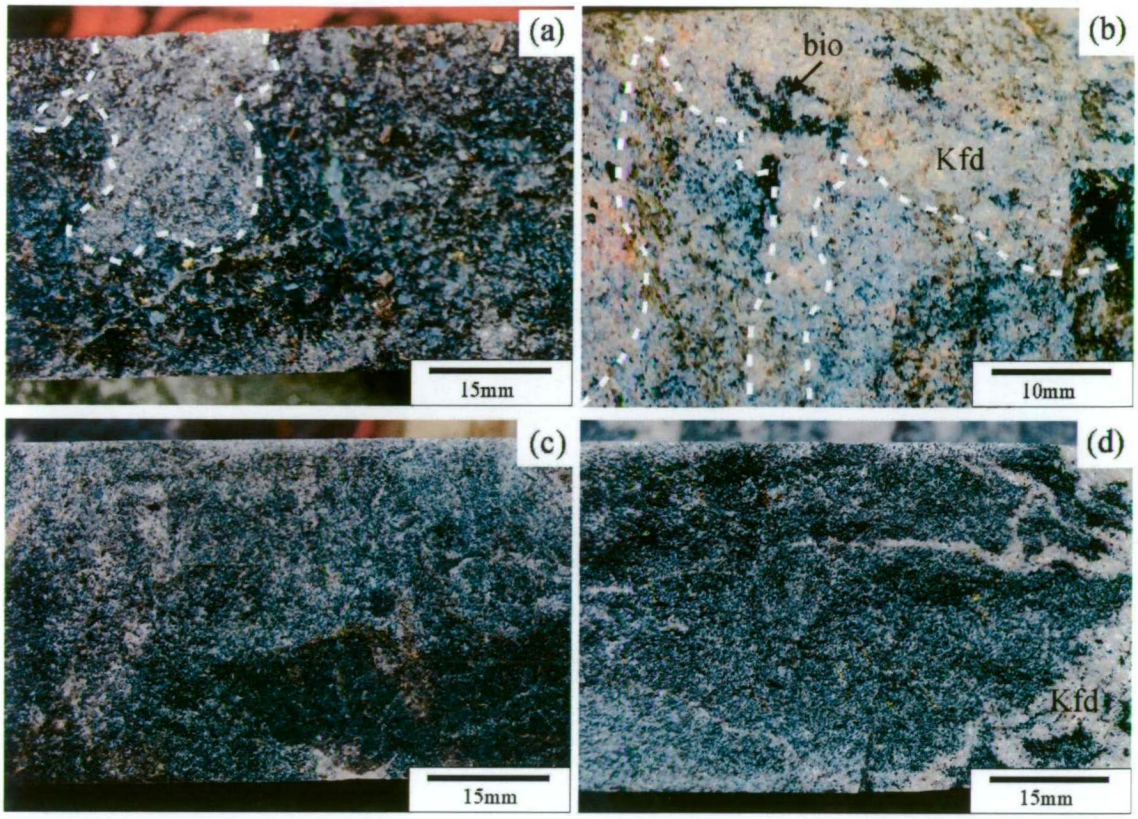

Figure 4-10. **(a)** Mineralised Phase 1 biotite pyroxenite with xenoliths of fine-grained K-feldspar biotite rock (outlined by dashed line). Note that mineralisation has overprinted both rock types (drill hole 2001-56_121.8m). **(b)** Mineralised Phase 1 syenite with early biotite alteration, overprinted by K-feldspar, coarse-grained biotite (top area) and mineralisation (drill hole 2001-63_112.0m). **(c)** Chalcopyrite-mineralised fine-grained K-feldspar biotite rock (drill hole 2001-56_70.0m). **(d)** Chalcopyrite-bornite mineralised fine-grained K-feldspar biotite rock cross-cut by early irregular anatomising K-feldspar-biotite veins with coarse biotite vein haloes (drill hole 2001-56_90.0m). Mineral abbreviations; bio = biotite: Kfd = K-feldspar.

4.4.1.2. Magnetite-diopside ± albite veins and patches

Early-stage magnetite-diopside ± albite veins and patches occur in the southern and central areas of the Lower Main Zone and are spatially associated with mineralised zones (Fig. 4-11a, b and e). Early-stage magnetite patches are characterised by cores of vanadium-rich magnetite (*see* Chapter 6) and outer rims dominated by cloudy dark green diopside (Fig. 4-12a-e). Early-stage magnetite-diopside ± albite veins have been cross-cut by early coarse K-feldspar-biotite veins (Fig. 4-12e), and fine-grained thin stringers of biotite (Fig. 4-12c), and are overprinted by main-stage disseminated Cu-Fe sulphides (Fig. 4-12c).

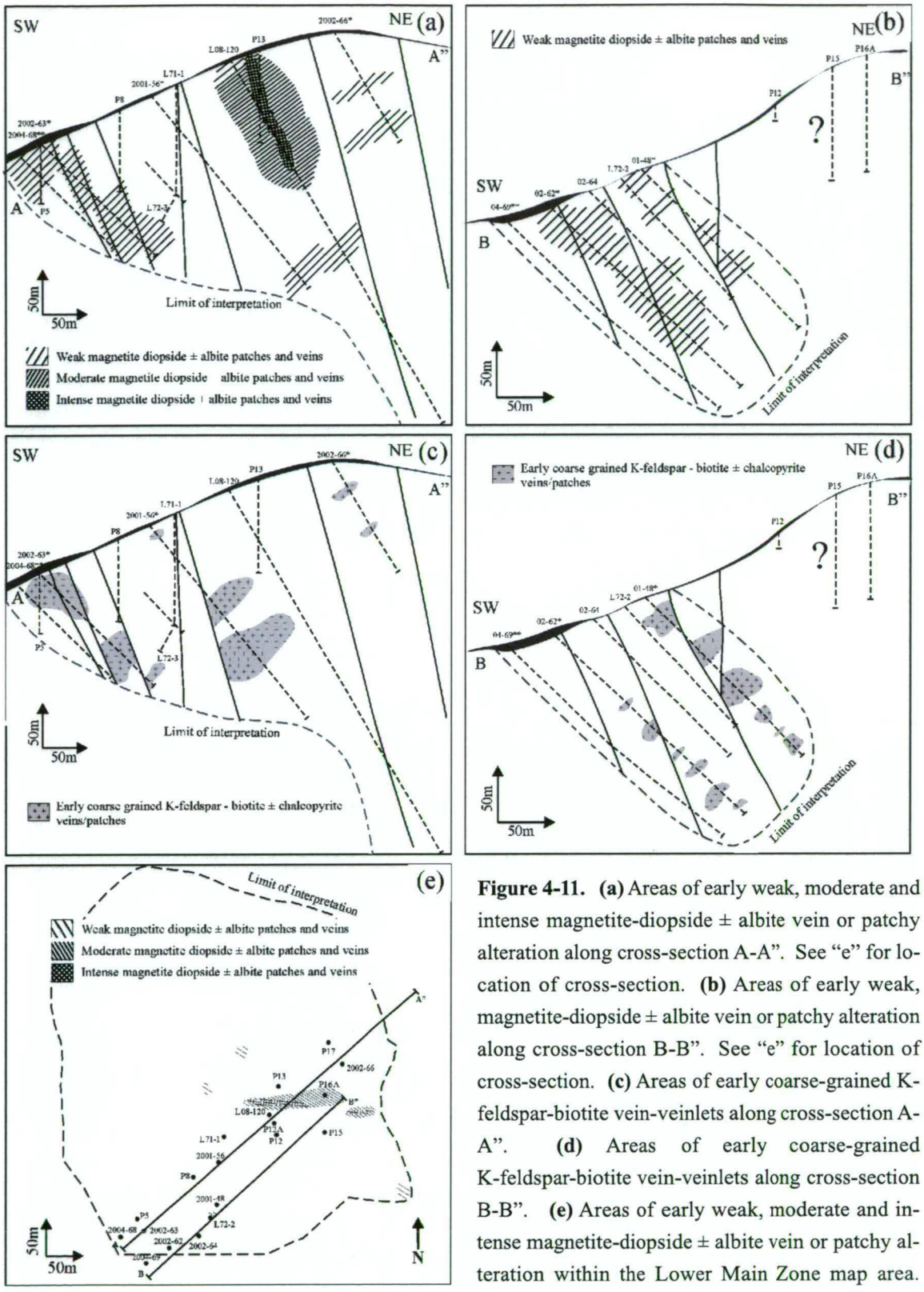

Figure 4-11. **(a)** Areas of early weak, moderate and intense magnetite-diopside ± albite vein or patchy alteration along cross-section A-A". See "e" for location of cross-section. **(b)** Areas of early weak, magnetite-diopside ± albite vein or patchy alteration along cross-section B-B". See "e" for location of cross-section. **(c)** Areas of early coarse-grained K-feldspar-biotite vein-veinlets along cross-section A-A". **(d)** Areas of early coarse-grained K-feldspar-biotite vein-veinlets along cross-section B-B". **(e)** Areas of early weak, moderate and intense magnetite-diopside ± albite vein or patchy alteration within the Lower Main Zone map area. Interpretations are primarily based on detailed logging of marked drill holes (*), quick logging of marked drill holes (**). Field mapping and drill logging were supplemented by historical company logs for drill holes that were unavailable for relogging (data provided by Teck Ltd).

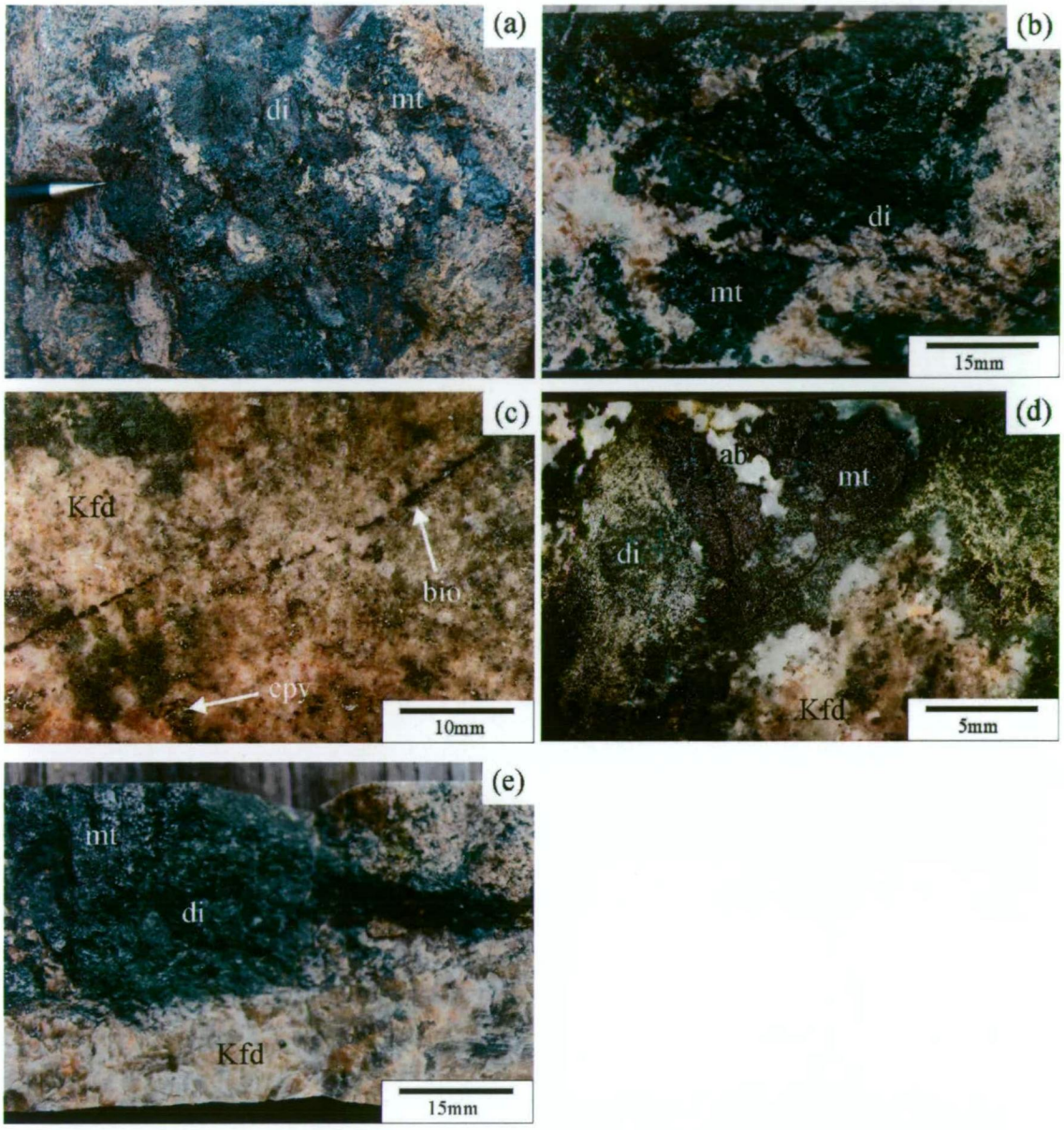

Figure 4-12. **(a)** An outcrop containing a large patch of early magnetite-diopside alteration in the southern area of the Lower Main Zone (347325mE, 6200583mN). **(b)** Early magnetite-diopside alteration that has been cross-cut by a veinlet of chalcopyrite (drill hole 2002-62_131.2m). **(c)** Chalcopyrite mineralised Phase 1 syenite from the Lower Main Zone with early coarse diopside and magnetite alteration patches. Note that early diopside-magnetite alteration is cross-cut by biotite veinlet and is overprinted by chalcopyrite mineralisation (sample 07AB-G7, 347330mE, 6200580mN). **(d)** Early patchy magnetite-diopside and albite alteration of Phase 1 syenite from the central area of the Lower Main Zone (347430mE, 6200735mN). **(e)** Mineralised Phase 1 syenite with a patch of early coarse-grained magnetite-diopside, that is in turn cross-cut by coarse K-feldspar vein (drill hole 2002-63_135.1m). Mineral abbreviations; ab = albite, bio = biotite, cpy = chalcopyrite, di = diopside, Kfd = K-feldspar and mt = magnetite.

4.4.1.3. Coarse-grained K-feldspar-biotite veins and coarse-grained biotite vein or patches

Early coarse-grained K-feldspar ± biotite veins and coarse-grained biotite veins or patches cross-cut early Phase 1 syenite and biotite pyroxenite in the south-central area of the Lower Main Zone (Fig. 4-11c-d). The veins are generally irregular, up to 5cm in thickness and are characterised by coarse-grained euhedral K-feldspar laths with coarse-grained biotite and anhedral light green apatite, and chalcopyrite and bornite (Fig. 4-13a-d). Early-stage coarse-grained K-feldspar-biotite veins are surrounded by alteration envelopes of Cu-Fe sulphides.

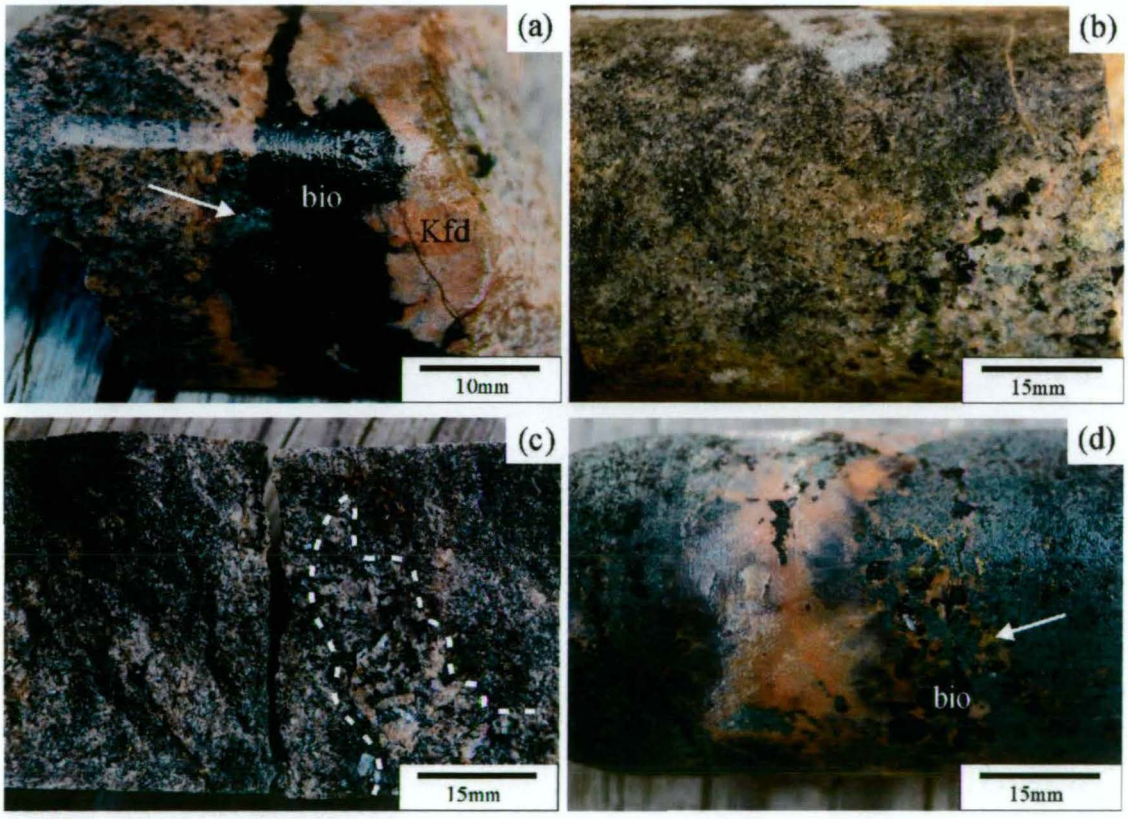

Figure 4-13. **(a)** Early coarse-grained K-feldspar-biotite vein that has cross-cut Phase 1 syenite. Note chalcopyrite and green apatite (arrow) with coarse biotite (drill hole 2002-62_97.5m). **(b)** Phase 1 syenite cross-cut by weakly mineralised coarse biotite and K-feldspar vein (drill hole 2001-56_16.0m). **(c)** Early chalcopyrite mineralised coarse-grained K-feldspar-biotite vein that has cross-cut fine-grained K-feldspar-biotite rock (drill hole 2001-48_126.0m). **(d)** Phase 1 biotite pyroxenite cross-cut by early chalcopyrite mineralised coarse K-feldspar and biotite vein. White arrow indicates chalcopyrite mineralisation in vein (drill hole 2001-48_172.1m). Mineral abbreviations; bio = biotite and Kfd = K-feldspar.

4.4.2. Transitional-stage

4.4.2.1. Inner zone assemblages

Inner-zone alteration of Phase 1 syenite and fine-grained K-feldspar-biotite rock is most intense at the surface in the southern area of the Lower Main Zone (Figs. 4-14a-d and 4-15a, b). Mineralisation occurs as a patchy, but mappable sulphide zonation pattern which

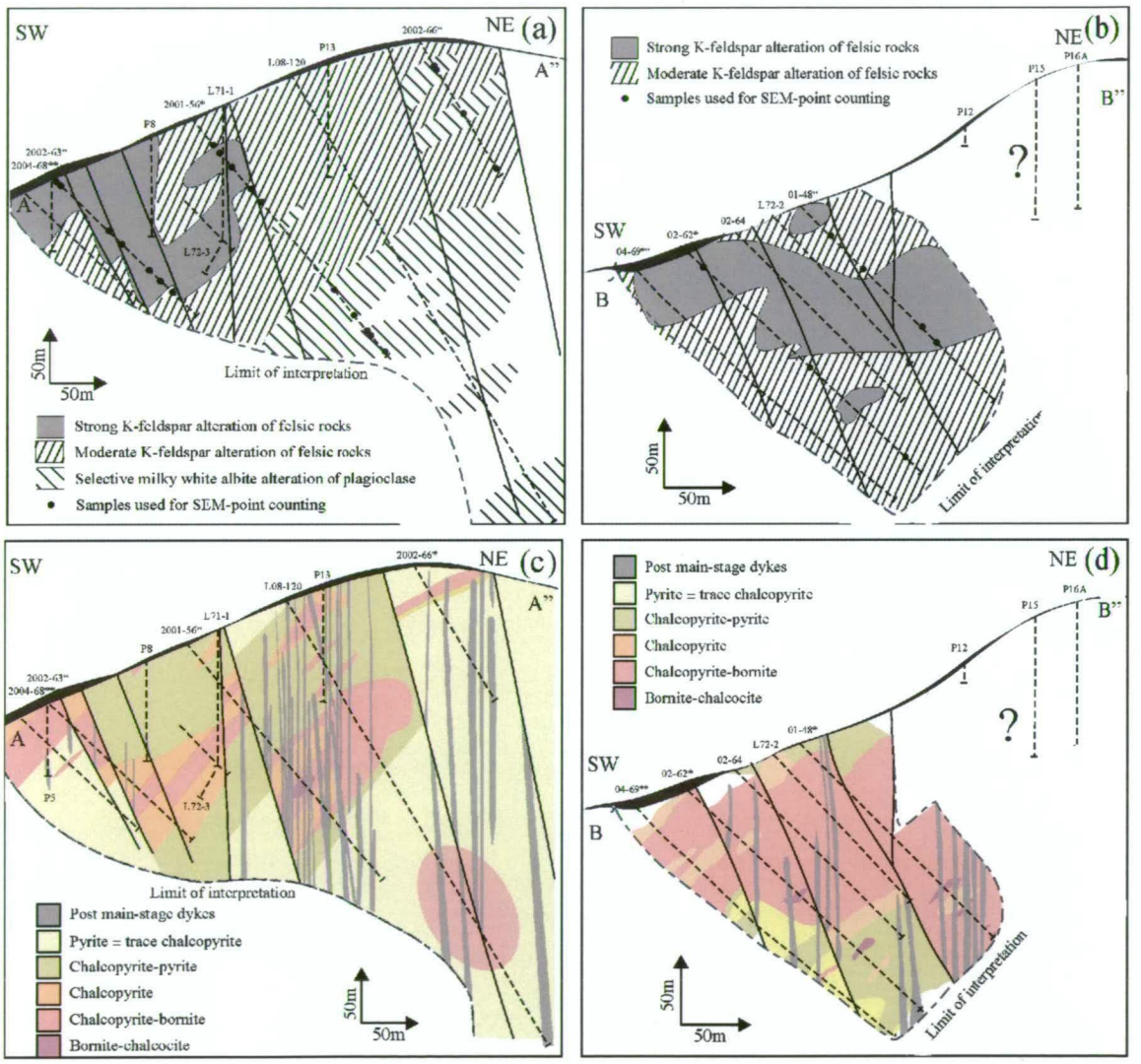

Figure 4-14. Alteration zonation patterns for cross-sections A-A" **(a, c)** and B-B" **(b, d)**. See Figure 4-14 for location of cross-sections in the Lower Main Zone. **(a-b)** Areas of selective albite-epidote-sericite, moderate K-feldspar and strong K-feldspar alteration of felsic rocks in the Lower Main Zone. Note that black dots along drill holes denotes sample locations used for SEM point counting to cross-check and quantify K-feldspar abundance estimates from detailed core logging. **(c-d)** Interpreted sulphide zonation pattern of the Lower Main Zone. Interpretations are primarily based on detailed logging of marked drill holes (*), quick logs of marked drill holes (**) and field mapping. Interpretation was aided by historical company logs for drill holes that were unavailable for relogging (data provided by Teck Ltd).

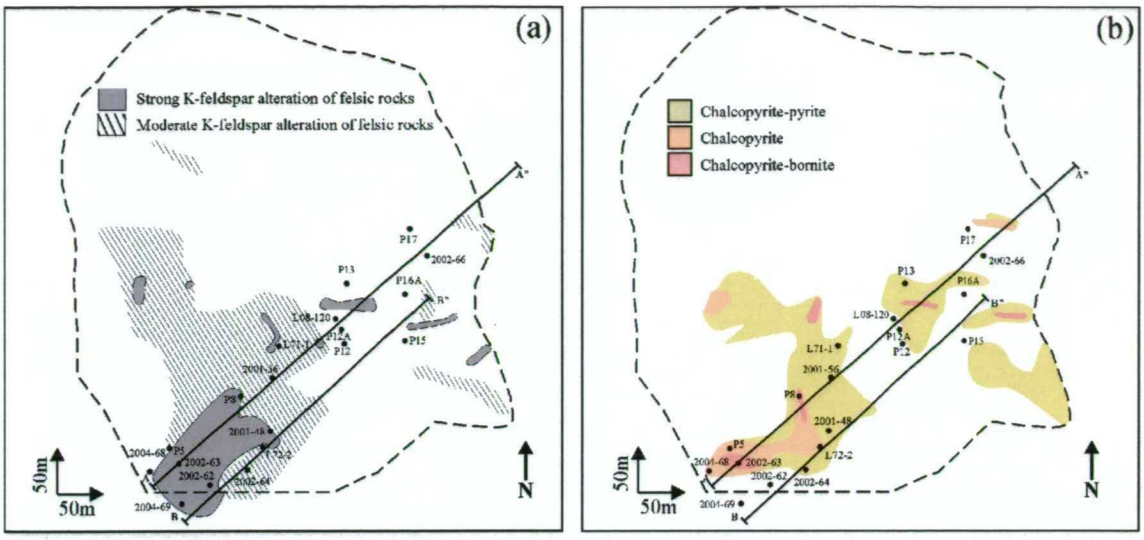

Figure 4-15. Alteration zonation patterns of the Lower Main Zone map area. **(a)** Areas of moderate K-feldspar and strong K-feldspar alteration of felsic rocks. **(b)** Interpreted sulphide zonation patterns.

is accompanied by localised areas of K-feldspar alteration in the syenite and fine-grained K-feldspar biotite rock (Figs. 4-14a-d, 4-15a-b and 4-16a). Sulphide mineralisation has formed fine-grained (<0.5mm) anhedral patches associated with albite, clinozoisite, titanite, sericite, chlorite, fluorite, quartz (trace), garnet (trace) and/or magnetite (Fig. 4-16b-f). Actinolite, albite, clinozoisite and titanite are commonly intergrown with sulphides where in contact with biotite, and in a number of samples it appears that sulphides and their associated alteration assemblage have replaced biotite (Fig. 4-16b-f).

Transitional-stage mineralisation in biotite pyroxenite is characterised by fine disseminated sulphides and rarely shows net-texture (Fig. 4-17a). Sulphides occur as anhedral grains and primary diopside in contact with sulphides has corroded margins and needles of actinolite along its margins (Fig. 4-17b). Also, (primary) biotite grains in contact with sulphides are rimmed by titanite (Fig. 4-17c), and in places relicts of biotite exist, where not all biotite has been replaced by sulphides (Fig. 4-17d; also *see* Chapter 5).

4.4.2.2. Peripheral zone assemblages

Syenite intersected by drill holes (e.g., drill hole 2001-56 at >220 m) and as outcrops in the north-eastern area of the Lower Main Zone (Fig. 4-14a), are characterised by fresh to weakly sericite altered grey to salmon pink K-feldspar and selectively pervasively altered Ca-rich plagioclase by milky white albite, sericite, muscovite, pyrite and clinozoisite (Fig.

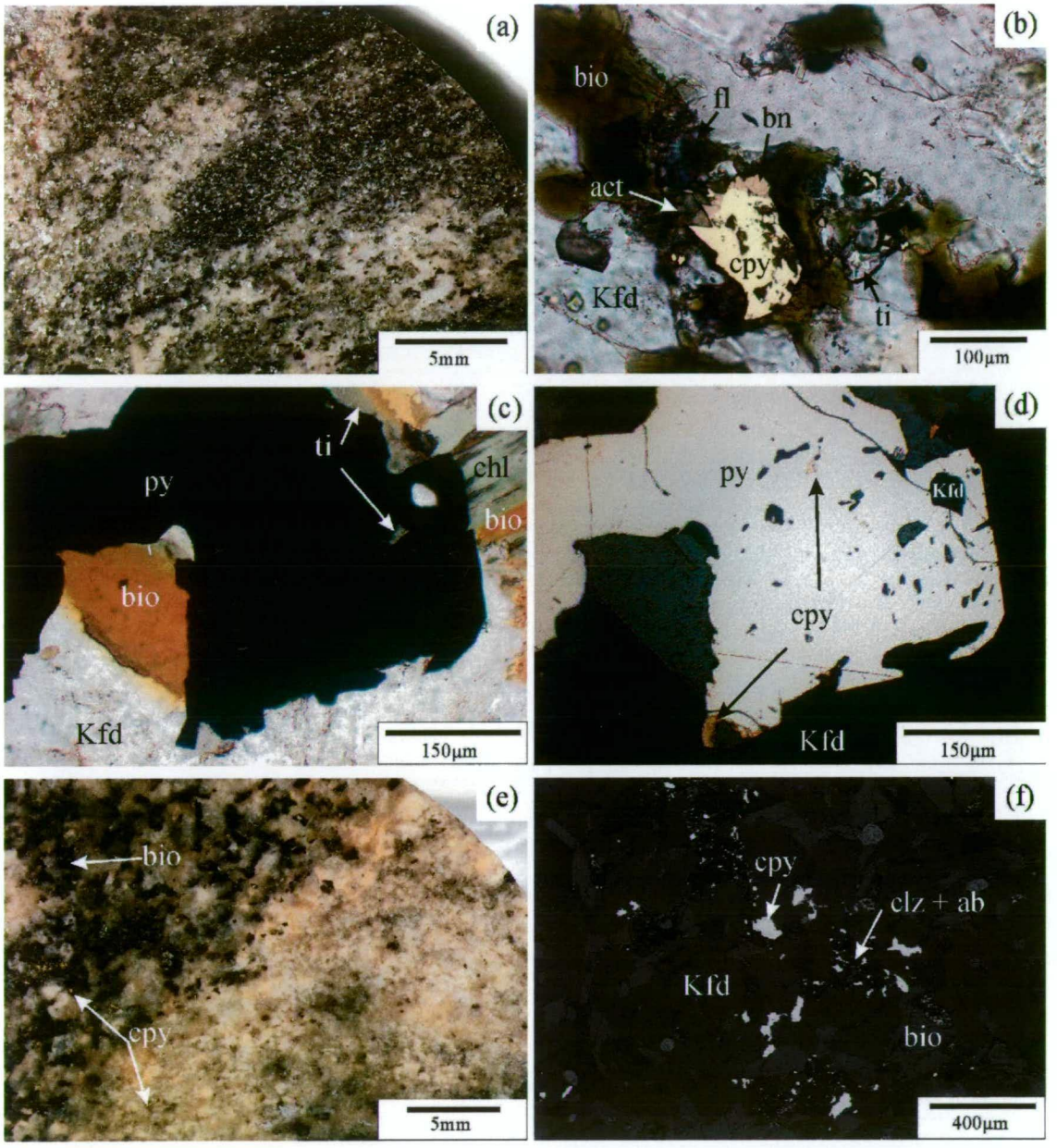

Figure 4-16. **(a)** Foliated fine-grained K-feldspar biotite rock overprinted by pervasive, fabric destructive K-feldspar alteration, which in turn has been overprinted by pyrite and chalcopyrite mineralisation (drill hole 2002-66_68.3m). **(b)** Fine-grained K-feldspar biotite rock with chalcopyrite and bornite mineralisation. Note actinolite alteration has occurred at the contact between biotite and Cu-Fe sulphide (347325mE, 6200720mN). **(c-d)** Pyrite with chalcopyrite, titanite and K-feldspar inclusions which appears to have overprinted biotite and K-feldspar. Chlorite alteration of biotite occurs along biotite margins. Photomicrograph in plane polarized light **(c)** and reflected light (d; drill hole 2001-56_106.1m). **(e)** Contact between mafic-poor (R) and mafic-rich (L) syenite. Both are Phase 1 syenite and are overprinted by chalcopyrite mineralisation. Note that mafic minerals are strongly associated with sulphides (drill hole 2002-63_106.7m). **(f)** Back-scatter electron image of chalcopyrite associated with fine-grained albite and clinozoisite patches in Phase 1 syenite from the Lower Main Zone (drill hole 2001-48_153m). Mineral abbreviations ab = albite, act = actinolite, bio = biotite, bn = bornite, chl = chlorite, clz = clinozoisite, cpy = chalcopyrite, fl = fluorite, Kfd = K-feldspar, py = pyrite, and ti = titanite.

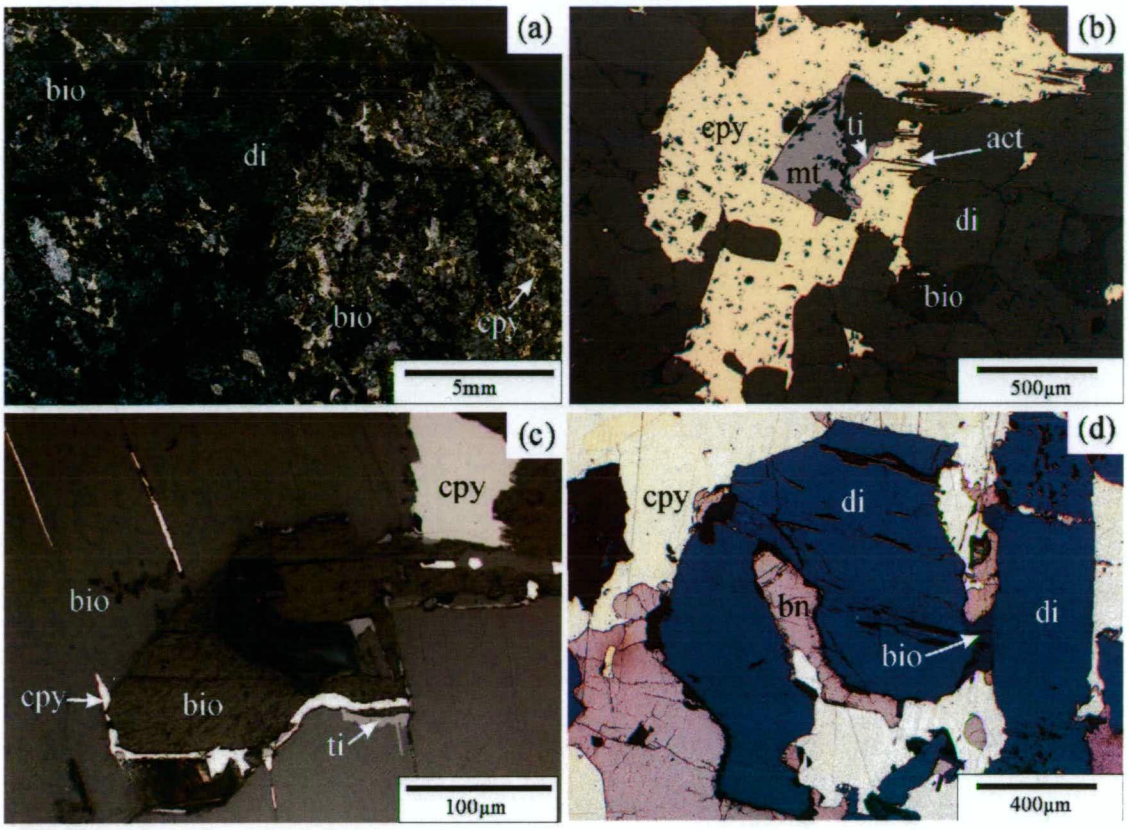

Figure 4-17. **(a)** Chalcopyrite-pyrite mineralised biotite pyroxenite with net-textured sulphides and coarse patches of biotite from the Lower Main Zone (drill hole 2001-56_199.8 m). **(b)** Photomicrograph of biotite pyroxenite in reflected light showing diopside with actinolite, titanite and magnetite alteration along margins in contact with chalcopyrite (drill hole 2001-56_157 m). **(c)** Biotite from biotite pyroxenite in reflected light showing the presence of chalcopyrite and titanite along biotite grain boundaries and along biotite cleavage planes (dill hole 2001-56_157 m). **(d)** Diopside in altered biotite pyroxenite from the Bishop Zone in reflected light. Diopside and biotite show corroded margins at contacts with chalcopyrite and bornite (drill hole 1996-44_244m). Mineral abbreviations; bio = biotite, bn = bornite, cpy = chalcopyrite, di = diopside, mt = magnetite; ti = titanite.

4-18a-d). Diopside and biotite are fresh to moderately chlorite, epidote and pyrite altered. Biotite pyroxenite from peripheral zones is fresh to moderately epidote altered. Patchy epidote alteration was also observed in Phase 2 biotite pyroxenite (e.g., Fig. 4-19e). Diopside and biotite show weak to moderate epidote and amphibole alteration along grain boundaries and magnetite shows weak hematite alteration in places. It is difficult to determine the exact timing of epidote alteration in the Phase 1 biotite pyroxenite, due to a lack of cross-cutting relationships, but it is assigned to the transitional-stage.

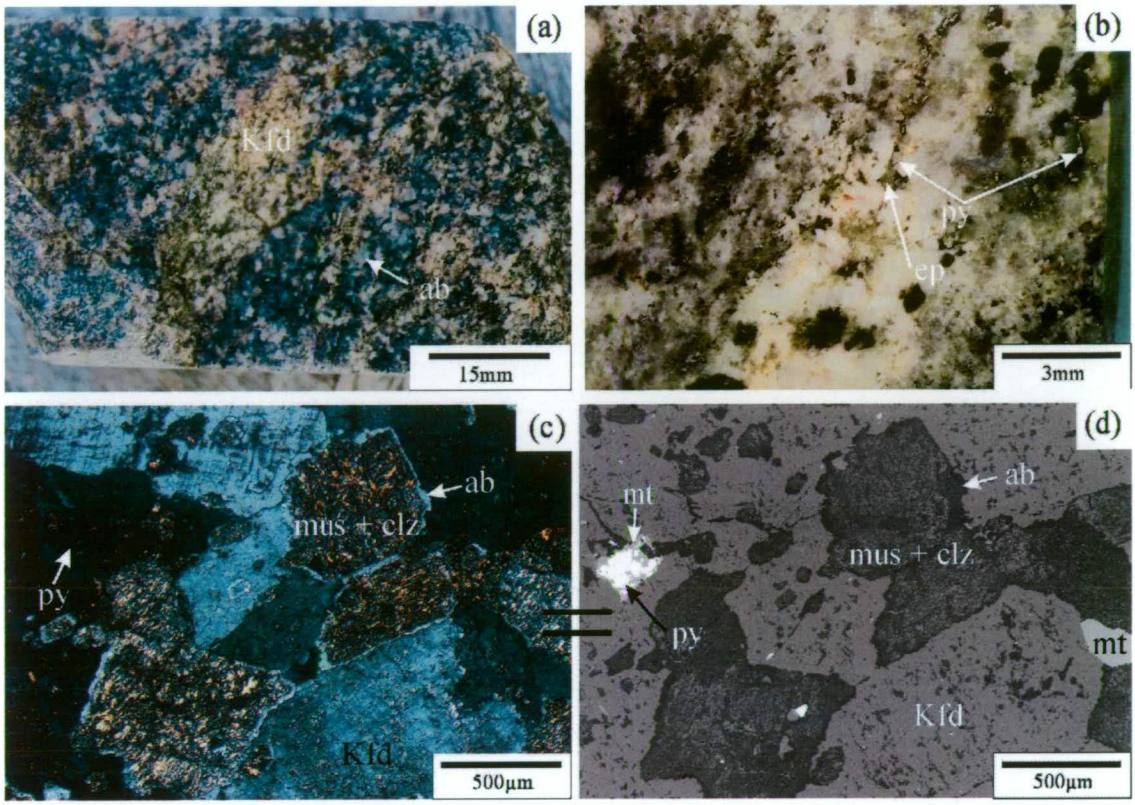

Figure 4-18. **(a)** Syenite from the peripheral zone, showing selectively-pervasive replacement of plagioclase by albite (tabular fine-grained milky white mineral) and weak potassic alteration (salmon pink). Mafics are epidote and pyrite alterated (drill hole 66-2002_81.3m). **(b)** Pyrite with trace chalcopyrite in Phase 1 syenite, showing pyrite and epidote preferentially forming along grain margins of biotite and diopside. **(c)** Pyrite mineralised Phase 1 syenite in cross-nicols showing selective replacement of plagioclase by albite, muscovite and clinozoisite. **(d)** Back-scatter electron image of "c". Images b, c and d are all from drill hole 2002-66_82.7m. Mineral abbreviations; ab = albite, clz = clinozoisite, ep = epidote, Kfd = K-feldspar, mt = magnetite, mus = muscovite and py = pyrite.

4.4.3. Late stage

4.4.3.1. Albite-diopside vein-veinlets and patches

Albite-diopside alteration occurs broadly across the Lower Main Zone in localised patches and is relatively minor (Fig. 4-19a-d and 4-20a-c). Sparse sub-vertical east- and north-trending planar vein sets occupy the Lower Main Zone (Figs. 4-21 and 4-22a). Albite-diopside veins and veinlets range from planar to irregular, are up to 50mm in width, and have overprinted mineralised Phase 1 rocks and barren Phase 2 biotite pyroxenite (Fig. 4-19a-d). Albite-diopside patches are overprinted by late-stage epidote (Figs. 4-19c, d).

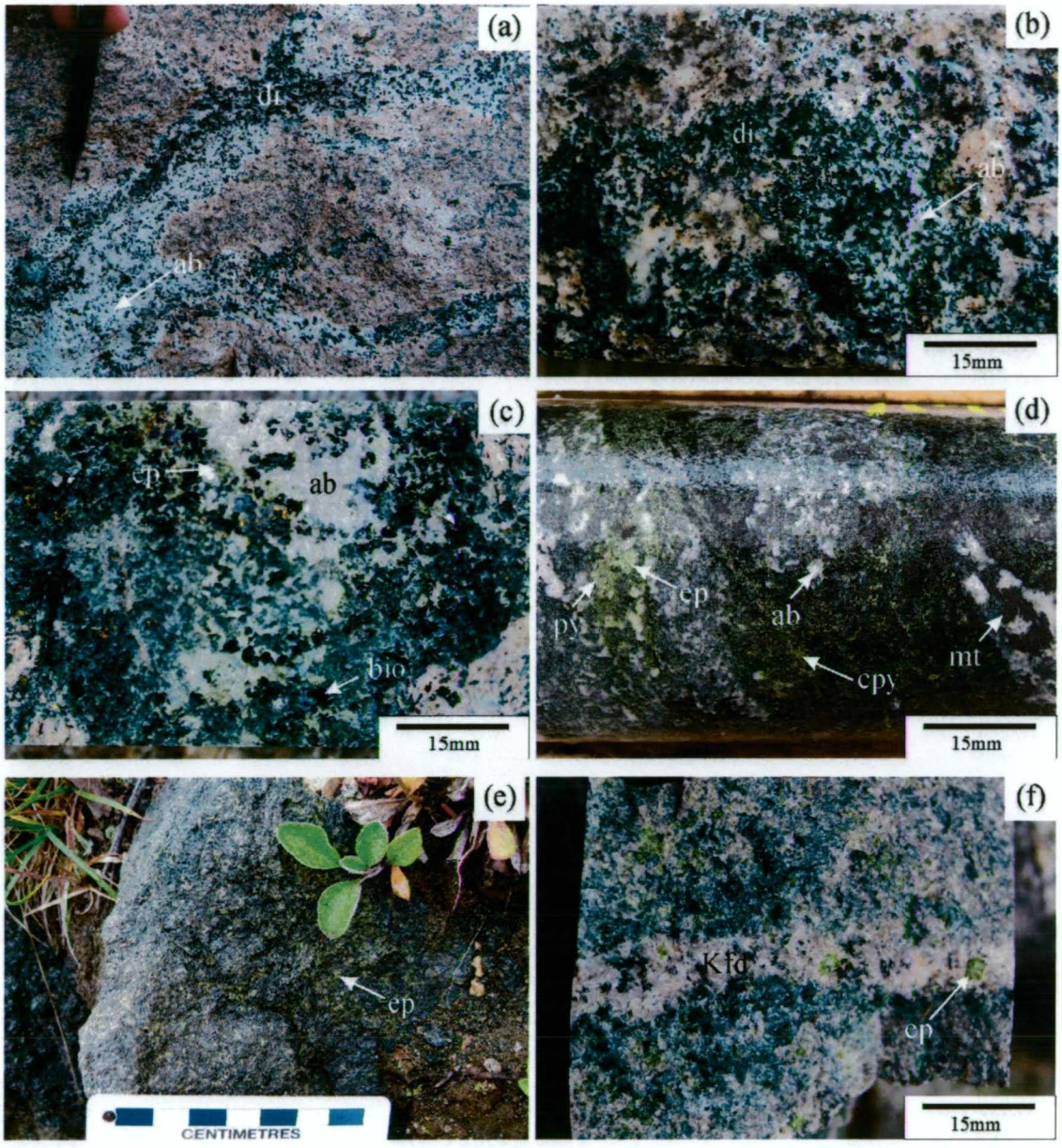

Figure 4-19. **(a-b)** Syenite from the Lower Main Zone and Main Zone that has been overprinted by late irregular patches of albite-diopside alteration (347587mE, 6200609mN and drill hole L95-25_150.8m respectively). **(c)** Mineralised feldspathic pyroxenite from the Bishop Zone that has been overprinted by late patchy albite alteration. Late albite alteration appears to have been overprinted by late epidote alteration (drill hole 1996-44_218.0m). **(d)** Mineralised biotite pyroxenite from the Lower Main Zone that has been locally albite altered. Late albite alteration appears to have been overprinted by late epidote alteration (drill hole L08-120_119.6m; photo courtesy of P. Baxter). **(e)** Phase 2 biotite pyroxenite from the Lower Main Zone that shows strong selective pervasive replacement of diopside by epidote (347428mE, 6200638mN). **(f)** Mineralised Phase 1 syenite and early K-feldspar biotite vein that show selective pervasive replacement of plagioclase and mafic minerals by epidote (drill hole 2001-56_81.9m). Mineral abbreviations; ab = albite, bio = biotite, cpy = chalcopyrite, di = diopside, ep = epidote, Kfd = K-feldspar, mt = magnetite; py = pyrite.

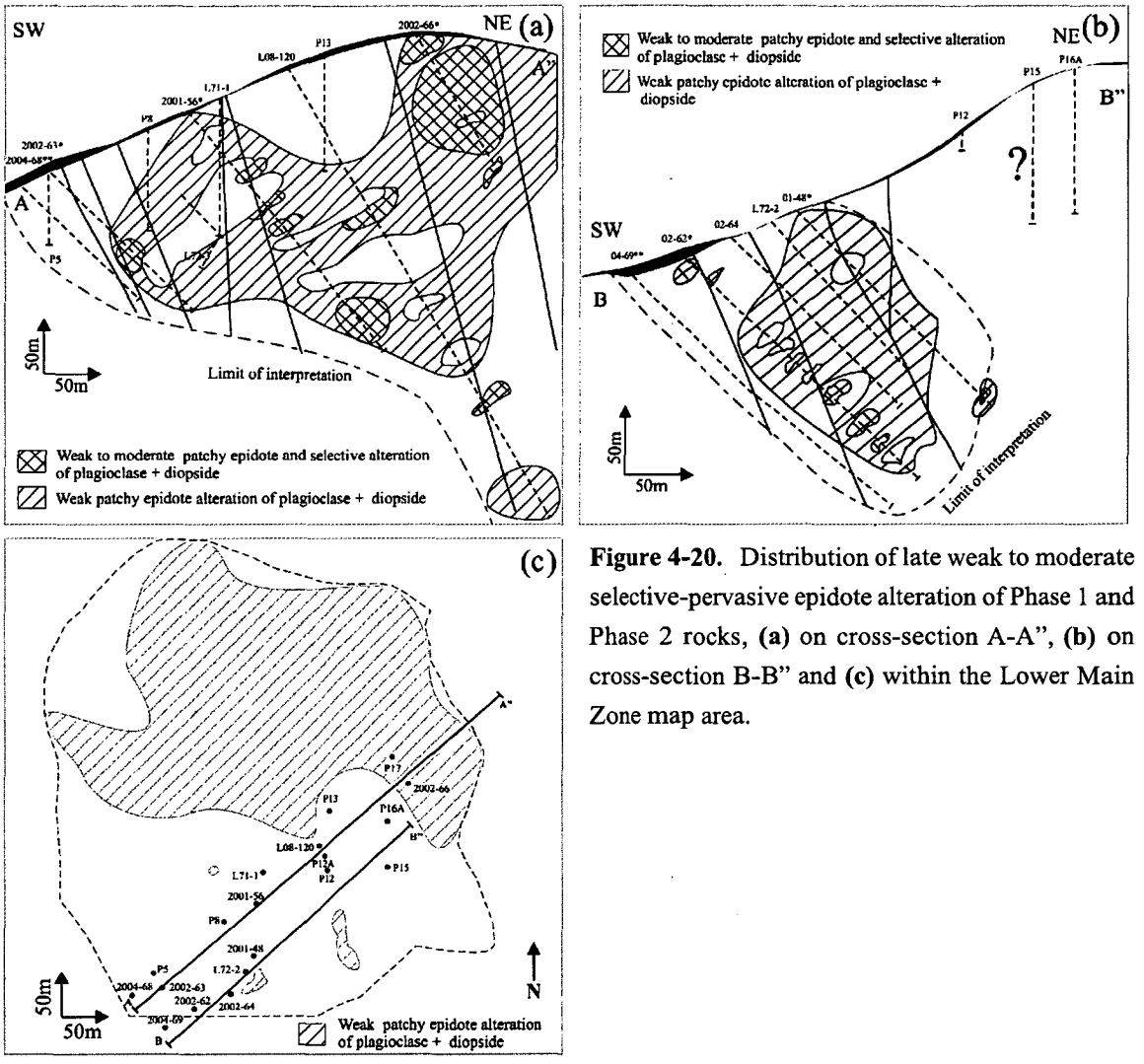

Figure 4-20. Distribution of late weak to moderate selective-pervasive epidote alteration of Phase 1 and Phase 2 rocks, **(a)** on cross-section A-A", **(b)** on cross-section B-B" and **(c)** within the Lower Main Zone map area.

4.4.3.2. Weak to strong selective-pervasive epidote alteration

Weak to locally strong selective-pervasive epidote alteration of plagioclase and diopside occurs throughout the Lower Main Zone and has affected Phase 1 and 2 rocks (Figs. 4-19c-f and 4-20a-c). Selective-pervasive replacement occurs in small (<10cm) areas and can range from weak to strong within individual outcrops. Weak epidote alteration is more prominent in Phase 1 and Phase 2 rocks in the northern area of the Lower Main Zone and is locally strong in Phase 1 and Phase 2 biotite pyroxenite. Weak epidote alteration occurs in monzonite, which is associated with small patches of hematite dusting of feldspar and pyrite. Late epidote alteration overprints late albite alteration in biotite pyroxenite and early biotite K-feldspar veins in Phase 1 syenite (Fig 4-19f). Late epidote alteration has been cross-cut by coarse K-feldspar ± biotite veins and veinlets (Fig. 4-23a, b).

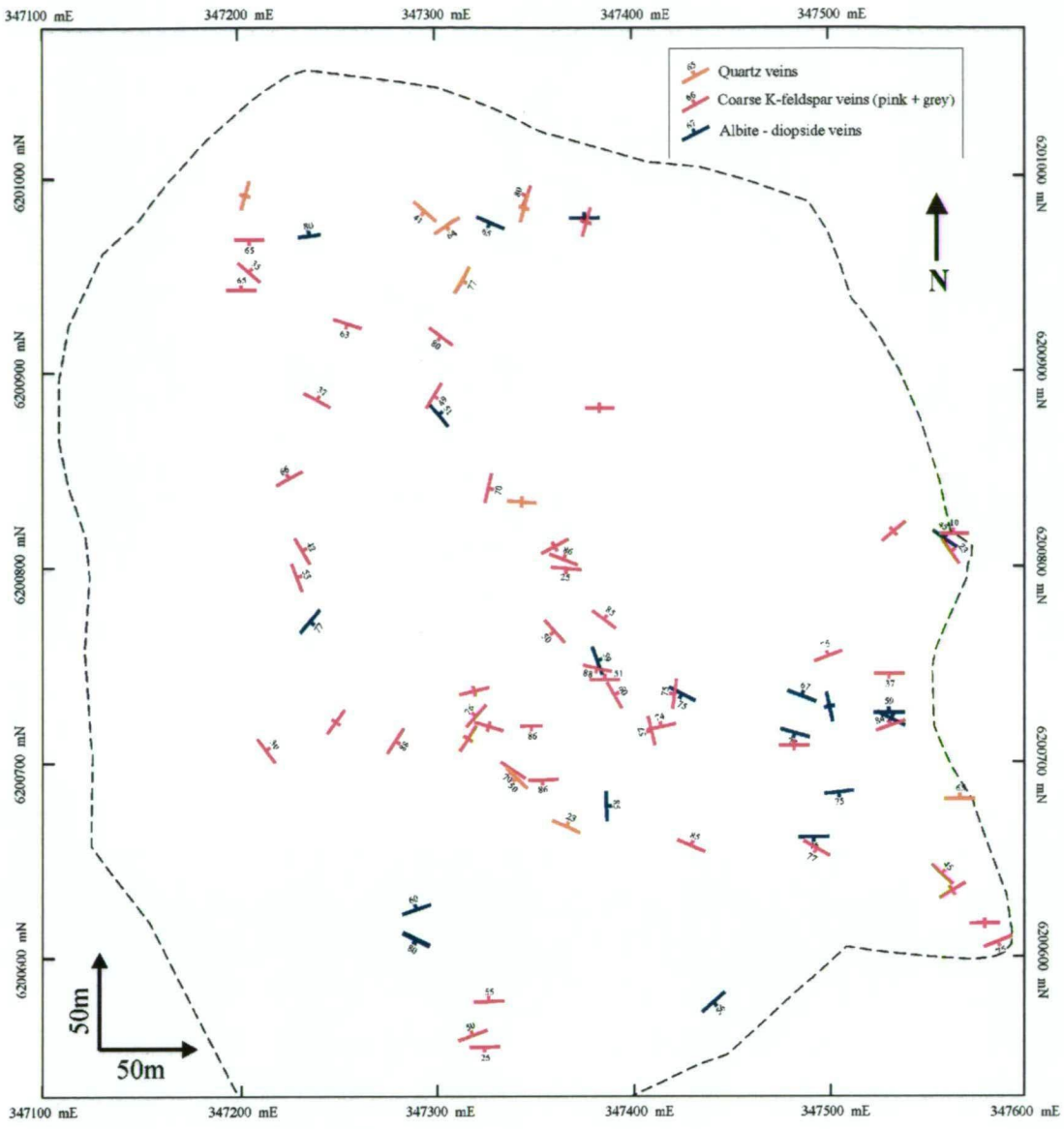

Figure 4-21. Distribution of late-stage planar veins within the Lower Main Zone map area as observed in field mapping.

4.4.3.3. Coarse-grained K-feldspar ± biotite vein-veinlet sets

Late coarse-grained K-feldspar ± biotite vein-veinlets are common throughout the Lower Main Zone and are up to 4 cm thick (Fig. 4-23a, b). Vein sets predominantly strike east to northeast and dip sub-vertically; although vein sets in the western and southern areas of the Lower Main Zone predominantly dip moderately towards the northeast and south-west (Figs 4-21 and 4-22b). Based on the lack of cross-cutting relationships it is unclear if the moderately dipping vein sets represent a separate event. The late coarse K-feldspar veins are distinguishable from early coarse K-feldspar veins in that they are barren, mostly planar and have cross-cut both Phase 2 and Phase 1 rocks.

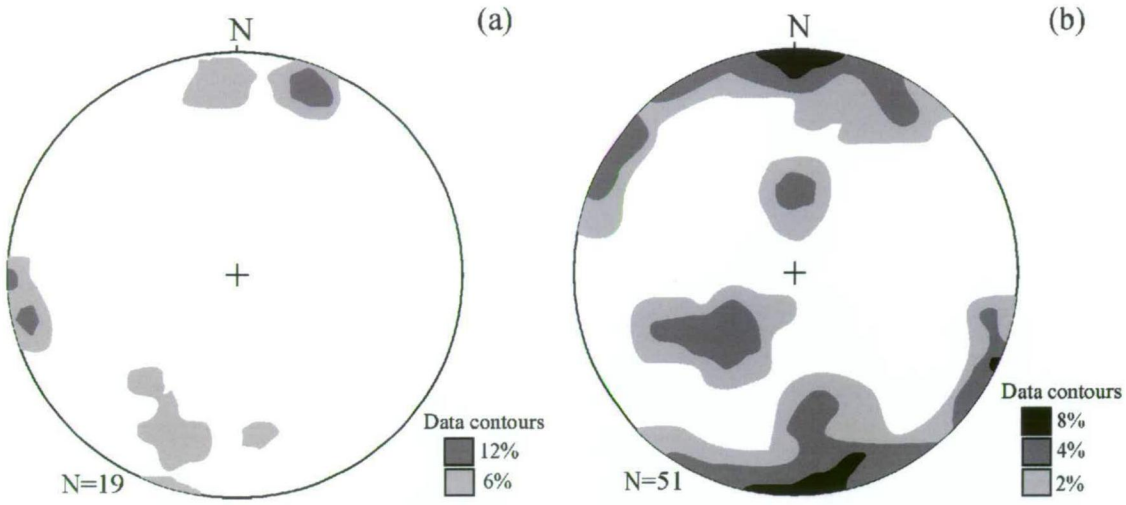

Figure 4-22. (a) Stereographic projection contours for poles to plane of late-stage albite-diopside vein populations in the Lower Main Zone. **(b)** Stereographic projection contours for poles to plane of late-stage coarse K-feldspar biotite vein sets in the Lower Main Zone. Data contours for stereographic projections were calculated using the GEOrient software program (Holcombe, 2006).

4.4.3.4. Quartz ± pyrite-chalcopyrite veins-veinlets

Late quartz veins-veinlets occur within the northern and south-central area of the Lower Main Zone and are spatially associated with quartz-bearing Phase 3 leucosyenite dykes (Fig. 4-21). The quartz veins are colourless to white and in some cases contain blebs of pyrite and chalcopyrite (Fig. 4-24a). Rocks cut by quartz veins show strong hematite dusting of feldspar and vein margins are malachite stained (Fig. 4-24a, b). In some areas quartz veins are surrounded by alteration envelopes with biotite in wall rock selectively altered to muscovite, carbonate and pyrite, and feldspar shows strong hematite dusting (Fig. 4-24b).

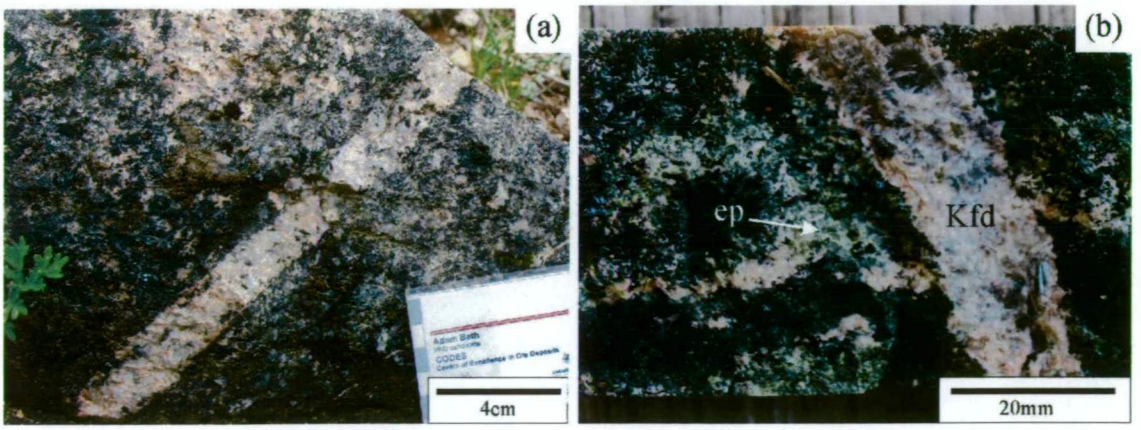

Figure 4-23. (a-b) Planar late stage coarse K-feldspar biotite veins cross-cutting Phase 2 epidote altered feldspathic pyroxenite (a = 034727mE, 6200931mN; b = drill hole 1996-44_205.3m, Bishop Zone). Mineral abbreviations; ep = epidote and Kfd = K-feldspar.

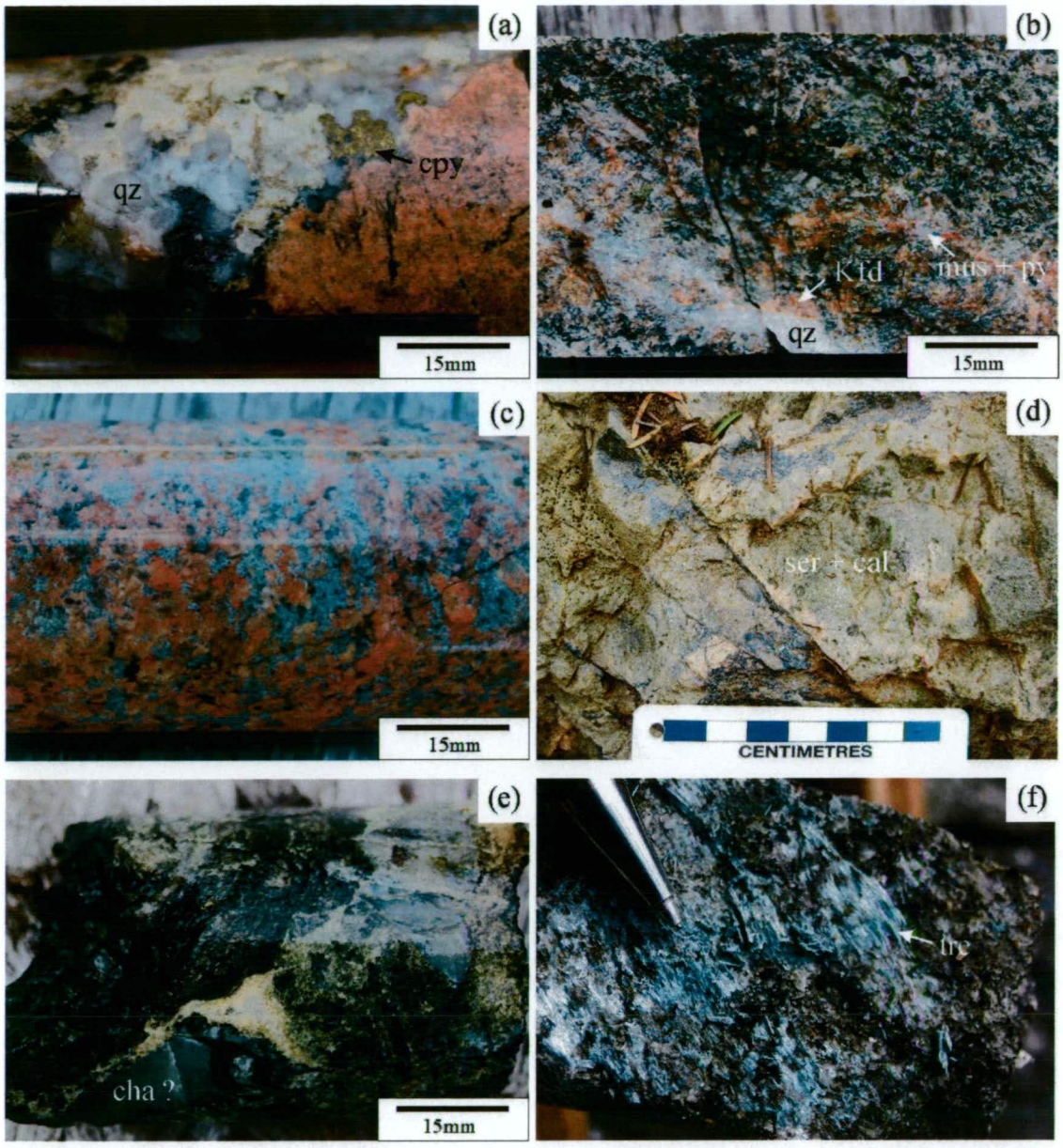

Figure 4-24. **(a)** Late stage irregular quartz vein with chalcopyrite and carbonate. Host is fine-grained K-feldspar biotite wall rock with strong hematite dusting of feldspar (drill hole 2001-56_95.1m). **(b)** Late stage quartz vein with a vein envelope of muscovite and hematite dusting of feldspar in syenite wall rock (drill hole 2002-63_64.1m). **(c)** Phase 3 coarse K-feldspar dike with selective pervasive replacement of biotite by muscovite-calcite and strong hematite dusting of K-feldspar (drill hole 2002-66_100.0m). **(d)** Pervasively sericite-calcite altered Phase 1 syenite adjacent to an east-striking fault within the Lower Main Zone (347352mE, 6200543mN). **(e)** Broken fragments of a late chalcedony? vein within a fault zone (drill hole 2002-62_47.2m). **(f)** Phase 1 biotite pyroxenite that has been cross-cut by a late stage blue tremolite vein (drill hole 2001-56_157.4m). Mineral abbreviations; cal = calcite, cha = chalocedony, cpy = chalcopyrite, Kfd = K-feldspar, mus = muscovite, py = pyrite, qz = quartz, ser = sericite; tre = tremolite.

4.4.3.5. Selective pervasive muscovite-carbonate-pyrite alteration of biotite

Late-stage selective-pervasive muscovite-carbonate-pyrite alteration is predominantly confined to late Phase 3 coarse K-feldspar dykes, and is characterised by the selective replacement of biotite by muscovite-carbonate-pyrite and strong hematite dusting of K-feldspar (Fig. 4-24c).

4.4.3.6. Local pervasive calcite-sericite alteration, chalcedony veins and tremolite veinlets

The alteration assemblages associated with late north-northeast and southeast striking subvertical brittle fault sets include pervasive and selective-pervasive calcite alteration of feldspar and mafics in wall rocks adjacent to faults (Fig. 4-24d, e). Wall rocks adjacent to faults also host chalcedony veins (Fig. 4-24e), and in biotite pyroxenite thin veinlets infilled with a cobalt blue fibrous mineral that was reported by Nixon and Peatfield (2003) to be tremolite based on X-ray diffraction analysis (Fig. 4-24f).

4.5. Discussion

4.5.1. Fluids related to potassic alteration, metal zonation and mineralisation in the Lower Main Zone

A number of characteristics of the Lower Main Zone are consistent with features found in porphyry systems. These include alteration assemblages of biotite and K-feldspar in the bornite-rich core of the deposit (Figs. 4-10a-d, 4-11a-c and 4-16a) and the increased occurrence of albite alteration (Figs. 4-11, 4-14b and 4-18a) in felsic rocks that are peripheral to mineralisation.

The cause of potassic alteration in the Lower Main Zone may be explained by the exsolution of fluids from metaluminous magmas with a high K/Na (e.g., syenites; Seedorff et al., 2005). These fluids will commonly produce potassic and sericitic alteration on cooling (Seedorff et al., 2005). However, as shown in the current study, sericitic alteration is not well developed in the Lower Main Zone. The lack of sericitic alteration in the Lower Main Zone, which is predicted by models for porphyry systems of Seedorff et al. (2005), may reflect magma-derived mineralising fluids with higher log $(mKCl + K^+)/(mHCl + H^+)$ than modeled for by those workers. Hence, the lack of sericitic or advanced argillic alteration in porphyries associated with alkaline rather than calc-alkaline (Sillitoe, 2002; Holliday and Cooke, 2007), likely reflects a control on the K^+/H^+ ratio by magma chemistry (Burnham, 1979; Sillitoe, 2010).

The general absence of quartz veining associated with mineralisation in Lower Main Zone may also provide clues to composition of the fluids. In particular, silcification is common

in the core of some porphyry deposits (e.g., Seedorff et al., 2005; Sillitoe, 2010); however quartz veins are rare in the silica-undersaturated alkalic porphyry Cu deposits in British Columbia (e.g., Galore Creek, Lorraine and Mount Polley; Lang et al., 1995b). Studies have shown that silica is transported as H_4SiO_4 or $H_3SiO_4^-$ (e.g., Rimstidt, 1997); however to date there is no experimental data on the solubility of silica in fluids that are relatively complex, such as those that likely occur in real porphyry environments. Recently, Akinfiev and Diamond (2009) modeled data on the quartz solubility in the water-salt-CO_2 system. They concluded under a wide range of P-T conditions that the presence of CO_2 in aqueous fluids lowers silica solubility, but the presence of salts (KCl and NaCl) may increase or decrease the solubility of quartz. In other studies Knauss and Wolery (1988) demonstrated that at low temperatures quartz solubility increases almost four orders of magnitude from a pH of approximately 6 to pH of 11.8, and they concluded that quartz solubility is pH dependant. In another study, Azimov and Bushmin (2007) showed that congruent dissolution of quartz and alkali-aluminum silicates in hydrothermal solutions at temperatures between 400 and 800 °C was almost independent of acidity, but more sensitive to temperature. No fluid inclusion data exists for the Lower Main Zone, due to the fact that reliable fluid inclusion assemblages have not been identified. Hence it is difficult to determine if the fluids, which were related to mineralisation, were comparatively silica-rich or silica-poor compared to fluids from calc-alkaline porphyry-Cu systems. Thus at this stage it is unclear if: (1) early magmatic CO_2-rich fluids suppressed quartz-solubility in fluids exsolved from the magma chamber. The separation of CO_2 from aqueous fluid as the fluid asended may have allowed the aqeuous fluid to remain silica undersaturated in the porphyry environment , or (2) fluids had relatively high pH (compared to porphyry deposits with abundant quartz alteration) and were able to keep silica in solution for longer, and hence suppressing quartz precipitation in the porphyry environment.

The current study has shown that zinc tends to be relatively more enriched in Phase 1 rocks in the northeast area of cross-section A-A" compared to the southeast area (Fig. 4-2d). Based on interpretations of the geology the Lower Main Zone, it is inferred that the north-eastern area of the cross-section is the outer part of the porphyry system. The distribution of lead appears to be patchier than zinc (Fig. 4-2e), but on average also appears to be more enriched in rocks in Phase 1 rocks in the north-eastern area of the Lower Main Zone. Traces of sphalerite were identified in some samples from the peripheral zones using the EDS-SEM point counting method; although galena was generally not identified in samples studied (Appendix J). Rocks in the pyrite-rich domain of the Bishop Zone, in contrast, do contain abundant sphalerite and galena (Chapter 5), which demonstrates that there are relatively strong enrichments of base metal sulphides in the peripheral zones of Lorraine. Peripheral enrichment of lead and zinc around porphyry Cu deposits, such as at Bingham (Utah) and Mineral Park (Arizona; Sillitoe, 2010), has been explained by hy-

persaline fluids formed during potassic alteration (Bodnar, 1995; Heinrich et al., 1999; Ulrich et al., 1999; Wilkinson et al., 2008; Sillitoe, 2010). These hypersaline fluids contain chlorides that form complexes with metals, and Pb and Zn remain in solution because they are not appreciably concentrated in the sulphides present in the main porphyry Cu orebody (Sillitoe, 2010). The cooling of the hypersaline fluid as it moves outwards and in contact with external wall rocks and the mixing of the fluid with meteoric water in the propylitic halos is considered to be the main cause of Zn and Pb precipitation (Hemley and Hunt, 1992; Sillitoe, 2010). These reactions may explain the occurrence of elevated Zn and Pb in the upper parts of the Lower Main Zone and in the Bishop Zone; although stable isotope work conducted in the current study (see Chapter 8), confirmed that magmatic (or metamorphic) fluids are likely related to mineralisation; meteoric fluid input has not been identified. The notion that saline fluids played a role during mineralisation in the Lower Main Zone is supported by the occurrence of relict salt-crystals in chalcocite from the potassic altered rocks of the Lower Main Zone (Chapter 5). The extent of saline fluid dispersion that may have occurred across the Lower Main Zone is unclear due to a lack of fluid inclusion data.

The distribution of gold and silver in the Lower Main Zone is shown in figures 4-2b-c and 4-3b-c. Zones of gold and silver enrichment correlate well with zones where copper is elevated. The occurrence of electrum inclusions in bornite in some samples from Lorraine, may explain the positive correlation of gold and silver with copper (Fig. 4-4a-b). Sillitoe (2010) noted that small (<20 μm) grains of native gold may occur as inclusions or as solid solution in bornite and to a lesser extent in chalcopyrite in porphyry systems. Various authors (e.g., Simon et al., 2000; Kesler et al. 2002; Sillitoe, 2010) have also noted gold grades tend to be up to ~50 percent higher in bornite-rich domains than chalcopyrite-dominated potassic assemblages. This has been explained by experimental observation that bornite solid solution is capable of holding up to one order of magnitude more gold than the intermediate solid solution precursor of chalcopyrite (Simon et al., 2000; Kesler et al. 2002; Sillitoe, 2010). In the Lower Main Zone, zones that are dominated by bornite on average have greater abundances of gold than zones that are bornite-free, supporting the contention that significant amounts of gold were incorporated into the bornite solid solution at the time of deposition.

4.5.2. Comparison of the Lower Main Zone with other alkalic porphyries

Alteration assemblages and zonation patterns of the Lower Main Zone are comparable with other Mesozoic alkalic porphyry deposits of British Columbia, such as Galore Creek, Mt. Polley and Mt. Milligan (Byrne et al., 2008; Jackson, 2008; Jago, 2008; Micko et al., 2008; Pass et al., 2008; Jago and Tosdal, in prep.; Micko et al., in prep.; Pass et al., in prep.). Similarities include (1) early magnetite alteration (2) inner zones of intense K-

feldspar alteration and hematite dusting of feldspar in syenite and fine-grained K-feldspar biotite rock, (3) outer zones with albite, epidote and weak sericite alteration, (4) a characteristic sulphide zonation pattern with a bornite dominated inner zone that grades out to bornite-chalcopyrite, chalcopyrite > pyrite and an outer pyrite ± minor chalcopyrite (*see* Table 4-3).

The Lower Main Zone, also has a number of characteristics that are unique when compared with other alkalic porphyries in British Columbia; (1) the presence of ultramafic rocks in mineralised zones and the occurrence of disseminated and net-textured sulphides in some ultramafic rocks, (2) the presence of fine-grained K-feldspar biotite rock with F-rich biotite and fine-grained disseminated sulphides, (3) a general absence of breccias (cf. Mt. Polley and Galore Creek) or quartz veining (cf. Mt. Milligan and Red Chris), (4) the occurrence of mineralisation hosted in deformed (biotite-banded) rocks, (5) an absence of a garnet-rich alteration zone peripheral to the inner bornite-chalcopyrite zone (cf. Mt. Polley and Galore Creek) and (6) a predominance of replacement style mineralisation. Most of these features appear to relate to the exotic nature of the Lorraine wall rocks.

4.5.3. The relationship between mineralisation and ductile fabric(s)

The distribution of sulphide zonation patterns and Cu-grade contours have been used to argue that the Lorraine deposit is tilted (e.g., Sillitoe, 2007). The dominant E-trending biotite-rich fabric in the Lower Main Zone is sub-vertical and deformation has folded early magnetite veins, which favours the notion that the deformational fabric post-dates tilting and mineralisation (Sillitoe, 2007; Garratt and Lindinger, 2008). In contrast, a number of fine-grained K-feldspar biotite rock and syenite observed in drill core from the Lower Main Zone have an earlier foliation overprinted by K-alteration and sulphide mineralisation (e.g., Fig. 4-16a), suggesting that either an early solid-state deformation event occurred prior to transitional-stage mineralisation or that a late mineralising event, which post-dates tilting, occurred in parts of the Lower Main Zone. As outlined in Chapter 3, biotite-rich banding may be related to the solid-state deformation caused by deformation of roof rocks above an active magma chamber or high temperature deformation around the margin of dykes, due to stretching and ductile deformation of adjacent wall rocks (e.g., Vernon and Johnson, 2004), and based on the close timing relationships between mineralisation and magmatism it appears plausible that the solid-state deformation event coincides with magmatic-hydrothermal activity and tilting of the Lower Main Zone.

Table 4-3. Alteration and mineralisation relationships in the alkalic porphyry deposits (modified after Tosdal et al. 2008).

Deposit	Mineralisation			Alteration			References
Mt. Polley	**Pre-breccia**: Disseminations and blebs of cpy (± bn ± py?) in rare clasts and xenoliths. Spatially restricted cpy disseminations and rare veins in host rocks (timing uncertain)	**Syn-breccia veins and cement**: Bn centres located within zones of abundant cpy, adjacent zones contain lesser cpy and py	**Post-breccia**: Veins: cpy ± ab ± bn; mylonitic bn > cpy veins; colloform cpy-ten-cc veins Intrusions: limited and localized disseminated and rarely veined cpy	**Potassic:** Kfd,-mt- car (act - Leak Zone) ± bio ± sulfate ± cpy ± bn **Sodic:** Ab + Kfd **Calc-potassic:** Gn (found across the deposit in all assemblages)	**Adjacent: Propylitic 2:** Ep-ab-chl-py-cc (± gn)	**Shallow/peripheral: Propylitic 1:** Py-chl-cc ± hm ± ser ± ze (± gn) **Late**: Ser-py-cc; sulphate-cc **Peripheral**: Rh-qz	Lang et al.(1995); Jackson et al.(2008); Pass et al.(2008)
Southwest Zone (Galore Creek)	**Early:** Pervasive disseminated mt-bio	**Main Stage:** Hydrothermal breccia, zones from core of cpy-(bn) to cpy>py into py>cpy. Replacement ± cement	**Peripheral:** Ep-chl-gnt-py ± (cpy) alteration and veins and ah-cpy veinlets **Late:** Qtz-Fe-carbonate-spec hm ± (py) veins	**Deep:** Bio - mt ± Kfd ± (rutite)	**Gradational from the core**; Ferroan di - mt-(ti) ± bio ±(ferro-act) ± ab	**Peripheral:** Chl-mt , gn-ep-py, Kfd-ah ± car **Late:** Structurally controlled qz-Fe-car-spec hm ± (py) veins	Enns et al.(1995); Lang et al.(1995); Byrne et al. (2008)
Mt. Milligan	**Early:** Qz-Kfd-mt-cpy-(py) veinlets	**Transitional:** Py-cc-(mt)-(cpy) veins	**Peripheral:** Py-ep-ab-act-cc-chl **Late:** Dol-ank-ser-qz-py-en- (cpy)	**Deep:** Bio-Kfd-mt-qz	Ab-act/ur-chl-(ep)-(cal)	**Peripheral:** Ep-chl-act/ur-cal-(ab). **Late:** Dol-ser-chl-(Kfd)-(ab)-py-hm alteration halos around late-stage faults	Sketchley et al.(1995); Delong.(1996); Jago.(2008)

Table 4-3. (*continued*).

Lorraine (Lower Main Zone)	**Early:** Mt-cpx-ab-cpy (patches/veins) bio-Kfd veins.	**Transitional:** Disseminated mt-cpy-bn-cc-py. Core of bn-cpy to cpy>py to cpy<py. Selective replacement of biotite by Cu-Fe sulfides and mt.	**Peripheral:** Disseminated py>cpy-chl-ser-ab-mus and clz **Late:** Cpy-py-qz veins	**Deep:** Kfd metasomatism (positive correlation between Cu and Kfd)-ab patches-ti ± mt ± clz/ep ± gn. Ca-rich pl absent. Localized coarse Kfd veins +/- coarse bio.	**Gradational from the core:** Selective replacement of pl with ser-mus and clz. Remnants of Ca-rich pl preserved in felsic rocks. Localised selective replacement of bio with chl in py>cpy zones.	**Peripheral:** Ser-mus-clz selective replacement of pl. Ca-rich pl preserved **Late:** Ser-car ± py alteration halos around late-stage faults. Ep-hm-py. Mt-cpx-Kfd-cpy polymictic bx. Qtz veins with cpy+py	Wilkinson et al. (1976); Nixon and Peatfield (2003); Peatfield and Nixon (2003)
Ridgeway	**Early:** Qz-mt-bn-cpy-Kfd-bio-(act) veins	**Transitional:** Qz-cpy-Kfd-(chl) veins	**Peripheral:** Epi-chl-py-cc-qz- preh-ze-(cpy)-(bn) **Late:** Qz-py-ser-cc-(chl)-(cpy)-(fl)	**Deep:** (Act)-bio-Kfd-ab-qz-mt	**Shallow:** Ab-chl-qz-py-cal	**Peripheral:** Chl-ab-hm-mt-ep **Late:** Ser-py alteration halos around late-stage faults	Harper.(2000); Wilson.(2003); Wilson et al.(2003); Wilson et al.(2007a)

Mineral acronyms: ab = albite; act = actinolite; ah = anhydrite; ank = ankerite; bio = biotite, phlogopite; bn = bornite; cal = calcite; car = carbonate; cc = chalcocite; chl = chlorite; clz = clinozoisite; cpx = clinopyroxene; cpy = chalcopyrite, cp; di = dioside; dol = dolomite; en = enargite/ tennantite; ep = epidote; fl = fluorite; gn = garnet, grandite; hm = hematite; kfd = K-feldspar, orthoclase; mt = magnetite; mus = muscovite; pl = plagioclase; py = pyrite; qz = quartz; rh = rhodochrosite; ser = sericite; ten = tennantite; ti = titanite, sphene, sp; ur = uralite; ze = zeolite.

Other acronyms: bx = breccia

*note- brackets indicate minor abundance

4.6. Conclusions

• Mineralisation and alteration in the Lower Main Zone are spatially and temporally associated with the emplacement of syenite intrusives. Some syenites are mineralised; others are weakly mineralised or cross-cut mineralisation. The absolute timing of mineralisation has been constrained between 178.8 and 178.4 Ma (*see* Chapter 3), implying that the Lower Main Zone formed in an active magmatic complex over a relatively short time frame, consistent with modern concepts on porphyry formation (e.g., Arribas et al., 1995). The formation of an alkalic porphyry Cu-Au deposit temporally and spatially associated with felsic magmatism, such as in the Lower Main Zone, is consistent with other alkalic porphyry Cu-Au deposit in British Columbia (e.g. Galore Creek; Enns et al., 1995), New South Wales (e.g. Ridgway; Wilson et al., 2003), Philippines (Didipio; Wolfe, 2001) and Greece (Skouries; Kroll et al., 2002).

• The Lower Main Zone has a sulphide zonation pattern comparable to other alkalic porphyry Cu-Au deposits in British Columbia; however mineralisation produced finely disseminated replacement-style Cu-Fe sulphides in fine-grained K-feldspar biotite rock, biotite pyroxenite and syenite. Features such as stockwork veining and breccias, which are common in most porphyry deposits, are only minor features at Lorraine. There is textural evidence that biotite in the fine-grained K-feldspar biotite rock and biotite pyroxenite has been replaced by Cu-Fe sulphides (also *see* Chapter 5).

• The Lower Main Zone appears to have formed in a magmatic complex, and has alteration and sulphide zonation patterns that are consistent with porphyry formation. Mineralisation textures in the Lower Main Zone allow Lorraine to be classified as a replacement-style alkalic Cu-Au-Ag ± PGE porphyry deposit.

CHAPTER 5
DETAILED DESCRIPTION OF TRANSITIONAL STAGE MINERALISATION

5.1. Introduction

Porphyry Cu deposits are geochemical anomalies of Cu and S, and most researchers agree that these elements originate from underlying magma chambers and are transported to the site of mineralisation by aqueous magmatic fluids (e.g., Evans, 1993; Hedenquist and Lowenstern, 1994; Audetat and Pettke, 2006). These aqueous fluids associated with mineralisation cause intense hypogene potassic alteration (Beane, 1982), which causes the replacement of primary rock-forming minerals by orthoclase, albite, magnetite, biotite and other secondary minerals in the core of porphyry deposits (e.g., Lowell and Guilbert, 1970; Pollard, 1984; Wilson et al., 2003; Seedorff et al., 2005). Aqueous fluids can also produce intense quartz stockwork veining (e.g., Brimhall, 1977; Carten et al., 1988; Cline and Bodnar, 1994; Seedorff et al., 2005) and/or hydrothermal breccias that can show a diverse range of characteristics (i.e. variations in cement or matrix composition, nature of fragments, geometry and dimension of breccia bodies, etc; Sillitoe, 1985; Landtwing et al., 2002; Byrne et al., 2008; Jackson, 2008; Pass et al., 2008). At Lorraine, mineralisation occurred in areas of K-feldspar alteration, and mineralisation produced a sulphide zonation pattern that overprints a number of different rock types (e.g., Sillitoe, 2007). These observations are consistent with characteristics of other alkalic porphyry Cu-Au deposits of British Columbia (Chapter 4); however Lorraine lacks large-scale hydrothermal breccias, which are common at other silica-undersaturated alkalic porphyry deposits in British Columbia (e.g., Mt. Polley, Galore Creek; Enns et al., 1995; Fraser et al., 1995; Byrne et al., 2008; Jackson, 2008; Pass et al., 2008). Mineralisation at Lorraine is inferred to be predominantly replacement-style (Chapter 4). Replacement textures are described in detail in this chapter, together with mineralised rocks from the Bishop Zone and Main Zone. Comparisons are also made here with Galore Creek replacement-style mineralisation (Central Replacement Zone), where sulphide distributions are controlled by host rock lithologies, and the selective replacement of biotite and magnetite by chalcopyrite has been recorded (Micko et al., 2008).

Previous authors (e.g., Bishop et al., 1995), have also described net-textured sulphides at Lorraine in biotite pyroxenite, and have hypothesised that these rocks may represent a magmatic component from a "deep" root zone of a porphyry deposit. These "net-textures" are investigated in detail in this chapter to determine if there is evidence of a primary magmatic sulphide component in ultrabasic rocks at Lorraine. Other possibilities, such as desulpidisation reactions, relating to metamorphism and oxidisation of primary magmatic

sulphides in ultrabasic bodies (e.g., Cawthorn and Meyer, 1993; Boer and Meyer, 1994; Maier and Barnes, 1999), are also considered in this chapter in light of the new textural data.

5.1.1. Methods employed

This chapter describes altered rocks based on data collected from transmitted and reflected light microscopy and observations made using the FEI Quanta 600 scanning electron microscope (SEM) facility in the Central Science Laboratory at the University of Tasmania. The SEM is equipped with secondary back-scattered electron, cathodoluminescence (CL) detectors and two energy dispersive spectrometers (EDS). The EDS was used for qualitative and semi-quantitative elemental analysis and spectrometers are interfaced to the Mineral Liberation Analysis (MLA) software package which has been used to determine mineral types.

This study used a point counting method on the SEM. Over 10,000 spots were analysed on individual thin sections or polished slabs using EDS and minerals types were determined using the MLA software package. This method proved to be effective for accurately quantifying mineral assemblages in individual thin sections and polished slabs, and the current study uses data from EDS-SEM analysis to compare modal abundance of plagioclase, albite, K-feldspar, clinopyroxene, biotite, quartz and epidote in unaltered versus altered rocks. The current study also compares the modal abundance of major mineral phases of felsic rock from different sulphide zones.

5.2. Petrographic descriptions

5.2.1. Samples selected for the current study

Representative mineralised samples used in this study were collected from the Lower Main Zone and Bishop Zone. Representative samples have been located using the Universal Transverse Mercator (zone 10; NAD83). Sample locations from the Lower Main Zone are plotted on the Lower Main Zone map and cross-sections A-A" and B-B" (Figs. 3-3 and 3-4a and b).

At Lorraine, mineralisation predominantly occurs as fine-grained sulphides disseminated in the host rocks, including fine-grained K-feldspar biotite rocks, biotite pyroxenite, feldspathic pyroxenite and syenite with variable abundance of mafic minerals (Chapter 3). Syenites and biotite pyroxenites are common host rocks in the Bishop Zone, and syenite

is the dominant host rock type in the Main Zone. The following subsections describe the petrography of these three major host rock types.

5.2.2. Fine-grained K-feldspar biotite rocks

Mineralised fine-grained K-feldspar biotite rocks predominately occur in the central area of the Lower Main Zone (Figs. 3-3 and 4-15). Sulphides are abundant in fine-grained K-feldspar biotite rocks that are adjacent to syenitic veins and zones of K-feldspar alteration (Fig. 5-1a-c), indicating that mineralisation and K-feldspar alteration are most likely related. The mineralised rocks are medium grey and comprise anhedral alkali feldspar, biotite, clinopyroxene, magnetite, and fine-grained disseminated pyrite and/or Cu-Fe sulphides (Figs. 5-1b, c, 5-2a, b), which in some samples are partly weathered to pitch-limonite (Fig. 5-3a, b). Mineralised fine-grained K-feldspar biotite rocks include accessory apatite, fluorite, titanite, and rarely contain quartz, sphalerite and/or galena, and sulphides are spatially associated with biotite or turbid feldspar (Figs. 5-2a, b, 5-3a, b and 5-4a-c).

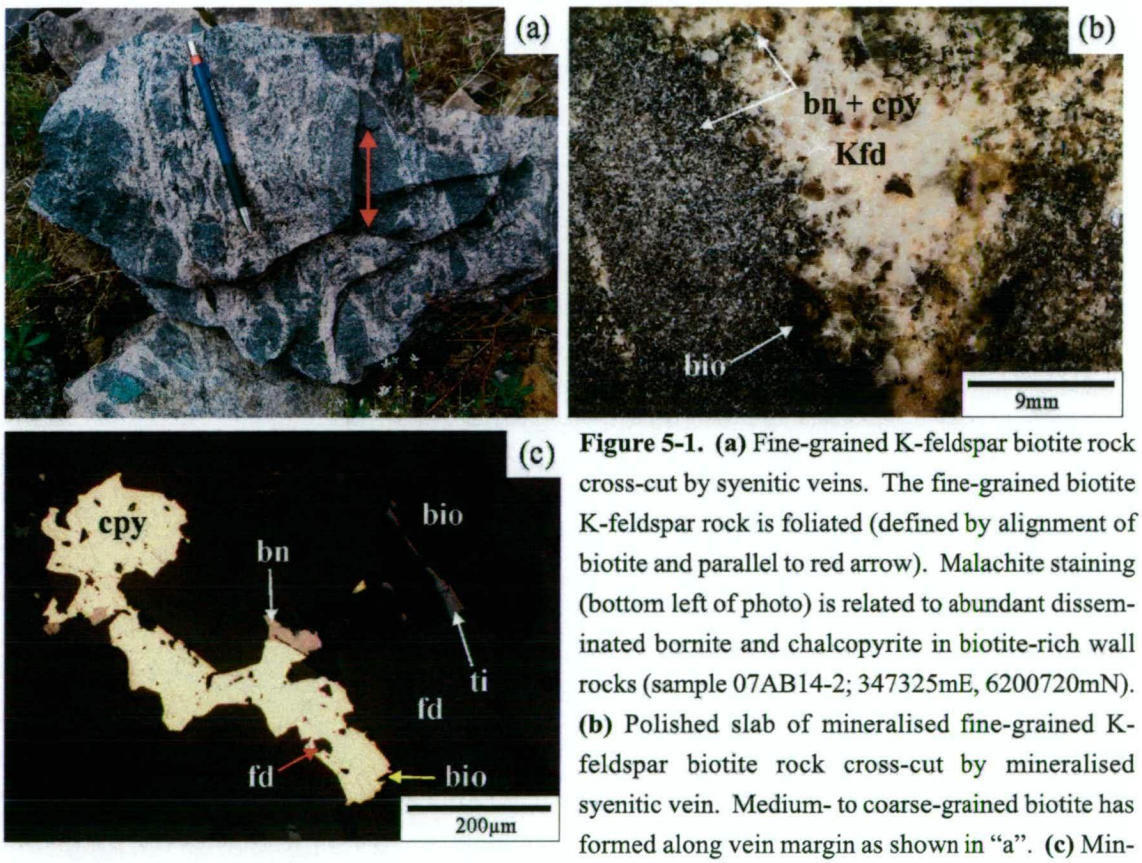

Figure 5-1. (a) Fine-grained K-feldspar biotite rock cross-cut by syenitic veins. The fine-grained biotite K-feldspar rock is foliated (defined by alignment of biotite and parallel to red arrow). Malachite staining (bottom left of photo) is related to abundant disseminated bornite and chalcopyrite in biotite-rich wall rocks (sample 07AB14-2; 347325mE, 6200720mN). **(b)** Polished slab of mineralised fine-grained K-feldspar biotite rock cross-cut by mineralised syenitic vein. Medium- to coarse-grained biotite has formed along vein margin as shown in "a". **(c)** Mineralised fine-grained K-feldspar biotite rock shown in reflected light (same sample as in "a" and "b". Bornite and chalcopyrite mineralisation forms irregular-shaped contacts with K-feldspar and biotite in the host rock. Sulphides also include inclusions of K-feldspar and biotite, which are inferred to be relicts of the host rock, which had been partly replaced by the sulphides. Mineral abbreviations: bio = biotite, bn = bornite, cpy = chalcopyrite, Kfd = K-feldspar, ti = titanite.

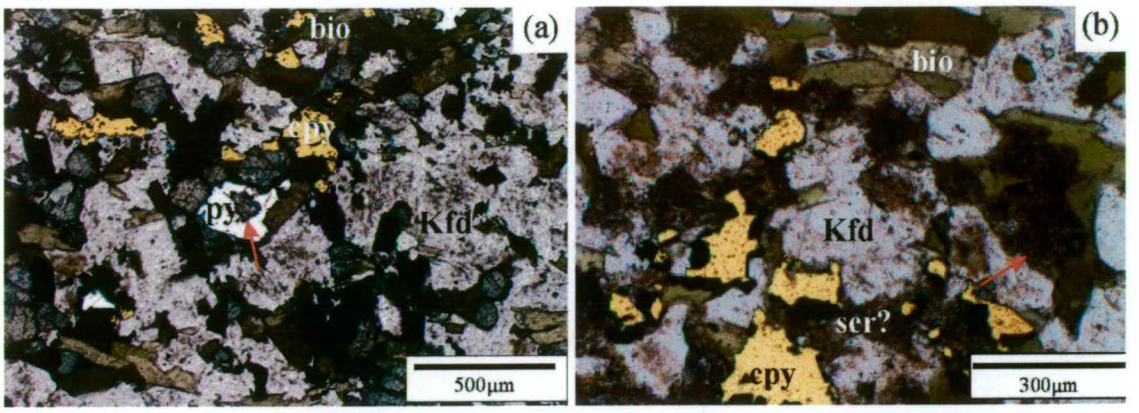

Figure 5-2. **(a)** Photomicrograph of chalcopyrite-pyrite altered rock from the central area of the Lower Main Zone photographed in combined transmitted light and reflected light. Clinopyroxene and biotite are unaltered, although pyrite appears to have grown around clinopyroxene (red arrow). Pyrite is inferred to have replaced clinopyroxene. Feldspar is weakly to moderately turbid (drill hole 2001-56_217 m). **(b)** Chalcopyrite altered rock from the central area of the Lower Main Zone in combined transmitted light and reflected light. Clinopyroxene appears to have been partially replaced by sericite (red arrow). Chalcopyrite is anhedral (drill hole 2001-56_88.9 m). Mineral abbreviations: bio = biotite, cpy = chalcopyrite, Kfd = K-feldspar, py = pyrite, ser = sericite.

Feldspars in the mineralised fine-grained K-feldspar biotite rock are commonly turbid. The turbid patches contain small (<10 µm) inclusions of chalcopyrite and bornite (Fig. 5-3a, b). In contrast, biotite has irregular-shaped green margins (Fig. 5-4a, b), and/or includes fluorite, actinolite, chlorite or titanite along grain margins where it is in contact with Cu-Fe sulphides (Fig. 5-4a-d). These green margins contain anomalous Cu (i.e. up to ~7000 vs. <5 ppm for most brown biotite; *see* Chapter 6), and it is inferred that Cu-enrichment occurred along biotite margins during mineralisation.

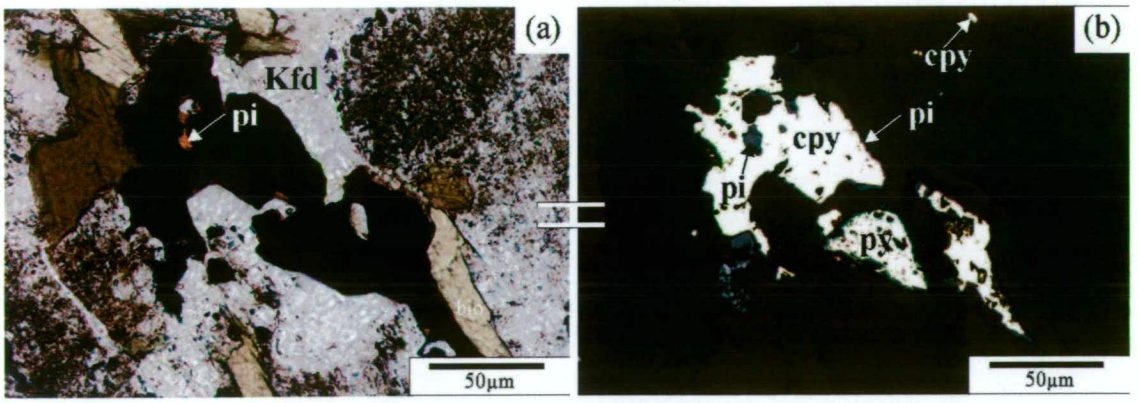

Figure 5-3. **(a)** Mineralised fine-grained K-feldspar biotite rock from the Lower Main Zone with chalcopyrite and pyrite mineralisation in plane polarised light. Feldspar includes turbid patches with small (<5 µm) inclusions of chalcopyrite (see "b"). Chalcopyrite is also rimmed by red pitched-limonite due to weathering (sample 07AB-52, 347332mE, 6200986mN). **(b)** Same as "a" except in reflected light. Mineral abbreviations: bio = biotite, cpy = chalcopyrite, Kfd = K-feldspar, py = pyrite, pi = pitch limonite.

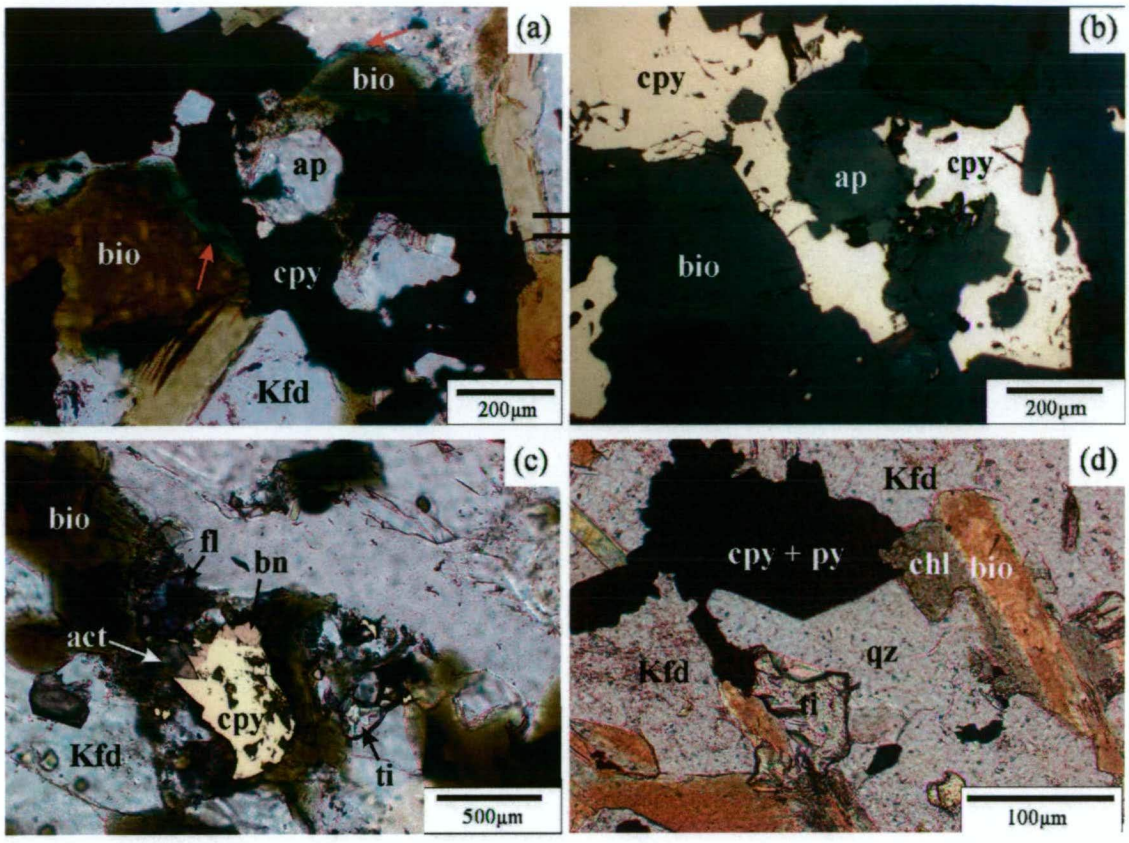

Figure 5-4. Fine-grained K-feldspar biotite rock with chalcopyrite ± bornite from the Lower Main Zone. **(a)** Contact between chalcopyrite and biotite. Biotite has green margins along contacts with chalcopyrite (red arrows). Viewed in transmitted light (drill hole 2001-56_88 m). **(b)** Same as "a" except in reflected light. Photomicrograph shows the distribution of chalcopyrite and the occurrence of K-feldspar inclusions in chalcopyrite. **(c)** Chalcopyrite and bornite in contact with biotite, with actinolite, fluorite (fl), and titanite (ti) alongside sulphides viewed in combined reflected and transmitted light (sample 07AB 14-2; 347325mE, 6200720mN). **(d)** Chalcopyrite-pyrite altered rock viewed under transmitted light. Biotite has been partially altered to chlorite (chl). Titanite (ti) also occurs along contact between biotite and sulphides, possibly as a result of alteration of biotite (drill hole 2001-56_106.1 m). Mineral abbreviations: act = actinolite, ap = apatite, bio = biotite, bn = bornite, cpy = chalcopyrite, chl = chlorite, fl = fluorite, Kfd = K-feldspar, ti = titanite.

Fine-grained K-feldspar biotite rocks from the outer pyrite-zone of Bishop Zone (i.e. drill hole 1996-44_88.8 m; Fig. 4-1) contain anomalous sphalerite, galena and pyrite, and these sulphide minerals occur in patches with turbid feldspar, fluorite and apatite (Fig. 5-5a-d). Turbid feldspars comprise albite and K-feldspar, which contain small (<10 µm) inclusions of galena (Fig. 5-5c, d), and biotite in contact with turbid feldspar and sulphides also has green margins (Fig. 5-5a).

In both the Lower Main Zone and Bishop Zone, fine-grained K-feldspar biotite rocks contain bornite, chalcopyrite, pyrite, galena and/or sphalerite which is spatially associated

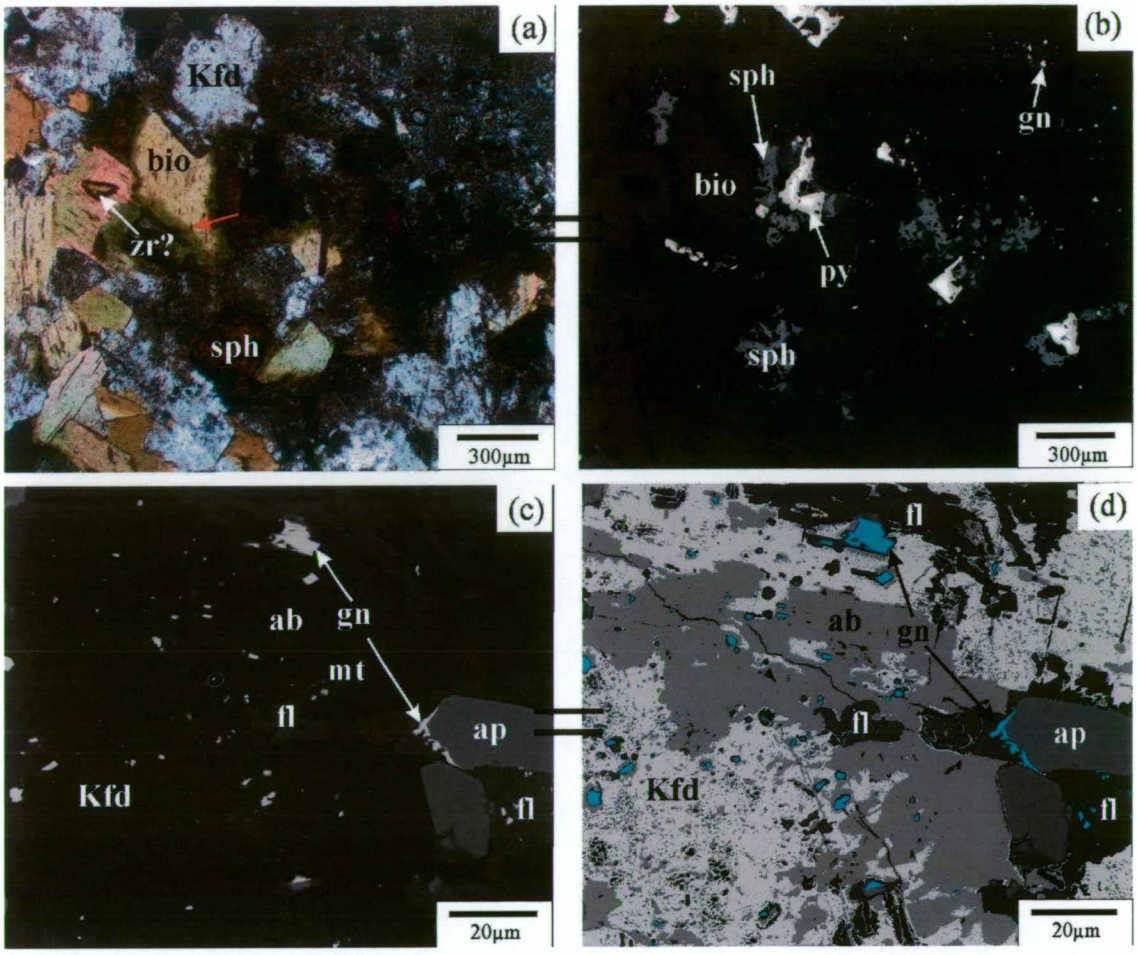

Figure 5-5. Fine-grained K-feldspar biotite rock with galena (gn), sphalerite (sph), pyrite (py) and minor chalcopyrite (cpy) from the Bishop Zone (drill hole 1996-44_88.9 m). **(a)** Albite, sericite, pyrite, galena, titanite, fluorite (fl) and sphalerite alteration patches that have overprinted fine-grained biotite and K-feldspar. Biotite has altered green margins in contacted with albite or sphalerite (red arrow). Biotite also includes high relief mineral, probably zircon (zr?). Viewed in transmitted light. **(b)** Same as "a" except viewed in reflected light. Sphalerite intergrown with pyrite and titanite, and small inclusions of galena in altered patches. **(c and d)** Albite, sericite, pyrite, galena, titanite and sphalerite alteration patches viewed under (c) back-scattered electron and (d) enhanced using false colours (i.e. galena is light blue). Albite patches contain abundant fluorite and galena. Fine-grained galena concentrated along the contacts between albite and K-feldspar. Mineral abbreviations: ab = albite, ap = apatite, bio = biotite, fl = fluorite, gn = glanet, Kfd = K-feldspar, mt = magnetite, py = pyrite, sph = sphalerite, zr = zircon.

with turbid feldspar and altered green biotite margins. Hydrothermal green biotites and/or turbid feldspars have been recorded in number of porphyry Cu deposits (e.g., Butte, Montana, Brimhall, 1977; Copper Mountain Porphyry district, British Columbia, Lang, 1996), and these features at Lorraine therefore appear consistent with porphyry-style hydrothermal alteration that usually accompanies mineralisation.

5.2.3. Biotite pyroxenite and feldspathic pyroxenite

Unaltered biotite pyroxenites and feldspathic pyroxenites were described in detail in Chapter 3. These are characterised by aligned euhedral to subhedral green diopside with anhedral biotite or biotite phenocrysts, variable amounts of anhedral feldspar, and accessory apatite and magnetite, which occur as inclusions in biotite and diopside. Mineralised biotite pyroxenites and feldspathic pyroxenites are texturally similar to barren biotite pyroxenites and feldspathic pyroxenites (Fig. 5-6a-c), or contain patches of coarse-grained biotite and/or coarse-grained apatite (Fig. 5-6d-f). The latter texture is common in bornite-chalcopyrite mineralised biotite pyroxenites, whereas the former is more common in chalcopyrite-pyrite mineralised biotite pyroxenite.

5.2.3.1. Chalcopyrite-pyrite mineralised biotite pyroxenite

Chalcopyrite-pyrite mineralised biotite pyroxenites from the Lower Main Zone contain medium grained subhedral diospide, anhedral fine- to medium-grained biotite and fine-grained subhedral to anhedral magnetite, pyrite and apatite (Figs. 5-7 and 5-8a-d). These sulphides have been described as "net-textured" by some authors (e.g., Bishop et al., 1995). The current study has investigated relationships between sulphides and primary magmatic minerals (i.e. diopside and biotite) in detail, and found that sulphides and magnetite predominantly occur in discrete zones with subhedral diopside. Zones that are relatively sulphide-poor contain aligned subhedral diopside with anhedral biotite (Fig. 5-7). Texturally, these poorly mineralised zones appear to resemble unaltered biotite pyroxenites (Chapter 3). In contrast, zones that contain abundant sulphides also contain subhedral diopsides that are not aligned and are closely spaced relative to the poorly mineralised domains (Fig. 5-7). These areas of the rock may represent areas where the diopside framework has been reorganised or recrystallised.

The present study also found that diopsides in contact with Cu-Fe sulphides have actinolite along crystal grain margins (Fig. 5-8a), and sulphides contain inclusions of diopside and actinolite (Fig. 5-8a, b). Diopside does not contain primary sulphide inclusions, but does contain globular magnetite and apatite inclusions, similar to those in unmineralised biotite pyroxenites (Chapter 3). Secondary sulphide inclusions occur along fractures in diopsides. Diopsides in mineralised biotite pyroxenites are strongly pleochroic, particularly along their margins, which, as pointed out by Deer et al. (1992) relates to abundant Fe (particularly Fe^{3+}) in diopside. Back-scattered electron images and microprobe analysis show that diopside from mineralised biotite pyroxenites have irregular-shaped outer margins that are more Fe-rich and have lower *mg*-numbers compared to diopside from unaltered biotite pyroxenite (Fig. 5-9a, b; Chapter 6). Irregular-shaped outer margins of diopside from mineralised biotite pyroxenite are inferred to represent a sub-solidus exchange of Fe and Mg between diopside, possibly during alteration (Chapter 6).

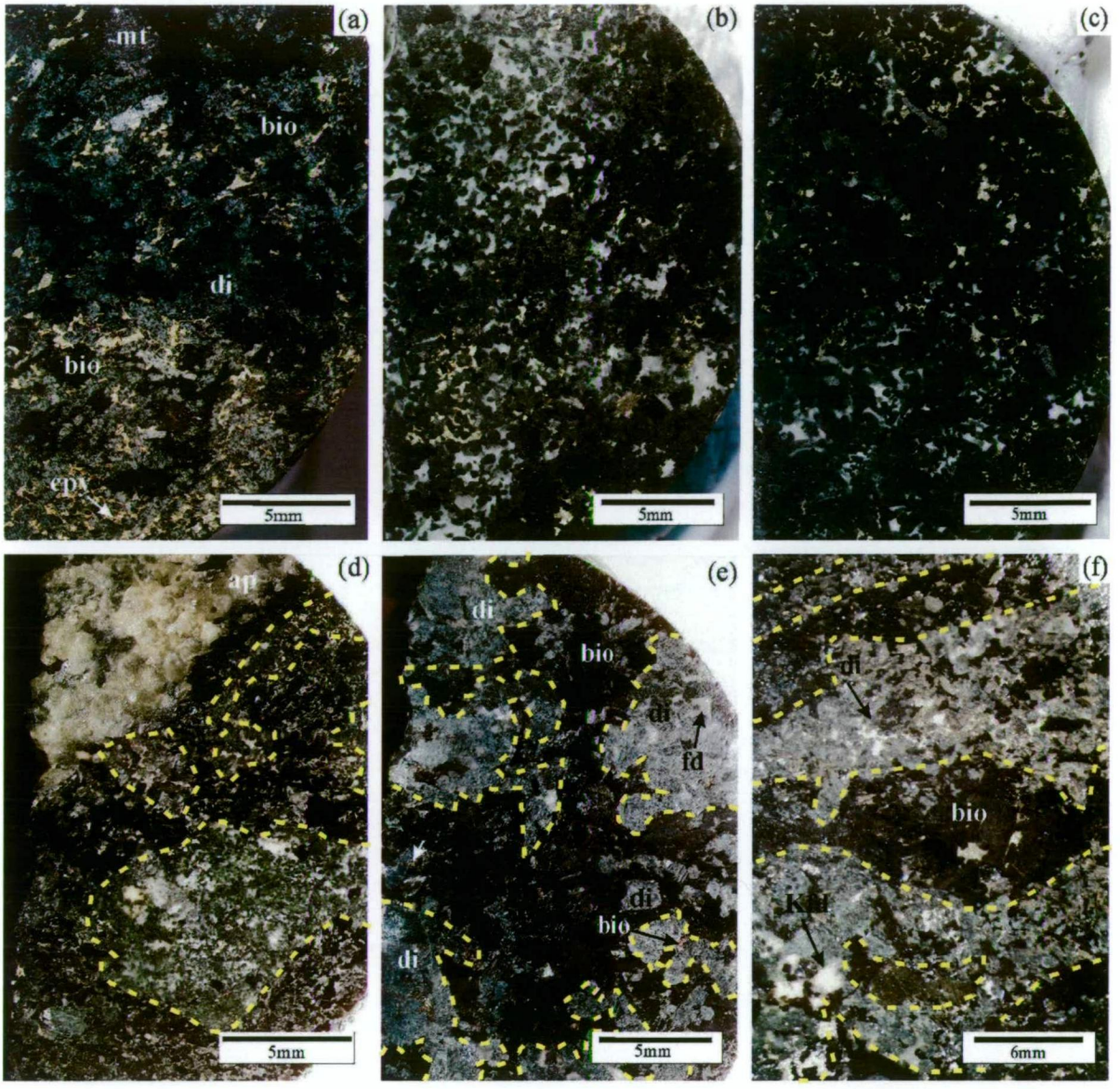

Figure 5-6. Various mineralised samples of biotite pyroxenite and feldspathic pyroxenite from the Lower Main Zone and Bishop Zone areas. **(a)** Chalcopyrite-pyrite altered biotite pyroxenite with localised net-textured sulphides and coarse patches of biotite from the Lower Main Zone as shown in Figs. 5-7, 5-8, 5-10 and 5-11 (drill hole 2001-56_199.8 m). **(b)** Chalcopyrite altered feldspathic pyroxenite from the Lower Main Zone as shown in Fig. 5-13a-h (drill hole 2001-56_157 m). **(c)** Chalcopyrite-pyrite altered feldspathic pyroxenite from the Lower Main Zone (drill hole 2001-56_198.1 m). **(d)** Bornite-chalcopyrite altered biotite pyroxenite with irregular patches of coarse biotite and a patch of coarse apatite that includes Cu-Fe sulphides from the Lower Main Zone. Yellow dash line denotes contact between coarse biotite patches, and patches dominated by feldspar (drill hole 2001-48_173.9m). **(e)** Bornite-chalcopyrite altered biotite pyroxenite with irregular patches of coarse-grained biotite from the Bishop Zone (drill hole 1996-44_234.4 m). **(f)** Bornite-chalcopyrite altered biotite pyroxenite with coarse bands of biotite from the Lower Main Zone (drill hole 2001-56_145 m). Mineral abbreviations: ap = apatite, bio = biotite, cpy = chalcopyrite, di = diopside, fd = feldspar, Kfd = K-feldspar, mt = magnetite.

Figure 5-7. Chalcopyrite-pyrite altered biotite pyroxenite with "net-textured" sulphides, magnetite under combined reflected and transmitted light. Diopsides are roughly aligned in the biotite-rich area of the thin section (see red arrow), whereas the part of the sample mineralised is biotite-poor and consists of finer grained diopsides crystals that are more closely packed and are not aligned. It is inferred that the diopside framework in the mineralised domains have been compacted, reorganisation and/or recrystallised during mineralisation (drill hole 2001-56_199.8 m). Mineral abbreviations: ap = apatite, bio = biotite, cpy = chalcopyrite, di = diopside, mt = magnetite, py = pyrite.

Biotite in contact with sulphides has irregular-shaped margins. In some cases, biotite has green rims along contacts with chalcopyrite (Fig. 5-8d). Detailed SEM work has revealed that irregular-shaped inclusions of biotite occur in chalcopyrite (Fig. 5-10), which appears to be relicts of biotite that have been partially replaced by chalcopyrite. In contrast, biotites do not contain primary sulphide inclusions; however sheet-like sulphide grains were identified along biotite cleavage planes (i.e. similar to those in feldspathic biotite pyroxenites, *see* below) and between biotite grains, which suggests that sulphides were deposited after biotite.

5.2.3.2. Chalcopyrite-pyrite mineralised feldspathic pyroxenite

Chalcopyrite and pyrite altered feldspathic pyroxenite comprise medium-grained subhedral diopside, coarse-grained biotite, medium-grained feldspar (Fig. 5-11a-d) and coarse-grained K-feldspar oikocrysts (not shown). Copper-Fe sulphides and titanite occur between biotite-clinopyroxene grains, on biotite-biotite grain boundaries, along biotite cleavage planes (Figs. 5-11a-f), and also occur as small (<10 μm) inclusions in turbid

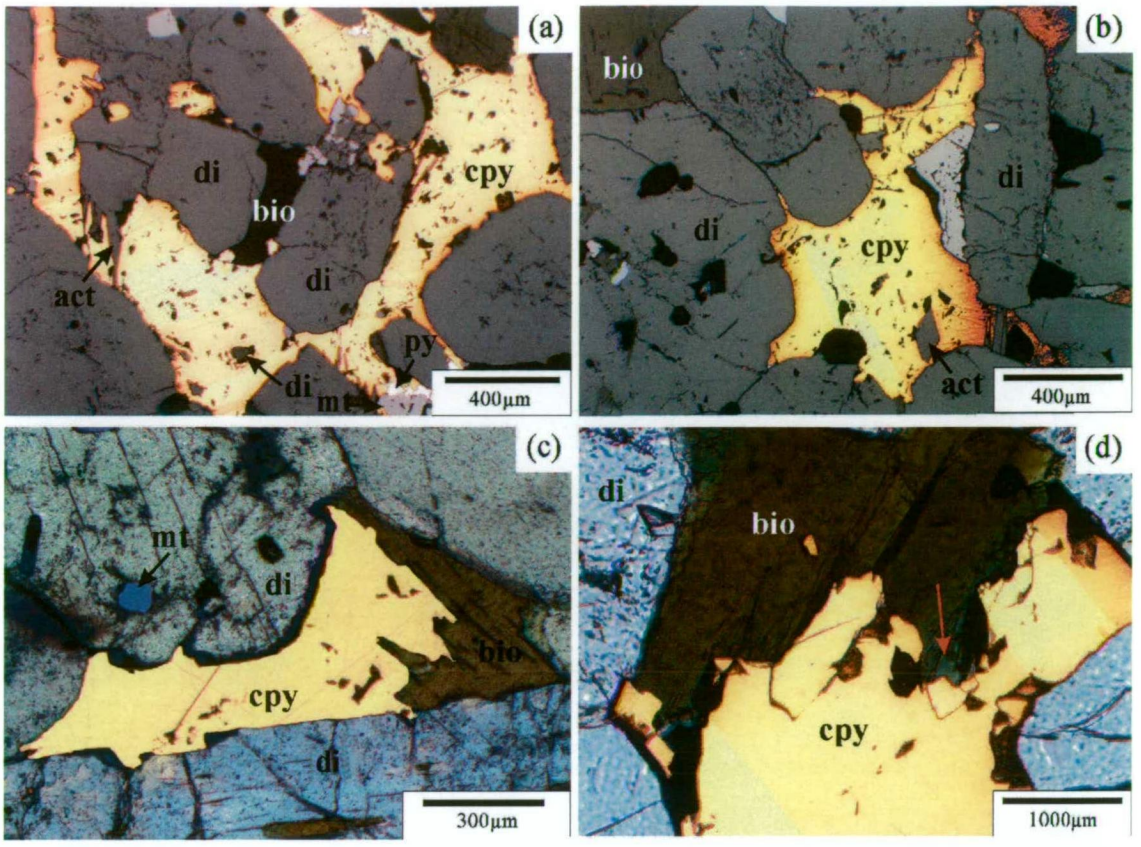

Figure 5-8. **(a)** Chalcopyrite-pyrite mineralised biotite pyroxenite from the Lower Main Zone viewed in reflected light, and showing subhedral diopside with anhedral chalcopyrite. Note the occurrence of actinolite along the margin of diopside, diopside inclusions in chalcopyrite and relict biotite between diopside crystals (drill hole 2001-56_199.8 m). **(b)** Anhedral chalcopyrite between subhedral diopside in chalcopyrite-pyrite mineralised biotite pyroxenite in reflected light and as shown in "a". Note the occurrence of actinolite along diopside grain margins. **(c)** Contact between chalcopyrite and biotite is sharp and irregular (combined transmitted light and reflected light; same sample as "a"). **(d)** Contact between biotite and chalcopyrite in combined transmitted and reflected light. Note that the biotite grain has a green margin, possibly as a result of chemical modification during chalcopyrite deposition (same sample as "a"). Mineral abbreviations: act = actinolite, ap = apatite, bio = biotite, cpy = chalcopyrite, di = diopside, mt = magnetite.

feldspar patches adjacent to coarse-grained biotite (Fig. 5-11d). Fine-grained needles of actinolite have formed on diopside grain boundaries with Cu-Fe sulphides (Figs. 5-11g, h). The actinolite and chalcopyrite are inferred to have partly altered the diopside. The titanite that occurs along biotite grain boundaries in contact with chalcopyrite is inferred to have formed due to recrystallisation of high-Ti biotite to a lower-Ti green biotite.

5.2.3.3. Bornite-chalcopyrite mineralised biotite pyroxenite and feldspathic pyroxenite

Altered biotite pyroxenites and feldspathic pyroxenites include fine- to medium-grained patches of anhedral albite and K-feldspar with euhedral diopside, patches of coarse-grained biotite with medium- to coarse-grained apatite and patches dominated by coarse-grained apatite (Figs. 5-12a, b and 5-13a-d). Contacts between the feldspar- and biotite-rich

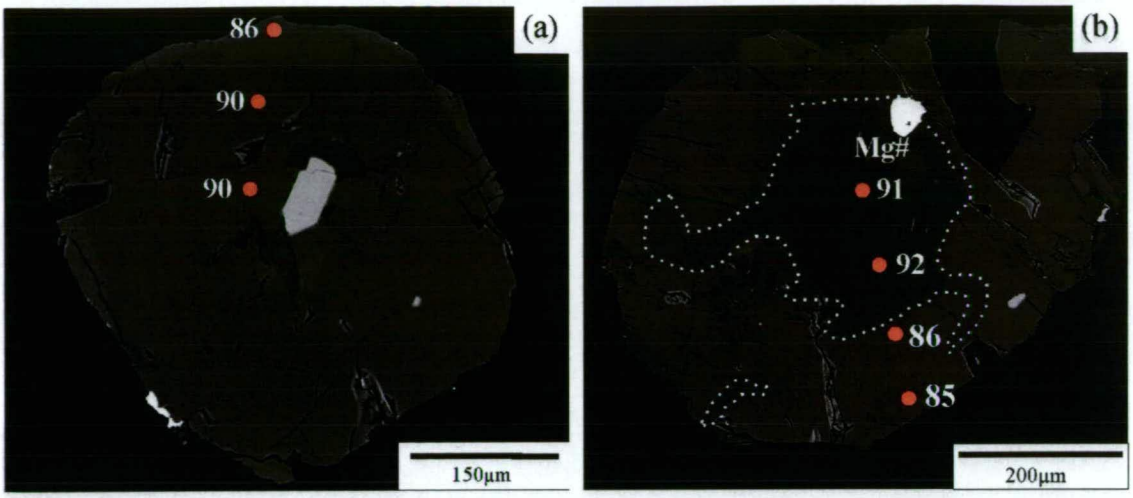

Figure 5-9. Back-scatter electron images of diopside from altered biotite pyroxenite and unaltered biotite pyroxenite from the Lower Main Zone. **(a)** Diopside in unaltered biotite pyroxenite shows only very minor evidence of compositional zoning along the rim (drill hole 2002- 66_75 m). **(b)** Diopside in altered biotite pyroxenite has an inner darker core with *mg*-number >90 and lighter rim with *mg*-number <86. The white dashed line denotes the contact between irregular darker patches and lighter patches (drill hole 2001-48_173.9 m).

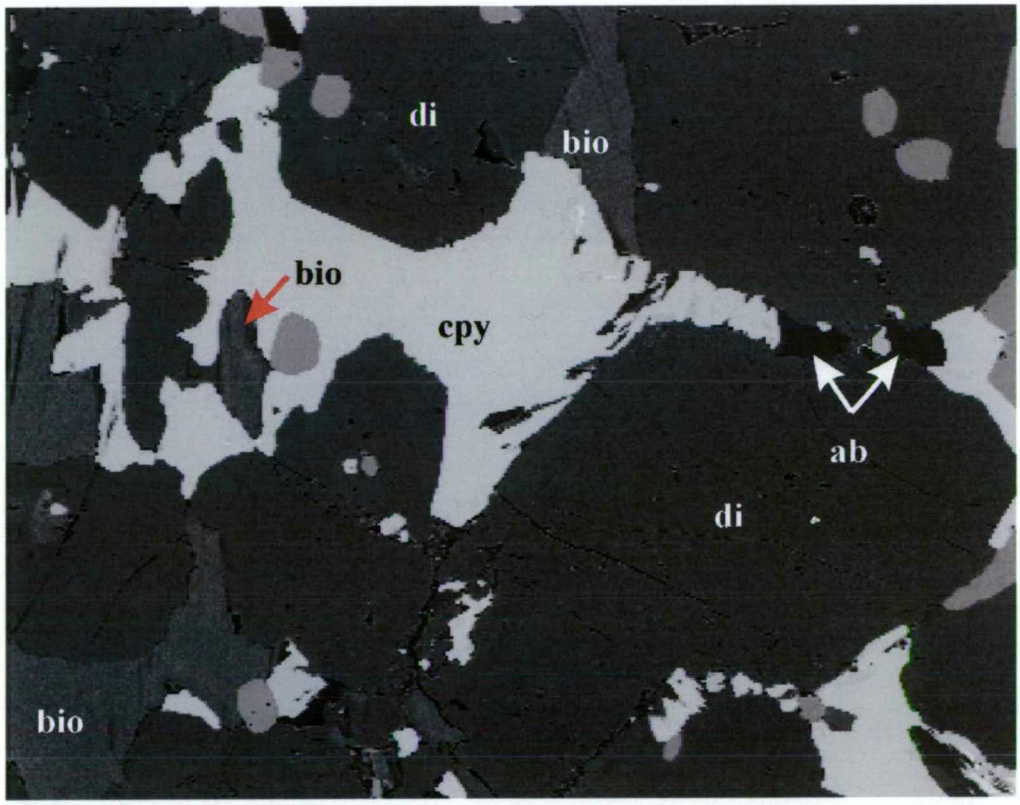

Figure 5-10. Back-scatter electron image of chalcopyrite-pyrite altered biotite pyroxenite showing the relationship between sulphides and silicate minerals within the sample (as shown in Fig. 5-8a-d). Red arrows denote contacts between biotite and chalcopyrite. The contacts are irregular and are inferred to indicate that chalcopyrite has partially replaced biotite. Diopside in contact with Cu-Fe sulphides also shows irregular margins. It is inferred that chalcopyrite has also partially replaced diopside (drill hole 2001-56_199.8 m). Mineral abbreviations: ab = albite, ap = apatite, bio = biotite, cpy = chalcopyrite, di = diopside.

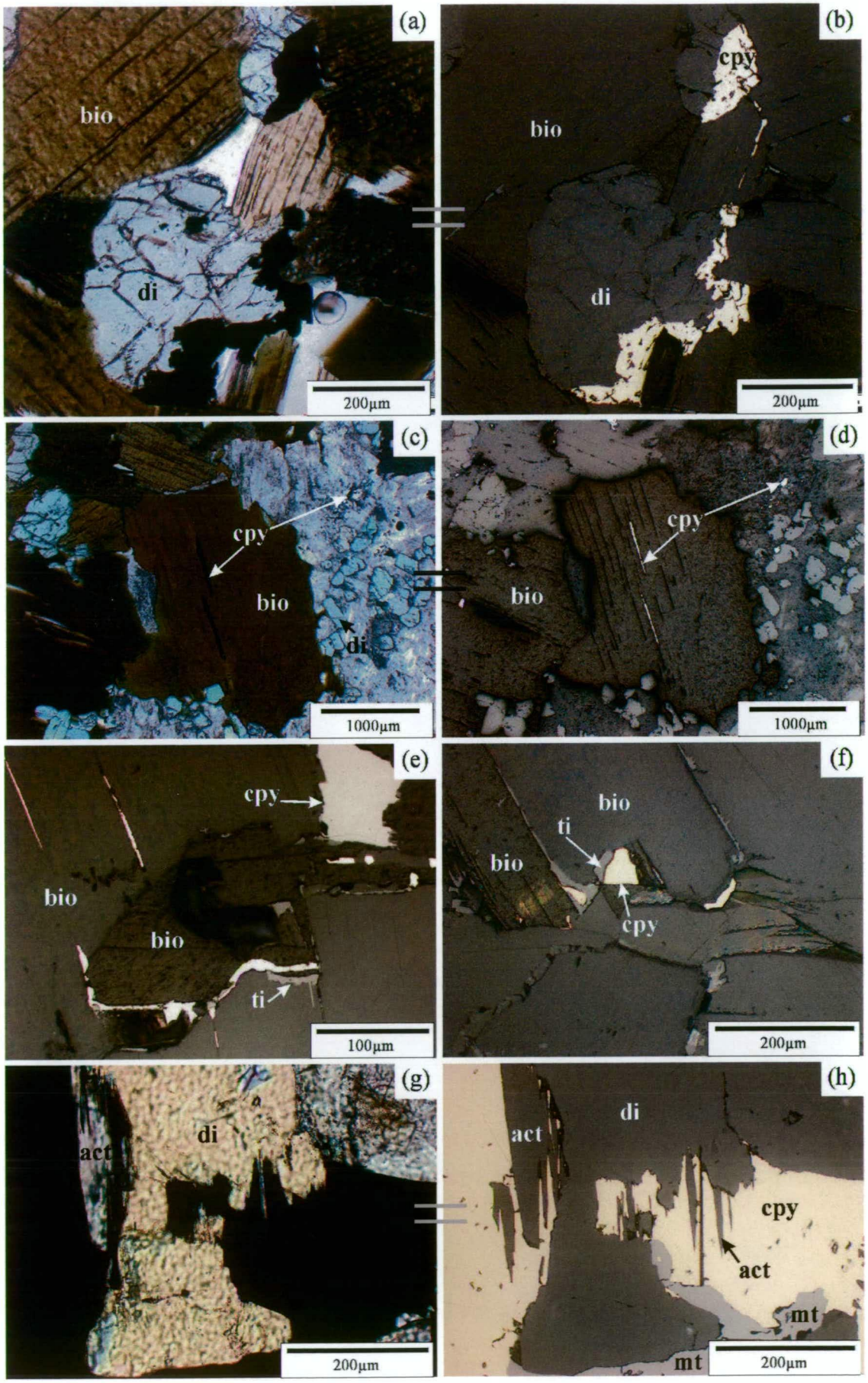
(a)
bio
di
200µm
(b)
cpy
bio
di
200µm
(c)
cpy
bio
di
1000µm
(d)
cpy
bio
1000µm
(e)
cpy
bio
bio
ti
100µm
(f)
bio
ti
bio
cpy
200µm
(g)
act
di
200µm
(h)
di
act
cpy
act
mt
mt
200µm

Figure 5-11. Chalcopyrite altered feldspathic pyroxenite from the Lower Main Zone (drill hole 2001-56_157 m, also *see* Fig. 5-6e). **(a)** Chalcopyrite occurs along the diopside grain boundary and along cleavage planes in biotite. Diopside rims are irregular and support the conclusion that diopside has been partially replaced by chalcopyrite along its margins. Viewed in transmitted light. **(b)** Same as "a" except in reflected light. **(c)** Chalcopyrite occurs along cleavage planes in biotite or as fine grains in albite patches. Viewed in transmitted light. **(d)** Same as "c" except in reflected light. **(e)** Titanite and chalcopyrite occur along biotite grain boundaries and biotite cleavage planes. Viewed in reflected light. **(f)** Titanite and chalcopyrite occurring along biotite grain boundaries. It is inferred that biotite has been replaced by chalcopyrite and titanite along grain boundaries. Viewed in reflected light. **(g)** An irregular contact between diopside and chalcopyrite in cross-polarised light. Needles of actinolite occur along diopside margins that are in contact with chalcopyrite. It is inferred that chalcopyrite has replaced diopside. It is also inferred that alteration of diopside resulted in the formation of actinolite. **(h)** Same as "g" except in reflected light. Mineral abbreviations: act = actinolite, bio = biotite, cpy = chalcopyrite, di = diopside, mt = magnetite, ti = titanite.

patches contain Cu-Fe sulphides. The feldspars that are spatially associated with Cu-Fe sulphides are turbid, and have fine-grained inclusions of Cu-Fe sulphides (Fig. 5-13c, d, 5-14 and 5-15b). Diopsides in contact with Cu-Fe sulphides share irregular-shaped contacts with euhedral actinolite (Fig. 5-15a, b). It is inferred that Cu-Fe sulphides have partially replaced diopside, and actinolite has formed along diopside margins as a result of alteration. In some areas diopside is partly brown (Fig. 5-15a), where partial replacement of diopside by hydrothermal biotite has occurred. Diopside and biotite contain inclusions of magnetite and apatite, similar to those in unaltered biotite pyroxenite (Chapter 3), but do not contain inclusions of bornite and/or chalcopyrite. In contrast, coarse- and medium-grained apatite in some samples contains sulphide inclusions with negative crystal shapes. These inclusions can be large (up to 80 μm), occur along crystal growth planes, and are inferred to represent sulphide liquids that were trapped during apatite growth (*see* below).

5.2.3.4. Bornite-chalcopyrite rich zones in mineralised pyroxenite

Exceptional bornite-chalcopyrite rich zones occur in biotite pyroxenite and feldspathic pyroxenite from the Bishop Zone. These highly enriched zones are <10 cm in apparent thickness (i.e. based on drill hole intersection; 1996-44_244m), and comprise subhedral diopside (15-20 %), magnetite (10-15 %) and apatite (5-10 %) and anhedral chalcopyrite (50-60 %) bornite (5-10 %), feldspar (1-3 %), pyrophanite ($MnTiO_3$; trace), titanite (trace), biotite (trace) and epidote (trace; Fig. 5-16a-c). These rocks resemble those described as having net textured sulphides by Bishop et al. (1995).

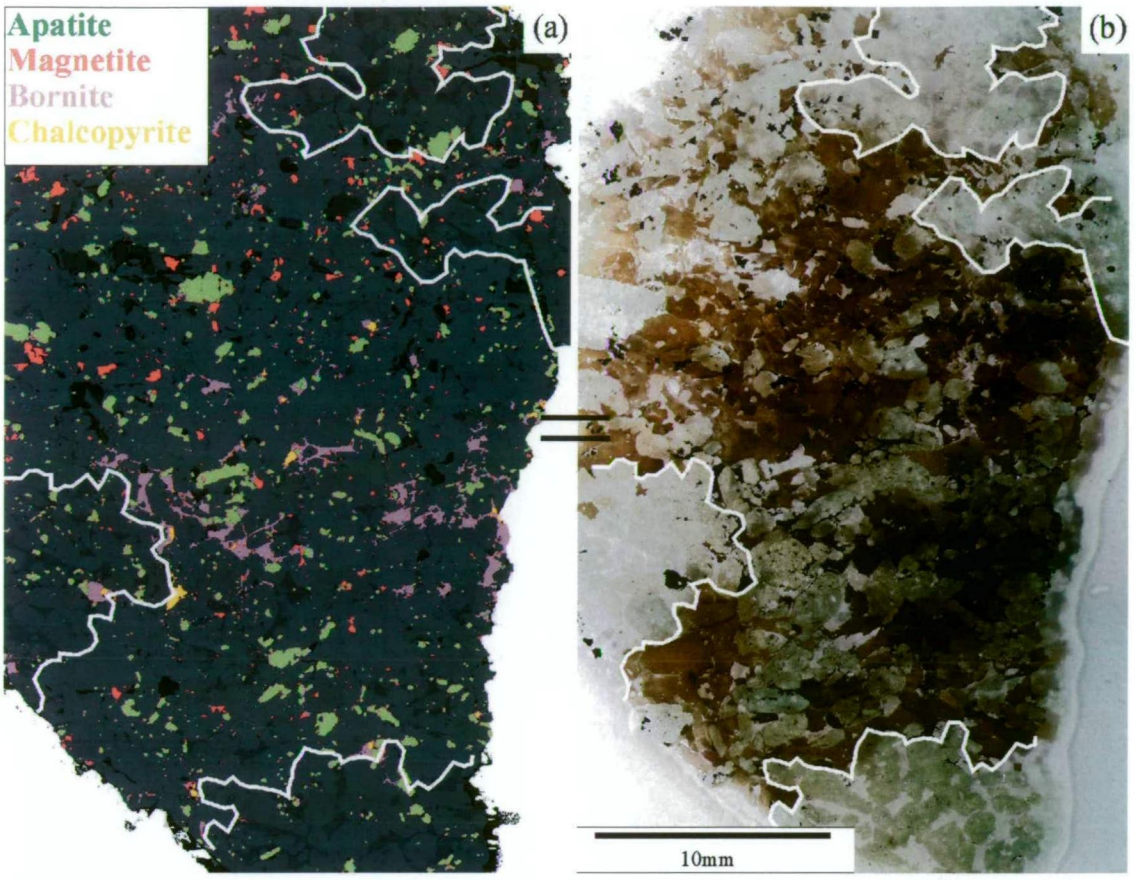

Figure 5-12. Bornite-chalcopyrite biotite pyroxenite with irregular patches of coarse-grained biotite from the Bishop Zone (drill hole 1996-44_234.4 m; also *see* Fig. 5-6h). **(a)** Back-scattered electron map of thin section with false colour coding of selected minerals. White line separates biotite dominated patch from patches dominated by anhedral feldspar. **(b)** Same as "a" except viewed in normal light.

Diopside grains are green, 1-3 mm in size, unaltered and contain inclusions of K-feldspar, albite, calcite and epidote. Biotite occurs as an anhedral phase. Diopside and biotite show embayed, irregular and straight grain boundaries where in contact with Cu-Fe sulphides (Fig. 5-16d, i). The Cu-Fe-sulphide and magnetite-rich framework is dominated by chalcopyrite with irregular-shape blebs of magnetite which range from 0.5 mm up to 20 mm in size (Fig. 5-16a). Etching of polished slabs using aqua regia has revealed that chalcopyrite has distinct crystal shapes when viewed in reflected light (Fig. 5-16b, e). These chalcopyrite grain-shapes may represent annealed textures, crystalline textures or possibly pseudomorphs of silicate phases replaced by chalcopyrite. Bornite mostly occurs at the interface between magnetite blebs and chalcopyrite and is irregular in shape (Fig. 5-16a). Back-scattered electron images reveal that magnetite blebs have thin rims (<30 μm) with pyrophanite and titanite, and in almost all cases pyrophanite occurs along the inner part of the rim and titainite occurs along the outer part of the rim (Fig. 5-17a). Apatite grains occur along the margin of magnetite crystals. Both apatite and magnetite have hairline fractures filled with Cu-Fe-sulphide (Fig. 5-17a, b), and apatite contains small (<20 μm)

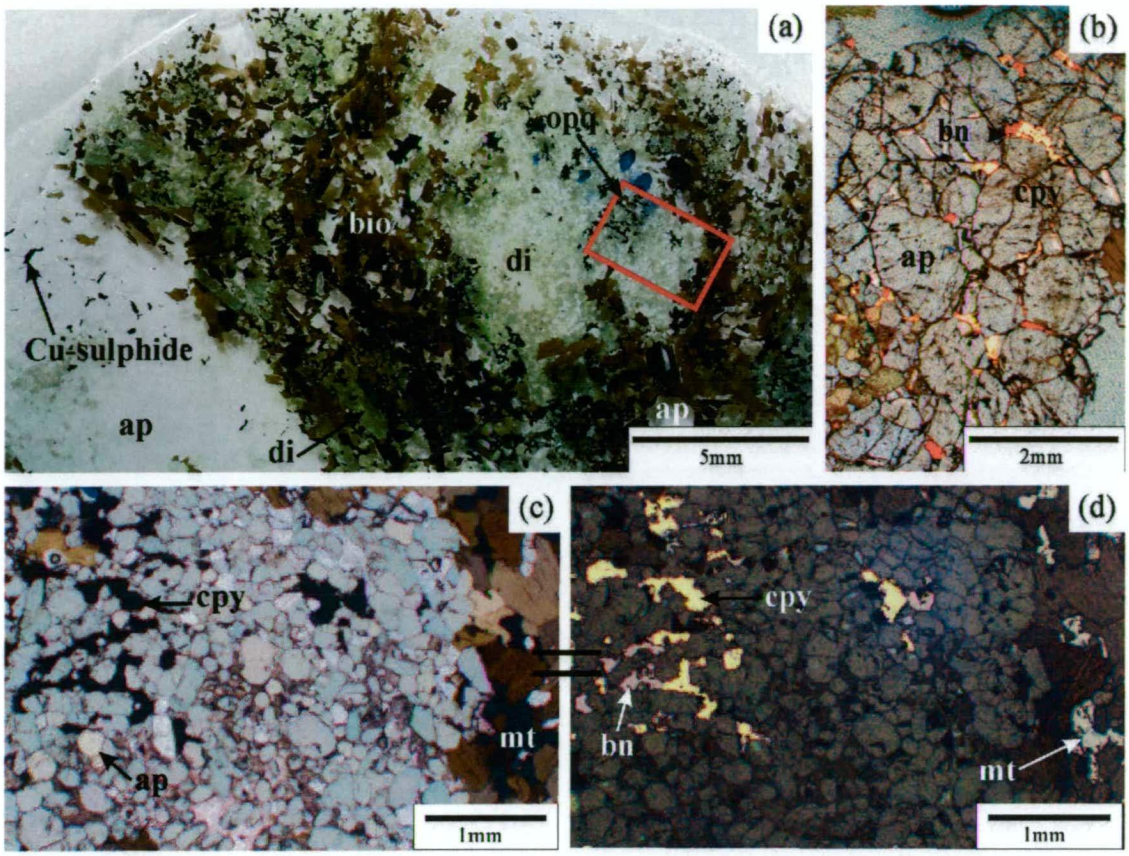

Figure 5-13. **(a)** Bornite-chalcopyrite mineralised biotite pyroxenite with irregular coarse-grained patches of biotite from the Lower Main Zone (drill hole 2001-56_173.9 m). Note left hand side of the thin section includes a patch of coarse grained apatite with anhedral Cu-Fe sulphides. Red box denotes the field of view for photomicrographs shown in "c" and "d". **(b)** Coarse grained patch of apatite with anhedral chalcopyrite and bornite in combined plane polarised and reflected light (same sample as "a"). **(c)** Coarse grained patch of biotite and apatite, and finer grained zone dominated by diopside and feldspar in plane polarised light (same sample as "a"). Note the occurrence of fine-grained disseminated Cu-Fe sulphides (bornite and chalcopyrite) in feldspar dominated zones. **(d)** Same as "c" except in reflected light. Mineral abbreviations: ap = apatite, bio = biotite, cpy = chalcopyrite, di = diopside, mt = magnetite, ti = titanite.

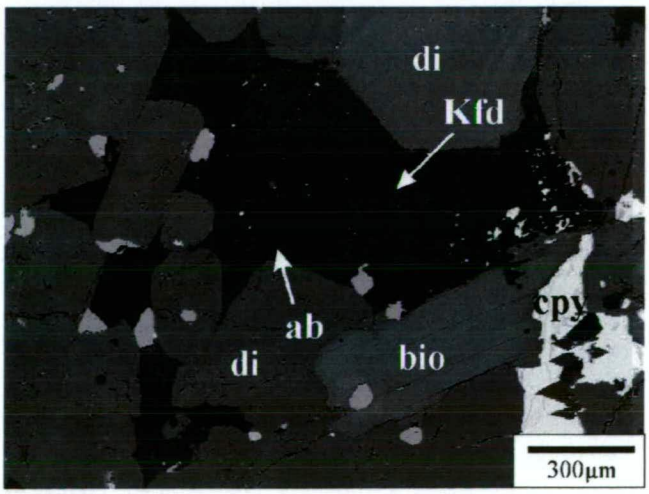

Figure 5-14. Back-scatter electron images of bornite-chalcopyrite biotite pyroxenite with irregular patches of coarse-grained biotite from the Bishop Zone (drill hole 1996-44_234.4 m). Euhedral to subhedral diopside with subhedral biotite and anhedral K-feldspar, albite and Cu-Fe sulphides. Cu-Fe sulphides occur as inclusions in albite. Mineral abbreviations: ab = albite, act = actiolite, ap = apatite, bio = biotite, cpy = chalcopyrite, di = diopside, Kfd = K-feldspar, mt = magnetite.

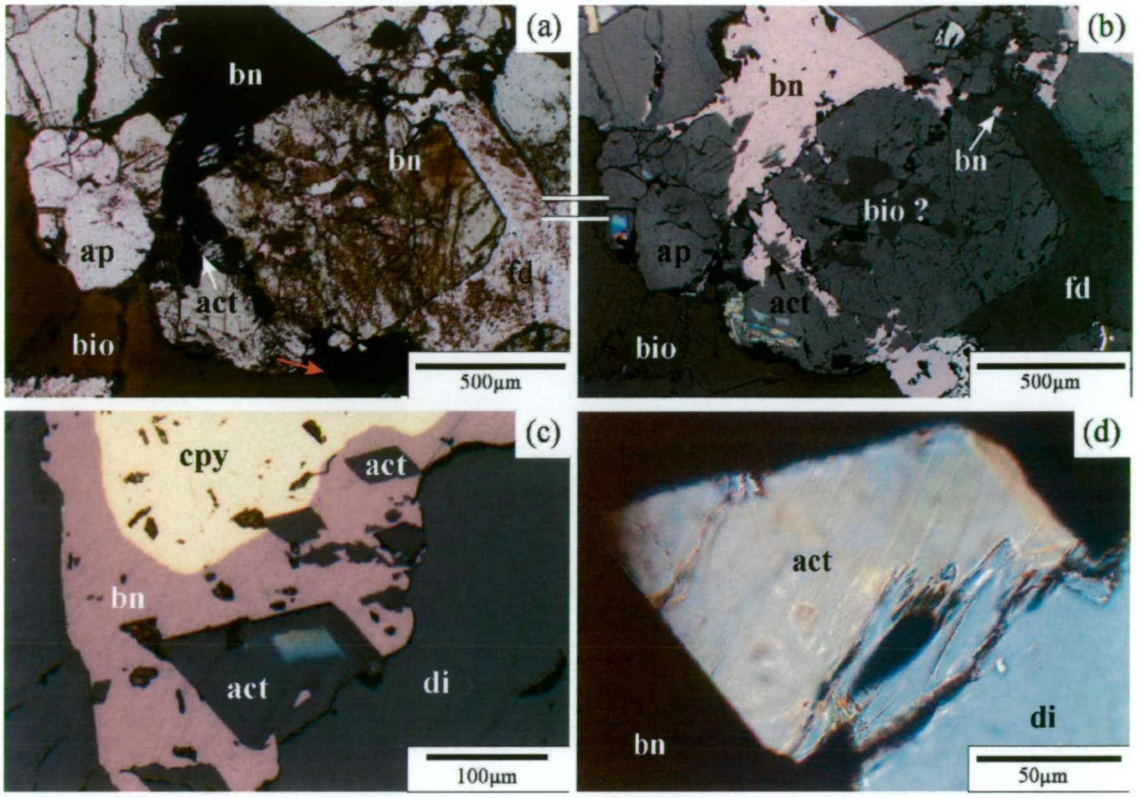

Figure 5-15. **(a)** Bornite-chalcopyrite mineralised biotite pyroxenite from the Bishop Zone viewed in plane polarised light (drill hole 1996-44_234.4 m). Diopside has been partially altered to actinolite along its contacts with bornite. Diopside also has irregular margins where in contact with bornite and brown in places reflecting biotite alteration of diopside. **(b)** Same as "a" except in reflected light. **(c)** Photomicrograph of bornite in contact with diopside and the formation of actinolite along the margin between diopside and bornite. Viewed in reflected light (same sample as "a"). **(d)** Closer view of the contact between actinolite, diopside and bornite as shown in "c". Actinolite has a sharp contact with diopside and appears to have nucleated and grown along the grain boundary of diopside. Viewed in transmitted light. Mineral abbreviations: act = actiolite, bn = bornite, cpy = chalcopyrite, di = diopside, fd = feldspar.

fluid inclusions (two phase: liquid + vapour bubble). Analyses of salt residue from a decrepitated fluid inclusion, which had spilt its content onto the surface of the host crystal, revealed that the fluid inclusions contain abundant dissolved halite and sylvite (Figs. 5-17b, c).

5.2.3.5. Apatite and apatite-hosted inclusions in bornite-chalcopyrite mineralised biotite pyroxenite

Apatite in bornite-chalcopyrite mineralised biotite pyroxenites range from fine- to coarse-grained, and can occur as coarse-grained patches in some biotite pyroxenites (Figs. 5-6d and 5-13a, b). Apatites have complex growth zonations (Fig. 5-18a-d), are coarser grained and are enriched in sulphur (S^{6+}; up to 1.1 wt. % SO_3) compared to apatite from their barren counterparts (<0.5 wt. % SO_3; Chapter 6). Some medium- to coarse-grained apatites have

cores with lower sulphur abundances (e.g., 0.26 wt. % SO_3; Fig. 5-18d), and margins with higher concentrations of S (e.g., 0.58 wt. % SO_3; Fig. 5-18d). The S-rich margins likely reflect an increase in the activity of S^{6+} (e.g., Frei, 1996; Streck and Dilles, 1998; Bath et al., 2006; Cleverley, 2006), and were most likely precipitated during hydrothermal alteration, whereas the S-poor cores may represent primary magmatic apatite, which are typically fine-grained in unaltered biotite pyroxenites (Chapter 3).

Bornite-chalcopyrite mineralised biotite pyroxenites also contain albite in feldspar-rich patches. These feldspar-rich patches are apatite-poor, and apatite in contact with albite in mineralised biotite pyroxenite has corroded margins (Fig. 5-19a-d). These corroded margins may reflect localised, partial dissolution of apatite during alteration and mineralisation of the feldspar rich patches. Dissolved apatite may have been locally reprecipitated as coarsed grained apatite in biotite-rich zones or as coarse-grained apatite patches with Cu-Fe sulphides (Fig. 5-13a, b).

Some coarse-grained apatite crystals in mineralised biotite pyroxenite contain small (<15 μm) secondary fluid inclusions (two-phase, consisting of coexisting liquid and vapour at room temperature; Fig. 5-18f). Others have small to medium size (<10 to 80 μm) Cu-Fe sulphide inclusions (Fig. 5-18e) with negative crystal shapes consisting of bornite + chalcopyrite. Small secondary fluid inclusion assemblages transect apatite growth zones, and inclusions contain dissolved KCl and NaCl, which were identified using EDS on the contents of a decrepitated fluid inclusion (Fig. 5-17b and c). These secondary saline fluid inclusions are either related to transitional-stage alteration and mineralisation, or a later hydrothermal event. Their high salinity is inferred to reflect a magmatic-hydrothermal origin. The Cu-Fe sulphide inclusions occur along crystal growth zones and are thought to represent primary inclusions, which were trapped during the growth of S-rich apatite. These Cu-Fe sulphide inclusions were only identified in apatite from bornite-chalcopyrite mineralised biotite pyroxenites.

5.2.4. Syenite

Syenites of the Lower Main Zone are fine- to medium-grained, equigranular to rarely porphyritic and massive to foliated rocks (Chapter 3; Figs. 3-14a-c and 3-15a, b). They range from light grey to salmon pink (Fig. 5-20a-f), and have a foliation defined by the alignment of K-feldspar laths (primary igneous foliation; Fig. 3-14a), or have biotite-rich bands (solid-state deformation fabric; Chapter 3; Fig. 3-14b). Syenites range from mafic-rich (i.e. >15 %) to mafic-poor (i.e. <5 %; Figs. 5-20e). The primary mafic minerals are diopside and biotite.

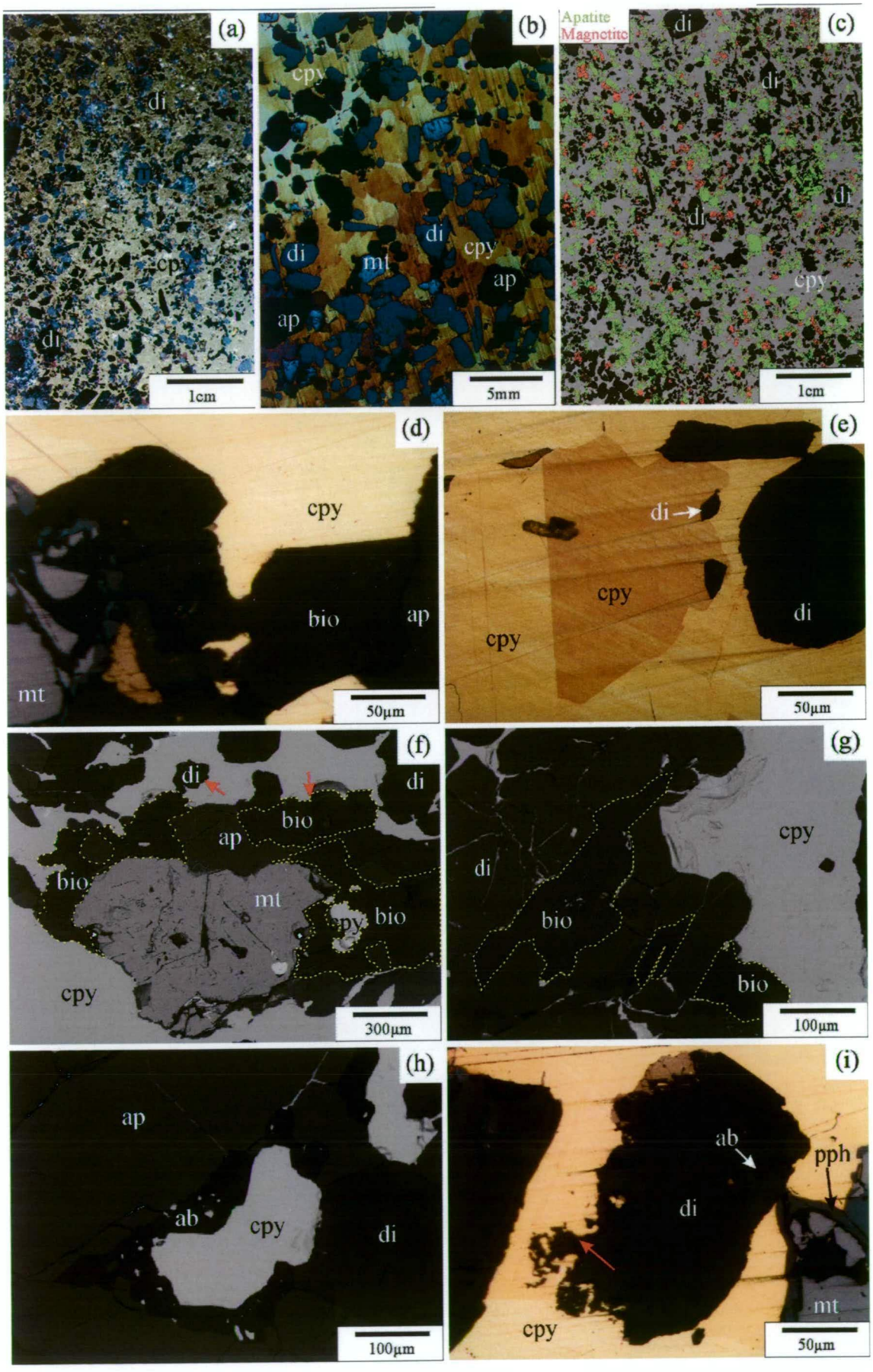
(a)
di
cpy
di
1cm
(b)
cpy
di
mt
di
cpy
ap
ap
5mm
Apatite
Magnetite
(c)
di
di
di
di
cpy
1cm
(d)
cpy
bio
ap
mt
50μm
(e)
di
cpy
cpy
di
50μm
(f)
di
di
bio
ap
bio
mt
cpy
bio
cpy
300μm
(g)
cpy
di
bio
bio
100μm
(h)
ap
ab
cpy
di
100μm
(i)
ab
pph
di
cpy
mt
50μm

←

Figure 5-16. Bornite-chalcopyrite rich zones in mineralised pyroxenite from the Bishop Zone (drill hole 1996-44_244 m). **(a)** Polished slab viewed in normal light showing euhedral to subhedral diopside and apatite with a chalcopyrite-magnetite-bornite matrix. **(b)** Etched surface (with aqua regia) of polished slab showing complex shapes of chalcopyrite. Shapes may represent annealed textures, crystal shapes of chalcopyrite or pseudomorphs of biotite, which has formed corroded margins with chalcopyrite and appears to have been partially replaced by chalcopyrite. Viewed in reflected light. **(c)** False colour coded image of polished slab. Image shows the distribution of diopside (dark grey), magnetite (red), apatite (light green) and chalcopyrite (light grey). **(d)** Biotite with an irregular contact with chalcopyrite. It is inferred that chalcopyrite has partially replaced biotite. Viewed in reflected light. **(e)** Etched surface of chalcopyrite in bornite-chalcopyrite rich zones in mineralised pyroxenite. Chalcopyrite also includes inclusions of diopside. Inclusions are inferred to represent relicts of diopside in chalcopyrite (reflected light). **(f)** Chalcopyrite in contact with magnetite, apatite, biotite and diopside. Both diopside and biotite have irregular margins in contact with chalcopyrite (see arrows). Irregular margins are inferred to represent corroded contacts between chalcopyrite and silicate minerals, with the former inferred to have replaced the latter. Back-scattered electron image. **(g)** A patch of diopside and biotite with chalcopyrite occurring along fractures and grain boundaries of diopside and biotite. It is inferred that chalcopyrite formed later than diopside and biotite. Back-scattered electron image. **(h)** Patch of albite and chalcopyrite that occurs along fractures and grain boundaries of apatite and diopside. Back-scattered electron image. **(i)** Back-scatter electron image of diopside in contact with chalcopyrite. Diopside has been partially replaced by chalcopyrite, based on the corroded grain boundary. Mineral abbreviations: ap = apatite, bio = biotite, cpy = chalcopyrite, di = diopside, mt = magnetite, pph = pyrophanite.

Unmineralised syenites have unaltered to weakly turbid medium- to coarse-grained euhedral to subhedral K-feldspar (50 to 70 %), which shows simple twinning (Chapter 3). They also contain plagioclase (5 to 15 %), which is fine- to medium-grained, subhedral to anhedral and ranges in composition from albite to oligoclase (Chapter 6), and comprise fine- to medium-grained euhedral to subhedral unaltered diopside and fine- to medium-grained anhedral biotite, with accessory fine-grained anhedral to subhedral magnetite, apatite and titanite. The subsections below describe details relating to mineralisation in syenites.

5.2.4.1. Pyrite-chalcopyrite mineralised syenite

Pyrite-chalcopyrite mineralised syenites were collected from the peripheral zones where pyrite is more abundant than chalcopyrite in the Lower Main Zone and the Bishop Zone. These samples contain weakly turbid hematite dusted K-feldspar (Figs. 5-20a-c and 5-21a) that have tartan and simple twinning, consistent with microcline and orthoclase respectively. The samples include localised patches of fine-grained diopside and albite, which also contain fine-grained inclusions of pyrite and chalcopyrite that predominantly

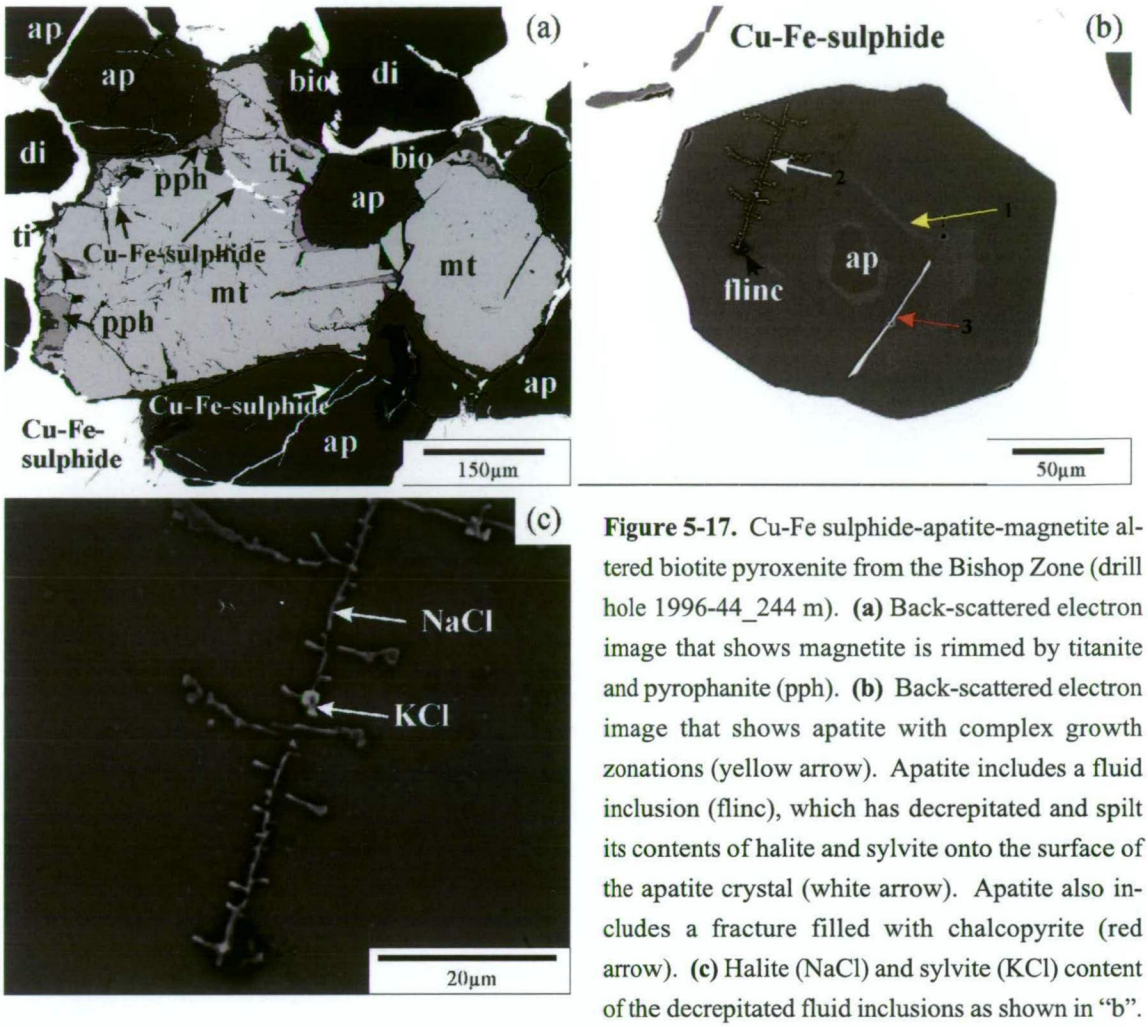

Figure 5-17. Cu-Fe sulphide-apatite-magnetite altered biotite pyroxenite from the Bishop Zone (drill hole 1996-44_244 m). **(a)** Back-scattered electron image that shows magnetite is rimmed by titanite and pyrophanite (pph). **(b)** Back-scattered electron image that shows apatite with complex growth zonations (yellow arrow). Apatite includes a fluid inclusion (flinc), which has decrepitated and spilt its contents of halite and sylvite onto the surface of the apatite crystal (white arrow). Apatite also includes a fracture filled with chalcopyrite (red arrow). **(c)** Halite (NaCl) and sylvite (KCl) content of the decrepitated fluid inclusions as shown in "b". Mineral abbreviations: ap = apatite, bio = biotite, di = diopside, mt = magnetite, pph = pyrophanite, ti = titanite.

occur along diopside grain boundaries (Fig. 5-21c, d). Pyrite and chalcopyrite also occur along biotite crystal margins, and in small (<200 µm) patches of sericite altered K-feldspar (Fig. 5-21a, b). Pyrite-chalcopyrite mineralised syenites also contain plagioclase that has been selectively altered to sericite, muscovite, pyrite and clinozoisite (Chapter 4; Fig. 4-18a-d).

5.2.4.2. Chalcopyrite mineralised syenite

Chalcopyrite-bearing syenites were collected from the Lower Main Zone and the Bishop Zone. The samples contain medium-grained microcline that is moderately turbid (Fig. 5-22a, c and e), and commonly show tartan twinning. Fine-grained patches of turbid diopside, have Cu-Fe sulphides along individual diopside grain margins (Fig. 5-22a, b). An-

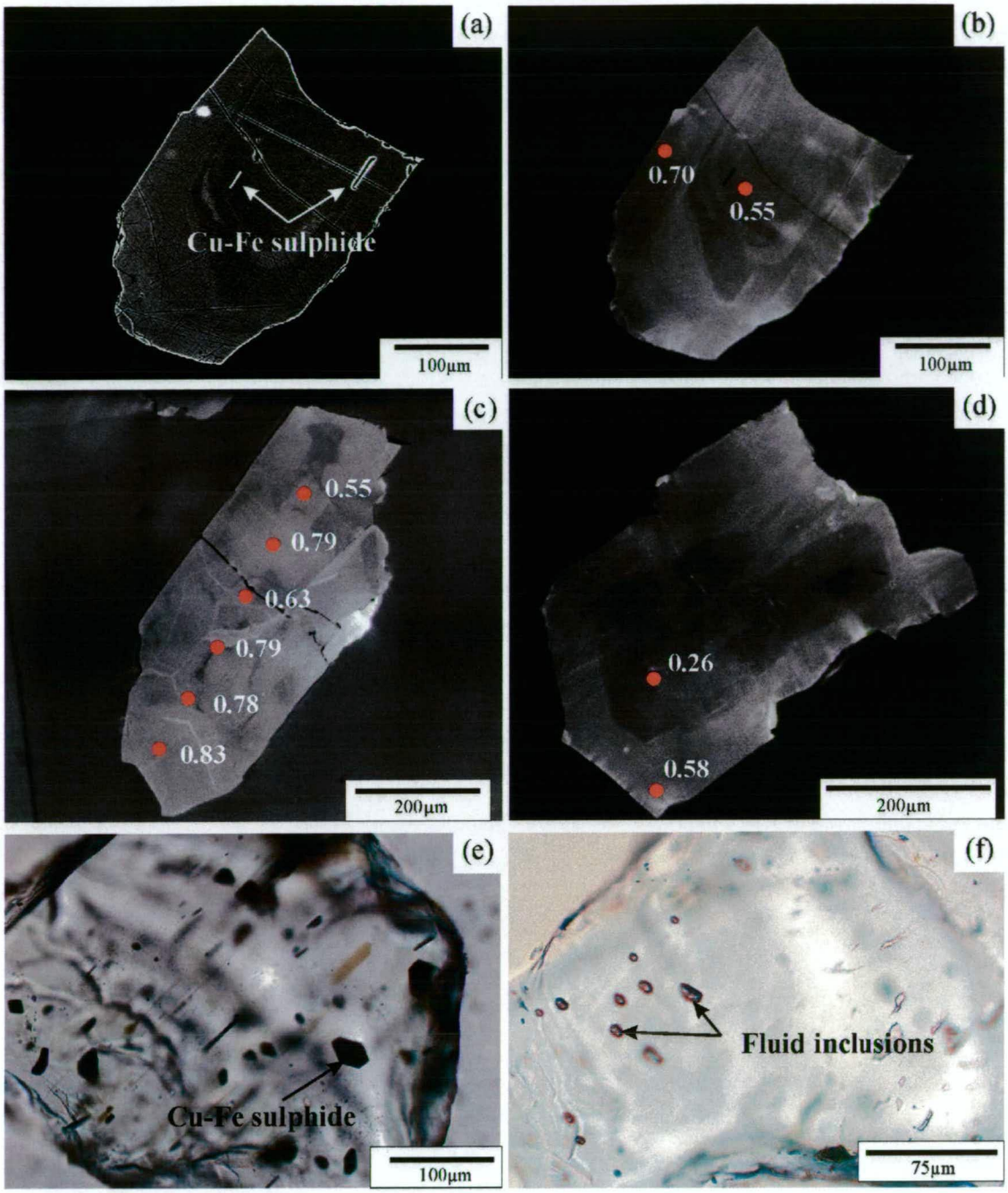

Figure 5-18. Apatite grains from altered biotite pyroxenite in back-scattered electron, plane polarised light and CL with EPMA spot location (red dots) and SO_3 (wt. %) abundance. **(a)** Back-scattered electron image of apatite showing complex zonation patterns and inclusions of Cu-Fe sulphides. Voids are inferred to have contained Cu-Fe sulphides that were removed during polishing. Copper-Fe sulphide inclusions have negative crystal shapes and it is inferred that sulphides were trapped during the growth of apatite (drill hole 2002-58_158.3 m). **(b)** Same as "a" except viewed in CL. **(c)** Medium grained apatite from altered biotite pyroxenite. The apatite grain is enriched in S relative to apatite from unaltered biotite pyroxenites (drill hole 1996-44_244 m). **(d)** Apatite grain composed of a darker inner zone with SO_3 of 0.26 wt. %, and an outer brighter zone that is comparatively enriched in SO_3 (0.58 wt. %; same sample as "a"). **(e)** Apatite grain from mineralised biotite pyroxenite containing bornite and chalcopyrite inclusions with negative crystal shapes (same sample as "a"). **(f)** Medium grained apatite with small (<15 µm) secondary fluid inclusions along fractures (same sample as "a").

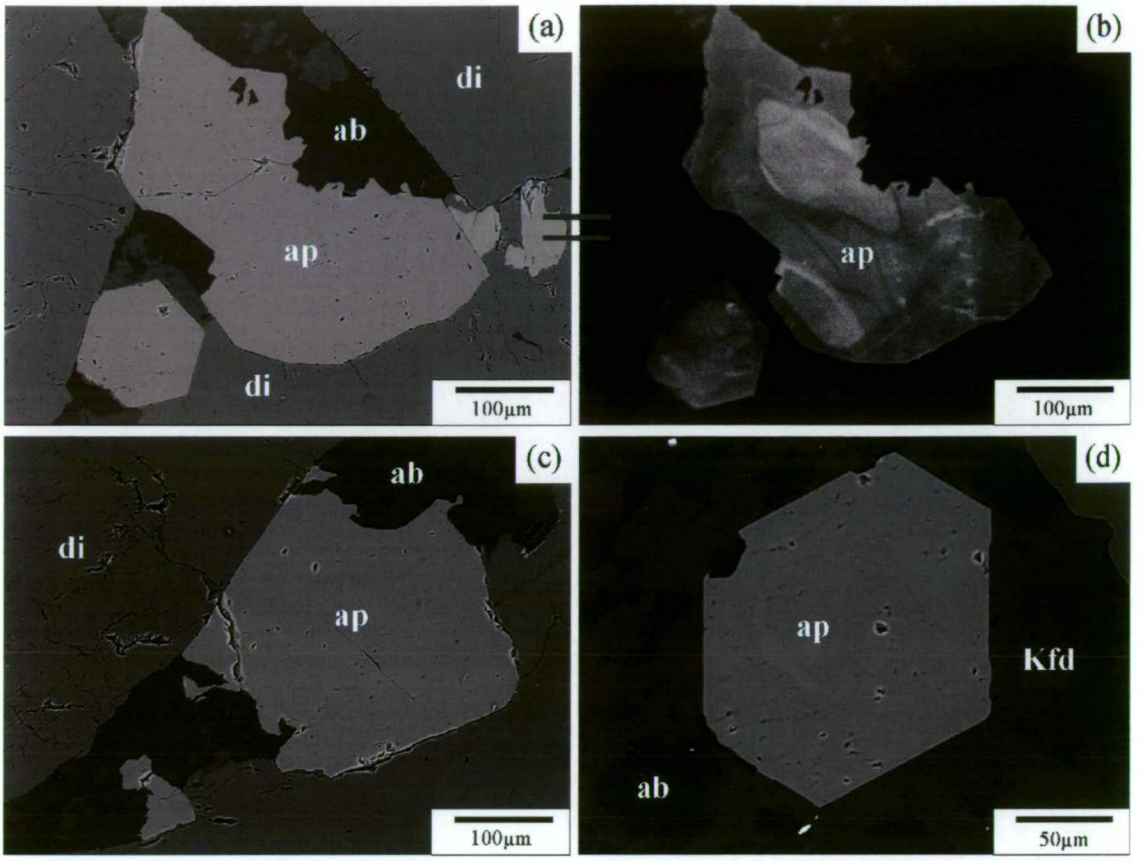

Figure 5-19. Photomicrographs of apatite in back-scattered electron (a, c and d) and catholumincence images (b). Apatite is from bornite-chalcopyrite altered biotite pyroxenite with coarse bands of biotite from the Bishop Zone (drill hole 1996-44_234.4 m). Apatite in contact with albite has irregular margins **(a)** and albite appears to cross-cut apatite growth zonations (shown by CL), suggesting albite has replaced apatite **(b)**. In contrast apatite, has sharp straight contacts with diopside **(c)** and K-feldspar **(d)**. Mineral abbreviations: ab = albite, ap = apatite, di = diopside, Kfd = K-feldspar.

hedral fine-grained biotite varies from unaltered to selective altered by magnetite, titanite chlorite and/or chalcopyrite (Fig. 5-22c, d and e). Chalcopyrite disseminations occur in patches together with anhedral albite (Fig. 5-22f).

5.2.4.3. Bornite-chalcopyrite mineralised syenite

Bornite and chalcopyrite altered syenites from Lower Main Zone and the Bishop Zone are dominated by turbid K-feldspars that are euhedral to subhedral, medium-grained hematite dusted or grey (in parts of the Bishop Zone; Fig. 5-20d-f). Many of the K-feldspar laths are rimmed by fine-grained albite (Figs. 5-23a and 5-24b, e), which is intergrown with epidote-clinozoisite, titanite, bornite and chalcopyrite (Figs. 5-23a, 5-24d, e and 5-25a-d). Some albite occurs together with andraditic to grossular fine-grained garnet. Fine-grained disseminated Cu-Fe sulphides are spatially associated with biotite, diopside and magnetite (Fig. 5-23b-d). Biotite that is in contact with bornite and chalcopyrite has been partially replaced by sericite and minor calcite (Fig. 5-23c, d), or chlorite (Fig. 5-23e) and

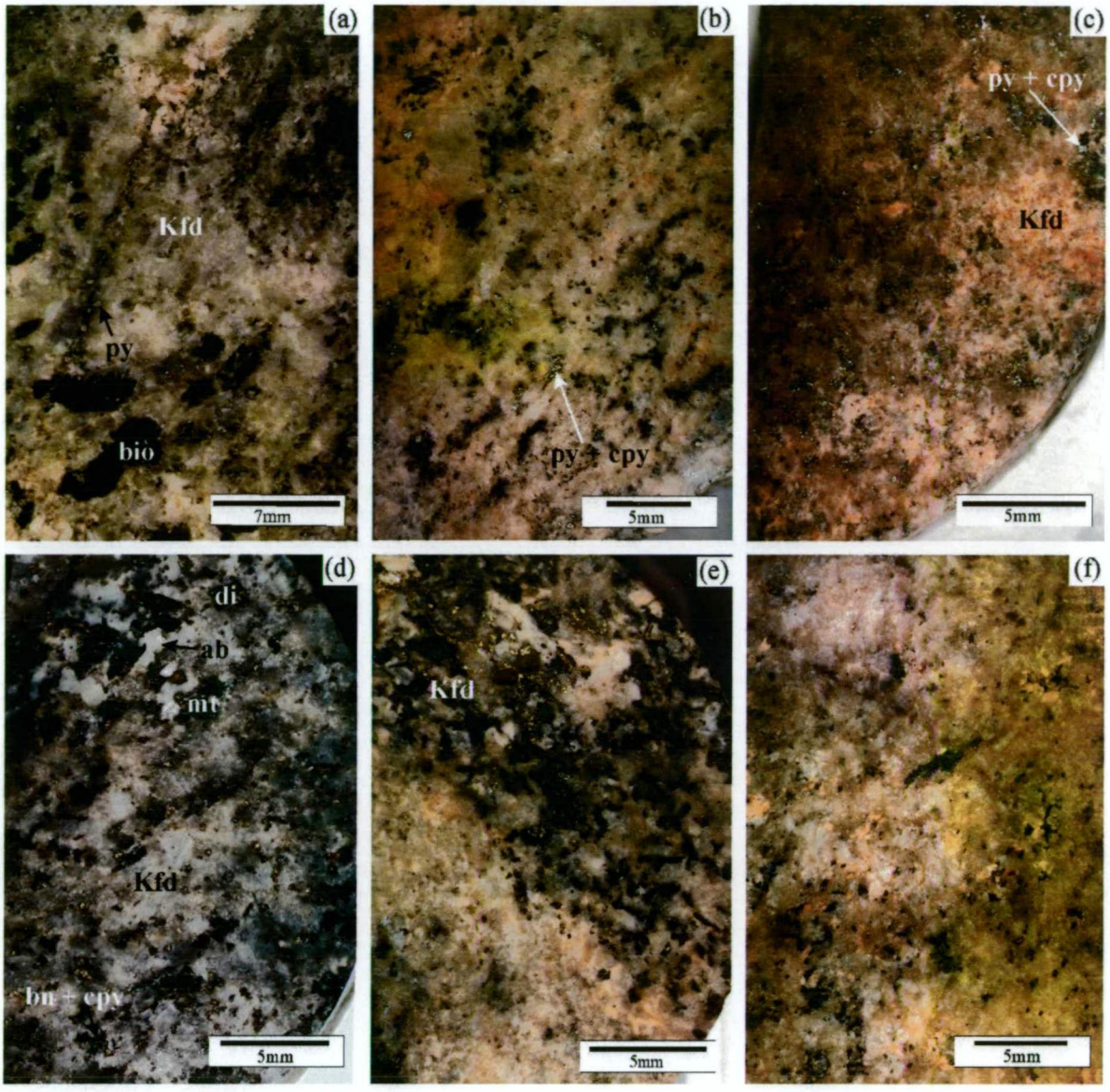

Figure 5-20. Examples of altered syenite from the Lower Main Zone and the Bishop Zone. (a-c) Representative samples of pyrite and chalcopyrite altered syenite and (d-f) representative samples of bornite-chalcopyrite altered syenite. **(a)** Weak pyrite-chalcopyrite altered biotite-diopside syenite rock from the eastern area of the Lower Main Zone (sample 02GNX5-9-4; 347531mE, 6200727mN). **(b)** Chalcopyrite-pyrite altered biotite-diopside syenitic rock from the Lower Main Zone with sulphide showing a close spatial association with mafic minerals (drill hole 2001-56_62.0 m). **(c)** Chalcopyrite-pyrite-sphalerite altered biotite-diopside syneitic rock from the Bishop Zone with sulphides spatially associated with biotite and chalcopyrite (drill hole 1996-44_135.4 m). **(d)** Bornite-chalcopyrite altered diopside-biotite syenitic rock from the Bishop Zone showing a strong spatial association between diopside, biotite, bornite, chalcopyrite and magnetite. There is also a patch of albite associated with mineralisation (black arrow; drill hole 1996_43-167.0 m). **(e)** Contact between biotite-diopside syenite and mafic-poor syenite. Both rocks show chalcopyrite-bornite mineralisation. Note that mafic sites are strongly associated with sulphides (Lower Main Zone; drill hole 2002-63_106.7 m). **(f)** Bornite-chalcopyrite altered syenite from the Lower Main Zone (drill hole 2002-63_81.0 m). Right-hand side of polished slab has been stained for K-feldspar (yellow), highlighting that secondary K-feldspar is abundant in the slide. Mineral abbreviations: ab = albite, bio = biotite, bn = bornite, cpy = chalcopyrite, di = diopside, Kfd = K-feldspar, mt = magnetite, py = pyrite.

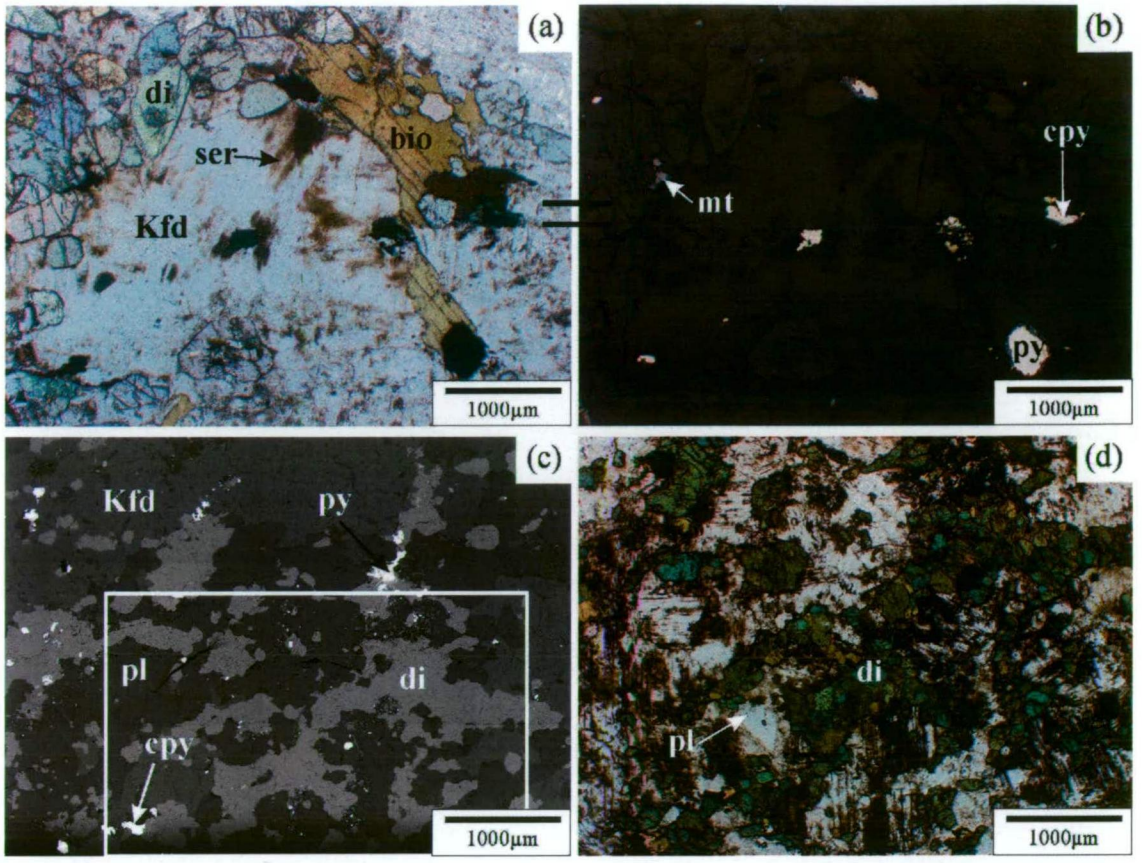

Figure 5-21. Pyrite-chalcopyrite altered Phase 1 syenite from the Lower Main Zone (a-b) and Main Zone (c-d). **(a)** Syenite consists of coarse- to medium-grained anhedral to subhedral K-feldspar with localised turbid patches associated with pyrite. Biotite is subhedral and medium-grained. Pyrite predominantly occurs along biotite margins (drill hole 2001-56_271.9 m). **(b)** Same as "a" except in reflected light. **(c)** Back-scattered electron image of diopside syenite. Fine to medium-grained diopside occur in patches with plagioclase and minor K-feldspar. Pyrite and minor chalcopyrite occur along grain boundaries between diopside and plagioclase. White box denote area of "d" (drill hole, 1995-24_194.0 m). **(d)** Plagioclase and diopside rich patch that contain pyrite and minor chalcopyrite in syenite, as shown in "c". Mineral abbreviations: bio = biotite, cpy = chalcopyrite, di = diopside, Kfd = K-feldspar, mt = magnetite, pl = plagioclase, py = pyrite, ser = sericite.

medium-grained magnetite can be found along grain boundaries where diopside in contact with Cu-Fe sulphides (Fig. 5-23e, f).

Syenites in the Lower Main Zone contain rare veinlets of bornite, chalcopyrite, chalcocite, quartz and aegerine (Fig. 5-26a-c). Intergrowths of chalcocite have small (<10 µm) inclusions of halite + fluid/vapour near grain boundaries (Fig. 5-26c, d). Empty pits were also observed in chalcocite, which may represent leaked fluid- and/or vapour-rich inclusions or dissolved halite crystals. The preservation of halite-rich inclusions (i.e. inclusions with >90 vol. % halite + vapour? and/or fluid?) in chalcocite indicates that salt crystals were trapped during the crystallisation of sulphides, which supports the contention that

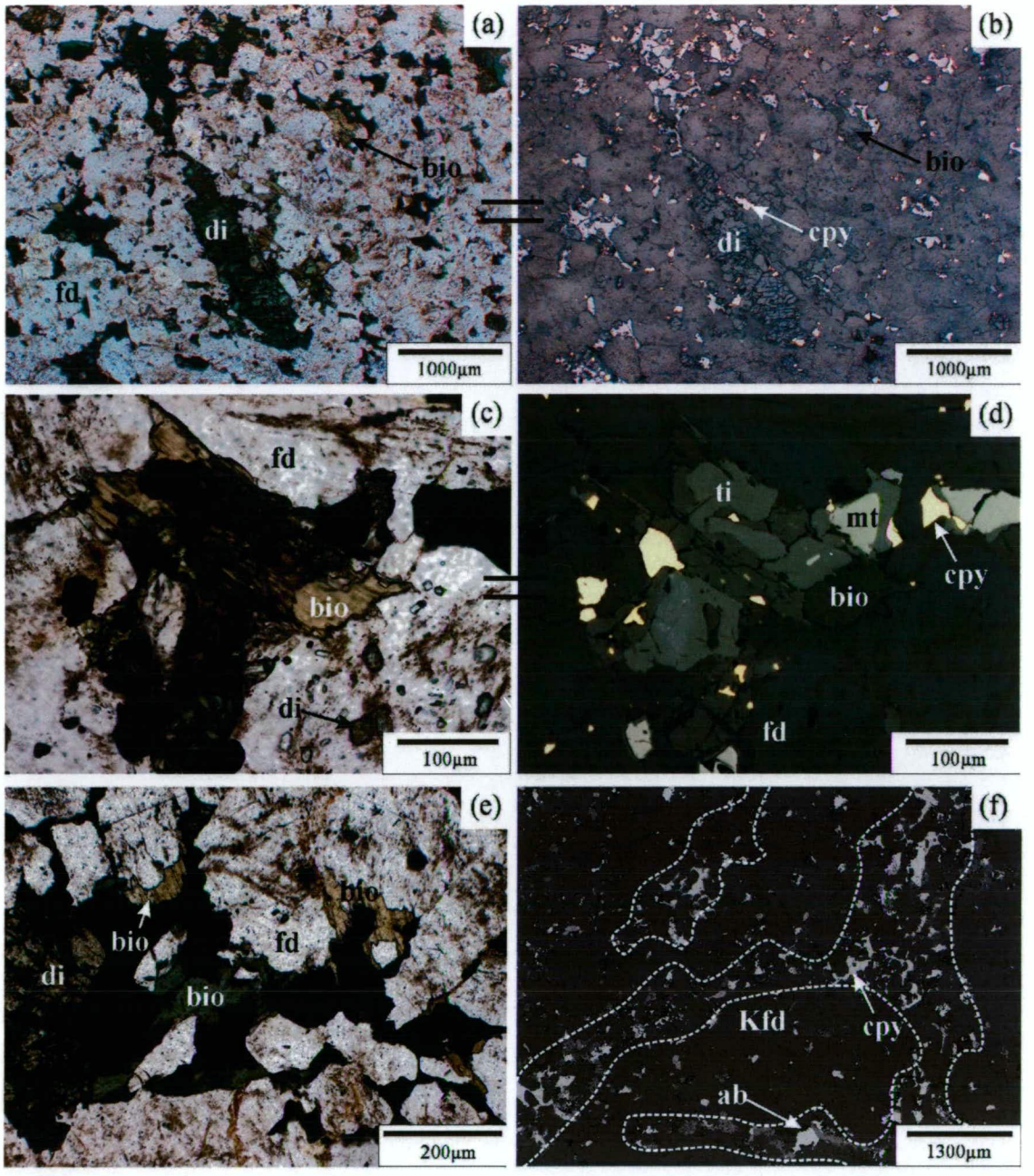

Figure 5-22. Chalcopyrite altered syenite from the Lower Main Zone (sample 07AB-G7; 347330mE, 6200580mN). **(a)** Syenite consists of medium-grained diopside which is turbid and fractured. The syenite also contains magnetite and chalcopyrite, which is spatially associated with biotite, diopside, albite and titanite. **(b)** Same as "a" except in reflected light. **(c)** Biotite with titanite, magnetite and chalcopyrite. It is inferred that titanite, magnetite and chalcopyrite have replaced biotite. **(d)** Same as "e" except in reflected light. **(e)** Anhedral biotite and opaque minerals, magnetite and chalcopyrite. Biotite is green where in contact with magnetite or chalcopyrite, and partially altered to chlorite locally. **(f)** Back-scattered electron image showing unevenly distributed fine-grained chalcopyrite. Chalcopyrite occurs in patches that appear to be interconnected and also contain albite. Mineral abbreviations: ab = albite, bio = biotite, cpy = chalcopyrite, di = diopside, fd = feldspar, Kfd = K-feldspar, mt = magnetite, ti = titanite.

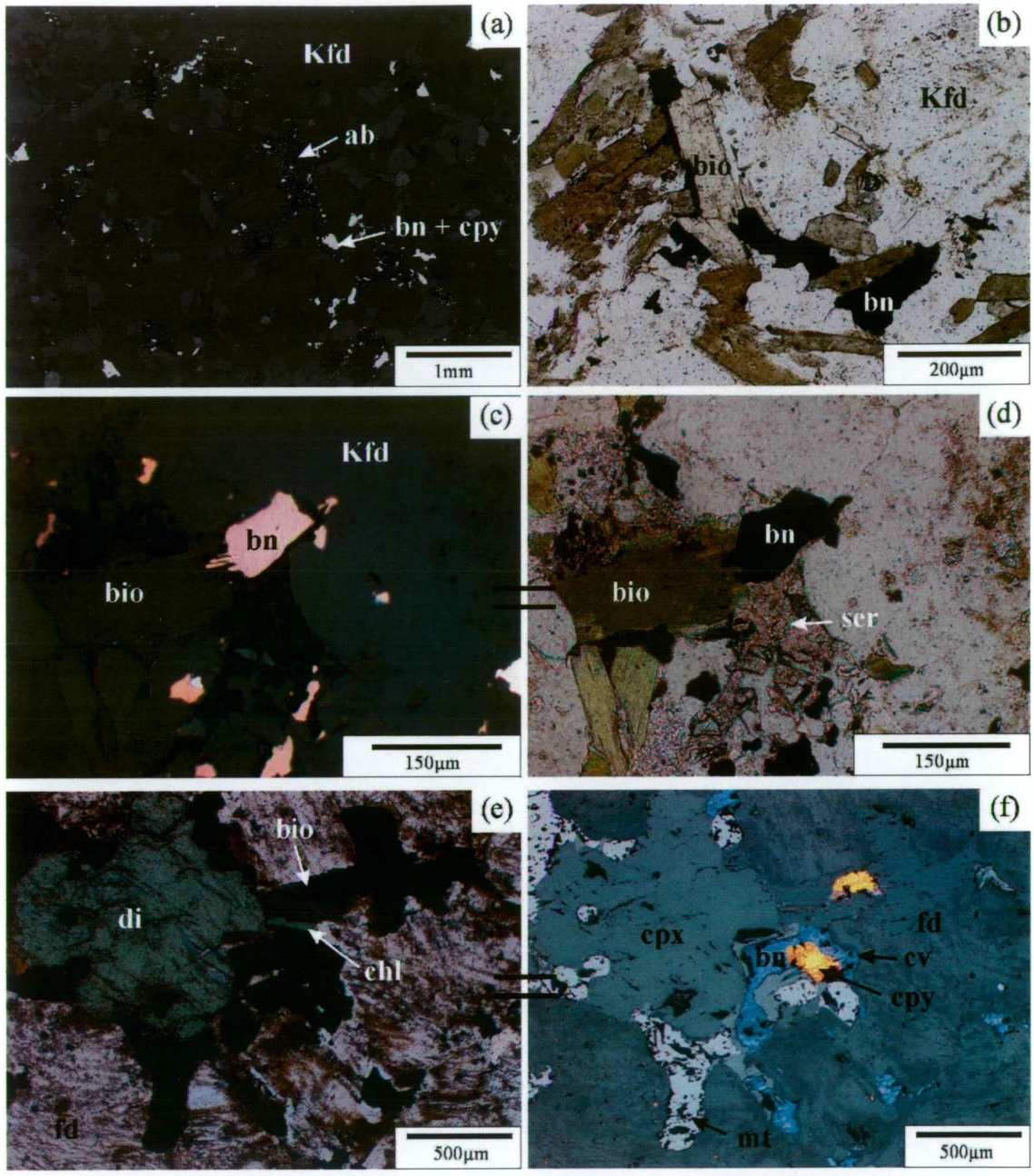

Figure 5-23. Bornite and chalcopyrite altered syenite from the Lower Main Zone (a-d; drill hole 2001-48_153m) and Bishop Zone (e-f; drill hole 1996-44_225 m). **(a)** Back-scattered electron image of syenite with fine-grained chalcopyrite and bornite, which is locally concentrated in patches with albite. **(b)** Bornite occurs along grain boundaries of fine to medium-grained biotite and is inferred to have selectively replaced biotite. Viewed in transmitted transmitted light. **(c)** Bornite and sericite occurs along K-feldspar grain boundaries in syenite. It is inferred that bornite has replaced biotite. Viewed in reflected light. **(d)** Same as "c" except in plane-polarised light. **(e)** Magnetite, chalcopyrite and bornite (with covellite?) that occur along the grain boundaries of diopside in syenite. Magnetite and chalcopyrite are inferred to have replaced diopside. Viewed in transmitted light. **(f)** Same as "e" except in reflected light. Note that bornite has secondary covellite (?; cv) along its margins. Mineral abbreviations: ab = albite, bio = biotite, bn = bornite, cpx = clinopyroxene, cpy = chalcopyrite, di = diopside, fd = feldspar, Kfd = K-feldspar, mt = magnetite, ser = sericite.

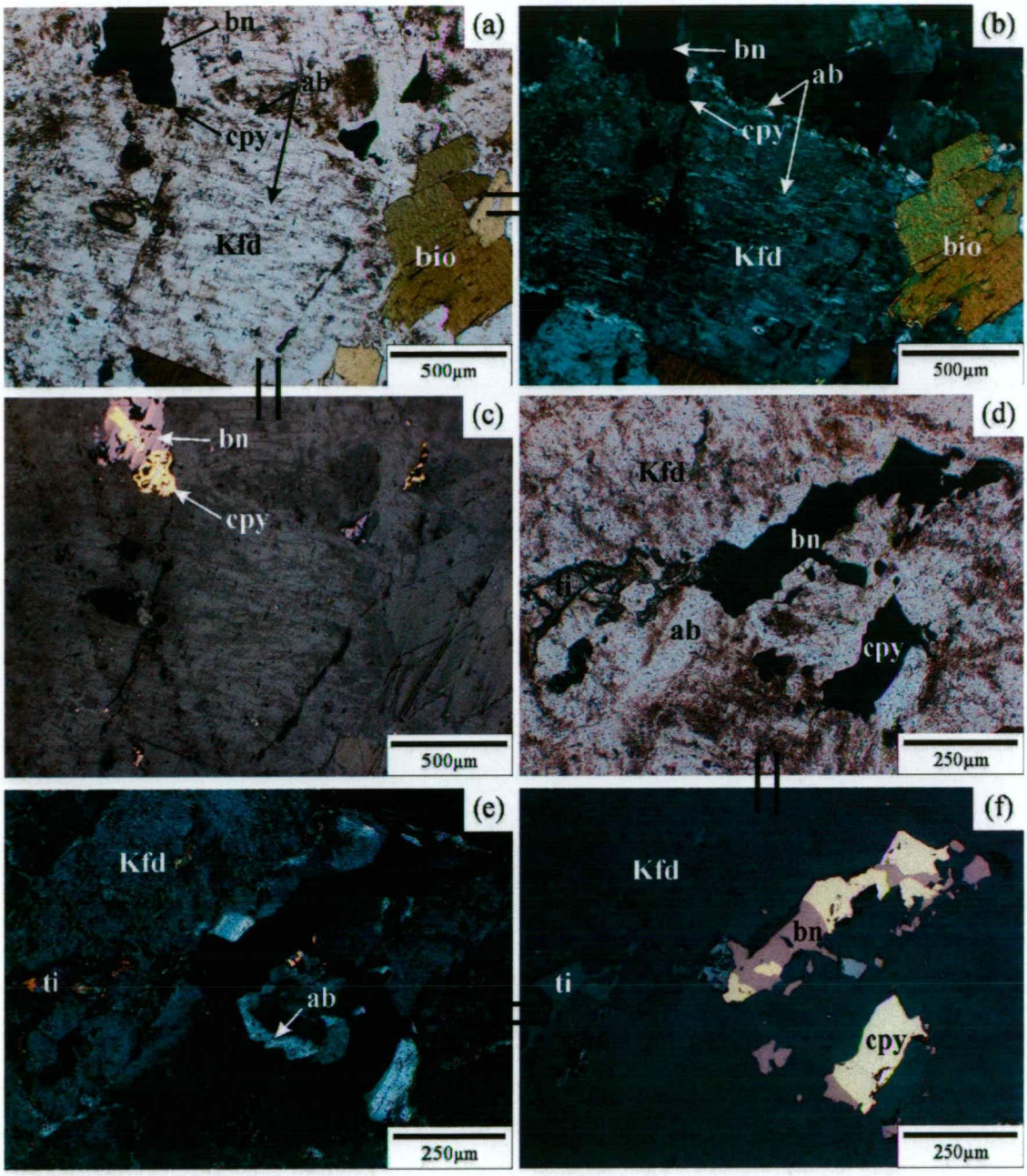

Figure 5-24. Bornite-chalcopyrite altered syenite from the Bishop Zone (a-b; drill hole 1996-43_167.3 m) and the Lower Main Zone (c-f; drill hole 2001-56_62 m). **(a)** Potassium-feldspar rimmed and cross-cut by sub-parallel thin patches of fine-grained albite. Bornite and chalcopyrite occur in albite patches. Viewed in transmitted transmitted light. **(b)** Same as "a" except in cross polarised light. **(c)** Same as "a" except in reflected light. **(d)** Bornite and chalcopyrite mineralisation in syenite. A patch of titanite occurs adjacent to bornite and chalcopyrite. Copper-Fe sulphides are spatially associated with albite patches. Viewed in plan polarised light. **(e)** Same as "d" except in cross polarised light. **(f)** Same as "d" except in reflected light. Mineral abbreviations: ab = albite, bio = biotite, bn = bornite, cpy = chalcopyrite, Kfd = K-feldspar, ti = titanite.

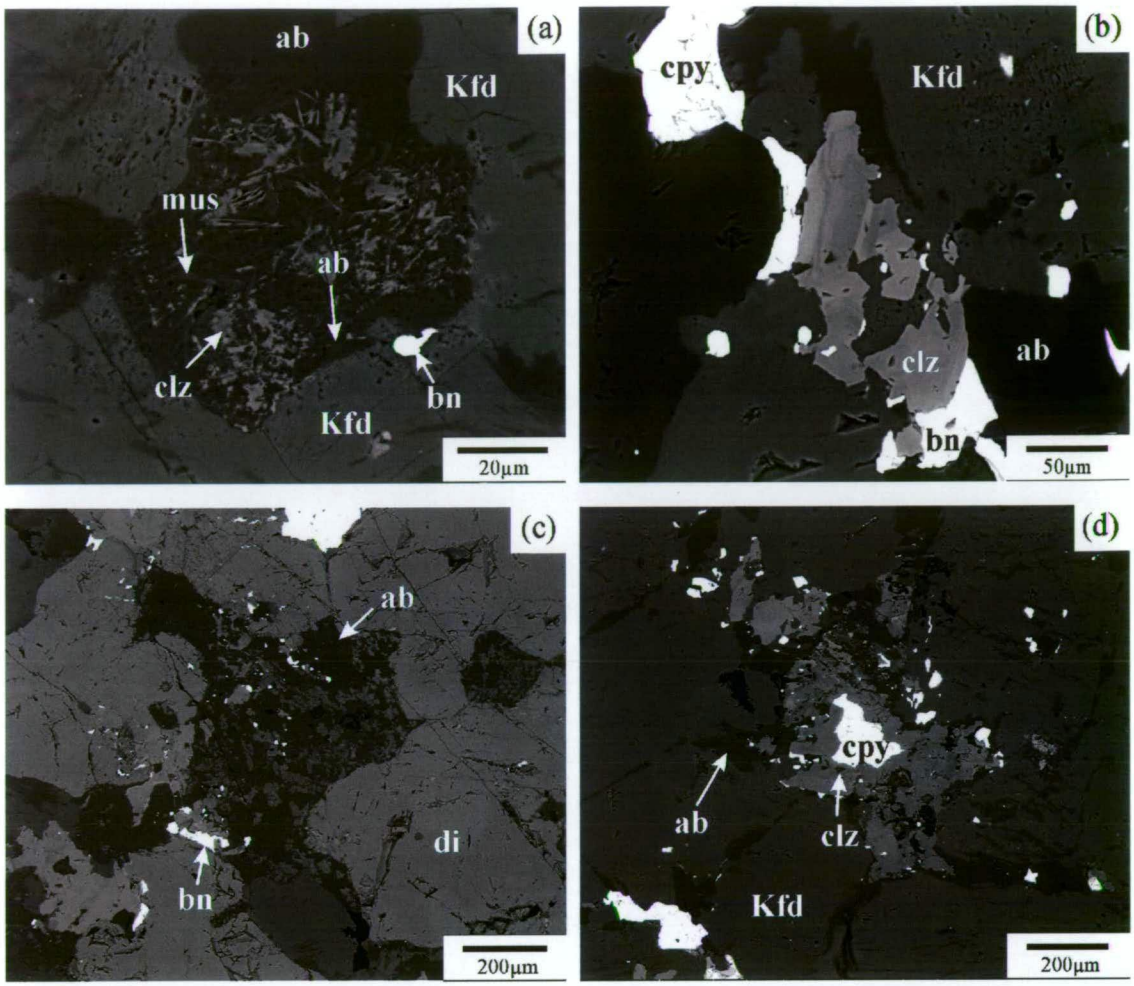

Figure 5-25. Back-scatter electron images of bornite and chalcopyrite altered syenite from the Bishop Zone (drill hole 1996-44_225.0 m). **(a)** Disseminated bornite in a patch of intergrown albite, clinozoisite and muscovite, which are inferred to have selectively replaced calcic plagioclase. **(b-d)** Chalcopyrite and bornite in patches with albite and epidote-clinozoisite. Mineral abbreviations: ab = albite, bn = bornite, clz = clinozoisite, cpy = chalcopyrite, di = diopside, Kfd = K-feldspar, mus = muscovite.

mineralising fluids were chloride-rich. Roedder (1984) noted that porphyry Cu deposits tend to form at very high temperatures (~400 to 800 °C), and are usually associated with very high salinities (~40->60 wt. % salts). These highly saline inclusions in chalcocite may reflect precipitation of salt crystals during vapour separation or halite supersaturation of the mineralising fluids (e.g., Richards and Kerrich, 1993).

5.2.4.4. Point counting results

Energy dispersive spectrometers-SEM point count analyses of monzonite and syenite were calculated to allow division of these rocks into the following categories based on sulphide mineralogy; (1) unaltered, (2) pyrite > chalcopyrite, (3) chalcopyrite > pyrite, (4) chalcopyrite, (5) chalcopyrite > bornite and (6) bornite > chalcopyrite. For the purpose of this study altered rocks without sulphides were avoided. Results have been plotted onto a se-

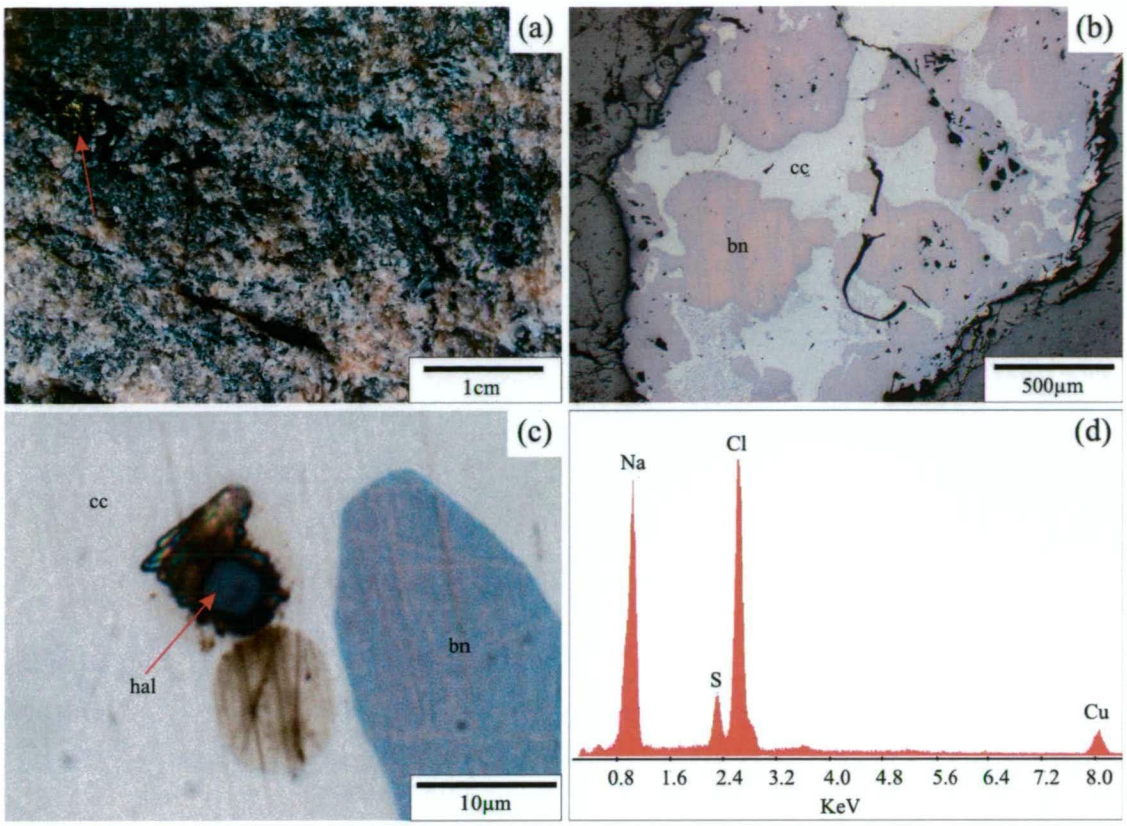

Figure 5-26. Bornite-chalcocite-chalcopyrite-quartz-aegerine veinlet from the Lower Main Zone (**a** – red arrow; drill hole 2002-62_143.2 m). **(b-c)** Chalcocite contains inclusions of halite crystals near bornite grains. **(d)** Electron dispersion spectrum (EDS) of halite inclusion in chalcocite. Mineral abbreviations include; bn = bornite, cc = chalcocite, hal = halite.

ries of scatter diagrams that discriminate sulphide mineralogy versus various mineral phases (vol. %) to determine if any general trends could be identified between sulphide and silicate mineralogies (Fig. 5-27a-g).

Syenites show a general increase in K-feldspar contents, from unaltered to chalcopyrite-altered syenites, and a decrease in plagioclase and clinopyroxene contents in altered syenites. The data for albite are scattered, but in general albite contents are higher in altered rocks. Biotite contents increase slightly in the altered rocks, whereas epidote and quartz is variable but generally increases in the altered rocks (Fig. 5-27e-g).

5.3. Discussion

5.3.1. Ore-forming processes: sulphide deposition in biotite pyroxenites

Earlier workers (e.g., Bishop et al., 1995) have hypothesised that net-textured sulphides in biotite pyroxenites could represent a magmatic sulphide component of the Lorraine porphyry Cu-Au deposits (e.g., Fig. 5-7). However the concept of sulphide segregation from a mafic magma is at odds with the presence of bornite in some biotite pyroxenites with

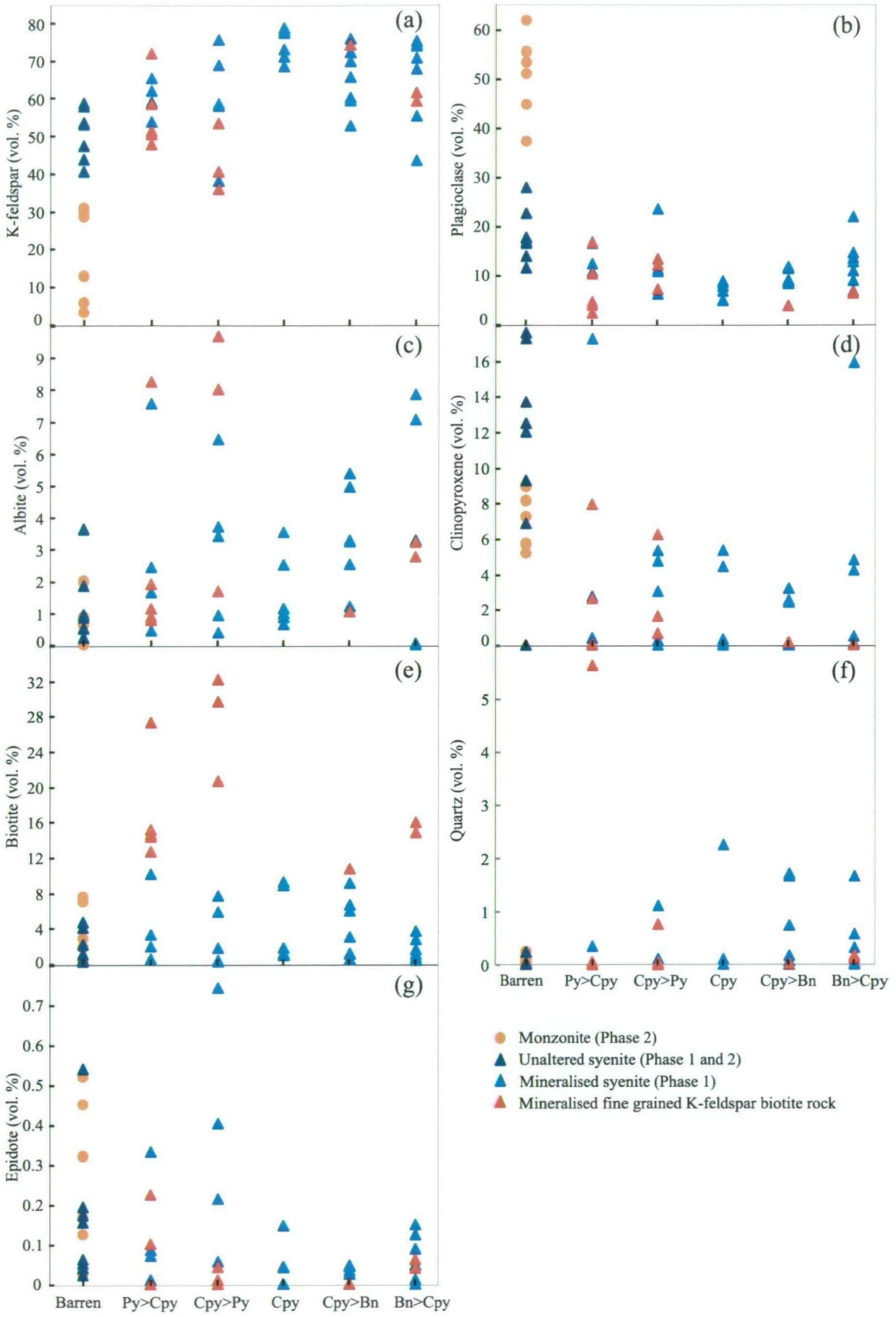
(a)
K-feldspar (vol. %)
(b)
Plagioclase (vol. %)
(c)
Albite (vol. %)
(d)
Clinopyroxene (vol. %)
(e)
Biotite (vol. %)
(f)
Quartz (vol. %)
(g)
Epidote (vol. %)
Barren
Py>Cpy
Cpy>Py
Cpy
Cpy>Bn
Bn>Cpy
Monzonite (Phase 2)
Unaltered syenite (Phase 1 and 2)
Mineralised syenite (Phase 1)
Mineralised fine grained K-feldspar biotite rock

net-textured sulphides, and the absence of pyrrhotite. Elsewhere, magmatic sulphide ores are commonly dominated by pyrrhotite, which occurs together with pentlandite and chalcopyrite, and with cubanite being a minor additional phase (Naldrett, 1989b; Maier and Barnes, 1999). A magmatic sulphide component at Lorraine is also at odds with the absence of primary sulphide inclusions in igneous minerals (i.e. diopside and biotite), and also with the high abundance of oxide minerals in the ore, which in some mineralised biotite pyroxenites exceeds 30 vol. % of the opaque phases. Magmatic sulphides ores typically contain between 5 and 15 % oxides (e.g., Naldrett, 1989b; Maier and Barnes, 1999). Keith et al. (1997; 1998) documented the occurrence of primary sulphide globules in latite lavas and dykes from the Bingham porphyry Cu deposit, which are considered to have precipitated following mixing of wet alkalic mafic magmas within a felsic magma chamber. These magmatitic sulphide globules in latite from Bingham comprise mixtures of pyrite, pyrrhotite and chalcopyrite, and are Ni-rich (i.e. up to 2.38 wt. % Ni; Keith et al., 1997). They are also distinctly different to sulphide inclusions identified in S-rich apatite from mineralised biotite pyroxenite at Lorraine, which comprise chalcopyrite and bornite.

Some authors have described anhedral disseminated bornite and chalcopyrite associated with magnetite in mafic to ultrabasic rocks from amphibolite- to granulite-grade metamorphic complexes (e.g., Okeip, South Africa, Cawthorn and Meyer, 1993; Curaçá Valley deposit, Brasil, Maier and Barnes, 1999). In the case of the Curaçá Valley deposit, mineralisation is exclusively associated with orthopyroxenites, lesser diorite and glimmerites (biotite rock), whereas the gneissic country rocks were reported to be generally free of sulphides (Maier and Barnes, 1999). In the case of the Okiep copper district, anhedral bornite and chalcopyrite are hosted in orthopyroxenites, norites and diorites (Cawthorn and Meyer, 1993). Models for these deposits have invoked desulphidsation of primary magmatic sulphide assemblages dominated by pyrrhotite and chalcopyrite during high-grade metamorphism, to assemblages consisting of chalcopyrite, bornite and magnetite (Cawthorn and Meyer, 1993; Boer and Meyer, 1994), e.g:

$$5\ \text{Chalcopyrite} + 5\ \text{Pyrrhotite} + 6\ H_2O + [16\ O] = \text{Bornite} + 3\ \text{Magnetite} + 6\ H_2S + 5\ SO_2 \quad \textbf{(5.1)}$$

Figure 5-27. Point count analysis results showing abundance of selected minerals in syenite, monzonite and fine-grained K-feldspar biotite rock from various sulphide zones. Results show that there is a general increase in K-feldspar for syenites that contain Cu-Fe sulphides versus unaltered samples. There is also a general decrease in plagioclase and clinopyroxene. Biotite, albite and epidote show much more variable abundances in various mineralised zones. On average biotite and albite are enriched in these zones. On average epidote is depleted in the mineralised zones. Data is listed in Appendix J.

Maier and Barnes (1999) noted that Cu-Fe sulphides in the Curaçá Valley deposit potentially could have been introduced during hydrothermal alteration, although they considered this scenario less likely. In particular they suggested that a relatively high mica, bornite and light REE content of many mineralised pyroxenites and diorites may conceivably indicate a hydrothermal origin of Cu mineralisation; however the absence of sulphides in adjacent gneissic country rocks was inferred to indicate that this scenario was less likely.

The current study compared mineralised biotite biotite pyroxenites from Lorraine with mineralised pyroxenites from high-grade (amphibolite- to granulite-grade) metamorphic complexes. The reason for the comparison is that some mineralised rocks in the Lower Main Zone are deformed and previous workers have speculated that sulphides were originally magmatic in ultrabasic rocks (e.g., Bishop et al., 1995) and later re-equilibrated during metamorphism may have occurred. In this study, the author compared Lorraine rocks with metamorphosed ultrabasic rocks from Okeip, South Africa and the Curaçá Valley deposit, Brasil (Crawford and Meyer, 1993; Maier and Barnes, 1999), which are mineralised.

At Lorraine, mineralised biotite pyroxenites are spatially associated with K-feldspar altered and mineralised syenites and fine-grained K-feldspar biotite rocks. This means that Lorraine is unlike deposits of the Curaçá Valley and Okiep copper districts in that mineralisation is not exclusively associated with ultrabasic and mafic rocks. In fact, most of the mineralisation in the Lower Main and Main zones, and a large proportion of the mineralisation in the Bishop Zone is hosted in syenites. Mineralised biotite pyroxenites in the Bishop Zone, and the Lower Main Zone, have been overprinted by a deposit-scale sulphide zonation pattern, which has also overprinted the syenites and fine-grained K-feldspar biotite rocks (e.g., Sillitoe, 2007). This deposit-scale sulphide zonation pattern appears consistent with porphyry-style sulphide zonation (e.g., Wilson et al., 2003; Cannell et al., 2005). Other points that discredit a high-grade metamorphic-style of mineralisation for biotite pyroxenites at Lorraine include:

- An absence of high-grade regional metamorphic sequences in the Lorraine district and in the Quesnel arc terrane (possibly with the exception of localised foliated K-feldspar biotite rocks with folded K-feldspar veins in the Lower Main Zone). Intrusives, volcanic and sedimentary rocks of the Quesnel terrane in the Hogem district are reported to have been metamorphosed to low grades (typically prehnite-pumpellyite facies but locally to lower greenschist facies; Ferri and Melville, 1994; Schiarizza and Tan, 2005).

- A general absence of mineralised biotite pyroxenites in other areas of the Duck-

ling Creek Syenite Complex away from the Lorraine deposit.

• A close temporal and spatial relationship between syenite intrusive and mineralisation at Lorraine (Chapter 3).

The metamorphic desulphidation model of Cawthorn and Meyer (1993) also requires the introduction of an oxidised fluid in order to covert pyrrhotite and chalcopyrite to bornite and magnetite. Cawthorn and Meyer (1993, p.591) noted the presence of anhydrite in the pyroxenites and norites of Okiep, South Africa, implying that highly oxidised fluids may have been involved in mineralisation at that location.

The current study has shown petrographic evidence of disequilibrium textures between sulphides and biotite and diopside in mineralied biotite pyroxenites at Lorraine. There are also distinct differences in the textures and abundance of biotite and diopside between mineralised and barren biotite pyroxenites. Significant disequilibrium and textural variations include; (1) bornite and chalcopyrite altered biotite pyroxenite that contains irregular patches dominated by coarse- to medium-grained biotite and apatite (Figs. 5-6g-i and 5-13a, b), (2) diopside crystals that occur in contact with Cu-Fe sulphides and that have actinolite-altered margins (Figs. 5-11h and 5-15c, d), (3) biotite crystals in contact with albite and Cu-Fe sulphides that have irregular-shaped green margins (Figs. 5-8c, d and 5-10), (4) turbid feldspar with fine-grained inclusions of Cu-Fe sulphides (Fig. 5-11c, d) and (5) diopside with irregular-shaped rims with lower *mg*-number that are strongly pleochroic (Fig. 5-16b). These textures are interpreted to be the products of hydrothermal alteration at Lorraine that are associated with Cu-Au mineralisation. In particular the occurrence of actinolite inclusions and actinolite along diopside margins is consistent with the replacement of diopside by actinolite, chalcopyrite and bornite at subsolidus temperatures (i.e. <550 °C at <3 kbar; Deer et al., 1992). Replacement textures, deposit-scale porphyry-style sulphide and alteration zonation patterns (Chapter 4), and a temporal and spatial association of mineralisation with a pulse of shoshonitic syenite magmatism in the Lower Main Zone (Chapter 3) provide evidence for replacement-style mineralisation in an alkalic porphyry environment at Lorraine.

5.3.2. Deposition of apatite and Cu-Fe sulphides in bornite-chalcopyrite mineralised biotite pyroxenite

The bornite-chalcopyrite mineralised biotite pyroxenites have medium- to coarse-grained apatite, and patches dominated by medium- to coarse-grained apatite with anhedral chalcopyrite and bornite. The apatite crystals contain Cu-Fe sulphide inclusions, which are inferred to have been trapped during the crystallisation of S-rich apatite in biotite pyroxenites, and reflect a period of alteration where the activity of S^{6+} in the mineralised biotite

pyroxenites was relatively high. The hydrothermal fluids may have contained hydrofluoric and phosphoric acid, and so could have reacted with diopside in pyroxenite wall rocks to form apatite (e.g., equation 5.2; Lentz, 1998), while aqueous Cu and S reacted with Fe released from mafic minerals to form chalcopyrite (e.g., equation 5.3). Relevant reactions may be:

$$5\ \text{Diopside} + 3\ H_3PO_{4(aq)} + HF_{(aq)} + 20\ H_2O = \text{Fluorapatite} + 5\ Mg(OH)_{2(aq)} + 10\ Si(OH)_{4(aq)} \quad \textbf{(5.2)}$$

and

$$\text{Biotite} + SO_4^{2-}{}_{(aq)} + 6^1/_2\ H^+_{(aq)} + \tfrac{1}{2}\ CuCl_2^-{}_{(aq)} + 4Cl^-_{(aq)} = {}^1/_2\ \text{Chalcopyrite} + \text{K-feldspar} + 2^1/_2\ MgCl_{2\ (aq)} + 4^1/_4\ H_2O + {}^{15}/_8\ O_2 \quad \textbf{(5.3)}$$

Reaction 5.3 suggests that for every two moles of biotite replaced, one mole of chalcopyrite can precipitate. The reactions also predicts that Fe^{2+} liberated from biotite will be oxidised to Fe^{3+} as S^{6+} is reduced to S^{2-}. Hydrogen ions are consumed during biotite replacement, driving the fluids to higher pH values and stabilising feldspar.

5.3.3. Alteration of syenite and fine-grained K-feldspar biotite rocks

Altered syenite and fine-grained biotite-K-feldspar rocks display a number of textures that were not observed in their unaltered counterparts, which include (1) the presence of diopside-magnetite and albite patches (Fig. 4-12a-e), (2) patches of fine-grained albite with Cu-Fe sulphide inclusions (Figs. 5-22f, 5-23a and 5-25a), (3) chlorite alteration of biotite in pyrite-bearing rocks (Fig. 5-4d), (4) titanite alteration of biotite in altered rocks (Figs. 5-4c), (6) the presence of clinozoisite-epidote with albite and Cu-Fe sulphides (Fig. 5-27a-d), (7) selective replacement of plagioclase by albite, clinozoisite-epidote and muscovite (Fig. 4-18c, d), (8) turbid K-feldspar (Figs. 5-5a, 5-22a, 5-23e) and (9) green-coloured rims on biotite grains in contact with Cu-Fe sulphides (Figs. 5-4a, 5-5a and 5-22e).

The textures in the altered felsic rocks suggest disequilibrium between Cu-Fe sulphides and the minerals that characterise the unaltered rocks. In particular, the association of albite patches with Cu-Fe sulphides appears to be consistent in all altered rock types at Lorraine. Albite patches and Cu-Fe sulphides have partially replaced biotite or are associated with green biotite rims. In addition, the formation of titanite, clinozoisite-epidote, chlorite and/or sericite associated with Cu-Fe sulphides is evidence for sub-solidus alteration of the host rocks during Cu-Au mineralisation.

5.3.4. Comparison with alteration assemblages from Galore Creek, Copper Canyon and Mt. Polley

Figure 5-28 shows photomicrographs of altered rocks from the Galore Creek-Copper Canyon area to make comparisons with altered rocks from Lorraine. There are a number of distinct differences between alteration assemblages at Lorraine and Galore Creek-Copper Canyon, such as the presence of abundant anhydrite, gypsum, and garnet; however there are also some notable similarities, including green margins around primary biotite (Fig. 5-28a), embayed and irregular margins of biotite in contact with sulphides (Fig. 5-28b), inclusions of relicts of biotite and K-feldspar in Cu-Fe sulphides (Fig. 5-28c, d) and apatite enrichment in some bornite-chalcopyrite mineralised rocks (Fig. 5-28e). Apatite enrichment has also been observed in bornite-cemented breccias from Mt. Polley's NE-zone (Fig. 5-28f). These apatites, like those from mineralised biotite pyroxenites at Lorraine, are also enriched in sulphur (Chapter 6).

Based on these data it appears that replacement-style mineralisation, which occurred in some mineralised zones at Lorraine, also occurred in some mineralised zones at Galore Creek and Copper Canyon. Replacement-reactions, which led to porphyry Cu mineralisation at Lorraine may have been similar to reactions that occurred between mineralising fluids and reactive wall rocks at Galore Creek and Copper Canyon. Mineralising fluids that passed through wall rocks at Lorraine, Galore Creek, Copper Canyon and Mt. Polley may have been phosphorous-rich, resulting in the enrichment of apatite in some mineralised zones.

5.4. Conclusions

Based on detailed petrographic studies of mineralised rocks from Lorraine, a number of key observations and conclusions have been made:

- Mineralised fine-grained K-feldspar biotite rocks, biotite pyroxenite, feldspathic pyroxenite and syenite contain sulphides that are spatially associated with turbid feldspar patches, biotite grains with embayed and green-coloured rims and/or diopside grains with corroded margins that have actinolite crystals along their grain boundaries in contact with Cu-Fe sulphides. These textures are concluded to indicate partial to complete replacement of biotite and diopside by Cu-Fe sulphides during transitional-stage alteration and mineralisation at Lorraine.

- The formation of actinolite along grain margins of primary igneous diopside, and the occurrence of actinolite inclusions in bornite and chalcopyrite, indicates that mineralisation and alteration of diopside in biotite pyroxenite occurred at sub-

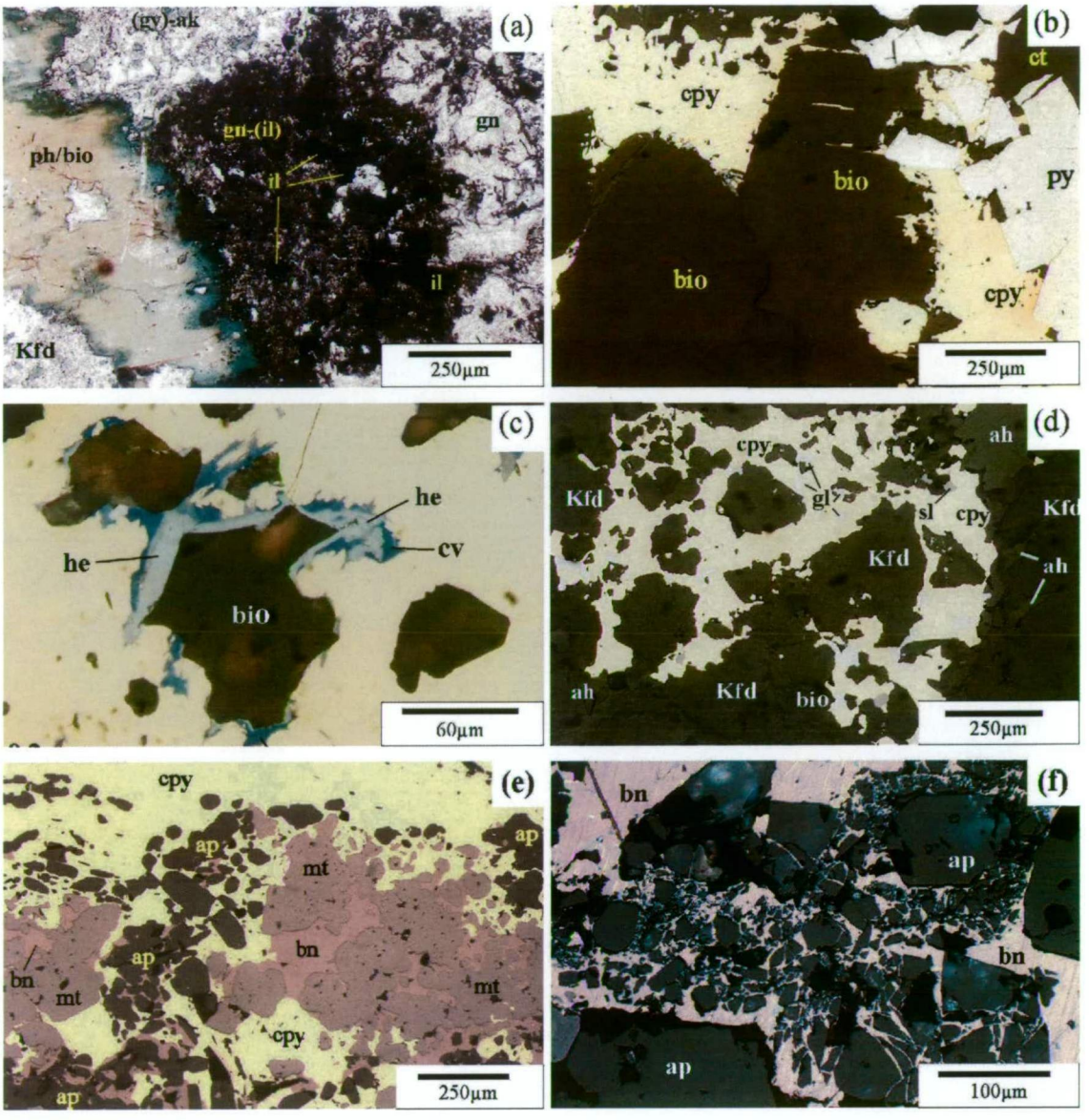

Figure 5-28. **(a)** Pyrite and chalcopyrite mineralised fine-grained syenite from Galore Creek showing a zone of garnet and illmenite alteration and the formation of green margins along biotite as a result of alteration. Photomicrograph in plane polarised light (drill hole GC-395_53.0 m, photo courtesy of Nova Gold Resources Inc.). **(b)** K-feldspar phyric syenite porphyry from the Copper Canyon porphyry Cu deposit in reflected light. The rock shows biotite with irregular magins in contact with chalcopyrite and pyrite. It is inferred that biotite has been replaced by chalcopyrite (drill hole CC04-22_210.3 m, photo courtesy of Nova Gold Resources Inc.). **(c)** Photomicrograph of mineralisation in volcanic with intermediate composition from the Galore Creek area in reflected light. The rock contains chalcopyrite mineralisation with irregular shape biotite inclusions (relicts?). Biotite inclusions have hematite and covellite along margins (drill hole GC03-442_304.7 m, photo courtesy of Nova Gold Resources Inc.). **(d)** Photomicrograph of chalcopyrite mineralisation in pseudoleucite-bearing syenite from Galore Creek in reflected light. Chalcopyrite includes irregular-shaped inclusions of K-feldspar. These are inferred to be relicts of K-feldspar that have been replaced by chalcopyrite (drill hole GC03-441_446.0 m, photo courtesy of Nova Gold Resources Inc.). **(e)** Magnetite-bornite-chalcopyrite-apatite rock from Galore Creek in reflected light. Rock includes patches of magnetite with bornite, and also patches of subhedral apatite (drill hole GC04-480_48 m; photo courtesy of Nova Gold Resources Inc.). **(f)** Bornite and apatite cement from a hydrothermal breccia with altered monzonite clasts from NE-zone ore body, Mt. Polley, in reflected light (UTM zone 10; 592775mE, 5825410mN;

Figure 5-28. *continued*
NAD83; Belich 912). Mineral abbreviations: ah = anhydrite, ak = ankerite, ap = apatite, bio = biotite, bn = bornite, cpy = chalcopyrite, cv = covellite, gl = galena, gn = garnet, gy = gypsum, he = hematite, il = ilmenite, Kfd = K-feldspar, mt = magnetite, ph = phlogopite, py = pyrite, ti = titanite.

solidus conditions (i.e. <550 °C; Deer et al., 1992).

- Chalcopyrite and bornite-chalcopyrite mineralised syenites contain turbid diopside, with sulphides in albite-rich patches and along margins of turbid diopside and biotite. The turbid diopside is an alteration product.

- The sulphide mineralogy of "net textured" Cu-Fe sulphides in ultrabasic rocks at Lorraine is inconsistent with the sulphide mineral assemblage of primary magmatic sulphides reported elsewhere (e.g., Naldrett, 1989a, 1989b; Keith et al., 1997; Keith et al., 1998).

- Based on an absence of district-scale high-grade metamorphism, and the association of sulphides with altered syenites and fine-grained K-feldspar biotite rocks, a model that involves desulphidsation of primary magmatic sulphides in ultrabasic rocks can also be ruled out.

- Biotite pyroxenites with net-textures fit within the deposit-scale porphyry sulphide zonation patterns in both the Bishop Zone and the Lower Main Zone.

- The replacement of primary minerals by sulphides in host rocks at Lorraine is similar to replacement of biotite and K-feldspar by sulpides in mineralised rocks at the alkalic Galore Creek-Copper Canyon porphyry-Cu deposits, British Columbia (i.e. replacement of biotite by Cu-Fe sulphides). Apatite enrichment in bornite chalcopyrite mineralised pyroxenites is also consistent with apatite enrichment in chalcopyrite and bornite mineralised rocks at Galore Creek and Mt. Polley.

CHAPTER 6
MINERAL GEOCHEMISTRY

6.1. Introduction

The chemical composition of rock forming minerals have been investigated extensively by petrologists over the past century (e.g., Deer et al., 1992 and references therein), and data sets have provided useful information towards constraining conditions during crystallisation. In particular, these data sets have provided useful information such as the relative activity of elements in melts or fluids, speciation of elements and temperature and pressure at which mineral assemblages equilibrated. These data sets have also allowed petrologists to characterise the chemical composition of minerals from particular geological environments.

The major and trace element composition of mineral phases from shoshonitic intrusives at Lorraine have not previously been characterised, and one of the aims of this chapter is to quantify the composition of minerals in unaltered rocks at Lorraine and compare their compositions to other arc-related shoshonites. A second aim of the current study is to identify minerals formed from hydrothermal alteration and to compare their compositions with mineral phases from other porphyry environments of alkalic and calc-alkalic character.

6.1.1. Data and terminology used in this chapter

The aim of this chapter is threefold, which includes: 1) to characterise and compare the mineral compositions of unmineralised Phase 1 and 2 rocks with selected unaltered shoshonitic samples from other locations; 2) to compare the composition of minerals from unmineralised Phase 1 and 2 rocks from Lorraine with minerals from mineralised Phase 1 rocks from Lorraine and 3) to compare the mineral compositions of Phase 1 mineralised rocks from Lorraine with the compositions of alteration minerals from other porphyry environments.

6.1.1.1. Shoshonitic rocks

For the current study the chemical composition of primary igneous minerals of Lorraine rocks were compared with the same mineral type from other arc-related alkalic lavas or intrusions. In particular, mineral phases from Fijian shoshonites, Nicola Group shoshonites and Zippa Mountain biotite pyroxenite were compared with the Lorraine rocks that have been classified as shoshonitic in composition (see Chapter 7). Fijian shoshonites were selected as they formed in a modern, well-studied, post-collisional arc-terrane setting (Fig. 6-1a). They formed between 4 and 5 Ma following a collisional event with the Ontong Java Plateau and the fossil Vitiaz trench at 12 Ma (Hamburger and Isacks, 1987; Rogers and Setterfield, 1994; Chen and Brudzinski, 2001; Green, 2001; Leslie, 2004). Shoshonitic magmatism at Lorraine is also thought to have occurred some seven million years after the collision of the Quesnel Terrane with ancestral North America (see Chapter 2; Nixon

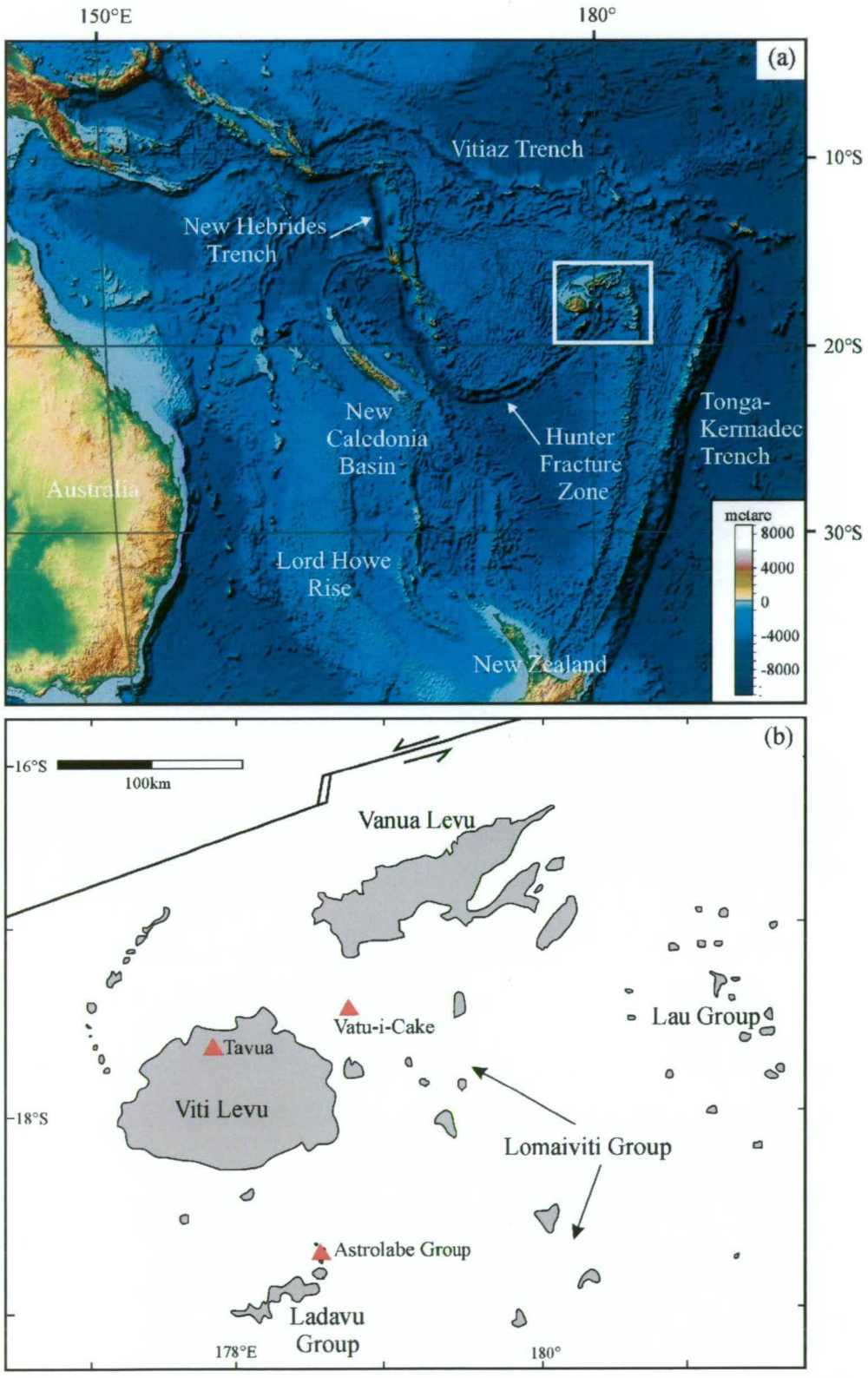

Figure 6-1. **(a)** Digital land surface and sea floor elevation map of the southwestern Pacific. The white rectangle denotes the area of the Fijian Islands shown in "b". Modified from Amante and Eakins (2008). **(b)** Map of the Fijian Islands with the location of the Astrolabe Group, Tavua and Vatu-i-Cake shoshonites. Modified from Leslie (2004).

et al., 1993; Mihalynuk et al., 2004). Hence shoshonites from Lorraine and Fiji appear to have formed in similar tectonic environments, validating the comparison with Lorraine rocks. These rocks were also chosen because they are particularly well-documented (Leslie, 2004).

The Nicola Group shoshonites formed in the Quesnel terrane in south-central British Columbia and crop out in the Mount Polley area (Fig. 6-2), and these rocks have been characteristed by Logan and Bath (2006), and formed in the same terrane as the Lorraine shoshonites. However, they were emplaced in the Late Triassic and are therefore older than the Lorraine shoshonites. The Nicola Group shoshonites are diopside-rich; most of them do not contain olivine. Despite not being the extrusive equivalent of Lorraine shoshonites, the Nicola Group shoshonites do provide an opportunity to compare the mineral and whole rock geochemistry of Lorraine shoshonites with extrusive shoshonites in the Quesnel terrane.

The Zippa Mountain biotite pyroxenite occurs in the Stikine terrane in north-western British Columbia (Fig. 6-2). Previous studies of these rocks have been conducted by Coulson et al. (1999; 2007). Although now exposed on opposite sides of the Cache Creek complex, the Stikine and Quesnel terranes are considered by some workers to have formed a single, continuous magmatic arc that lay east of the Cache Creek accretionary complex in the Paleozoic and early Mesozoic (Chapter 2; Wernicke and Klepacki, 1988; Mihalynuk

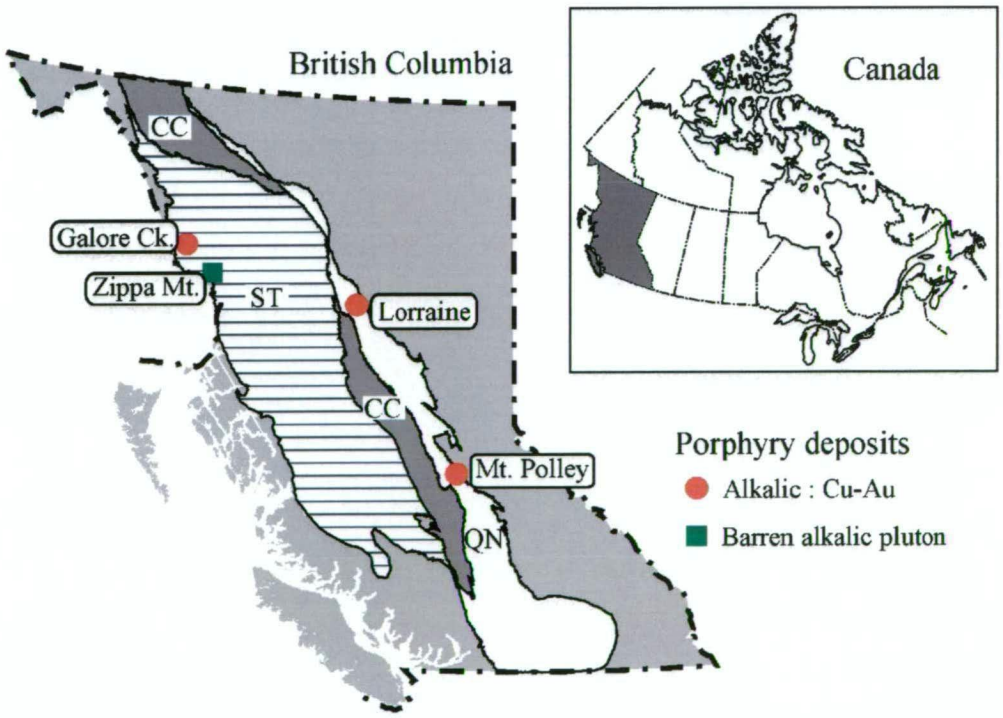

Figure 6-2. Tectono-stratigraphic setting and location of the Lorraine deposit along with other Late Triassic to Early Middle Jurassic Cu-Au porphyry deposits in British Columbia. Terranes; Stikine (ST); Cache Creek (CC); Quesnel (QN; modified from Nixon and Peatfield, 2003). Labels show the location of selected Late Triassic to Early Jurassic alkalic porphyry deposits in the Quesnel and Stikine terranes (McMillan et al., 1995) and the location of the barren Zippa Mount pluton. Inserted is a map of Canada with provincial and territorial boarders. Grey filled area represents the province of British Columbia.

et al., 1994a). Hence biotite pyroxenites from Lorraine and Zippa Mount appear to have formed in a similar tectonic setting. Texturally, the Zippa Mount biotite pyroxenites appear to be very similar to those at Lorraine, and therefore they are used here for comparison. Main differences between Lorraine biotite pyroxenites and Zippa Mount biotite pyroxenite is that the later crystallised as cumulates in a zoned pluton as opposed to dykes. Another significant difference is that the Zippa Mountain pluton forms contacts with carbonate-rich wall rocks, where skarn alteration assemblages have formed; such wallrocks have not been identified at Lorraine.

6.1.1.2. Alteration minerals from porphyry environments

The current study also compares the chemical composition of minerals from alteration zones. In particular mineral phases from the Mt. Polley NE-zone porphyry-Cu Au deposit (Quesnel Terrane, British Columbia; Fig. 6-2), the Santa Rita porphyry-Cu deposit (New Mexico, USA; Jacobs and Parry, 1976) and Endeavour 26 North porphyry-Cu deposit of the Macquarie Arc (NSW, Australia; Cross, 2000) were compared with the compositions of altered rocks from Lorraine.Biotites from Santa Rita were selected as they are from a well studied porphyry deposit where both magmatic and hydrothermal biotites have been clearly characterised.

6.1.1.3. Terminology

The terminology used in this chapter is different to that used in earlier chapters. In particular the use of Phase 1 and Phase 2 has been omitted, and rocks have been described as either unaltered or mineralised. Unaltered rocks include both Phase 1 and 2 rocks, whereas mineralised rocks strictly refer to Phase 1 or fine-grained K-feldspar biotite rock. It is important to note that no significant geochemical differences exist between the compositions of minerals in unaltered Phase 1 rocks and unaltered Phase 2 rocks. Hence for the purpose of this chapter these two were grouped together.

6.2. Analytical method

6.2.1. Sample preparation

Over 2000 mineral grains from over 80 samples were selected for analysis of diopside, biotite, magnetite, feldspar and apatite. Rocks were crushed and 0.3 to 1 mm rock chips were separated using sieves in preparation for analysis. Individual crystals were hand-picked using a binocular microscope and tweezers. Selected crystals were organized on top of a strip of double-sided tape. A 25mm steel ring was placed around the grains and 5 mL of epoxy resin was poured into the casting and dried to form an epoxy grain mount. Grain mounts were polished, cleaned (ultrasonic bath), wiped with a tissue soaked with metholated spirits and dried in an oven that had been preheated to 50 °C.

6.2.2. Electron probe microanalyser (EPMA)

Analyses were carried out on carbon-coated mounts using the Cameca SX 100 microprobe of the Central Science Laboratory at the University of Tasmania. A series of mounts were prepared for individual EPMA sessions of either diopside, biotite, apatite, feldspar or magnetite. Specific standards and beam conditions were used based on the mineral chosen for individual sessions. Known standards were used at the beginning, middle and end of probe sessions in order to assess accuracy and correct for machine drift during probe sessions. Correction factors and adjustments for machine drift were applied to data when the average measured value of the standard was not in one standard deviation of the accepted value.

Preparing epoxy mounts rather than using existing thin sections for analytical work was made for a number of reasons, which included (1) a single crystal type for large number of different samples could be analysed in one single session, which improves analytical precision for data sets and is cost effective, (2) euhedral crystals could be orientated in the preferred orientation, which is vital for accurate analysis of halogens in apatite (i.e. apatite crystals were orientated so that their c-axis was orientated parallel at right-angles to the beam to minimise the effect of halogen migration towards the beam during the analysis), (3) specialised beam conditions and external standards could be run for specific crystal types to improve accuracy and reduce analytical time and (4) epoxy mounts could also be used for LA-ICP-MS analysis (trace elements) and exact crystal spots probed using the EPMA could be later analysed again using the LA-ICP-MS, hence allowing accurate values for internal references needed to accurately calculate trace element data. This also allows data to be compared from the two above analytical methods, and therefore improving quality control of data.

6.2.2.1. Diopside

Elements Si, Ti, Al, Fe, Mn, Mg, Ca, Na, K and Cr were analysed using a beam diameter of 5μm, an accelerating voltage of 15 keV and a beam current of 20 nA. A diopside external standard (Utas1 cpx) was used for quality control.

6.2.2.2. Apatite and biotite

Biotite and apatite were analysed for Si, Ti, Al, Mn, Mg, Ca, Na, K, P, S, Cl and F using a beam diameter of 20 μm, an accelerating voltage of 15 keV and a beam current of 10 nA. Chlorine in biotite was analysed; however chlorine was almost always below the detection limit (i.e. approx. 900 ppm). For apatite, in an effort to minimise problems with peak-intensity variation related to anisotropic diffusion of fluorine under electron beam exposure, short counting times for major elements (10-20 seconds) and eight repeated five second counting times for F over a forty second period of the same point were conducted. According to Stormer et al. (1993) using cumulative beam exposure reduces the effects of F migration towards the beam, and therefore improves the accuracy of F analysis.

Standards Utas4 topaz and Durango apatite were used for quality control. Topaz is less susceptible to F migration compared to apatite, and therefore topaz was used to determine the accuracy of the F analysis. Apatite standard grains were analysed with *c*-axis parallel and perpendicular to the beam to observe the effects of fluorine migration for different crystal orientations. Results showed that when apatite was orientated with the *c*-axis parallel to the beam, the F values were ~15 % greater than the known concentration of the standard (i.e. 4.06 wt. % with stdev of 0.12 wt. % vs. 3.53 wt. % respectively). In contrast, the apatite standard orientated with the *c*-axis perpendicular to the beam recorded F values that were 0 to 6.5 % greater than the known value (i.e. avg. of 3.68 wt. % with stdev. of 0.094 wt. % vs. 3.53 wt. % respectively). However it is important to note that three areas of Durango apatite recorded F values between 3.54 and 3.61 throughout the probe session, whereas another four areas of the grain consistently recorded values between 3.70 and 3.80 throughout the probe session, suggesting that the Durango apatite standard is not homogenous with respect to F.

The topaz standard recorded an average F concentration that was 0.1 wt. % (or 0.5 %) greater than the mean (i.e. avg. = 20.75 wt. %, stdev. = 0.18 wt. % vs. 20.65 wt. %) and showed no significant change in the measured concentration of F from the start to the end of the analytical session, suggesting machine drift for F was not significant. Analysis of the topaz standard demonstrated that F concentrations for topaz were within one standard deviation of the accepted value, suggesting that measured values were statistically comparable to the known value. Thus given the variation in F values for the Durango apatite and that the known Utas4 topaz standard was in one standard deviation of the measured value, I concluded that no correction factor needed to be applied to the F analysis from microprobe sessions. However it should be noted that the measurement error for F on apatite is significantly larger because of the orientation effect. Despite this, the standard deviations for apatite from individual samples are low, suggesting that measured F concentrations are precise. Biotite is not reported in the scientific literature to suffer from the effects of anisotropic diffusion of F to the degree of apatite, and the topaz standard was also used as external standard for the analysis of F in biotite. Chlorine in biotite was also analysed; however chlorine was almost always below the detection limit (i.e. ~900 ppm).

The Durango apatite was used as an external standard for elements Ca, P, S, Cl, Na, Fe and Si for apatite analysis. For biotite, the Utas cpx1 and Utas4 phlogopite and Utas2 hornblende were used as standards for Si, Ti, Al, Fe, Mg, Mn, Ca, Na and K. The Utas4 phlogopite standard is based on average values from over one hundred analyses on the Cameca SX 100 microprobe at the University of Tasmania.

In this chapter results for apatite-biotite geothermometryof Zhu and Sverjensky (1991, 1992) was used to estimate the temperature (with respect to OH and F substitution) in mineralised and unaltrered rocks. For this, apatite and biotite were separated from the rock. Temperature values were calculated based on the composition of apatite and average

composition of biotite in each sample. It is important to note that grain boundaries of biotite that were avoided to reduce to effects of sub-solidus chlorine-hydroxyl exchange (e.g., Piccoli and Candela, 1994; Coulson et al., 2001). It is also important to note that the variation in X_{Fe}, F and OH (calculated) between biotites from each sample was small. Hence the errors of each calculated temperature shown in Fig. 6-29a are smaller that the size of the data point on the graph.

6.2.2.3. Magnetite

Approximately 200 magnetite grains and inclusions were analysed using the Cameca SX 100 electron microprobe at the University of Tasmania. Elements analysed included Si, Ti, Al, O, V, Cr, Fe, Mg, Ca, Mn, Ni, Zn and Co using a beam diameter of 2μm, an accelerating voltage of 20 keV and a beam current of 15nA. Silicon, Mg, Ca, Ni, Zn and Co were almost always below the detection limit (i.e. approximatlely 200, 250, 150, 350, 500 and 400 ppm respectively). Titanium and Al varied from below detection limit (i.e. approximately 150 and 200 ppm respectively) to >1 wt. %. Chromium was commonly above detection limit (i.e. 300 ppm), and V, Mn and Fe were above the detection limit (300, 400 and 650 ppm respectively) in all samples. Ferric and ferrous iron abundances were calculated using methods of Sauerzapf et al. (2008). Oxygen was also analysed. High background levels of O contributed to large detection limits of 4000 to 4500 ppm. Analytical results for the above elements (including O) from four known standards were used to check for machine drift and analytical accuracy.

Standards used included Minas Gerais (Brazil) magnetite, Ilmenite Mountain Miask (USSR) ilmenite, Tiebaghi Mine (New Caledonia) chromite and gahnite from Brazil (Jarosewich et al., 1980). Measured Fe had a mean value in 0.01% of the known value of the magnetite standard (i.e. avg. = 70.74 wt. %; stdev. = 0.53 wt. % vs. 70.69 wt. % respectively). Vanadium abundance was known for the chromite standard only and the average measured concentration was statistically higher than the known concentration (i.e. avg. = 0.063 wt. %; stdev. = 0.009 wt. % vs. 0.054 wt. % respectively). Hence a correction factor was applied for vanadium. Average measured chromium concentrations were statistically comparable to the known chromite standard (i.e. avg. = 41.31 wt. %; stdev = 0.20 wt. % vs. 41.39 wt. % respectively). Aluminium concentrations were known for chromite and gahnite standards and for both standards the measured value was statistically slightly higher than the accepted values.

6.2.2.4. Feldspar

Feldspars were analysed for Si, Ti, Al, Mg, Mn, Fe, Ca, Na, K, Sr and Ba using a beam diameter of 10 μm and an accelerating voltage of 15 keV and a beam current of 10 nA. Approximately 350 feldspar grains were analysed from over 35 samples. The standard used for the analysis was the Utas1 plagioclase to monitor and adjust for analytical accuracy and machine drift.

6.2.3. Laser-ablation inductively coupled plasma mass-spectrometry (LA-ICP-MS)

Trace and select major elements Li, Cl, K, Ca, Sc, Ti, V, Mn, Fe, Co, Ni, Cu, Zn, Ge, As, Rb, Sr, Y, Zr, Nb, Mo, Sn, Ba, La, Ce, La, Ce, Nd, Sm, Eu, Gd, Dy, Er, Yb, Hf, W, Pb, Th and U for diopside, apatite and biotite were analysed using a Nd:YAG 193 nm UV laser manufactured by New Wave fitted to an Agilent 7500cs ICP-MS at the University of Tasmania. The samples were ablated under He and Ar gas before introduction to the plasma. Targets for the analysis were spots that had previously been analysed with EPMA. Prior to each analysis, the laser was fired at a low pulse rate (1 Hz) for three seconds to remove surface contamination. The laser was then fired at 10 Hz repetition rate and holes 50 μm in diameter were ablated (or 35 μm for small apatite inclusions in diopside or biotite). Acquisition time consisted of a 30 second measurement of the gas background with the laser blocked, followed by 70 second measurement of the target. Ablated material from the crystal was transported by the carrier gas to the torch of the ICPMS that is equipped with a fast-switching quadrupole mass spectrometer. To correct for instrument drift the international standard NIST612 (doped synthetic silicate glass) was ablated twice at the beginning of the analysis, at 90 minute intervals during the analysis and at the end of the analysis. A secondary standard, BCR-2 (basaltic glass) was ablated twice at the beginning of analytical sessions at 10 Hz repetition rate and holes of 50 μm in diameter, which was consistent with laser conditions used on samples. Correction factors were applied to the data for unknown samples based on the difference between the measured abundance of elements in BCR-2 vs. the known abundance of elements in BCR-2.

6.2.3.1. Data reduction and interpretation

Data reduction and interpretation was carried using methods described by Gilbert and Danyushevsky (2007). Formulated Microsoft Excel™ spreadsheets designed by Gilbert and Danyushevsky at the University of Tasmania were used for the data reduction process. For an outline of the methodology, the reader is referred to Gilbert and Danyushevsky (2007). Calcium abundance in diopside and apatite, and K abundance in biotite determined from EPMA analysis were used as external reference standards for data reduction.

6.2.4. Quality of data: LA-ICP-MS vs. EPMA

Based on calculated values using the methodology of Gilbert and Danyushevsky (2007), detection limits (i.e. the lowest concentration that can be confidently measured above the background) for diopside were typically between 0.01 to 0.05 ppm for REE, Zr, Y and Sr, 0.06 to 0.1 ppm for V, Co and Li, 0.2 to 0.4 ppm for Mn, Zn and Cu, and 2 to 5 ppm for Ti and Fe. Analytical precision (%) for almost all elements was between 3 and 5 %. One exception is Cu which has analytical precision typically between 15 and 25 %. Analytical error (i.e. an expression of analytical noise and sample variability) was commonly between 1 and 5 %.

A comparison of LA-ICP-MS vs. EPMA analysis of Fe, Ti and Mn for biotite and diopside (Fig. 6-3a-f). The accidental ablation of micro-inclusions during LA-ICP-MS analysis may also account for discrepancies between the two techniques; although all integration intervals from LA-ICP-MS analysis were selected where no obvious spikes in the counts per second were evident. Overall there are strong to moderate 1:1 correlations for Fe, Ti and Mn for biotite and moderate 1:1 correlations for Fe, Ti and Mn in diopside (Figs. 6-3a-f); although manganese is systematically high in diopside for LA-ICP-MS analysis relative to EPMA.

The Mn and Fe data for biotite from both probe and LA-ICP-MS fits well along the 1:1 line. In contrast, the Mn and Fe concentrations for diopside are on average higher when analysed by LA-ICP-MS compared to microprobe data. Both biotite and diopside were analysed during the same LA-ICP-MS session and therefore the same BCR-2 secondary standard was used. Hence it is unlikely to be a problem with the primary or secondary standard from LA-ICP-MS analysis, although possible matrix effect variations between standards and diopside cannot be ruled out. One other explanation is that diopside crystals are zoned and during LA-ICP-MS analysis the crystals were ablated from inner zones to outer zones. Outer zones in diopside are relatively Mn- and Fe-rich and would increase the value of these elements during the analysis. Hence discrepancies for Fe and Mn in diopsides between probe and LA-ICP-MS data are inferred to reflect variations in the amount of material analysed and fact that many diopside crystals are zoned, whereas biotites by comparison are weakly zoned and this affect was by comparison is less obvious.

6.3. Clinopyroxene

6.3.1. Clinopyroxene in unaltered biotite pyroxenite, syenite and monzonite

Cations for pyroxene were calculated using the PYROX program of Yavuz (2001). Pyroxenes from Lorraine plot in the diopside field on the ternary classification diagram of Morimoto (1988; Fig. 6-4a, b); although most pyroxenes plot slightly above the diopside field towards the wollastonite endmember (i.e. Wo>50). According to Deer et al. (1978) diopsides with Wo>50 occur in alkaline igneous rocks, skarns and metasomatised mafic rocks.

Unaltered biotite pyroxenites have diopside with *mg*-numbers (molar ratio of Mg to the sum of Mg and Fe) between 83 and 97, unaltered syenites have diopside with *mg*-numbers between 76 and 94, and monzonites have diopside with *mg*-numbers between 83 and 92 (Fig. 6-5a-h). A direct comparison between the three groups of diopsides (i.e. unaltered biotite pyroxenite, syenite and monzonite) has been made based on equivalent *mg*-number (e.g., *mg*-number 90 to 95, 85 to 90 and 80 to 85). Diopside in biotite pyroxenites with *mg*-numbers between 90 and 95 are on average enriched in Cr, but depleted in Fe^{3+} and Mn compared to diopside from syenite and monzonite, and diopsides in biotite pyroxenite

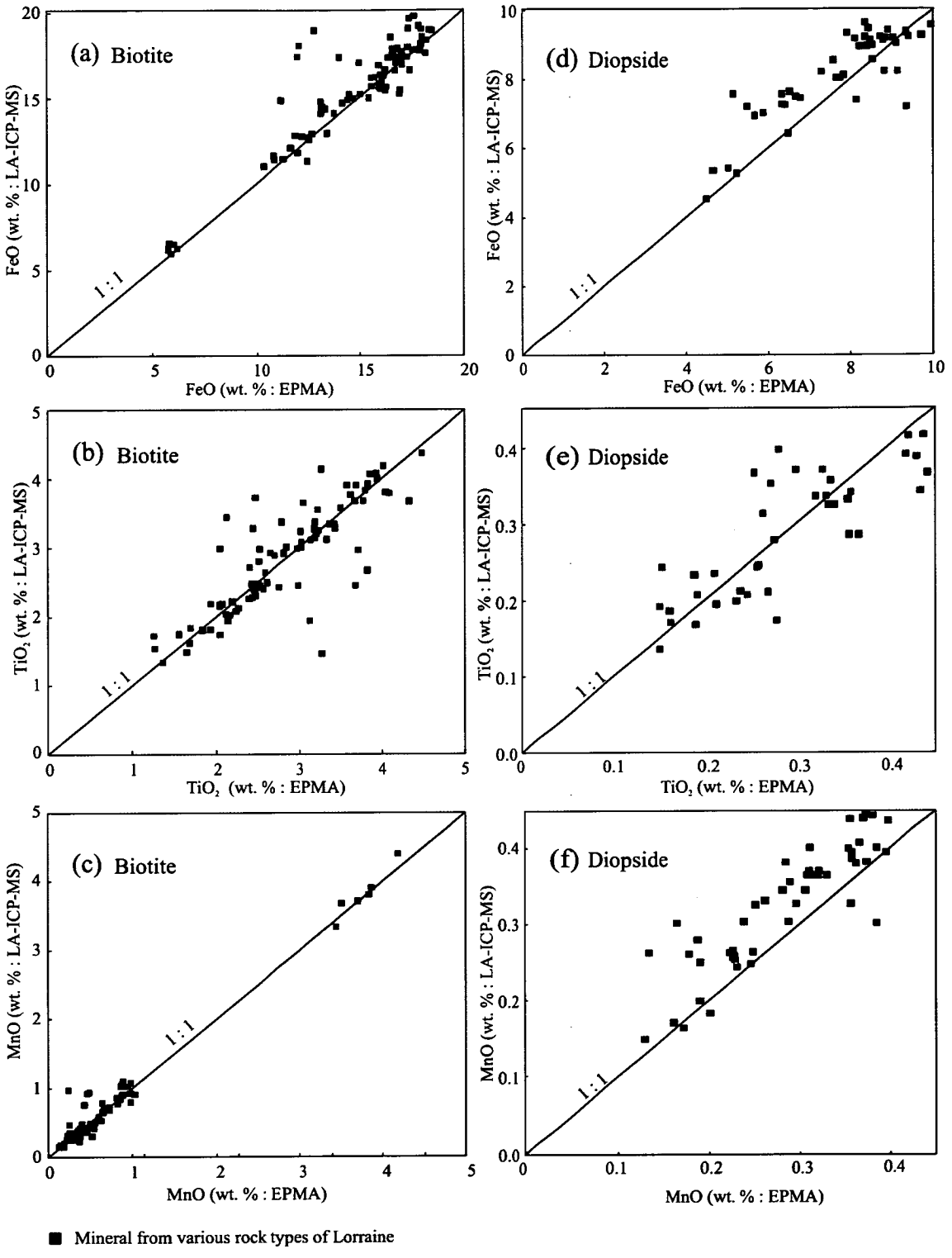

Figure 6-3. Major element composition of (a-c) biotite and (d-f) diopside from LA-ICP-MS vs. EPMA analysis from the same location on the same biotite or diopside grain. Laser-ICP-MS data was reduced using K for biotite and Ca for diopside from microprobe analysis as reference standard elements.

with *mg*-number between 85 and 90 are also depleted in Mn compared to diopside from syenites and monzonites.

A key substitution reaction in diopsides is equilibria involving the tschermakitic ($CaAl_2SiO_6$; CaTs) component, which is potentially useful for estimating the pressure of crystallisation with appropritate mineral assemblages (e.g., anorthite-clinopyroxene-quartz; Wood, 1976). Wood (1976) demonstrated that the tschermakitic component of clinopyroxene increases with pressure, and that clinopyroxenes with ~8 mole % of CaTs component equilibrated at ~10 kbar at temperatures between 900° to 1200 °C respectively. Unaltered biotite pyroxenites have an average mole fraction CaTs component of ~4 mole %, and syenites and monzonites have average mole fraction CaTs components of ~6 mole % (Yavuz, 2001), which could be interpreted as indicating that Lorraine diopsides equilibrated at <10 kbar. However in these equilibria, the anorthite content of plagioclase must also be considered. As shown below, plagioclase at Lorraine show evidence of low temperature re-equilibration (<550 °C; Figs. 6-30), whereas diopside is inferred to have equilibrated at ~720 °C (Chapter 8). Therefore the plagioclase-diopside geobarometer was not applied to these rocks.

6.3.2. Comparison of diopsides from Lorraine rocks with clinopyroxene from Fijian and Nicola Group shoshonitic lavas

Lorraine diopside compositions were compared with clinopyroxenes from Fijian shoshonitic lavas (Leslie, 2004; A.J. Crawford, unpublished data). Clinopyroxenes from

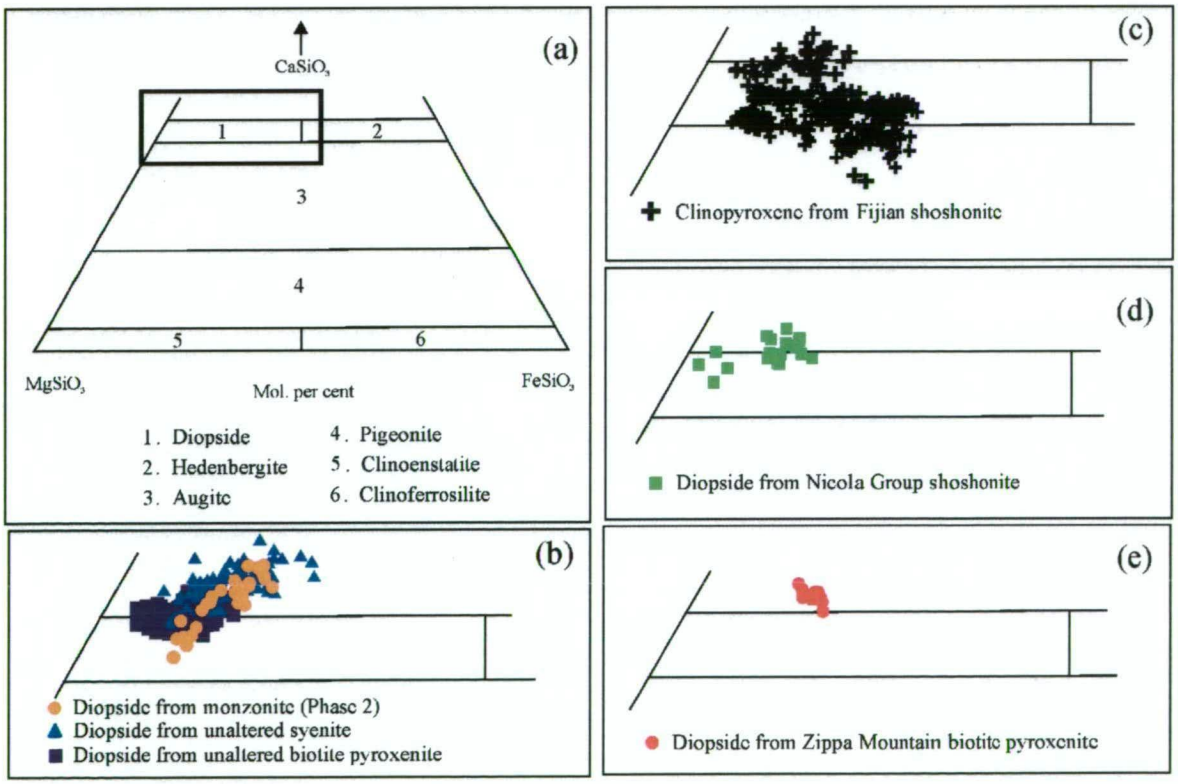

Figure 6-4. **(a)** Nomenclature of clinopyroxenes diagram after Morimoto (1988). Composition of **(b)** pyroxene from unaltered biotite pyroxenite, monzonite and syenite of Lorraine, **(c)** clinopyroxene from Fijian shoshonite lavas (data provided by A.J. Crawford and sourced from Leslie, 2004), **(d)** pyroxene from Nicola Group shoshonite lavas. Data for Nicola Group shoshonites from Bath and Logan (unpublished data; Appendix E) and **(e)** pyroxene from Zippa Mountain biotite pyroxenite (Appendix F). Note all data is EPMA.

Fijian shoshonites range from diopside to augite in composition (Morimoto, 1988; Fig. 6-4c). Clinopyroxene compositions from the biotite pyroxenite overlap with the field for Fijian clinopyroxenes on the classification diagram of Morimoto (1988; Fig. 6-4b, c); although diopsides from Lorraine monzonites and syenites are on average more calcium-rich than Fijian clinopyroxenes (Fig. 6-5g).

Clinopyroxenes from Fijian shoshonites have *mg*-numbers between 74 and 97, and predominantly overlap with the range of *mg*-number for Lorraine diopsides (i.e. 76 to 97; Figs. 6-3a-h and 6-5a-h). Plots of Si, Al, Cr, Ca, Ni, V, Y and Co vs. *mg*-number for Lorraine diopsides predominantly overlap with the field for Fijian diopsides (Figs. 6-3 and 6-5); however Lorraine diopsides are enriched in Na, Sr, La and Zn relative to diopsides with the equivalent *mg*-number from Fiji. Titanium is on average lower in diopside from biotite pyroxenite compared to Fijian clinopyroxenes; although diopside in syenite and monzonite mainly overlap with the field for Fijian clinopyroxenes.

Clinopyroxenes from the Nicola Group shoshonitic lavas predominantly plot in the diopside field (Rock, 1990; Fig. 6-4d), and have *mg*-numbers between 83 and 98 (Figs. 6-5a-h and 6-6a-h). Lorraine diopsides overlap with the field for Nicola Group basalts for Fe^{3+} (calculated), Ca and Y. In contrast, Nicola Group diopsides predominantly have lower Si, Na, Zr, Sr relative to Lorraine diopsides at equivalent *mg*-numbers. Nicola Group diopsides also have, on average, higher amounts of Al and Ti compared to Lorraine diopsides with the equivalent *mg*-number (Fig. 6-5b, c). The crystallisation of diopside at greater pressure could potentially explain the higher average amounts of Al in Nicola Group diopsides compared to Lorraine diopsides. In particular the Nicola Group diopsides may have crystallised from magma sources at greater depths relative to the latter, prior to eruption. Alternatively diopsides in Nicola Group shoshonites may have crystallised from a more Al- and Ti-rich magma.

Diopsides in biotite pyroxenite have similar amounts of Mn to diopside in Nicola Group shoshonite, whereas syenites and monzonites are notably enriched in Mn relative to diopsides with the equivalent *mg*-number. Chromium in diopside from Nicola Group basalts increases with *mg*-number and overlaps with compositions of diopside from Lorriane biotite pyroxenite.

Sodium is distinctly enriched in diopside from Lorraine rocks compared to clinopyroxene from Fijian shoshonite and Nicola Group basalts (Fig. 6-5h). The relative enrichment of Na in Lorraine diopsides may be explained by the substitution of either jadeite ($NaAlSi_2O_6$)

→

Figure 6-5. Select major elements vs. *mg*-number for diopside from unaltered biotite pyroxenite, unaltered syenite and monzonite. Fields include diopside composition of Fijian shoshonite (black dashed line), Nicola Group shoshonite (green) and Zippa Mountain diopside (red line). Fields for Fijian shoshonite provided by A.J. Crawford (unpublished data). Note all data is from EPMA analysis.

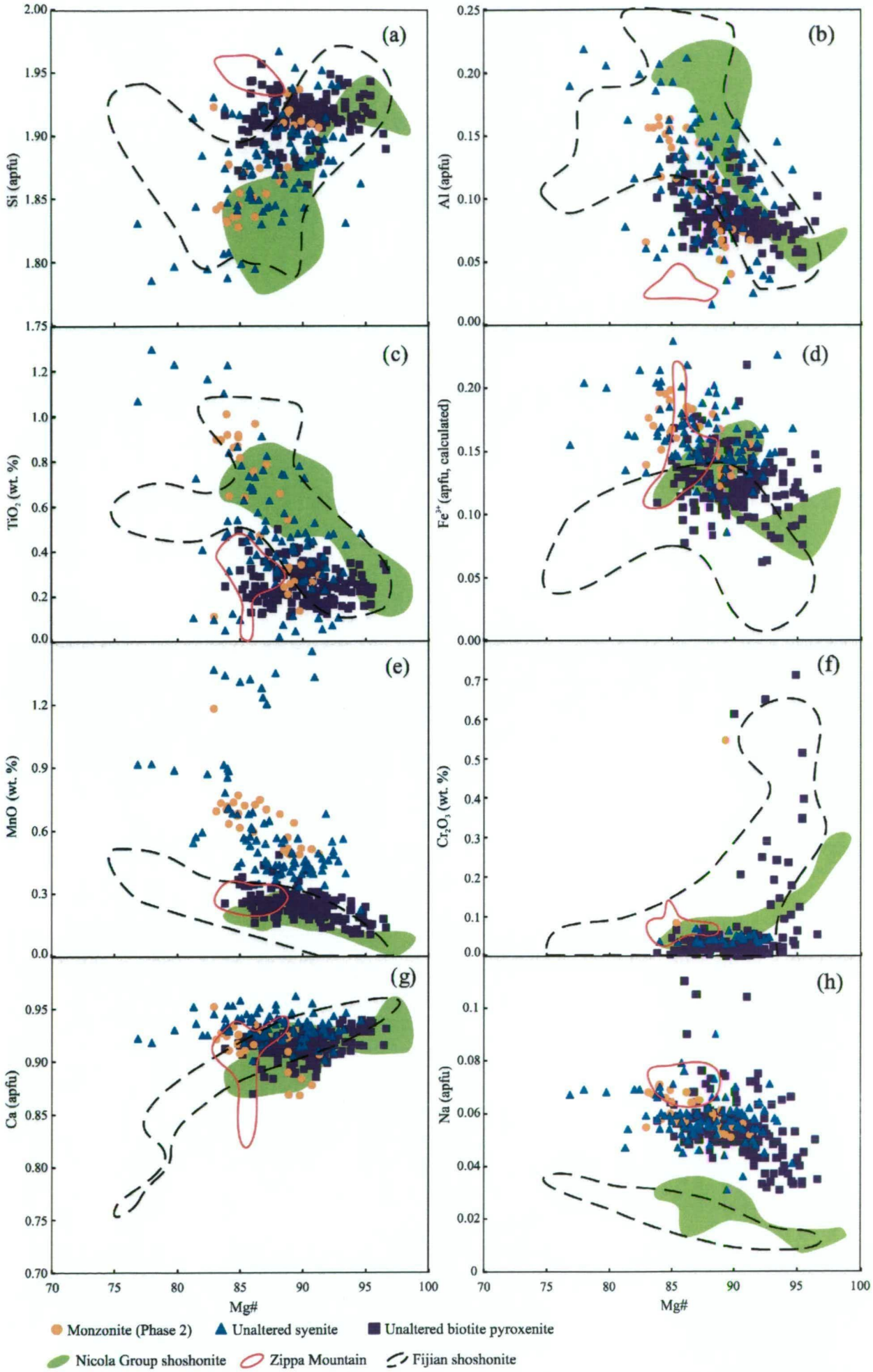
(a)
(b)
(c)
(d)
(e)
(f)
(g)
(h)
Si (apfu)
Al (apfu)
TiO2 (wt. %)
Fe3* (apfu, calculated)
MnO (wt. %)
Cr2O3 (wt. %)
Ca (apfu)
Na (apfu)
Mg#
Mg#
Monzonite (Phase 2)
Unaltered syenite
Unaltered biotite pyroxenite
Nicola Group shoshonite
Zippa Mountain
Fijian shoshonite

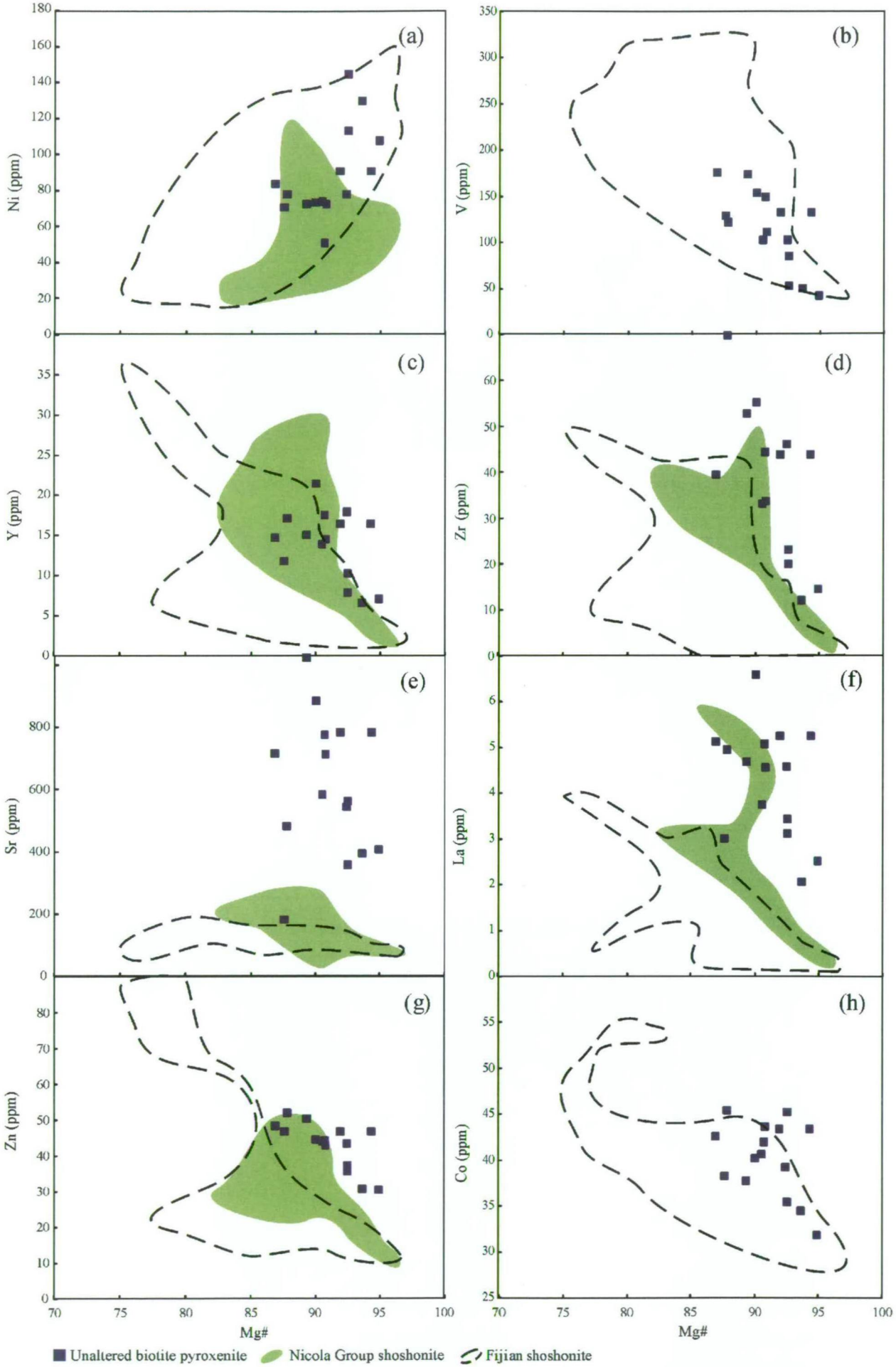
(a)
Ni (ppm)
(b)
V (ppm)
(c)
Y (ppm)
(d)
Zr (ppm)
(e)
Sr (ppm)
(f)
La (ppm)
(g)
Zn (ppm)
(h)
Co (ppm)
Mg#
Mg#
Unaltered biotite pyroxenite
Nicola Group shoshonite
Fijian shoshonite

Figure 6-6. Select trace elements vs. *mg*-number for diopsides from unaltered biotite pyroxenite. Fields include diopside compositions of Fijian shoshonite (black dashed line) and Nicola Group shoshonite (green). Data for Fijian shoshonite provided by A.J. Crawford (unpublished data), and Nicola Group shoshonites from Bath and Logan (unpublished data; Appendix E). Note all data, except *mg*-number is from LA-ICP-MS analysis. Magnesium and iron data is derived from EPMA analysis.

or aegirine ($NaFe^{3+}Si_2O_6$) component into diopside. Lorraine diopsides contain very minor amounts of M-site Al (i.e. avg. = 0.003 apfu) compared to Na (i.e. avg. = 0.06 apfu), and therefore the jadeite component of diopside appears to be very low. In contrast, Fe^{3+} is calculated to be relatively abundant in the M-site (i.e. avg. = 0.14 apfu) of Lorraine diopsides, which supports the contention that aegirine controls Na-substitution into diopsides (i.e. avg. Lorraine diopside has ~6 mole % aegirine). The positive correlation between Na and Fe^{3+} supports this conclusion (Fig. 6-7).

Deer et al (1978; 1992) suggested that the aegirine component of diopsides tends to increase with decreasing temperature for the aegirine-diopside binary system. Hence the relatively higher abundance of aegirine component in Lorraine diopsides compared to clinopyroxenes from Fijian and Nicola Group shoshonites could be inferred to indicate that diopside from Lorraine equilibrated at lower temperatures. The fact that Lorraine diopsides are hosted by intrusive bodies supports the contention that diopsides in these rocks formed in a relatively slow cooling environment compared to clinopyroxene in Fijian and Nicola Group lavas. The slow cooling environment likely allowed Lorraine diopsides to equilibrate at lower temperatures. Alternatively a precursor melt with a relatively higher activity of Na and Fe3+ could also explain the relatively higher abundance of these elements in diopsides from Lorraine compared to diopsides from the Nicola Group.

6.3.3. Comparison of diopside from biotite pyroxenites from Lorraine and Zippa Mountain

Major elements in clinopyroxene from biotite pyroxenite of the zoned Zippa Mountain intrusive complex, are compared with diopside from biotite pyroxenite from Lorraine on figures 6-4 and 6-5. Zippa Mountain clinopyroxenes plot above the diopside field towards wollastonite endmember on the Morimoto (1988; Fig. 6-4e) classification diagram. Zippa Mountain diopsides have *mg*-number between 83 and 89, and on average have higher Si, Na, Fe^{3+} (calculated) and Cr, but lower Al and Ca compared to Lorraine biotite pyroxenites with the equivalent *mg*-number (Fig. 6-5). Manganese and Ti abundance in diopsides from both Lorraine and Zippa Mountain pyroxenites are similar. The lower abundance of Al and higher abundance of Na in Zippa Mountain diopsides (Fig. 6-5b, h), compared with Lorraine diopsides, is consistent with the equilibration of Zippa Mountain diopsides at relatively lower pressures (i.e. CaTs ~2 vs. ~4 mole %) and lower temperatures (i.e. aegirine component ~8 mole % vs. ~6 mole % for Lorraine). Alternatively, Zippa Mountain diopsides may have crystallised from a magma that was comparatively Al-poor and Na-rich.

6.3.4. Rare earth elements in clinopyroxene from Lorraine biotite pyroxenite, Fijian shoshonite and Nicola Group shoshonite

Rare earth elements in diopsides from biotite pyroxenite, Fijian shoshonite, and Nicola Group shoshonite were chondrite normalised and plotted onto multi-element diagrams (Fig. 6-8a-c; Sun and McDonough, 1989). The group of diopsides from Lorraine biotite pyroxenite have *mg*-numbers between 90 and 95. Dotted lines show the upper and lower REE range of clinopyroxene from Fijian and Nicola Group shoshonites with *mg*-numbers between 90 and 95. Clinopyroxene from Fijian and Nicola shoshonites with *mg*-numbers between 90 and 95 have a lower abundance of REE compared to diopsides with *mg*-numbers <90. They also have a lower abundance of REE compared to diopsides from Lorraine biotite pyroxenites with the equivalent *mg*-number.

The substitution of REE occurs into the M2-site of clinopyroxene is thought to be facilitated by two different components $(Na_{0.5}REE_{0.5})MgSi_2O_6$ and $(REE)MgAlSiO_6$ (Wood and Blundy, 1997, 2001; Francis and Minarik, 2008). Hence an increase in the abundance of Na or Al in clinopyroxenes may result in an increase in the abundance of REE in clinopy-

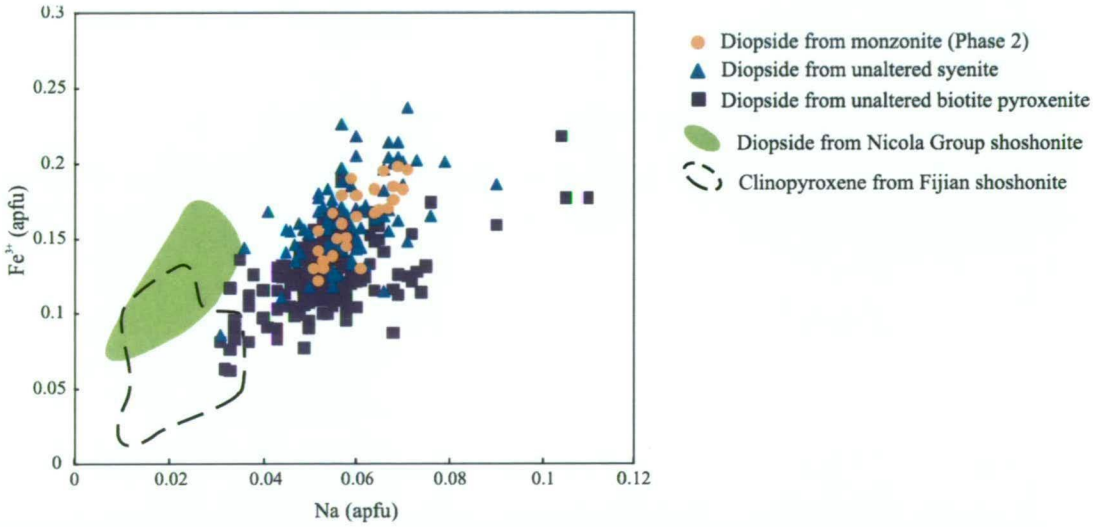

Figure 6-7. Fe^{3+} versus Na (apfu) for diopside from Lorraine rocks. The figure also includes fields for clinopyroxene from Fijian shoshonites and Nicola Group shoshonites (apfu = atoms per formula unit). Note all data is from EPMA analysis.

roxene. Lorraine diopsides are enriched in Na compared to clinopyroxenes from Fijian and Nicola Group shoshonites, and therefore it appears most likely that the higher abundance of REE in Lorraine diopsides, with the equivalent *mg*-number, could be explained by the substitution of Na + REE ↔ 2 Ca into the M2-site. Alternatively, a higher activity of REE in ultrabasic magmas may explain the higher abundance of REE in Lorraine diopsides relative to clinopyroxene from Fijian or Nicola Group shoshonites.

Diopside from all above rock types are relatively enriched in MREE. The Lorraine pyroxenites are most anomalous in Nd, whereas diopside from Fijian shoshonites and Nicola Group basalts are most anomalously enriched in Sm. The above REE patterns are consis-

tent with the contention that MREE partition preferentially into clinopyroxene relative to alkalic mafic magmas (e.g., Fedele et al., 2009).

6.3.5. Effects of alteration on diopside compositions in biotite pyroxenite

The major and trace element geochemistry of diopside in mineralised biotite pyroxenites were compared with diopside in unaltered biotite pyroxenites. Back-scattered electron images and microprobe data show that diopsides in mineralised biotite pyroxenite have irregular-shaped outer zones with lower mg-number compared to cores (Fig. 6-9b). However in contrast, diopsides in unaltered biotite pyroxenite do not show the irregular zonation pattern (Fig. 6-9a). Diopside from mineralised biotite pyroxenite have outer zones with mg-numbers <85, and less abundant Ni and Sr, but on average, altered rims are more abundant in Al, Ti, Mn, V, Y, Fe3+ and Zr compared to their cores and diopsides from un-

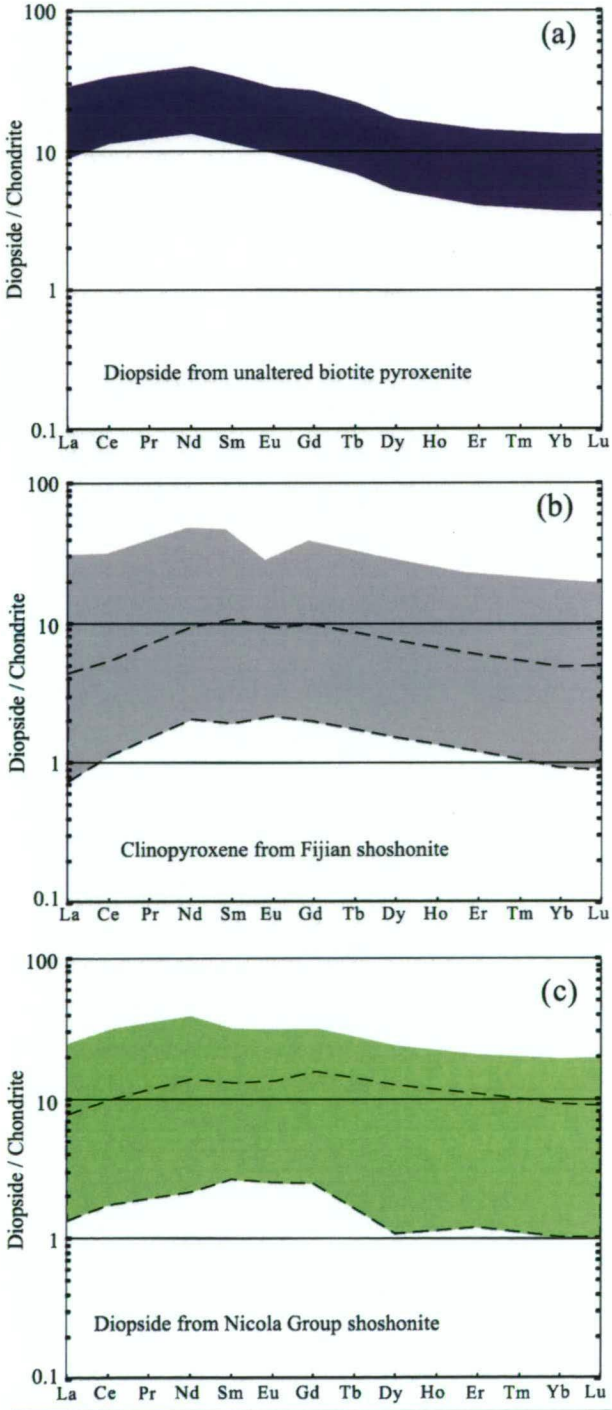

Figure 6-8. Chondrite normalised REE patterns (Sun and McDonough, 1989) for diopside from **(a)** unaltered biotite pyroxenite, **(b)** Fijian shoshonite and **(c)** Nicola Group shoshonite. Data for Fijian shoshonite provided by A.J. Crawford (unpublished data), and Nicola Group shoshonites from Bath and Logan (unpublished data). Note that all data is from LA-ICP-MS analysis.

altered biotite pyroxenite (Figs. 6-10a-h and 6-11a-h). Chromium and Ca concentrations are not significantly different in diopside from mineralised biotite pyroxenite vs. unaltered biotite pyroxenite.

The abundance of LREE in diopside from mineralised biotite pyroxenite are between 10 and 50 times chondrite value (Fig. 6-12b), and overlap with the range for diopsides from unaltered biotite pyroxenite (9 to 22 times chondrite). Medium and HREE composition of diopside from mineralised and unaltered biotite pyroxenites also overlap; however some diopsides from mineralised biotite pyroxenites are notably enriched in MREE and HREE. The higher abundance of REE in diopsides from mineralised biotite pyroxenite appears to reflect lower *mg*-numbers (i.e. grey dashed line denotes the range of REE compositions for diopsides with *mg*-number <85; Fig. 6-12b). Diopsides from mineralised biotite pyroxenites with lower *mg*-numbers are, on average, more abundant in Na and Al.

Also, some diopsides with *mg*-number <85 in mineralised biotite pyroxenite have negative Eu-anomalies. The diopsides with strong negative Eu-anomalies are from mineralised fine-grained feldspar rich patches in bornite-chalcopyrite mineralised biotite pyroxenites (Fig. 5-13c, d). These feldspar-rich patches with fine-grained diopside most likely represent the recrystallisation of the biotite pyroxenite during metasomatism, and therefore the unique strong negative anomalous Eu of these diopsides is most likely a product of metasomatism.

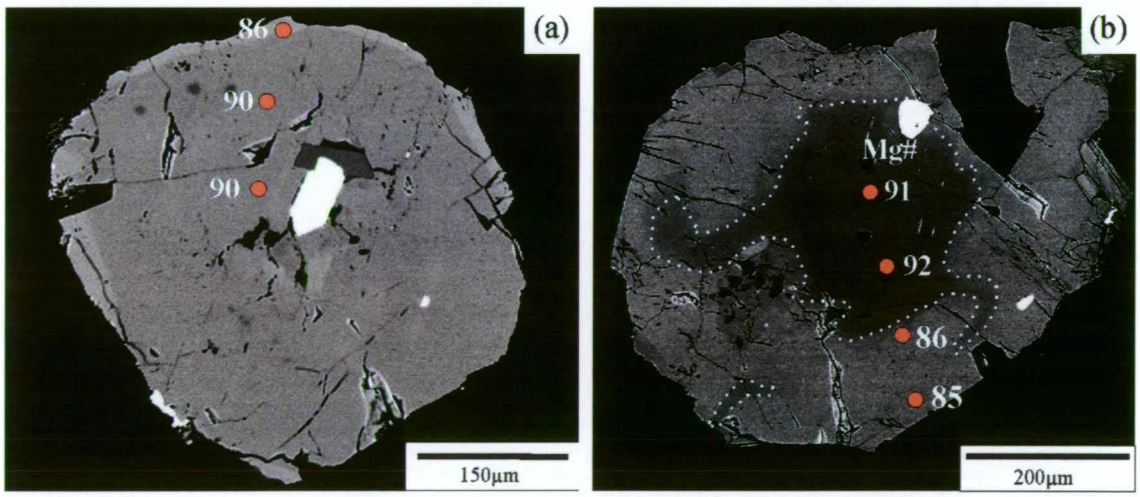

Figure 6-9. Back-scatter electron images of diopside from mineralised biotite pyroxenite and unaltered biotite pyroxenite from the Lower Main Zone. **(a)** Diopside in unaltered biotite pyroxenite shows only very minor evidence of compositional zoning along the rim (drill hole 2002-66_75 m). **(b)** Diopside in mineralised biotite pyroxenite has an inner darker core with Mg-number >90 and lighter rim with *mg*-number <86. The white dashed line denotes the contact between irregular darker patches and lighter patches (drill hole 2001-48_173.9 m).

Figure 6-10. Select major elements vs. *mg*-number for diopsides from unaltered biotite pyroxenite and mineralised biotite pyroxenite. Fields include diopside compositions from Fijian shoshonite (black dashed line) and Nicola Group shoshonite (green). Data for Fijian shoshonite provided by A.J. Crawford (unpublished data), and Nicola Group shoshonites from Bath and Logan (unpublished data). All EMPA data.

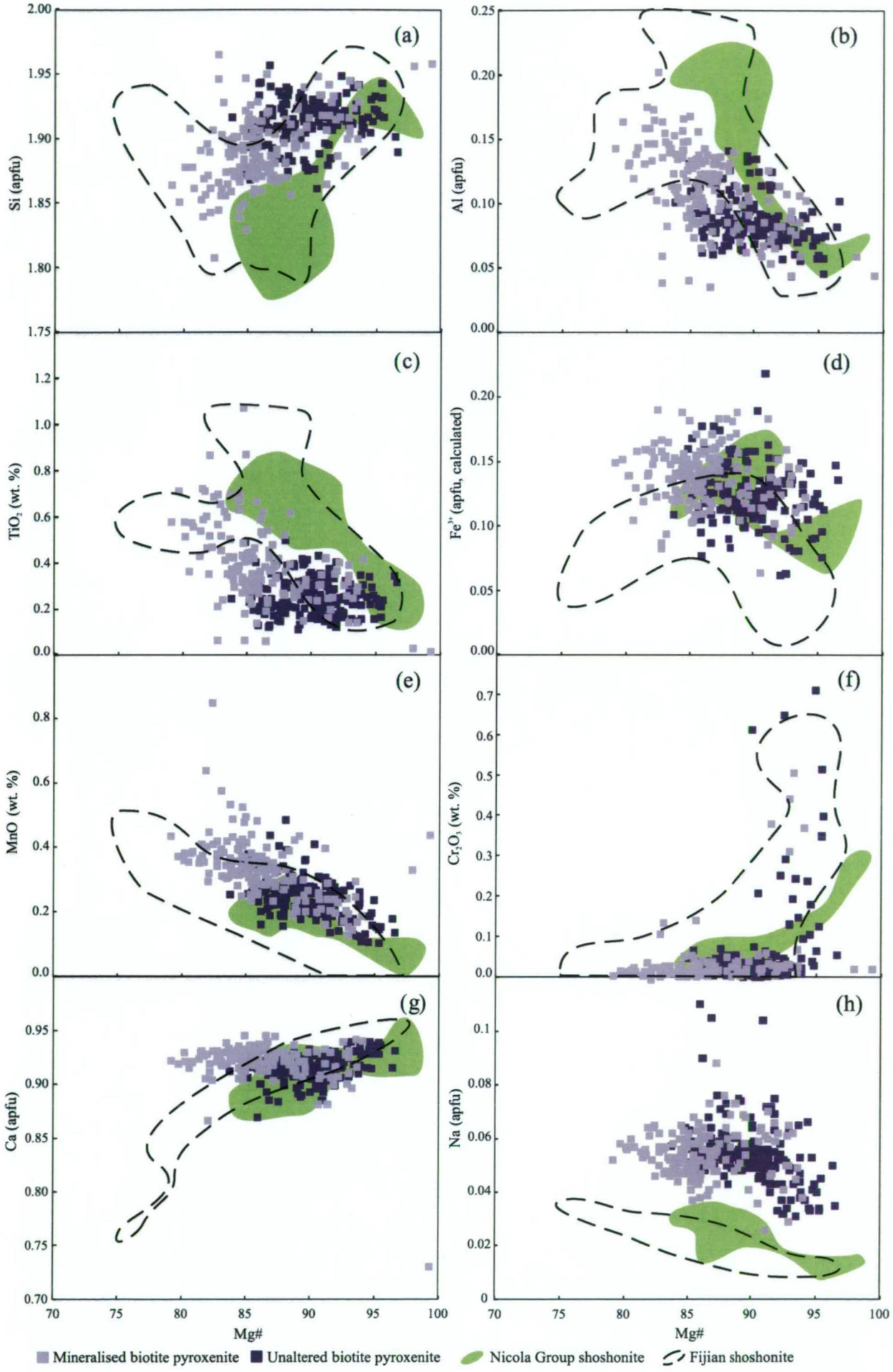
(a)
(b)
(c)
(d)
(e)
(f)
(g)
(h)
Si (apfu)
Al (apfu)
TiO2 (wt. %)
Fe3+ (apfu, calculated)
MnO (wt. %)
Cr2O3 (wt. %)
Ca (apfu)
Na (apfu)
Mg#
Mg#
Mineralised biotite pyroxenite
Unaltered biotite pyroxenite
Nicola Group shoshonite
Fijian shoshonite

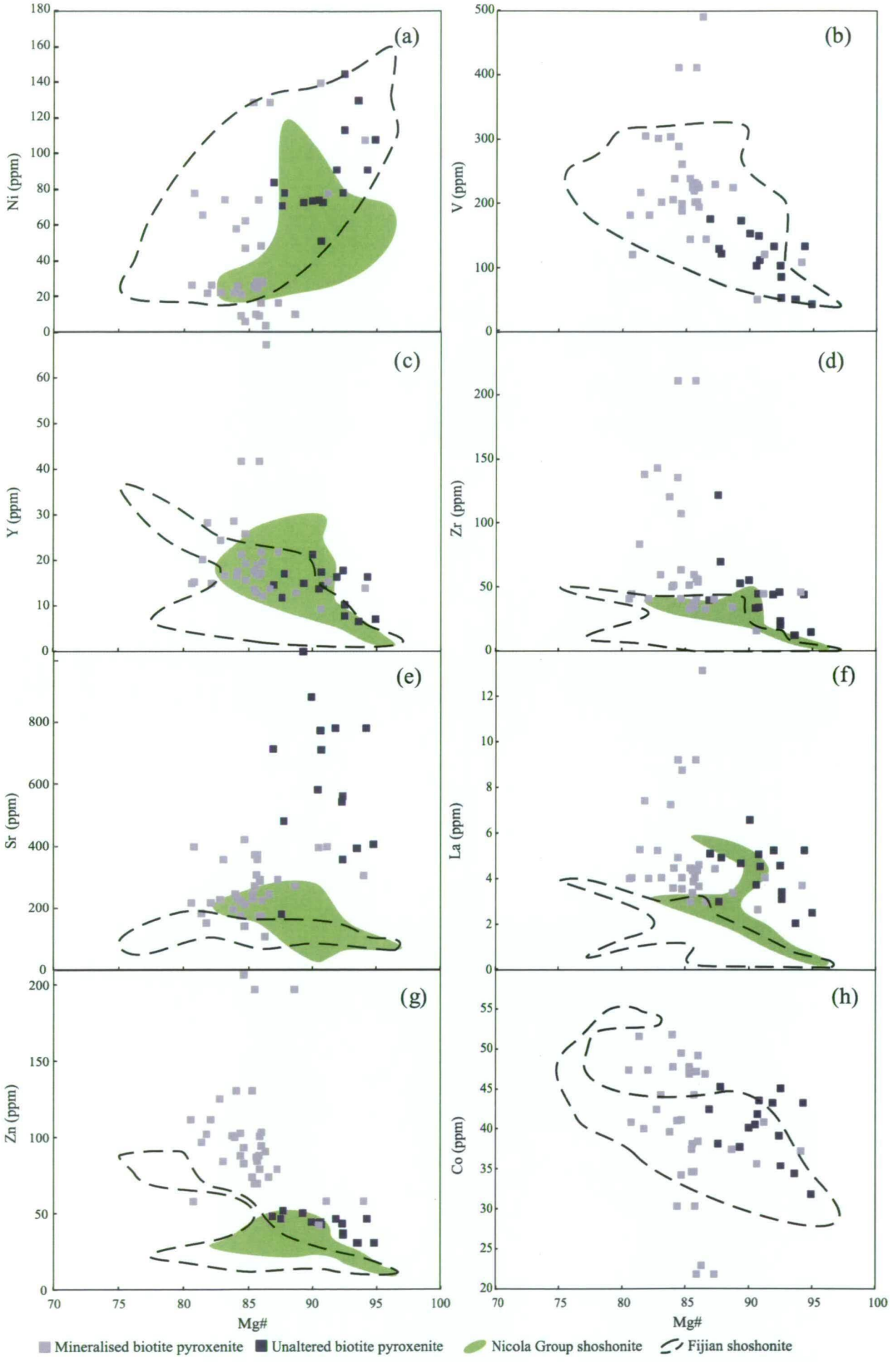
(a)
Ni (ppm)
(b)
V (ppm)
(c)
Y (ppm)
(d)
Zr (ppm)
(e)
Sr (ppm)
(f)
La (ppm)
(g)
Zn (ppm)
(h)
Co (ppm)
Mg#
Mg#
Mineralised biotite pyroxenite
Unaltered biotite pyroxenite
Nicola Group shoshonite
Fijian shoshonite

Figure 6-11. Select trace elements vs. *mg*-number for diopsides from unaltered biotite pyroxenite and mineralised biotite pyroxenite. Fields include diopside compositions from Fijian shoshonite (black dashed line) and Nicola Group shoshonite (green). Data for Fijian shoshonite provided by A.J. Crawford (unpublished data), and Nicola Group shoshonites from Bath and Logan (unpublished data). LA-ICP-MS data.

6.3.6. Copper composition of diopsides

The abundance of copper in diopside from mineralised and unaltered biotite pyroxenite, Nicola Group shoshonite and Fijian shoshonite were compared in Figure 6-13. Diopsides from Nicola Group and Fijian shoshonites show an increase in Cu with decreasing *mg*-number, which may reflect an increase in the activity of Cu in the melt during fractionation (A.J. Crawford, pers. commun., 2009). In contrast, diopsides from mineralised and unaltered biotite pyroxenites have relatively low Cu contents (i.e. < 3ppm, Fig. 6-13), and do not show a relative increase in Cu with decreasing *mg*-number. Hence, Lorraine diopsides, unlike Fijian and Nicola Group diopsides, show no evidence for an increase in Cu with fractionation or a loss of copper from diopside during slow cooling. The fact that diopside in both mineralised and barren biotite pyroxenites both contain very low concentrations of Cu is considered here to favour a model where Cu was introduced to biotite pyroxenite after the crystallisation of diopside, as opposed to the precipitation of primary magmatic sulphides from Cu-rich ultrabasic magmas.

Results show that some diopsides are relatively enriched in copper. These samples show elevated copper counts per second for the full duration of the LA-ICP-MS analysis, and hence do not appear to represent the ablation of large copper-rich inclusions (i.e. no obvious inclusion spikes). However it is possible that nano-size copper-rich inclusions occur in diopside. If so, then these inclusions are too small to see under using the SEM and must be uniformaly distributed to produce a constant elevated response. Why some samples are enriched in copper and others are not is unclear. The introduction of Cu to diopside

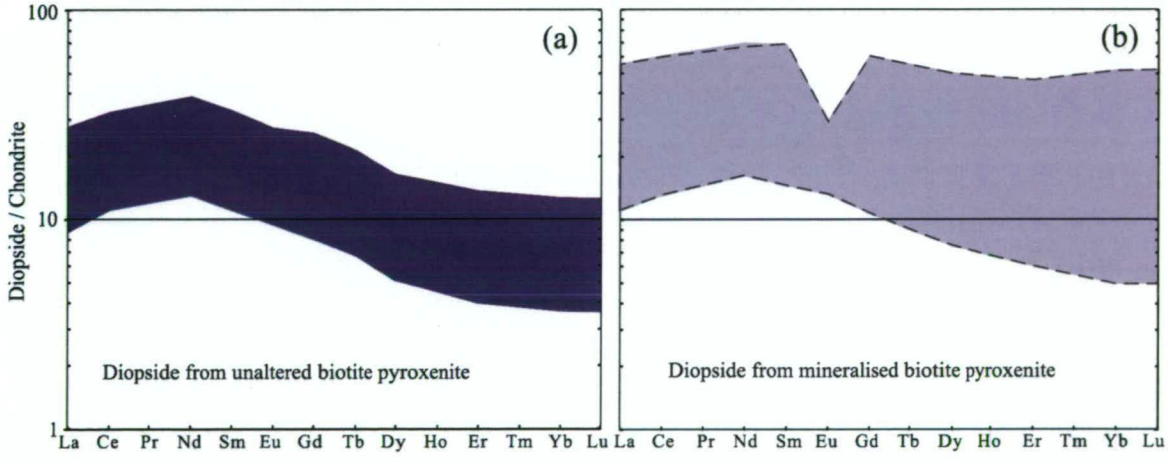

Figure 6-12. Chondrite normalised REE patterns (Sun and McDonough, 1989) for diopside from **(a)** unaltered biotite pyroxenite and **(b)** mineralised biotite pyroxenite. Dashed line shows the distribution of diopisde in altered biotite pyroxenite with *mg*-number <85. LA-ICP-MS data.

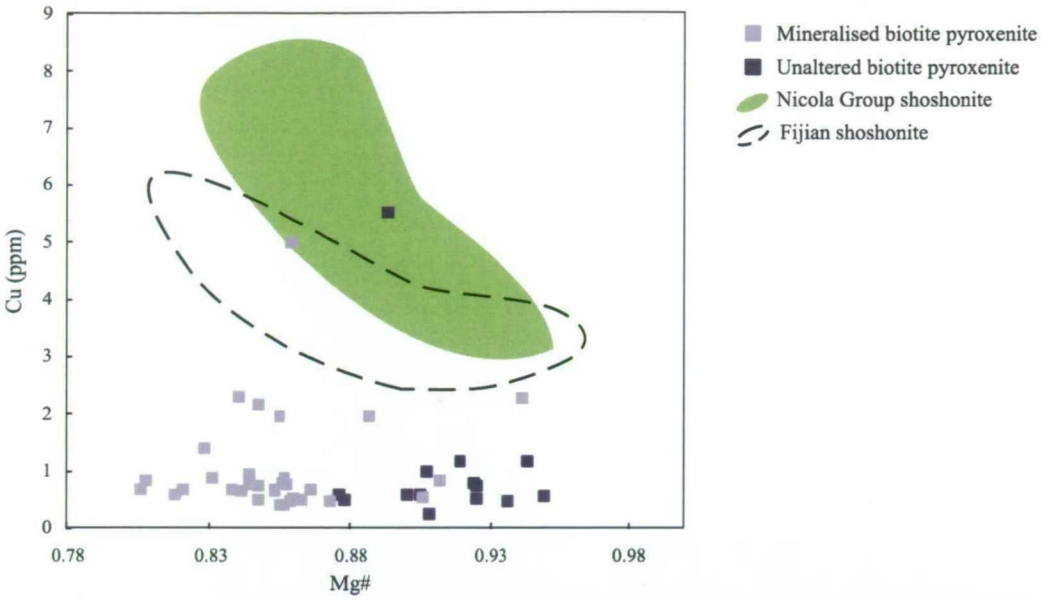

Figure 6-13. Cu vs. *mg*-number for diopsides from unaltered biotite pyroxenite and mineralised biotite pyroxenite. Note that diopsides from both mineralised and unaltered biotite pyroxenite contain less Cu than diopside from shoshonitic lavas. Lavas also show an increase in Cu with lower *mg*-number, which is not evident in Lorraine diopsides. Data for Fijian shoshonite provided by A.J. Crawford (unpublished data), and Nicola Group shoshonites from Bath and Logan (unpublished data). Cu is is LA-ICP-MS data, whereas *mg*-number was calculated from EPMA data.

during alteration is one possible explanation; however some of the highest-grade samples have diopsides with Cu values of <1 ppm, which is similar to unaltered samples. Hence there is no strong evidence for the loss or gain of Cu from diopside during metasomatism.

6.4. Biotite

6.4.1. Classification of Lorraine biotite

Microprobe analyses were entered into the MICA+ software program (Yavuz, 2003a, b) to calculate the formula of biotite. The MICA+ program calculated atoms per formula unit (apfu) for biotite based on 24 (O, OH, F and Cl) atoms, as well as calculating the water content of biotite, Fe^{3+}/Fe^{2+} ratios and *mg*-number. The composition of biotite was plotted on the International Mineral Association (IMA) recommended *mgli* (Mg-Li) vs. *feal* (Fe_{tot}+Mn+Ti) mica nomenclature diagram of Tischendorf et al. (2001). Biotites from unaltered biotite pyroxenite and monzonite have compositions consistent with Mg biotite (Fig. 6-14a, b).

Figure 6-14. **(a)** Nomenclature of micas (*mgli* vs. *feal* diagram after Tischendorf et al. (2001). **(b)** Composition of biotites from unaltered biotite pyroxenite and monzonite of Lorraine on the mica nomenclature diagram. **(c)** Biotites from unaltered biotite pyroxenite and monzonite from Lorraine plotted on a mole % ternary diagram of $Al_2O_3 - (CaO + Na_2O + K_2O) - (\sum FeO + MnO + MgO)$ of Deer et al. (2003). The ternary diagram shows discrimination fields for igneous biotite versus metamorphic biotite. **(d)** Lorraine biotites from unaltered biotite pyroxenite and monzonite on the ternary $10 \times TiO_2 - (FeO_{tot} + MnO) - MgO$ discrimination diagram for biotites (Nachit et al., 1985). **(e)** The composition of biotites from biotite pyroxenite and monzonite plotted on the binary Al_2O_3 vs. MgO tectonomagmatic discrimination diagram Abdel-Rahman (1994). **(f)** Biotites from unaltered biotite pyroxenite plotted on the binary Al_2O_3 vs. $\sum FeO$ diagram with evolutionary trends for micas from alkaline igneous rock types (after Mitchell, 1995). All EPMA data.

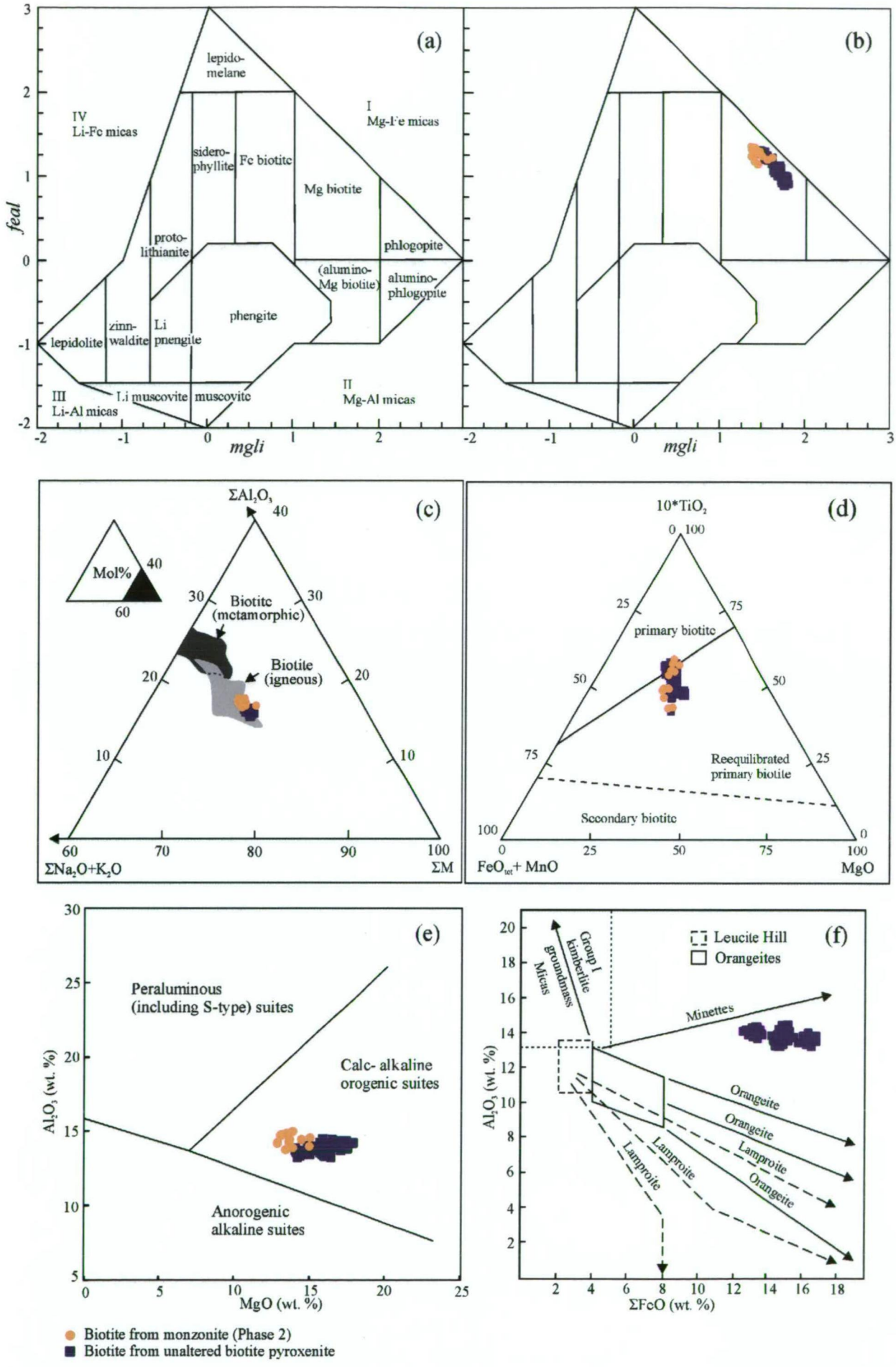
(a)
lepido-melane
IV Li-Fe micas
I Mg-Fe micas
sidero-phyllite
Fe biotite
Mg biotite
proto-lithianite
phlogopite
(alumino-Mg biotite)
alumino-phlogopite
phengite
zinn-waldite
Li pnengite
lepidolite
III Li-Al micas
Li muscovite
muscovite
II Mg-Al micas
feal
mgli
(b)
mgli
(c)
ΣAl2O3
Mol%
Biotite (metamorphic)
Biotite (igneous)
ΣNa2O+K2O
ΣM
(d)
10*TiO2
primary biotite
Reequilibrated primary biotite
Secondary biotite
FeOtot+ MnO
MgO
(e)
Peraluminous (including S-type) suites
Calc- alkaline orogenic suites
Anorogenic alkaline suites
Al2O3 (wt. %)
MgO (wt. %)
(f)
Leucite Hill
Orangeites
Group I kimberlite groundmass Micas
Minettes
Orangeite
Lamproite
Al2O3 (wt. %)
ΣFeO (wt. %)
Biotite from monzonite (Phase 2)
Biotite from unaltered biotite pyroxenite

Biotite from unaltered biotite pyroxenite and monzonite have compositions consistent with igneous biotite on the Al_2O_3 – (CaO+Na_2O+K_2O) – (FeO_{tot}+MnO+MgO) ternary discrimination diagram of Deer et al. (2003; Fig. 6-14c). Biotites have compositions that range from primary igneous to re-equilibrated primary biotite on the ternary 10 x TiO_2 – (FeO_{tot}+MnO) – MgO discrimination diagram of Nachit et al. (1985; 6-14d), and plot in the field for calc-alkaline orogenic field on the Al_2O_3 vs. MgO tectonomagmatic discrimination diagram of Abdel-Rahman (1994; 6-14e). Unaltered biotite pyroxenites contain biotites with compositions that appear to resemble biotites in minettes on the evolutionary trend of Al_2O_3 vs. ∑FeO (and Al_2O_3 vs. TiO_2) for biotite from mafic-ultrabasic alkaline igneous rocks (Mitchell, 1995; Fig. 6-14f). Biotites from monzonite plot in the same field as primary biotites from monzonites and granodiorites of the Santa Rita stock (Santa Rita porphyry Cu deposit, New Mexico, USA) on the F vs. X (Phl) diagram of Jacobs and Parry (1976; Fig. 6-15). Biotites from unaltered biotite pyroxenite have similar abundance of F, but relatively higher X (Phl) values compared to those from monzonite and granodiorite from the Santa Rita pluton.

6.4.2. Biotite in unaltered biotite pyroxenite and monzonite

Biotites from unaltered biotite pyroxenite have *mg*-number between 58 and 72, and Si and Al that increase with increasing *mg*-number and Ti, Fe^{3+} (calculated), Mn and F that decrease (Fig. 6-16a-h). Monzonite biotites have a lower range of *mg*-number (56 to 64) and are on average enriched in Al and Mn, but depleted in Si and Na compared to biotite

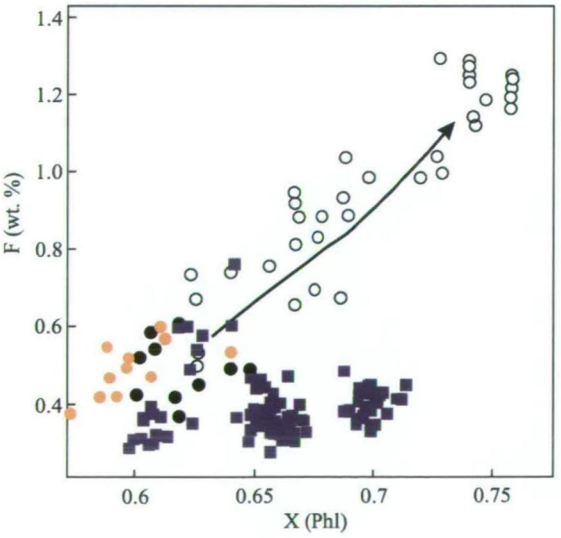

Figure 6-15. Comparison of the composition of biotites fromLorraine monzonite and unaltered biotite pyroxenite relative to primary igneous and secondary biotites from the Santa Rita pluton (New Mexico, USA) and Santa Rita porphyry-Cu deposit, respectively, on the F vs. mole fraction of phlogopite X (Phl) binary diagram (after Jacobs and Parry, 1976). EPMA data.

→

Figure 6-16. Select major elements vs. *mg*-number for biotites from unaltered biotite pyroxenite and monzonite. Fields include Zippa Mountain biotite (red line). EPMA data.

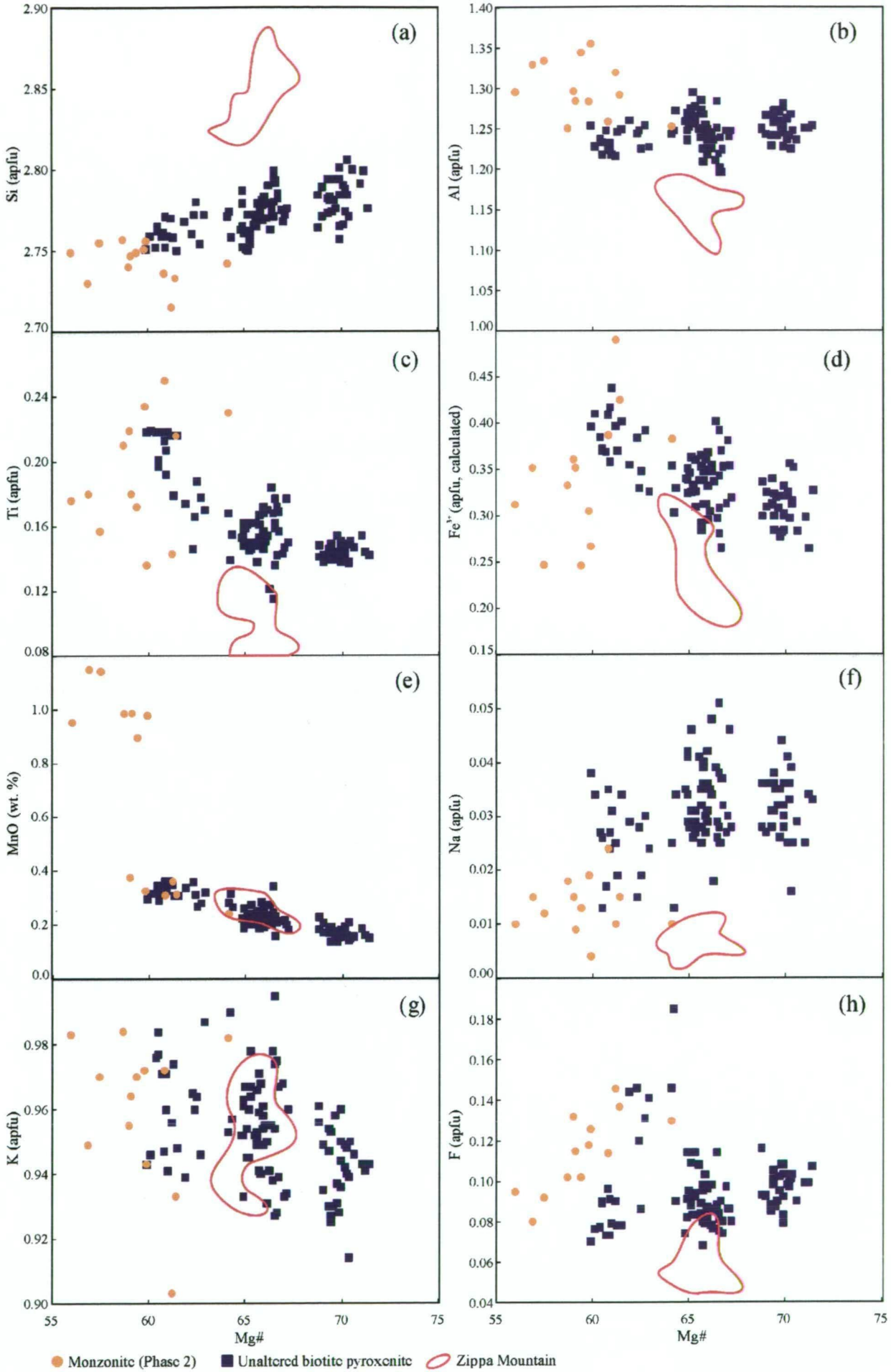
(a)
Si (apfu)
2.90
2.85
2.80
2.75
2.70
(b)
Al (apfu)
1.40
1.35
1.30
1.25
1.20
1.15
1.10
1.05
1.00
(c)
Ti (apfu)
0.24
0.20
0.16
0.12
0.08
(d)
Fe3+ (apfu, calculated)
0.45
0.40
0.35
0.30
0.25
0.20
0.15
(e)
MnO (wt. %)
1.0
0.8
0.6
0.4
0.2
0.0
(f)
Na (apfu)
0.05
0.04
0.03
0.02
0.01
0.00
(g)
K (apfu)
0.98
0.96
0.94
0.92
0.90
(h)
F (apfu)
0.18
0.16
0.14
0.12
0.10
0.08
0.06
0.04
55
60
65
70
75
Mg#
Monzonite (Phase 2)
Unaltered biotite pyroxenite
Zippa Mountain

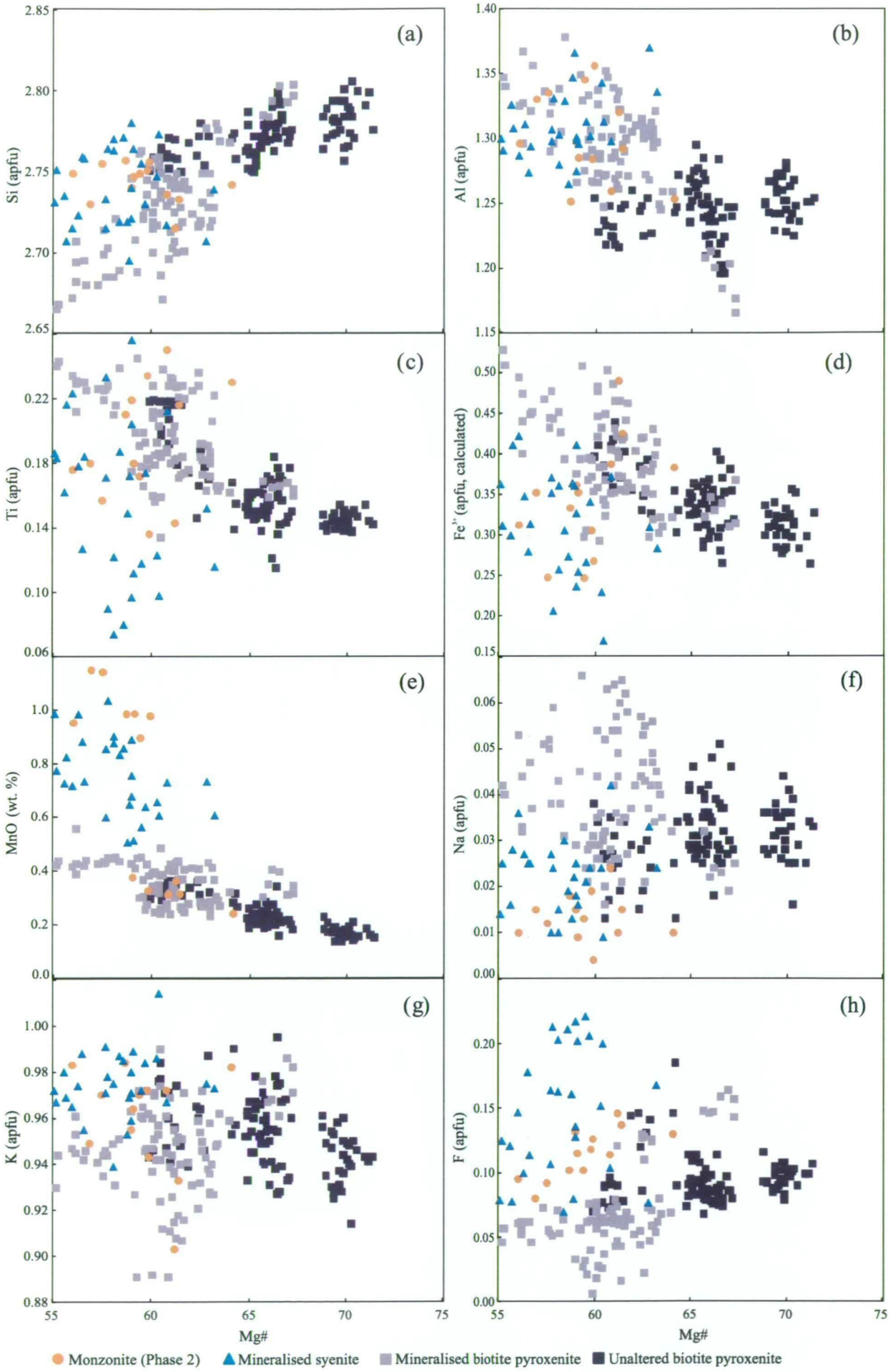
(a)
Si (apfu)
2.85
2.80
2.75
2.70
2.65
(b)
Al (apfu)
1.40
1.35
1.30
1.25
1.20
1.15
(c)
Ti (apfu)
0.22
0.18
0.14
0.10
0.06
(d)
Fe3+ (apfu, calculated)
0.50
0.45
0.40
0.35
0.30
0.25
0.20
0.15
(e)
MnO (wt. %)
1.0
0.8
0.6
0.4
0.2
0.0
(f)
Na (apfu)
0.06
0.05
0.04
0.03
0.02
0.01
0.00
(g)
K (apfu)
1.00
0.98
0.96
0.94
0.92
0.90
0.88
(h)
F (apfu)
0.20
0.15
0.10
0.05
0.00
55
60
65
70
75
Mg#
Monzonite (Phase 2)
Mineralised syenite
Mineralised biotite pyroxenite
Unaltered biotite pyroxenite

←

Figure 6-17. Select major elements vs. *mg*-number for biotites from unaltered biotite pyroxenite and monzonite relative to biotite from mineralised biotite pyroxenite and mineralised syenite. EPMA data.

from biotite pyroxenite. Trace elements Ni, Zr and Ba are enriched in biotite from biotite pyroxenite compared to monzonite (Fig. 6-18a, d, e). In contrast, Nb, Rb and Zn appear to be depleted in biotite from biotite pyroxenite compared to monzonite (Fig. 6-17c, f, g). A decrease in the abundance of Ni and an increase in the abundance of Rb and Zn are consistent with fractionation trends (i.e. compatible and incompatible elements respectively); however a decrease in Zr and Ba is at odds with fractionation trends. Alternatively, Zr and Ba may have partitioned into other phases, such as zircon and K-feldspar respectively, which are more common in felsic rock types.

6.4.3. Comparison of biotite from Lorraine biotite pyroxenite with Zippa Mountain biotite pyroxenite

Twenty biotite grains from Zippa Mountain biotite pyroxenite were analysed for major elements and compared with biotite from Lorraine pyroxenite. Zippa Mountain biotites have *mg*-number between 62 and 67, and are enriched in Si, but depleted in Al, Ti, Fe^{3+} (calculated), Na and F compared to biotite from Lorraine with the equivalent *mg*-number (Fig. 6-16a-h). Manganese and K abundance is comparable in Lorraine biotite pyroxenite and Zippa Mountain biotite pyroxenite. A notable lower abundance of Ti in biotite from Zippa Mountain may mean that Zippa Mountain biotites equilibrated at lower temperatures than Lorraine biotites (e.g., Henry et al., 2005). Alternatively Zippa Mountain biotites may have crystallised from an ultrabasic magma source that was relatively depleted in Ti, Al, Na and F, but enriched in Si.

6.4.4. Effects of alteration on biotite composition in Lorraine rocks

Biotites from mineralised biotite pyroxenites have lower *mg*-number of between 55 and 65, and are depleted in Si, Ni and F, but have higher Al, Ti, Fe^{3+} (calculated) and Mn compared to biotites from unaltered biotite pyroxenite (Figs. 6-17a and 6-18a-h). Biotites from mineralised biotite pyroxenites have a similar range of *mg*-number and Si, Al, Ti and K to those in unaltered monzonite and mineralised syenite; although Na and Fe^{3+} (calculated) are relatively more abundant, and F and Mn are relatively depleted in biotite from mineralised biotite pyroxenite compared to biotite from monzonite and mineralised syenite. The small shift in diopside *mg*-number and the large shift in biotite *mg*-number imply alteration temperature was lower than primary mineral equilibration. Biotites in Phase 1 syenites generally have similar compositions to Phase 2 monzonite. One exception is the amount of F in syenites, which is on average higher in mineralised syenites compared to unmineralised syenites (*see* section 6.9.4.).

Alteration is inferred to have resulted in the loss of Mg, Si, F and Ni from biotite in biotite pyroxenite. A possible sink for the release of Mg and F from biotite may be the biotite in

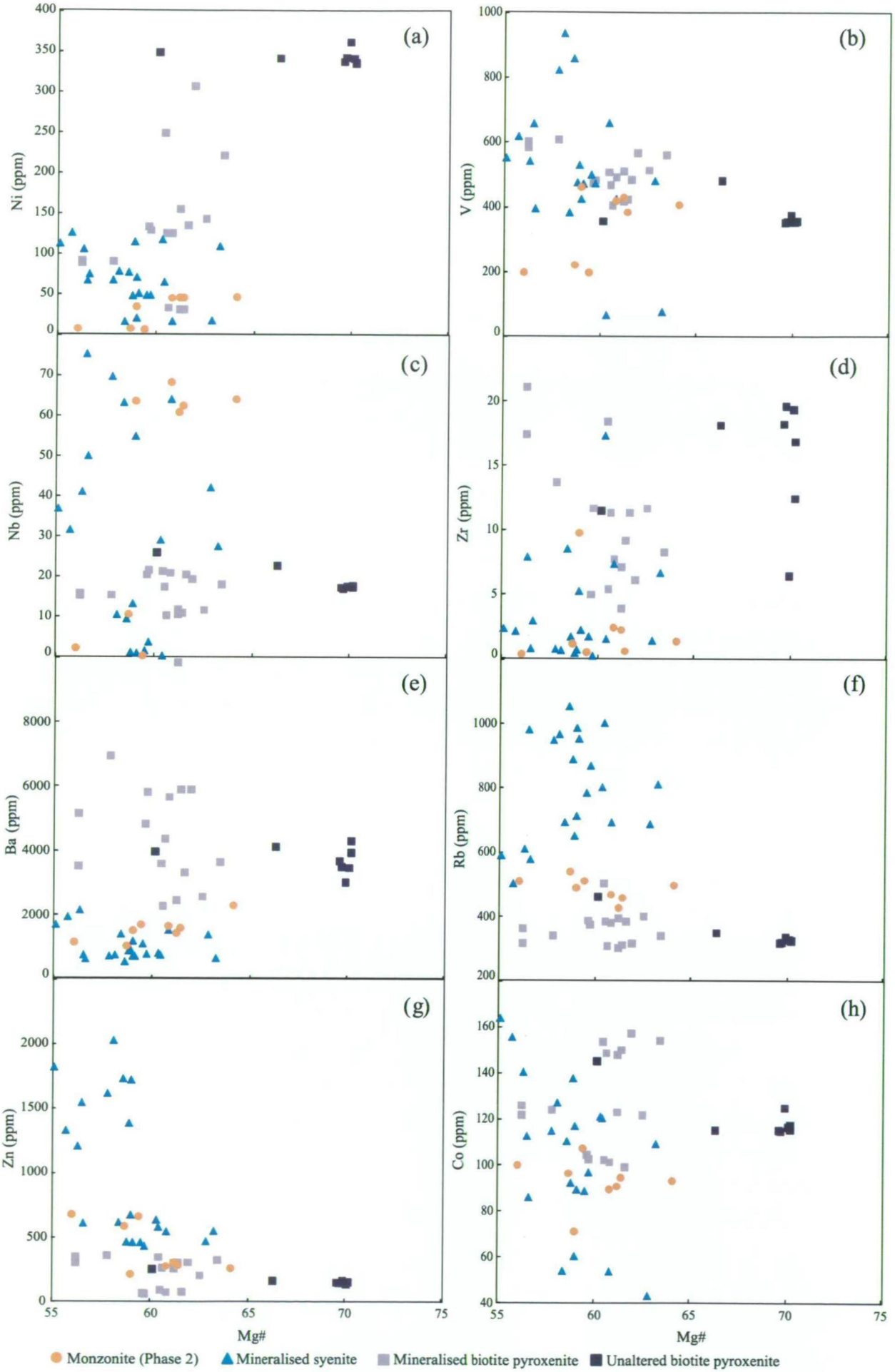
(a)
Ni (ppm)
(b)
V (ppm)
(c)
Nb (ppm)
(d)
Zr (ppm)
(e)
Ba (ppm)
(f)
Rb (ppm)
(g)
Zn (ppm)
(h)
Co (ppm)
Mg#
Mg#
Monzonite (Phase 2)
Mineralised syenite
Mineralised biotite pyroxenite
Unaltered biotite pyroxenite

Figure 6-18. Select trace elements vs. *mg*-number for biotites from unaltered biotite pyroxenite and monzonite relative to biotite from mineralised biotite pyroxenite and mineralised syenite. LA-ICP-MS data.

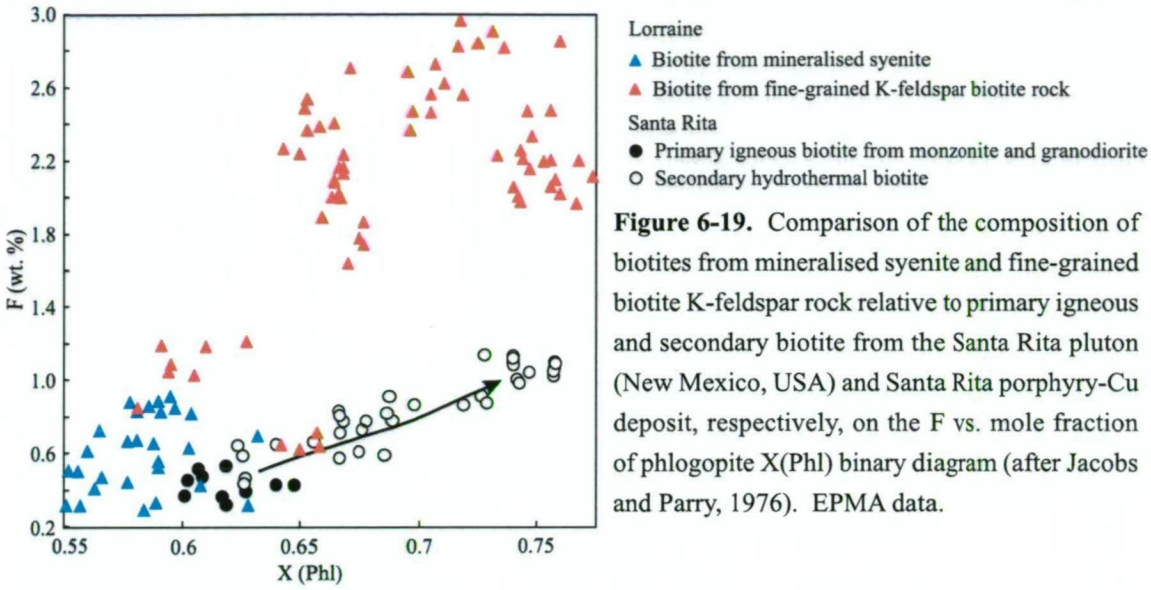

Figure 6-19. Comparison of the composition of biotites from mineralised syenite and fine-grained biotite K-feldspar rock relative to primary igneous and secondary biotite from the Santa Rita pluton (New Mexico, USA) and Santa Rita porphyry-Cu deposit, respectively, on the F vs. mole fraction of phlogopite X(Phl) binary diagram (after Jacobs and Parry, 1976). EPMA data.

fine-grained K-feldspar biotite rocks which are relatively enriched in Mg and F. Biotites in fine-grained K-feldspar biotite rocks are more enriched in F compared to secondary biotite from the Santa Rita porphyry-Cu deposit (New Mexico, USA; Jacobs and Parry, 1976; Fig. 6-19), and are also inferred to represent hydrothermal secondary biotite due to their spatial association with altered rocks and mineralisation in the central area of the Lower Main Zone (*see* Figs. 3-3 and 4-15a, b).

Secondary biotite in fine-grained K-feldspar biotite rock have variable amounts of Cu (i.e. <1 ppm to ~7000 ppm; Fig. 6-20). In the Lower Main Zone, the greatest amount of Cu-enrichment in biotite occurs in F-rich biotite in fine-grained biotite rocks from mineralised zones (Fig. 6-20). Copper enrichment in biotite is strongest along rims (i.e. particularly biotite with green rims; Fig. 6-21a; also *see* Chapter 5). The green margins of biotite that are also Ti-, Ba- and Fe-poor, and Mg-, F- and Cu-rich (Fig. 6-21a-f) and are inferred to

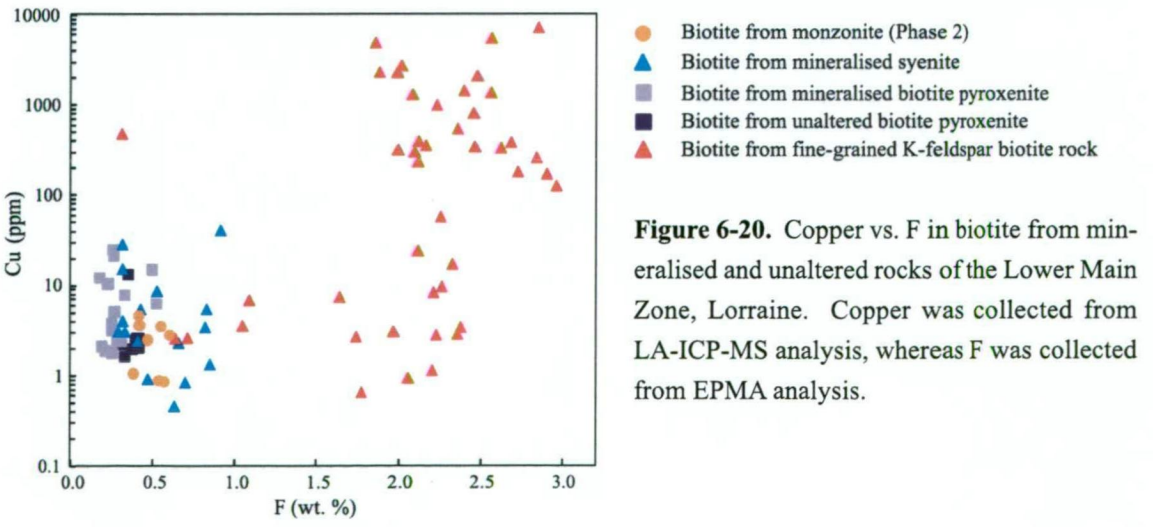

Figure 6-20. Copper vs. F in biotite from mineralised and unaltered rocks of the Lower Main Zone, Lorraine. Copper was collected from LA-ICP-MS analysis, whereas F was collected from EPMA analysis.

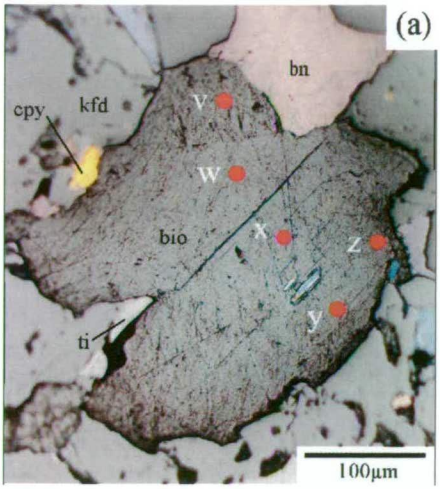

Figure 6-21. **(a)** Photomicrograph of F- and Cu-rich biotite (bio) from mineralised fine grained K-feldspar biotite rock from the Lower Main Zone (sample 07AB 14-2; 347325mE, 6200720mN) in reflected light. Red dots labelled v-z denote locations of EPMA. Other minerals in the photomicrographs include K-feldspar (Kfd), bornite (bn), chalcopyrite (cpy) and titanite (ti). **(b-f)** Chemical composition of the biotite grain shown in "a" for points v to z. Chemical compositions are from EPMA analysis.

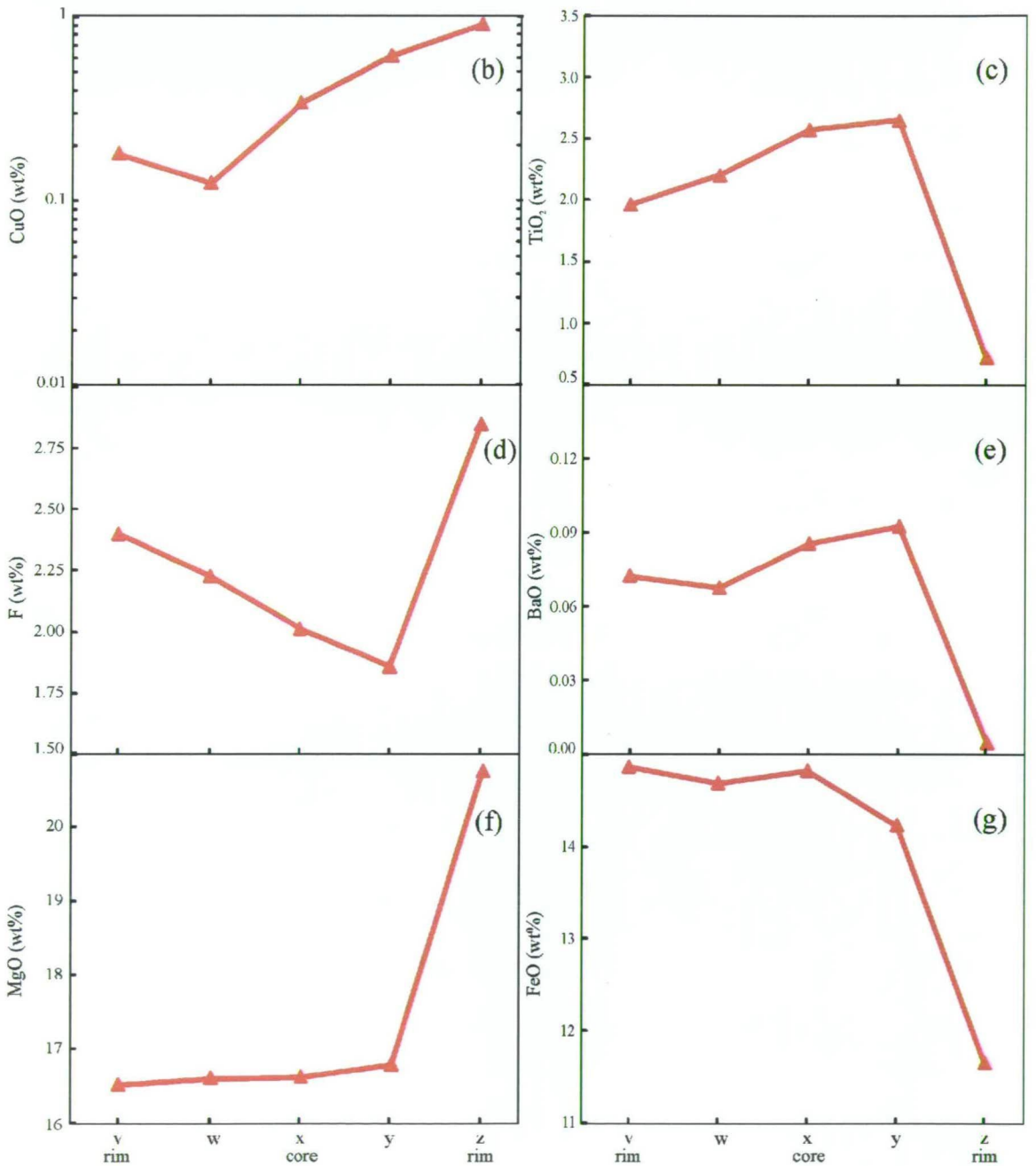

be related to main-stage mineralisation.

Hence, rocks from Lorraine contain primary igneous biotite, and/or secondary F-rich biotite. Primary igneous biotite in mineralised biotite pyroxenite contains lower *mg*-numbers compared to biotite in barren biotite pyroxenites. This likely reflects re-equilibration of biotite in mineralised biotite pyroxenites during alteration and mineralisation (*see* discussion).

6.5. Apatite

6.5.1. Classification of Lorraine apatite

Over 200 apatite grains from unaltered and mineralised biotite pyroxenite and fine-grained K-feldspar biotite rock were analysed using the EPMA, and approximately 40 grains from from mineralised and unaltered biotite pyroxenites were analysed using the LA-ICP-MS. All apatite are classified as fluor-apatite (Fig. 6-22).

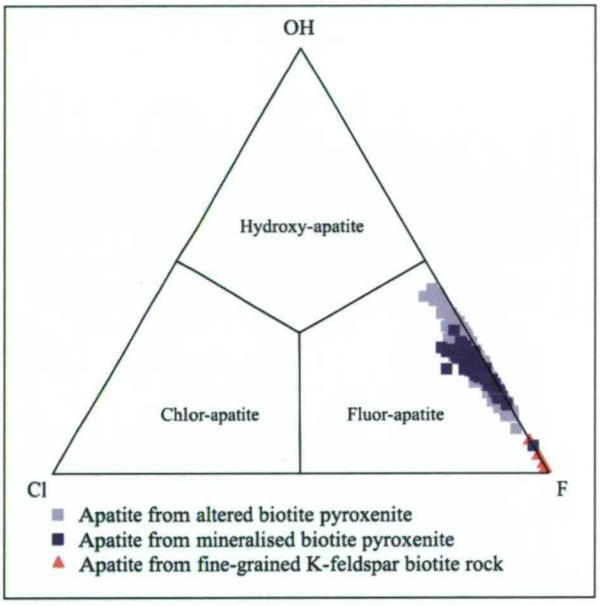

Figure 6-22. Composition and classification of apatite from unaltered biotite pyroxenite, mineralised biotite pyroxenite and fine-grained K-feldspar biotite rock on the OH – Cl – F ternary diagram. Adapted after Deer et al. (1992). Fluorine and Cl were collected from EPMA analysis.

6.5.2. Composition of apatite in unaltered and mineralised biotite pyroxenite

Apatites in unaltered biotite pyroxenites are fine-grained and contain 0.2 to 0.6 wt. % SO_3, whereas apatites in mineralised biotite pyroxenites are fine- to medium-grained and contain 0.2 to 1.1 wt. % SO_3 (Figs. 6-23a-h and 6-24a, b). Medium-grained apatites from mineralised biotite pyroxenite are enriched in SO_3 or show S-rich rims and S-poor cores (Fig. 6-24a, b).

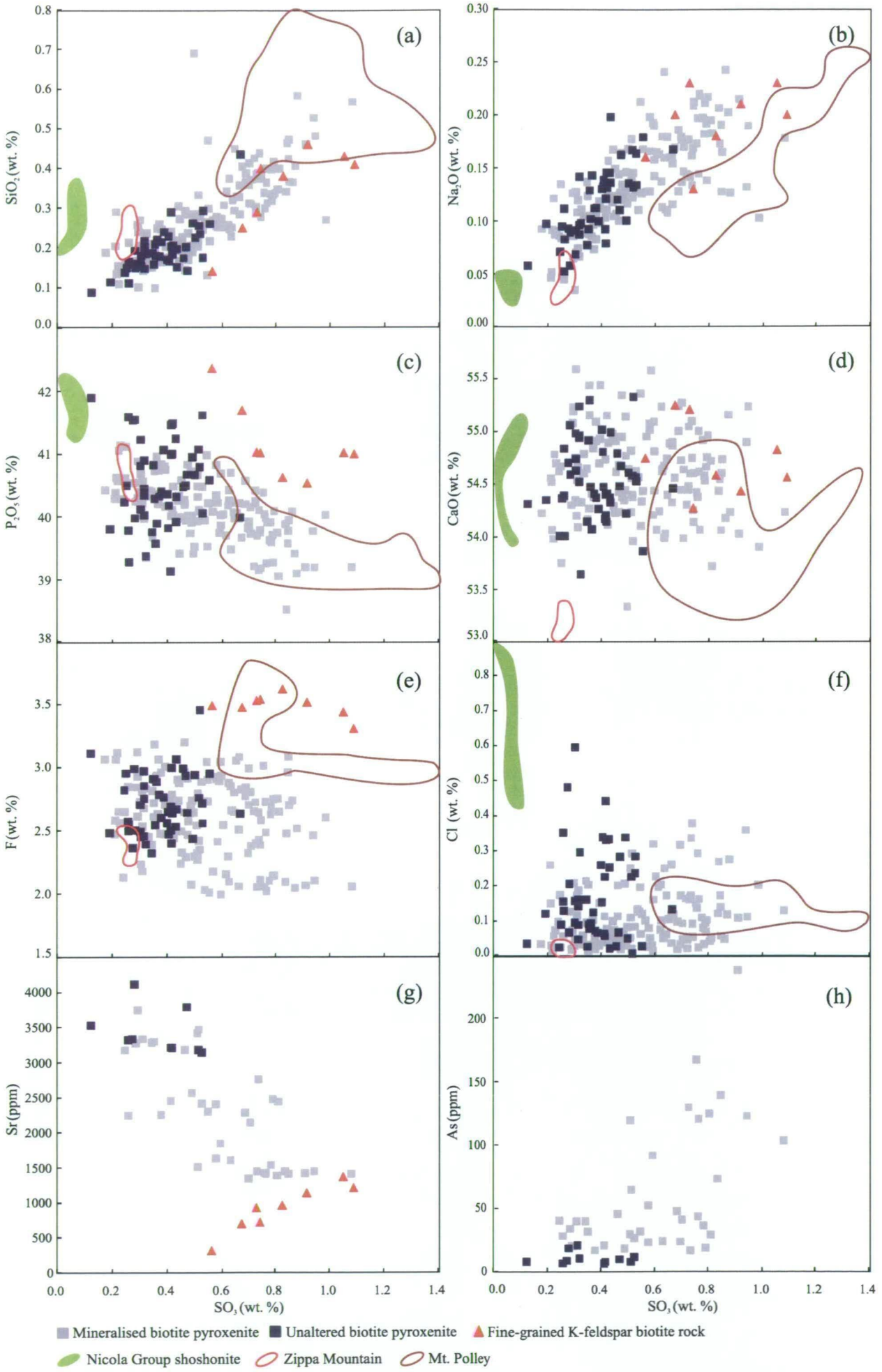
(a)
(b)
(c)
(d)
(e)
(f)
(g)
(h)
SiO2 (wt. %)
Na2O (wt. %)
P2O5 (wt. %)
CaO (wt. %)
F (wt. %)
Cl (wt. %)
Sr (ppm)
As (ppm)
SO3 (wt. %)
SO3 (wt. %)
Mineralised biotite pyroxenite
Unaltered biotite pyroxenite
Fine-grained K-feldspar biotite rock
Nicola Group shoshonite
Zippa Mountain
Mt. Polley

←

Figure 6-23. Select major and trace elements vs. SO_3 for apatites from unaltered biotite pyroxenite, mineralised biotite pyroxenite and fine-grained K-feldspar biotite rock. Fields include apatite from diopside-hosted melt inclusions from the Nicola Group shoshonite (green area), hydrothermal apatite from NE-zone (brown line) and apatite from Zippa Mountain biotite pyroxenite (red line). EPMA data.

Binary diagrams of Na_2O and SiO_2 vs. SO_3 show positive correlations (Fig. 6-23a, b), whereas P_2O_5 generally decreases with increasing SO_3 (Fig. 6-23c) for apatite from mineralised and unaltered biotite pyroxenite. These trends are consistent with common substitution reactions (Yuanming and Fleet, 2002, p.31):

$2\ P^{5+} = S^{6+} + Si^{4+}$

$P^{5+} + Ca^{2+} = S^{6+} + Na^{+}$

Apatites in fine-grained biotite K-feldspar rocks are notably enriched in F compared to apatite in mineralised and unaltered biotite pyroxenites. There is no obvious difference in the F composition of apatite in mineralised and unaltered biotite pyroxenites. No correlation was identified for CaO vs. SO_3 (Fig. 6-23d), and Fe and Mn are commonly below detection limits. Strontium is depleted in apatite from mineralised biotite pyroxenite compared to apatite from unaltered biotite pyroxenite (Fig. 6-23g). Arsenic in contrast, is more abundant in apatites from mineralised biotite pyroxenite compared to unaltered biotite py-

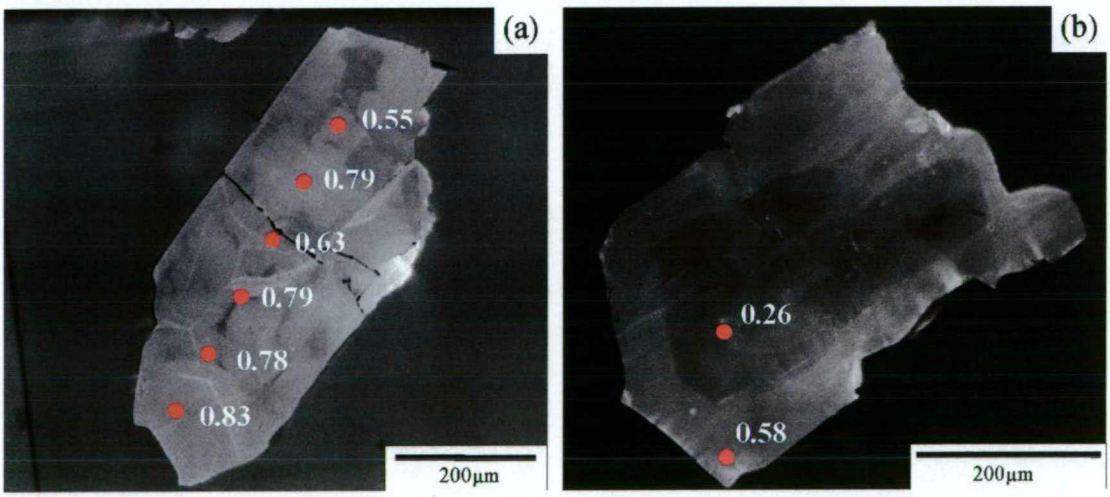

Figure 6-24. Apatite grains from altered biotite pyroxenite in CL with EMPA spot location (red dots) and SO_3 (wt. %) abundance. **(a)** Apatite from mineralised biotite pyroxenite that is enriched in S relative to apatite from unaltered biotite pyroxenite (drill hole 1996-44_244 m). **(b)** Apatite grain from mineralised biotite pyroxenite that is composed of a darker inner zone with SO_3 of 0.26 wt. %, and an outer brighter zone that is comparatively enriched in SO_3 (0.58 wt. %; sample drill hole 2002-58_158.3 m). It is inferred that the S-rich outer zone is apatite that grew as a hydrothermal overgrowth on pre-existing magmatic apatite.

roxenite (Fig. 6-23h), which likely reflects a relative increase in the activity of As during alteration. The volatile site of apatite grains from mineralised and unaltered biotite pyroxenite is dominated by F and OH (calculated), with Cl being a minor component, ranging from below detection limit (~450 ppm) to 0.6 wt. % (Fig. 6-23e, f).

6.5.3. Comparison of Lorraine apatite with apatite from Mount Polley ore, Nicola Group basalt and Zippa Mountain biotite pyroxenite

Apatite grains hosted in bornite-cement from the NE-zone at Mount Polley (N = 25), co-trapped apatite grains hosted in melt inclusions from the Nicola Group shoshonites (N = 4) and apatite grains hosted in biotite pyroxenite from Zippa Mountain pluton (N = 4) were analysed in this study for major elements using the EPMA. Results show that apatite in melt inclusions from Nicola Group shoshonites have the lowest concentration of SO_3 (<0.09 wt. %), Zippa Mountain biotite pyroxenite have intermediate compositions (0.23 to 0.27 wt. %) and apatite from the NE-zone have the highest concentration of SO_3 (0.6 to 1.37 wt. %; Fig. 6-23a-h). The low SO_3 content of apatite in melt inclusions from Nicola Group shoshonites may reflect a relatively low activity of SO_4^{2-} in mafic magmas during the crystallisation of apatite and diopside. In contrast, the high SO_3 content of apatite from the NE-zone may reflect a relative high activity of SO_4^{2-} in hydrothermal fluids.

Apatites from unaltered biotite pyroxenites have intermediate SO_3 contents that are comparable to apatite from Zippa Mountain biotite pyroxenite. In contrast, apatites in mineralised biotite pyroxenite and fine-grained biotite K-feldspar rock have SO_3 compositions which range from intermediate to high, and overlap with the composition of Zippa Mountain apatites and hydrothermal apatite from Mount Polley.

Silicon and Na also tend to be more enriched in apatite from Mount Polley ore zone and mineralised biotite pyroxenite and fine-grained biotite K-feldspar rock, which is consistent with the exchange reactions of P and Ca with Si, Na and S (*see* above). Chlorine is notably enriched in apatites in melt inclusions from Nicola Group shoshonites. The host melt inclusions also contain abundant Cl (i.e. ~1000 to 2200 ppm), which reflects a high activity of Cl in the magma during the crystallisation of Nicola Group apatite (*see* Chapter 7).

6.5.4. Rare earth elements in apatite

The rare earth element composition of apatite from mineralised and unaltered biotite pyroxenite was normalised to chondrite (Sun and McDonough, 1989), and plotted on chondrite-normalised diagrams (Fig. 6-25a and b). Apatites from both mineralised and unaltered biotite pyroxenite have similar average abundances of REE, and have slight negative Eu-anomalies. The REE composition of apatite from mineralised and unaltered bi-

otite pyroxenite was compared with the REE composition of hydrothermal apatite from the Mount Polley NE-zone, which is hosted in bornite cement. Lorraine apatites are comparatively enriched in MREE, but are depleted in LREE compared to Mt. Polley apatites (Fig. 6-25c). Mount Polley apatites show a more concave-up REE-pattern compared to Lorraine apatites. This may reflect the fact that LREE are relatively mobile in hydrothermal solutions compared to MREE and HREE (Jenner, 1996; Hollings and Wyman, 2004), and are therefore more likely to be relatively enriched in minerals that precipitate from hydrothermal solutions.

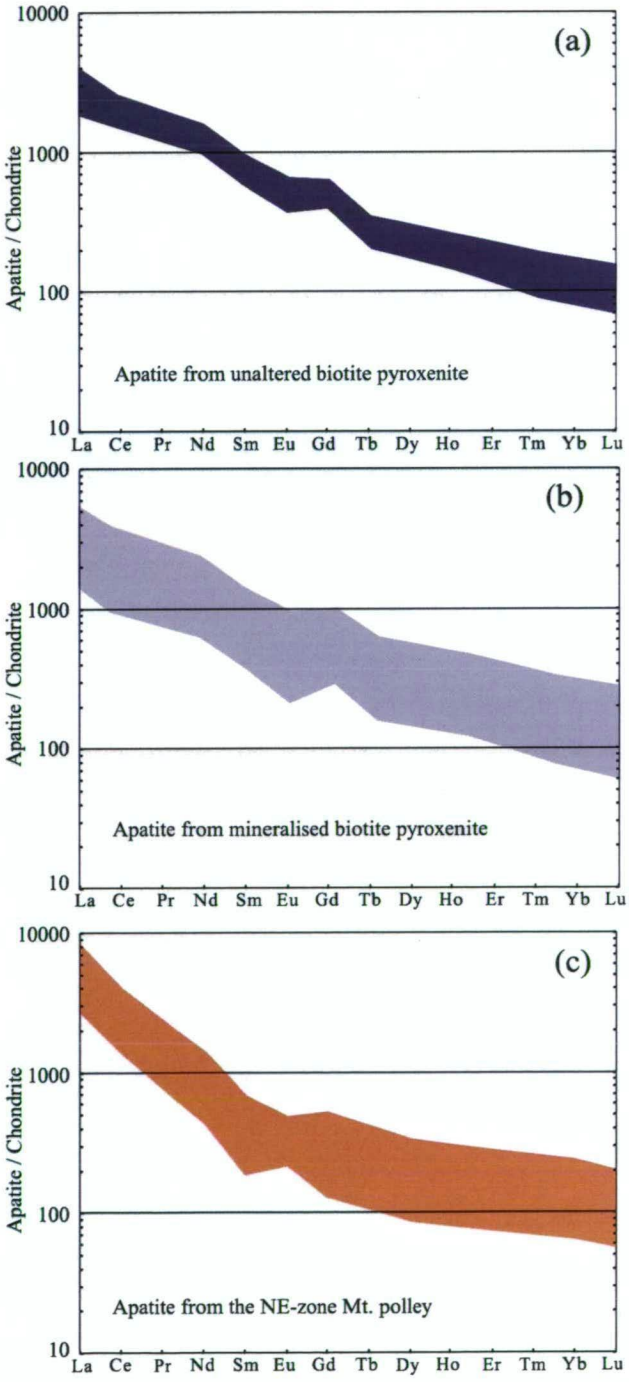

Figure 6-25. Chondrite normalised REE patterns (Sun and McDonough, 1989) for apatites from **(a)** unaltered biotite pyroxenite, **(b)** mineralised biotite pyroxenite and **(c)** apatite in bornite-cement from the NE-zone, Mt. Polley. LA-ICP-MS data.

6.6. Magnetite

6.6.1. Magnetite in biotite pyroxenite and magnetite-diopside veins

Magnetites in mineralised and unaltered biotite pyroxenite, and from magnetite-diopside-chalcopyrite veins were analysed using the EPMA. Those in biotite pyroxenite occurs as (1) small inclusions in diopside, (2) inclusions in biotite and (3) euhedral to subhedral magnetite grains on grain boundaries (also *see* Chapter 5). Magnetite inclusions in diopsides are thought to represent the earliest generation of magnetite, whereas magnetite inclusions in biotite and discrete euhedral to subhedral magnetite crystallised late in the crystallisation path. Magnetites in magnetite-diopside-chalcopyrite veins are inferred to represent hydrothermal magnetite (Fig. 4-11a-e).

Approximately 200 magnetite grains, and inclusions of magnetite in diopside were analysed using the EPMA. Vanadium occurs in all magnetites analysed (V_2O_3 ranges from 0.1 to 0.65 wt. %; Fig. 6-26a-f). Magnetite inclusions in diopside from unaltered biotite pyroxenite, on average, have the lowest concentrations of V_2O_3 (0.05 to 0.45 wt. %), whereas magnetites from magnetite-diopside-chalcopyrite veins have the highest concentrations of V_2O_3 (0.5 to 0.65 wt. %). Subhedral to euhedral magnetites in mineralised biotite pyroxenite have V_2O_3 between 0.25 and 0.65 wt. %. Ferric oxide, which was calculated using methods by Sauerzapf et al. (2008), is mostly between 66 and 68 wt. %, whereas FeO is mostly between 29 and 31 wt. %, which is close to pure endmember composition for magnetite (i.e. ~69 wt. % and 31 wt. % respectively). However, magnetite inclusions in diopside, and magnetite in some barren biotite pyroxenite can contain as little as 60 wt. % Fe_2O_3 (excluding one outlier) and up to 34 wt. % FeO (Fig. 6-26a, b). These magnetites are relatively enriched in Ti (*see* below). Magnetites in unaltered biotite pyroxenite are enriched in Cr compared to magnetite from mineralised biotite pyroxenite and magnetite veins (Fig. 6-26c).

Titanium is generally very low (i.e. ~300ppm Ti) in magnetite from mineralised and unaltered biotite pyroxenite and magnetites in magnetite-diopside-chalcopyrite veins; although magnetite inclusions in diopside (in both mineralised and unaltered biotite pyroxenite) and some magnetites in unaltered biotite pyroxenites have between 1 and 5 wt. % TiO_2 (Fig. 6-25f). According to Frost and others (1988; 1991; 1991), Fe-Ti oxides tend to re-equilibrate on cooling in plutonic rocks. In particular, Fe-Ti oxides can re-equilibrate by oxide-oxide re-equilibration, intra oxide re-equilibration (or oxyexsolution) and oxide silicate reactions at intermediate temperatures (Frost et al., 1988; Frost, 1991; Frost and Lindsley, 1991; Cross, 2000). Intra oxide re-equilibration at intermediate temperatures tends to result in near pure magnetite and ilmenite endmembers.

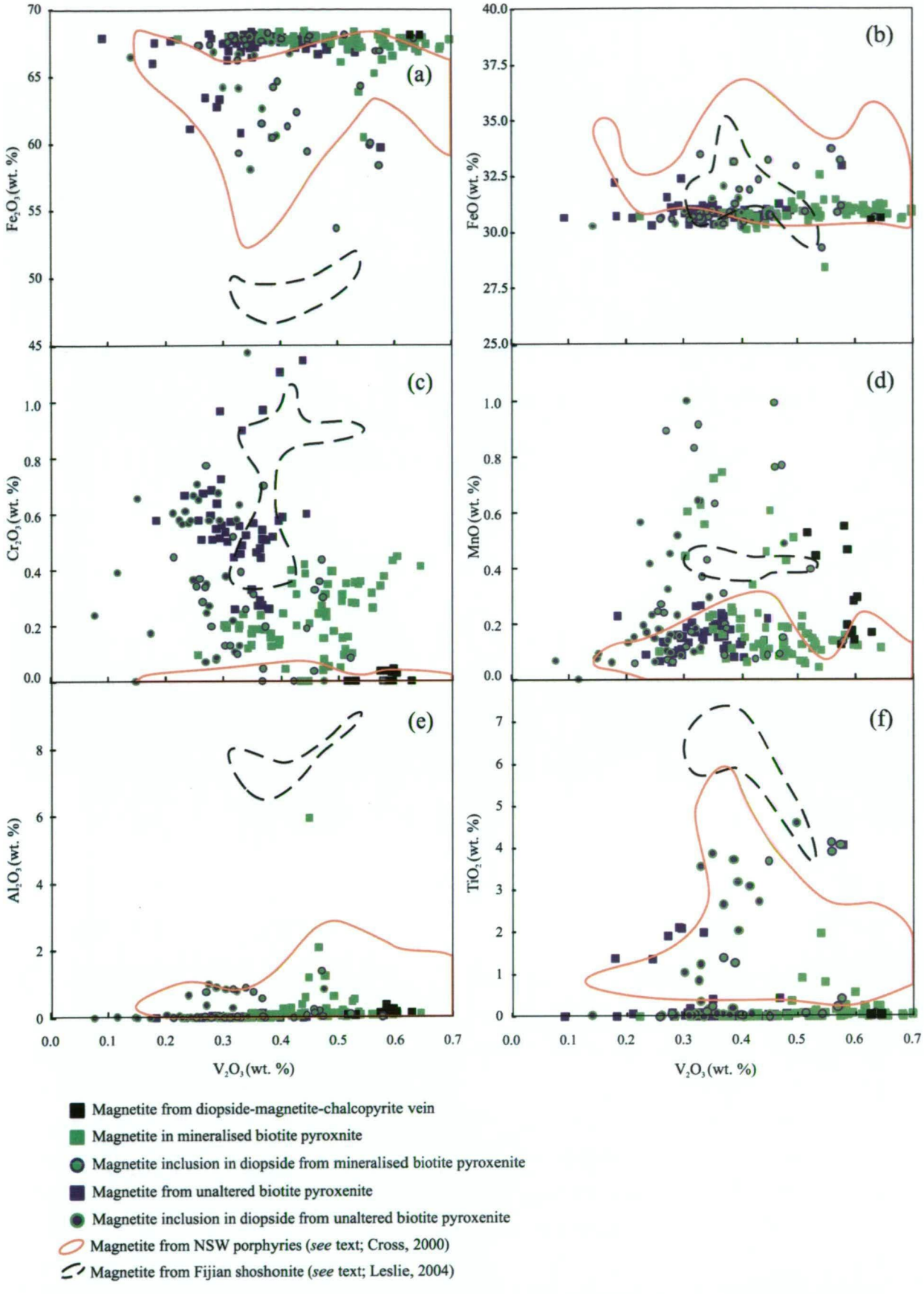

Figure 6-26. Geochemistry of magnetite from magnetite-diopsde-chacopyrite veins, unaltered biotite pyroxenite and mineralised biotite pyroxenite. Fields shown include magnetite from Fijian shoshonite (black dashed line; Leslie, 2004) and hydrothermal magnetite from Endeavour 26 North porphyry-Cu deposit, NSW (orange line; Cross, 2000). EPMA data.

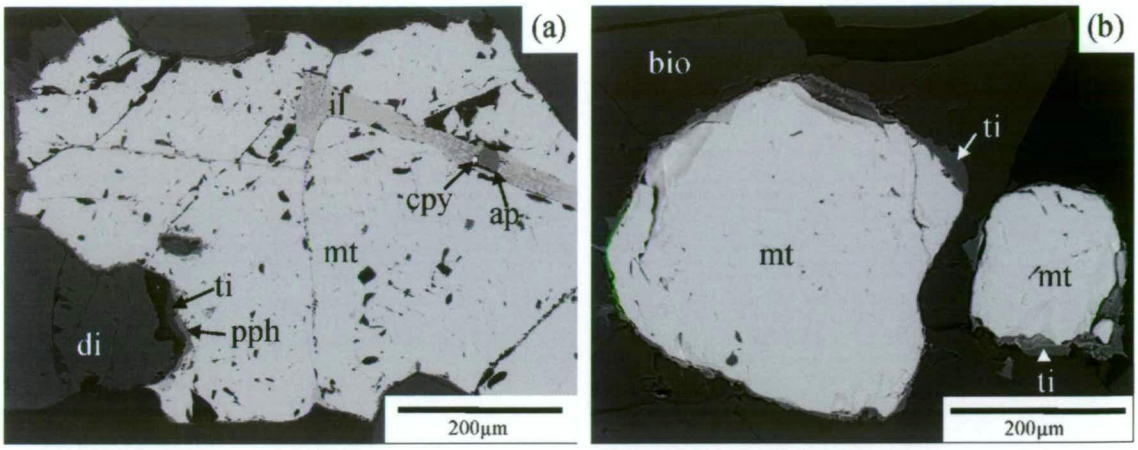

Figure 6-27. (a) Back-scatter electron image of magnetite in mineralised biotite pyroxenite from the Bishop Zone. Magnetite conatins an inclusion of ilmenite, and has a thin rim of pyrophanite and titanite (drill hole 2002-58_158.2 m). **(b)** Back-scatter electron image of magnetite with biotite from unaltered feldspathic pyroxenite from the Lorraine area. Magnatite includes a thin rim of titanite (sample 14-5-1, 348669mE, 6200520mN). Mineral abbreviations: ap = apatite, bio = biotite, cpy = chalcopyrite, di = diopside, il = ilmenite, mt = magnetite, pph = pyrophanite and ti = titanite.

Ilmenite is relatively uncommon in mineralised and unaltered biotite pyroxenite, but can occur as inclusions in magnetite (Fig. 6-27a). Other Ti-bearing phases, which are associated with magnetite, are titanite and/or pyrophanite ($MnTiO_3$; Fig. 6-27a, b). These phases form rims (~10 µm) around magnetite in both mineralised and unaltered biotite pyroxenite (Figs. 6-27b and 5-17a). These Ti-rich phases may have formed during from the exsolution of Ti from magnetite during the slow cooling of intrusive rocks and/or during hydrothermal alteration.

6.6.2. Comparison of Lorraine magnetite from biotite pyroxenite with magnetites from Fijian shoshonite and hydrothermal magnetites from Endeavour 26 North porphyry-Cu deposit, NSW

The composition of magmatic magnetites from Fijian shoshonites (Astrolabe Group; Leslie, 2004) and the composition of hydrothermal magnetite from Endeavour 26 North porphyry-Cu deposit, NSW (Cross, 2000), were compared with magnetite from Lorraine (Fig. 6-26a-f). The V_2O_3 composition of magnetite from Fijian shoshonite ranges from 0.3 to 0.55, and overlaps with the composition of magnetite in mineralised and unaltered biotite pyroxenite and magnetite diopside veins. Magnetites from Fijian shoshonite are depleted in Fe_2O_3, but are enriched in FeO, Al_2O_3 and TiO_2 compared to magnetite in Lorraine rocks, which is consistent with the contention that magnetites in relatively fast cooling volcanic rocks are less likely to re-equilibrate and exsolute Ti, Al and other impurities compared to magnetites in their intrusive counterparts (e.g., Cross, 2000). Chromium abundance of magnetite in Fijian shoshonites overlap with the range for those in unaltered

biotite pyroxenite; however Fijian shoshonites also contain chromite and Cr-magnetite inclusions in olivine, and spinel in Fijian shoshonites can contain up to 50 wt. % Cr_2O_3 (Leslie, 2004). Ferrous iron (calculated) abundance in magnetites from Fijian shoshonites overlap with magnetite from unaltered biotite pyroxenite, and MnO contents of magnetites from Fijian shoshonites are comparatively higher than those of most magnetites from unaltered biotite pyroxenite.

The V_2O_3 composition of hydrothermal magnetites from Endeavour 26 North porphyry-Cu deposit, NSW, range from 0.15 to 1.4 wt. %, and their abundances of MnO and Al_2O_3 are similar to magnetite from mineralised and unaltered biotite pyroxenites (Fig. 6-26d, e and f). Chromium, however, is depleted in hydrothermal magnetite from Endeavour 26 North porphyry-Cu deposit compared to magnetite from unaltered biotite pyroxenite. Magnetite from both mineralised and unaltered biotite pyroxenite are on average depleted in TiO_2 relative to hydrothermal magnetite from the Endeavour 26 North porphyry-Cu deposit, which may reflect a slower cooling environment and re-equilibration of magnetites in the former case.

6.7. Feldspar

6.7.1. Composition of feldspars from Lorraine

More than 370 feldspar grains from 36 samples of mineralised and unaltered syenite, fine-grained K-feldspar biotite rock, monzonite and mineralised and unaltered feldspathic pyroxenite were analysed using the EPMA. Feldspar compositions were plotted onto ternary diagrams (Fig. 6-28a-e). Feldspars from mineralised and unaltered feldspathic pyroxenite and syenite have plagioclase compositions that range from albite (An_0) to oligoclase (An_{19}; Fig. 6-28a-c), fine-grained K-feldspar biotite rocks have plagioclase compositions that range from albite (An_0) to andesine (An_{34}; Fig. 6-28d), and monzonites have plagioclase compositions that range from albite (An_1) to labradorite (An_{67}; Fig. 6-28e).

Microprobe results show that Lorraine rocks have a broad range of alkali feldspar compositions, with some feldspars consisting of intermediate compositions between albite and orthoclase end-members (Fig. 6-28a-f). However, K-feldspar (i.e. $>Or_{15}$) from mineralised and unaltered syenites has a median composition of $\sim Or_{90}$, monzonite has a median composition of $\sim Or_{82}$, fine-grained K-feldspar biotite rock has a median composition of $\sim Or_{89}$ and a small population of K-feldspar from feldspathic pyroxenite has a median composition of $\sim Or_{63}$. Both mineralised and unaltered rocks at Lorraine have K-feldspar compositions that dominantly range between Or_{70} and Or_{95}. Feldspathic pyroxenites have grains of intermediate compositions between albite and orthoclase end-members. Monzonites

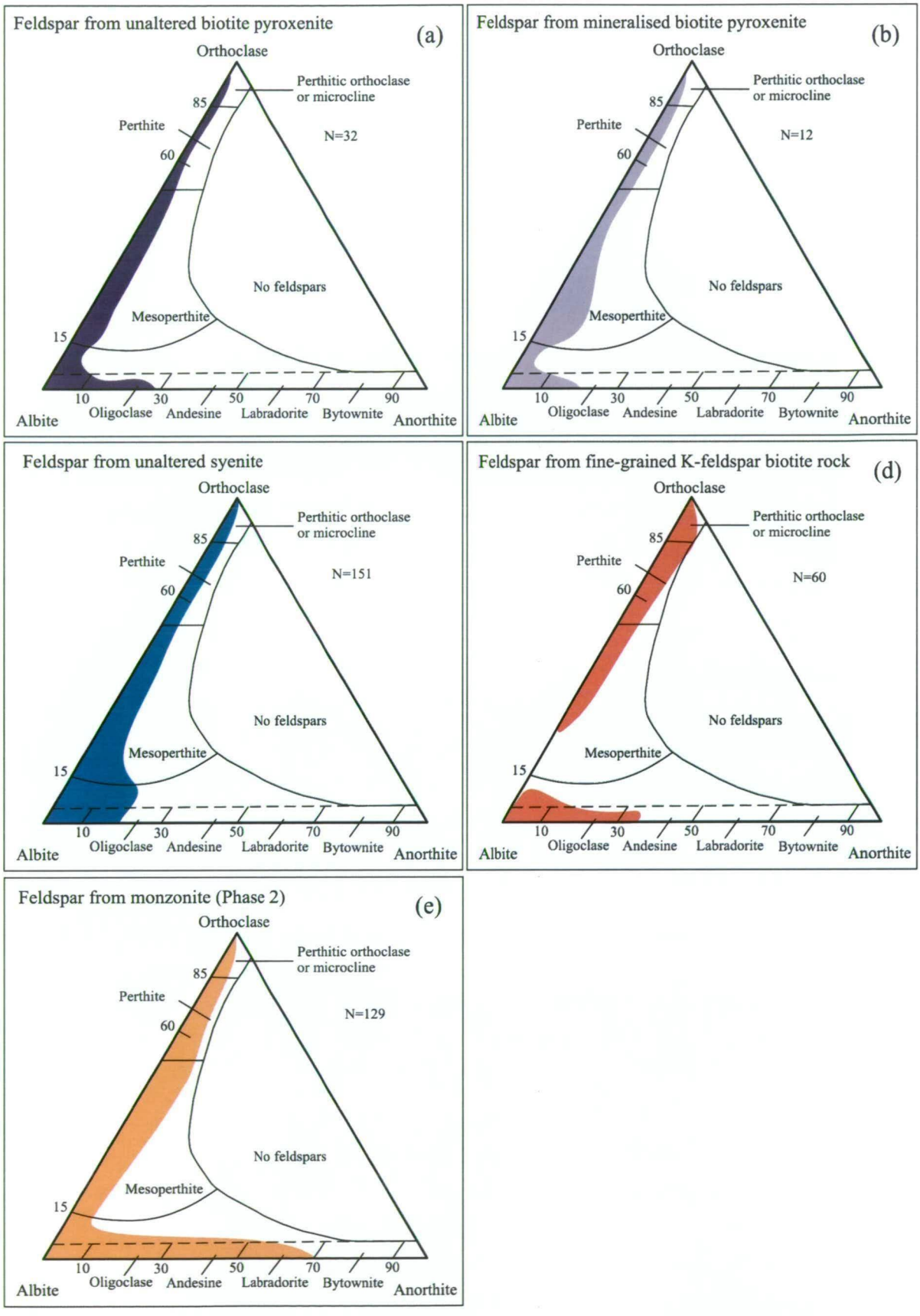

Figure 6-28. Ternary diagrams that show fields for feldspar in **(a)** unaltered feldspathic pyroxenite **(b)** mineralised feldspathic pyroxenite, **(c)** syenite, **(d)** fine-grained K-feldspar biotite rock and **(e)** monzonite. The fields shown are mostly low temperature results of exsolution in intrusive rocks. EPMA data.

also have, on average, more Na-rich K-feldspars compared to syenites and fine-grained K-feldspar biotite rock.

6.8. Mineral geothermometers

6.8.1. Apatite-biotite

The biotite-apatite geothermometer of Zhu and Sverjensky (1991, 1992) was used to estimate the temperature at which apatite and biotite pairs equilibrated (with respect to OH and F) in mineralised and unaltered biotite pyroxenite and altered fine-grained K-feldspar biotite rock. Temperature estimates are based on EPMA, with hydroxyl ions calculated using the method of Yavuz (2003a). The formula used to calculate temperature is:

$$T\,(^{o}C) = ((8852 - 0.024P\,(bars) + 5000X_{Fe}) / (1.987 \ln K_d^{Ap/Bio} + 3.3666)) - 273.15$$

where

$$X_{Fe} = (Fe^{2+} + Al^{[VI]}) / (Fe^{2+} + Mg + Al^{[VI]})$$

and

$$K_d^{Ap/Bio} = (X_F/X_{OH})^{Ap} / (X_F/X_{OH})^{Bio}$$

and X_F and X_{OH} are mole fractions of F and OH in apatite and biotite.

According to Steifert et al. (2000) the effects of changes in pressure are negligible, and the analytical error associated with fluorine analysis is the largest source of uncertainty in calculating temperatures . A pressure of 1 kbar was assumed in calculations here. The mean error (1σ) of the geothermometer is ± 50 °C (Steifert et al., 2000).

Temperature estimates were made for 47 apatite grains paired with average biotite compositions from 8 samples of unaltered biotite pyroxenite. Temperature estimates range from approximately 540 to 640 °C with a median ~600 °C (stdev. = ~30°C; Fig. 6-29a). Temperature estimates were also made for 105 apatite analyses paired with average biotite compositions for 8 samples from mineralised biotite pyroxenite. Mineralised biotite pyroxenite range from approximately 490 to 670 °C and have a median of ~570 °C (stdev. = 45 °C; Fig. 6-29a).

Temperature estimates were also made for F-rich, altered, fine-grained K-feldspar biotite rock. Biotite in these rocks has a major element composition consistent with the hydrothermal alteration field of Beane (1974). Five apatite-biotite pairs were analysed, giving a median temperature estimate of ~540 °C (stdev. = 65 °C; Fig. 6-29a).

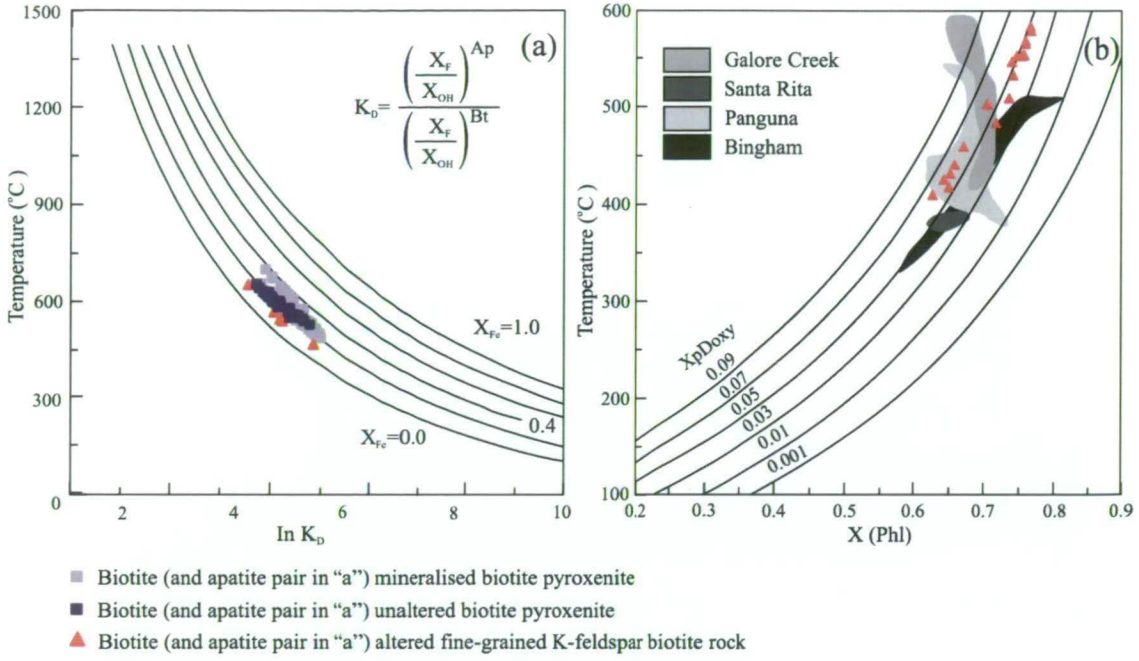

Figure 6-29. **(a)** Distribution of unaltered biotite pyroxenite, mineralised biotite pyroxenite and fine-grained K-feldspar biotite rock on revised apatite-biotite geothermometer of Zhu and Sverjensky (1992). (b) Compositions of biotite from fine-grained K-feldspar biotite rock on Beane's (1974) Temperature vs. X(Phl) diagram. Contours show fixed mole fraction of proton-deficient oxyannite. Fields also include biotites from Galore Creek, Santa Rita, Panguna and Bingham porphyry deposits from Beane (1974). EPMA data used.

The average temperature estimate of biotite-apatite pairs in the altered fine-grained K-feldspar biotite rock is similar to temperature estimates using the single Mg^{2+}-Fe^{2+}-Fe^{3+} biotite thermometer of Beane (1974) for hydrothermal biotite in porphyry Cu environments, which yielded a median temperature of 550 °C (stdev. = 20 °C; Fig. 6-29b). In the case of biotite pyroxenite (both mineralised and unaltered), the single biotite geothermometer yields significantly lower temperatures (~400 °C) compared to the apatite-biotite geothermometer. According to Beane (1974), alteration-related biotites generally have molar Mg/Fe >1.5 and Fe^{3+}/Fe^{2+} <0.3. Igneous biotites generally have Mg/Fe <1.0. Biotite from some altered fine-grained K-feldspar biotite rock fit the criteria for alteration biotite. Biotites from unaltered and mineralised biotite pyroxenite, mineralised syenite, monzonite and unaltered fine-grained K-feldspar biotite rock do not fit the general criteria for alteration biotite of Beane (1974). Fluorine-rich biotites from mineralised fine-grained K-feldspar biotite rock fit the criteria for alteration biotite of Beane (1974). It is inferred that fine-grained F-rich biotite represents an early phase of hydrothermal alteration (Chapter 4). Using the apatite-biotite geothermometer, it is inferred that early biotite alteration occurred at approximately 540°C. The above temperature range for altered fine-grained K-feldspar biotite rock is consistent with that for hydrothermal biotite from Galore Creek and Bingham porphyry Cu deposits (Beane, 1974).

6.8.2. Two feldspar geothermometer

A two feldspar geothermometer was used to estimate the temperature of feldspar-pairs in mineralised Phase 1 syenite and unaltered post-main stage Phase 2 monzonite. Microprobe spot analyses of adjacent plagioclase and K-feldspar crystals were carried out, and temperature estimates reported here are based on the assumption that equilibrium was obtained between crystal pairs. Temperature estimates were calculated using the pressure dependant two-feldspar thermometer formula of Haselton et al. (1983):

$$T_K = \frac{[(X_{Or}^{A-F})^2(18810 + 17030X_{Ab}^{A-F} + 0.364P) - (X_{An}^{Plag})^2(28230\text{-}39520X_{Ab}^{Plag})]}{\left[10.3(X_{Or}^{A-F})^2 + 8.3143\ln\left(\frac{(X_{Ab}^{A-F})^2(2 - X_{Ab}^{Plag})}{X_{Ab}^{A-F}}\right)\right]}$$

A pressure (P) of 1000 bars was assumed for the calculation and mole fractions refer to the ternary system. The results show that feldspar-pairs in mineralised syenite feldspar and unaltered biotite pyroxenites yield temperatures mostly between 380 and 500 °C, whereas phase 2 monzonite two feldspar compositions yield a temperature range of between 350 and 820 °C (Fig. 6-30). Thus it appears that the monzonite contains feldspar pairs that equilibrated at both magmatic and sub-solidus temperatures, whereas mineralised syenite and unaltered biotite pyroxenite has feldspar pairs that have completely re-equilibrated at sub-solidus temperatures. In the case of feldspar-pairs from mineralised syenite, this equilibration provides a minimum temperature estimate for K-feldspar metasomatism during transitional stage mineralisation.

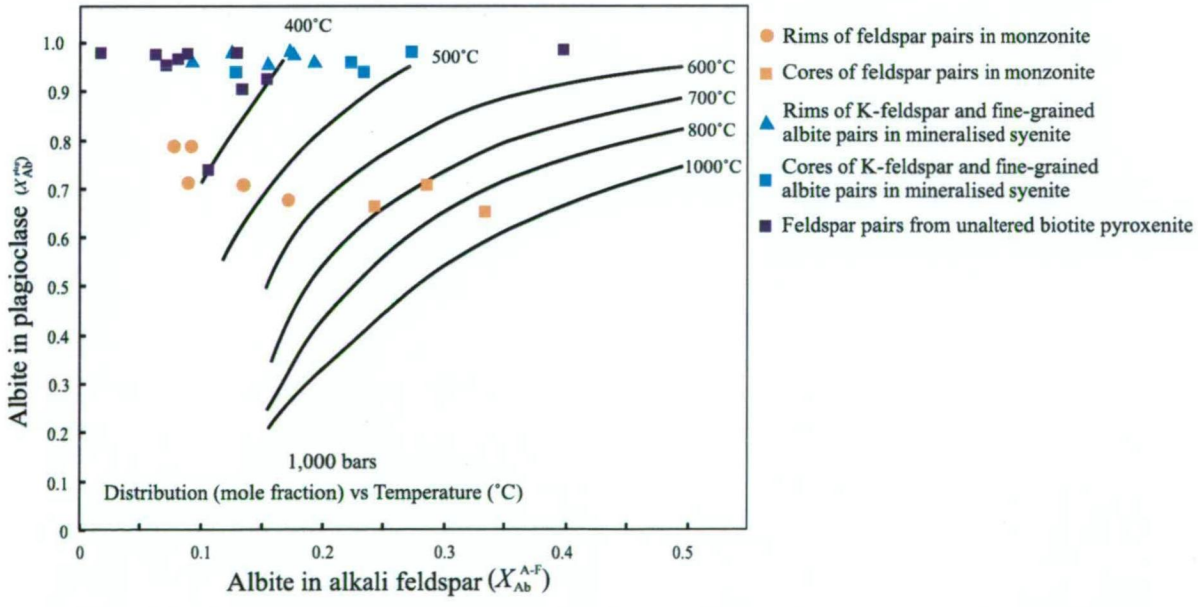

Figure 6-30. The distribution of albite component between alkali feldspar and plagioclase in feldspar pairs from mineralised Phase 1 syenite from the Lower Main Zone (drill hole 2001-56_55.8 m), an unaltered Phase 2 monzonite dyke from the Lower Main Zone (drill hole 2001-56_266.3 m) and an unaltered feldspathic pyroxenite from the Bishop Zone (drill hole 1996-44_128.0 m). Isotherms were derived from the equation of Haselton et al. (1983; see formula in text). Assuming 1000 bar pressure. EPMA data used.

6.9. Discussion

6.9.1. The composition of rock-forming minerals in unaltered biotite pyroxenite vs. other alkaline igneous rocks

One of the aims of this chapter was to compare the compositions of diopside, biotite, apatite and magnetite with mineral compositions of other alkaline mafic and ultrabasic arc-related rocks. In particular, mineral phases from Fijian shoshonites (Leslie, 2004; A.J. Crawford, unpublished data), biotite pyroxenites from the Zippa Mountain pluton (British Columbia) and Nicola Group basalts (British Columbia) were selected for the comparison.

The comparison demonstrates that major and trace elements in diopsides from unaltered biotite pyroxenite overlap in composition with clinopyroxene from Fijian shoshonite and Nicola Group shoshonites with equivalent *mg*-number (excluding Na and REE). This supports the contention that diopsides in the unaltered Lorraine biotite pyroxenite crystallised from mafic alkalic arc magmas. The relatively higher abundance of Na and REE in diopsides from Lorraine and Zippa Mountain diopsides may be a temperature effect or due to relatively higher activities of Na in the Lorraine and Zippa Mountain melts. In the case of temperature, the fact that Lorraine and Zippa Mountain diopsides formed in an intrusive body, implies that diopsides in these rocks may have equilibrated at lower temperatures due to slow cooling, as opposed to lavas which may be exhumed and cooled rapidly.

The composition of diopsides in Lorraine rocks have relatively consistent Wo ($CaSiO_3$) components and plot between diopside and hedenbergite end-members on the clinopyroxene nomenclature diagram of Morimoto (1988). The above trend is similar to clinopyroxene from Fijian shoshonites, as opposed to the trend for med-K calc-alkaline mafic rocks from the Vanuatu arc (e.g., Barsdell and Berry, 1990; Fig. 6-31). This supports the conclusion that diopside in Lorraine rocks has compositions that are consistent with diopsides in alkalic igneous rocks.

Biotites in unaltered biotite pyroxenite and monzonite plot in the igneous and re-equilibrated fields on generic discrimination diagrams for micas (Fig. 6-13c, d), and have compositions that are comparable to biotite (or phlogopite) from alkalic intrusives (e.g., minette; Fig. 6-13f). Hence it is inferred that biotite in biotite pyroxene and monzonite represent igneous biotite that has partly re-equilibrated in a slow cooling intrusive. In contrast, biotite in fine-grained biotite K-feldspar rock are notably F-rich, and are generally more enriched in F compared to secondary biotite from the Santa Rita porphyry-Cu deposit in New Mexico (e.g., Jacobs and Parry, 1976). Biotites in fine-grained K-feldspar biotite rock are in some cases enriched in Cu, which supports the contention that they are related to a Cu-bearing alteration event. Hence it is inferred that the Lower Main Zone contains both igneous and hydrothermal biotite.

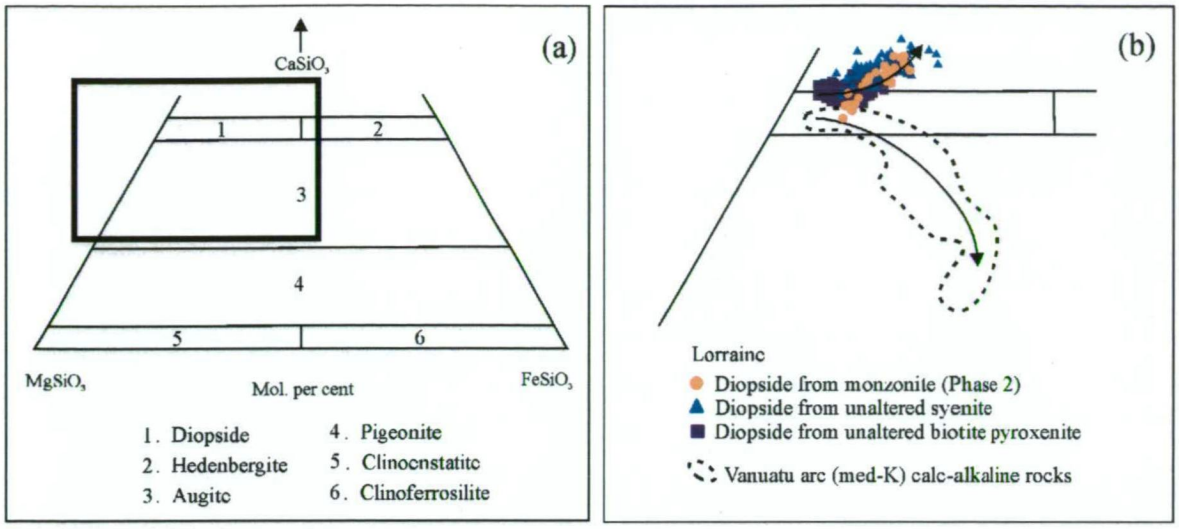

Figure 6-31. **(a)** Nomenclature of clinopyroxenes diagram after Morimoto (1988). **(b)** Comparision of pyroxene from unaltered biotite pyroxenite, monzonite and syenite of Lorraine with the composition a field of clinopyroxene from the med-K calc-alkaline lavas of the Vanuatu arc from Barsdell and Berry (1990). EPMA data used.

Apatites in unaltered biotite pyroxenite have compositions that overlap those from biotite pyroxenite of the Zippa Mountain pluton. In contrast, apatites from the Nicola Group basalts are lower in S and higher in Cl than apatites from unaltered biotite pyroxenite. The low S in apatite from Nicola Group shoshonites could reflect a more reduced melt composition.

Hydrothermal apatites from the Mt. Polley alkalic porphyry Cu deposit are also enriched in S^{6+} compared to apatite from the unaltered biotite pyroxenite, and apatites in fine-grained biotite K-feldspar rock also appear to be enriched in S^{6+} compared to apatite in biotite pyroxenite. The hydrothermal fluid has a higher SO_4^{2-} activity than the biotite pyroxenite.

Magnetites from unaltered biotite pyroxenite have Cr and V compositions that overlap with Cr-poor magnetite compositions from Fijian shoshonite. The abundance of Cr and V in magnetite appears to be useful for discriminating between magmatic and hydrothermal magnetite, and an overlap in the composition of Cr and V in magnetites from Fijian shoshonites with those in unaltered biotite pyroxenite supports the contention that the latter are also magmatic. The Ti-content in magnetite from both unaltered and mineralised biotite pyroxenite are generally very low, which is inferred to reflect exsolution of Ti-rich phases during slow cooling of intrusive bodies.

6.9.2. The compositions of biotite and diopside in unaltered vs. mineralised biotite pyroxenite

Biotites from mineralised biotite pyroxenites, on average, have lower *mg*-numbers than biotites from unaltered biotite pyroxenite, and the range of *mg*-numbers for biotite from mineralised biotite pyroxenite strongly overlaps with the range for biotite from monzonite and unaltered syenite (Fig. 6-32a-f). The abundance of Si and F in biotites from mineralised biotite pyroxenite is distinctly lower than biotite from unaltered biotite pyroxenite, and Al, Ti, Fe^{3+} and Mn is, on average, higher in biotites from mineralised biotite pyroxenite compared to unaltered biotite pyroxenites. Biotite in mineralised biotite pyroxenite have Si, Al, Ti and Fe^{3+} compositions that overlap with the composition of biotite from monzonites and unaltered syenites. Hence it appears plausible that the composition of biotite in mineralised biotite pyroxenites could be explained by the re-equilibration of biotite with a fluid source that was derived from a syenite and/or monzonite source(s). Based on apatite-biotite geothermometry it is inferred that re-equilibration occurred at between 550 and 600 °C.

Irregular outer zones of diopsides from mineralised biotite pyroxenites have *mg*-number <85 (Fig. 6-9b), which on average is lower than diopsides from unaltered biotite pyroxenite. Outer zones of diopside from mineralised biotite pyroxenite are also, more abundant in Al, Ti, Fe^{3+} and Mn compared to average diopside from unaltered biotite pyroxenites (Fig. 6-33a-f). Diopsides in unaltered syenites and monzonites also have, on average, lower *mg*-number and higher Al, Ti, Fe^{3+} and Mn compared to those from unaltered biotite pyroxenites,. Hence it is also possible that the irregular outer zones of diopside from mineralised biotite pyroxenite were formed as a result of re-equilibration with a fluid derived from the adjacent monzonite and syenite.

6.9.3. The composition of apatite and magnetite in unaltered biotite pyroxenite vs. mineralised biotite pyroxenite

Apatites in mineralised biotite pyroxenites are fine- to medium-grained and can be S-rich (Fig. 6-24a) or include outer zones with higher abundance of S (Fig. 6-24b). Abundances of S of outer zones of apatite match those of hydrothermal apatites from Mt. Polley, whereas the relative low S content of inner zones of apatite are consistent with apatite in unaltered biotite pyroxenite and apatite from biotite pyroxenite of the barren Zippa Mountain pluton. It is inferred that the outer S-rich zones of apatite in mineralised biotite pyroxenite represent overgrowths of hydrothermal apatite. The occurrence of sulphide inclusions in S-rich apatite appears to support the contention that apatite crystallised in biotite pyroxenite during mineralisation and alteration (*see* Chapter 5).

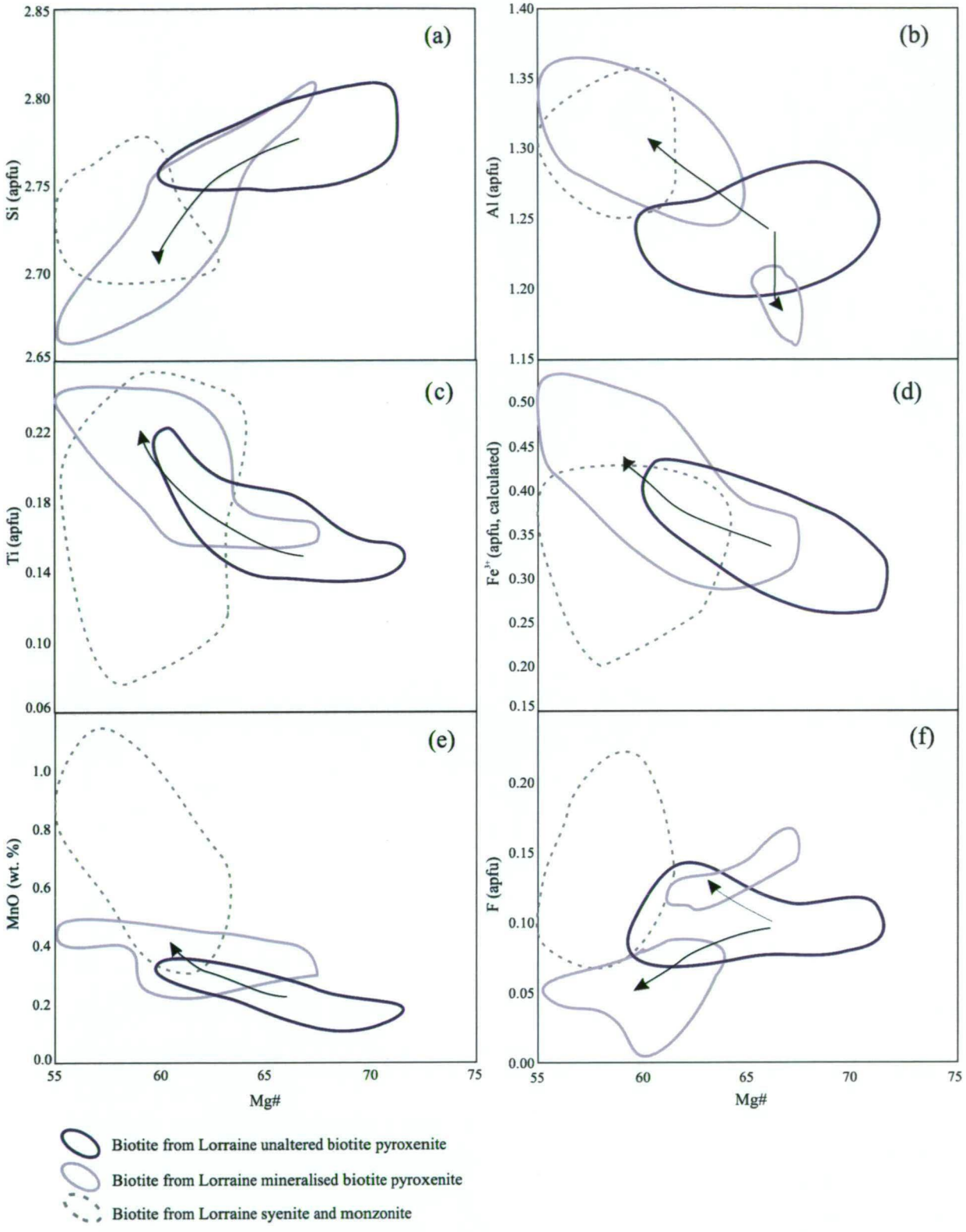

Figure 6-32. Comparison of the distribution of biotite compositions of mineralised biotite pyroxenite vs. unaltered biotite pyroxenite on major element vs. *mg*-number bi-variant diagrams. Arrow denotes the general trend(s) of biotite from unaltered biotite pyroxenite to mineralised biotite pyroxenite. Bi-variant diagrams also show the distribution of biotites from unaltered syenite and monzonite.

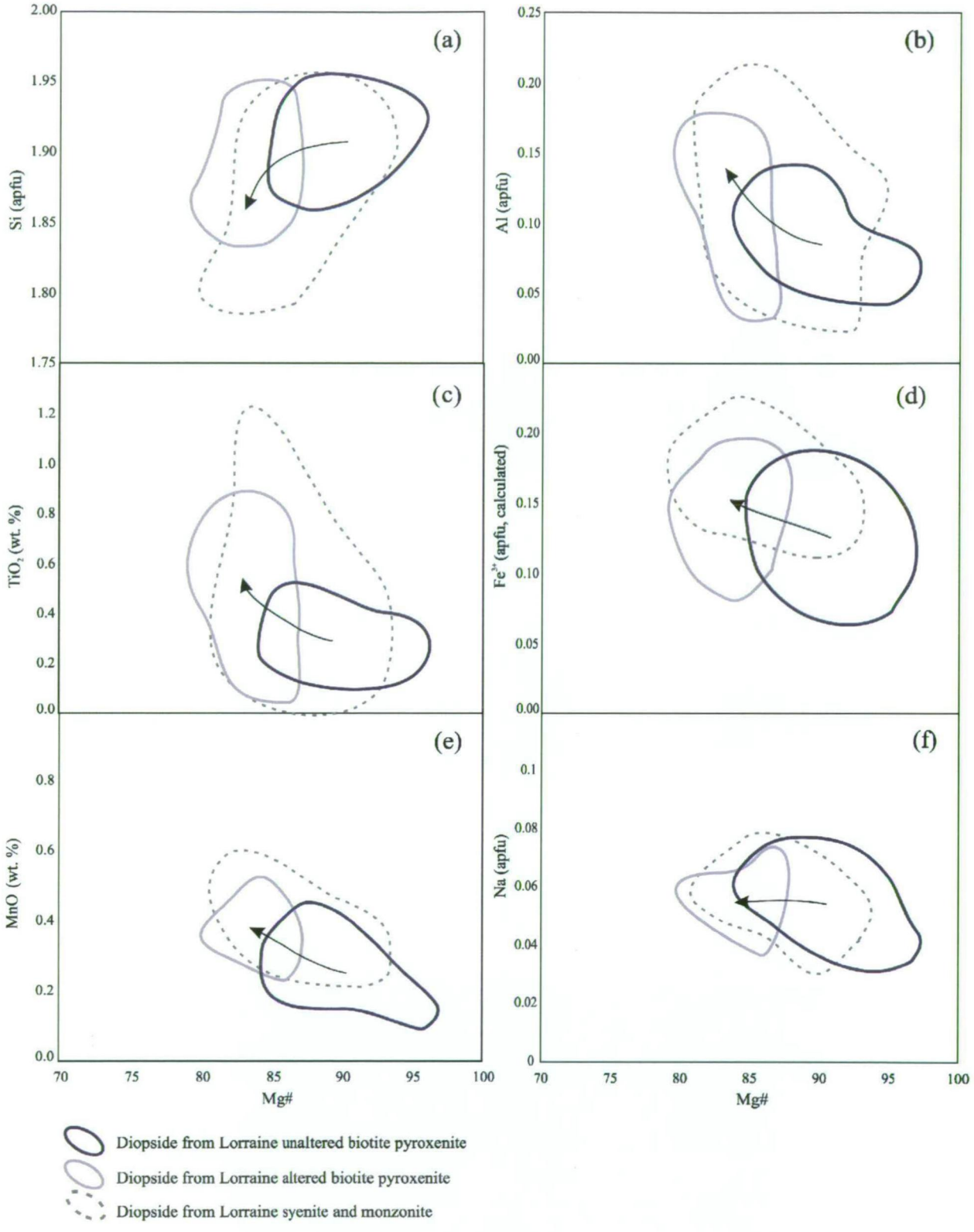

Figure 6-33. Bi-variant diagrams showing the distribution of select major elements vs. mg-number in outer zones of diopside from mineralised biotite pyroxenite and unaltered biotite pyroxenite. Arrow denotes the general trend of diopside from unaltered biotite pyroxenite to mineralised biotite pyroxenite. Bi-variant diagrams also show the distribution of diopsides from unaltered syenite and monzonite.

Magnetites in mineralised biotite pyroxenites are notably V-rich and Cr-poor compared to those in unaltered biotite pyroxenite. The content of V and Cr in magnetite from mineralised biotite pyroxenite is comparable to hydrothermal magnetite from the Endeavour 26 North porphyry-Cu deposit, NSW. In contrast, the Cr content of magnetite from unaltered biotite pyroxenite is notably higher than hydrothermal magnetite from the Endeavour 26 North porphyry-Cu deposit, but comparable in abundance to magnetite from Fijian shoshonites. Hence the relative enrichment of V and depletion of Cr in magnetite from mineralised biotite pyroxenite is a signature of hydrothermal alteration.

6.9.4. An estimation of the fluorine concentration in hydrothermal fluids

Fluorine is a common constituent in hydrothermal systems (e.g., Aksyuk, 2000; Aksyuk, 2002; Ayati et al., 2008). Abundant fluorine in hydrothermal solutions can promote the transportation of U, W, Mo, Sn, Be, REE, Ta, Zr, Hf and Nb by forming fluoride complexes with these elements (e.g., Bailey, 1977; Manning, 1981; Eugster, 1985; Keppler and Wyllie, 1991; Zhu and Sverjensky, 1991; Candela and Piccoli, 1995; Wood and Samson, 1998; Charoy, 1999; Aksyuk, 2000; Wood, 2004). Fluorine-rich biotite occurs as an alteration phase in a number of porphyry-Cu deposits (e.g., Selby and Nesbitt, 2000; Ayati et al., 2008), and it is possible that F in hydrothermal solutions may have played a role in the mobilisation and remobilization of metals in porphyry environments. Aksyuk (2000;2002) was able to show that evolving fluids from a known magmatic source could be tracked based on the F compostion of mineral phases through different alteration domains (i.e. biotite and muscovite). Aksyuk (2000;2002) was also able to quantify the concentration of fluorine in hydrothermal solutions based on biotite compositions.

At Lorraine, biotite analysed in fine-grained K-feldspar biotite rocks are considered here to have formed during an early phases of potassic alteration that pre-dates Cu-Fe sulphide mineralisation (see Chapter 4). However an understanding of early alteration is an important step towards determining the hydrothermal evolution of the Lorraine porphyry Cu-Au system. Some early alteration F-rich biotites are enriched in Cu (Fig. 6-20). Hence there appears to be a relationship between some early Cu mineralisation and F-metasomatism at Lorraine (Chapter 4). Here the author calculates the composition of HF in hydrothermal fluids that were in equilibrium with hydrothermal fluorine-rich biotites, using the methods of Aksyuk (2000; 2002; Fig. 6-19). The author has also calculated the composition of fluids in equilibrium with biotite at magmatic temperatures.

The method used here to evaluate fluorine composition of hydrothermal fluids at Lorraine was that of Aksyuk (2000; 2002). This method used a calibrated biotite fluorimeter to estimate the fluorine composition of the fluids that were in equilibrium with biotite. The equation:

$$\text{Log } M_{HF} = (X_F/(1 - X_F)) - 1722/T(K) - 1.107\ X_{Mg} + 0.216\ (Al\text{-}2) + 0.8958 + \log aH_2O$$

is used here to calculate the HF (moles/litre) concentration of hydrothermal fluids. Where MHF = concentration of fluids (moles/dm^3), XF = mole fraction of F in biotite, XMg = fraction of Mg in the octahedral-site, Al = aluminium atoms in biotite formula, T = temperature in degrees Kelvin and aH_2O = the activity of water in fluid under the given temperature, which was assumed to be 1. Temperatures were obtained from method shown in section 6.8.

Geothermometry results show that early fine-grained biotite alteration in fine-grained K-feldspar biotite rocks occurred at between about 350 and 600 °C (Fig. 6-29) by a fluid that had concentrations of between approximately log -3.5 and log -2.0 M_{HF} respectively. In other words the fluid is calculated to have had a HF concentration of between approximately 15 and 200 ppm (assuming a fluid density of 1 g/cm^3), and calculations indicate that the concentration of HF in solution diminished significantly with decreasing temperature (Fig. 6-34). Lower concentrations may have been driven by a decrease in the solubility of fluoride in solution with decreasing temperature (e.g., Zhu and Sverjensky, 1991). Higher temperature (>500 °C) and relatively fluorine-rich fluids interacted with wall rocks in the central area of the Lower Main Zone and in parts of the Bishop Zone.

Two trends were identified in the data set with respect to M_{HF} versus temperature (Fig. 6-34). Trend one biotites were in equilibrium with fluids that had higher M_{HF} at a given temperature compared to trend two biotites and occur in both the Bishop and the Lower Main zones. Trend one biotites were in equilibrium with fluids that had a higher activity of HF at a given temperature compared to fluids in equilibrium with biotite in both unaltered and altered biotite pyroxenite. Biotites from both altered and unaltered biotite pyroxenites plot along trend 2. Biotites from altered and unaltered syenites also appear to have equilibrated with fluids that had M_{HF} values to trend two. Hence, it is likely that fluids exsolved from biotite pyroxenites and syenites had M_{HF} values similar to fluids that resulted in trend 2 metasomatism

.

The source of fluids that result in trend one metasomatism remains unclear. Based on stable O-D isotope studies (Chapter 8) it has been shown that F-rich trend one biotites from

fine-grained K-feldpsar biotite rocks were in equilibrium with a fluid that was either magmatic or metamorphic in origin. In the case of a magmatic origin, the author was not able to identify an intrusive body that contained biotites that would plot along trend 1. Hence unlike studies by Aksyuk (2002), where secondary biotite compositions fall along the same trend as magmatic biotites,the author has not been able to link secondary trend one biotites to a magmatic source. It is plausible that the magmatic source that generated F-rich metasomatism in the Lower Main and Bishop zones is concealed at depth.

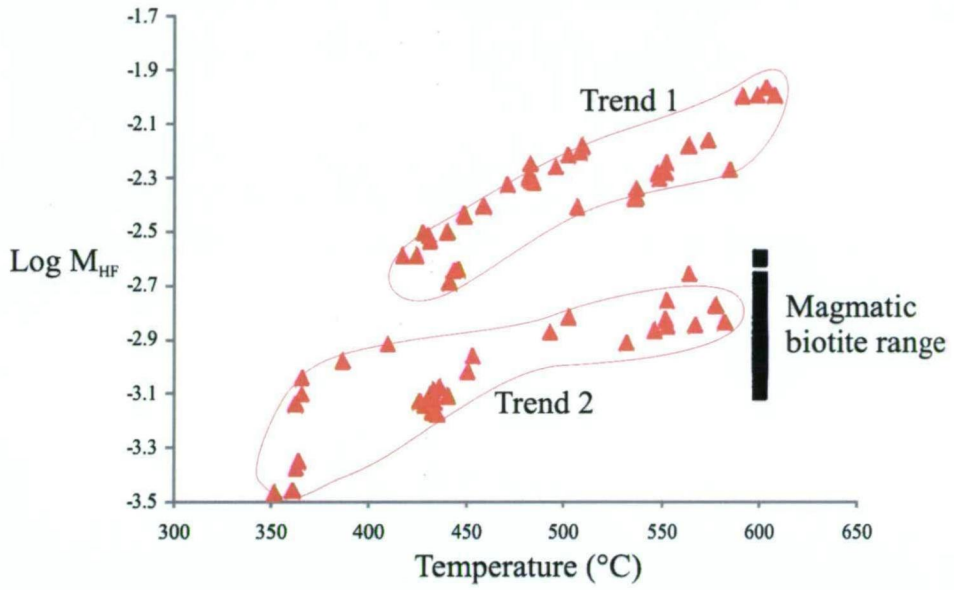

Fig. 6-34. HF concentrations (M. mol/dm^3) in fluids that were in equilibrium with fine-grained biotite (red) and biotite from magmatic rocks. Note that there are two trends. Trend 1 represents a group of biotites that were in equilibrium with fluids that were relatively enriched in HF compared to trend 2 biotite at a given temperature. Calculated from EPMA data.

6.10. Conclusions

Based on major and trace element geochemistry of mineral phases a number of conclusions can be made:

- Diopsides from unaltered biotite pyroxenite and monzonite have major and trace element abundances and *mg*-numbers that are similar to diopsides from Fijian and Nicola Group shoshonites. Sodium, however, is enriched in diopside in Lorraine rocks compared to Fijian and Nicola Group shoshonites. The abundance of Na in Lorraine diopside is similar to primary diopside from the Zippa Mountain pluton.

- Lorraine diopsides have a higher aegirine component than clinopyroxene from Fijian or Nicola Group shoshonites. The relatively higher proportion of aegirine in Lorraine diopsides compared to clinopyroxenes from Fijian and Nicola Group shoshonites probably indicates that diopside from Lorraine equilibrated at lower

temperatures. The fact that Lorraine diopsides occur in intrusive bodies supports the contention that diopsides in these rocks formed in a relatively slow cooling intrusive complex compared to clinopyroxene in Fijian and Nicola Group lavas. Alternatively, the higher abundance of Na in Lorraine diopsides could also be explained by a relatively higher activity of Na and Fe^{3+} in the melt.

• Diopsides in biotite pyroxenite from Lorraine have a low abundance of Cu compared to diopside from Fijian shoshonites and Nicola Group shoshonites. Lorraine diopsides, unlike Fijian and Nicola Group diopsides, show no evidence of an increase in Cu with fractionation (i.e. decreasing *mg*-number).

• Biotites from unaltered biotite pyroxenite have higher *mg*-number compared to those from unaltered monzonite and mineralised biotite pyroxenite. Biotites from mineralised biotite pyroxenite have similar major element compositions to biotites from monzonite and mineralised syenite. It is inferred here that alteration has changed the composition of biotite in mineralised biotite pyroxenite to compositions closer to those of biotite from the felsic rocks.

• Diopsides in mineralised biotite pyroxenite have irregular-shaped outer zones with lower *mg*-number compared to cores and to diopsides from unaltered biotite pyroxenite. This is attributed to alteration which has transformed the composition of outer zones of diopside grains to a lower *mg*-number.

• Apatites and magnetites from mineralised biotite pyroxenite have high S and low Cr, respectively, compared to apatite and magnetite from unaltered biotite pyroxenite. It is concluded that the high S in apatite and low Cr (and higher V) in magnetite in mineralised biotite pyroxenite. Magnetite in mineralised biotite pyroxenite is mostly coarser grained compared to magnetite in unaltered rocks, and thus it has been inferred that V-rich magnetite precipitated from hydrothermal solutions.

• Apatite-biotite pairs in mineralised and unaltered biotite biotite pyroxenite have, on average, equilibrated at ~570 °C and ~600 °C respectively, and apatite-biotite pairs in fine-grained K-feldspar biotite rocks appeared to have equilibrated at between 400 and 600 °C.

CHAPTER 7
IGNEOUS GEOCHEMISTRY

7.1. Introduction

Based on research over the past thirty years, there appears to be a general consensus that melting along arcs occurs in the mantle in response to an ingress of aqueous fluids and/or melt from the subducting plate (e.g., Gill, 1981; Tatsumi et al., 1986; Hawkesworth et al., 1993; Woodhead et al., 1993; Pearce and Peate, 1995; Tatsumi and Eggins, 1995; Hawkesworth et al., 1997; Peate et al., 1997; Sun and Stern, 2001; Hollings and Wyman, 2004). The resulting magmas that form as a result of partial melting of the sub-arc mantle tend to be enriched in non-conservative large ion lithophile elements (LILE; e.g., Ba and Rb), but have negative anomalies in the conservative high field strength elements (HFSE; e.g., Nb, Ta and Ti) when compared to normal mid-ocean ridge basalt (N-MORB; Tatsumi et al., 1986; Woodhead et al., 1993; Pearce and Peate, 1995; Hollings and Wyman, 2004). High field strength elements are thought to behave conservatively and are retained either in the down-going slab or the metasomatised mantle, or (less likely perhaps) they are buffered by a high concentration in the mantle source (Pearce and Peate, 1995). In contrast, LILE prefer to partition into aqueous slab-derived fluids (Pearce and Peate, 1995; Hollings and Wyman, 2004). As such, ratios of non-conservative to conservative elements can provide insights into slab-derived fluid input into the mantle or crustal contamination (Pearce and Peate, 1995; Sun and Stern, 2001). Conservative element ratios of mafic magmas can also provide insights into the degree of melting of the peridotite mantle source (Pearce and Parkinson, 1993).

At Lorraine, biotite pyroxenite dykes are mineralised, and also cross-cut mineralised rocks (Chapter 3), implying that biotite pyroxenites were emplaced both pre- and post-mineralisation. Based on cross-cutting relationships and absolute ages of syenites, it is inferred that pyroxenite emplacement closely coincided with the timing of mineralisation in the Lower Main Zone (*see* Chapter 3). Hence, biotite pyroxenites from Lorraine provide an opportunity to study the chemistry of ultrabasic rocks that are temporally and spatially associated with Cu-Au mineralisation at Lorraine.

For the current study, the major and trace element chemistry of the biotite pyroxenites are compared with monzonite and syenite from Lorraine. The major and trace element geochemistry of biotite pyroxenites are also compared with arc-related shoshonite lavas, arc tholeiites and calc-alkaline arc rocks.

7.2. Tools and methods

Intrusive rocks consist of masses of interlocking crystals that formed during cooling of a magma source. During cooling, physical processes such as crystal settling, flotation, flow differentiation, filter pressing, selective nucleation, gas streaming and gravitational liquid separation may have resulted in the accumulation of specific phases (e.g., Hall, 1987, p.218). Therefore, the bulk composition of an intrusive rock may differ significantly from its parent magma composition. Biotite pyroxenites at Lorraine consist largely of aligned euhedral to subhedral diopside crystals that touch adjacent diopside crystals (Fig. 3-11a-d). It therefore appears plausible that biotite pyroxenites consist of accumulated diopside crystals. However, Phase 2 biotite pyroxenites are vertically dipping, 1 to >5 m in thickness and cross-cut mineralised Phase 1 biotite pyroxenites and syenites. Recent workers have inferred that these biotite pyroxenites are dykes (e.g., Sillitoe, 2007; Devine et al., 2007; Garratt and Lindinger, 2008), and therefore the diopsides in biotite pyroxenites should not represent the cumulate portion of a magma chamber. Also, based on the density of diopside (i.e. ~3.2 to 3.4 g/cm^3; Deer et al., 1992), it is unlikely that the crystals would float in mafic magma (i.e. 2.8 to 3.1 g/cm^3; Hall, 1987), and therefore accumulation of diopside by flotation can be ruled out. Alternatively, diopside crystals may have been entrained in the magma and perhaps were concentrated at the choke point in magma conduits. Aligned K-feldspar phenocrysts (parallel to dyke contacts) in feldspathic biotite-pyroxenite dykes and aligned diopside crystals in some feldspathic pyroxenite dykes (Figs. 3-1a, b, 3-11a and 5-7) appear to support the contention that K-feldspar and diopside were entrained and transported in magmas. The purpose of the comparison of Lorraine rocks with lavas and melt inclusions is to test if the bulk rock chemical compositions of biotite pyroxenites from Lorraine have major and trace element concentrations or element ratios that may resemble parent mafic magmas.

The trace element composition of mafic igneous rocks can reflect the source of magma, depth and extent of partial melting, petrogenetic processes associated with melt formation and magma evolution (e.g., Hawkesworth et al., 1993; Woodhead et al., 1993; Hofmann, 1997; Hollings and Wyman, 2004; Leslie, 2004). In the case of island arc basalts, the sub-arc mantle wedge, subducted oceanic crust and sediments may all contribute to parental basaltic magmas. Pearce and Peate (1995) used projections of M/Yb vs. Nb/Yb, where M represents the element of interest to assess the effects of partial melting, fractional crystallisation or input from slab-derived sediments. In particular Yb and/or Nb are used as the common denominator as they are considered conservative and incompatible elements that are least affected by partial melting and fractional crystallisation. In the case that element "M" is conservative, then the rock should plot in the mantle-array (N-MORB, E-MORB, OIB), based on the assumption that slab fluid-derived components will not have the same vector as the mantle-array (Pearce and Peate, 1995). According to Pearce and

Peate (1995), most volcanic arc basalts plot in the mantle-array when M is Zr, Hf, Ti, HREE, Y, Sc Ga, Ni, Cr or Co, or other major and minor elements other than K, Na or P; however Zr and Hf may also act as non-conservative elements when crust or subducted sediment undergoes melting rather than dehydration (e.g., Sun and Stern, 2001).

Lanthanum and Sm are conservative elements, and La/Sm ratios are affected by changes in source fertility and in the extent of partial melting of the peridotitic mantle (Ryan et al., 1996; Leslie, 2004), due to the difference in the bulk distribution coefficients between the two elements (e.g., Rollinson, 1993; Jenner, 1996; Kerrich and Wyman, 1996). The melting of clay minerals at temperatures greater than 800 °C may also increase La/Sm (Johnson and Plank, 1999); however, La/Sm is thought to be unaffected by changes in slab fluid input (Ryan et al., 1996; Leslie, 2004). Therefore, La/Sm is considered a useful proxy for partial melting, mantle fertility and sediment melt input (Leslie, 2004). These ratios, along with others, are used as tools to compare Lorraine biotite pyroxenite with rocks that have crystallised from mafic magmas along magmatic arcs. The composition of melt inclusions from the Nicola Group basalts (Mount Polley area British Columbia; Logan and Bath, 2006; Fig. 6-2) are inferred to represent actual mafic melts, and are therefore used as an additional tool to compare with Lorraine biotite pyroxenites.

7.3. Sample preparation and analytical methods

7.3.1. Whole rock

Samples analysed in this study were collected from the Lower Main, Main and Bishop zones during detailed core logging and bedrock mapping. Additional samples collected from the Main Zone and other parts of the Duckling Creek Syenite Complex were supplied by Dr Graham Nixon (British Columbia Geological Survey Branch) and Fionnuala Devine (Teck Ltd).

Seventy four whole rock samples were crushed, milled and prepared for major and selected trace element analyses at the University of Tasmania and the British Columbia Geological Survey Branch in Victoria, Canada. Rocks were crushed using the tungsten carbide hydraulic press and small chips (3-15 mm) were then separated and washed in an ultrasonic cleaner for 10 minutes. Clean chips free of xenoliths and visible veins were then dried and milled. Samples to be analysed for major elements (plus selected trace elements) were pulverised using a tungsten carbide mill. Samples to be analysed for trace elements were milled using a alumina-ceramic mill. In addition, 12 samples supplied by Fionnuala Devine were milled at the British Columbia Geological Survey Branch using a tungsten

carbide mill and a Cr-Fe mill for major and trace element geochemistry respectively. Mills were cleaned using quartz and thoroughly scrubbed with synthetic cleaning pads in hot soapy water, rinsed and then dried using compressed air between samples to reduce any chances of contamination. All mills had previously been tested for possible trace element contaminants by milling quartz and analysing milled quartz for contamination. Ceramic alumina and Cr-Fe mills did not add significant amounts of trace element contaminants to milled quartz during tests, and possible contaminants were below detection limit (pers. comm., P. Robinson, 2008 and R. Lett, 2008, respectively).

Major elements and selected trace elements (S, Nb, Zr, Sr, Cr, Ba, V, La, Y, Rb, Pb, Zn, Cu and Ni) were analysed using X-ray fluorescence (XRF) via a Phillips 1480 X-ray spectrometer at the University of Tasmania. For each sample, 400 mg of ignited sample, 5.2 g of flux (12:22 type) and 3-4 drops of 25 % LiBr solution were mixed. Samples then underwent two six-minute heating cycles to produce a fused disc for major element analysis. Samples for trace element analysis are pressed composite pellets of ~10 g – 15 g of sample homogenised with ~0.36 g Palaroid (3.6 % weight to weight ratio), and mixed with 2 to 3 ml of acetone. The mixture was redried and hand crushed in an agate mortar, then encased in a Borax sheath and pressed to 10 tonnes.

Trace elements (Li, Be, Sc, V, Cr, Mn, Co, Ni, Cu, Zn, Ga, As, Rb, Sr, Y, Zr, Nb, Mo, Ag, Cd, Sn, Sb, Cs, Ba, La, Ce, Pr, Nd, Sm, Eu, Gd, Tb, Dy, Ho, Er, Tm, Yb, Lu, Hf, Ta, W, Tl, Pb, Bi, Th and U) were analysed using an Agilent HP4500 quadrupole inductive coupled mass spectrometer (ICP-MS) at the University of Tasmania. For trace element analyses, mafic samples were digested using the HF-HNO_3 Savillex (low pressure) digestion, whereas felsic samples required a high pressure HF-H_2SO_4 PicoTrace digestion in order to dissolve refractory minerals (e.g., zircon).

7.3.2. Melt inclusions

With the assistance of Prof. V.S. Kamenetsky, one set of 0.3-0.5 mm diopside fractions (~150) from five shoshonitic basalt samples were placed into low-inertia heating stage at the University of Tasmania, which was designed at the Vernadsky Institute, Moscow (Sobolev and Slutskii, 1984). Melt inclusions in these crystals were homogenised at 1180 °C (inferred trapping temperature) and then rapidly cooled to avoid crystallisation. Diopside grains were then glued into epoxy mounts and polished. Grains that hosted large (>40 μm) non-decrepitated silicate melt inclusions were selected for analysis and polished until melt inclusions were exposed at the surface. The diopside grains were then lifted from the epoxy mount using a soldering iron and glued into a final epoxy mount. The final mount was carefully polished and then cleaned in an ultrasonic cleaner for 40 min-

utes, wiped with a tissue that had been dipped in methanol and then placed in a pre-heated (~50 °C) oven to dry for 30 minutes.

Exposed melt inclusions were analysed for Si, Al, Fe, Na, K, Ca, F, Cl, Mn, Ti, P, S, Ba and Mg using the Cameca SX50 electron microprobe at the University of British Columbia. An accelerating voltage of 15 keV, a low beam current of 15 nA, a large beam diameter of 5-10 μm and a counting time of 3 sec were chosen to avoid volatilisation of the alkali elements from melt inclusions. Sodium, the element most prone to volatilisation (Neilson and Sigurdsson, 1981), was always analysed first. One to three spots were analysed on each inclusion, and to avoid overlap with the host diopside during analyses, measurements were made near the centre of the melt inclusion.

Those inclusions which were analysed using microprobe were also analysed for trace elements using a Nd:YAG 193nm UV laser manufactured by New Wave fitted to an Agilent 7500cs ICP-MS at the University of Tasmania. Elements analysed included Li, Be, B, Al, Ca, Ti, Ni, Cu, Zn, Rb, Sr, Y, Zr, Nb, Mo, Ag, Sn, Ba, La, Ce, Nd, Sm, Eu, Gd, Dy, Er, Yd, W, Au, Pb, Th and U. The samples were ablated under He and Ar gas before introduction to the plasma. Prior to each analysis, the laser was fired at a low pulse rate (1 Hz) for three seconds to remove surface contamination. The laser beam was then fired at 10 Hz repetition rate and holes 35 μm in diameter were ablated. Acquisition time consisted of a 30 second measurement of the gas background with the laser blocked, followed by 70 second measurement of the target. Ablated material from the crystal was transported by the carrier gas to the torch of the ICPMS, which is equipped with a fast switching quadrupole mass filter. To correct for instrument drift the international standard NIST612 (doped synthetic silicate glass) was ablated twice at the beginning of the analytical session, at 90 minute intervals during the analysis and at the end of the analysis. A secondary standard, BCR-2 (basaltic glass) was ablated twice at the beginning of analytical sessions at 10 Hz repetition rate and 35 μm hole diameter, which was consistent with laser conditions used on samples. Correction factors were applied to the data for unknown samples based on the difference between the measured abundance of elements in BCR-2 versus the known abundance of elements in BCR-2. Aluminum ratios obtained from microprobe analysis were used as an internal standard.

7.4. Lorraine results

7.4.1. Presentation of data

Data ratios for Lorraine rocks have been classified based on rock type, and on the basis of alteration. Altered syenites are distinguished based on their abundant pink turbid K-

feldspar (Fig. 5-20a-c, e and f), fine-grained disseminated biotite (Fig. 4-10b) and/or fine grained disseminated sulphides, which have replaced primary biotite and diopside or secondary fine-grained biotite (Fig. 5-20b, e). These rocks contain >300 ppm of Cu and typically contain >55 vol. % K-feldspar (Fig. 5-27a). Altered biotite pyroxenites, show epidote, albite, magnetite alteration (Fig. 4-19c-e), coarse patches of biotite (Fig. 5-6d-f), coarse patches of apatite (Fig. 5-6d) and/or fine-grained sulphides that have replaced diopside and/or biotite (Fig. 4-17a-d). These rocks typically contain >300 ppm of Cu. Lorraine rocks can also be overprinted by late-stage alteration assemblages (*see* Chapter 4); however rock samples, which have been overprinted by late-stage alteration assemblages, were avoided for geochemical analysis.

7.4.2. Classification of Lorraine rocks

The suite of rocks from Lorraine varies from mafic to felsic compositions, with SiO_2 contents of 38 to 63 wt. % (excluding late Phase 3 leucosyenite with >70 wt.% silica), and plots in the alkaline field on the alkali versus silica plot (Irvine and Baragar, 1971; Fig. 7-1a, b). Both mineralised and unaltered syenites plot in the silica-undersaturated and silica-saturated fields of Lang et al. (1994; Fig. 7-1b). Most mineralised syenites plot in the silica-undersaturated field, probably due to an increase in potassium from metasomatism. Unaltered syenites vary from silica-undersaturated to just silica-saturated. Syenites have nepheline normative CIPW norms (Fig. 3-1b); however nepheline or primary quartz is uncommon in syenite samples.

Whole rock data from Lorraine were plotted onto the Zr/TiO_2 vs. Nb/Y trace element discrimination plot, after Winchester and Floyd (1977; Fig. 7-1c). Unaltered rocks plot in the sub-alkaline basalt to andesite/basalt fields. A small population of mineralised syenites and fine-grained K-feldspar biotite rocks plot in the alkaline basalt and trachyandesite fields.

Altered and unaltered rocks from Lorraine plot in the shoshonitic field on the K_2O vs. SiO_2 magmatic series discrimination diagram of Pecerillo and Taylor (1976) and Rickwood (1989; Fig. 6-1d). Altered and unaltered syenite and unaltered monzonite plot in the oceanic arc field on the Zr/Al_2O_3 vs. TiO_2/Al_2O_3 tectonic discrimination diagram (Fig. 7-1e) for shoshonitic and potassic volcanics of Müller et al. (1992). Syenite and monzonite plot in the late oceanic arc field on the Zr/Al_2O_3 vs. P_2O_5/Al_2O_3 oceanic arc discrimination diagram of Müller et al. (1992; Fig. 7-1f); although some mineralised syenites have lower P_2O_5/Al_2O_3 ratios compared to unaltered syenite and monzonite, and plot in the initial oceanic arc field.

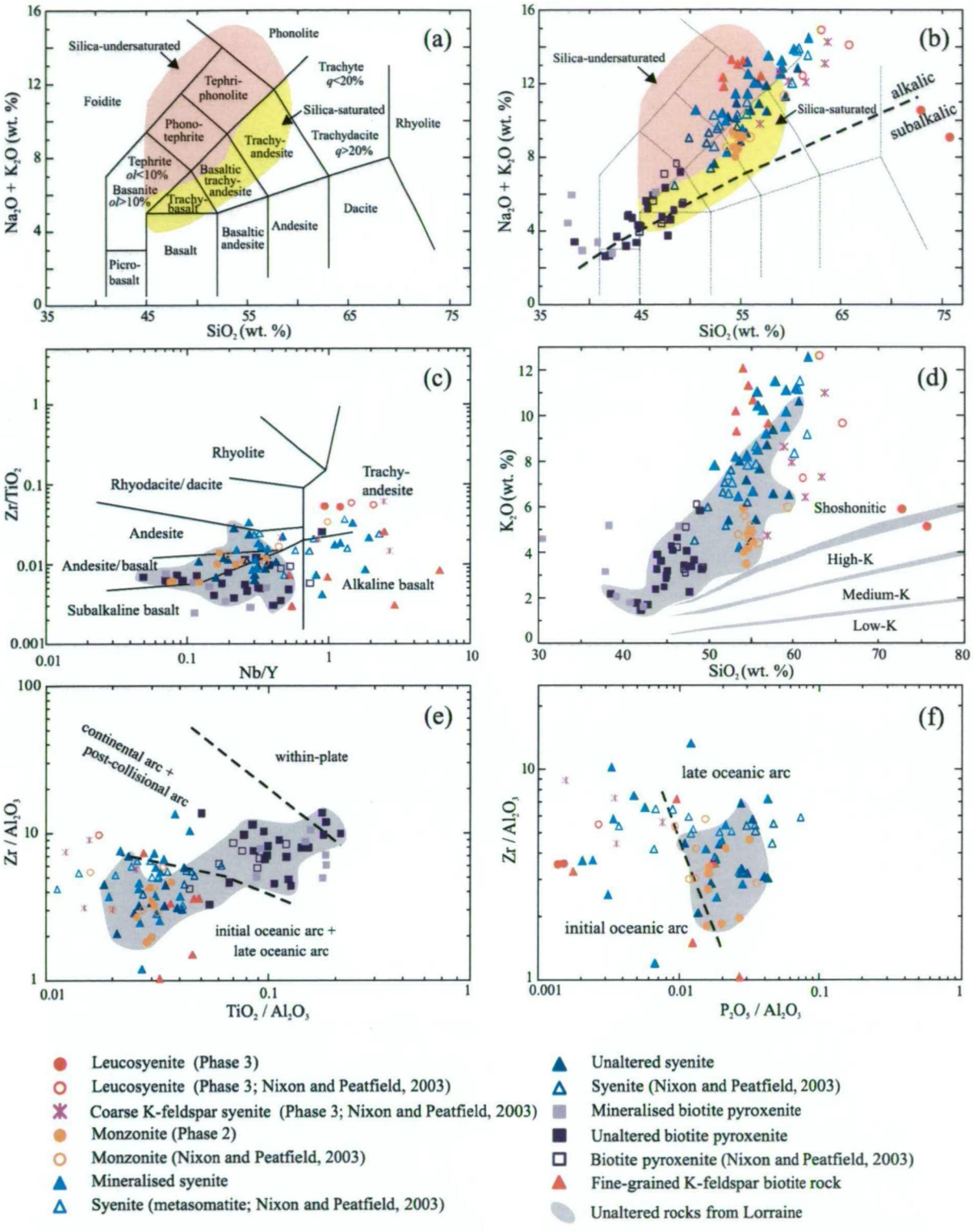

Figure 7-1. Major- and trace-element discrimination diagrams for mineralised and unaltered intrusive rocks of the Lorraine deposit. (a) Total alkali vs. silica (TAS) diagram with rock names (Le Maitre, 1989). (b) Whole rock data of Lorraine intrusives plotted on the TAS diagram with discrimination fields for alkaline vs. subalkaline (Irvine and Baragar, 1971) and silica-saturated vs. silica undersaturated fields (Lang et al., 1994). (c) Zr/TiO_2 vs. Nb/Y igneous rock discrimination plot (Winchester and Floyd, 1977). (d) K_2O vs. SiO_2 magma series discrimination plot of Peccerillo and Taylor (1976) and Rickwood (1989). (e) Zr/Al_2O_3 vs. TiO_2/Al_2O_3 tectonic discrimination diagram of Müller et al. (1992). (f) Zr/Al_2O_3 vs. P_2O_5/Al_2O_3 oceanic arc discrimination diagram of Müller et al. (1992). Data listed in Appendix D.

Altered and unaltered biotite pyroxenite plot in the continental arc and post-collisional arc field on the Zr/Al_2O_3 vs. TiO_2/Al_2O_3 tectonic discrimination diagram for shoshonitic and potassic volcanics of Müller et al. (1992; Fig. 7-1e). The classification of ultrabasic rocks as continental arc and post-collisional arc rocks is at odds with the data for coeval syenites from Lorraine, which plot in the oceanic arc field. Hence the tectonic discrimination diagram of Müller et al. (1992) cannot definitively assign all coeval rocks at Lorraine to one particular tectonic setting.

7.4.3. Effects of hydrothermal alteration on whole rock geochemistry

Hydrothermal alteration in porphyry copper environments is thought to have an effect on the abundance of 'mobile' elements (e.g., K, Na, Ca, Mg, Ba, Sr and Rb; Beane, 1982; Seedorff et al., 2005), but a lesser effect on the redistribution of 'immobile' elements (e.g., Zr, Ti, Nb, Y, REE, Th and U; Anthony and Titley, 1994).

Ratios of Zr/TiO_2, Zr/Al_2O_3, Ti/Al_2O_3, Nb/Y and P_2O_5/Al_2O_3 were used to evaluate element mobility as a result of hydrothermal alteration and mineralisation. Element ratios of Zr/TiO_2, Zr/Al_2O_3 and TiO_2/Al_2O_3 for mineralised and barren rocks, at Lorraine are similar for most rocks; although a small population of mineralised syenites has higher and lower Zr/Al_2O_3 ratios compared to the range for unaltered syenite (Figs. 7-1f). It is inferred that the above elements behaved as immobile elements in most mineralised samples in the Lower Main Zone. In contrast, Nb/Y ratios for mineralised syenites are higher than the range for unaltered syenite. It is inferred that alteration/metasomatism has resulted in the depletion of Y and/or enrichment of Nb in some mineralised rocks with higher Nb/Y ratios (Figs. 7-1c). A number of mineralised syenites are depleted in P relative to Al (Figs. 7-1f), suggesting that alteration may have resulted in the depletion of P in some syenites.

A plot of K_2O vs. Na_2O was used to compare the alkali contents of the various rock types at Lorraine (Fig. 7-2). Fields designated by Jensen and Barton (2000) for average igneous rocks, average potassic igneous rocks and a field for Galore Creek metasomatic rocks were used to compare with Lorraine data. Mineralised, fine-grained K-feldspar biotite rocks and most mineralised syenites plot in the metasomatic field, whereas most unaltered syenites plot in the fields for potassic and average igneous rocks. Monzonite plots predominantly in the average igneous rock field. Hence mineralised syenites from Lorraine have higher K and lower Na compared to their unaltered counterparts. Moreover, mineralised and unaltered syenites plot along a trend which is consistent with metasomatic vectors shown by Jensen and Barton (2000), which favours the formation of K-feldspar at the expense of plagioclase (Fig. 7-2). Unmineralised and mineralised biotite pyroxenites show no obvious distinction in alkali content, and therefore the presence or absence of sulphides

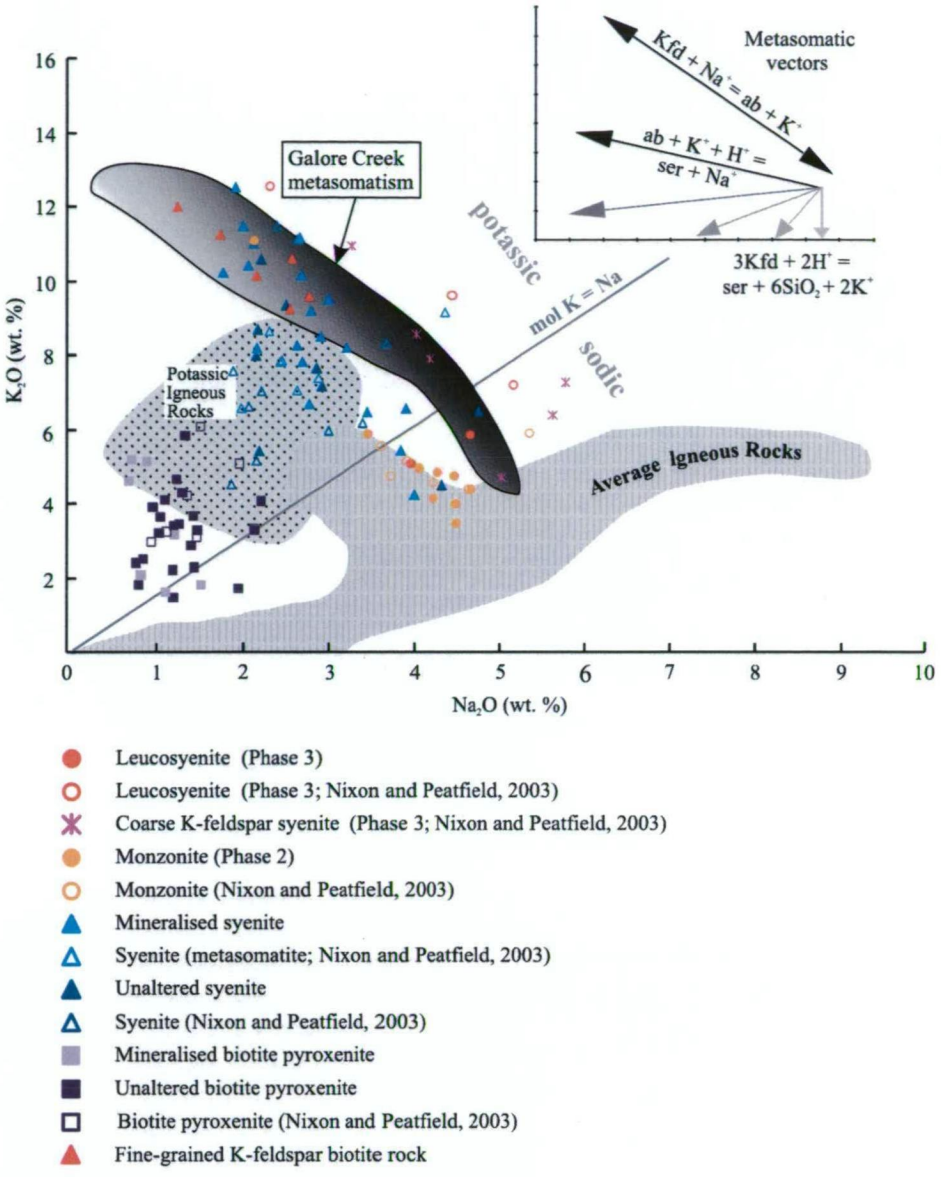

Figure 7-2. Whole rock plot of K_2O vs. Na_2O for various mineralised and barren rock types from Lorraine. Data are overlain on top of fields for average igneous rocks, potassic igneous rocks and for rocks that have undergone metasomatism at Galore Creek (modified from Jensen and Barton, 2000). The mineralised syenite and fine-grained K-feldspar biotite rocks from Lorraine appear to mostly fall in the field of metasomatised rocks from Galore Creek. The insert shows several metasomatic vectors. The vector for K-feldspar (Kfd) – albite (ab) best explains the distribution of whole rock data for mineralised syenite and fine-grained K-feldspar biotite rocks from Lorraine (modified after Jensen and Barton, 2000). Ser = sericite. Data listed in Appendix D.

has no obvious relationship with the alkali content of ultrabasic rocks at Lorraine.

Hydrothermal alteration can also have an effect on the volatile content of the host rocks. Secondary hydrous minerals such muscovite and chlorite can form as a result of low temperature alteration (e.g., Cathelineau, 1988). Water from these minerals can be detected in whole rock analysis as loss on ignition (LOI). Unaltered rocks from Lorraine have LOI ratios as high as 1.5 wt. % (Fig. 7-3). Some mineralised biotite pyroxenites and syenites

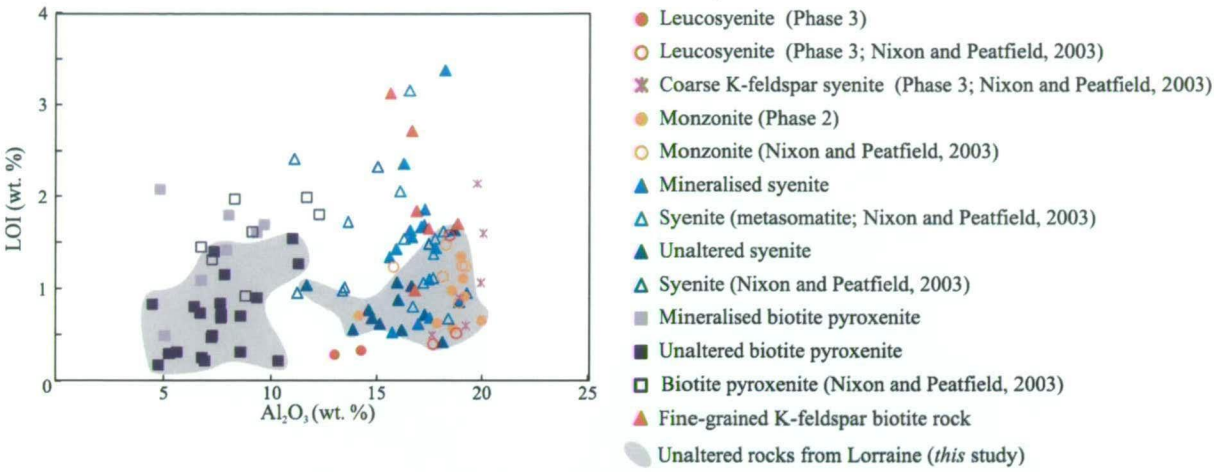

Figure 7-3. Loss on ignition (LOI) vs. Al_2O_3 for barren and mineralised rocks from Lorraine. The grey field highlights the distribution of compositions for unaltered rocks. Data listed in Appendix D.

have LOI ratios >1.5 wt. %. Altered rocks with >1.5 wt. % tend to contain muscovite and/or chlorite, which have selectively replaced plagioclase and mafics, respectively (e.g., Fig. 4-18c).

7.4.4. Major and trace element patterns of unaltered intrusive at Lorraine

A series of plots of various major and trace elements contents versus MgO are presented in Figures 7-4a-j and 7-5a-j to determine if any correlations exist between the suite of unaltered mafic to felsic intrusives. The suite of rocks from Lorraine have MgO concentrations that range from 0.2 to 14 wt. %. Rocks plot along negative linear or "dog leg" trends for SiO_2, Al_2O_3, Na_2O, K_2O and Sr vs. MgO and positive linear or "dog leg" trends for TiO_2, Cr, Fe_2O_3, MnO, CaO, P_2O_5, Ni, V and Co vs. MgO. In particular, trends for Al_2O_3, Cr, and CaO vs. MgO show "dog leg" trends, with the slope change along the main trend

Figure 7-4. Bivariate plots of major oxides vs. MgO for whole rock geochemistry of unaltered rocks from the Lower Main Zone and Lorraine area. The dashed line represents the field for Fijian shoshonites, after Leslie (2004). Average biotite (bio), diopside (di), K-feldspar (Kfd), plagioclase (pl) and magnetite (mt) compositions from Lorraine rocks have been plotted for to compare mineral compositions with whole rock trends. Results show that it is difficult to account for the numerous linear or "dog leg" tends by the accumulation of diopside alone. Data listed in Appendix D.

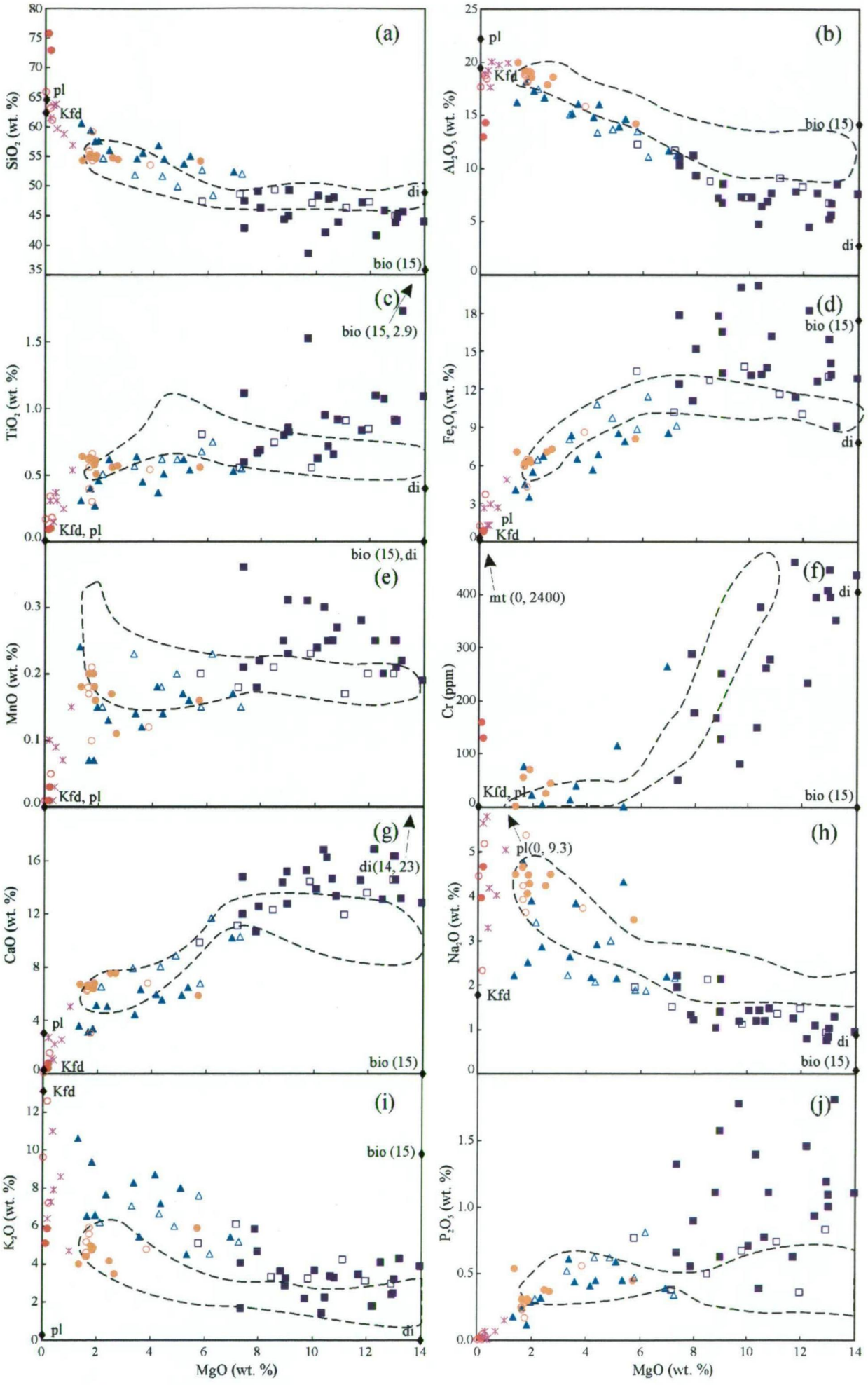
(a)
SiO2 (wt. %)
pl
Kfd
di
bio (15)
(b)
Al2O3 (wt. %)
pl
Kfd
bio (15)
di
(c)
TiO2 (wt. %)
bio (15, 2.9)
di
Kfd, pl
(d)
Fe2O3 (wt. %)
bio (15)
di
pl
Kfd
(e)
MnO (wt. %)
bio (15), di
Kfd, pl
(f)
Cr (ppm)
mt (0, 2400)
di
Kfd, pl
bio (15)
(g)
CaO (wt. %)
di(14, 23)
pl
Kfd
bio (15)
(h)
Na2O (wt. %)
pl(0, 9.3)
Kfd
di
bio (15)
(i)
K2O (wt. %)
Kfd
bio (15)
pl
di
(j)
P2O5 (wt. %)
MgO (wt. %)
MgO (wt. %)

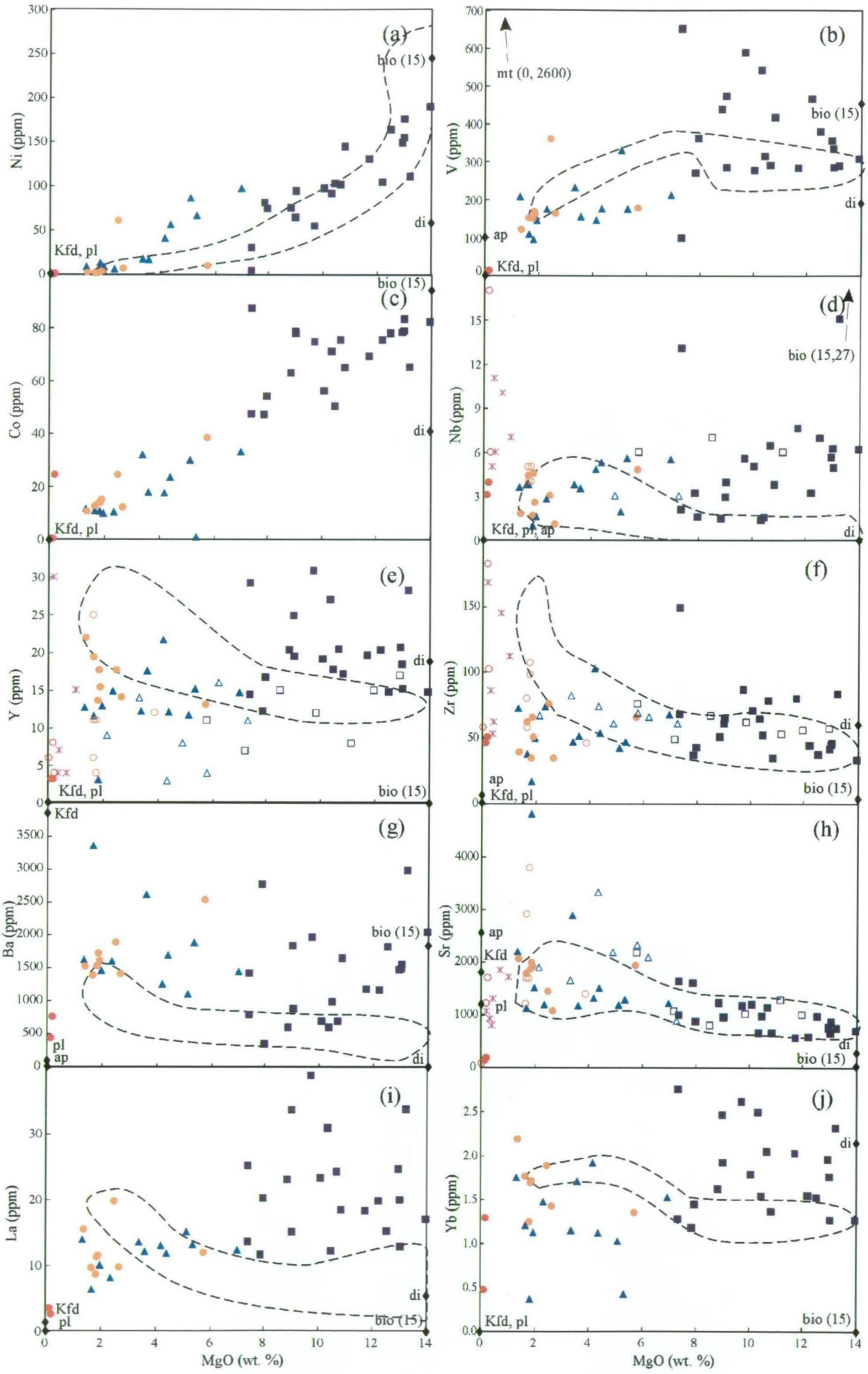
(a)
Ni (ppm)
bio (15)
di
Kfd, pl
bio (15)
(b)
V (ppm)
mt (0, 2600)
bio (15)
di
ap
Kfd, pl
(c)
Co (ppm)
di
Kfd, pl
(d)
Nb (ppm)
bio (15,27)
Kfd, pl, ap
di
(e)
Y (ppm)
di
Kfd, pl
bio (15)
(f)
Zr (ppm)
di
ap
Kfd, pl
bio (15)
(g)
Ba (ppm)
Kfd
bio (15)
pl
ap
di
(h)
Sr (ppm)
ap
Kfd
pl
di
bio (15)
(i)
La (ppm)
di
Kfd
pl
bio (15)
(j)
Yb (ppm)
di
Kfd, pl
bio (15)
MgO (wt. %)
MgO (wt. %)

occurring at approximately 9 wt. % MgO. The slope change along the "dog leg" trend most likely marks a shift from diopside and biotite to feldspars as the dominant phases.

Zirconium and Nb levels remain relatively constant across the MgO fractionation range (Fig. 7-5d, f). Yttrium, La and Yb are predominantly enriched in pyroxenite relative to syenite and monzonite, but do not define coherent trends (Fig. 7-5e, i and j). Pyroxenite and syenite have variable contents of Ba (i.e. <600 to 3000 ppm), whereas monzonite predominantly has relatively consistent Ba ratios between approximately 1400 and 1800 ppm (Fig. 7-5g).

7.4.4.1. Multi-element variation diagrams

Trace elements and selected major elements from whole rock analyses of biotite pyroxenite, syenite, fine-grained K-feldspar biotite rocks and monzonite were normalised to primitive mantle ratios (Sun and McDonough, 1989) and plotted onto a series of multi-element variation diagrams (Fig. 7-6a-d). All rock types plot along a negative slope from left to right with positive anomalies for LILE (Li, K, Rb and Ba) as well as Sr, Pb and Sn, and relative negative anomalies for HFSE (Ti, Nb, Ta, Zr and Hf), which is consistent with patterns for arc rocks (e.g., Pearce and Parkinson, 1993). The patterns are also consistent with those of arc-related shoshonites (*see* section 7.6.5.).

7.5. Comparison of Lorraine rocks with Fijian shoshonites

7.5.1. Samples for comparison

Major and trace element geochemical data for primitive shoshonitic lava from the Tavua Volcano, the Astrolabe Group and Vatu-i-Cake, all in Fiji are from the PhD study of Leslie (2004; Fig. 6-1a, b), and are used here to compare with whole rock data from Lorraine.

←

Figure 7-5. Bivariate plots of selected trace elements vs. MgO for whole rock geochemistry of unaltered rocks from the Lower Main Zone and Lorraine area. The dashed line represents the field for Fijian shoshonites after Leslie (2004). Average biotite (bio), diopside (di), K-feldspar (Kfd), plagioclase (pl) and magnetite (mt) compositions from Lorraine rocks have been plotted for to compare mineral compositions with whole rock trends. Results show that it is difficult to account for the numerous linear tends by the accumulation of diopside alone. Data listed in Appendix D.

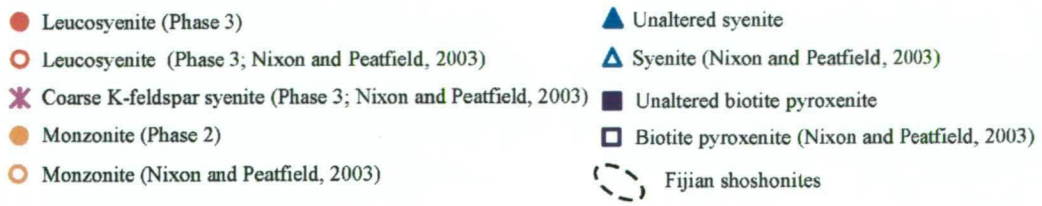

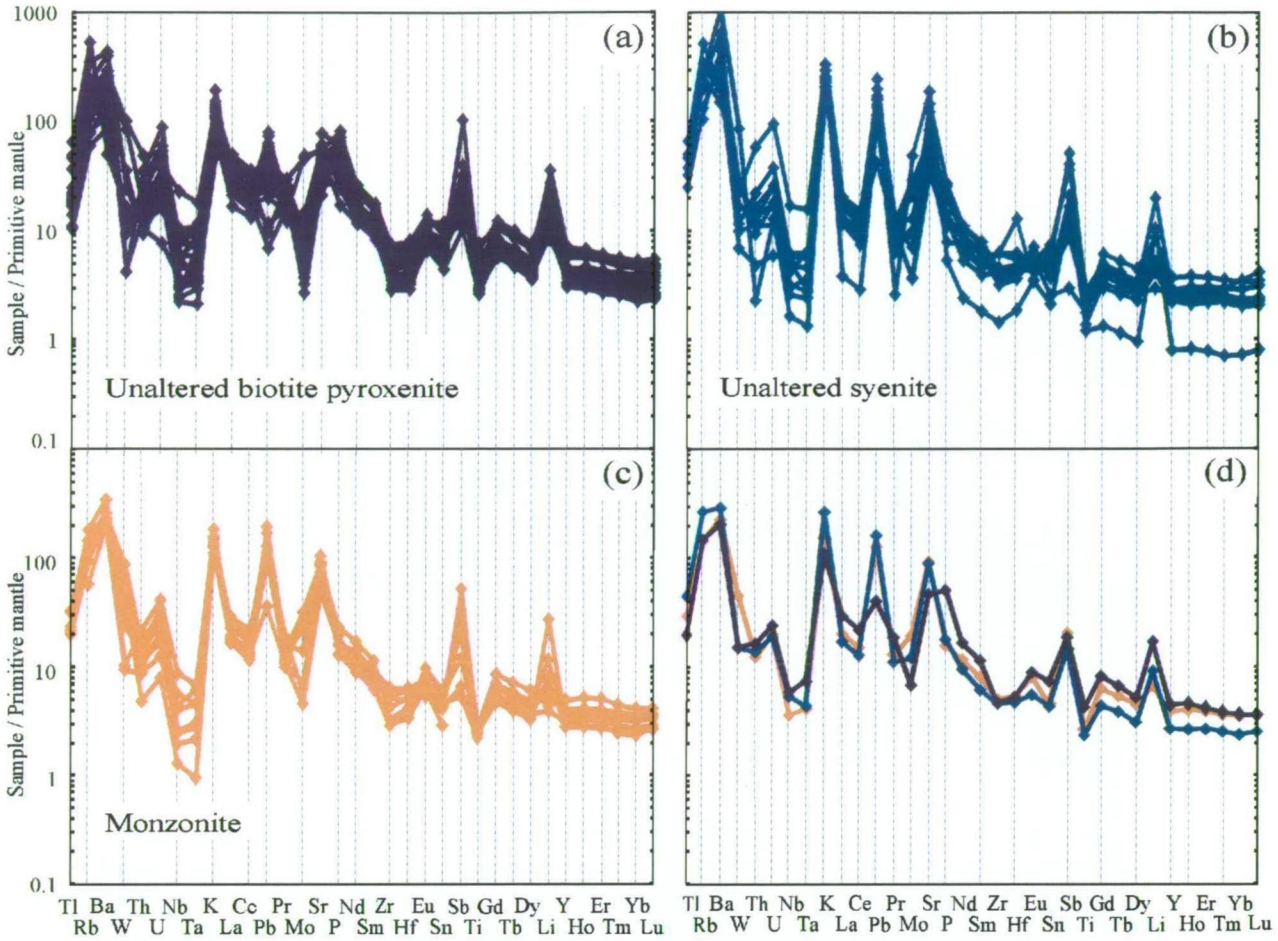

Figure 7-6. Primitive mantle (Sun and McDonough, 1989) normalised multi-element variation diagrams showing the distribution of whole rock trace element patterns for **(a)** unaltered biotite pyroxenite, **(b)** unaltered syenite, **(c)** unaltered monzonite and **(d)** average biotite pyroxenite (purple), syenite (blue) and monzonite (yellow). Data listed in Appendix D.

The data from Leslie (2004), includes 37 analyses of shoshonitic volcanic rocks that contain olivine and clinopyroxene phenocrysts.

7.5.2. Major and trace elements

Fields for the Fijian shoshonites and Lorraine are presented on a series of major and trace element vs. MgO plots (Figs. 7-4a-j and 7-5a-j). Tavua Group rocks range from 1.7 to 13.6 wt. % MgO, Astrolabe rocks range from 2.0 to 13.8 wt. % MgO and Vati-i-Cake lavas range between 10.4 and 15.2 wt. % MgO. Shoshonites from Fiji have a similar range of MgO compared to the suite of biotite pyroxenite, monzonite and syenite from Lorraine (Figs. 7-4a-j and 7-5a-j). The Lorraine rocks and Fijian shoshonites plot along similar trends on SiO_2, Ni, and V vs. MgO scatter plots (Figs. 7-4a and 7-5a, b). Fijian shoshonites with less than 6 wt. % MgO overlap with Lorraine in plots of Al_2O_3, Cr, CaO, Na_2O and Sr vs. MgO; although Fijian shoshonites with greater than 6 wt. % MgO have more abundant in Al_2O_3, Na_2O and less Fe_2O_3 and P_2O_5 compared to Lorraine rocks. Both Fijian and

Lorraine rocks show "dog leg" trends in the Al_2O_3, and Cr vs. MgO plots. Notable differences between the two suites are (1) Ba is on average more enriched, but also highly variable in Lorraine rocks, (2) Nb, Y and Zr do not change with decreasing MgO in Lorraine rocks, (3) P_2O_5 and La have weak positive correlations with MgO at Lorraine; however Fijian shoshonites show no correlation between P_2O_5 vs. MgO, and have a negative correlation for La vs. MgO. Key differences are the higher P and REE-Y for some Lorraine biotite pyroxenites, reflecting their apatite-accumulative nature.

7.5.3. Comparison of trace element ratios for biotite pyroxenite with Fijian shoshonites, mafic arc rocks from the western Pacific and the mantle-array

Biotite pyroxenite dominantly plot in the enriched MORB field on the Zr/Yb vs. Nb/Yb of Pearce and Peate (1995; Fig. 7-7a), and they overlap with the Nb/Yb range for Fijian shoshonites, being most similar to Astrolabe Group lavas. The array of Nb/Yb ratios for biotite pyroxenites are on average higher than calc-alkaline (med-K) rocks from Vanuatu, Togan-Kermadec arc tholeiites and Tabar-Feni arc shoshonites, suggesting derivation from a relatively enriched (or less depleted) mantle source. In contrast, Nb/Yb ratios for biotite pyroxenite overlap with Mariana arc shoshonites; although Zr/Yb ratios for Mariana arc shoshonites are higher than for biotite pyroxenites and plot along a vector that trends outside the mantle-array. Sun and Stern (2001) suggested that the Mariana shoshonites have been contaminated by melts of marine sediments derived from the subducting slab, which contributed enrichments of Th, REE and HFSE relative to the mantle-array. Biotite pyroxenites do not show evidence of increased Zr/Yb relative to the mantle-array, and therefore there appears to be no evidence of Zr-enrichment from slab-derived sediment melt or crustal contamination.

Lanthanum/Sm ratios pose problems when dealing with unaltered biotite pyroxenites from Lorraine, as many unaltered biotite pyroxenites show evidence of apatite accumulation (i.e. apatites are LREE-enriched; *see* Chapter 6). For the purpose of this section the author focused on those samples that show the least evidence of phosphorous enrichment (i.e. <0.8 wt. % P_2O_5). Lanthanum/Sm ratios for biotite pyroxenite are restricted between approximately 3.5 and 4.5, and are higher than the mantle-array, as are all arc suites plotted (Figs. 7-7b and 7-8a-h). The La/Sm ratios are lower than apatite (4.9 to 6.2) but higher than diopside (1.1 to 1.6). This limited range of La/Sm ratios likely reflects that biotite pyroxenites were generated from a magma source with La/Sm ratio between 3.5 and 4.5.

The Togan-Kermadec arc tholeiites and calc-alkaline (med-K) basalts from Vanuatu have a wide range of La/Sm ratios (i.e. ~1 to 5 and 1 to 6.5 respectively) and overlap with the range for biotite pyroxenite. Fijian shoshonites from the Astrolabe Group have a lower

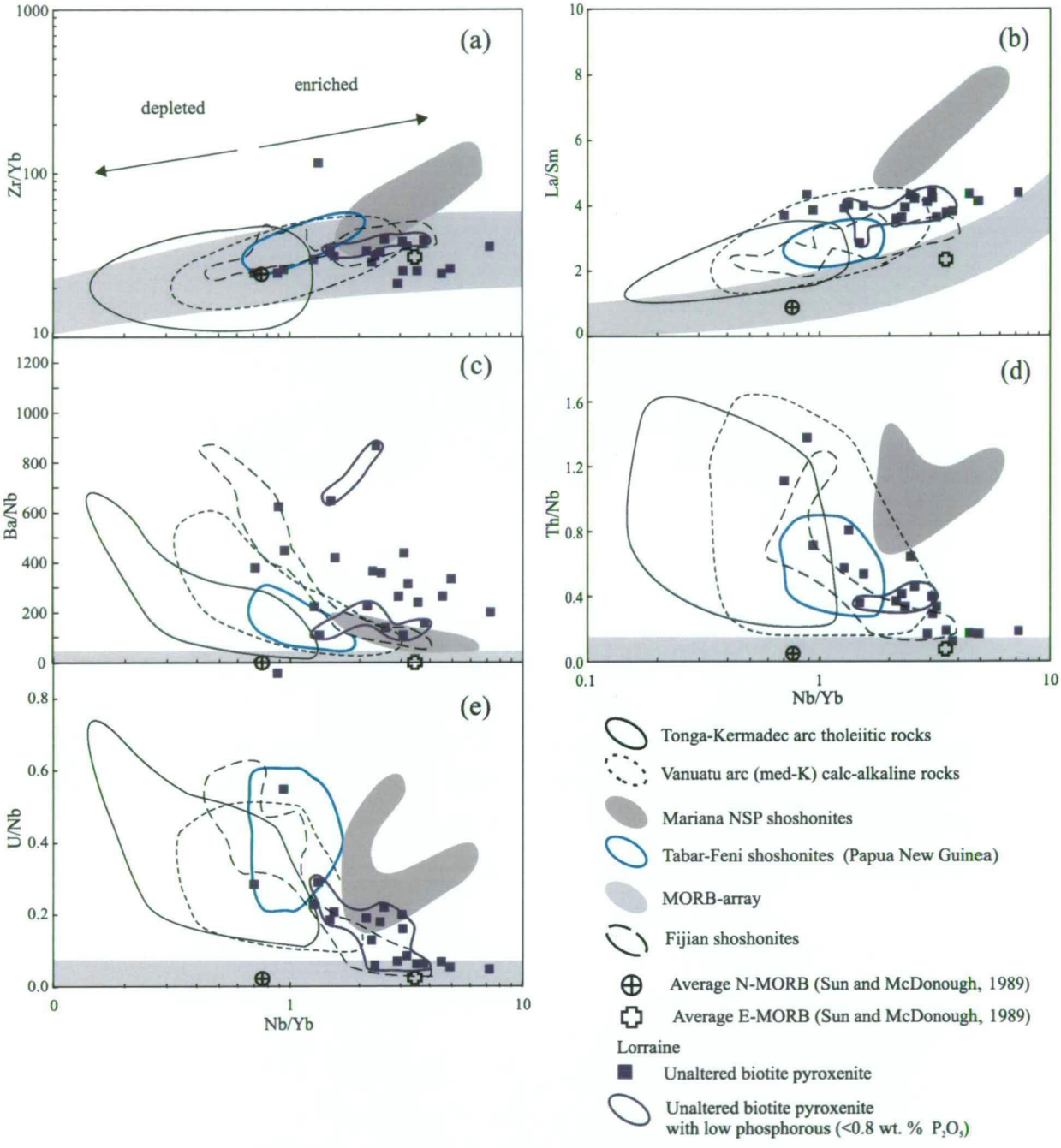

Figure 7-7. **(a)** Zr/Yb vs. Nb/Yb diagram (after Pearce and Peate, 1995) with illustrated fields for enriched and depleted mantle sources independent of slab-derived components, and the distribution of Lorraine biotite pyroxenite relative to basalts from the western Pacific arcs. **(b)** La/Sm vs. Nb/Yb with biotite pyroxenite compositions relative to mantle-array and basalts from the western Pacific arcs. This diagram illustrates the relative relationship between LREE and MREE. **(c-e)** Ba/Nb, Th/Nb and U/Nb vs. Nb/Yb. Fields for western Pacific arc basalts were compiled by Leslie (2004). (Data sources for fields include; Barsdell, 1988; Crawford et al., 1988; Barsdell and Berry, 1990; Kennedy et al., 1990; Eggins, 1993; Gamble et al., 1993; Rogers and Setterfield, 1994; Monzier et al., 1997; Turner et al., 1997; Stracke and Hegner, 1998; Sun and Stern, 2001; Leslie, 2004; Raos and Crawford, 2004).

range of La/Sm ratios (i.e. 2.5 to 3.5), whereas shoshonites from the Tavua and Vati-i-Cake Groups have La/Sm ratios that overlap with biotite pyroxenite (i.e. ~1.5 to 4 and ~2 to 5 respectively). In particular, shoshonites from the Vati-i-Cake Group with greater than 13.5 wt. % MgO have La/Sm ratios >3, and are similar to, or overlap with biotite pyroxenite. It is inferred that higher La/Sm ratios are caused due to lower degrees of partial melting of a peridotite mantle source, an increase in mantle fertility and/or a higher degree of slab-derived sediment input. One or more of the above processes may explain the relative high La/Sm ratios of the Lorraine biotite pyroxenite.

Barium/Nb ratios for biotite pyroxenites are highly variable and range from approximately 100 to 900 (Figs. 7-7c and 7-8b). These ratios are higher than the mantle-array (i.e. ~0-50), but are comparable to the range for Tonga-Kermadec arc tholeiites (~25-700), and Vanuatu arc (med-K) calc-alkaline lavas (~100-650) due to the lower Nb of the latter two groups. In contrast, Mariana and Tabar-Feni arc shoshonites have, on average, lower Ba/Nb ratios than the biotite pyroxenites (i.e. ~50-250 and ~50-350 respectively). Fijian shoshonites show a large range in Ba/Nb ratios, with the Tavua Group lavas the highest (~400-900), Vati-i-Cake intermediate (~350-450) and Astrolabe Group the lowest (~50-200). Hence the range of Ba/Nb for Fijian shoshonites is comparable to the range for Lorraine biotite pyroxenite, but the biotite pyroxenites plot at higher ratios of Ba/Nb for any Nb/Yb level, reflecting their very high Ba contents. The Ba enrichment may have been derived from slab-derived fluids.

Thorium/Nb ratios for biotite pyroxenites range from approximately 0.2 to 0.9 (excluding two outliers), and like other arc-related magmas, biotite pyroxenites have higher Th/Nb ratios relative to the mantle-array (Figs. 7-8d and 7-9g). Th/Nb ratios for biotite pyroxenite overlap with the field for Tabar-Feni arc shoshonites and Astrolabe Group shoshonites from Fiji. However, Fijian shoshonites from Tavua and Vati-i-Cake groups tend to have higher Th/Nb ratios than pyroxenites (i.e. 0.7-1.1 and 1.2-1.3 respectively). Arc tholeiites and calc-alkaline (med-K) arc lavas have a wide range of Th/Nb ratios (~0.2-1.6), and shoshonites from the Mariana arc have higher Th/Nb ratios than the biotite pyroxenites (~0.7 to 1.5). Thorium is considered to behave as an immobile element with respect to fluids derived from dehydration of subducted slab, and enrichment in Th relative to Nb in mafic arc magmas may be explained by slab-derived sediment melting (e.g., Mariana shoshonites).

Uranium/Nb ratios of biotite pyroxenites range from 0.05 to 0.3 (excluding one outlier), with some plotting in the mantle-array (Figs. 7-7e and 7-8h). Biotite pyroxenites show a similar array of U/Nb ratios to Astrolabe Group shoshonites from Fiji; however Lorraine pyroxenites predominantly have lower U/Nb ratios than Tabar-Feni shoshonites, Mariana

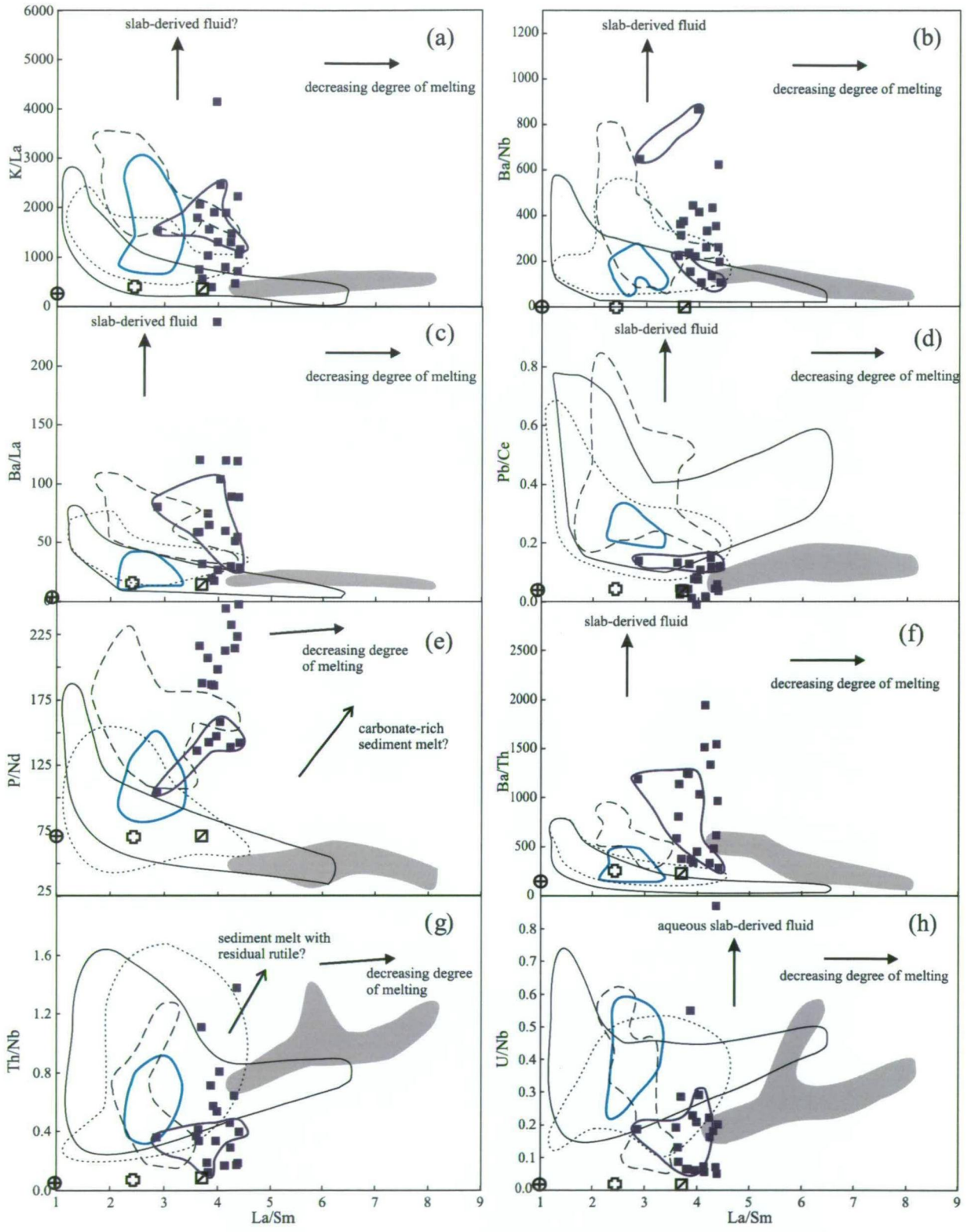
(a)
slab-derived fluid?
decreasing degree of melting
K/La
(b)
slab-derived fluid
decreasing degree of melting
Ba/Nb
(c)
slab-derived fluid
decreasing degree of melting
Ba/La
(d)
slab-derived fluid
decreasing degree of melting
Pb/Ce
(e)
decreasing degree of melting
carbonate-rich sediment melt?
P/Nd
(f)
slab-derived fluid
decreasing degree of melting
Ba/Th
(g)
sediment melt with residual rutile?
decreasing degree of melting
Th/Nb
(h)
aqueous slab-derived fluid
decreasing degree of melting
U/Nb
La/Sm
La/Sm
Tonga-Kermadec arc tholeiitic rocks
Vanuatu arc (med-K) calc-alkaline rocks
Mariana NSP shoshonites
Tabar-Feni shoshonites (Papua New Guinea)
Fijian shoshonites
Average N-MORB (Sun and McDonough, 1989)
Average E-MORB (Sun and McDonough, 1989)
Average OIB (Sun and McDonough, 1989)
Lorraine
Unaltered biotite pyroxenite
Unaltered biotite pyroxenite with low phosphorous (<0.8 wt. % P_2O_5)

←

Figure 7-8. **(a-h)** Plots of selected trace element ratios vs. La/Sm, which illustrates the composition of Lorraine biotite pyroxenites relative to western Pacific arc basalts, N-MORB, E-MORB, OIB (Sun and McDonough, 1989) and Tongan sediment composition (Plank and Langmuir, 1998). Data fields and vectors were compiled by Leslie (2004). See Figure 7-8 for a list of data sources.

shoshonites, Tauva and Vati-i-Cake shoshonites. Arc tholeiites and calc-alkaline rocks show a wide range in U/Nb ratios, which overlaps with the range for biotite pyroxenites. Uranium is considered to behave as a non-conservative element, and enrichment in U relative to Nb in mafic arc magmas may be explained by slab-derived fluids.

Potassium/La and Ba/La ratios are higher in pyroxenites relative to the mantle-array, and overlap with ratios for arc rocks from the western Pacific (Fig. 7-8a, c). Surprisingly perhaps, Pb/Ce ratios of pyroxenites are only slightly higher than the MORB-array (for low P biotite pyroxenites from Lorraine), and have compositions similar to shoshonites from the Mariana arc (Fig. 7-8d). Lead is considered to be non-conservative, whereas Ce is considered to be moderately conservative, and therefore slab-derived aqueous fluids should increase the Pb/Ce ratio of mafic magmas derived from the sub-arc mantle. Hence the notable low Pb/Ce ratios of biotite pyroxenites may be explained by a relatively low input of Pb from slab derived fluids or maybe from pelagic clay melting(?).

Phosphorous/Nd ratios in biotite pyroxenites range from approximately 140 to 250 and are higher than N-MORB (~75; Fig. 7-8e). Biotite pyroxenites also have higher P/Nd ratios than Mariana shoshonites (30-70) and Astrolabe Group shoshonites. Calc-alkaline (med-K), arc tholeiites and Tabar-Feni arc shoshonites predominantly have lower P/Nd ratios than pyroxenites. Tauva and Vati-i-Cake shoshonites from Fiji have P/Nd ratios that overlap with the range for pyroxenite (110-230 and 150-180 respectively). Leslie (2004) suggested that addition of a melt of carbonate-rich sediment to the mantle source may have led to increased P/Nd ratios in Fijian shoshonites. Green and Wallace (1988) also suggested that carbonatitic melts in the mantle should be an effective transporting agents for P and LREE. The ultimate source of P (and Sr) may well have come from subducted P-rich fish debris and carbonate-rich nano-fossils or other biogenic sources, which is also the proposed source of P- and Sr-enrichment in Fijian shoshonites, and for other western Pacific arc lavas (e.g., Leslie, 2004; Raos and Crawford, 2004).

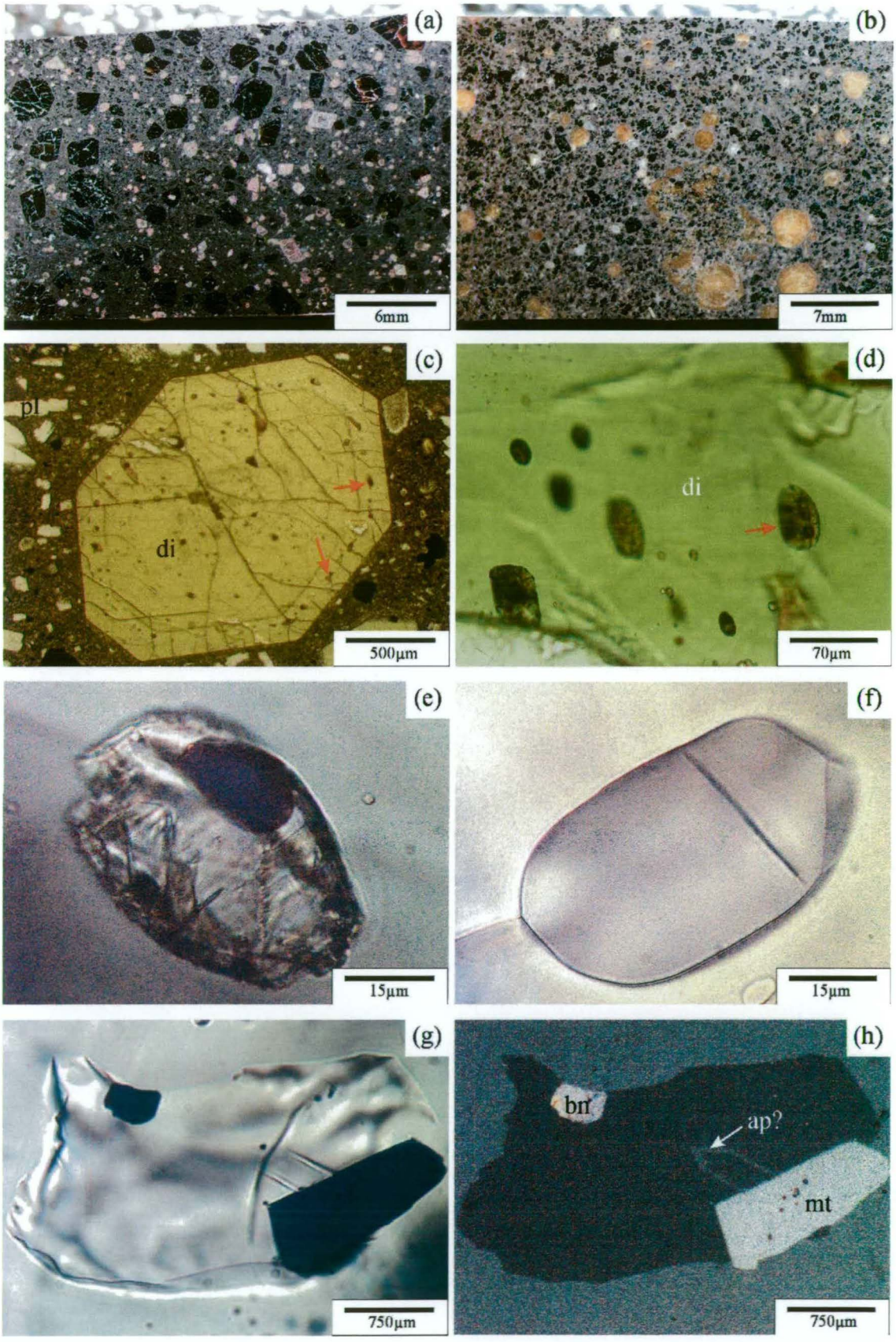

Figure 7-9. **(a)** Diopside-plagioclase phyric basalt. **(b)** Analcime-diopside phyric basalt from the Nicola Group Volcanics in the Mt. Polley area (a; sample 05ABA 13-105; 586016mE, 5819125mN; b; sample 05JLO 32-246-2; 600846mE, 5804521mN). **(c)** Euhedral diopside from "a" with melt inclusions along

Figure 7-9. *continued*

crystal growth plane (red arrows; di = diopside, pl = plagioclase). **(d)** Melt inclusions assemblage in diopside from "a". **(e)** Unheated melt inclusion in diopside with crystals along wall of inclusion and a vapour bubble. **(f)** Remelted homogenised inclusion. Inclusion was heated to 1180 °C and quenched in He gas. **(g)** Remelted inclusion with co-trapped crystals of bornite (bn), magnetite (mt) and apatite (ap).

7.6. Comparison of Lorraine rocks with alkaline basalt and diopside-hosted melt inclusions from the Nicola Group Volcanics, BC

7.6.1. Samples

Diopside + plagioclase phyric and analcime + diopside phyric alkaline basalts of the Nicola Group volcanics from the Mt. Polley area (Fig. 6-2) were selected for a melt inclusion study (Fig. 7-9a, b). Whole rock major and trace element analysis was previously carried out on the samples by Logan and Bath (2006). As part of the current study over 40 melt inclusions hosted in euhedral diopside were analysed for major elements using the EPMA, and eight inclusions were analysed for trace elements using LA-ICP-MS at the University of Tasmania. Melt inclusions occur along crystal growth zones (Fig. 7-9c, d), and range from <1 μm to 200 μm in size. Unheated inclusions contain fine-grained silicate daughter crystals that predominantly occur along the wall of inclusions, glass, and a vapour bubble (Fig. 7-9e). Some inclusions also contain co-trapped crystals of magnetite, apatite and/or Cu-Fe sulphides (Fig. 7-9g, h). Inclusions reheated to 1180 °C are glassy, and some inclusions contain co-trapped crystals of magnetite, apatite and Cu-Fe sulphides.

7.6.2. Classification of basaltic glasses and whole rock geochemistry

Reheated melt inclusions have SiO_2 contents of 46-57 wt %, and plot in the alkaline field on the alkali versus silica diagram (Irvine and Baragar, 1971; Fig. 7-10b). Whole rock data for the host basalts range from alkaline to sub-alkaline, and rocks plot in the basalt, trachy-basalt and basaltic trachy-andesite fields (Fig. 7-10a, b). Basaltic glasses and whole rocks plot in the sub-alkaline basalt to andesite/basalt fields on the Zr/TiO_2 vs. Nb/Y diagram (Winchester and Floyd, 1977; Fig. 7-10c). Melt inclusions plot in the shoshonitic field, whereas the whole rocks dominantly plot in shoshonitic field, but also in the high- and medium-K fields on the K_2O vs. SiO_2 magmatic series discrimination diagram of Pecerillo and Taylor (1976) and Rickwood (1989; Fig. 7-10d). The basaltic glasses and whole rock samples plot in the late oceanic arc field on the Zr/Al_2O_3 vs. TiO_2/Al_2O_3 tectonic discrimination diagram for shoshonitic and potassic volcanics of Müller et al. (1992; Fig. 7-10e, f).

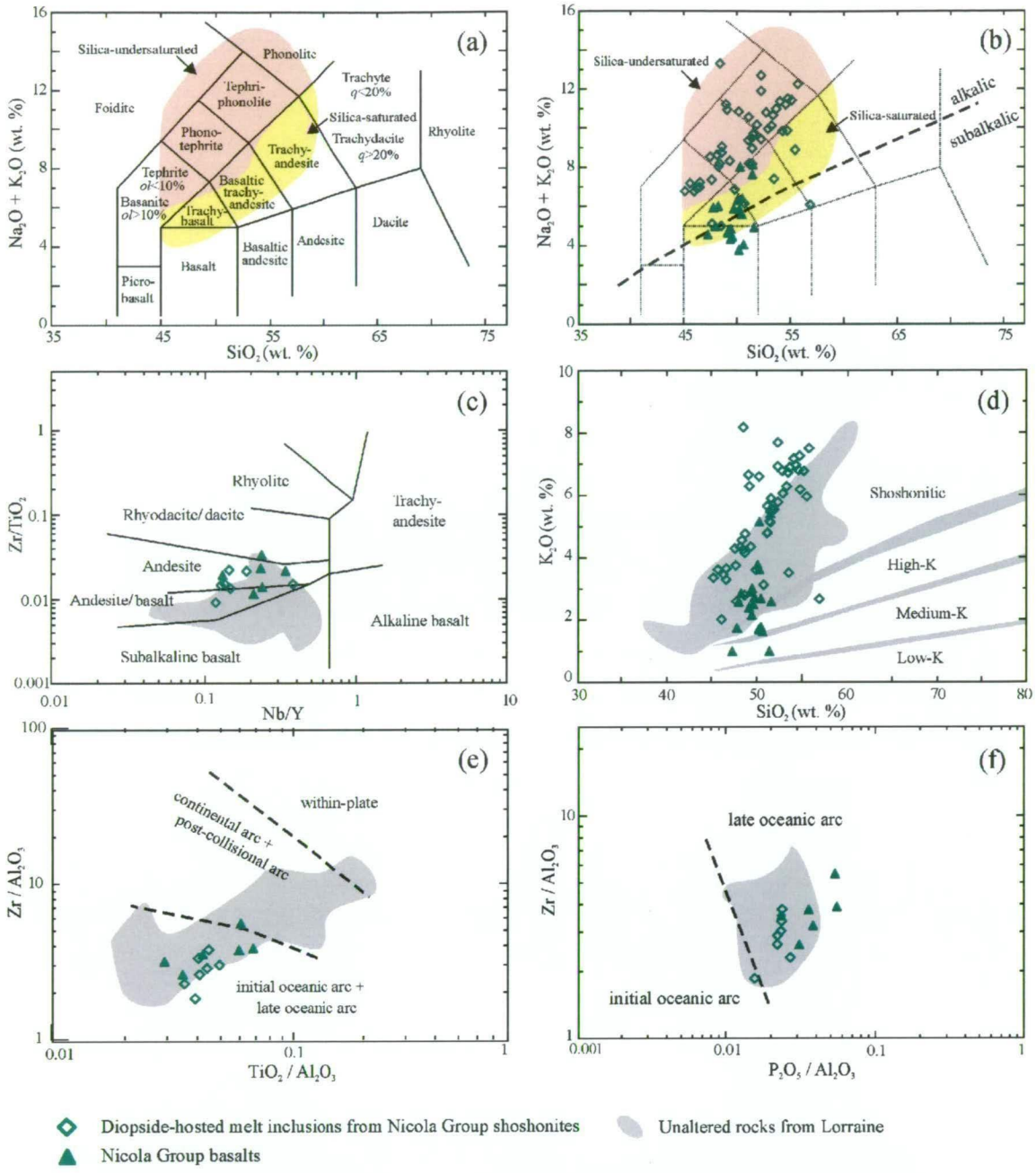

Figure 7-10. Major- and trace-element discrimination diagrams for Nicola Group basalts (closed green triangles) and diopside hosted melt inclusions from basalts (open green diamonds). Note that whole rock data for Nicola Group basalt is from Logan and Bath (2006). **(a)** Total alkali vs. silica (TAS) diagram with rock names (Le Maitre, 1989) and silica-saturated vs. silica-undersaturated fields (Lang et al., 1994). **(b)** Whole rock data of Mt. Polley plotted on the TAS diagram with discrimination fields for alkaline vs. subalkaline (Irvine and Baragar, 1971). **(c)** Zr/TiO_2 vs. Nb/Y igneous rock discrimination plot (Winchester and Floyd, 1977). **(d)** K_2O vs. SiO_2 magma series discrimination plot of Peccerillo and Taylor (1976) and Rickwood (1989). **(e)** Zr/Al_2O_3 vs. TiO_2/Al_2O_3 tectonic discrimination diagram of Müller et al. (1992). **(f)** Zr/Al_2O_3 vs. P_2O_5/Al_2O_3 oceanic arc discrimination diagram of Müller et al. (1992).

Figure 7-11. Bivariant plots of major oxides vs. MgO for Nicola Group basalts (closed green triangles) and diopside hosted melt inclusions from basalts (open green diamonds). The grey field represents the compositions of unaltered intrusive rocks from Lorraine (this study). The dashed line shows the field for Fijian shoshonites from Leslie (2004). Note that whole rock data for Nicola Group basalt is from Logan and Bath (2006). Average biotite (bio), diopside (di), K-feldspar (Kfd), plagioclase (pl) and magnetite (mt) compositions from Lorraine rocks have been plotted to compare mineral compositions with whole rock trends.

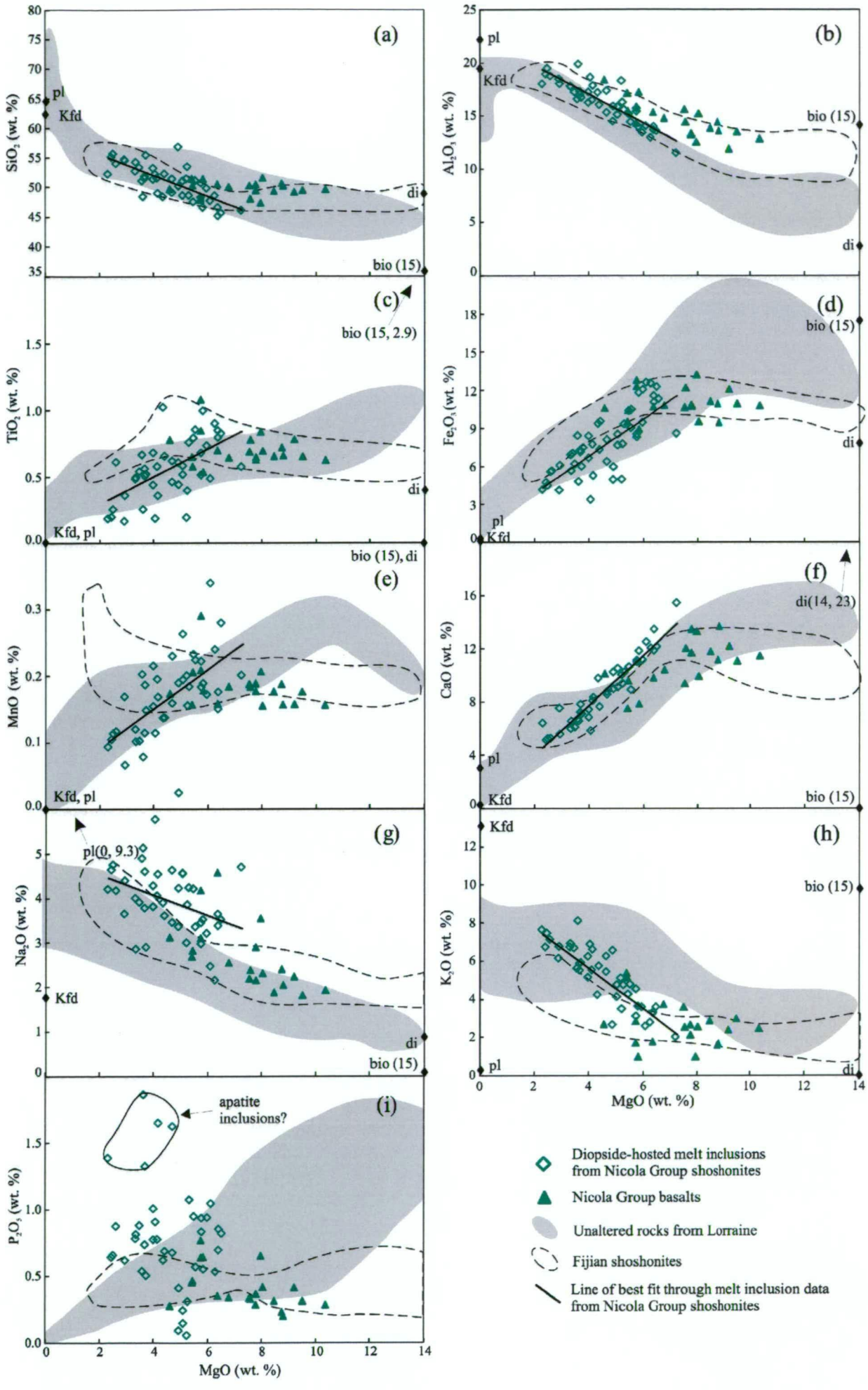
(a)
SiO2 (wt. %)
pl
Kfd
di
bio (15)
(b)
Al2O3 (wt. %)
pl
Kfd
bio (15)
di
(c)
TiO2 (wt. %)
bio (15, 2.9)
di
Kfd, pl
(d)
Fe2O3 (wt. %)
bio (15)
di
pl
Kfd
(e)
MnO (wt. %)
bio (15), di
Kfd, pl
(f)
CaO (wt. %)
di(14, 23)
pl
Kfd
bio (15)
(g)
Na2O (wt. %)
pl(0, 9.3)
Kfd
di
bio (15)
(h)
K2O (wt. %)
Kfd
bio (15)
pl
di
(i)
P2O5 (wt. %)
apatite inclusions?
MgO (wt. %)
MgO (wt. %)
Diopside-hosted melt inclusions from Nicola Group shoshonites
Nicola Group basalts
Unaltered rocks from Lorraine
Fijian shoshonites
Line of best fit through melt inclusion data from Nicola Group shoshonites

7.6.3. Major oxides

A series of plots of various major and trace elements vs. MgO are presented in Figures 7-11a-i and 7-12a-h to compare trends of Nicola Group basalts and diopside-hosted melt inclusions with Lorraine rocks and Fijian shoshonites. The Nicola Group basalts have MgO concentrations from ~4 to 10 wt. %, and diopside-hosted melt inclusions that range from ~2 to 7 wt. %. Whole rock and melt inclusions predominantly plot in the same field as Lorraine rocks for SiO_2, TiO_2, Fe_2O_3, CaO, Ni, Nb, Y, Zr, Ba and Yb vs. MgO; although basalts are on average, richer in Al_2O_3 relative to Lorraine rocks with equivalent MgO. They also tend to have lower abundances of La. Nicola Group basalts have lower abundances of P_2O_5 compared to most biotite pyroxenite. Some melt inclusions have anomalous P_2O_5, probably related to melting of co-trapped apatite during reheating (?). Nicola Group Volcanics overlap with the field for Fijian shoshonites for almost all elements plotted against MgO on Figures 7-11a-i and 7-12a-h, with the exception of Ba, which is more enriched in Nicola Group basalts that contain less than 8 wt. % MgO.

7.6.4. Trace element ratios

Basalt and diopside-hosted melt inclusions predominantly plot between N- and E-MORB on the Zr/Yb vs. Nb/Yb of Pearce and Peate (1995; 7-13a), and have a similar range to the Fijian shoshonites. Nb/Yb ratios overlap with the range for biotite pyroxenite from Lorraine and vary from 0.8 to 2. Basalts and melt inclusions have La/Sm ratios between 2 and 4.5 (excluding one outlier) and some plot in the same field as biotite pyroxenite on the La/Sm vs. Nb/Yb plot; others have La/Sm ratios <3, and plot in the field of Tabar-Feni shoshonite (Figs. 7-13b and 7-14a-h). Analcime-diopside phyric basalts have higher La/Sm (i.e. >3) compared to diopside-plagioclase phyric basalts (i.e. <3). Ba/Nb ratios for basalts and diopside-hosted melt inclusions are highly variable; these range from 200 to 1200. Approximately half of the basalt samples have higher Ba/Nb than the range for Lorraine pyroxenites (Fig. 7-13c and 7-14b). At a given MgO, Ba/Nb of the basalts and melt inclusions are higher than those of Fijian shoshonites, as are the Lorraine biotite pyroxenites, supporting derivation of the latter from a Nicola Group-like shoshonitic magma. Thorium/Nb ratios range from 0.2 to 0.9 and overlap with ratios for pyroxenites (Figs. 7-13d and 7-14g). In contrast, U/Nb ranges from 0.2 to 0.65 and are on average higher for basalts than pyroxenite (Figs. 7-13e and 7-14h). Higher U/Nb ratios may reflect a relative higher input of U in basalts from slab-derived fluids.

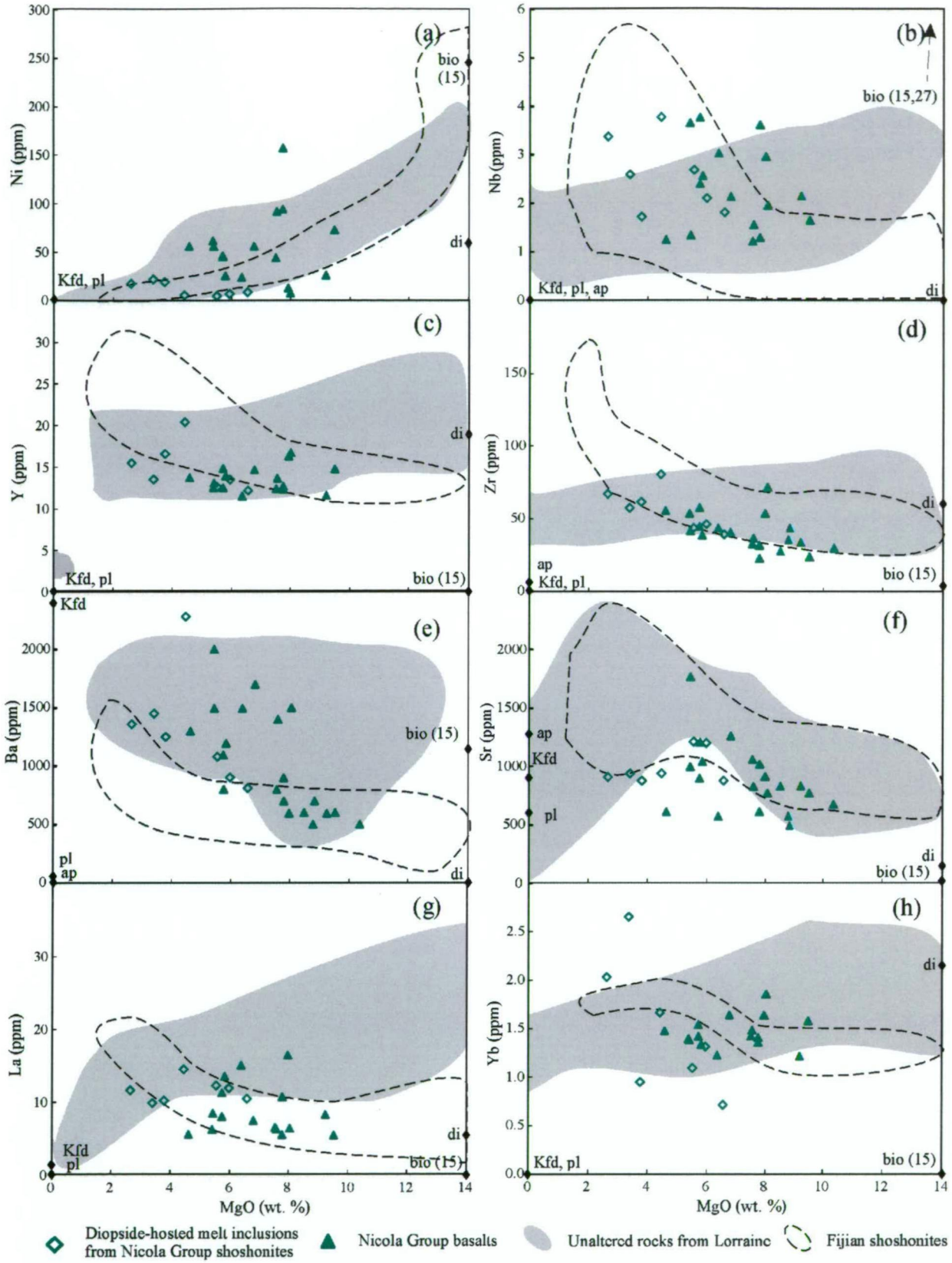

Figure 7-12. Bivariant plots of selected trace elements vs. MgO for Nicola Group basalts (closed green triangles) and diopside hosted melt inclusions from basalts (open green diamonds). The grey field represent the compositions of unaltered intrusive from Lorraine. The dashed line highlights the field for Fijian shoshonites from Leslie (2004). Note that not all basalts from the Nicola Group have a complete set of trace elements (i.e. Zr, Sr and Ba were analysed using XRF, whereas other elements were analysed using ICPMS). Also note that whole rock data for Nicola Group basalt is from Logan and Bath (2006).

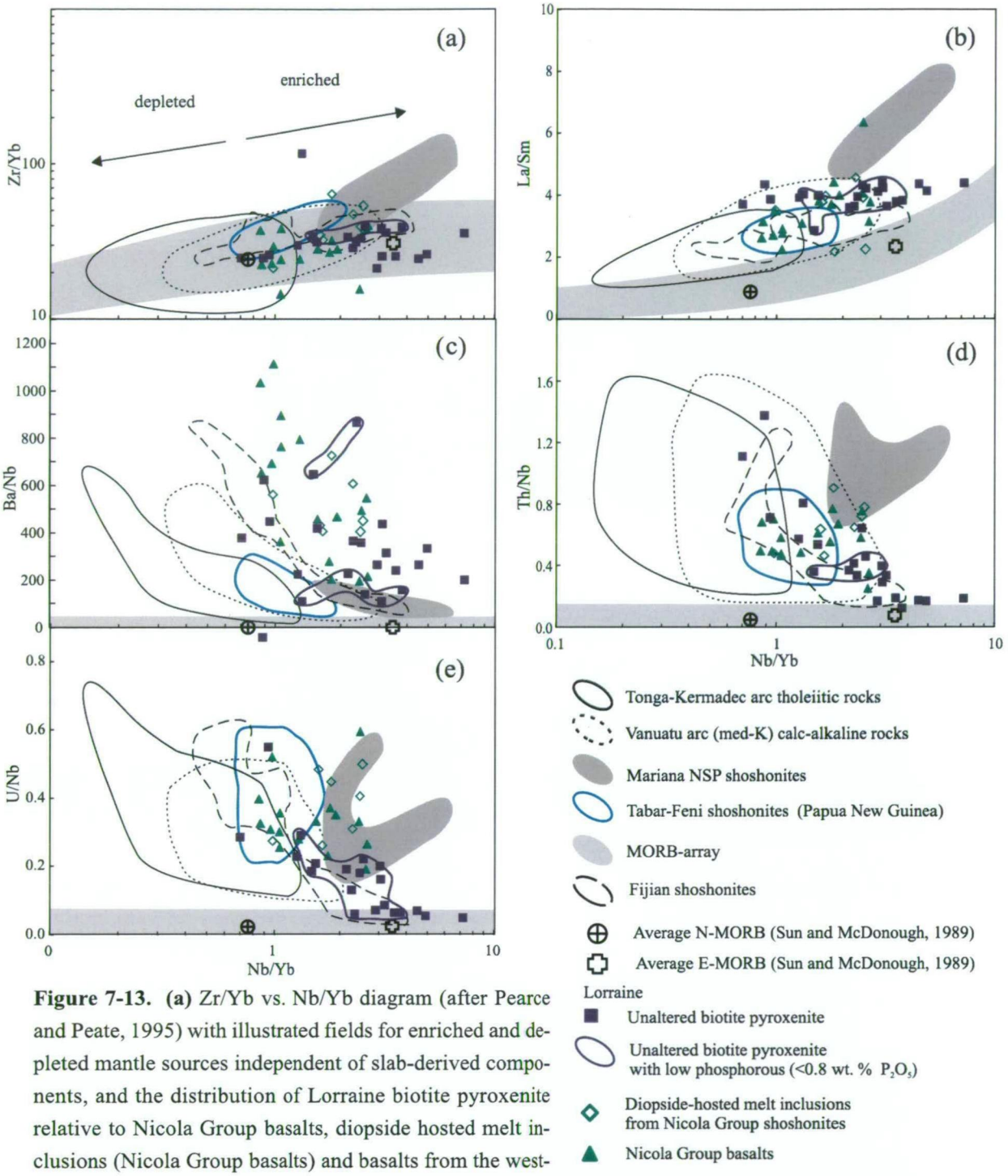

Figure 7-13. **(a)** Zr/Yb vs. Nb/Yb diagram (after Pearce and Peate, 1995) with illustrated fields for enriched and depleted mantle sources independent of slab-derived components, and the distribution of Lorraine biotite pyroxenite relative to Nicola Group basalts, diopside hosted melt inclusions (Nicola Group basalts) and basalts from the western Pacific arcs. **(b)** Lanthanum/Sm vs. Nb/Yb with biotite pyroxenite compositions relative to MORB-array and basalts from the western Pacific. This diagram illustrates the relative relationship between LREE and MREE. **(c-e)** Barium/Nb, Th/Nb and U/Nb vs. Nb/Yb (see text for details). Data fields for western Pacific arc basalts were compiled by Leslie (2004). Note that whole rock data for Nicola Group basalt is from Logan and Bath (2006).

Figure 7-14. **(a-h)** Plots of selected trace element ratios vs. La/Sm, which illustrates the composition of Lorraine biotite pyroxenites relative to Nicola Group basalts, diopside-hosted melt inclusions (Nicola Group basalts) and western Pacific arc basalts, N-MORB, E-MORB, OIB (Sun and McDonough, 1989) and Tongan sediment composition (Plank and Langmuir, 1998). Data fields and vectors were compiled by Leslie (2004). See Figure 6-7 for a list of data sources. Also note that whole rock data for Nicola Group basalt is from Logan and Bath (2006).

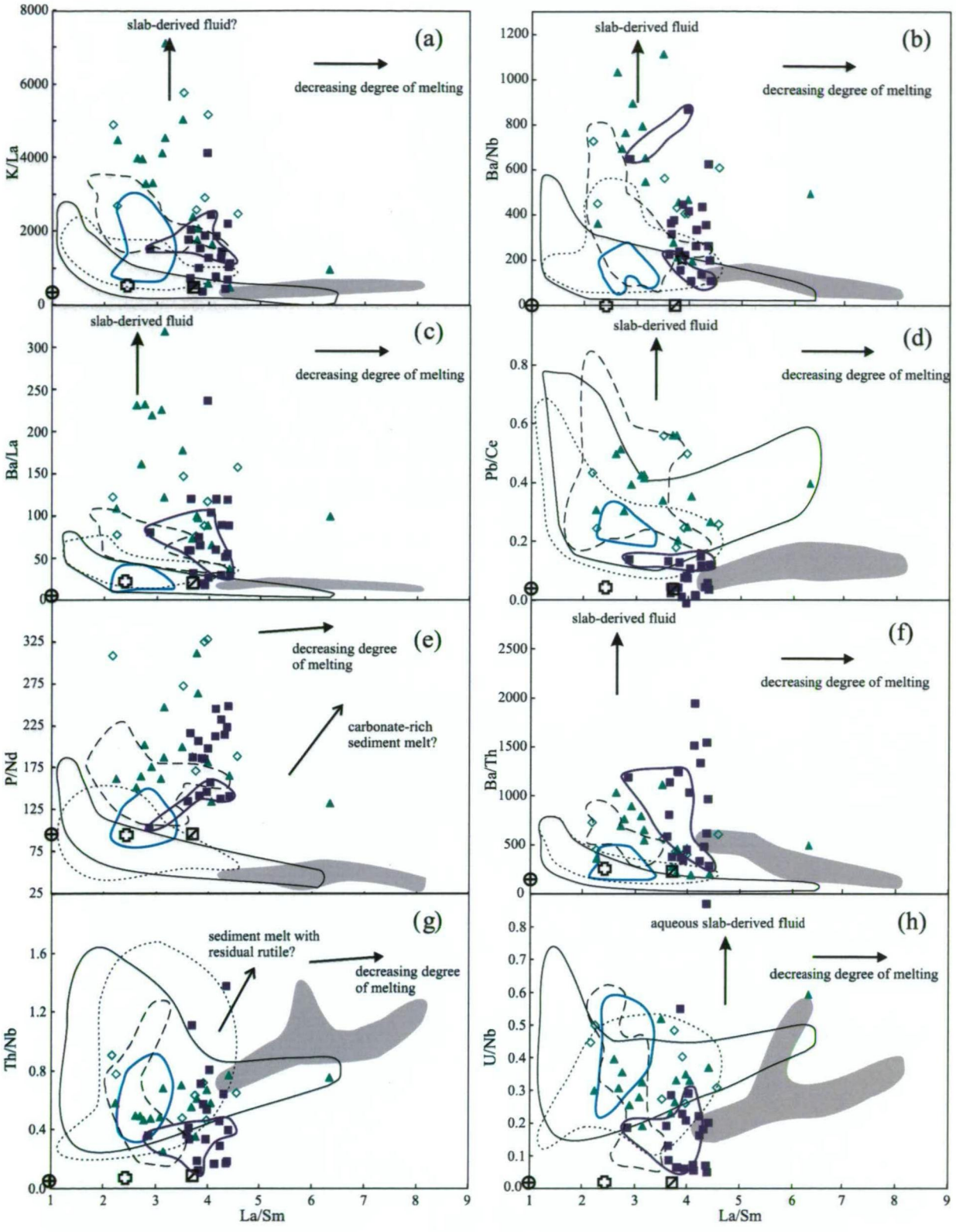

Tonga-Kermadec arc tholeiitic rocks

Vanuatu arc (med-K) calc-alkaline rocks

Mariana NSP shoshonites

Tabar-Feni shoshonites (Papua New Guinea)

Fijian shoshonites

Diopside-hosted melt inclusions from Nicola Group shoshonites

Nicola Group basalts

Average N-MORB (Sun and McDonough, 1989)

Average E-MORB (Sun and McDonough, 1989)

Average OIB (Sun and McDonough, 1989)

Lorraine

Unaltered biotite pyroxenite

Unaltered biotite pyroxenite with low phosphorous (<0.8wt. % P_2O_5)

7.6.5. N-MORB-normalised multi-element patterns for biotite pyroxenite, basalts from the western Pacific and Nicola Group basalt and melt inclusions

Average trace and major element ratios of biotite pyroxenites (~10 wt. % MgO), average Nicola Group basalt and melt inclusions were normalised to N-MORB (Sun and McDonough, 1989) and plotted together with typical basalt from Tonga-Kermadec arc (tholeiite), Vanuatu (med-K calc-alkaline) and Fijian shoshonite (Fig. 7-15).

All of the western Pacific arc-related suites, Lorraine biotite pyroxenites and Nicola Group basalts and melt inclusions are depleted in Zr, Ti, Y and HREE (Gd, Dy, Er and Yb) compared to N-MORB, but relatively enriched in all other elements. Lorraine biotite pyroxenites are enriched in Rb, Ba, Nb, REE and P compared to arc rocks from the western Pacific and Nicola Group basalts, but the biotite pyroxenites are depleted in Pb relative to Fijian shoshonites and Nicola Group basalts. Barium/Rb, U/Th, Ce/La and U/Nb ratios are lower for biotite pyroxenites, compared to average Nicola Group basalt and melt inclusion, but higher for Sm/Zr and Gd/Ti. In general, the average trace element composition of biotite pyroxenite shows similar patterns to Nicola Group basalts and melt inclusions.

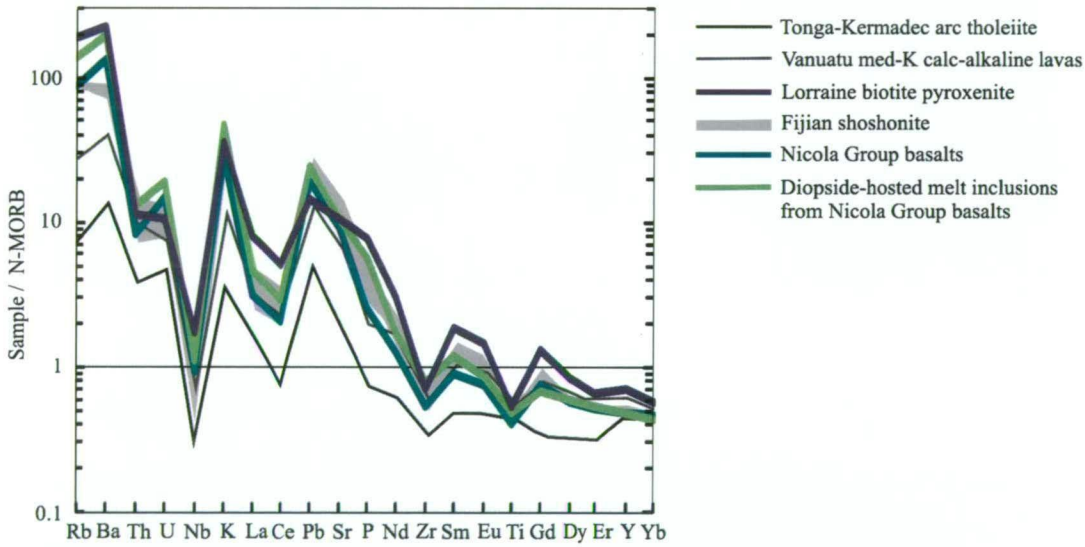

Figure 7-15. N-MORB (Sun and McDonough, 1989) normalised multi-element variation diagram showing average biotite pyroxenite, average Nicola Group basalts, average diopside-hosted melt inclusions (Nicola Group basalts) and western Pacific arc basalts. Data for western Pacific basalts were compiled by Leslie (2004). Note that whole rock data for Nicola Group basalt is from Logan and Bath (2006).

7.6.6. Metals and volatile elements in shoshonitic melts

Copper, Ni, Zn, Pb, Mo, Sn, U, Au and Ag were analysed in melt inclusions in order to assess the metal content of shoshonitic magmas of the Nicola Group. Mo, Sn, Au and Ag were almost always below detection limit. However some inclusions had detectable Mo and Sn concentrations of ~2 ppm and ~5 ppm respectively.

Copper abundances in inclusions range from ~190 to 845 ppm, with an average (median) concentration of ~290 ppm. Basalts have copper concentrations that range from approximately 100 to 290 ppm, and an average of ~160 ppm. Nickel and Zn are enriched in basalts (avg. 55 and 90 ppm respectively) compared to melt inclusions (avg. 12 and 55 ppm respectively). Lead and U are similarly abundant in melt inclusions relative to whole rock (avg. ~7 and ~1 ppm respectively). Volatile elements Cl and S were analysed in melt inclusions using the EPMA. Chlorine ranges from ~1000 to 2200 ppm (avg. 1660 ppm), whereas S was either below the detection limit or close to the detection limit for most analyses (i.e. ~300 ppm). The water content, which is inferred to be the difference in the total mass analysed and 100 wt. %, ranges from 0 to 3.4 wt. % and averages 1.8 wt. %.

Three unheated inclusions were ablated to compare the abundance of Cu in unheated inclusions with reheated inclusions. Kamenetsky and Danyushevsky (2005) demonstrated that Cu and Ag in melt inclusions trapped in quartz can show exceptional volatility when reheated. Reheated inclusions in quartz can absorb significant amounts of Cu and Ag from contaminated environments, such as a dirty furnace (i.e., 2.8 ppm vs. 396 ppm Cu for unheated and reheated inclusions respectively). Unheated inclusions in this study had concentrations between 276 and 300 ppm of Cu, and fall in the range of reheated inclusions. Silver was below the detection limit (~0.6 ppm) in both reheated and unheated inclusions. Hence no detectable enrichment of Ag or Cu occurred during reheating.

7.7. Copper in unaltered rocks from Lorraine

Over the past two decades a number of studies have highlighted the importance of mafic magmas in the formation of porphyry-Cu systems (e.g., Keith et al., 1997; Keith et al., 1998; Keith, 2002; Halter et al., 2005). For example, Keith et al. (1997; 1998) inferred that the introduction of mafic alkaline magmas into a silicic magma chamber beneath the Bingham porphyry-Cu deposit led to the enrichment of Cu, S and other volatiles prior to mineralisation. They postulated that these mafic alkaline magmas were enriched in Cu and S (and other volatiles) relative to felsic magmas (Keith et al., 1997; Keith et al., 1998), due to the relatively higher solubility of Cu and S in mafic magmas (e.g., Haughton et al., 1974; Banks, 1982; Keith et al., 1997; Keith et al., 1998). During magma mixing sulphide globules may have formed owing to the lower solubility of sulphur in Fe-poor felsic magmas, and these sulphide globules are thought to have sequestered Cu and other precious metals from the melt prior to resorption and exsolution of an ore fluid (Keith et al., 1997; Keith et al., 1998; Keith, 2002). Intermixing of mafic alkaline magmas with felsic magmas, may also lead to the enrichment of both compatible and incompatible "elements" such as P, Ba, Ni and Cr (Keith et al., 1997). The mafic magmas may also play a role in

heating large silicic magma chambers, and hence induce and promote convection, which may lead to fluid separation in a cupola (Keith, 2002).

Unaltered rocks from Lorraine were analysed in order to assess the magmatic Cu content of biotite pyroxenite, syenite and monzonite. Results show that:

- Most unaltered biotite pyroxenites have very low concentrations of Cu (i.e. 10 to 40 ppm); although some Phase 2 biotite pyroxenites are enriched in Cu (i.e. up to ~230 ppm).
- Unaltered syenites have highly variable Cu contents (i.e. 10 to ~200 ppm).
- Monzonites have variably low Cu concentrations (i.e. 20 to 70 ppm).

The average unaltered biotite pyroxenite at Lorraine is depleted in Cu compared to monzonite and syenite. They are also depleted in Cu relative to Nicola Group shoshonite and Fijian shoshonites and Bingham mafics with the equivalent Si content. Alternatively, some biotite pyroxenites are enriched in Cu and have similar abundances of Cu and Si to the Bingham mafics, Nicola Group shoshonites and Fijian shoshonites. These Cu-enriched biotite pyroxenites contain small (<5 μm) inclusions of chalcopyrite in magnetite or ilmenite (e.g., Fig. 6-26a), which may have been trapped during magnetite growth or may have formed following the exsolution of copper impurities from the magnetite structure in slowly cooled ultrabasic dykes (e.g., Cross, 2000). These Cu-enriched biotite pyroxenites may have crystallised from a relatively Cu-rich mafic magma source compared to the Cu-poor biotite pyroxenites.

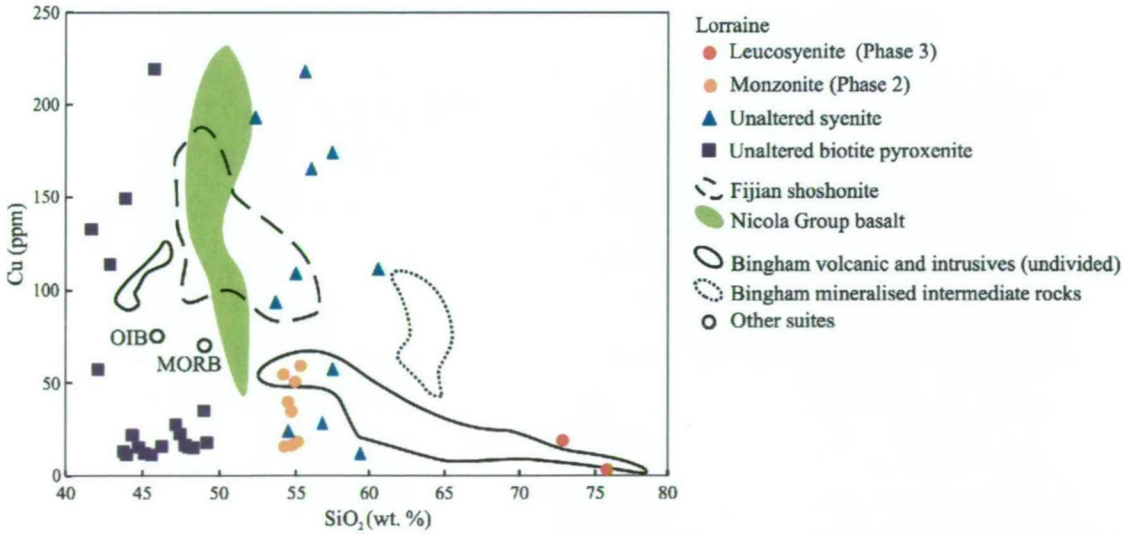

Figure 7-16. Cu (ppm) vs. SiO_2 (wt. %) for Lorraine rocks, Fijian shoshonites, Nicola Group basalts and Bingham volcanic and intrusive rocks. The diagram also shows the average composition of MORB and OIB. Adapted after Keith et al. (1997). Note that whole rock data for Nicola Group basalt is from Logan and Bath (2006).

7.8. Discussion

7.8.1. Evidence for the accumulation of diopside in Lorraine rocks?

Diopside is the dominant Ca-rich phase in biotite pyroxenite at Lorraine. Diopside, however, does not contain K, and therefore K should not accumulate in biotite pyroxenites as a result of physical processes (e.g., flow differentiation). Hence K is used here as a proxy for fractionation that is independent of diopside. Thus, a plot of K_2O vs. CaO was used to assess diopside fractionation, and also to identify rocks that are anomalously enriched in diopside, as a result of physical processes (Fig. 7-17). Syenites and biotite pyroxenites plot along a single linear trend on the K_2O vs. CaO diagram, whereas monzonites have lower K_2O ratios relative to syenites with the equivalent CaO. The linear trend of biotite pyroxenites and syenite intersects 20 wt. % CaO for $K_2O = 0$; however the average Lorraine diopside composition is CaO = 23.2 wt. % (stdev. = 0.3 wt. % for biotite pyroxenite). Hence the above trend cannot be explained solely as a diopside accumulation trend. Mixing between biotite and diopside also cannot explain the trend because the data do not form an array on K_2O vs. MgO plot between these two minerals (Fig. 7-4i). The trend for biotite pyroxenite and syenite on the K_2O vs. CaO diagram is also sub-parallel and overlaps with the trend for basalts from the Nicola Group and melt inclusions hosted in diopside. The trend shown by melt inclusions is inferred to represent a fractionation trend. Hence, the similarities between Lorraine rocks and Nicola Group basalts on the K_2O vs. CaO diagram appears to support the contention that fractionation was the dominant process for variations in Ca and K in Lorraine rocks rather than a diopside accumulation trend. Although biotite pyroxenites, on average, have slightly higher CaO ratios relative to Nicola Group basalts with the equivalent MgO, which could be explained by adding diopside to successive liquids, in approximately similar amounts.

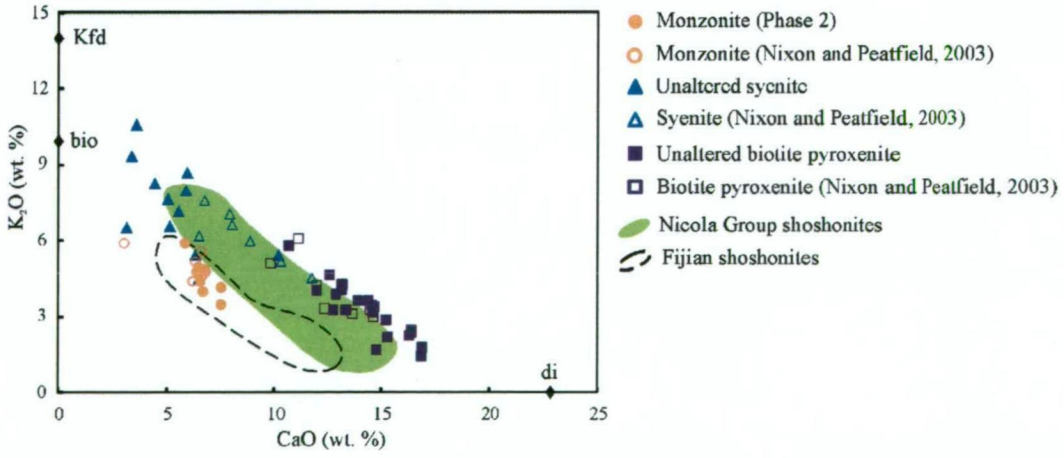

Figure 7-17. K_2O vs. CaO scatter plot of Lorraine whole rock compositions relative to diopside, biotite and K-feldspar compositions. Plot also includes a field for Nicola Group basalt and melt inclusions (green) and Fijian shoshonites (dashed line) for comparison.

7.8.2. Major and trace element patterns of Lorraine intrusives

The suite of biotite pyroxenite to syenite and monzonite shows variations of major and trace elements that could be explained by the fractionation of magnetite, diopside, apatite and olivine? (i.e. decreasing TiO_2, Fe_2O_3, MgO, CaO, P_2O_5, V; increasing K_2O, Na_2O, Al_2O_3 and SiO_2; Figs. 7-4 and 7-5). Lorraine rocks generally do not have negative Eu-anomalies and therefore the fractionation of plagioclase is considered to have been relatively minor (Fig. 7-6a-c). Trace element patterns of Lorraine rocks have positive anomalies of LILE (e.g., Rb, K and Ba) and negative anomalies of HFSE (e.g., Ti, Nb and Ta) on primitive mantle and N-MORB normalised multi-element variation diagrams (Figs. 7-6a-c and 7-15). The trace element patterns of the Lorraine rocks on multi-element diagrams generally appear to be consistent with the accepted paradigm for subduction zone magma genesis, which invokes aqueous fluids expelled from the down going slab mobilising non-conservative elements, whereas conservative elements are retained in the down going slab (e.g., Gill, 1981; Tatsumi et al., 1986; Morris et al., 1990; Pearce and Peate, 1995; Tatsumi and Eggins, 1995; Kepezhinskas and Defant, 1996; Ryan et al., 1996). In particular, Lorraine rocks have negative anomalies for Nb, Zr and Ti. Negative anomalies for Nb and Ti may be explained by residual Nb- and Ti-rich phases in the eclogite residue of slab melting (e.g., rutile and ilmenite (Ti only)).

7.8.2.1. Time-perspective evolution of Lorraine rocks

One of the greatest difficulties with concluding on a time-progressive history on Lorraine rocks is that most of the Phase 1 rocks from the Bishop, Lower Main and Main zones are altered. So from an igneous petrology perspective it is difficult to compare altered rocks with unaltered rocks to gain insights into the igneous evolution. The author did however, look at comparing Phase 2 rocks from the Lower Main Zone, Bishop Zone and Main Zone with least altered Phase 1 rocks that occur on the Lorraine property but away from the mineralised zones. No significant difference was identified between the two populations. Hence there is no obvious evolution in the chemistry between Phase 1 and Phase 2 rocks, when comparing Phase 1 biotite pyroxenites with Phase 2 biotite pyroxenites and Phase 1 syenites with Phase 2 syenites. There is however a significant shift in the chemistry between Phase 1 and 2 syenites with Phase 3 leucosyenites. This is shown in Figure 7-1 where Phase 3 leucosyenites fall in the subalkaline field. Thus the transition from alkalic magamatism to sub-alkalic magamatism did occur at Lorraine and this transition to sub-alakalic magmatism is thought to have occurred at ~177 Ma (Mihalynuk, written commun., 2007).

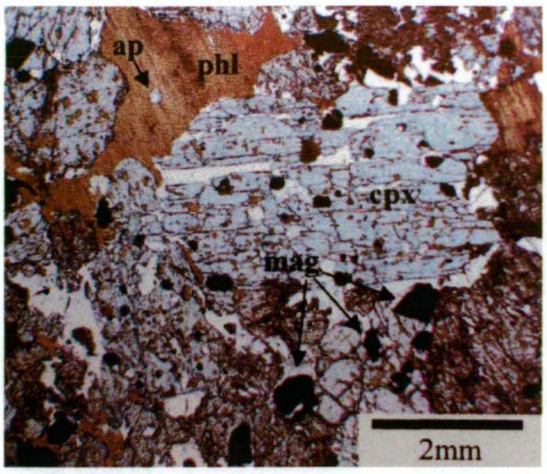

Figure 7-18. Photomicrograph of a phlogopite-clinopyroxenite (D2) xenolith in Astrolabe Group shoshonite from Fiji. The xenolith comprises phlogopite (phl), clinopyroxene (cpx), magnetite (mag) and apatite (ap). Photomicrograph taken in plane polarised light. Sourced from Leslie (2004).

7.8.3. Why is there no olivine in Lorraine rocks?

According to Bowen's reaction series (Bowen, 1928), olivine should crystallise prior to pyroxene during low-pressure fractionation of mafic magmas; however olivine has not been identified in biotite pyroxenites at Lorraine (although it is possible that traces of olivine may have been overlooked in some samples). The high *mg*-number of diopsides from Lorraine biotite pyroxenites match those in Fijian shoshonites, which coexist with olivine Fo_{74} to Fo_{94} (Leslie, 2004), so the absence of olivine in Lorraine biotite pyroxenites appears enigmatic. Some authors (e.g., Iacono-Marziano et al., 2007, 2008; Pass et al., 2008; Iacono-Marziano et al., 2009; Pass et al., in prep.) have noted that the presence of carbonate in the melt can react with olivine and silica to produce clinopyroxene and carbon dioxide. Thus, a relatively high activity of carbonate in ultrabasic magmas at Lorraine may have suppressed the crystallisation of olivine.

Alternatively, Zanetti et al. (1999) noted that the crystallisation of hydrous phases may result in an increase of CO_2/H_2O values in the residual melt, which in turn can react with previous phases to form diopside and even carbonates. Perhaps at Lorraine the onset of biotite crystallisation in ultrabasic magmas may have increased the CO_2/H_2O ratio in the residual melt, which may have reacted with any olivine that had previously crystallised. Shoshonitic lavas from Fiji contain xenoliths of phlogopite-clinopyroxenite (Leslie, 2004; Fig. 7-18), where olivine is rare. According to Leslie (2004) these xenoliths are thought to have been derived from the conduit wall. Also, some shoshonitic lavas from the Nicola Group Volcanics contain diopsides with high *mg*-numbers (i.e. >90), but do not appear to contain olivine. Hence the apparent absence or rare occurrence of olivine in some shoshonitic rocks does not appear to be limited to Lorraine shoshonites, and appear to pose broader petrological problems, which are beyond the scope of the current study.

7.8.4. Source of mafic magmas

Comparison of the major and trace element composition of Lorraine biotite pyroxenite with N-MORB, mafic volcanics from the western Pacific arcs and shoshonites and high-K rocks from Nicola Group basalts has provided clues to the source of mafic magma at Lorraine. Arc-related magmas are derived from the partial melting of variably enriched or depleted peridotite mantle source(s) that may have been contaminated with slab-derived components (i.e. slab-derived fluids or melts; Gill, 1981; Tatsumi et al., 1986; Hawkesworth et al., 1993; Woodhead et al., 1993; Pearce and Peate, 1995; Tatsumi and Eggins, 1995; Hawkesworth et al., 1997; Peate et al., 1997; Sun and Stern, 2001; Hollings and Wyman, 2004). The contention that parental shoshonite magmas for the Lorraine biotite pyroxenite were derived from a relative enriched mantle source is supported by Zr/Yb and Nb/Yb ratios that range between N-MORB and E-MORB (Figs. 7-7a and 7-13a), and high Ba/Nb ratio support the arguement that slab-derived fluids were also added to the sub-arc mantle wedge source. However U/Nb is not notably higher than the mantle-array, and therefore slab-derived fluids were not enriched in U. Thorium/Nb and Zr/Nb ratios are not significantly different from the mantle-array, and therefore there is very little evidence for a slab-derived melt that was relatively enriched in Th or Zr, which is the case for the Mariana arc shoshonites (e.g., Sun and Stern, 2001). Alternatively, high P/Nd may reflect a contribution of P from slab-derived carbonate-rich sediment melts (in addition to aqueous fluids) in the sub-arc mantle wedge. The ultimate source of P (and Sr) may well have come from subducted P-rich fish debris and carbonate-rich nano-fossils or other biogenic sources, which has been proposed as the source of P- and Sr-enrichment in Fijian shoshonites and other arc rocks from the western Pacific (e.g., Raos, 2001; Leslie, 2004; Raos and Crawford, 2004).

7.8.5. What evidence is there for the subduction of carbonate-rich sediments during arc magmatism at Lorraine?

The concept that carbonate- and phosphorous-rich sediments were subducted beneath the Quesnel terrane appears to be consistent with the geology of the Cache Creek accretionary complex, which occurs to the west of the Quesnel terrane and is composed of abundant exotic shallow marine carbonate-rich Tethyan fauna and cherts (Monger and Ross, 1971; Monger and Price, 2000). Cherts and carbonate-rich sediments are Upper Carboniferous to Triassic in age, and the latter are also characterised by the distinct Permian Veerbeekinid fusilinids that are known elsewhere only in the Tethyan domain of southern Asia (Monger and Ross, 1971). It is inferred that the exotic fauna formed on seamounts that originated in the Tethyan sea, and were transported across the Panthalassa ocean and then accreted

along the margin of the Quesnel and Stikine terranes (Mihalynuk et al., 1994a; Johnston and Borel, 2007). The onset of accretion of seamounts bearing Tethyan fauna along the Quesnel terrane occurred sometime between the Latest Permian to Middle Triassic and subduction is thought to have continued until middle Jurassic with final closure of the arc (Mihalynuk et al., 1994a). Alkalic arc magmatism first occurred in the Quesnel terrane in the Middle Triassic (e.g., Nicola Group Volcanics), and therefore appears to temporally and spatially coincide with the subduction of carbonate-rich sediments. Hence it is inferred here that conditioning of the sub-arc mantle wedge by fluids and melt derived from subducted carbonate-rich sediments may have been an important with respect to the onset of alkalic silica-undersaturated arc magmatism that dominates the Quesnel and Stikine terranes during the Middle Triassic to early Middle Jurassic.

7.9. Conclusions

Based on whole rock major and trace element geochemistry, it is argued that:

- Barren biotite pyroxenite and unaltered syenite rocks have major and trace element geochemistry that plot broadly along trends that may be explained by magmatic fractionation processes (Figs. 7-4 and 7-5), supporting the contention for a genetic link between ultrabasic to felsic rock types at Lorraine.

- Biotite pyroxenites have trace element ratios that are comparable to shoshonitic lavas from Fiji with similar abundance of magnesium. In particular, non-conservative/conservative element ratios frequently overlap (Figs. 7-7 and 7-8). It is inferred that similar trace element ratios occur due to input from of slab-derived fluids or partial melts of slab-derived sediments.

- Biotite pyroxenites also have similar trace element ratios to the older alkaline basalts and diopside-hosted melt inclusions of the Nicola Group Volcanics that formed within the same arc (Figs. 7-10, 7-11 and 7-12). In particular, the volcanic rocks and melt inclusions have high P/Nd ratios compared to the N-MORB, shoshonite from Mariana and Tabar-Feni arc, arc tholeiites and arc calc-alkaline rocks. A possible explanation for the high P/Nd in mafic rocks from the Quesnel terrane is that P was contributed from the subducted carbonate- and phosphorous-rich sediments.

CHAPTER 8
RADIOGENIC AND STABLE ISOTOPES

8.1. Introduction

Arc magmatism is the product of interactions between the subducting lithosphere and sediments with the overlying mantle asthenosphere, and these magmas are enriched in LILE and depleted in HFSE relative to REE (e.g., Pearce and Peate, 1995; Tatsumi and Eggins, 1995; Sun and Stern, 2001). However based on the major and trace element geochemistry of arc-related rocks it is difficult to assess the relative contribution of the mantle asthenosphere source and possible contaminants. It is also difficult to determine how much crustal assimilation occurred, if any. Alternatively as shown by Sun and Stern (2001), mixing models involving a mantle derived melts with various contaminants can, using radiogenic isotopes, place constraints on the source and relative extent of contamination in mafic magmas. Although as pointed out by Tatsumi and Eggins (1995), the effective use of radiogenic isotopes requires that the isotopic composition of all possible contributing sources be known and that they display sufficient compositional contrast. In this chapter, radiogenic isotopes Sr, Nd and Pb from Lorraine rocks are used to attempt to constrain petrogenetic models.

As shown by Ito and Stern (1986), O isotopes can be used to assess the source components and degree of contamination in mafic magmas, and with H isotopes can also be used to constrain the source(s) of fluids involved in ore deposition in mineralised rocks (e.g., Taylor, 1979). Hence, another aim of this chapter is compare the stable isotope composition of mineral phases from barren and mineralised rocks, in order to characterise the O and H isotopic composition of unaltered ultrabasic rocks at Lorraine and to constrain the source of the fluids relating to mineralisation.

8.1.1. Terminology used in this chapter

The terminology used in this chapter is consistent with Chapters 6 and 7. In particular rocks have been described as either unaltered or mineralised. Unaltered rocks include both Phase 1 and 2 rocks (Chapters 2 to 5), whereas mineralised rocks strictly refer to Phase 1 or fine-grained K-feldspar biotite rock.

8.2. Analytical methods

8.2.1. Sample preparation

The author made biotite, diopside, apatite and galena separates by hand-picking coarse- to fine-grained material from crushed rock and veins using tweezers and a binocular microscope. Biotite and diopside crystals that contained magnetite inclusions were separated

using a magnet, and then discarded to avoid contamination. Magnetite was also separated using a magnet and then hand-picked using tweezers and a binocular microscope. Magnetite and diopside samples, which were used for O-isotope analysis, were further purified by density separation (polytungstate) at the National Isotope Centre, GNS Science, Te Pu Ao, New Zealand. This process was overseen by Dr Kevin Faure.

8.2.2. Strontium, Nd and Pb isotopes

Strontium, Nd and Pb isotope ratios for diopside, apatite and galena in mineralised and unaltered rocks from Lorraine were analysed at the University of Melbourne by Dr Roland Maas using the NU Plasma multi-collector-ICP-MS equipped with a CETAC Aridus desolvator and glass expansion Opalmist nebuliser operated at ~40 µl/min uptake. The procedures broadly followed those described by Maas et al. (2005).

Prior to analyses apatite fractions weighing 2.5-3 mg were washed in warm, 0.01 M distilled HNO_3, followed by dissolution in concentrated HNO_3. Diopside separates were cleaned in 2 M HNO_3, spiked with Sm-Nd tracer and dissolved in 3:1 HF-HNO_3 amd 6 M HCl on a hotplate. Galena cubes were cleaned in dilute HNO_3, dissolved in concentrated HNO_3 and analysed without further purification. In the case of diopside and apatite, a total of 60 % of the sample solution was spiked with a mixed $^{147}Sm/^{150}Nd$ tracer and dried. Strontium and LREE-rich fractions were then extracted using small columns of EICHROM™ Sr- and RE-resin, respectively. Neodymium and Sm were purified on 1 ml columns of EICHROM™ LN resin, using dilute HCl. The remainder of the sample solution was spiked with a mixed ^{233}U-^{205}Pb tracer, followed by extraction of Pb and U on small anion resin (HBr/HCl; Manhes et al., 1978) and EICHROM™ TRU-resin columns (Luo et al., 1997).

Routine blanks were ≤100 pg for Sr and Nd, and ~10 pg for Pb and U. $^{87}Sr/^{86}Sr$ was normalised to $^{88}Sr/^{86}Sr = 8.37521$, and is reported relative to SRM987 = 0.71023. $^{143}Nd/^{144}Nd$ is reported relative to LaJolla = 0.511860, and internal precision (2σ error) for Sr and Nd were ≤±0.000020 and ~±0.000010, whereas external precision (2 std. dev.) is estimated at ±0.000040 and ±0.000020, respectively. Eimer and Amendt, modern seawater and BCR-2 yielded $^{87}Sr/^{86}Sr$ of 0.70800 ± 3 (2σ), 0.70916 ± 2 (2σ) and 0.70500 ± 3 (2σ), respectively, and $^{143}Nd/^{144}Nd$ in JNd-1 and BCR2 is 0.512115 ± 15 (2σ) and 0.512640 ± 15 (2σ), respectively. Initial Sr-Nd isotope ratios were calculated for an age of 0.18 Ga. Mass bias in U isotope dilution runs were corrected internally, using the natural $^{238}U/^{235}U$ = 137.88 after correction for spike impurities. Mass bias during Pb runs were corrected externally using analyses of SRM981 run at similar signal intensities. The external precision of this correction is estimated at ± 0.1 %.

8.2.3. Oxygen Isotopes

Oxygen was extracted from biotite, diopside and magnetite for isotope analyses using a CO_2-laser and BrF_5 (Sharp, 1990) at the National Isotope Centre, GNS Science, Te Pu Ao, New Zealand. Analyses were carried out by Dr Kevin Faure. Oxygen isotope values are reported as $\delta^{18}O$, relative to VSMOW (Vienna Standard Mean Ocean Water). Samples were normalised to the international quartz standard (NBS-28) using a value of 9.6 ‰. Values for four NBS-28 standards analysed with the samples had values that varied by less than 0.1 ‰. Samples and standards were heated overnight in an oven to 150 °C, to remove any adsorbed water, prior to loading into the vacuum extraction line. The samples were then evacuated for approximately 6 hours and left overnight in a vapour of BrF_5. Blank BrF_5 runs were done until yield was less than 0.1 μmoles oxygen. Oxygen was passed through a fluorine-getter (in-line Hg diffusion pump), and converted to CO_2 by a graphite furnace, yields recorded and CO_2 analysed on a Geo20-20 mass spectrometer.

8.2.4. Hydrogen Isotopes

Hydrogen isotope values in biotite were analysed on a HEKAtech high temperature elemental analyser coupled with a GV Instruments IsoPrime mass spectrometer at the National Isotope Centre, GNS Science, Te Pu Ao, New Zealand and analyses were also carried out by Dr Kevin Faure. Samples were pyrolysed at 1400 °C, in silver capsules. All samples were analysed in triplicate. All results are reported with respect to VSMOW, normalised to the international standard IAEA-CH-7 (-100.33 ‰), NBS-22 (-120.0 ‰) and NBS-30 (-65 – 100.33 ‰).

8.3. Results

8.3.1. Radiogenic isotopic compositions of Lorraine rocks

The Sr and Nd isotopic compositions of diopside from an unaltered biotite pyroxenite, a mineralised biotite pyroxenite and an unaltered monzonite samples were analysed (Table 8-1). Diopsides from unaltered biotite pyroxenite have an initial $^{87}Sr/^{86}Sr$ value of 0.7036 and initial εNd value of +4.7, and diopsides from an unaltered monzonite have $^{87}Sr/^{86}Sr$ value of 0.7037 and εNd value of +5.3 (Fig. 8-1). Apatite and diopside in mineralised biotite pyroxenite have initial $^{87}Sr/^{86}Sr$ values of 0.7037 and 0.7036 and initial εNd values of +4.7 and +4.8 respectively. Thus mineralised and unaltered biotite pyroxenites at Lorraine cannot be distinguished based on their $^{87}Sr/^{86}Sr$ and εNd values. The monzonites have $^{87}Sr/^{86}Sr$ values consistent with biotite pyroxenite; however, based on the above data set, monzonites have slightly higher εNd values than biotite pyroxenites (Fig. 8-1).

Table 8-1. Strontium and Nd isotopes of selected mineral phases of Lorraine rocks.

Sample	Rock type	Area	Sample type	Easting/ drill hole	Northing/ depth	Mineral	Rb ppm[1]	Sr ppm[1]	$^{87}Rb/^{86}Sr$	$^{87}Sr/^{86}Sr$[2]	Sm ppm	Nd ppm	$^{147}Sm/^{144}Nd$	$^{143}Nd/^{144}Nd$[3]	εNd_n[4]	geol. age[6]	$^{87}Sr/^{86}Sr_i$[5]	εNd_i[5]
06AB 100-1	Phase 2 Monzonite	Lower Main Zone	surface outcrop	347505	6200899	diopside	0.06	425	0.00041	0.7037	7.64	26.10	0.1770	0.5129	4.88	0.18	0.7037	5.3
44-244	Mineralised biotite pyroxenite	Bishop Zone	drill core	1996-44*	244.0†	diopside	0.06	425	0.00041	0.7037	3.92	14.03	0.1688	0.5129	4.14	0.18	0.7037	4.8
15-7-1	Unaltered biotite pyroxenite	Lorraine	surface outcrop	348560	6200804	diopside	0.06	425	0.00041	0.7036	3.04	10.52	0.1744	0.5129	4.21	0.18	0.7036	4.7
44-234	Mineralised biotite pyroxenite	Bishop Zone	drill core	1996-44*	234.0†	apatite	0.29	1507	0.00056	0.7036	104.8	523.6	0.1210	0.5128	2.98	0.18	0.7036	4.7
44-234	Mineralised biotite pyroxenite	Bishop Zone	drill core	1996-44*	234.0†	apatite	0.29	1507	0.00056	0.7036	113.8	570.6	0.1206	0.5128	2.93	0.18	0.7036	4.7

* Drill hole no.

† Depth (m)

[1]Analyses at CODES using LA-ICPMS

[2]Relative to SRM987 = 0.710230

[3]Relative to La Jolla = 0.511860

[4]Now

[5]Initial

[6]Age (Ga)

Present-day CHUR is 0.512638, decay constants are 1.42E-11/yr (Rb) and 6.54E-12/yr (Sm)

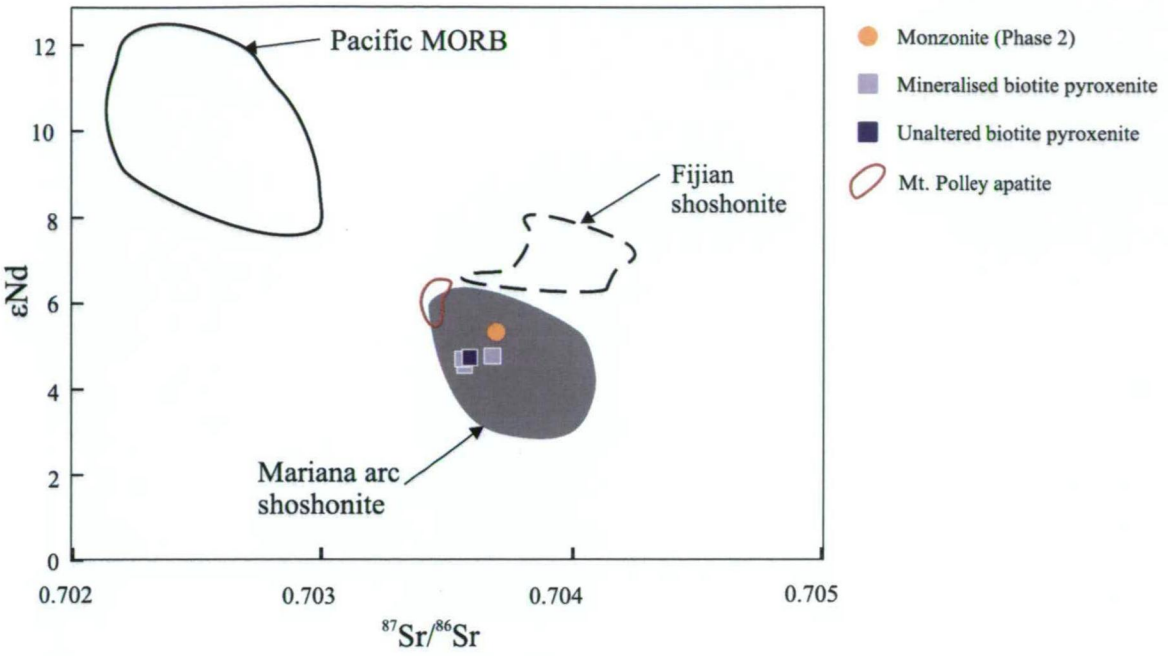

Figure 8-1. εNd vs. $^{87}Sr/^{86}Sr$ plot for diopside and apatite from mineralised biotite pyroxenite, and for diopside from unaltered biotite pyroxenite and monzonite from Lorraine. Lorraine data is superimposed on fields for Pacific MORB and western Pacific arc-related shoshonites compiled by Leslie (2004). All data are listed in Table 8-1.

Lead isotopes from galena in a fine-grained K-feldspar biotite rock was analysed (Table 8-2). Lead isotope compositions are consistent with four additional galena samples analysed by Mortensen (written commun., 2009) from the Lorraine district, with $^{206}Pb/^{204}Pb$ values between 18.93 and 18.97, $^{207}Pb/^{204}Pb$ values between 15.61 and 15.66 and $^{208}Pb/^{204}Pb$ values between 38.50 and 38.71 (Fig. 8-2a, b). Lead-isotope values for galena most likely represent magmatic values. One being that stable and radiogenic isotopes of alteration phases are not statistically significantly different to magmatic phases for any of the other isotope systems studied here. The second is that common-Pb values are within error of model values used for dating magmatic rocks. However future work should be carried out on magmatic phases such as K-feldspar phenocrysts in unaltered magmatic rocks to confirm this.

8.3.2. Comparison of radiogenic isotope compositions of Lorraine rocks with western Pacific shoshonites, OIB and MORB

Initial εNd and initial $^{87}Sr/^{86}Sr$ values of biotite pyroxenite and monzonite are compared with western Pacific shoshonites, OIB and MORB in Figure 8-1. The Lorraine rocks overlap with the field for Mariana arc shoshonites. Initial $^{87}Sr/^{86}Sr$ values of Lorraine rocks also overlap with Fijian shoshonites and apatite from the Mt. Polley ore-zone, but have

Table 8-2. Lead istope data from Lorraine.

Sample	Drill hole	Depth	Mineral	Pb^{206}/Pb^{204}	Pb^{207}/Pb^{204}	Pb^{208}/Pb^{204}
1996-44	1996-44	88.8m	galena	18.933	15.605	38.502
Lorraine[a]	-	-	galena	18.947	15.637	38.638
Lorraine[a]	-	-	galena	18.959	15.649	38.675
Lorraine[a]	-	-	galena	18.969	15.661	38.714
Lorraine[a]	-	-	galena	18.969	15.628	38.623

[a]Data provided by Mortensen written commun., 2009.

lower initial εNd values (i.e. more radiogenic) than Fijian shoshonites and apatite from the Mt. Polley ore-zone. Compared to Pacific MORB, Lorraine rocks have lower initial εNd and higher initial $^{87}Sr/^{86}Sr$ compositions (i.e. more radiogenic).

Lorraine galena has similar $^{206}Pb/^{204}Pb$ values to Mariana arc shoshonites and Fijian shoshonites (Fig. 8-2a, b). Lorraine galena also has overlapping $^{207}Pb/^{204}Pb$ values with Mariana arc shoshonites and plot in the same field on the $^{207}Pb/^{204}Pb$ vs. $^{206}Pb/^{204}Pb$ diagram. In contrast, Lorraine galena has higher $^{207}Pb/^{204}Pb$ values than Fijian shoshonites but overlapping $^{208}Pb/^{204}Pb$ values, and has more radiogenic Pb than N-MORB on the $^{208}Pb/^{204}Pb$ vs. $^{206}Pb/^{204}Pb$ diagram (Fig. 8-2).

8.3.3. Oxygen and hydrogen isotopes

8.3.3.1. Biotite

Biotite in the unaltered biotite pyroxenite is thought to represent primary igneous biotite, and has measured δD values of -95.5 to -81.2 and $\delta^{18}O$ values of 3.4 to 5.4 ‰ (Table 8-3). Re-equilibrated biotite in an mineralised biotite pyroxenite (*see* Chapter 6) has a measured δD value of -85.6 and $\delta^{18}O$ value of 4.9 ‰, overlaping with the values for the unaltered biotite pyroxenite. Hence, there is no evidence for a substantial change in the δD or $\delta^{18}O$ isotope values in biotite as a result of alteration. The D-O isotopic values of biotite from the biotite pyroxenites partially overlaps with the range of values for mantle phlogopite (Fig. 8-3; Kyser, 1986); although some Lorraine samples have lower δD and $\delta^{18}O$ values than mantle phlogopite. Biotite in fine-grained K-feldspar biotite rock and syenite have a range of δD values from -87 to -80.9 ‰, and $\delta^{18}O$ values from 3.6 to 5.1 ‰ (Fig. 8-3). Coarse-grained biotite in veins has the lowest δD and $\delta^{18}O$ values of -103 and 2.5 respectively (Table 8-3). Biotite isotopic values for unaltered and mineralised mafic and felsic rocks plot along a positive linear trend, but there is no obvious time perspective evolution with respect to stable isotopes. The linear trend is inferred to represent an isotopic fractionation trend. The linear isotope fractionation trend may have been driven

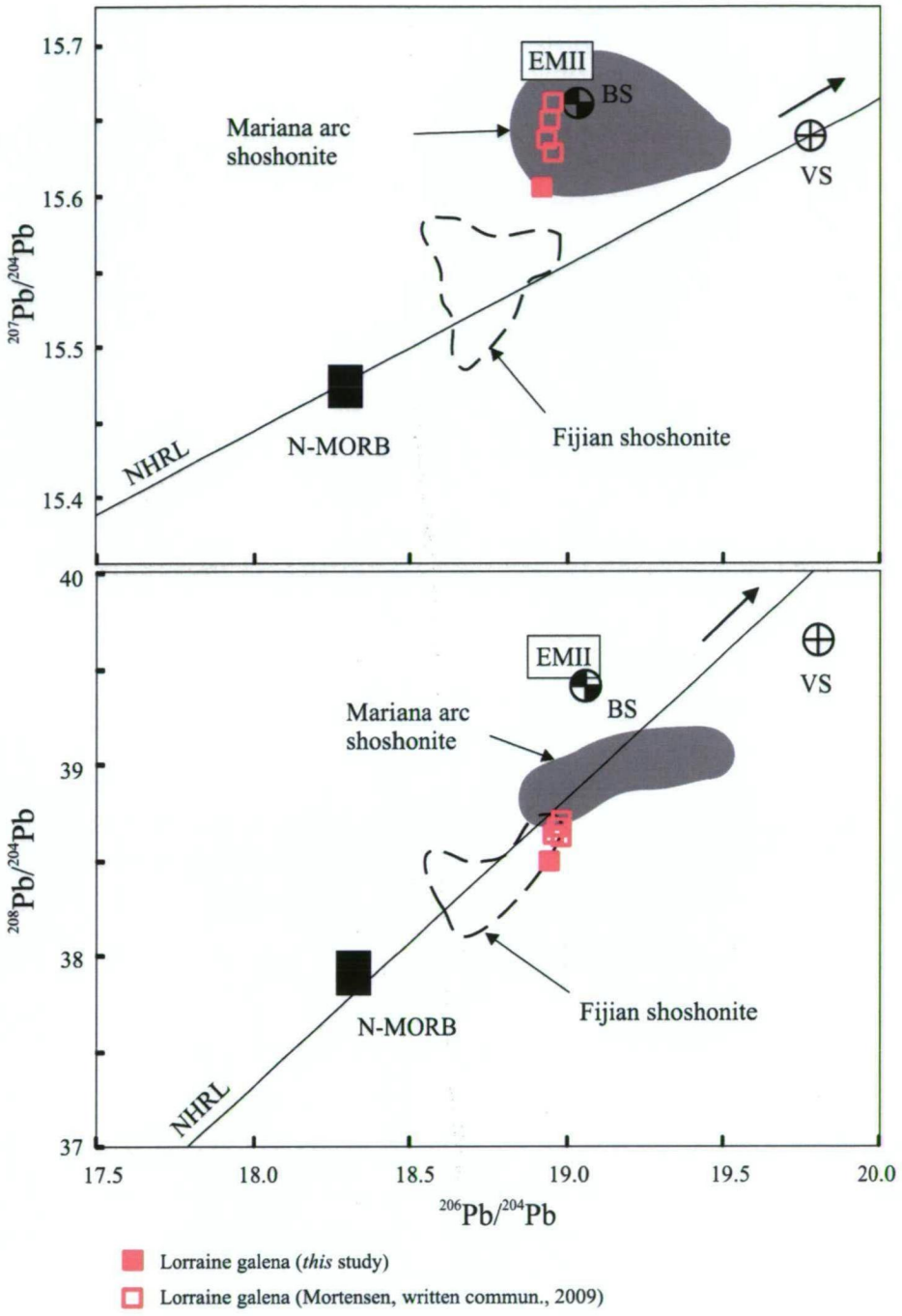

Figure 8-2. **(a)** $^{207}Pb/^{204}Pb$ vs. $^{206}Pb/^{204}Pb$ and **(b)** $^{208}Pb/^{204}Pb$ vs. $^{206}Pb/^{204}Pb$ diagrams showing the Pb isotopic composition of galena from Lorraine (closed pink box this study; open pink box; Mortensen, written commun., 2009; Table 8-2). The Lorraine data are superimposed on to the field defined as Fijian arc shoshonites (Leslie, 2004) and Mariana arc shoshonites (Sun and Stern, 2001). N-MORB, Mariana arc bulk marine sediment (BS), volcaniclastic turbidite sediments (VS), OIB (EMII) and northern hemisphere reference line (NHRL) data are also from Sun and Stern (2001).

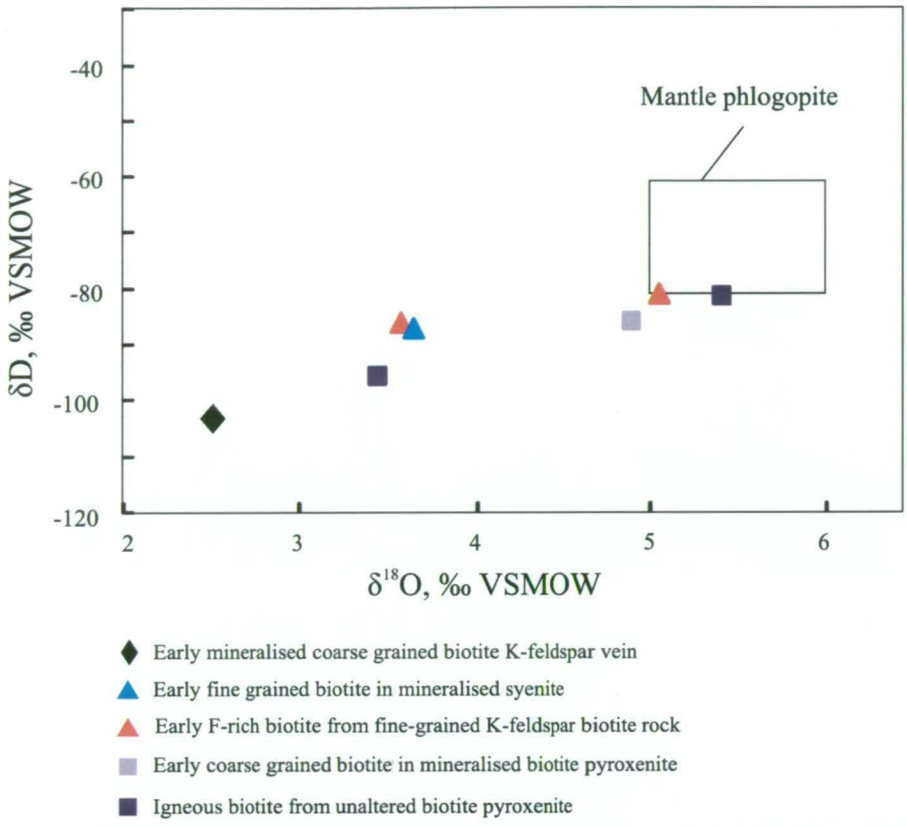

Figure 8-3. δD (‰) and $\delta^{18}O$ (‰) values for biotite from various rock types at Lorraine relative to the field for mantle phlogopite of Kyser (1986). Note that mineralised and unaltered biotite pyroxenites are all Phase 1 rocks. All data are listed in Table 8-3.

by the exsolution of dissolved water from the crystallising magma (i.e. loss of light stable isotopes), which would explain the lower δD and $\delta^{18}O$ values in biotite from some biotite pyroxenites relative to others (e.g., Nabelek et al., 1983; Kyser and O'Neil, 1984; Hall, 1987). Also, variations in temperature of O and H equilibrium between biotite and magmatic fluids may have also contributed to variations in the isotopic composition of biotites (e.g., Bottinga and Javoy, 1973; Suzuoki and Epstein, 1976).

8.3.3.2. Fluids in equilibrium with biotite

Suzuoki and Epstein (1976) and Bottinga and Javoy (1973) provided calibrated hydrogen and oxygen isotope fractionation factors between biotite and water at temperatures between 400 and 850 °C and 500 to 800 °C respectively, which were used here to calculate the isotopic composition of fluids (assuming equilibrium between mineral and fluid was attained). The fluids in equilibrium with biotite at 600 ± 50 °C in unaltered biotite pyroxenites (based on the biotite-apatite thermometer; *see* Fig. 6-27a) have calculated isotopic values of -68 and +6.1 ‰ for δD and $\delta^{18}O$ respectively, and hence are consistent with the isotopic range for both magmatic and metamorphic fluids defined by Sheppard (1986; Table 8-3).

Table 8-3. Oxygen and hydrogen isotope values of biotite, diopside and magnetite from the Lower Main Zone and Lorraine district. Data also includes the model composition of aqeous fluids in equilibrium with the selected mineral.

sample	Rock type	Location	Easting /DDH	Northing /depth	Mineral	T model (°C)	Measured		Model composition	
							$\delta^{18}O$ mineral	δD mineral	$\delta^{18}O$ fluid	δD fluid[d]
15-7-1	Unaltered biotite pyroxenite	Lorraine area	348560	6200804	biotite	600[a] ± 50	5.40 ± 0.1	-81.2 ± 4	8.0 ± 0.1[c]	-50 ± 4
05F0403-1	Unaltered biotite pyroxenite	Page Bowl	348305mE	6198987mN	biotite	600[a] ± 50	3.44 ± 0.1	-95.5 ± 4	6.0 ± 0.1[c]	-65 ± 4
56-165.1	Mineralised biotite pyroxenite	Lower Main Zone	2001-56*	165.1m†	biotite	570[a] ± 50	4.89 ± 0.1	-85.6 ± 4	7.4 ± 0.1[c]	-53 ± 4
07AB40	Fine grained K-feldspar biotite rock	Lower Main Zone	347295mE	6200720mN	biotite	550[a] ± 90	5.06 ± 0.1	-80.9 ± 7	7.6 ± 0.1[c]	-47 ± 7
66-30.4	Fine grained K-feldspar biotite rock	Lower Main Zone	2001-66*	30.4m†	biotite	550[a] ± 60	3.58 ± 0.1	-86 ± 4	6.1 ± 0.1[c]	-52 ± 4
56-62.0	mineralised syenite	Lower Main Zone	2001-56*	62.5m†	biotite	550[g] ± 60	3.65 ± 0.1	-87 ± 4	6.2 ± 0.1[c]	-53 ± 4
63-131	Coarse grained biotite K-feldspar vein	Lower Main Zone	2002-63*	131.0m†	biotite	550[g] ± 60	2.52 ± 0.1	-103 ± 4	5.0 ± 0.1[c]	-69 ± 4
15-7-1	Unaltered biotite pyroxenite	Lorraine area	348560	6200804	diopside	720[b] ± 50	5.89 ± 0.1		8.0 ± 0.1[e]	
96-244	Mineralised biotite pyroxenite	Bishop Zone	1996-44*	244m†	diopside	730[b] ± 50	5.69 ± 0.1		7.8 ± 0.1[e]	
07AB-32	Magnetite diopside vein	Lower Main Zone	347390	6200735	diopside	750[b] ± 50	4.98 ± 0.1		7.1 ± 0.1[e]	
63-76	Magnetite diopside vein	Lower Main Zone	2002-63*	76.0m†	diopside	790[b] ± 50	5.48 ± 0.1		7.5 ± 0.1[e]	
15-7-1	Unaltered biotite pyroxenite	Lorraine area	348560	6200804	magnetite	720[b] ± 50	2.29 ± 0.1		7.5 ± 0.1[f]	
96-244	Mineralised biotite pyroxenite	Bishop Zone	1996-44*	244m†	magnetite	730[b] ± 50	2.20 ± 0.1		7.4 ± 0.1[f]	
07AB-32	Magnetite diopside vein	Lower Main Zone	347390	6200735	magnetite	750[b] ± 50	2.36 ± 0.1		7.5 ± 0.1[f]	
63-76	Magnetite diopside vein	Lower Main Zone	1996-44*	76.0m†	magnetite	790[b] ± 50	2.34 ± 0.1		7.3 ± 0.1[f]	

*Drill hole no.

†Drill hole depth (m).

[a] Temperature estimation based on apatite-biotite geothermometer, errors are approximately 2 standard deviations (Zhu and Sverjensky, 1991).

[b] Temperature estimation based on the magetite-diopside oxygen isotope geothermometer of Chiba et al. (1989).

[c] Fluid composition calculated using the equation of Bottinga and Javoy (1973).

[d] Fluid composition calculated using the equation of Suzuoki and Epstein (1976).

[e] Fluid composition calculated using the equation of Zheng (1993).

[f] Fluid composition calculated using the equation of Cole et al. (1993).

[g] Assumed temperature.

Calculated fluids that were in equilibrium with biotite in the mineralised biotite pyroxenite (at 570 °C), fine-grained K-feldspar biotite rock (at 550 ± 60 °C) and syenite (at 550 ± 60 °C) had isotopic values between -55 and -47 ‰ for δD, and +6.1 and +7.6 ‰ for $\delta^{18}O$ (Table 8-3). The values overlap with the isotopic range for both magmatic and metamorphic fluids (Sheppard, 1986; Fig. 8-4). In addition, fluids in equilibrium with biotite from the biotite pyroxenite and one fine-grained K-feldspar biotite rock also plot within the field for fluids in equilibrium with high temperature hydrothermal biotite from the Santa Rita, Bingham and Ely porphyry copper deposits (Sheppard et al., 1971; Dilles et al., 1992). In contrast, fluids in equilibrium with biotite from the early coarse biotite-K-feldspar veins have calculated δD and $\delta^{18}O$ values of -69 and +5 ‰, respectively, and plot outside of the fields defined by Sheppard (1986). The above results support the contention

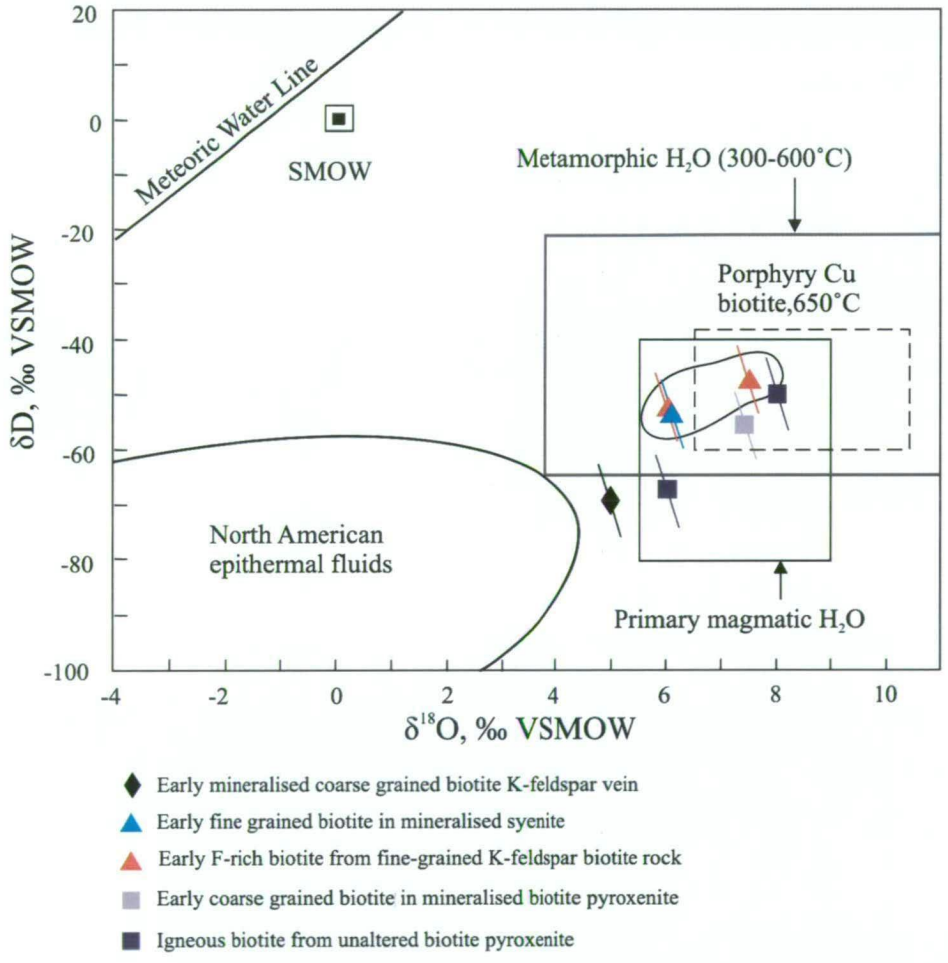

Figure 8-4. Calculated isotopic composition of water in equilibrium with biotite from mineralised rocks of the Lower Main Zone and one regional unaltered sample from the Lorraine-Jajay property normalised to Vienna standard mean ocean water (VSMOW). Fields for natural waters are from Sheppard (1986), and field for water in equilibrium with hydrothermal biotite at 650 °C from copper porphyry environments at Santa Rita, Bingham and Ely is from Sheppard et al. (1971) and Dilles et al. (1992). Also shown for comparison is the range of fluid compositions discharged from high-temperature volcanic fumaroles (Giggenbach, 1992). Bars show temperature errors from mineral geothermometry. O-D isotopic data are listed in Table 8-3.

that hydrothermal fluids were of magmatic derivation, and there appears to be no evidence of interaction between fluids and near-surface meteoric waters. Alternatively high-temperature (i.e. >550 °C) metamorphic fluids at Lorraine might have caused early biotite alteration at Lorraine, although subsequent mineralisation appears to be at odds with the lack of solid-state deformation in all mineralised zones at Lorraine (e.g., Bishop Zone and much of the Main Zone lack solid-state deformation fabrics).

8.3.3.3. Diopside

Oxygen isotopes were measured in diopside from unaltered biotite pyroxenite and mineralised biotite pyroxenite. Diopside from unaltered biotite pyroxenite has a $\delta^{18}O$ value of 5.9 ‰, and diopside from mineralised biotite pyroxenite has a $\delta^{18}O$ value of 5.7 ‰ (Table 8-3). Diopside from both mineralised and unaltered biotite pyroxenite have $\delta^{18}O$ values that overlap with the range for olivine and pyroxene phenocrysts from Mariana arc shoshonites ($'^{18}O$ = 5.4-6.3 ‰; Sun and Stern, 2001), and are close to mantle values ($'^{18}O$ = 5.71 ‰; Sun and Stern, 2001).

Zhao and Zheng (2003) calculated the fractionation effects of $\delta^{18}O$ between diopside and mafic magmas, and showed that diopside in equilibrium with mafic magma has only slightly lower $\delta^{18}O$ values than the magma (i.e. $\delta^{18}O$ is 0.36 or 0.5 lower in diopside than mafic magma at 1100 or 850 °C respectively). Therefore, the $\delta^{18}O$ of diopside can be used to approximate the minimum $\delta^{18}O$ values of mafic magmas (assuming that sub-solidus re-equilibration of $\delta^{18}O$ was minor). Hence it is inferred that ultrabasic magmas, which Lorraine biotite pyroxenite crystallised from, had only marginally lower $\delta^{18}O$ than mantle values (i.e. 5.4 ‰ vs. 5.71 ‰, assuming $\delta^{18}O$ in diopside equilibrated with a magma source at approximately 850 °C).

Oxygen isotopes were also measured in diopside from diopside-magnetite veins for comparison. Diospide in veins has $\delta^{18}O$ values of 5.0 and 5.5 ‰ lower than values for diopside from biotite pyroxenite. Hence hydrothermal diopside at Lorraine has slightly lower $\delta^{18}O$ values than diopside in magmatic rocks, which may be attributed to temperature-induced isotope fractionation.

8.3.3.4. Diopside-magnetite thermometry

Oxygen isotopes were measured in magnetite and diopside pairs from unaltered biotite pyroxenite and mineralised biotite pyroxenite for geothermometry. Temperature estimates are based on the diopside-magnetite thermometer for magmatic rocks of Chiba et al. (1989). Calculations indicate that oxygen isotopes in magnetite and diopside in unaltered biotite pyroxenite equilibrated at 720 ± 50 °C, and in mineralised biotite pyroxenite at 730

± 50 °C (Table 8-3). Hence there is no notable difference in the equilibrium temperature between diopside and magnetite pairs in mineralised biotite pyroxenite versus unaltered biotite pyroxenite, and it appears unlikely that alteration resulted in the re-equilibration of O isotopes in diopside from the host rock. The above temperature range for biotite pyroxenite is consistent with sub-solidus exchange between diopside and magnetite, and estimated temperatures are slightly lower than the typical range for mafic intrusives (e.g., magnetite-diopside pairs in gabbroic intrusives typically yield temperatures between 800-900 °C; Chiba et al., 1989).

The $\delta^{18}O$ values of diopside and magnetite pairs in diopside-magnetite veins were also measured, and calculated temperature estimates indicate temperatures of 750 to 790 °C. Hence it is inferred that early magnetite-diopside veins formed during high temperature alteration.

8.4. Discussion

8.4.1. Magma sources for ultrabasic rocks at Lorraine

Radiogenic isotopes and trace element composition of mafic arc-related magmas can provide constraints on the mantle source and degree of contamination of magma during transit (e.g., Gill, 1984; Ito and Stern, 1986; Woodhead, 1989; Lin et al., 1990; Stern et al., 1990; Stern et al., 1993; McCulloch et al., 1994; Sun and Stern, 2001; Boari et al., 2009). In particular, in the sub-arc mantle wedge melting occurs due to mixing between mantle and slab-derived components, and these slab-derived fluids and sediment melts may interact with the mantle wedge above subduction zones and modify its trace element and isotopic composition (e.g., Pearce and Parkinson, 1993; Hawkesworth et al., 1994; Pearce and Peate, 1995; Tatsumi and Eggins, 1995; Sun and Stern, 2001). In continental margin arc settings, interactions between cratonic rocks and mantle-derived magmas can also result in diverse major, trace and isotopic compositions of arc magmas (e.g., Pearce, 1983).

Hawkesworth et al. (1991) showed that REE data for rocks from destructive plate margin fall into two main groups: one with low Ce/Yb (Type-A arc rocks; Fig. 8-5) and a second with higher Ce content, but with similar Yb abundance (Type-B arc rocks; Fig. 8-5). Type-A rocks have restricted and depleted radiogenic isotope signatures, whereas Type-B rocks have a much greater range in Nd, Sr and Pb isotope ratios (Hawkesworth et al., 1994). Type-A rocks tend to form along oceanic island arc (Hawkesworth et al., 1994; Fig. 8-5), whereas Type-B rocks tend to form along continental island arcs or along island arcs where either: (1) slab-derived sediment input was high (e.g., McDermott et al., 1993; Hawkesworth et al., 1994); (2) trace elements were enriched in the source region of the mantle wedge (Morris and Hart, 1983; Rogers and Hawkesworth, 1989; Hawkesworth et

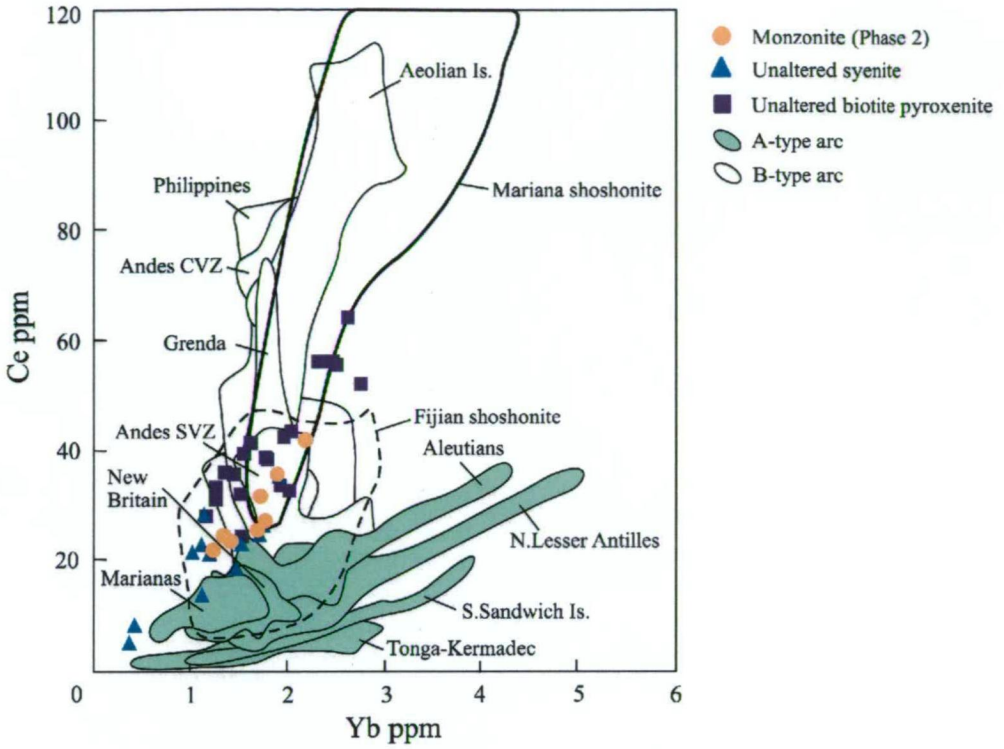

Figure 8-5. Ce vs. Yb variation diagram for Lorraine shoshonites in comparison to other arc rocks from around the world. Fields for A-type arc and B-type arc rocks are from Hawkesworth et al. (1993), and fields for Mariana arc shoshonites and Fijian arc shoshonites are from Sun and Stern (2001).

al., 1994) and/or (3) low degrees of partial melting of the mantle source had occurred (e.g., Hawkesworth et al., 1994). Hawkesworth et al. (1994) further noted that arc rocks with high Ce/Yb values and high K content, may form due to lower degrees of partial melting of the mantle source with residual garnet.

Lorraine shoshonites have high Ce/Yb values and mostly plot in the field for Type-B arc rocks (Fig. 8-5); however Lorraine rocks have low $^{87}Sr/^{86}Sr$ and high εNd values compared to most arc rocks, which were formed along continental margins where contamination has occurred between magmas and the overlying crust (e.g., Central Andes; Hildreth and Moorbath, 1988; Fig. 8-6). Shoshonitic rocks from the Marianas, like Lorraine, have high Ce/Yb, low $^{87}Sr/^{86}Sr$ and high εNd values (Sun and Stern, 2001; 1994; Figs. 8-5, 8-6 and 8-7), whereas shoshonitic rocks from Fiji have both high and low Ce/Yb values, low $^{87}Sr/^{86}Sr$ and high εNd values (Roger and Setterfield, 1994; Sun and Stern, 2001; Figs. 8-5, 8-6 and 8-7). Similarities between Lorraine shoshonites, Mariana shoshonites and Fijian shoshonites may represent similar processes during the formation of parental melts. This section uses mixing models (e.g., Sun and Stern, 2001), to test if mixing between crustal sources can potentially explain the isotopic and geochemical characterisitics of Lorraine shoshonites.

Data for Lorraine rocks include Sr and Nd isotopic values from diopside and apatite, and

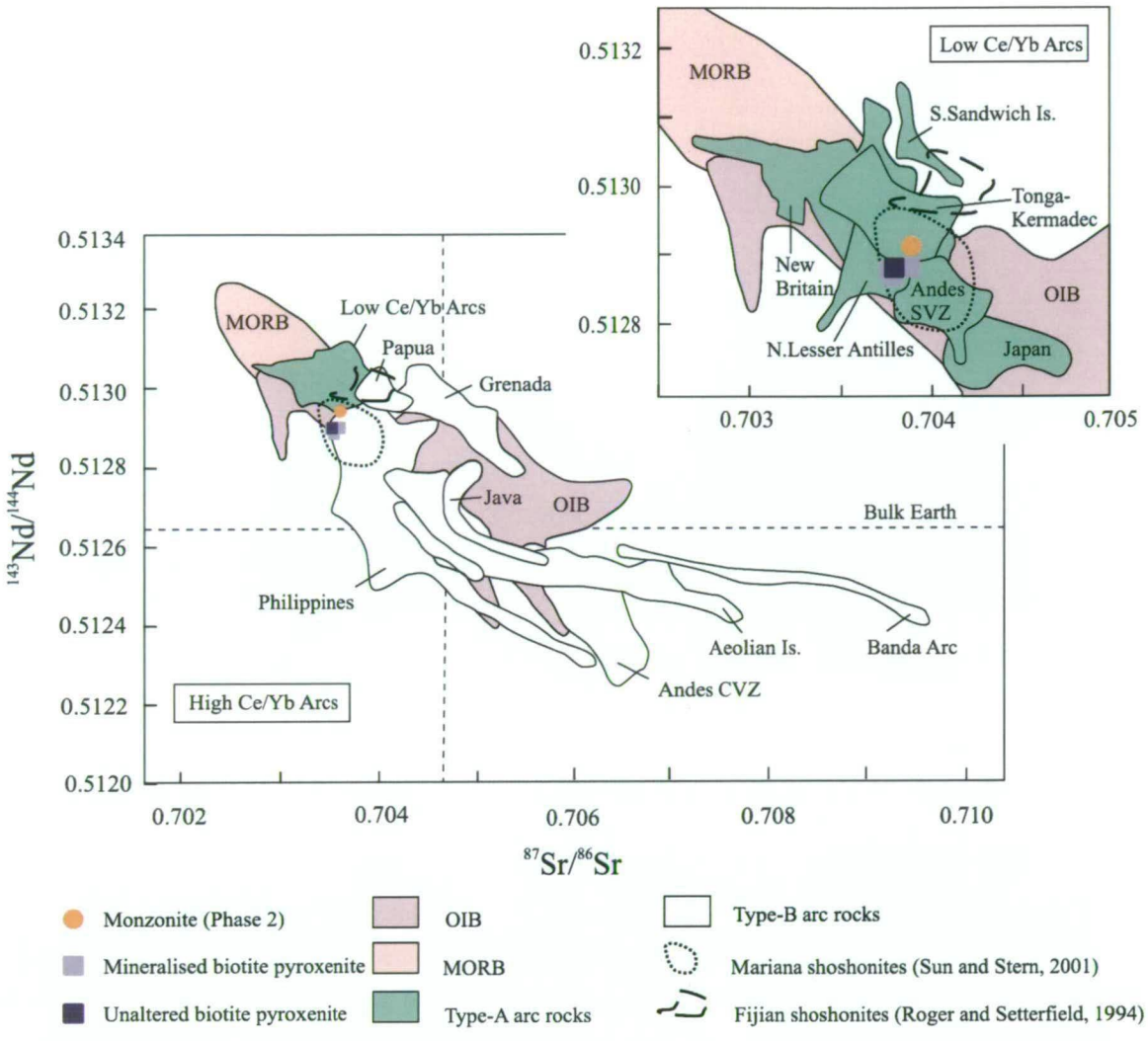

Figure 8-6. Nd vs. Sr isotope ratios for Lorraine rocks compared to arc rocks with low and high Ce/Yb ratios. Modified after Hawkesworth et al. (1994). Lorraine isotope data shown in Table 8-1.

Pb isotopic values from galena. For the purpose of this section it has been assumed that the range of Pb isotopic values of galena are similar to magmatic rocks at Lorraine.

8.4.1.1. Geochemical evidence for a slab-derived sedimentary component

Subducted sediments are thought to play an important role in shaping the trace element and isotopic compositions of arc magmas. However, one of the challenges with testing a model for the contribution of aqueous fluids and sediment melts derived from the subducted slab is that a representative record of the sediments that were subducted is often missing. Also, it is difficult to determine the proportion of sediment scraped off the slab during subduction. For arc rocks of the Quesnel terrane, the Cache Creek accretionary complex offers insights into the nature of sediments scrapped off the slab during the Mesozoic (Chapter 2); however to the author's knowledge there are no records of an intact ob-

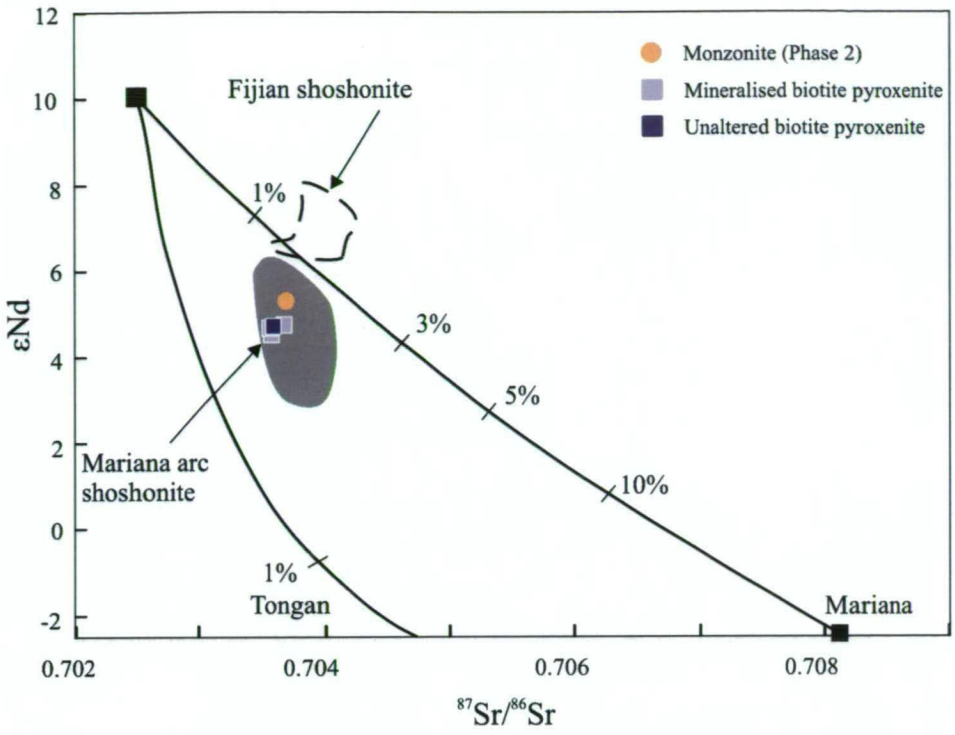

Figure 8-7. εNd vs. $^{87}Sr/^{86}Sr$ mixing models for N-MORB with OIB and seafloor sediments from various areas of the western Pacific. Lorraine data (Table 8-1) are superimposed on mixing models along with areas for Mariana arc shoshonites and Fijian shoshonites. Fields for Fijian shoshonites was sourced from Leslie (2004), and the field for Mariana arc shoshonite is from Sun and Stern (2001). Marine bulk sediment trace element and isotopic compositions were derived from Plank and Langmuir (1998), and EMII and N-MORB end-members were derived from Sun and Stern (2001). Mixing model calculations are shown in Appendix H.

ducted oceanic slab in British Columbia that could be used to quantify the average composition of the sediment load that was subducted beneath the Quesnel arc in the Triassic to early Jurassic.

Plank and Langmuir (1998) quantified the average major element, trace element and radiogenic isotopic ratios of several hundred meters of sediments from the modern-day seafloor (ocean drilling project) from the seaward side of the Mariana and Tongan trenches. The composition of these sediments in areas adjacent to trenches of modern-day arcs provides a means of linking sediment composition and input into arc-magmas. In particular a simple two end-member mixing of an N-MORB magma and average seafloor sediment compositions (e.g., Sun and Stern, 2001) is used here to test if sediment input derived from the slab could potentially explain the isotopic composition of Lorraine rocks.

Mixing models have been calculated involving εNd vs. $^{87}Sr/^{86}Sr$, $^{87}Sr/^{86}Sr$ vs. $^{206}Pb/^{204}Pb$ and εNd vs. $^{206}Pb/^{204}Pb$ for an N-MORB (Figs. 8-7 and 8-8a, b). Mixing models of $^{87}Sr/^{86}Sr$ vs. $^{206}Pb/^{204}Pb$ and εNd vs. $^{206}Pb/^{204}Pb$ calculated by Sun and Stern (2001) for a mantle derived melt (i.e. N-MORB) contaminated with variable proportions of average oceanic slab sediment and average volcanic turbidite from the oceanic crust seaward of the Mariana

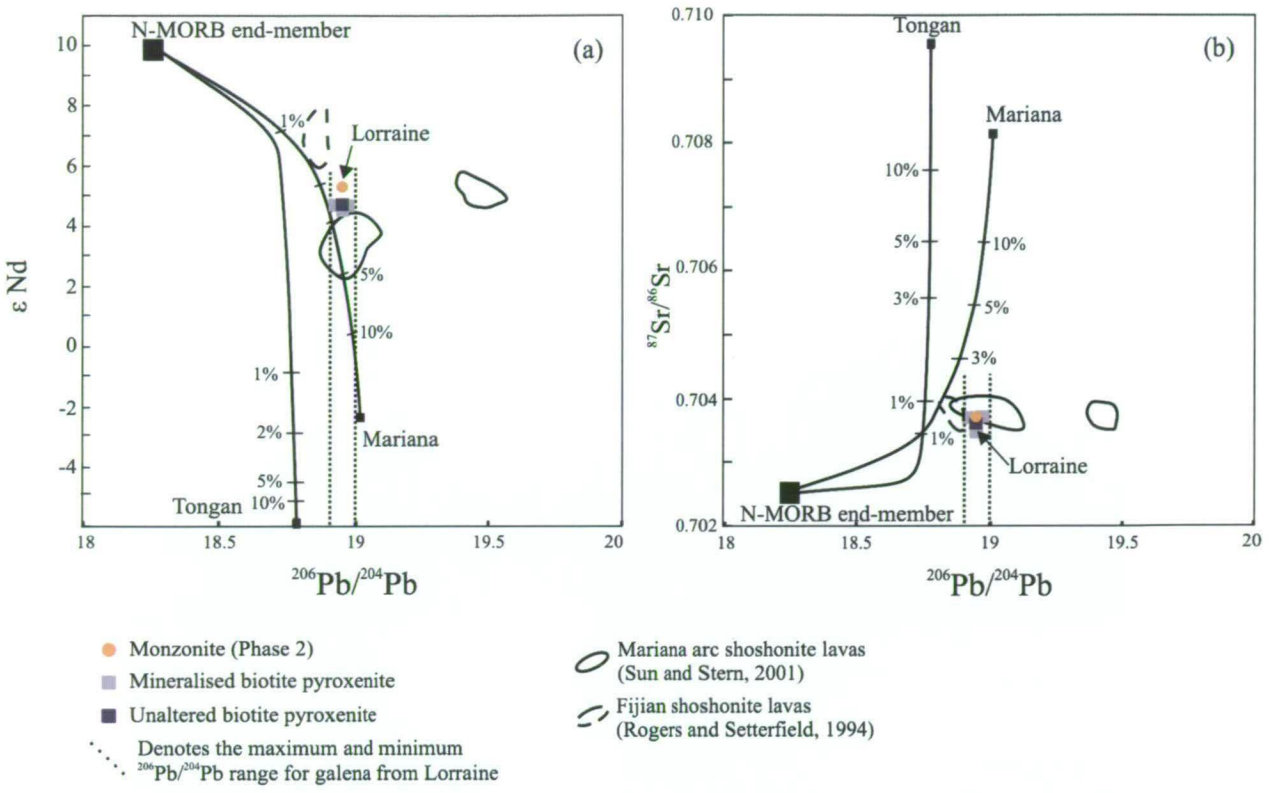

Figure 8-8. εNd vs. $^{206}Pb/^{204}Pb$ and $^{87}Sr/^{86}Sr$ vs. $^{206}Pb/^{204}Pb$ models for mixing an N-MORB source with variable proportions of sediments from seafloor seaward of the trench of the Mariana and Tongan arcs. Mixing models shown in **(a)** and **(b)** are sourced from Sun and Stern (2001). Seafloor sediment isotopic and trace element data are provided by Plank and Langmuir (1998). Black open polygons represent the distribution of Mariana arc shoshonites from Sun and Stern (2001). Data from Lorraine is superimposed on the each of the diagrams, and demonstrates that mixing of approximately 1.5 to 2.5 % of Mariana-like sediment with an N-MORB could potentially explain the isotopic characteristics of Lorraine rocks. Mixing model calculations are shown in Appendix H.

trench are used for comparison (Fig. 8-8a and b). The Lorraine data plot between the mixing lines of N-MORB – Mariana bulk marine sediment on the εNd vs. $^{87}Sr/^{86}Sr$ diagram (Fig. 8-7). For $^{87}Sr/^{86}Sr$ vs. $^{206}Pb/^{204}Pb$ and εNd vs. $^{206}Pb/^{204}Pb$, Lorraine rocks plot closest to mixing curves of N-MORB with Mariana-arc bulk sediment, which comprises volcanoclastics, limestone, clay and chert. Mixing models show that mixing of approximately 1.5 to 2.5 % of Mariana-like bulk marine sediment with an N-MORB could potentially explain the radiogenic isotopic compositions of Lorraine rocks.

8.4.1.2. Is there evidence of crustal or limestone assimilation?

Recent work by Iacono-Marziano et al. (2007; 2008; 2009) proposed that crustal carbonate assimilation could explain silica-undersaturated characterisitics of alkalic magmas at Mount Vesuvius, Italy. Pass et al. (in prep.) presented Sr and Pb isotope data and abundances of Pb and Sr in Norian limestone from the Nicola Group in the Mount Polley area

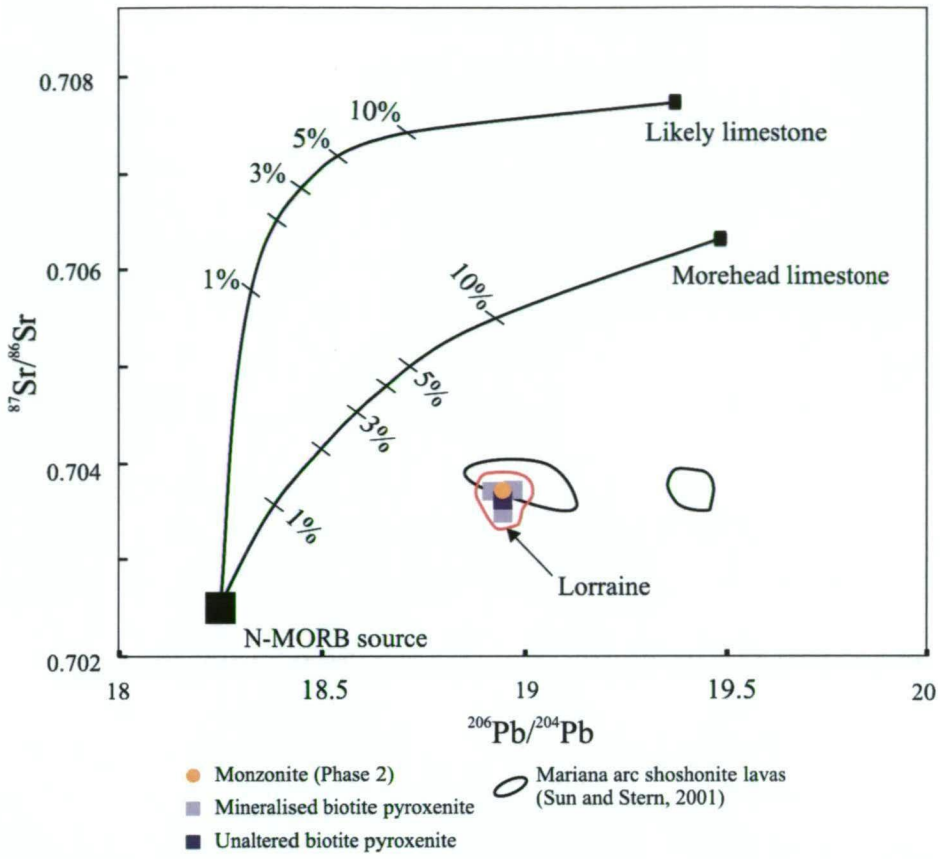

Figure 8-9. $^{87}Sr/^{86}Sr$ vs. $^{206}Pb/^{204}Pb$ model for mixing an N-MORB source with Norian age limestone of the Nicola Group from the Mt. Polley area. Limestone data was sourced from Pass et al. (in prep.). Mixing model calculations are shown in Appendix H.

(Fig. 6-2). Isotope data from the two samples from Pass et al. (submitted; Appendix H) are used here to test if mixing between N-MORB and crustal limestone in the Quesnel terrane could potentially explain the Pb and Sr isotopic characteristics of Lorraine rocks.

Mixing models of an N-MORB source with Mt. Polley limestone shows sharp increases in 87Sr/86Sr (i.e. 0.7025 to 0.7035 or 0.7025 to 0.7058) with only relatively small amounts of limestone assimilation (i.e. 1 wt. %; Fig. 8-9). In contrast, 206Pb/204Pb remains relatively unchanged (i.e. 18.25 to 18.40 or 18.25 to 18.32) due to the low concentration of Pb in Mt. Polley limestone. Hence, the above mixing model of limestone with a N-MORB magma cannot explain the Sr and Pb isotopic composition of Lorraine rocks.

Alternatively, assimilation of Pb- and Nd-richer source(s), such as sedimentary or igneous wall rocks, could potentially explain the isotopic composition of the Lorraine rocks. In particular, at the time of arc magmatism at Lorraine, it is thought that the Quesnel terrane was in the process of being accreted to ancestral North America (e.g., Mihalynuk et al., 1994a; Chapter 2), and therefore it is possible that the source magmas for the Lorraine intrusives assimilated older cratonic wall rocks. However, there is no evidence for "inher-

ited" zircons in Lorraine rocks, and conservative element ratios (e.g., Zr/Nb vs. Nb/Yb) on the diagrams of Pearce and Peate (1995), show that Lorraine rocks plot in the mantle-array (Fig. 7-7a). The Lorraine rocks have similar trace element ratios to Nicola Group basalts, which are believed to have formed more than 30 million years prior to the accretion of Quesnellia to ancestral North America (Chapters 2). Hence, based on the data presented in the current study there appears to be no geochemical evidence that magmas that were emplaced at Lorraine had assimilated cratonic rocks from ancestral North American, which is reported to have more crustal isotopic compositions than arc rocks of the Quesnel terrane (i.e. εNd ~ -5 to -28; Patchett and Gehrels, 1998).

The Lorraine monzonites do not have more evolved isotopic compositions compared to biotite pyroxenites (Table 8-1; Fig. 8-1). It is therefore unlikely that the felsic rocks formed as a result of assimilation of older cratonic rocks or as a result of anatexsis melting of older cratonic rocks. However, the assimilation or anatexsis melting of arc rocks with similar chemical and isotopic characteristic would not likely be detected through isotopic and trace element studies, and therefore cannot be ruled out.

One other possibility is that a partial melt derived from the mantle had a significantly higher content of Sr than the N-MORB end-member used in Figure 8.9 and by Sun and Stern (2001). Therefore the two end-member mixing model shown in Figure 8.9 could be considered irrelevant. Certainly a mantle derived melt that is enriched in Sr would show a different mixing trajectory with Norian limestone from the Nicola Group in the Mount Polley area then is shown in Figure 8.9. Hence, without data from a true mantle end member (i.e. mantle xenoliths) the Sr and Pb isotope data alone cannot prove or disprove that crustal limestone assimilation caused alkalic magmatism at Lorraine. However there are a number of similarities between the Lorraine rocks and shoshonitic rocks from the Fijian and the Mariana arcs. These similarities include timing of alkalic magmatism relative to major tectonic events (i.e. post-collisional alkalic magmatism), the major and trace element patterns consistent with a slab-derived input (Chapter 7) and similarities in the isotopic composition of these rocks. The author infers that these similarities are consistent with tectonic –scale processes as opposed to local crustal assimilation events.

8.4.2. Oxygen and strontium isotopes

The oxygen-isotope $\delta^{18}O$ ‰ vs. $^{87}Sr/^{86}Sr$ diagram of Ito and Stern (1986) was used to compare the composition of Mariana arc magmas with diopside from mineralised and unaltered biotite pyroxenite (Fig. 8-10). Diopsides from both mineralised and unaltered biotite pyroxenites plot along the mixing curve between MORB and pelagic marine sediments that occur seaward of the Mariana trench. Lorraine diopsides plot in the same field as arc rocks of the Mariana arc, and the mixing model shows that mixing of 1.5 and

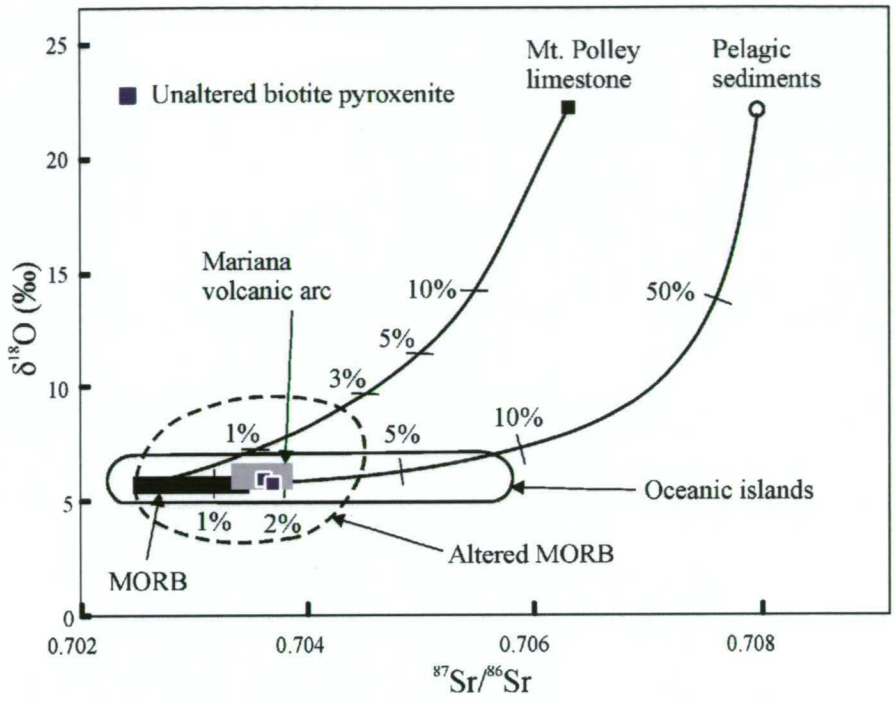

Figure 8-10. $\delta^{18}O$ (‰) vs. $^{87}Sr/^{86}Sr$ diagram of Ito and Stern (1986). The diagram shows the distribution of Mariana arc rocks, MORB, weathered MORB, OIB, bulk pelagic marine sediment, and a mixing model between a MORB source with bulk pelagic sediment, together with data from the Lorraine biotite pyroxenite. Mixing model calculations are shown in Appendix H.

2 wt. % of Mariana-like sediment into a MORB source could potentially explain the $\delta^{18}O$ ‰ vs. $^{87}Sr/^{86}Sr$ composition of Lorraine diopsides.

8.4.3. Sulphur isotopes

Deyell and Tosdal (2005) presented initial sulphur-isotope data for sulphides from the Lower Main Zone and revealed that high-grade bornite > chalcopyrite mineralised syenite have $\delta^{34}S$ values between -4.0 and -16.6 ‰, whereas lower grade chalcopyrite-pyrite zones have $\delta^{34}S$ values between 0 and -10 ‰.

Deyell and Tosdal (2005) presented data for drill hole 2002-62, which was logged in detail in the present study and occurs in cross-section B-B' (Fig. 3-3b). Sulphide zonation patterns were compared with sulphur-isotope data for drill hole 2002-62 (Fig. 8-11). Initial sulphur patterns range from -16.6 to -3.0 ‰ $\delta^{34}S$ along drill hole 2002-62. The most negative $\delta^{34}S$ (‰) values occur within the bornite-chalcopyrite zone; however high-grade bornite-chalcopyrite zones have highly variable initial $\delta^{34}S$ (‰) values and no obvious increase in $\delta^{34}S$ (‰) occurs into the chalcopyrite-pyrite zone along this drill hole (Fig.

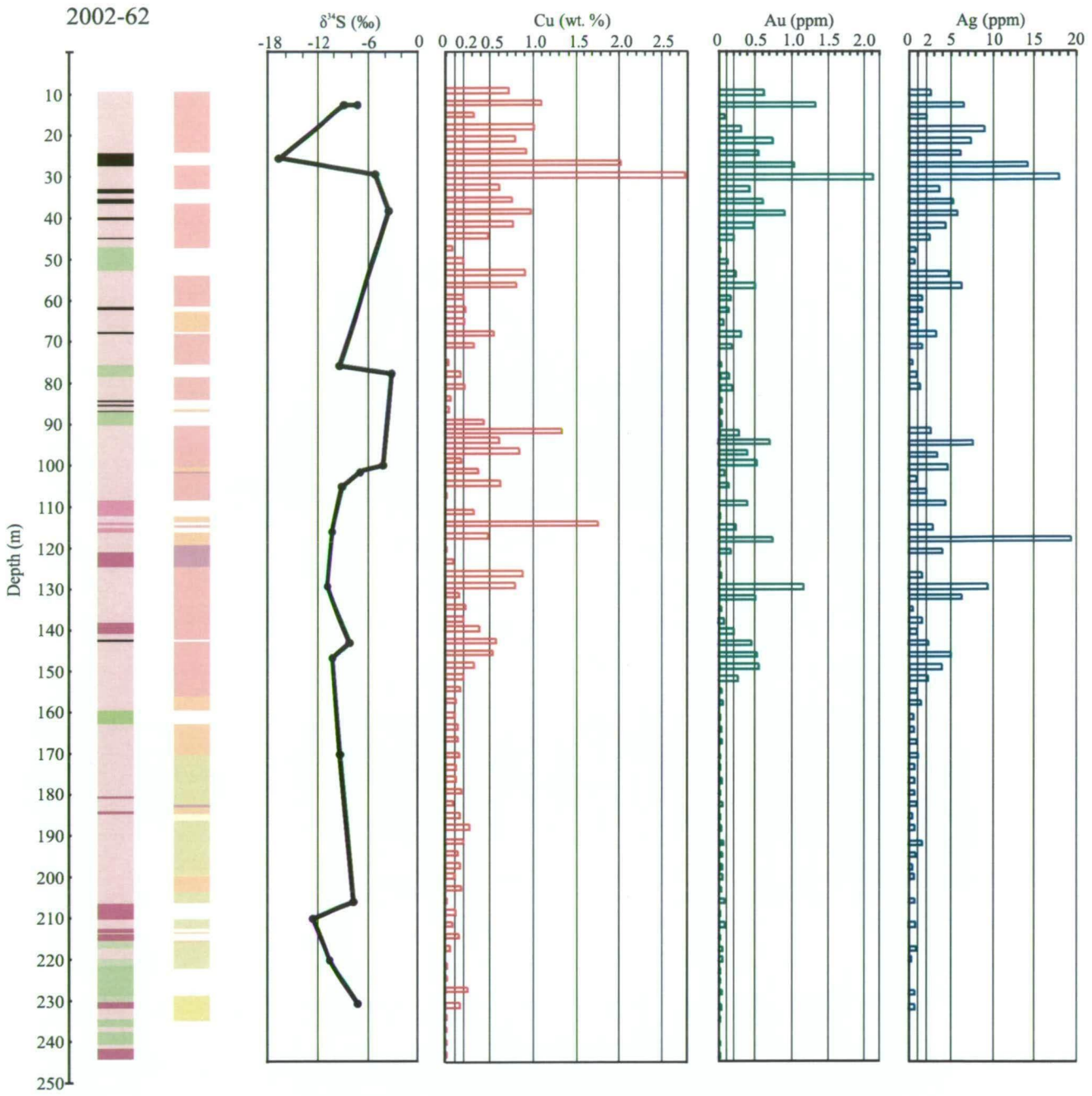
2002-62
δ34S (‰)
-18 -12 -6 0
Cu (wt. %)
0 0.2 0.5 1.0 1.5 2.0 2.5
Au (ppm)
0 0.5 1.0 1.5 2.0
Ag (ppm)
0 2 5 10 15 20
Depth (m)
10 20 30 40 50 60 70 80 90 100 110 120 130 140 150 160 170 180 190 200 210 220 230 240 250
Lithology
Phase 2 syenite
Phase 2 feldspathic biotite pyroxenite
Phase 2 biotite pyroxenite
Phase 1 syenite
Phase 1 biotite pyroxenite
Fine-grained K-feldspar biotite rock
Fault
Pyrite ± trace chalcopyrite
Chalcopyrite-pyrite
Chalcopyrite
Chalcopyrite-bornite
Bornite-chalcocite

←

Figure 8-11. Simplified geology, sulphide mineralogy, Cu, Ag and Au grades and $\delta^{34}S$ data for drill hole 2002-62 from the Lower Main Zone (see cross-section B-B"; Figs. 3-3b, 4-12a and b). Sulphur isotope data of sulphide minerals from Deyell and Tosdal (2005).

8-11).

According to Harper (2000), Wilson (2003), Deyell and Tosdal (2005) and Wilson et al. (2007), the most negative $\delta^{34}S$ (‰) values typically occur towards the top of mineralised monzonite/syenite pipes in porphyry environments, with a return to near-zero values with distance upwards and/or outwards from the pipe. The general $\delta^{34}S$ (‰) trend in porphyry environments is believed to be related to sulphide deposition from an oxidised (sulphate predominant) fluid rather than contamination by biogenic sulphur (Rye, 1993; Wilson et al., 2007). The trend of increasing negative $\delta^{34}S$ (‰) values towards the core of mineralised Cu-Au alkaline porphyry deposits has been recorded at Ridgeway (Wilson et al., 2003), Northparkes (Heithersay and Walshe, 1995), Didipio (Wolfe, 2001), Galore Creek (Byrne et al., 2008), Mt. Polley (Deyell and Tosdal, 2005; Pass et al., in prep.) and Afton (Deyell and Tosdal, 2005), and hence appears to be a common characteristic of alkalic Cu-Au porphyry deposits globally. Based on $\delta^{34}S$ (‰) data from drill hole 62-2002 it can be stated that strong negative values occur within inner bornite-chalcopyrite zones at Lorraine; however there is a lack of data from peripheral pyrite zones, and it is unclear if $\delta^{34}S$ (‰) return to near-zero values within the Lower Main Zone.

8.5. Conclusions

- Rocks from Lorraine have more radiogenic $^{87}Sr/^{86}Sr$, εNd and Pb isotopic compositions than N-MORB (Figs. 8-1 and 8-2), and can be explained by partial melting of a mantle wedge, contaminated with slab-derived fluids and/or sediment melts. Calculations indicate that ~1.5 to 2.5 % contamination by modern-day seafloor sediment of an N-MORB source could potentially produce magma with similar stable and radiogenic isotopic compositions to the Lorraine rocks (Figs. 8-7, 8-8a, b and 8-10).

- There is no notable variation in the radiogenic or stable isotopic composition of mineral phases in unaltered vs. mineralised biotite pyroxenite (Figs. 8-1 and 8-3), and therefore fluids which caused alteration were either isotopically in equilibrium with gangue minerals in the host rock, or did not perturb the isotopic composition of gangue minerals in the host rock.

- $\delta^{18}O$ and δD values measured from different generations of biotite have been used to calculate the $\delta^{18}O$ and δD values of fluids. The data indicate that fluids in equilibrium with biotite from mineralised and unaltered biotite pyroxenite, mineralised syenite and fine-grained K-feldspar biotite rock plot within the magmatic

field of Sheppard (1986; Fig. 8-4). Hence it is inferred that magmatic fluids transported and deposited metals at Lorraine. There is no evidence of mixing of magmatic fluids with external water or seawater, but mixing with metamorphic water cannot be ruled out (Fig. 8-4).

• Sulphides in Lorraine rocks have strong negative $\delta^{34}S$ (‰) values in bornite-chalcopyrite and pyrite-chalcopyrite mineralised inner zones (Deyell and Tosdal, 2005; Fig. 8-11). Negative $\delta^{34}S$ (‰) values in the inner zone of porphyry Cu-Au deposits are consistent with other alkalic porphyries in BC, NSW and Philippines (Heithersay and Walshe, 1995; Wolfe, 2001; Wilson et al., 2003; Deyell and Tosdal, 2005; Byrne et al., 2008; Pass et al., in prep.).

CHAPTER 9
DISCUSSION AND CONCLUSIONS

9.1. Introduction

The Lorraine porphyry Cu-Au deposit occurs in the Quesnel terrane in north-central British Columbia, and mineralisation was spatially and temporally related to the emplacement of biotite pyroxenite and syenite dykes. This thesis has investigated the biotite pyroxenites and syenites, which are spatially associated with porphyry-Cu mineralisation, and has compared their chemical composition with arc-related shoshonitic lavas of the Nicola Group (British Columbia), Fiji and Marianas. This section summarises the findings of the present study, and sets them in a Cordilleran tectonic context.

9.2. Tectonic setting and genesis of shoshonitic magmas at Lorraine

The western Canadian Cordillera is composed of a collage of arc terranes that collided with ancestral North America between the late Early Jurassic and Late Jurassic (Monger, 1993; Mihalynuk et al., 1994a; Monger and Price, 2000; Mihalynuk et al., 2004; Johnston and Borel, 2007). Leading up to, and during the accretion of arc terranes, major changes in the configuration of subduction are thought to have occurred. In addition, medium-K calc-alkaline through to high-K calc-alkaline to shoshonitic magmatism occurred in the Quesnel terrane between the Middle Triassic to early Middle Jurassic, which also coincides with a period of accretion of oceanic plateaus along the western margin of the arc (e.g., Mihalynuk et al. 1994a). Inferred oroclinal bending of the Stikinia-Quesnellia arc and amalgamation of the two arcs is thought to have occurred in the Middle Jurassic (Mihalynuk et al., 1994a; Mihalynuk et al., 2004). In the Lorraine district, active calc-alkaline to alkaline arc volcanism occurred between the Middle to Late Triassic during the formation of the Takla Group (Ferri and Melville, 1994, p.53); and was followed by the emplacement of granodiorite intrusives at ca. 189 Ma (Hogem granodiorite), and calc-alkaline to high-K diorite and monzodiorite intrusives at ca. 185 Ma (Thane and Denti plutons; Nixon and Peatfield, 2003). Following the accretion of the Quesnel terrane with ancestral North America at ca. 186 Ma (Nixon et al., 1993), the post-collisional shoshonitic intrusives of the Duckling Creek Syenite Complex were emplaced at ca. 179 to 177Ma (*this* study). The hypabyssal and volcanic igneous rocks of the Quesnel terrane in the Hogem district can be subdivided into five temporally, geochemically and spatially distinct series:

- Middle to Late Triassic Takla Group Volcanics: calc-alkaline to alkaline

(e.g., Ferri and Melville, 1994).

• Late Triassic? to Early Jurassic Hogem granodiorite: calc-alkaline granodiorite (189 ± 6 Ma; hornblende K-Ar cooling age; Nixon and Peatfield, 2003).

• Late Triassic? to Early Jurassic Thane and Detni Plutons: calc-alkaline to high-K diorite and monzodiorite (185 ± 14 Ma hornblende K-Ar cooling age; Nixon and Peatfield, 2003).

• Latest Early Jurassic Duckling Creek Syenite Complex: shoshonitic biotite pyroxenite, monzonite and syenite (ca. 179 to 177 Ma; zircon U-Pb; *this* study).

• Early to Middle Cretaceous calc-alkaline diorites, granodiorites and granites of the Mesilinka and Osilinka intrusives (Nixon and Peatfield, 2003).

Shoshonitic rocks from the Duckling Creek Syenite Complex at Lorraine have trace element signatures typical of shoshonitic arc-related lavas from the western Pacific. They are notably enriched in LILE, LREE, Sr and P, but depleted in HFSE and HREE compared to N-MORB. Lorraine rocks also have similar trace element ratios to whole rock samples and diopside-hosted melt inclusions of the Nicola Group medium-K to shoshonitic lavas, which are older (Middle to Late Triassic), but also formed in the Quesnel terrane. Rocks from Lorraine have more evolved $^{87}Sr/^{86}Sr$ and εNd isotopic compositions than N-MORB, and can be explained by partial melting of a mantle wedge, contaminated with slab-derived fluids and/or sediment melts. Factors contributing to the formation of shoshonitic magmatism at Lorraine include a low degree of partial melting (i.e. high La/Sm ratios compared to N-MORB, Fig. 7-8b), a mantle source that was enriched in large ion lithophile elements LILE relative to REE, but depleted in HFSE relative to REE and a mantle source that was enriched in P and Sr.

Based on the above conclusions, a petrogenic tectonic model is devised for the genesis of parental magmas for Lorraine rocks, which includes the introduction of slab-derived fluids and melts into the sub-arc mantle wedge during subduction. However, the majority of global arc-related shoshonitic suites are not directly related (in the temporal sense) to active "steady state" plate subduction, and most appear to be associated with rifting of mature arcs following subduction-polarity reversal, cessation of subduction, collision with oceanic plateau and/or plate detachment (e.g., Morrison, 1980; Stern et al., 1984; McInnes and Cameron, 1994; Rogers and Setterfield, 1994; Chen and Brudzinski, 2001; McInnes et al., 2001; Sun and Stern, 2001; van de Zedde and Wortel, 2001; Barley et al., 2002; Leslie, 2004). For example, Fijian shoshonite lavas are inferred to have formed at 5 to 4

Ma (Rogers and Setterfield, 1994) following the detachment of the stalled Pacific plate along the fossil Vitiaz trench at ~12 Ma, due to a collisional event with the Ontong Java Plateau (Hamburger and Isacks, 1987; Chen and Brudzinski, 2001; Green, 2001; Leslie, 2004). The detached part of the Pacific slab is inferred to have remained in the upper mantle and contributed subducted material (e.g., Hamburger and Isacks, 1987; Chen and Brudzinski, 2001; Green, 2001). Leslie (2004) estimated that an "infiltration time" of ~7 Ma was required to conductively heat the overlying metasomatised mantle sufficiently to produce shoshonitic parental melts at Fiji (based on a minimum mantle flow rate of 5.5 cm/year).

The above model for the generation of shoshonitic parental magmas of Fiji could also potentially be used as an analogue for the genesis of shoshonitic magmatism at Lorraine. In particular, shoshonitic rocks of the Lorraine deposit were emplaced at ca. 179 Ma, which post-dates accretion of the Quesnel terrane to ancestral North America at ca. 186 Ma (in north-central British Columbia; Nixon et al., 1993; Mihalynuk et al., 2004; Fig. 9-1a-b). At ca. 186 Ma the model of Mihalynuk et al. (2004) predicts final collapse of the Slide Mountain ocean basin to the east, and the emplacement of the Quesnel terrane atop a pericratonic backstop. Accretion of the Quesnel terrane may have been driven by impingement of non-subductable Cache Creek terrane (Mihalynuk, written commun., 2010). Hence, subduction beneath the Quesnel terrane may have either ceased or slowed by the time parental shoshonitic melts were generated leading up to the pulse of shoshonitic magmatism at Lorraine. Although difficult to test in ancient arcs, slowing or cessation of the subducting slab due to collisional events may have promoted localised slab detachment beneath Lorraine (Fig. 9-1a), leading to partial melting of the subduction-modified mantle.

According to van de Zedde and Wortel (2001), shallow slab detachment can increase the temperature of the sub-arc mantle wedge by more than 500 °C due to asthenosphere upwelling, and thereby promote partial melting. Hence, the slab detachment model potentially provides a mechanism to invoke heating of the mantle wedge following and/or during the amalgamation of terranes, while maintaining the infiltration of slab-derived components that are required to explain the major element, trace element and isotopic composition of biotite pyroxenites at Lorraine (Fig. 9-1b). Following slab-detachment hot upwelling mantle infiltrated the sub-arc mantle wedge, and slab-derived hydrous fluids and melts were released from the downgoing slab (Fig. 9-1b). The release of slab-derived fluids and melts into the sub-arc mantle wedge caused metasomatisim of the mantle. The ultimate source of P (and Sr) could have come from subducted P-rich fish debris and carbonate-rich nano-fossils or other biogenic sources, which is also the proposed source of P- and Sr-enrichment in Fijian shoshonites and other arc rocks from the western Pacific (e.g., Leslie, 2004; Raos and Crawford, 2004). Fluids and melts released from the downgoing slab also promoted partial melting in the mantle. Partial melting in the mantle gen-

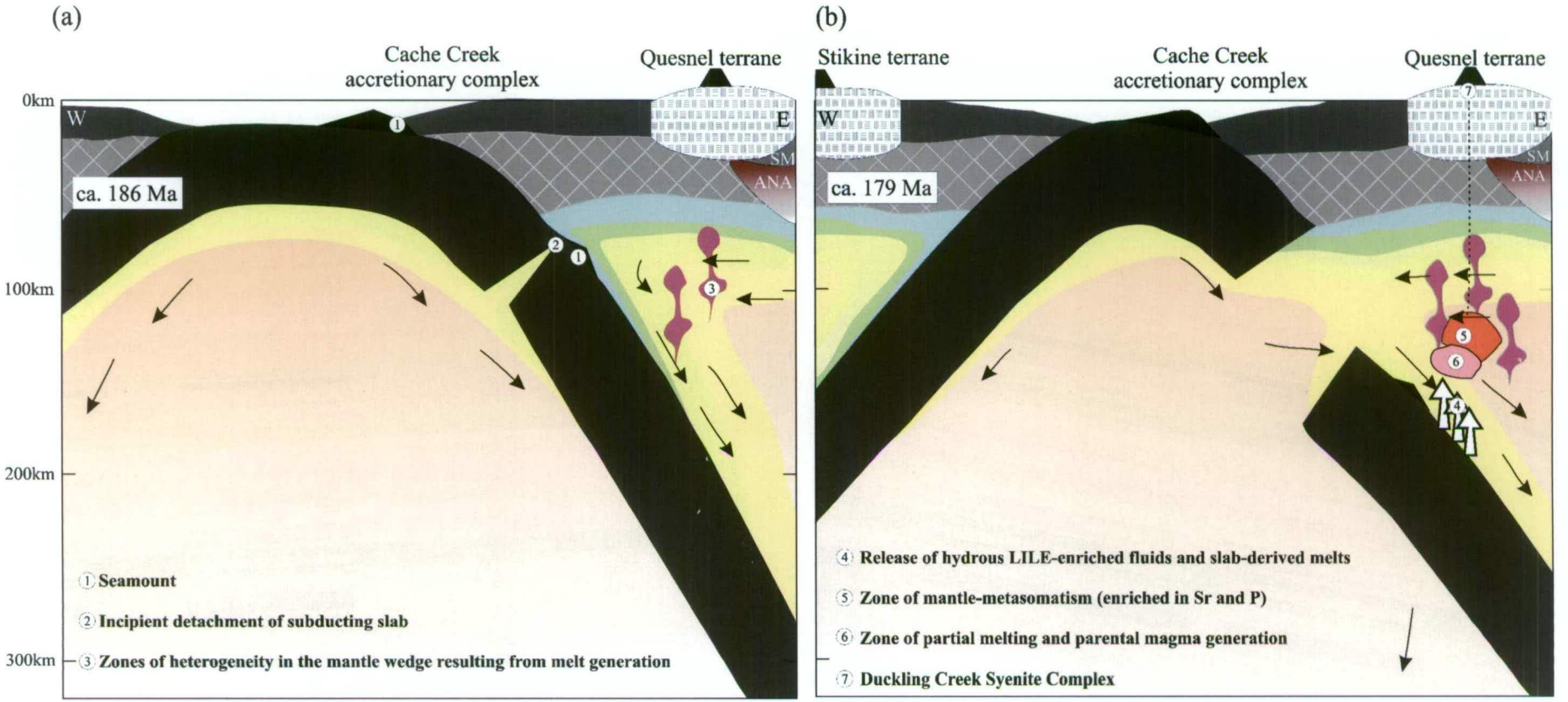

Figure 9-1. E-W schematic cross section of a proposed tectonic regime for the Quesnel, Cache Creek and Stikine terranes in the late Early Jurassic at (a) ca. 186 Ma and (b) ca. 179 Ma, illustrating the petrogenesis of shoshonitic magmatism in the Duckling Creek Syenite Complex. **(a)** Incipient detachment of the down-going slab, along with heterogeneities in the mantle wedge relating to earlier arc magmatism. **(b)** Hydrous fluids and slab-derived melts released from the downgoing slab, which subsequently metasomatised and generated partial melting in the mantle above the detached slab. Spatial and temporal concepts for the above model were inspired by Nixon et al. (1993), Mihalynuk et al. (1994a; 2004) and Ferri and Melville (1994). Note red areas represent relatively hot areas in the mantle, whereas green and blue represent relatively cooler areas. Modified for the Mesozoic Quesnel terrane from Raos (2001) and Monzier et al. (1997). Acronyms used include: ancestral North America = ANA, Slide Mountain terrane = SM.

erated ultrabasic magmas, which subsequently rose from the mantle into the upper crust in the Lorraine district.

An alternative mechanism for the generation of shoshonitic magmatism at Lorraine could be the onset of oblique subduction during amalgamation of terranes. A Tertiary analogue to this model is the shoshonitic magmatism of the Alkaline Volcanic Province in the Mariana arc, which formed at the northern termination of a propagating back-arc rift axis, inferred to have either provided unusually fertile sources or triggered an unusual process of melt generation (Stern et al., 1984; Sun and Stern, 2001). Additional features of the Alkaline Volcanic Province of the Mariana arc is the presence of the Ogasawara oceanic plateau colliding with the trench just to the north of the alkalic province, and the highly oblique subduction along the portion of the arc where the Alkaline Volcanic Province lies (Seno and Maruyama, 1984; Sun and Stern, 2001). Hence collision of oceanic plateaux within the Cache Creek terrane with the western margin of the Quesnel terrane could have produced localised highly oblique subduction, which inturn promoted shoshonitic arc magmatism beneath the Lorraine part of the arc. Other factors such as post-arc extention, decompression melting and upwelling of the subduction-metasomatised asthenosphere could have also contributed to the generation of shoshonitic magmatism (e.g., Luhr, 1997; Paquette et al., 2003; Richards, 2009).

The occurrence of felsic intrusives at Lorraine, such as syenite and monzonite dykes and stocks, could have formed by fractionation of ultrabasic or mafic magmas in larger magma chambers in the crust at depth. Alternatively, some authors (e.g., Sintron and Detrick, 1992; Marsh, 1995, 1998; Danyushevsky et al., 2002; Leslie, 2004) have advocated that mafic magmas can pass through a complex sequence of interconnected chambers with well-developed mush columns at depth which allows fractionation en route (Fig. 9-2). The mush columns are considered to contain crystals and residual melts that were left behind by passing magma batches. Also, current data sets suggest that anatexis melting of crustal rocks cannot be ruled out for the generation of felsic rocks at Lorraine. However, if anatexis melting is invoked then the radiogenic isotopic composition of the source rocks would have $^{87}Sr/^{86}Sr$ of approximately 0.7037 and εNd of approximately +5.3. These values are not distinctly different to ultrabasic rocks at Lorraine. Hence, if anatexsis melting is invoked then there is no evidence for the melting of older crustal rocks with evolved isotopic signatures for the generation of monzonites.

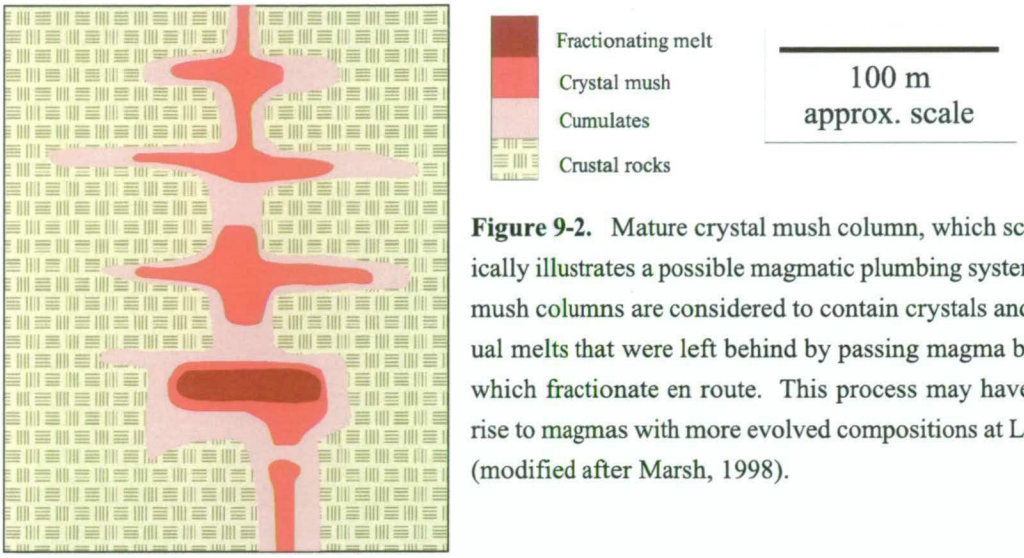

Figure 9-2. Mature crystal mush column, which schematically illustrates a possible magmatic plumbing system. The mush columns are considered to contain crystals and residual melts that were left behind by passing magma batches, which fractionate en route. This process may have given rise to magmas with more evolved compositions at Lorraine (modified after Marsh, 1998).

9.3. Deposit-scale geology, mineralisation and alteration

Lorraine's Lower Main Zone is hosted by a magmatic complex within the Duckling Creek Syenite Complex, which comprises three main phases (e.g., Devine et al. 2007):

- Phase 1: moderately southward dipping biotite pyroxenite and syenite dykes.
- Phase 2: steeply dipping biotite pyroxenite and syenite dykes, and monzonite dykes and stocks.
- Phase 3: leucosyenite and coarse grained K-feldspar syenite dykes.

Mineralisation in the Lower Main Zone is hosted by Phase 1 dykes, and is associated with magnetite and diopside alteration and K-silicate alteration. Alteration patterns, copper grade contours and sulphide zonation patterns dip moderately to the south and are sub-parallel to the dip of Phase 1 dykes. Thus it is inferred that Phase 1 dykes were the focus on mineralisation, and the dykes and ore zones were tilted soon after their formation. The concept of tilted zones was earlier proposed by Teck Ltd geologists (e.g., Devine et al., 2007) and Sillitoe (2007) based on the orientation of dykes in the Lorraine district and the occurrence of a tilted sulphide zonation pattern in the Bishop Zone.

Paragenetic reconstructions in this study have revealed early-, transitional- and late-stages of alteration in the Lower Main Zone. Early alteration consists of (1) high temperature (~550 °C) pervasive, fine-grained F-rich biotite and K-feldspar alteration, (2) localised very high temperature (i.e. ~ 780 °C) magnetite-diopside veins and patches, and (3) localised coarse-grained K-feldspar ± biotite veins or patches that include or have selvages of Cu-Fe sulphides.

Transitional-stage alteration consists of inner K-feldspar alteration of syenites and fine-grained K-feldspar biotite rocks, and fine-grained disseminated sulphides associated with fine-grained patches of albite, clinozoisite, titanite, sericite, chlorite, fluorite, quartz (trace), garnet (trace) and/or magnetite. Inner-zone transitional-stage alteration also includes fine-grained disseminated Cu-Fe sulphides in biotite pyroxenites. Copper-Fe sulphides in biotite pyroxenite form corroded contacts with diopside, with actinolite along diopside margins in contact with Cu-Fe sulphides, and titanite along biotite margins in contact with Cu-Fe sulphides. The replacement of diopside with actinolite implies temperatures <550 °C (at <3 kbar pressure) during hydrothermal alteration (e.g., Deer et al., 1992, p.244). The above transitional-stage alteration assemblages account for most of the mineralisation in the Lower Main Zone. Late alteration assemblages are generally Cu-Fe sulphide poor.

9.3.1. Replacement textures and implications for ore-forming processes

The current study shows petrographic evidence of disequilibrium textures between biotite and diopside with assemblages of sulphides, actinolite, titanite, albite, clinozoisite and magnetite. Thus, I propose that Fe^{2+} derived from predominantly primary igneous ferromagnesian minerals was an important reactant for the deposition of Cu-Fe sulphides in the Lower Main Zone.

A balanced chemical equation (9.1) shows how biotite and sulphate can react to form chalcopyrite and K-feldspar. Equation (9.1) suggests 2 moles of biotite are required to form 1 mole of chalcopyrite. Equation (9.1) predicts Fe^{2+} from biotite is oxidised to Fe^{3+} during the reduction of S^{6+} to S^{2-}. Equation (9.1) also shows consumption of H^+ ions during the replacement of biotite by chalcopyrite, suggesting the alteration drove the fluids to a higher pH consistent with the feldspar-pyroxene alteration assemblages observed at Lorraine.

$$\text{Biotite} + SO_4^{2-} + 6\tfrac{1}{2}\,H^+ + \tfrac{1}{2}\,CuCl_{2\,(aq)}^- + 4\,Cl^-_{(aq)} =$$

$$\tfrac{1}{2}\,\text{Chalcopyrite} + \text{K-feldspar} + 2\tfrac{1}{2}\,MgCl_{2\,(aq)} + 4\tfrac{1}{4}\,H_2O + \tfrac{15}{8}\,O_2 \quad (9.1)$$

The hypothesis of an oxidised sulphate-predomant, transitional-stage fluid within the Lower Main Zone is supported by the presence of coarse-grained S-rich apatite in mineralised biotite pyroxenite (i.e. apatite contains up to 1.1 wt. % SO_3), hematite dusting of feldspar in mineralised syenite, and the negative $\delta^{34}S$ (‰) values reported for bornite and chalcopyrite by Deyell and Tosdal (2005), which has been inferred to have formed as a result of S-isotope sulphate-sulphide fractionation under oxidising conditions (Rye, 1993; Wilson et al., 2007).

9.3.2. Chemical composition of mineral phases in unaltered and altered rocks

Deposit-scale mapping and core logging have shown that both altered and unaltered biotite pyroxenites dykes occur in the Lower Main and Bishop zones (Sillitoe, 2007; *this* study), with altered Phase 1 biotite pyroxenites cross-cut by unaltered biotite pyroxenite. The current study has compared the chemical compositions of minerals in altered biotite pyroxenite to those from unaltered biotite pyroxenite to assess the effects of mineralisation and alteration. Results of the comparison revealed that:

- Biotites from altered biotite pyroxenites have lower *mg*-numbers, lower abundances of Si and F, and contain more abundant Al, Ti, Fe^{3+} (calculated) and Mn than biotite from unaltered biotite pyroxenite. The composition of biotites in altered biotite pyroxenites resemble the biotites in altered syenite and unaltered monzonites.

- Diopsides in altered biotite pyroxenites have irregular-shaped outer zones with lower *mg*-number compared to cores and to diopsides from unaltered biotite pyroxenites. These have been inferred to represent metasomatised margins.

- Apatites from altered biotite pyroxenites have outer zones with higher abundances of S compared to apatites from unaltered biotite pyroxenites. The S content of apatite from altered biotite pyroxenite is similar to hydrothermal apatite from high-grade mineralised zones at Mount Polley.

- Magnetites from altered biotite pyroxenites are V-rich but Cr-poor compared to magnetite from unaltered biotite pyroxenites. The V and Cr compositions of magnetite from altered biotite pyroxenite are similar to these in hydrothermal magnetite from alkalic porphyry deposits in New South Wales.

It has been inferred that the trend towards lower *mg*-numbers in biotite and irregular-shaped outer zones of diopside from altered biotite pyroxenite reflect re-equilibration of biotite and diopside with a fluid derived from a monzonite or syenite source. The fluid source is inferred to have delivered Cu and S to the wall rocks. An inferred higher activity of S^{6+} during mineralisation is supported by the relatively high S content of medium-grained apatite and of apatite outer zones in mineralised biotite pyroxenite.

9.3.3. Isotopic composition of hydrothermal fluids

$\delta^{18}O$ and δD values measured from different generations of biotite have been used to calculate the $\delta^{18}O$ and δD values of fluids. The data indicate that fluids in equilibrium with

biotite from fresh, unaltered biotite pyroxenite plot within the magmatic field of Taylor (1979) and Ohmoto (1986). The data also shows that early fluorine-rich biotite from fine-grained K-feldspar biotite rocks, early biotite in syenite and early coarse-grained biotite in mineralised biotite pyroxenite were in equilibrium with a fluid with isotopic compositions consistent with magmatic, metamorphic or high temperature porphyry environments (Sheppard et al., 1971; Taylor, 1979; Ohmoto, 1986; Dilles et al., 1992). The hypothesis that regional high temperature metamorphism (i.e., amphibolite-grade) resulted in localised early biotite and mineralisation within the Lower Main Zone is at odds with the prehnite-pumpellyite to lower greenschist grades, which are characteristic of the Quesnel terrane in the Hogem district (e.g., Ferri and Melville, 1994; Nelson and Bellefontaine, 1996; Schiarizza and Tan, 2005). Alternatively, the hypothesis of a magmatic-hydrothermal fluid source is consistent with the close timing of alteration and mineralisation relative to the emplacement of syenite dykes in the Lower Main Zone.

9.3.4. Temperature of equilibrium for host rock and alteration assemblages

Temperature constraints for unaltered rocks from Lorraine rocks have been estimated using major element and isotopic composition of mineral pairs. Calculations indicate that:

- Diopside-magnetite pairs in unaltered biotite pyroxenite equilibrated at ~720 °C (oxygen isotopes; Table 8-3).

- Biotite-apatite pairs in unaltered biotite pyroxenite equilibrated at ~600 °C (F-OH exchange; Fig. 6-28a).

- Feldspar pairs in monzonite between ~350 and 850 °C (two-feldspar solvus; Fig. 6-29).

Hence, it is inferred that the above mineral pairs in unaltered rocks equilibrated at sub-solidus temperatures during the slow cooling of the host intrusives. Alternatively, temperature constraints of altered rocks include:

- Early alteration F-rich biotite alteration occurred at ~550 °C in fine-grained K-feldspar biotite rock (OH-F exchange for apatite-biotite pairs and phlogopite mole fraction in biotite; Fig. 6-28a, b).

- Early alteration magnetite-diopside patches equilibrated at ~780 °C (oxygen isotopes; Table 8-3).

- Biotite-apatite pairs in altered biotite pyroxenites equilibrated at ~570 °C (OH-F exchange; Fig. 6-28a).

- Feldspar pairs in altered syenite ~380 and 500 °C (two-feldspar solvus; Fig. 6-29).

Early potassic and magnetite-diopside alteration is inferred to have occurred at high temperatures. The average temperature of apatite-biotite pairs in altered biotite pyroxenite (570 °C) is similar to temperature estimates from apatite-biotite pairs in unaltered biotite pyroxenite (600 °C). This suggests that either mineralisation occurred at temperatures ~570 °C and/or that lower temperature fluids did not significantly affect the F-OH system of biotite and apatite in biotite pyroxenites during subsequent mineralisation and alteration. A minimum temperature estimate of mineralisation is provided by the feldspar pairs in altered syenite of 380 to 500 °C (Fig. 6-29). The temperature range in altered rocks appears to be consistent with moderate to high temperature conditions for porphyry-Cu deposits reported elsewhere (e.g., Beane, 1974; Carten et al., 1988).

9.3.5. The role of ultrabasic magmas in porphyry formation at Lorraine

The current study found that most unaltered biotite pyroxenites have low concentrations of Cu when compared to western Pacific shoshonites, Nicola Group shoshonites and alkaline mafic intrusives from the Bingham porphyry Cu-Au deposit. Alternatively however some unaltered Phase 2 biotite pyroxenites from the Lower Main and Bishop zones have higher Cu concentrations that are comparable to Fijian shoshonites, Nicola Group shoshonites and alkaline mafic intrusive rocks from Bingham (Fig. 7-17). These Cu-enriched unaltered biotite pyroxenites may have crystallised from a relatively Cu-rich mafic magma source compared to the Cu-poor biotite pyroxenites. Alternatively, Keith et al. (1998) noted that generally <1 % of magmatic sulphides are preserved in slowly cooled intrusives or lavas, and hence, Cu-depleted biotite pyroxenites may have initially had higher concentrations of Cu, and subsequently lost Cu during cooling.

Diopside from unaltered biotite pyroxenites (and altered biotite pyroxenites) also contain mostly low concentrations of Cu compared to diopside from Fijian shoshonites and Nicola Group shoshonites (Fig. 6-13). In addition, diopside from Fijian and the Nicola Group shoshonites show an increase in the concentration of Cu with decreasing *mg*-number, which may reflect an increase in the activity of Cu in the melt during fractionation of these rocks (A.J. Crawford, pers. comm., 2009). In contrast, diopsides in unaltered biotite pyroxenite do not show an increase in Cu with a decrease in *mg*-number. This may reflect either: (1) a low activity of Cu in the melt during the crystallisation of diopside; or (2) a loss of Cu from diopside during slow cooling.

Thus, based on the current data set there appears to be very little evidence to support the contention that biotite pyroxenites at Lorraine crystallised from alkaline mafic magmas that were anomalously enriched in Cu; however these magmas may have lost copper during slow cooling. Alternatively, some ultrabasic magmas may have been enriched in Cu compared to others. If so, then Cu-enriched ultrabasic magmas may have potentially introduced metals and other volatiles into felsic magma chambers at depth prior to the formation of the Lorraine porphyry Cu-Au deposit. This model has been proposed for the formation of the giant Bingham porphyry Cu-Au deposits (Keith et al., 1997; Keith et al., 1998) and the Northparkes alkalic porphyry Cu-Au deposit, NSW (Lickfold et al., 2007).

9.4. Timeline for the genesis of the Lower Main Zone

The Lorraine Lower Main Zone porphyry-Cu deposit formed in an active magmatic complex over a geologically short time frame. Radiogenic isotopic signatures of ultrabasic rocks, and age determinations of syenites have enabled constraints on the source of ultrabasic and felsic magmas and the timing of magmatism and mineralisation.

- **~186 Ma**, Accretion of the Quesnel terrane against the western margin of ancestral North America/Pericratonic belt (e.g., Nixon et al. 1993).
- **182.6 ± 3.2 Ma**, Emplacement of the oldest known syenite in the Lower Main Zone (Phase 1), and the first known event of shoshonitic magmatism in the Duckling Creek Syenite Complex.
- **178.8 to 178.4 Ma**, Pulse of ultrabasic to felsic shoshonitic magmatism in the Lower Main Zone (Phase 1), Cu-Au mineralisation, tilting of the Lower Main Zone and post-tilting shoshonitic ultrabasic to felsic magmatism (Phase 2).
- **~177 Ma**, Emplacement of late sub-alkaline to alkaline quartz-bearing leucosyenite dykes and coarse K-feldspar dykes.

9.5. Conclusions

The Lower Main Zone of the Lorraine porphyry Cu-Au deposit occurs in the Quesnel terrane (island arc) in north-central British Columbia, and mineralisation formed during a period of ultrabasic to felsic shoshonitic magmatism sometime between 178.8 and 178.4 Ma. This period of shoshonitic magmatism post-dates the accretion of Quesnel terrane with ancestral North America by ~7 million years (i.e. accretion occurred at ca. 186 Ma; Nixon et al., 1993; Mihalynuk et al., 1994a; Mihalynuk et al., 2004). Collision between

Quesnel and ancestral North America at ca. 186 Ma. It is proposed in the present study that the impingement of non-subductable Cache Creek terrane along the western side of the Quesnel arc (e.g., Mihalynuk, written commun., 2010; Fig. 9-1a) may have either initiated slab-detachment or oblique subduction. The collision event is inferred to have led to shoshonitic magmatism at Lorraine by ca. 179 Ma.

The Lower Main Zone comprises Phase 1 biotite pyroxenite and syenite dykes. These dykes are tilted and pre-date mineralisation. Phase 1 dykes are cut by steeply dipping Phase 2 (post-mineralisation) biotite pyroxenite, syenite and monzonite dykes and Phase 3 (late) leucosyenite and coarse K-feldspar dykes. The absolute timing of mineralisation and tilting has been constrained to between 178.8 and 178.4 Ma, implying that the Lower Main Zone formed within an active magmatic complex over a relatively short geological time frame, consistent with modern concepts on porphyry formation (e.g., Arribas et al., 1995).

Major and trace element geochemistry and isotopic composition of biotite pyroxenite from the Lorraine deposit have arc signatures. In particular, unaltered biotite pyroxenites, syenites and monzonites are depleted in high field strength elements in comparison with rare earth elements, are enriched in large ion lithophile elements and P in comparison with rare earth elements and have $^{87}Sr/^{86}Sr$ (avg. = 0.7036), εNd (+4.7 to +5.3) and stable isotope $\delta^{18}O$ (diopside = 5.89) compositions that are similar to post-collisional arc-related shoshonites from the Mariana arc and Fiji. The slightly evolved isotopic signature of Lorraine shoshonites may be explained by the contribution of slab-derived fluids and slab-derived melts into the sub-arc mantle wedge. More specifically, high P and Sr in Lorraine shoshonites may be related to the melting of slab-derived carbonate- and phosphorous-rich sediments in the mantle.

Alteration in the Lower Main Zone is defined by early-, transitional- and late-stage assemblages. Early-stage alteration is characterised by: (1) pervasive and texturally destructive fine-grained F-rich biotite and K-feldspar alteration; (2) veins and patches of magentite-diopside ± albite and/or Cu-Fe sulphides; (3) early coarse-grained K-feldspar-biotite veins that are associated with chalcopyrite and bornite mineralisation. Transitional-stage mineralisation is characterised by K-feldspar (hematite dusted) alteration of syenites. K-feldspar altered syenites commonly contain fine-grained disseminated sulphides, disposed predominatly along the margins of fine-grained biotite, diopside or in fine-grained anhedral patches of albite and clinozoisite. In addition, transitional-stage alteration also produced fine-grained dissminated sulphides and localised net-textured sulphides. Primary magmatic diopside in mineralised biotite pyroxenite have actinolite-altered margins, and sulphides include relicts of biotite and diopside, inferring that sulphides have replaced primary igneous biotite and diopside. Transitional-stage mineralisation also produced a por-

phyry-style sulphide zonation pattern, in the Bishop and Main zones (Sillitoe, 2007). The sulphide zonation pattern overprint a variety of rocks types, including biotite pyroxenites, fine-grained K-feldspar biotite rocks and syenite. Late-stage alteration assemblages are characterised by: (1) localised albite-diopside vein-veinlets and patches; (2) localised selective alteration of diopside and plagioclase by epidote; (3) planar coarse-grained K-feldspar ± biotite vein-veinlet sets; (4) quartz ± pyrite-chalcopyrite veins -veinlets and (5) localised selective-pervasive muscovite-carbonate-pyrite alteration of biotite in Phase 3 coarse-grained K-feldspar syenite dykes.

The Lower Main Zone has a sulphide zonation pattern comparable to other alkalic porphyry deposits in British Columbia; however mineralisation produced finely disseminated Cu-Fe sulphides in fine-grained K-feldspar biotite rock, biotite pyroxenite and syenites. Features such as stockwork veining and breccias, which are common in most porphyry deposits (e.g., Gustafson and Hunt, 1975; Titley and Beane, 1981; Titley, 1982; Enns et al., 1995; Fraser et al., 1995; Frei, 1995; Schroeter, 1995; Hedenquist and Arribas, 1998; Sillitoe, 2000; Cannell et al., 2005; Seedorff et al., 2005; Logan and Mihalynuk, 2005a, b; Audetat and Pettke, 2006; Byrne et al., 2008; Jago, 2008; Pass et al., in prep.), are not well developed at Lorraine. There is textural evidence that biotite in the fine-grained K-feldspar biotite rock and biotite pyroxenite has been replaced by Cu-Fe sulphides. The replacement of biotite by Cu-Fe sulphides has also been identified in the Central Replacement Zone at Galore Creek (e.g., Micko et al., 2008; Fig. 5-28a-d), and this appears to be the closest analogue to mineralisation observed in the Lower Main Zone at Lorraine.

Hence the Lower Main Zone formed in a magmatic complex, and has alteration and sulphide zonation patterns that are consistent with porphyry formation. Mineralisation textures in the Lower Main Zone allow Lorraine to be classified as a replacement-style alkalic Cu-Au-Ag ± PGE porphyry deposit.

9.6. Recommendations for further study

9.6.1. Shoshonitic rocks of the Quesnel terrane

Shoshonitic vs. calc-alkaline rocks: The current study has shown that the Lower Main Zone Lorraine porphyry-Cu deposit formed in an active shoshonitic magmatic complex. These melts are inferred to have formed from mixing between slab-derived components and a mantle source; however a comparison of the trace element and isotopic composition of Duckling Creek shoshonites has not been carried out on older calc-alkaline rocks in the Hogem district (e.g., Hogem granodiorite). This comparison could be used test if the source of shoshonitic magmas had a stronger signature of slab-derived components than

calc-alkaline rocks in the district. Hence a comparative study of the major element, trace element and Pb-, Sr- Nd- and O-isotope values of the Hogem calc-alkaline and shoshonite rocks would be useful to further test this model and to understand the evolution of arc-related rocks in Hogem district.

Distict-scale structural studies: What are the limits of tilting in the Duckling Creek Syenite Complex? Does tilting just affect the Duckling Creek Syenite Complex or the entire Hogem Batholith. Are there discrete fault bound structural domains in the Hogem Batholith?

9.6.2. Lower Main Zone, Lorraine porphyry-Cu deposit

Future drilling and deposit-scale 3D modeling: Further drilling, combined with 3D modeling would be useful to constrain the distribution of mineralisation in the Lower Main Zone. In particular, there is the potential to extend the area of known mineralised zones via deeper drilling in the southern area of the Lower Main Zone, as mineralisation has not been closed off at depth in this area. Additional drilling could also be conducted in the central area of the Lower Main Zone around the F-rich, fine-grained K-feldspar biotite rock.

Detailed deposit-scale structural geology: The absence of orientated drill core in the Lower Main Zone has limited the investigation of the solid-state deformation fabric(s) and prevents any correlations with surface exposures. If a future drilling program enables *in situ* measurements of structural features, then further work could be conducted to define the evolving stress conditions during porphyry emplacement, and to constrain any significant local structural controls on mineralisation or post-mineral structures which displace mineralisation.

REFERENCES CITED

Abdel-Rahman, A. M., 1994, Nature of biotites from alkaline, calc-alkaline, and peraluminous magmas: Journal of Petrography, v. 35, p. 525-541.

Akinfiev, N.N., and Diamond, L.W., 2009, A simple predictive model of quartz solubility in water-salt-CO_2 systems at temperatures up to 1000 degrees C and pressures up to 1000 MPa: Geochimica et Cosmochimica Acta, v. 73, p. 1597-1608.

Aksyuk, A.M., 2000, Estimation of fluorine concentrations in fluids of mineralized skarn systems: Economic Geology and the Bulletin of the Society of Economic Geologists, v. 95, p. 1339-1347.

Aksyuk, A.M., 2002, Experimentally established geofluorimeters and the fluorine regime in granite-related fluids: Petrology, v. 10, p. 557-569.

Anthony, E. Y., and Titley, S. R., 1994, Patterns of element mobility during hydrothermal alteration of the Sierrita porphyry copper deposit, Arizona: Economic Geology, v. 89, p. 186-192.

Arif, J., and Baker, T., 2004, Gold paragenesis and chemistry at Batu Hijau, Indonesia: implications for gold-rich porphyry copper deposits: Mineralium Deposita, v. 39, p. 523-535.

Arribas, A., Hedenquist, J. W., Itaya, T., Okada, T., Concepcion, R. A., and Garcia, J. S., 1995, Contemporaneous formation of adjacent porphyry and epithermal Cu-Au deposits over 300 ka in Northern Luzon, Philipines: Geology, v. 23, p. 337-340.

Audetat, A., Pettke, T., Dolejs, D., and Bodnar, R., 2002, Magmatic anhydrite in the Cu-porphyry-related magma at Santa Rita, New Mexico (USA): Geochimica et Cosmochimica Acta, v. 66, p. A37-A37.

Audetat, A., and Pettke, T., 2006, Evolution of a porphyry-Cu mineralized magma system at Santa Rita, New Mexico (USA): Journal of Petrology, v. 47, p. 2021-2046.

Ayati, F., Yavuz, F., Noghreyan, M., Haroni, H.A., and Yavuz, R., 2008, Chemical characteristics and composition of hydrothermal biotite from the Dalli porphyry copper prospect, Arak, central province of Iran: Mineralogy and Petrology, v. 94, p. 107-122.

Azimov, P.Y., and Bushmin, S.A., 2007, Solubility of minerals of metamorphic and metasomatic rocks in hydrothermal solutions of varying acidity: thermodynamic modeling at 400-800°C and 1-5 kbar: Geochemistry International, v. 45, p. 1210-1234.

Bailey, J.C., 1977, Fluorine in granitic rocks and melts - review: Chemical Geology, v. 19, p. 1-42.

Baker, T., Ash, C. H., and Thompson, J. F. H., 1997, Geological setting and characteristics of the Red Chris porphyry copper-gold deposit, northwestern British Columbia: Exploration and Mining Geology, v. 6, p. 297-316.

Banks, N. G., 1982, Sulfur and Copper in Magma and Rocks, *in* Titley, S. R., ed., Advances in Geology of the Porphyry Copper Deposits: Southwestern North America, The University of Arizona Press, p. 227-257.

Barley, M. E., Rak, P., and Wyman, D., 2002, Tectonic controls on magmatic-hydrothermal gold mineralization in the magmatic arcs of SE asia: Geological Society of London Special Publication, v. 204, p. 39-47.

Barrie, T. C., 1993, Petrochemistry of shoshonitic rocks associated with porphyry copper-gold deposits of central Quesnellia, British Columbia, Canada: Journal of Geochemical Exploration, v. 48, p. 225-258.

Barsdell, M., 1988, Petrology and petrogenesis of clinopyroxene-rich tholeiitic lavas, Merelava Volcano, Vanuatu: Journal of Petrology, v. 29, p. 927-964.

Barsdell, M., and Berry, R. F., 1990, Origin and evolution of primitive island arc ankaramites from western Epi, Vanuatu: Contributions to Mineralogy and Petrology, v. 81, p. 148-155.

Bateman, R., Busacca, A. J., and Sawka, N. W., 1983, Cretaceous deformation in the western foothills of the Sierra Nevada, California: Bulletin of the Geological Society of America, v. 94, p. 30-42.

Bath, A., and Cooke, D., 2008, The importance of biotite for the deposition of sulfides at the Lower Main Zone, Lorraine Cu-Au porphyry deposit, north-central British Columbia, Shallow- and Deep-Level Alkalic Mineral Deposits: Developing an Integrated Exploration Model; Year 3 - Porphyry Module Final Update to Project Sponsors, Mineral Deposit Research Unit (UBC) and CODES Centre of Excellence in Ore Deposits (Utas), Unpub. Report, p. 7.1-7.9.

Bath, A. B., Logan, J. M., and Kamenetsky, V. S., 2006, Apatite in Cu-sulfide ore from the Mount Polley alkalic porphyry, BC Canada: Geochimica et Cosmochimica Acta, v. 70, p. A40-A40.

Baxter, P., and Devine, F., 2007, Report on the 2006 Airborne Radiometric, Geological Mapping, Geochemical Soil Sampling and Diamond Drilling Program. Lorraine-Jajay Property Omineca Mining Division, BC, Unpub. Report, Teck Cominco Limited, p. 58.

Beane, R. E., 1974, Biotite stability in porphyry copper environment: Economic Geology, v. 69, p. 241-256.

Beane, R. E., 1982, Hydrothermal alteration in silicate rocks; southwestern North America, *in* Titley, S. R., ed., Advances in geology of porphyry copper deposits; southwestern North America, University of Arizona Press, Tucson, AZ, United States (USA), p. 117-137.

Bishop, S. T., Heah, T. S., Stanley, C. R., and Lang, J. R., 1995, Alkalic intrusion hosted copper-gold mineralization at the Lorraine deposit, north-central British Columbia, *in* Schroeter, T. G., ed., Porphyry Deposits of the northwestern Cordillera of North America, Canadian Institute of Mining, Metallurgy and Petroleum: Vancouver, Canadian Institute of Mining, Metallurgy and Petroleum, Special Volume 46, p. 623-629.

Boari, E., Tommasini, S., Laurenzi, M. A., and Conticelli, S., 2009, Transition from Ultrapotassic Kamafugitic to Sub-alkaline Magmas: Sr, Nd, and Pb Isotope, Trace Element and Ar-40-Ar-39 Age Data from the Middle Latin Valley Volcanic Field, Roman Magmatic Province, Central Italy, 2009, p. 1327-1357.

Bodnar, R.J., 1995, Experimental-determination of the pvtx properties of aqueous-solutions at elevated-temperatures and pressures using synthetic fluid inclusions - H_2O-NaCl as an example: Pure and Applied Chemistry, v. 67, p. 873-880.

Boer, R. H., and Meyer, F. M., 1994, Stable isotopic evidence for crustal contamination and desulfuridation of the cuperiferous Koperberg Suite, Namaqualand, South Africa: Geochimica et Cosmochimica Acta, v. 58, p. 2677-2687.

Bottinga, Y., and Javoy, M., 1973, Comments on oxygen isotope geothermometry: Earth and Planetary Science Letters, v. 20, p. 250-265.

Bowen, N. L., 1928, The evolution of the igneous rocks, Princeton University Press (reprinted by Dover Publications, New York, 1956).

Brimhall, G. H., Jr., 1977, Early fracture-controlled disseminated mineralization at Butte, Montana: Economic Geology, v. 72, p. 37-59.

Brown, D. A., Logan, J. M., Gunning, M. H., Orchard, M. J., and Bamber, W. E., 1991, Stratigraphic Evolution of the Paleozoic Stikine Assemblage in the Stikine and Iskut Rivers Area, Northwestern British-Columbia: Canadian Journal of Earth Sciences, v. 28, p. 958-972.

Burnham, C.W., 1979, Magmas and hydrothermal fluids, in Barnes, H.L., ed., Geochemistry of hydrothermal ore deposits, 2nd Edition: New York, John Wiley and Sons, p. 71-136.

Byrne, K., Tosdal, R., and Chamberlain, C., 2008, Magmatic-hydrothermal evolution and zonation of a breccia-centered Cu-Au alkalic porphyry: Southwest Zone, Galore Creek, Shallow- and Deep-Level Alkalic Mineral Deposits: Developing an Integrated Exploration Model; Year 3 - Porphyry Module Final Update to Project Sponsors, Unpub. Report, Mineral Deposit Research Unit (UBC) and CODES Centre of Excellence in Ore Deposits (Utas), Unpub. Report, p. 7.1-7.9.

Bysouth, G. D., Campbell, K. V., Barker, G. E., and Gagnier, G. K., 1995, Tonalite-trondhjemite fractionation of peraluminous magma and the formation of syntectonic porphyry copper mineralization, Gibralter mine, central British Columbia, *in* Schroeter, T. G., ed., Porphyry Deposits of the Northwestern Cordillera of North America: Vancouver, Canadian Institute of Mining, Metallurgy and Petroleum, Special Volume 46, p. 201-213.

Candela, P.A., and Piccoli, P.M., 1995, Model ore-metal patitioning from melt into vapor and vapor/brine mixtures: Mineralogical Assocition of Canada Short Course, v. 23, p. 101-127.

Candela, P. A., and Piccoli, P. M., 2005, Magmatic Processes in the Development of Porphyry-Type Ore Systems, *in* Hedenquist, J. W., Thompson, J. F. H., Goldfarb, R. J., and Richards, J. P., eds., One Hundredth Anniversary Volume 1905-2005, Economic Geology, p. 25-37.

Cannell, J., Cooke, D. R., Walshe, J. L., and Stein, H., 2005, Geology, mineralization, alteration, and structural evolution of the El Teniente porphyry Cu-Mo deposit: Economic Geology, v. 100, p. 979-1003.

Carten, R. B., Geraghty, E. P., Walker, B. M., and Shannon, J. R., 1988, Cyclic development of igneous features and their relationship to high-temperature hydrothermal features in the Henderson porphyry molybdenum deposit, Colorado: Economic Geology, v. 83, p. 266-296.

Carter, N. L., and Tsenn, M. C., 1986, Flow properties of continental lithosphere: Tectonophysics, v. 136, p. 27-63.

Casselman, M. J., McMillan, W. J., and Newman, K. M., 1995, Highland Valley porphyry copper deposits near Kamloops, British Columbia: A review and update with emphasis on the Valley deposit, *in* Schroeter, T. G., ed., Porphyry Deposits of the Northwestern Cordillera of North America, Canadian Institute of Mining, Metallurgy and Petroleum, Special Volume 46, p. 161-191.

Cathelineau, M., 1988, The chlorite and illite geothermometers: Chemical Geology, v. 70, p. 182-182.

Cawthorn, R. G., and Meyer, F. M., 1993, Petrochemistry of the Okiep copper district basic intrusive bodies, northwestern Cape province, South Africa: Economic Geology, v. 88, p. 590-605.

Charoy, B., 1999, Beryllium speciation in evolved granitic magmas: phosphates versus silicates: European Journal of Mineralogy, v. 11, p. 135-148.

Chen, W. P., and Brudzinski, M. R., 2001, Evidence of a large-scale ramnant of subducted lithosphere beneath Fiji: Science, v. 292, p. 2475-2479.

Chiba, H., Chacko, T., Clayton, R. N., and Goldsmith, J. R., 1989, Oxygen isotope fractionation involving diopside, forsterite, magnetite, and calcite: Application to geothermometry: Geochimica et Cosmochimica Acta, v. 53, p. 2985-2995.

Cleverley, J. S., 2006, Using the chemistry of apatite to track fluids in Fe-oxide Cu-Au systems: 16th Annual V.M. Goldschmidt Conference, Melbourne, 2006, p. A105.

Cline, J. S., and Bodnar, R. J., 1991, Can Economic Porphyry Copper Mineralization Be Generated by a Typical Calc-Alkaline Melt: Journal of Geophysical Research-Solid Earth and Planets, v. 96, p. 8113-8126.

Cline, J. S., and Bodnar, R. J., 1994, Direct Evolution of Brine from a Crystallizing Silicic Melt at the Questa, New-Mexico, Molybdenum Deposit: Economic Geology and the Bulletin of the Society of Economic Geologists, v. 89, p. 1780-1802.

Cooke, D. R., Hollings, P., and Walsh, J. L., 2005, Giant porphyry deposits: Characteristics, distribution, and tectonic controls: Economic Geology, v. 100, p. 801-818.

Cooke, D. R., Wilson, A. J., House, M. J., Wolfe, R. C., Walsh, J. L., Lickfold, V., and Crawford, A. J., 2007, Alkalic porphyry Au-Cu and associated mineral deposits of the Ordovician to Early Silurian Macquarie Arc, New South Wales: Australian Journal of Earth Sciences, v. 54, p. 445-463.

Coulson, I. M., Russell, J. K., and Dipple, G. M., 1999, Origins of the Zippa Mountain pluton: a late triassic, arc-derived, ultrapotassic magma from the Canadian Cordillera: Canadian Journal of Earth Sciences, v. 36, p. 1415-1434.

Coulson, I.M., Dipple, G.M., and Raudsepp, M., 2001, Evolution of HF and HCl activity in magmatic volatiles of the gold-mineralized Emerald Lake pluton, Yukon Territory, Canada: Mineralium Deposita, v. 36, p. 594-606.

Coulson, I. M., Westphal, M., Anderson, R. G., and Kyser, T. K., 2007, Concomitant skarn and syenitic magma evolution at the margins of the Zippa Mountain pluton: Mineralogy and Petrology, v. 90, p. 199-221.

Crawford, A. J., Greene, H. G., and Exon, N. F., 1988, Geology, petrology and geochemistry of submarine volcanoes around Epi Island, New Hebrides island arc, *in* Greene, H. G., and Wong, F. L., eds., Geology and offshore resources of Pacific island arcs: Vanuatu region, 8, Circum-Pacific Council for Energy and Mineral Resources, Earth Science Series, p. 301-327.

Cross, A. J., 2000, An Investigation of the Minor and Trace Element Chemistry of Hydrothermal Porphyry- and Skarn-Related Magnetite: Unpub. M.Sc thesis, University of Canberra, 171 p.

Danyushevsky, L. V., Sobolev, A. V., and Falloon, T. J., 2002, Melt inclusions in olivine phenocrysts; using diffusive re-equilibration to determine the cooling history of a crystal, with implications for the origin of olivine-phyric volcanic rocks: Journal of Petrology, v. 43, p. 1651-1671.

Deer, W. A., Howie, R. A., and Zussman, J., 1978, Single-Chain Silicates, Longman, 668 p.

Deer, W. A., Howie, R. A., and Zussman, J., 1992, An Introduction to the Rock-Forming Minerals. 2nd Edition, Longman, 696 p.

Deer, W. A., Howie, R. A., and Zussman, J., 2003, Micas, The Geological Society of London, 758 p.

Delong, R. C., 1996, Geology, alteration, mineralization and metal zonation of the Mt. Milligan porphyry copper-gold deposits: Unpub. M.Sc. thesis, University of British Columbia, 196 p.

Devine, F., Chamberlain, C., Baxter, P., Davies, A. G. S., Jago, C. P., and Henry, C. D., 2007, Geological map of the Lorraine Area: Including the Main zone, Lower Main zone, Bishop zone, Ekland Ridge and extensions, Teck Cominco Ltd, Unpub. Map.

Deyell, C. L., and Tosdal, R. M., 2005, Alkalic Cu-Au deposits of British Columbia: sulfide isotope zonation as a guide to mineral exploration Geological Fieldwork 2004, BC Ministry of Energy, Mines and Petroleum Resources, Paper 2005-1, p. 191-208.

Dilles, J. H., Solomon, G. C., Taylor, H. P., and Einaudi, M. T., 1992, Oxygen and hydrogen isotope characteristics of hydrothermal alteration at the Ann-Mason porphyry copper deposit, Yerington, Nevada: Economic Geology, v. 87, p. 44-63.

Dilles, J. H., Einaudi, M. T., Proffett, J. M., and Barton, M. D., 2000, Overview of the Yerington porphyry copper district: Magmatic to nonmagmatic sources of hydrothermal fluids: Their flow paths and alteration effects on rocks and Cu-Mo-Fe-Au ores: Society of Economic Geologists Guidebook Series, v. 32, p. 55-66.

Eadie, E. T., 1976, K-Ar and Rb-Sr geochronology of the northern Hogem Batholith, B.C. : Unpub. B.Sc. thesis, The University of British Columbia, 46 p.

Eggins, S. M., 1993, Origin and differentiation of picritic arc magmas, Ambae (Aoba), Vanuatu: Contributions to Mineralogy and Petrology, v. 114, p. 79-100.

Eggleton, R. A., and Buseck, P. R., 1980, The orthoclase-microcline inversion: a high-resolution tranmission electron microscope study and strain analysis: Contributions to Mineralogy and Petrology, v. 74, p. 123-133.

English, J. M., Mihalynuk, M. G., Johnston, S. T., and Devine, F. A. M., 2002, Atlin TGI Part III: Geology and petrochemistry of the mafic rocks within the northern Cache Creek terrane and tectonic implications, Geological Fieldwork 2001 Paper 2002-1: Ministry of Energy and Mines, Victoria BC, p. 19-30.

English, J. M., Mihalynuk, M. G., and Johnston, S. T., 2010, Geochemistry of the northern Cache Creek terrane and implications for accretionary processes in the Canadian Cordillera: Canadian Journal of Earth Sciences, v. 47, p. 1-22.

Enns, S. G., Thompson, A. J. B., Stanley, C. R., and Yarrow, E. W., 1995, The Galore Creek porphyry copper-gold deposits, northwestern British Columbia, *in* Schroeter, T. G., ed., Porphyry deposits of the Northwestern Cordillera of North America, Quebec, Canadian Institute of Mining, Metallurgy and Petroleum Special Volume 46, p. 609-622.

Erdmer, P., Ghent, E. D., Archibald, D. A., and Stout, M. Z., 1998, Paleozoic and Mesozoic high-pressure metamorphism at the margin of ancestral North America in central Yukon: Geological Society of America Bulletin, v. 110, p. 615-629.

Eugster, H.P., 1985, Granites and hydrothermal ore-deposits - a geochemical framework: Mineralogical Magazine, v. 49, p. 7-23.

Evans, A. M., 1993, Ore Geology and Industrial Minerals; an introduction, Oxford: Blackwell Science, 389 p.

Evenchick, C. A., McNicoll, V. J., and Snyder, L. D., 2004, Stratigraphy, geochronology, and geochemistry of the Georgie River area, northwest British Columbia, and implications for mineral exploration: Canadian Journal of Earth Sciences, v. 41, p. 199-216.

Fedele, L., Zanetti, A., Morra, V., Lustrino, M., Melluso, L., and Vannucci, R., 2009, Clinopyroxene/liquid trace element partitioning in natural trachyte-trachyphonolite systems: insights from Campi Flegrei (southern Italy): Contibutions to Mineralogy and Petrology, v. 158, p. 337-356.

Ferri, F., Dudka, S., and Rees, C., 1992, Geology of the Uslika Lake area, northern Quesnel Trough, B.C. (94 C/3, 4 and 5). *In* Geological fieldwork 1991: British Columbia Ministry of Energy, Mines and Petroleum Resources, Paper 1992-1, p. 127-146.

Ferri, F., Dudka, S., Rees, C., and Meldrum, D. G., 1993, Geology of the Aiken Lake and Oslinka River areas, Northern Quesnel Trough (94 C/2,3,5,6 and 12). *In* Geological fieldwork 1992: British Columbia Ministry of Energy, Mines and Petroleum Resources, Paper 1993-1, p. 109 -134.

Ferri, F., and Melville, D. M., 1994, Bedrock geology of the Germansen Landing - Manson Creek area, British Columbia (93/9, 10, 15; 94C/2): B.C. Ministry of Energy, Mines and Petroleum Resources, v. Bulletin 91, p. 147.

Ferri, F., 1997, Nina Ceek Group and Lay Range Assemblage, north-central British Columbia: remnants of late Paleozoic oceanic and arc terranes: Canadian Journal of Earth Sciences, v. 34, p. 854-874.

Fournier, R. O., 1999, Hydrothermal processes related to movement of fluid from plastic into brittle rock in the magmatic-epithermal environment: Economic Geology, v. 94, p. 1193-1211.

Francis, D., and Minarik, W., 2008, Aluminum-dependent trace element partitioning in clinopyroxene: Contibutions to Mineralogy and Petrology, v. 156, p. 439-451.

Fraser, T. M., 1994, Geology, Alteration and Origin of Hydrothermal Breccias at the Mount Polley Alkalic Porphyry Copper-Gold Deposit, South-Central British Columbia: Unpub. M.Sc. thesis, The University of British Columbia, Vancouver, 261 p.

Fraser, T. M., Stanley, C. R., Nikic, Z. T., Pesalj, R., and Gorc, D., 1995, The Mount Polley alkalic porphyry copper-gold deposit, south-central British Columbia, *in* Schroeter, T. G., ed., Porphyry Deposits of the Northwestern Cordillera of North America, Canadian Institute of Mining, Metallurgy and Petroleum, Special Volume 46, p. 609-622.

Frei, R., 1995, Evolution of Mineralizing Fluid in the Porphyry Copper System of the Skouries Deposit, Northeast Chalkidiki (Greece) - Evidence from Combined Pb-Sr and Stable-Isotope Data: Economic Geology and the Bulletin of the Society of Economic Geologists, v. 90, p. 746-762.

Frei, R., 1996, Sulfur in bulk rock and igneous apatite; Tracing mineralized and barren trends in intrusions: Schweizerische Mineralogische Und Petrographische Mitteilungen, v. 76, p. 57-73.

Frost, B. R., Lindsley, D. H., and Anderson, D. J., 1988, Fe-Ti oxide silicate equilibria: assemblages with fayalite olivine: American Mineralogist, v. 73, p. 727-740.

Frost, B. R., 1991, Introduction to Oxygen Fugacity and its Petrologic Importance, *in* Lindsley, D. H., ed., Oxide Minerals: Petrologic and Magnetic Significance 25. Reviews in Mineralogy, Mineralogical Society of America, p. 1-8.

Frost, B. R., and Lindsley, D. H., 1991, Occurrence of Iron-Titanium Oxides in Igneous Rocks, *in* Lindsley, D. H., ed., Oxide Minerals: Petrologic and Magnetic Significance, 25, Mineralogical Society of America, p. 433-462.

Gabrielse, H., 1991, Late Paleozoic and Mesozoic terrane interactions in north-central British Columbia: Canadian Journal of Earth Sciences, v. 28, p. 947-957.

Gabrielse, H., Monger, J. W. H., Wheeler, J. O., and Yorath, C. J., 1991, Part A. Morphological belts, tectonic assemblages, and terranes, *in* Gabrielse, H., and Yorath, C. J., eds., Chapter 2 of Geology of the Cordillera Orogen in Canada, 4, Geological Survey of Canada, Geology of Canada, p. 15-28.

Gamble, J. A., Smith, I. E. M., McCulloch, M. T., Graham, I. J., and Kokelaar, B. P., 1993, The geochemistry and petrogenesis of basalts from the Taupo volcanic zone and Kermadec Island Arc, SW Pacific: Journal of Volcanology and Geothermal Research, v. 54, p. 265-290.

Garnett, J. A., 1974, Lorraine; *in* Geology and Exploration in British Columbia: *B.C. Ministry of Energy, Mines and Petroleum Resources*, p. 370-378.

Garnett, J. A., 1978, Geology and mineral occurrences of the southern Hogem Batholith: B.C. Ministry of Energy, Mines and Petroleum Resources, Bulletin 70, p. 75.

Garratt, G. L., and Lindinger, J. E. L., 2008, Summary Report on the Jajay-Lorraine-Jan-Tam-Misty Property: Vancouver, B.C., Omineca Mining Division, B.C., Unpub. Report, p. 114.

Garwin, S. L., 2000, The setting, geometry and timing of intrusion-related hydrothermal systems in the vicinity of the Batu Hijau porphyry copper-gold deposit, Sumbawa, Indonesia, University of Western Australia, 452 p.

Gerstenberger, H., and Haase, G., 1997, A highly effective emitter substance for mass spectrometric Pb isotope ratio determinations: Chemical Geology, v. 136, p. 309-312.

Ghent, E. D., Erdmer, P., Archibald, D. A., and Stout, M. Z., 1996, Pressure-temperature and tectonic evolution of Triassic lawsonite - aragonite blueschists from Pinchi Lake, British Columbia: Canadian Journal of Earth Sciences, v. 33, p. 800-810.

Giggenbach, W. F., 1992, Isotopic shifts in waters from geothermal and volcanic systems along convergent plate boundaries and their origin: Earth and Planetary Science Letters, v. 133, p. 495-510.

Gilbert, S., and Danyushevsky, L., 2007, Laser Ablation ICPMS Methodology: Hobart, Department of Earth Sciences, University of Tasmania, Unpub. Manual, p. 9. Accessed March 15, 2007.

Gill, J. B., 1981, Orogenic Andesites and Plate Tectonics: New York, Springer-Verlag.

Gill, J. B., 1984, Sr-Pb-Nd isotopic evidence that both MORB and OIB sources contribute to oceanic island arc magmas in Fiji: Earth and Planetary Science Letters, v. 68, p. 443-458.

Green, D. H., and Wallace, P. J., 1988, Mantle metasomatism by ephemeral carbonatite melts: Nature, v. 336, p. 459-461.

Green, H. W., 2001, A graveyard for buoyant slabs: Science, v. 292, p. 2445-2446.

Gustafson, L. B., and Hunt, J. P., 1975, Porphyry copper-deposit at El-Salvador, Chile: Economic Geology, v. 70, p. 857-912.

Hall, A., 1987, Igneous Petrology, Longman Scientific and Technical, 573 p.

Halter, W. E., Heinrich, C. A., and Pettke, T., 2005, Magma evolution and the formation of porphyry Cu-Au ore fluids: evidence from silicate and sulfide melt inclusions: Mineralium Deposita, v. 39, p. 845-863.

Hamburger, M. W., and Isacks, B. L., 1987, Deep earthquakes in the southwest Pacific: a tectonic interpretation: Journal of Geophysical Research, v. 92, p. 13,841-13,854.

Harper, B. J., 2000, Hydrothermal alteration at the Ridgeway porphyry gold – copper deposit, N.S.W.: Unpub. BSc (Hons) thesis, University of Tasmania, 130 p.

Haselton, H. T., Hovis, G. L., Hemingway, B. S., and Robie, R. D., 1983, Calorimetric investigation of the excess entropy of mixing in albite-sandine solid solutions: lack of evidence for Na, K, short-range order and implications for two-feldspar thermometry: American Mineralogist, v. 68, p. 398-413.

Haughton, D. R., Roeder, P. L., and Skinner, B., 1974, Solubility of sulfur in mafic magmas: Economic Geology, v. 69, p. 451-467.

Hawkesworth, C., Hergt, J. M., Ellam, R. M., and McDermott, F., 1991, Element fluxes associated with subduction related magmatism: Philosophical Transactions of the Royal Society of London Series A, v. 335, p. 393-405.

Hawkesworth, C. J., Gallagher, K., Hergt, J. M., and McDermott, F., 1993, Mantle and slab contributions in arc magmas: Annual Review of Earth and Planetary Sciences, v. 21, p. 175-204.

Hawkesworth, C. J., Gallagher, K., Hergt, J. M., and McDermott, F., 1994, Destructive plate margin magmatism: Geochemistry and melt generation: Lithos, v. 33, p. 169-188.

Hawkesworth, C. J., Turner, S. P., McDermott, F., Peate, D. W., and vanCalsteren, P., 1997, U-Th isotopes in arc magmas: Implications for element transfer from the subducted crust: Science, v. 276, p. 551-555.

Hedenquist, J. W., and Lowenstern, J. B., 1994, The Role of Magmas in the Formation of Hydrothermal Ore-Deposits: Nature, v. 370, p. 519-527.

Hedenquist, J. W., and Arribas, A., Jr., 1998, Evolution of an intrusion-centered hydrothermal system: Far Southeast-Lepanto porphyry and epithermal Cu-Au Deposits, Philippines: Economic Geology, v. 1998, p. 373-404.

Heinrich, C., 2005, The physical and chemical evolution of low-salinity magmatic fluids at the porphyry to epithermal transition: a thermodynamic study: Mineralium Deposita, v. 39, p. 864-889.

Heinrich, C. A., Gunther, D., Audetat, A., Ulrich, T., and Frischknecht, R., 1999, Metal fractionation between magmatic brine and vapor, determined by microanalysis of fluid inclusions: Geology, v. 27, p. 755-758.

Heithersay, P. S., and Walshe, J. L., 1995, Endeavour 26 North: A porphyry copper-gold deposit in the Late Ordovician, shoshonitic Godnumbla volcanic complex, New South Wales, Australia: Economic Geology, v. 90, p. 1506-1532.

Hemley, J. J., and Jones, W. R., 1964, Chemical aspects of hydrothermal alteration with emphasis on hydrogen metasomatism: Economic Geology, v. 59, p. 538-569.

Hemley, J.J., and Hunt, J.P., 1992, Hydrothermal ore-forming processes in the light of studies in rock-buffered systems: II. Some general geologic applications: Economic Geology and the Bulletin of the Society of Economic Geologists, v. 87, p. 23-43.

Henry, D. J., Guidotti, C. V., and Thomson, J. A., 2005, The Ti-saturation surface for low-to-medium pressure metapelitic biotites: Implications for geothermometry and Ti-substitution mechanisms: American Mineralogist, v. 90, p. 316-328.

Hildreth, W., and Moorbath, S., 1988, Crustal Contributions to Arc Magmatism in the Andes of Central Chile: Contributions to Mineralogy and Petrology, v. 98, p. 455-489.

Hobbs, B. E., 1966, Microfabrics of tectonites from the Wyangala Dam area, New South Wales, Australia: Bulletin of the Geological Society of America, v. 77, p. 685-706.

Hofmann, A. W., 1997, Mantle geochemistry: the message from oceanic volcanism: Nature, v. 385, p. 219-229.

Holcombe, R., 2006, GEOrient 9.2; Stereographic Projections and Rose Diagram Plots, Holcombe, Coughlin and Associates.

Holliday, J. R., Wilson, A. J., Blevin, P. L., Tedder, I. J., Dunham, P. D., and Pfitzner, M., 2002, Porphyry gold-copper mineralisation in the Cadia district, eastern Lachlan Fold Belt, New South Wales, and its relationship to shoshonitic magmatism: Mineralium Deposita, v. 37, p. 100-116.

Holliday, J. R., and Cooke, D. R., 2007, Advances in geological models and exploration methods for copper ± gold porphyry deposits, Proceedings of Exploration 07: Fifth Decennial International Conference on Mineral Exploration, p. 791-809.

Hollings, P., and Wyman, D. A., 2004, The Geochemistry of Trace Elements in Igneous Systems: Principles and Examples from Basaltic Systems, *in* Linnen, R. L., and Samson, I. M., eds., Rare-Element Geochemistry and Mineral Deposits 17: St. Catherines, Ontario, Geological Association of Canada, p. 1-16.

Iacono-Marziano, G., Gaillard, F., and Pichavant, M., 2007, Limestone assimilation and the origin of CO_2 emissions at the Alban Hills (Central Italy): constants from experimental petrology: Journal of Volcanology and Geothermal Research, v. 166, p. 91-105.

Iacono-Marziano, G., Gaillard, F., and Pichavant, M., 2008, Limestone assimilation by basaltic magmas: an experimental re-assessment and application to Italian volcanoes: Contributions to Mineralogy and Petrology, v. 155, p. 719-738.

Iacono-Marziano, G., Gaillard, F., Scaillet, B., Pichavant, M., and Chiodini, G., 2009, Role of non-mantle CO_2 in the dynamics of volcano degassing: The Mount Vesuvius example: Geology, v. 37, p. 319-322.

Irvine, T. N., and Baragar, W. R. A., 1971, A guide to the chemical classification of the common volcanic rocks: Canadian Journal of Earth Sciences, v. 8, p. 523-548.

Ito, E., and Stern, R. J., 1986, Oxygen- and Strontium- isotopic investigations of subduction zone volcanism: the case of the Volcano Arc and the Mariana Island Arc: Earth and Planetary Science Letters, v. 76, p. 312-320.

Jackson, M., Chamberlain, C., Tosdal, R., Rees, C., Ferreira, L., and Taylor, C., 2008, Breccia evolution and distribution of associated alteration and sulfide minerals on sections 29 and 18, northeast zone, Mount Polley alkalic Cu-Au porphyry deposit British Columbia, Shallow- and Deep-Level Alkalic Mineral Deposits: Developing an Integrated Exploration Model; Year 3 - Porphyry Module Final Update to Project Sponsors, Unpub. Report, Mineral Deposit Research Unit (UBC) and CODES Centre of Excellence in Ore Deposits (Utas), Unpub. Report, p. 4.1-4.7.

Jackson, M. L., 2008, Evolution of the Northeast zone breccia body, Mount Polley mine, British Columbia: Unpub. M.Sc. thesis, University of British Columbia, Vancouver, 232 p.

Jacobs, D. C., and Parry, W. T., 1976, A comparison of the geochemistry of biotite from some Basin and Range stocks: Economic Geology, v. 71, p. 1029-1035.

Jago, C. P., 2008, Metal- and alteration-zoning, and hydrothermal flow paths at the moderately-tilted, silica-saturated Mt. Milligan Cu-Au alkalic porphyry deposit: Unpub. M.Sc. thesis, University of British Columbia, Vancouver, 210 p.

Jago, C. P., and Tosdal, R. M., in prep., Mt. Milligan (British Columbia): an example of the younger silica-saturated alkalic porphyry Cu-Au deposit: Economic Geology.

Jago, P., and Tosdal, R., 2008, The Early Jurassic Mt. Milligan (British Columbia): an example of the younger silica-saturated alkalic porphyry Cu-Au deposit, Shallow- and Deep-Level Alkalic Mineral Deposits: Developing an Integrated Exploration Model; Year 3 - Porphyry Module Final Update to Project Sponsors, Unpub. Report, Mineral Deposit Research Unit (UBC) and CODES Centre of Excellence in Ore Deposits (Utas), Unpub. Report, p. 6.1-6.8.

Jarosewich, E., Nelen, J. A., and Norberg, J. A., 1980, Reference Samples for Electron Microprobe Analysis: Geostandards Newsletter, v. 4, p. 43-47.

Jenner, G. A., 1996, Trace element geochemistry of igneous rocks: geochemical nomenclature and analytical geochemistry, *in* Wyman, D. A., ed., Trace Element Geochemistry of Volcanic Rocks: Applications for Massive Sulphide Exploration, 12, Geological Association of Canada, p. 51-77.

Jensen, E. P., and Barton, M. D., 2000, Gold Deposits Related to Alkaline Magmatism: Chapter 8, *in* Hagemann, S. G., and Brown, P. E., eds., Gold in 2000, 13. Reviews in Economic Geology, Society of Economic Geologists, p. 279-314.

Johnson, A. M., and Pollard, D. D., 1973a, Mechanics of growth of some laccolithic intrusions in the Henry Mountains, Utah.I. : Tectonophysics, v. 18, p. 262-309.

Johnson, A. M., and Pollard, D. D., 1973b, Field observations, Gilbert's model, physical properties and flow of the magma .II. Bending and failure of overburden layers and sill formation: Tectonophysics, v. 18, p. 311-354.

Johnson, M. C., and Plank, T., 1999, Dehydration and melting experiments constrain the fate of subducted sediments, Geochemistry, Geophysics and Geosystems, 1, no.1999GC000014.

Johnston, S. T., and Erdmer, P., 1995, Hot-Side-up aureole in southwest Yukon and limits on terrane assembly of the northern Canadian Cordillera: Geology, v. 23, p. 419-422.

Johnston, S. T., and Borel, G. D., 2007, The odyssey of the Cache Creek terrane, Canadian Cordillera: Implications for accretionary orogens, tectonic setting of Panthalassa, the Pacific superwell, and break-up of Pangea: Earth and Planetary Science Letters, v. 253, p. 415-428.

Kay, R. W., 1980, Volcanic arc magmas: implications of a melting-mixing model for element recycling in the crust-upper mantle system: Journal of Geology, v. 88, p. 497-522.

Kamenetsky, V. S., and Danyushevsky, L. V., 2005, Metals in quartz-hosted melt inclusions: Natural facts and experimental artifacts: American Mineralogist, v. 90, p. 1674-1678.

Keith, J. D., Whitney, J. A., Hattori, K., Ballantyne, G. H., Christiansen, E. H., Barr, D. L., Cannan, T. M., and Hook, C. J., 1997, The role of magmatic sulfides and mafic alkaline magmas in the Bingham and Tintic mining districts, Utah: Journal of Petrology, v. 38, p. 1679-1690.

Keith, J. D., Christiansen, E. H., Maughan, D. T., and Waite, K. A., 1998, The Role of Mafic Alkaline Magmas in Felsic Porphyry-Cu and Mo-Systems, *in* Lentz, D. R., ed., Mineralized Intrusion-Related Skarn Systems, 26. Short Course Series: Quebec City, Mineralogical Association of Canada p. 211-273.

Keith, J. D., 2002, Could the combination of mafic and silicic magmas be vital to porphyry systems: a discussion, Geological Society of America annual meeting: Denver, Colorado, Abstract with Programs.

Kennedy, A. K., Hart, S. R., and Frey, F. A., 1990, Composition and isotopic constraints on the petrogenesis of alkaline arc lavas: Lihir Island, Papua New Guinea: Journal of Geophysical Research, v. 95, p. 6929-6942.

Kepezhinskas, P., and Defant, M. J., 1996, Contrasting styles of mantle metasomatism above subduction zones: constraints from ultramafic xenoliths in Kamchatka, *in* Bebout, G. E., Scholl, D. W., Kirby, S. H., and Platt, J. P., eds., Subduction Top to Bottom, American Geophysical Union, p. 307-314.

Keppler, H., and Wyllie, P.J., 1991, Partitioning of Cu, Sn, Mo, W, U, and Th between Melt and Aqueous Fluid in the Systems Haplogranite-H2o Hcl and Haplogranite-H2o Hf: Contributions to Mineralogy and Petrology, v. 109, p. 139-150.

Kerrich, R., and Wyman, D. A., 1996, The trace element systematics of igneous rocks in mineral exploration: an overview, *in* Wyman, D. A., ed., Trace Element Geochemistry of Volcanic Rocks: Applications for Massive Sulphide Exploration, 12. Short Course Notes, Geological Association of Canada, p. 1-50.

Kesler, S.E., Chryssoulis, S.L., and Simon, G., 2002, Gold in porphyry copper deposits: its abundance and fate: Ore Geology Reviews, v. 21, p. 103-124.

Knauss, K.G., and Wolery, T.J., 1988, The dissolution kinetics of quartz as a function of pH and time at 70-Degrees-C: Geochimica et Cosmochimica Acta, v. 52, p. 43-53.

Koo, J., 1968, Geology and mineralization in the Lorraine property area, Ominica Mining Division, B.C.: Unpub. M.Sc. thesis, The University of British Columbia, 107 p.

Kooiman, G. J. A., McLeod, M. J., and Sinclair, W. D., 1986, Porphyry tungstan-molybdenum orebodies, polymetallic veins and replacement bodies and tin-bearing greisen zones in the Fire Tower zone, Mount Pleasant, New Brunswick: Economic Geology, v. 81, p. 1356-1373.

Krogh, T. E., 1982, Improved accuracy of U-Pb zircon ages by the creation of more concordant systems using an air abrasion technique: Geochimica et Cosmochimica Acta, v. 46, p. 637-649.

Kroll, T., Muller, D., Seifert, T., Herzig, P. M., and Schneider, A., 2002, Petrology and geochemistry of the shoshonite-hosted Skouries porphyry Cu-Au deposit, Chalkidiki, Greece: Mineralium Deposita, v. 37, p. 137-144.

Kyser, T. K., and O'Neil, J. R., 1984, Hydrogen isotope systematics of submarine basalts: Geochimica et Cosmochimica Acta, v. 48, p. 2123-2133.

Kyser, T. K., 1986, Stable Isotope Variations in the Mantle, *in* Valley, J. W., Taylor, H. P. J., and O'Neil, J. R., eds., Stable Isotopes, 16, Mineralogical Society of America, p. 141-164.

Landtwing, M. R., Dillenbeck, E. D., Leake, M. H., and Heinrich, C. A., 2002, Evolution of the breccia-hosted porphyry Cu-Mo-Au deposit at Agua Rica, Argentina: progressive unroofing of a magmatic hydrothermal system: Economic Geology, v. 97, p. 1273-1292.

Lang, J. R., Stanley, C. R., and Thompson, J. F. H., 1994, Porphyry copper deposits related to alkalic igneous rocks in the Triassic-Jurassic arc terranes of British Columbia, *in* Bolm, J. G., and Pierce, F. W., eds., Bootprints Along the Cordillera, 20, Arizona Geological Society Digest, p. 219-236.

Lang, J. R., Stanley, C. R., Thompson, J. F. H., and Dunne, K. P. E., 1995a, Na-K-Ca magmatic-hydrothermal alteration in alkalic porphyry Cu-Au deposit, British Columbia, *in* Thompson, J. F. H., ed., Magmas, fluids, and ore deposits; Short Course Handbook, 23, University of British Columbia, Department of Geological Sciences, Vancouver, BC, Canada (CAN), p. 339-366.

Lang, J. R., Lueck, B., Mortensen, J. K., Russell, J. K., Stanley, C. R., and Thompson, J. F. H., 1995b, Triassic-Jurassic silica-undersaturated and silica-saturated alkalic intrusions in the Cordillera of British-Columbia - implications for arc magmatism: Geology, v. 23, p. 451-454.

Lang, J. R., 1996, Potassium Feldspar, *in* Thompson, A. J. B., and Thompson, J. F. H., eds., Atlas of Alteration: A Field and Petrographic Guide to Hydrothermal Alteration Minerals, Geological Association of Canada, Mineral Deposit Division, p. 78-79.

Le Maitre, R. W., 1989, A Classification of Igneous Rocks and Glossary of Terms, Blackwell Scientific Publications, Oxford, 193 p.

Lentz, D. R., 1998, Late-Tectonic U-Th-Mo-REE Skarn and Carbonatitic Vein-Dyke Systems in the South Eastern Grenville Province: A Pegmatite-Related Pneumatolytic Model Linked to Marble Melting (Limestone Syntexis): Chapter 15, *in* Lentz, D. R., ed., Mineralized Intrusion-Related Skarn Systems, 26: Quebec City, Mineralogical Association of Canada Short Course Series, p. 519-657.

Leslie, R. A. J., 2004, Primitive Shoshonites from Fiji: Mineralogy, Melt Inclusions and Geochemistry: Unpub. Ph.D thesis, University of Tasmania, Hobart, 333 p.

Lickfold, V., 2002, Intrusive history and volatile evolution of the Endeavour porphyry Cu-Au deposits, Northparkes district, NSW, Australia: Unpub. PhD thesis, University of Tasmania, 230 p.

Lickfold, V., Cooke, D. R., Smith, S. G., and Ullrich, T. D., 2003, Endeavour copper-gold porphyry deposits, Northparkes, New South Wales: Intrusive history and fluid evolution: Economic Geology and the Bulletin of the Society of Economic Geologists, v. 98, p. 1607-1636.

Lickfold, V., Cooke, D. R., Crawford, A. J., and Fanning, C. M., 2007, Shoshonitic magmatism and the formation of the Northparkes porphyry Cu–Au deposits, New South Wales: Australian Journal of Earth Sciences, v. 54, p. 279-306.

Lin, P. N., Stern, R. J., and Bloomer, S. H., 1989, Shoshonitic volcanism in the northern Mariana Arc: 2, Large-ion lithophile and rare earth element abundances: Evidence for the source of incompatible element enrichments in intraoceanic arcs: Journal of Geophysical Research, v. 94, p. 4497-4514.

Lin, P. N., Stern, R. J., Morris, J., and Bloomer, S. H., 1990, Nd- and Sr- isotopic compositions of lavas from the northern Mariana and southern Volcano arcs: Implications for origin of island arc melts: Contributions to Mineralogy and Petrology, v. 105, p. 381-392.

Logan, J. M., and Koyanagi, V. M., 1989, Preliminary Geology and Mineral Deposits of the Galore Creek Area, North-western British Columbia (104G/7W): Geological Fieldwork 1988, BC Ministry of Energy, Mines and Petroleum Resources, Paper 1989-1, p. 269-284.

Logan, J. M., Koyanagi, V. M., and Rhys, D. A., 1989, Geology and Mineral Occurrences of the Galore Creek Area (104A and B): B.C. Ministry of Energy, Mines and Petroleum Resources, Open File 1989-8.

Logan, J. M., and Koyanagi, V. M., 1994, Geology and mineral deposits of the Galore Creek area (104G/3, 4), Ministry of Energy, Mines and Petroleum Resources, Victoria BC, 95 p.

Logan, J. M., 2004, Preliminary lithogeochemistry and polymetallic VHMS mineralization in the Early Devonian(?) and Early Carboniferous volcanic rocks, Foremore property: B.C. Ministry of Energy, Mines and Petroleum Resources, Fieldwork 2003-1, p. 105-124.

Logan, J. M., 2005, Alkaline magmatism and porphyry Cu-Au deposits at Galore Creek, Northwestern British Columbia: B.C. Ministry of Energy, Mines and Petroleum Resources, Paper 2005-1, p. 237-248.

Logan, J. M., and Mihalynuk, M. G., 2005a, Regional Geology and Setting of the Cariboo, Bell, Springer and Northeast Porphyry Cu-Au Zones at Mount Polley, South-Central British Columbia: Geological Fieldwork 2004, BC Ministry of Energy, Mines and Petroleum Resources, Paper 2005-1, p. 249-270.

Logan, J. M., and Mihalynuk, M. G., 2005b, Porphyry Cu-Au deposits of the Iron Mask Batholith, southeastern British Columbia: Geological Fieldwork 2004, BC Ministry of Energy, Mines and Petroleum Resources, Paper 2005-1, p. 271-290.

Logan, J. M., and Bath, A. B., 2006, Geochemistry of Nicola Group Basalt from the Central Quesnel Trough at the Latitude of Mount Polley (NTS 093A/5, 6, 11, 12), Central British Columbia: *in* Geological Fieldwork 2005, BC Ministry of Energy, Mines and Petroleum Resources, v. 2006-1, p. 83-98.

Logan, J. M., Mihalynuk, M. G., Ullrich, T., and Friedman, R. M., 2007, U-Pb age of intrusive rocks and 40Ar/39Ar plateau ages of copper-gold-silver mineralization associated with alkaline intrusive centres at Mount Polley and the Iron Mask batholith, southern and central British Columbia: Geological Fieldwork 2006, British Columbia Ministry of Energy, Mines and Petroleum Resources, Paper 2007-1, p. 93-115.

Lowell, J. D., and Guilbert, J. M., 1970, Lateral and vertical alteration-mineralization zoning in porphyry ore deposits: Economic Geology, v. 65, p. 373-408.

Lowenstern, J. B., 1994, Dissolved volatile concentrations in an ore-forming magma: Geology, v. 22, p. 893-896.

Ludwig, K. R., 2001, Squid 1.02, Berkeley Geochronolgy Centre Special Publication 2.

Ludwig, K. R., 2003, Isoplot version 3.00: A geochronological toolkit for Microsoft Excel, Berkeley Geochronology Centre.

Luhr, J. F., 1997, Extensional tectonics and the diverse primitive volcanic rocks in the western Mexican volcanic belt: Canadian Mineralogist, v. 35, p. 473-500.

Luo, X., Rehkämper, M., Lee, D. C., and Halliday, A. N., 1997, High precision $^{230}Th/^{232}Th$ and $^{234}U/^{238}U$ measurements using energy-filtered ICP magnetic sector multiple collector mass spectrometry: International Journal of Mass Spectrometry Ion Processes, v. 171, p. 105-117.

Maas, R., Kamenetsky, M. B., Sobolev, A. V., Kamenetsky, V. S., and Sobolev, N. V., 2005, Sr-Nd-Pb isotopic evidence for a mantle origin of alkali chlorides and carbonates in the Udachnaya kimberlite, Siberia: Geology, v. 35, p. 549-552.

Maier, W. D., and Barnes, S.-J., 1999, The origin of Cu Sulfide Deposits in the Curaca Valley, Bahia, Brazil: evidence from Cu, Ni, Se and platinum-group element concentrations: Economic Geology, v. 94, p. 165-183.

Manhes, G., Minster, J. F., and Allègre, C. J., 1978, Comparative uranium-thorium-lead and rubidium-strontium study of the Saint Sèverin amphoterite: consequences for early solar system chronology: Earth and Planetary Science Letters v. 39, p. 14-24.

Manning, D.A.C., 1981, The effect of fluorine on liquidus phase-relationships in the system qz-ab-or with excess water at 1-Kb: Contributions to Mineralogy and Petrology, v. 76, p. 206-215.

Marsh, B. D., 1995, Solidification fronts and magmatic evolution: Mineralogical Magazine, v. 60, p. 5-40.

Marsh, B. D., 1998, On the interpretation of crystal size distributions in magmatic systems: Journal of Petrology, v. 39, p. 553-599.

McCulloch, M. T., Kyser, T. K., Woodhead, J. D., and Kinsley, L., 1994, Pb-Sr-Nd-O isotopic constraints on the origin of rhyolites from the Taupo Volcanic Zone of New Zealand - evidence for assimilation followed by fractionation from basalt Contributions to Mineralogy and Petrology, v. 115, p. 303-312.

McDermott, F., Defant, M. J., Hawkesworth, C. J., Maury, R. C., and Joron, J. L., 1993, Isotope and trace-element evidence for 3 component mixing in the genesis of the North Luzon arc lavas (Philippines): Contributions to Mineralogy and Petrology, v. 113, p. 9-23.

McInnes, B. I. A., and Cameron, E. M., 1994, Carbonated, alkaline hybridizating melts from a sub-arc environment: Mantle wedge samples from the Tabar-Lihir-Tanga-Feni arc, Papua New Guinea: Earth and Planetary Science Letters, v. 122, p. 125-141.

McInnes, B. I. A., Gregoire, M., Binns, R. A., Herzig, P. M., and Hannington, M. D., 2001, Hydrous metasomatism of oceanic sub-arc mantle, Lihir, Papua New Guinea: petrology and geochemistry of fluid-metasomatism mantle wedge xenoliths: Earth and Planetary Science Letters, v. 188, p. 169-183.

McMillan, W. J., Thompson, J. F. H., Hart, C. J. R., and Johnston, S. T., 1995, Regional geological and tectonic setting of porphyry deposits in British Columbia and Yukon Territory, *in* Schroeter, T. G., ed., Porphyry Deposits of the Northwestern Cordillera of North America, Canadian Institute of Mining, Metallurgy and Petroleum, Special Volume 46, p. 40-57.

Micko, J., 2007, Lithological distribution, hydrothermal alteration and mineralization at the Central Zone, Galore Creek alkalic Cu-Au porphyry deposit, NW British Columbia, MDRU-CODES: Shallow and deep alkalic deposits: Porphyry module , Year 2 meeting, Unpub. Report, p. 3.1-3.10.

Micko, J., Tosdal, R., Simpson, K., Chamberlain, C., and Schwab, D., 2008, Controls and Hydrothermal Zonation of Central Zone Mineralization at the Galore Creek Alkalic Cu-Au Porphyry Deposit, northwestern British Columbia, Shallow- and Deep-Level Alkalic Mineral Deposits: Developing an Integrated Exploration Model; Year 3 - Porphyry Module Final Update to Project Sponsors, Unpub. Report, Mineral Deposit Research Unit (UBC) and CODES Centre of Excellence in Ore Deposits (Utas), Unpub. Report, p. 2.1 - 2.7.

Micko, J., Tosdal, R. M., Simpson, K., Chamberlain, C., and Schwab, D., in prep., The hydrothermal genesis of the Central Zone, alkalic Cu-Au porphyry deposit, Galore Creek, northwestern British Columbia: Economic Geology.

Mihalynuk, M. G., Nelson, J., and Diakow, L. J., 1994a, Cache Creek terrane entrapment - oroclinal paradox within the Canadian Cordillera: Tectonics, v. 13, p. 575-595.

Mihalynuk, M. G., Smith, M. T., Hancock, K. D., and Dudka, S., 1994b, Regional and economic geology of the Tulsequah river and glacier areas (104K/12 & 13): *in* Geological Fieldwork 1993, Ministry of Energy and Mines, Victoria BC, Paper 1994-1, p. 321-342.

Mihalynuk, M. G., Johnston, S. T., English, J. M., Cordey, F., Villeneuve, M. E., Rui, L., and Orchard, M. J., 2003, Atlin TGI, Part II: Regional geology and mineralization of the Nakina area (NTS 104N/2W and 3): *in* Geological Fieldwork 2002, BC Ministry of Energy, Mines and Petroleum Resources, v. Paper 2003-1, p. 9-37.

Mihalynuk, M. G., Erdmer, P., Ghent, E. D., Cordey, F., Archibald, D. A., Friedman, R. M., and Johannson, G. G., 2004, Coherent French Range blueschist: Subduction to exhumation in < 2.5 m.y.?: Geological Society of America Bulletin, v. 116, p. 910-922.

Mitchell, R. H., 1995, Kimberlites, Orangeites and Related Rocks: New York, N.Y., Plenum Press, 410 p.

Monger, J. W. H., and Ross, C. A., 1971, Distribution of Fusulinaceans in Western Canadian Cordillera: Canadian Journal of Earth Sciences, v. 8, p. 259-&.

Monger, J. W. H., 1975, Upper Paleozoic rocks of the Atlin terrane, Geological Survey of Canada, p. 63.

Monger, J. W. H., 1977, Upper Paleozoic rocks of the northwestern British Columbia, Paper 77-1A: Geological Survey of Canada, p. 255-262.

Monger, J. W. H., and Irving, E., 1980, Northward displacement of north-central British Columbia: Nature, v. 285, p. 289-294.

Monger, J. W. H., 1993, Canadian Cordilleran Tectonics - from Geosynclines to Crustal Collage: Canadian Journal of Earth Sciences, v. 30, p. 209-231.

Monger, J. W. H., and Price, R. A., 2000, A Transect of the Southern Canadian Cordillera from Vancouver to Calgary, Geological Survey of Canada, 170 p.

Montoya, J. W., and Hemley, J. J., 1975, Activity relations and stabilities in alkali feldspar and mica alteration reactions: Economic Geology, v. 70, p. 577-594.

Monzier, M., Robin, C., Eissen, J., and Cotten, J., 1997, Geochemistry versus seismotectonics along the volcanic New Hebrides central chain (Soouthwest Pacific): Journal of Volcanology and Geothermal Research, v. 78, p. 1-29.

Morimoto, M., 1988, Nomenclature of pyroxenes: Mineralogical Magazine, v. 52, p. 535-550.

Morris, J. D., and Hart, S. R., 1983, Isotopic and incompatible trace element constraints on the genesis of island arc volcanics from Cold Bay and Amak Island, Aleutians, and implications for mantle structure: Geochimica et Cosmochimica Acta, v. 47, p. 2015-2030.

Morris, J. D., Leeman, W. P., and Tera, F., 1990, The subducted component in island arc lavas: constraints from Be isotopes and B-Be systematics: Nature, v. 344, p. 31-36.

Morrison, G. W., 1980, Characteristics and tectonic setting of the shoshonite rock association: Lithos, v. 13, p. 97-108.

Mortensen, J. K., 1992, Pre-Mid-Mesozoic tectonic evolution of the Yukon-Tanana terrane, Yukon and Alaska: Tectonics, v. 11, p. 836-853.

Mortensen, J. K., Ghosh, D.K., and Ferri, F., 1995, U-Pb geochronology of intrusive rock associated with copper-gold porphyry deposits in the Canadian Cordillera; *in* Porphyry Deposits of the Northwestern Cordillera of North America, T.G. Schroeter, Editor: Canadian Institute of Mining and Metallurgy, Special Volume 46, p. 142-158.

Müller, D., Rock, N. M. S., and Groves, D. I., 1992, Geochemical discrimination between shoshonitic and potassic volcanic rocks from different tectonic settings: a pilot study: Mineralogy and Petrology, v. 46, p. 259-289.

Nabelek, P. I., O'Neil, J. R., and Papike, J. J., 1983, Vapor phase exsolution as a controlling factor in hydrogen isotope variation in granitic rocks: the Notch Peak granitic stock, Utah: Earth and Planetary Science Letters, v. 66, p. 137-150.

Nachit, H., Razafimahefa, N., and Stussi, J. M., 1985, Composition chimique des biotites et typologie magmatique des granitoids: Comtes Rendus Hebdomadaires de l' Académie des Science, v. 301, p. 813-818.

Naldrett, A. J., 1989a, Magmatic Sulfide Deposits, Oxford University Press, 196 p.

Naldrett, A. J., 1989b, Sulfide melts-crystallization temperatures, solubilities in silicate melts, and Fe, Ni, and Cu partitioning between basaltic magmas and olivine, *in* Whitney, J. A., and Naldrett, A. J., eds., Ore deposits associated with magmas: Reviews in Economic Geology, 4, p. 5-20.

National Geophysical Data Centre, Surface of the Earth digital sea floor and land surface elevation image. National Oceanic and Atmospheric Administration, U.S. Department of Commerce, Website: http://www.ngdc.noaa.gov/mgg/image/2minrelief.html. Accessed August, 12, 2009.

Neilson, C. H., and Sigurdsson, S., 1981, Quantitative methods for electron microprobe analysis of sodium in natural and synthetic glasses: American Mineralogist, v. 66, p. 547-552.

Nelson, J., and Colpron, M., 2007, Tectonics and metallogeny of the British Columbia, Yukon and Alaskan Cordillera, 1.8 Ga to the present, *in* Goodfellow, W. D., ed., Mineral Deposits of Canada: A Synthesis of Major Deposit-Types, District Metallogeny, the Evolution of Geological Provinces, and Exploration Methods, Geological Association of Canada, Mineral Deposits Division: Special Publication No. 5, p. 755-791.

Nelson, J. L., and Bellefontaine, K. A., 1996, The geology and mineral deposits of north-central Quesnellia; Tezzeron Lake to Discovery Creek, central British Columbia: B.C. Ministry of Energy, Mines and Petroleum Resources, Bulletin 99, p. 112 pages.

Neuendorf, K. K. E., Mehl, J. P., and Jackson, J. A., 2005, Glossary of Geology: Fifth Edition: Alexandria, Virginia, American Geological Institute, 779 p.

Newell, J. M., and Peatfield, G. R., 1995, The Red-Chris porphyry copper-gold deposit, northwestern British Columbia, *in* Schroeter, T. G., ed., Porphyry Deposits of the Northwestern Cordillera of North America, Special Volume 46: Vancouver, Canadian Institute of Mining, Metallurgy and Petroleum, p. 674-687.

Nixon, G. T., Archibald, D. A., and Heaman, L. M., 1993, ^{40}Ar-^{39}Ar and U-Pb geochronometry of the Polaris Alaskan-type complex, British Columbia: Precise timing of Quesnellia-North America interaction: Geological Association of Canada; Mineralogical Association of Canada; annual meeting abstracts with programs, v. 18, p. A-76.

Nixon, G. T., Hammack, J. L., Ash, C. H., Cabri, L. J., Case, G., Connelly, J. N., Heaman, L. M., Laflamme, J. H. G., Nuttall, C., Paterson, W. P. E., and Wong, R. H., 1997, Geology and platinum-group-element mineralization of Alaskan-type ultramafic-mafic complexes in British Columbia: B.C. Ministry of Employment and Investment, v. Bulletin 93, p. 141.

Nixon, G. T., 2003, Geological setting of the Lorraine Alkaline Cu-Au porphyry, north-central British Columbia, Open File 2003-4 Map 1, British Columbia Ministry of Energy, Mines and Petroleum Resources.

Nixon, G. T., and Peatfield, G. R., 2003, Geological Setting of the Lorraine Cu-Au Porphyry Deposit, Duckling Creek Syenite Complex, North-central British Columbia: Open File 2003-4, British Columbia Ministry of Energy, Mines and Petroleum Resources, p. 1-24.

Nixon, G. T., Cabri, L. J., Laflamme, J. H. G., Sylvester, P., and Turbrett, M., 2004, Platinum-group elements in alkaline Cu-Au porphyries: Geofile 2004-6, British Columbia Ministry of Energy and Mines, Poster.

Ohmoto, H., 1986, Stable isotope geochemistry of ore deposits: Reviews in Mineralogy, v. 16, p. 491-559.

Paquette, J.-L., Menot, R.-P., Pin, C., and Orsini, J.-B., 2003, Episodic and short-lived granitic pulses in a post-collisional setting: Evidence from precise U-Pb zircon dating through a crustal cross-section in Corsica: Chemical Geology, v. 198, p. 1-20.

Parfenov, L. M., Nokleberg, W. J., Monger, J. W. H., Norton, I. O., Stone, D. B., Fujita, K., Khanchuk, A. I., and Scholl, D. W., 1999, Northern Pacific orogens: A collage of terranes and history of its formation: Geologiya I Geofizika, v. 40, p. 1563-1574.

Pass, H., Cooke, D., Ferreira, L., Rees, C., Simpson, K., and Chamberlain, C., 2008, Geochemistry, alteration and mineralization of long-section 17-34, Northeast Zone, Mt. Polley breccia-hosted alkalic Cu-Au porphyry deposit, Shallow- and Deep-Level Alkalic Mineral Deposits: Developing an Integrated Exploration Model; Year 3 - Porphyry Module Final Update to Project Sponsors, Mineral Deposit Research Unit (UBC) and CODES Centre of Excellence in Ore Deposits (Utas), Unpub. Report, p. 5.1-5.10.

Pass, H. E., Cooke, D. R., Davidson, G. J., Maas, R., Dipple, G. M., Rees, C., and Ferreira, L., in prep., Alteration and isotope geochemistry of the Northeast Zone, Mt. Polley alkalic Cu-Au porphyry deposit, British Columbia: A case for carbonate assimilation?: Economic Geology.

Patchett, P. J., and Gehrels, G. E., 1998, Continental influence on Canadian Cordilleran terranes from Nd isotopic study, and significance for crustal growth processes: Journal of Geology, v. 106, p. 269-280.

Paterson, S. R., Vernon, R. H., and Tobisch, O. T., 1989, A review of criteria for the identification of magmatic and tectonic foliations in granitoids: Journal of Structural Geology, v. 11, p. 349-363.

Pearce, J. A., 1983, Role of the sub-continental lithosphere in magma genesis at active continental margins, *in* Hawkesworth, C. J., and Norry, M. J., eds., Continental Basalts and Mantle Xenoliths: Nantwich, UK, Shiva, p. 230-249.

Pearce, J. A., and Parkinson, I. J., 1993, Trace element models for mantle melting: application to volcanic arc petrogenesis: Geological Society of London Special Publication, v. 76, p. 373-403.

Pearce, J. A., and Peate, D. W., 1995, Tectonic implications of the composition of volcanic arc magmas: Annual Review of Earth and Planetary Sciences, v. 19, p. 290-300.

Peate, D. W., Pearce, J. A., Hawkesworth, C. J., Colley, H., Edwards, C. M. H., and Hirose, K., 1997, Geochemical variations in Vanuatu arc lavas: the role of subducted material and a variable mantle wedge composition: Journal of Petrology, v. 38, p. 1331-1358.

Peatfield, G. R., and Nixon, G. T., 2003, Geological Setting of the Lorraine Alkalic Cu-Au Porphyry: Lower Main Zone, Open File 2003-4 Map 2, British Columbia Ministry of Energy, Mines and Petroleum Resources.

Peccerillo, A., and Taylor, S. R., 1976, Geochemistry of Eocene calc-alkaline volcanic rocks from the Kastamonu area, northern Turkey: Contributions to Mineralogy and Petrology, v. 58, p. 63-81.

Piccoli, P., and Candela, P., 1994, Apatite in felsic rocks - a model for the estimation of initial halogen concentrations in the Bishop Tuff (Long Valley) and Tuolumne intrusive suite (Sierra-Nevada Batholith) magmas: American Journal of Science, v. 294, p. 92-135.

Plank, T., and Langmuir, C. H., 1998, The chemical composition of subducted sediment and its consequences for the crust and mantle: Chemical Geology, v. 145, p. 325-394.

Pollard, P. J., 1984, An Introduction to Potassic Alteration in Porphyry Copper Deposits, *in* Laing, W. P., ed., Contributions of the Economic Geology Research Unit, Geology Department, James Cook University of North Queensland, p. 8.

Raos, A. M., 2001, The volcanic and geochemical evolution of a trachydacite-dominated island arc centre: Efate Island Group, Vanuatu arc, SW Pacific: Unpub. Ph.D thesis, University of Tasmania, 197 p.

Raos, A. M., and Crawford, A. J., 2004, Basalts from the Efate Island group, central section of the Vanuatu arc, SW Pacific: geochemistry and petrogenesis: Journal of Volcanology and Geothermal Research, v. 134, p. 35-56.

Rebagliati, C. M., Bowen, B. K., Copeland, D. J., and Niosi, D. W. A., 1995, Kemess South and Kemess North porphyry gold-copper deposits, northern British Columbia, *in* Schroeter, T. G., ed., Porphyry Deposits of the Northwestern Cordillera of North America: Vancouver, Canadian Institute of Mining, Metallurgy and Petroleum, Special Volume 46, p. 377-396.

Redmond, P. B., Einaudi, M. T., Inan, E. E., Landtwing, M. R., and Heinrich, C. A., 2004, Copper deposition by fluids cooling in intrusion-centered systems: New insights from the Bingham porphyry ore deposit, Utah: Geology, v. 32, p. 217-220.

Reesor, J. E., 1958, Dewar Creek map area with special emphasis on the White Creek Batholith, British Columbia: Geological Survey of Canada Memoirs, v. 292.

Richards, J. P., and Kerrich, R., 1993, The Porgera Gold Mine, Papua-New-Guinea - Magmatic Hydrothermal to Epithermal Evolution of an Alkalic-Type Precious-Metal Deposit: Economic Geology and the Bulletin of the Society of Economic Geologists, v. 88, p. 1017-1052.

Richards, J. P., 2009, Postsubduction porphyry Cu-Au and epithermal Au deposits: Products of remelting of subduction-modified lithosphere: Geology, v. 37, p. 247-250.

Rickwood, P. C., 1989, Boundary lines within petrologic diagrams which use oxides of major and minor elements: Lithos, v. 22, p. 247-263.

Rimstidt, J.D., 1997, Quartz solubility at low temperatures: Geochimica Et Cosmochimica Acta, v. 61, p. 2553-2558.

Rock, N. M. S., 1990, The international mineralogical association (IMA/CNMMN) pyroxene nomenclature scheme - computerization and its consequences: Mineralogy and Petrology, v. 43, p. 99-119.

Roddick, J. C., Loveridge, W. D., and Parrish, R. R., 1987, Precise U/Pb dating of zircon at the subnanogram Pb level: Chemical Geology, v. 66, p. 111-121.

Roedder, E., 1984, Fluid inclusions, Reviews in Mineralogy, Mineralogical Society of America, Michigan, v. 12, 644 p.

Rogers, N. W., and Setterfield, T. N., 1994, Potassium and incompatible element enriched in shoshonitic lavas from the Tavua volcano, Fiji: Chemical Geology, v. 118, p. 43-62.

Rollinson, H., 1993, Using geochemical data: evaluation, presentation, interpretation, Prentice and Hall, 352 p.

Rose, A. W., 1970, Zonal relations of wallrock alteration and sulfide distribution at porphyry copper deposits: Economic Geology, v. 65, p. 920-936.

Rose, A. W., and Burt, D. M., 1979, Hydrothermal Alteration, *in* Barnes, H. L., ed., Geochemistry of Hydrothermal Ore Deposit, John Wiley and Sons, p. 173-235.

Rusk, B.G., Reed, M.H., Dilles, J.H., Klemm, L.M., and Heinrich, C.A., 2004, Compositions of magmatic hydrothermal fluids determined by LA-ICP-MS of fluid inclusions from the porphyry copper-molybdenum deposit at Butte, MT: Chemical Geology, v. 210, p. 173-199.

Rusk, B.G., Reed, M.H., and Dilles, J.H., 2008, Fluid inclusion evidence for magmatic-hydrothermal fluid evolution in the porphyry copper-molybdenum deposit at Butte, Montana: Economic Geology, v. 103, p. 307-334.

Ryan, J., Morris, J., Bebout, G., and Leeman, B., 1996, Describing chemical fluxes in subduction zones: insights from "depth-profiling" studies of arc and forearc rocks, *in* Bebout, G. E., Scholl, D. W., Kirby, S. H., and Platt, J. P., eds., Subduction Top to Bottom, American Geophysical Union, p. 263-268.

Rye, R. O., 1993, The evolution of magmatic fluids in the epithermal environment - the stable isotope perspective: Economic Geology and the Bulletin of the Society of Economic Geologists, v. 88, p. 733-753.

Samson, I.M., and Wood, S.A., 1997, The relative solubilities of ferberite and scheelite as a function of temperature, pressure, pH and salinity: Applications to granitoid-related tungsten deposits: Mineral Deposits: Research and Exploration, Where Do They Meet?, p. 967-980.

Sauerzapf, U., Lattard, D., Burchard, M., and Engelmann, R., 2008, The titanomagnetite-ilmenite equilibrium: new experimental data and thermo-oxybarometric application to the crystallization of basic to intermediate rocks: Journal of Petrography, v. 49, p. 1161-1185.

Selby, D., Nesbitt, B.E., Muehlenbachs, K., and Prochaska, W., 2000, Hydrothermal alteration and fluid chemistry of the Endako porphyry molybdenum deposit, British Columbia: Economic Geology and the Bulletin of the Society of Economic Geologists, v. 95, p. 183-201.

Schiarizza, P., and Tan, S. H., 2005, Geology and mineral occurences of the Quesnel terrane between the Mesilinka River and Wrede Creek (NTS 94D/8, 9), North-Central British Columbia: B.C. Ministry of Energy, Mines and Petroleum Resources, Paper 2005-1, p. 109-130.

Schroeter, T. G., ed., 1995, Porphyry deposits of the northwestern cordillera of North America, Canadian Instituite of Mining, Metallurgy and Petroleum, Special Volume 46, 888 p.

Seedorff, E., 1988, Cyclic development of hydrothermal mineral assemblages related to multiple intrusions at the Henderson porphyry molybdenum deposit, Colorado: Canadian Institute of Mining and Metallurgy Special Volume, v. 39, p. 367-393.

Seedorff, E., Dilles, J. H., Proffett, J. M., Einaudi, M. T., Zurcher, L., Stavast, W. J., Johnson, D. A., and Barton, M. D., 2005, Porphyry deposits: characteristics and origin of hypogene features Economic Geology, 100th Anniversary Volume, p. 251-298.

Seno, T., and Maruyama, S., 1984, Paleogeographical reconstruction and origin of the Philippine Sea: Tectonophysics, v. 102, p. 53-84.

Sharp, Z. D., 1990, Laser-based microanalytical method for the in situ determination of oxygen isotope ratios of silicates and oxides: Geochimica et Cosmochimica Acta, v. 54, p. 1353-1357.

Shelley, D. M., 1985, Determining paleo-flow directions from groundmass fabrics in the Lyttleton radial dykes, New Zealand: Journal of Volcanology and Geothermal Research, v. 25, p. 69-79.

Sheppard, S. M. F., Nielsen, R. L., and Taylor, H. P., 1971, Hydrogen and oxygen isotope ratios in minerals from porphyry copper deposits: Economic Geology, v. 66, p. 515-542.

Sheppard, S. M. F., 1986, Characterization and Isotopic Variations in Natural Waters, *in* Valley, J. W., Taylor, H. P. J., and O'Neil, J. R., eds., Stable Isotopes in High Temperature Geological Processes, 16. Reviews in Mineralogy, Mineralogical Society of America, p. 165-184.

Sillitoe, R. H., 1985, Ore-related breccias in volcanoplutonic arcs: Economic Geology, v. 80, p. 1467-1514.

Sillitoe, R. H., 2000, Gold-rich porphyry deposits: Descriptive and genetic models and their role in exploration and discovery: Reviews in Economic Geology, v. 13, p. 315-345.

Sillitoe, R.H., 2002, Some metallogenic features of gold and copper deposits related to alkaline rocks and consequences for exploration: Mineralium Deposita, v. 37, p. 4-13.

Sillitoe, R. H., 2007, Geological Interpretation and Potential of the Lorraine Porphyry Copper and Gold and Nearby Prospects, Internal Company Report for Teck Cominco Ltd, Unpub. Report, p. 16.

Sillitoe, R.H., 2010, Porphyry copper systems: Economic Geology, v. 105, p. 3-41.

Sillitoe, R. H., Hall, C., and Grant, J. N., 1975, Porphyry tin deposits in Bolivia: Economic Geology, v. 70, p. 913-927.

Sillitoe, R. H., and Gappe, I. M., Jr., 1984, Philippine porphyry copper deposits: Geologic setting and characteristics, United Nations Economic Social Commission Asia-Pacific, Committee for Coordination of Joint Prospecting for Mineral Resources in Asian Offshore Areas, Technical Publication 14, 89 p.

Simon, G., Kesler, S.E., Essene, E.J., and Chryssoulis, S.L., 2000, Gold in porphyry copper deposits: Experimental determination of the distribution of gold in the Cu-Fe-S system at 400 degrees to 700 degrees C: Economic Geology and the Bulletin of the Society of Economic Geologists, v. 95, p. 259-270.

Sintron, J. M., and Detrick, R. S., 1992, Mid-ocean ridge magma chambers: Journal of Geophysical Research, B, Solid Earth and Planets, v. 97, p. 197-216.

Sketchley, D. A., Rebagliati, C. M., and DeLong, C., 1995, Geology, alteration and zoning patterns of the Mt. Milligan copper-gold deposits; in Porphyry Deposits of the Northwestern Cordillera of North America, *in* Schroeter, T. G., ed., Canadian Institute of Mining, Metallurgy and Petroleum, Special Volume 46, p. 650-665.

Sobolev, A. V., and Slutskii, A. B., 1984, Composition and crystallisation conditions of the initial melt of the Siberian meimechites in relation to the general problem of ultrabasic magmas: Soviet Geology and Geophysics, v. 25, p. 93-104.

Spilsbury, T. W., 1995, The Shaft Creek copper-molybdenum-gold-silver porphyry deposit, northwestern British Columbia, *in* Schroeter, T. G., ed., Porphyry Deposits of the Northwestern Cordillera of North America: Vancouver, Canadian Institute of Mining, Metallurgy and Petroleum, Special Publication 46, p. 239-246.

Stacey, J. S., and Kramers, J. D., 1975, Approximation of terrestrial lead isotope evolution by a 2-stage model: Earth and Planetary Science Letters, v. 26, p. 207-221.

Stanley, C. R., Holbek, P. M., Huyck, H. L. O., Lang, J. R., Preto, V. A. G., Blower, S. J., and Bottaro, J. C., 1995, Geology of the Copper Mountain alkalic porphyry copper-gold deposits, Princeton, British Columbia, *in* Schroeter, T. G., ed., Porphyry Deposits of the Northwestern Cordillera of North America: Vancouver, Canadian Institute of Mining, Metallurgy and Petroleum, Special Volume 46, p. 537-565.

Steifert, W., Kampf, H., and Wasternack, J., 2000, Compositional variation in apatite, phlogopite and other accessory minerals of the ultramafic Delitzsch complex, Germany: implication for cooling history of carbonatites: Lithos, v. 53, p. 81-100.

Stern, C. R., Frey, F. A., Futa, K., Zartman, R. E., Peng, Z. C., and Kyser, T. K., 1990, Trace-element and Sr, Nd, Pb and O isotopic composition of Pliocene and Quaternary alkali basalts of the Patagonian Plateau lavas of southernmost South-America: Contributions to Mineralogy and Petrology, v. 104, p. 294-308.

Stern, R. J., Smoot, N. C., and Rubin, M., 1984, Unzipping of the Volcano Arc, Japan: Tectonophysics, v. 102, p. 153-175.

Stern, R. J., Jackson, M. C., Fryer, P., and Ito, E., 1993, O, Sr, Nd and Pb isotopic composition of the Kasuga Cross-Chain in the Mariana Arc: a new perspective on the K-h relationship: Earth and Planetary Science Letters, v. 119, p. 459-475.

Stormer, J. C., Pierson, M. L., and Tacker, R. C., 1993, Variations in F and Cl X-ray intensity due to anisotropic diffusion in apatite during electron microprobe analysis: American Mineralogist, v. 74, p. 877-888.

Stracke, A., and Hegner, E., 1998, Rifting-related volcanism in an oceanicpost-collisional setting; the Tabar-Lihir-Tanga-Feni (TLTF) island chain, Papua New Guinea: Lithos, v. 45, p. 545-560.

Streck, M. J., and Dilles, J. H., 1998, Sulfur evolution of oxidized arc magmas as recorded in apatite from a porphyry copper batholith: Geology, v. 26, p. 523-526.

Streckeisen, A., 1976, To each plutonic rock its proper name: Earth Science Reviews, v. 12, p. 1-33.

Sun, C. H., and Stern, R. J., 2001, Genesis of Mariana shoshonites: contribution of the subduction component: Journal of Geophysical Research, v. 106, p. 589-608.

Sun, S. S., and McDonough, W. F., 1989, Chemical and isotopic systematics of oceanic basalts: implications for mantle composition and processes, *in* Saunders, A. D., and Norry, M. J., eds., Magmatism in Ocean Basins, v. 42, Geological Society of London Special Publication, p. 313-345.

Sutherland Brown, A., and Cathro, R. J., 1976, A perspective of porphyry deposits, *in* Sutherland Brown, A., ed., Porphyry Deposits of the Canadian Cordillera, Canadian Institute of Mining and Metallurgy, Special Volume 15, p. 7-16.

Suzuoki, T., and Epstein, S., 1976, Hydrogen isotope fractionation between OH-bearing minerals and water: Geochimica et Cosmochimica Acta, v. 40, p. 1229-1240.

Tatsumi, Y., Hamilton, D. L., and Nesbitt, R. W., 1986, Chemical characteristics of fluid phase release from a subducted lithosphere and the origin of arc magmas: evidence from high pressure experiments and natural rocks: Journal of Volcanology and Geothermal Research, v. 29, p. 293-309.

Tatsumi, Y., and Eggins, S., 1995, Subduction zone magmatism: Boston, Blackwell Science, 211 p.

Taylor, R. G., 1979, Oxygen and hydrogen isotope relationships in hydrothermal mineral deposits, *in* Barnes, H. L., ed., Geochemistry of hydrothermal ore deposits, third edition: New York, USA, John Wiley and Sons, p. 236-237.

Thirlwall, M. F., 2000, Inter-laboratory and other errors in Ph isotope analyses investigated using a Pb-207-Pb-204 double spike: Chemical Geology, v. 163, p. 299-322.

Tischendorf, G., Förster, H. J., and Gottesmann, B., 2001, Minor and trace-element composition of trioctahedral micas: a review: Mineralogical Magazine, v. 65, p. 249-276.

Titley, S. R., and Beane, R. E., 1981, Porphyry copper deposits: Part I. Geological settings, petrology, and tectogenesis: Economic Geology 75th Anniversary Volume, p. 214-235.

Titley, S. R., 1982, The style and progress of mineralization and alteration in porphyry copper systems, America Southwest, *in* Titley, S. R., ed., Advances in Geology of the Porphyry Copper Deposits, Southwestern North America: Tucson, Arizona, The University of Arizona Press, p. 37-58.

Tosdal, R., Cooke, D. R., Simpson, K., Bissig, T., Bath, A., Byrne, K., Jackson, M., Jago, C. P., Micko, J., Pass, H., and Chamberlain, C., 2008, MDRU-CODES: Shallow- and Deep-Level Alkalic Mineral Deposits: Developing an Integrated Exploration Model — Porphyry Module, Unpub. Report, 1.1 - 1.21 p.

Turner, S., Hawkesworth, C., Rogers, N., Bartlett, J., Worthington, T., Hergt, J., Pearce, J., and Smith, I., 1997, U-238-Th-230 disequilibria, magma petrogenesis, and flux rates beneath the depleted Tonga-Kermadec island arc: Geochimica et Cosmochimica Acta, v. 61, p. 4855-4884.

Ulrich, T., 1999, Genesis of the Bajo de la Alumbrera Porphyry Cu-Au Deposit, Argentina: Geological, Fluid Geochemical, and Isotopic Implications: Unpub. Ph.D thesis, Swiss Federal Institute of Technology Zurich, 142 p.

Ulrich, T., Gunther, D., and Heinrich, C.A., 1999, Gold concentrations of magmatic brines and the metal budget of porphyry copper deposits: Nature, v. 399, p. 676-679.

Ulrich, T., Gunther, D., and Heinrich, C. A., 2001, The evolution of a porphyry Cu-Au deposit, based on LA-ICP-MS analysis of fluid inclusions: Bajo de la Alumbrera, Argentina: Economic Geology, v. 96, p. 1743-1774.

Urai, J. L., Means, W. D., and Lister, G. S., 1986, Dynamic recrystallisation of minerals, *in* Hobbs, B. E., and Heard, H. C., eds., Mineral and Rock Deformation: Laboratory Studies, 36, American Geophysical Union Geophysical Monographs, p. 161-199.

van de Zedde, D. M. A., and Wortel, M. J. R., 2001, Shallow slab detachment as a transient source of heat at midlithospheric depths: Tectonics, v. 20, p. 868-882.

Vernon, R. H., 1968, Microstructures of high-grade metamorphic rocks at Broken Hill, Australia: Journal of Petrography, v. 9, p. 1-22.

Vernon, R. H., 1976, Metamorphic Processes: London, Murby.

Vernon, R. H., 1983, Restite, xenoliths and microgranitoid enclaves in granites: Journal of the Royal Society of New South Wales, v. 116, p. 77-103.

Vernon, R. H., 1986, K-feldspar megacrysts in granites - phenocrysts, not porphyroblasts: Earth Science Reviews v. 23, p. 1-63.

Vernon, R. H., Etheridge, M. A., and Wall, V. J., 1988, Shape and microstructure of microgranitoid enclaves: indicators of magma mingling and flow: Lithos, v. 22, p. 1-12.

Vernon, R. H., and Johnson, S. E., 2004, Empacement-related microstructures in the margin of a deformed pluton: the San Jose tonalite, Baja California, Mexico: Journal of Structural Geology, v. 26, p. 1867-1884.

Vila, T., and Sillitoe, R. H., 1991, Gold-Rich Porphyry Systems in the Maricunga Belt, Northern Chile: Economic Geology and the Bulletin of the Society of Economic Geologists, v. 86, p. 1238-1260.

Waite, K. A., Keith, J. D., Christiansen, E. H., Whitney, J. A., Hattori, K., Tingey, D. G., and Hook, C. J., 1997, Petrogenesis of the volcanic and intrusive rocks associated with the Bingham Canyon porphyry Cu-Au-Mo deposit, Utah, *in* John, D. A., and Ballantyne, G. H., eds., Geology and Ore Deposits of the Oquirrh and Wasatch Mountains, Utah SEG Guidebook, 29, Society of Economic Geologist, p. 69-90.

Weeks, R. M., Bradburn, R. G., Flintoff, G. R., Harris, G. R., and Malcolm, G., 1995, The Brenda mine: The life of a low-cost porphyry copper-molybdenum producer (1970-1990), southern British Columbia, *in* Schroeter, T. G., ed., Porphyry Deposits of the Northwestern Cordillera of North America: Vancouver, Canadian Institute of Mining, Metallurgy and Petroleum, Special Volume 46, p. 192-200.

Wernicke, B., and Klepacki, D. W., 1988, Escape hypothesis for the Stikine block: Geology, v. 16, p. 461-464.

Wilkinson, J.J., Wilkinson, C.C., Vry, V.H., Rusk, B.G., Seguel, J., Zentilli, M., and Jefferies, T.E., 2008, Ore fluid chemistry in super-giant porphyry copper deposits, Pacrim Congress 2008: Gold Coast, Queensland, Extended Abstracts: Melbourne, Australiasian Institute of Mining and Metallurgy, p. 295-299.

Wilkinson, W. J., Stevenson, R. W., and Garnett, J. A., 1976, Lorraine, *in* Sutherland Brown, A., ed., Porphyry Deposits of the Canadian Cordillera, Special Volume 15, Canadian Institute of Mining and Metallurgy, p. 397-401.

Wilson, A. J., 2003, The geology, genesis and exploration context of the Cadia gold-copper porphyry deposits, New South Wales, Australia: Unpub. Ph.D thesis, University of Tasmania, Hobart, 335 p.

Wilson, A. J., Cooke, D. R., and Harper, B. L., 2003, The Ridgeway gold-copper deposit: A high-grade alkalic porphyry deposit in the Lachlan fold belt, New South Wales, Australia: Economic Geology and the Bulletin of the Society of Economic Geologists, v. 98, p. 1637-1666.

Wilson, A. J., Cooke, D. R., and Richards, T., 2004, Veins, pegmatites and breccias: examples from the alkalic Cadia Quarry Au–Cu porphyry deposit, NSW, Australia., *in* Cooke, D. R., Deyell, C. L., and Pongratz, J., eds., 24 Carat Gold Workshop, University of Tasmania CODES, p. 45-56.

Wilson, A. J., Cooke, D. R., Harper, B. J., and Deyell, C. L., 2007a, Sulfur isotopic zonation in the Cadia district, southeastern Australia: exploration significance and implications for the genesis of alkalic porphyry gold-copper deposits, 2007a, p. 465-487.

Wilson, A. J., Cooke, D. R., Stein, H. J., Fanning, C. M., Holliday, J. R., and Tedder, I. J., 2007b, U-Pb and Re-Os geochronologic evidence for two alkalic porphyry ore-forming events in the Cadia District, New South Wales, Australia: Economic Geology, v. 102, p. 3-26.

Wilson, J. W. J., Kesler, S. E., Cloke, P. L., and Kelly, W. C., 1980, Fluid inclusion geochemistry of the Granisle and Bell porphyry copper deposits, British Columbia: Economic Geology, v. 75, p. 45-61.

Winchester, J. A., and Floyd, P. A., 1977, Geochemical discrimination of different magma series and their differentiation products using immobile elements: Chemical Geology, v. 20, p. 325-343.

Wolfe, R. C., 2001, Geology of the Dipipio region and paragenesis of the Dinkidi Cu-Au porphyry deposit: Unpub. PhD thesis, University of Tasmania, 201 p.

Wood, B. J., 1976, Mixing properties of tschermakitic clinopyroxenes: American Mineralogist, v. 61, p. 599-602.

Wood, B. J., and Blundy, J. D., 1997, A predictive model for rare earth element partitioning between clinopyroxene and anhydrous silicate melt: Contibutions to Mineralogy and Petrology, v. 129, p. 166-181.

Wood, B. J., and Blundy, J. D., 2001, The effect of cation charge on crystal-melt partitioning of trace elements: Earth and Planetary Science Letters, v. 188, p. 59-71.

Woodhead, J., Eggins, S., and Gamble, J., 1993, High-field strength and transitional element systematics in island-arc and back-arc basin basalts - evidence for multiphase melt extraction and depleted mantle wedge: Earth and Planetary Science Letters, v. 114, p. 491-504.

Woodhead, J. D., 1989, Geochemistry of the Mariana arc (western Pacific): Source composition and processes: Chemical Geology, v. 76, p. 1-24.

Woodsworth, G. J., 1976, Plutonic rocks of the McConnell Creek (94D west half) and Aiken Lake (94C east half) map-areas, Geological Survey of Canada Paper 76-1A, p. 69-73.

Woodsworth, G. J., Anderson, R. G., and Armstrong, R. L., 1991, Plutonic Regimes, Chapter 15, *in* Gabrielse, H., and Yorath, C. J., eds., Geology of the Cordillera Orogen in Canada, 4. Geology of Canada, Geological Survey of Canada, p. 491-531.

Yavuz, F., 2001, PYROX: A computer program for the IMA pyroxene classification and calculation scheme: Computers & Geosciences, v. 27, p. 97-107.

Yavuz, F., 2003a, Evaluating micas in petrologic and metallogenic aspect: I-definitions and structure of the computer program MICA(+): Computers & Geosciences, v. 29, p. 1203-1213.

Yavuz, F., 2003b, Evaluating micas in petrologic and metallogenic aspect: Part II-applications using the computer program Mica(+): Computers & Geosciences, v. 29, p. 1215-1228.

Yuanming, P., and Fleet, M., 2002, Composition of the Apatite-Group Minerals: Substitution Mechanisms, *in* Kohn, M. J., Rakovan, J., and Hughes, J. M., eds., Phosphates: Geochemical, Geobiological and Materials Importance, 48. Reviews in Mineralogy and Geochemistry: Washington, DC, Mineralogical Society of America, p. 13-49.

Zanetti, A., Mazzucchelli, M., Rivalenti, G., and Vannucci, R., 1999, The Finero phlogopite-peridotite massif: an example of subduction-related metasomatism: Contributions to Mineralogy and Petrology, v. 134, p. 107-122.

Zhang, G., and Hynes, A., 1992, Structures along Finlay-Ingenika Fault, McConnell Creek area, north-central British Columbia (94C/5; 94D/8, 9): British Columbia Ministry of Energy, Mines and Petroleum Resources, v. Paper 1992-1, p. 147-154.

Zhang, G., and Hynes, A., 1994, Fabrics and kinematic indicators associated with local structures along the Finlay-Ingenika Fault, McConnell Creek area, north-central British Columbia: Canadian Journal of Earth Sciences, v. 31, p. 1687-1699.

Zhao, Z. F., and Zheng, Y. F., 2003, Calculation of oxygen isotope fractionation in magmatic rocks: Chemical Geology, v. 193, p. 59-80.

Zhu, C., and Sverjensky, D. A., 1991, Partitioning of F-Cl-OH between minerals and hydrothermal fluids: Geochimica et Cosmochimica Acta, v. 55, p. 1837-1858.

Zhu, C., and Sverjensky, D. A., 1992, F-Cl-OH partitioning between biotite and apatite: Geochimica et Cosmochimica Acta, v. 56, p. 3435-3467.